FACULTY OF ENGINEERING OF PORTO UNIVERSITY
DEPARTMENT OF MECHANICAL ENGINEERING AND INDUSTRIAL MANAGEMENT

REPAIR OF COMPOSITE AND WOOD STRUCTURES

by

Raul Duarte Salgueiral Gomes Campilho
M.Sc. in Mechanical Engineering

A thesis submitted in conformity with the requirements for the
Doctoral Degree in Mechanical Engineering

Supervisor:
Marcelo F.S.F. de Moura
Faculty of Engineering, Porto University

Co-Supervisors:
José J.L. Morais
Engineering Department, University of Trás-os-Montes e Alto Douro

Joaquim J.M.S. Domingues
Mechanical Engineering Department, Instituto Superior de Engenharia do Porto

OPorto, March 2009

Abstract

Carbon-epoxy composites are being increasingly used in structures requiring high specific strength and stiffness, introducing an issue regarding their handling after damage. Repair of these structures should be evaluated, instead of their disposal, for cost saving and ecological purposes. Adhesively-bonded repairs present several advantages relatively to alternative methods, such as fewer sources of stress concentrations, attractive fatigue characteristics and possibility of joining different materials. Most of the design approaches for these structures are based on Finite Element Modelling coupled with strength of materials or fracture criteria, which have some limitations. Cohesive Zone Models are an appealing alternative to these methods, overcoming their limitations and exploiting their advantages, by the use of strength of materials criteria to model damage initiation and fracture mechanics to deal with propagation. In this work, a mixed mode (I+II+III) trapezoidal Cohesive Zone Model to be included in Finite Element simulations was developed to simulate thin layers of ductile adhesives in bonded assemblies. To reproduce the adhesives behaviour, after the elastic region a constant strength plateau follows, corresponding to the development of plasticity. The cohesive laws for the adhesive used in this work were derived by an inverse method. This also applied to the interlaminar and intralaminar fracture characterization of the composite used as damaged structure or patch. Preliminary validations of this technique were carried out with parametric studies of single-strap repairs and single-lap joints on carbon-epoxy laminates.

The developed numerical methodology is applied to the fracture behaviour prediction and geometric parameters optimization of repairs in thin carbon-epoxy laminates. Single and double-strap, and also scarf repairs, were examined experimentally and numerically under tension, compression and bending loads. Particular emphasis was paid to the fracture mechanisms and failure load. A purely numerical geometric optimization investigation was carried out for single and double-strap repairs on composite structures under the same loads. Some of the geometric alterations regarded in the literature to increase the repairs strength are addressed, such as patch outer and inner chamfering, laminate outer and inner chamfering, adhesive filleting at the patch edges and plug filling the repair hole with adhesive.

No accurate predictive tools are yet available to the designer for adhesively-bonded repairs of wood members with thin plates. To exploit this important field of application of composites, the numerical methodology developed was experimentally validated on repairs of wood structures under static bending. Repair techniques were proposed for three of the most common damage mechanisms under bending, i.e., compression failure, horizontal shear and cross-graining, aiming the full re-establishment of the beams undamaged strength. The possibility of wood failure was introduced in two different propagation planes, in addition to the patch interlaminar and adhesive layer cohesive failures.

The overall results of this dissertation show that, despite introducing several possibilities in the numerical models, these were always accurate in modelling the repairs fracture behaviour. The concurrent quantitative predictions of the repairs elastic stiffness, maximum load and corresponding displacement, as well as other parameters defined by the characteristics of each set of repair technique and loading, certify the suitability of the proposed methodology in simulating the fracture behaviour of bonded assemblies, opening a good perspective for a quicker design and reduction of costs due to extensive experimental characterization.

Résumé

Les composites carbone/époxy stratifiés sont de plus en plus employés en structures exigeant des résistances et des rigidités spécifiques élevées, ce qui entraîne des problèmes de réutilisation après l'endommagement. La réparation de ces structures est préférable à leur remplacement, pour des raisons économiques et écologiques. Les réparations collées présentent plusieurs avantages relativement aux autres méthodes, comme la réduction de concentrations de contraintes, la bonne tenue à la fatigue et la possibilité de lier différents matériaux. La plupart des méthodes de conception sont basées sur la modélisation par Eléments Finis alliée à des critères de la résistance des matériaux ou de la mécanique de la fracture, qui ont quelques limitations. Les Modèles de Dommage Cohésifs sont une alternative à ces méthodes, évitant leurs limitations et exploitant leurs avantages, en employant des critères de la résistance des matériaux pour modéliser l'initiation du dommage et de la mécanique de la fracture pour la propagation. Dans ce travail, un Modèle de Dommage Cohésif trapézoïdal en mode mixte (I+II+III) pour simulations d'Éléments Finis a été développé pour simuler des couches minces d'adhésifs ductiles dans des assemblages collés. Pour reproduire correctement le comportement des adhésifs, un plateau de contrainte apparaît après la région élastique, correspondant à la plasticité. Les lois cohésives pour l'adhésif utilisé ont été déterminées par une méthodologie inverse. Cette méthodologie également a été appliquée à la caractérisation inter laminaire et intra laminaire de rupture du composite utilisé comme structure ou *patch*. Des validations préliminaires de cette technique ont été effectuées avec des études paramétriques de joints et réparations de simple recouvrement sur des composites carbone/époxy stratifiés.

La méthodologie numérique développée a été appliquée pour prévoir la rupture et optimiser la géométrie des réparations en composites carbone/époxy stratifiés. Des réparations de simple et double recouvrement, et également en rampe, ont été examinées expérimentalement et numériquement en tension, compression et flexion. Les mécanismes de rupture et la charge maximum des réparations sont détaillés. Une recherche numérique d'optimisation géométrique a été effectuée pour des réparations de simple et double recouvrement sur les structures composites sous les mêmes cas de sollicitation. Quelques changements géométriques pour augmenter la résistance des réparations ont été considérés: le biseau extérieur et intérieur du *patch*, le biseau extérieur et intérieur du composite, le filet d'adhésif dans l'extrémité extérieure du *patch* et remplissant avec de l'adhésif le trou résultant de l'enlèvement du matériel endommagé.

Aucun outil prédictif précis n'est disponible à l'Ingénieur pour des réparations adhésives des membres en bois. Pour exploiter ce champ d'application des composites, la méthodologie numérique a été validée avec des essais expérimentaux pour des réparations des structures en bois sous flexion. On a proposé des techniques de réparation pour des mécanismes d'endommagement les plus communs en flexion: fracture en compression, cisaillement horizontal et croix granulation, de façon à rétablir la résistance initiale du bois. La possibilité de fracture du bois a été mise dans deux plans de propagation, en plus des fractures inter laminaires du *patch* et cohésives de la couche d'adhésif.

Les résultats de cette dissertation prouvent que, en dépit de l'introduction de plusieurs possibilités aux modèles numériques, les prévisions de ruptures des réparations ont toujours été précises. Les prévisions quantitatives simultanées de la rigidité élastique de réparations, de la charge maximale et du déplacement correspondant, comme d'autres paramètres définis par les caractéristiques de chaque technique de réparation et sollicitation, prouvent que la méthodologie proposée simule correctement le comportement des assemblages collés. De plus elle permet une conception plus rapide, avec la réduction des coûts dus à la caractérisation expérimentale vaste.

Resumo

A utilização dos compósitos de carbono-epóxido tem vindo a aumentar em aplicações que necessitam de materiais com elevada resistência e rigidez específicas, conduzindo ao problema da sua manipulação após sofrerem dano. Deve-se optar pela reparação destas estruturas, em detrimento da sua substituição, tanto por razões económicas como ecológicas. A utilização de reparações adesivas apresenta diversas vantagens relativamente aos métodos alternativos, tais como diminuição das concentrações de tensões, bom comportamento à fadiga e possibilidade de ligar materiais distintos. A maioria dos métodos de dimensionamento são baseados na modelação por Elementos Finitos acoplada a critérios de rotura da resistência dos materiais ou de fractura, que possuem algumas limitações. Os Modelos de Dano Coesivos são uma alternativa atraente, superando as suas limitações e explorando suas vantagens, pela utilização de critérios da resistência dos materiais para modelar a iniciação do dano e da mecânica da fractura para a propagação. Neste trabalho, foi desenvolvido um Modelo de Dano Coesivo trapezoidal em modo misto (I+II+III) para ser incorporado em simulações de Elementos Finitos, permitindo a modelação de camadas finas de adesivos dúcteis. Para reproduzir fielmente o comportamento dos adesivos, após a região elástica segue-se um patamar de tensão constante, correspondendo ao comportamento plástico. As leis coesivas para o adesivo usado neste trabalho foram obtidas por uma metodologia inversa, procedimento também aplicado à caracterização interlaminar e intralaminar da fractura do compósito usado como estrutura ou remendo. Foram realizadas validações preliminares desta técnica com estudos paramétricos de juntas e reparações por sobreposição simples em laminados de carbono-epóxido.

A metodologia numérica desenvolvida é aplicada à previsão do comportamento e à optimização de alguns parâmetros geométricos de reparações em laminados finos de carbono-epóxido. Foram avaliadas experimentalmente e numericamente reparações por sobreposição simples, dupla e por remendo embebido em tracção, compressão e flexão. Foi dada relevância aos mecanismos de rotura e à carga máxima. Um trabalho numérico de optimização da geometria foi também realizado em reparações por sobreposição simples e dupla em estruturas de carbono-epóxido sob as mesmas cargas. Algumas das alterações consideradas na literatura para aumentar a resistência das reparações são testadas, como o chanfro exterior e interior do remendo, o chanfro exterior e interior do laminado, a utilização de filetes de adesivo na extremidade exterior do remendo e o enchimento com adesivo do furo correspondente ao material danificado.

Neste momento, não se encontram disponíveis para o projectista ferramentas de previsão fiáveis para reparações adesivas em vigas de madeira. Para explorar esta aplicação dos materiais compósitos, a metodologia numérica foi validada experimentalmente com estas reparações sob flexão. Foram propostas técnicas de reparação para três dos mecanismos de dano mais comuns sob flexão: rotura por compressão, por corte horizontal e por desalinhamento do grão, com o objectivo da restituição da resistência inicial das vigas. A possibilidade de dano na madeira foi introduzida em dois planos de propagação, para além das roturas interlaminar do remendo e coesiva da camada de adesivo.

Os resultados apresentados nesta dissertação mostram que, apesar da introdução de diversas possibilidades de rotura nos modelos numéricos, estes reproduziram sempre fielmente os modos de rotura. Simultaneamente, as previsões quantitativas da rigidez elástica, carga máxima e respectivo deslocamento, assim como outros parâmetros definidos pelas características de cada técnica de reparação e solicitação, certificam a adequabilidade da metodologia proposta para prever o comportamento à fractura de conjuntos reparados por adesivos, abrindo uma boa perspectiva para um dimensionamento mais expedito e redução dos custos derivados de uma caracterização experimental detalhada.

Acknowledgements

I would like to express my sincere gratitude to the following individuals, for the guidance or technical contribution at some stage in this work, interesting discussions, writing and grammar review, friendship and moral support to the completion of this thesis, without which such a demanding task could not have been accomplished. I equally wish to thank my family for the lack of attention and support during these years. Finally, I show my gratitude to the Portuguese Foundation for Science and Technology for supporting the work here presented, through the individual grant SFRH/BD/30305/2006.

Abel Ferreira
Abílio de Jesus
Albertina Medeiros
Ana Almeida
Ana Barreto
André Roque
Anselmo de Moraes
Anselmo Vieira
António Ferreira
António Marques
António Ribeiro
Armindo Teixeira
Arnaldo Pinto
Avelino Pinheiro
Carla Roque
Carolina Garbe
Cassilda Tavares
Célia Novo
Clara Frias
Cristina di Angelis
Cristóvão Santos
Daniel Gonçalves
Daniel Rocha
Daniel Rodrigues
Dimitra Ramantani
Eduardo Marques
Fernando Neves
Filipe Chaves
Francisco Silva
Hannes Korber
Hélder Damaso
Hugo Faria
Jaqueline Silva
João Batista
João Gonçalves
Joaquim Domingues
Joaquim Fonseca
Joaquim Rocha
Jorge Almeida
Jorge Batista
Jorge Facão
José Chousal
José Esteves
José Gomes
José Morais
José Pereira
José Reina
José Xavier
Liyong Tong
Lucas Silva
Lúcia Dinis
Luís Durão
Luís Ferreira
Luís Magalhães
Manuel Silva
Marcelo Moura
Marco Parente
Mariana Banea
Mário Pinto
Mário Vaz
Miguel Figueiredo
Nuno Dourado
Paulo Castro
Paulo Neves
Paulo Nóvoa
Pedro Camanho
Pedro Martins
Pedro Moreira
Pedro Neves
Ricardo Lima
Rui Fazenda
Rui Martinho
Rui Silva
Sérgio Tavares
Sónia Santos
Sónia Vieira
Susana Oliveira
Tuani da Roza
Valentin Trummer
Victória Fernandez
Vitor Alves

Table of Contents

List of Tables

List of Figures

List of acronyms

2D – Two-Dimensional
3D – Three-Dimensional
3PB – Three-Point Bending
4ENF – Four-Point End Notched Flexure
4PB – Four-Point Bending
ASC – Average Stress Criterion
ASSC – Average Shear Stress Criterion
CBBM – Compliance-Based Beam Method
CBN – Cubic Boron Nitride
CBT – Corrected Beam Theory
CCM – Compliance Calibration Method
CFRP – Carbon-Fibre Reinforced Plastic
CLPT – Classical Laminate Plate Theory
CNC – Computer Numerical Control
CT – Compact-Tension
CZM – Cohesive-Zone Model
DBT – Direct Beam Theory
DCB – Double Cantilever Beam
DL – Double-Lap
DS – Double-Strap
ELS – End-Loaded Split
ENF – End-Notched Flexure
FEM – Finite Element Method
FEUP – Faculdade de Engenharia da Universidade do Porto
FPZ – Fracture Process Zone
FRP – Fibre Reinforced Plastic
GFRP – Glass-Fibre Reinforced Plastic
HOTA – High Order Theory Approach
HSS – High Speed Steel
IEO – Inner Edge of the Overlap
IES – Inner Edge of the Scarf
INEGI – Instituto de Engenharia Mecânica e Gestão Industrial
ISEP – Instituto Superior de Engenharia do Porto
LEFM – Linear-Elastic Fracture Mechanics
LVDT – Linear Variable Differential Transformer
MIM – Moiré Interferometry Method
MNSC – Maximum Normal Stress Criterion
MSC – Maximum Stress Criterion
MSSC – Maximum Shear Strain Criterion
OEO – Outer Edge of the Overlap
OES – Outer Edge of the Scarf
RPM – Revolutions Per Minute
SEN – Single-Edge Notched
SL – Single-lap
SS – Single-Strap
TDCB – Tapered Double Cantilever Beam
UTAD – Universidade de Trás-os-Montes e Alto Douro
VCCT – Virtual Crack Closure Technique

List of symbols

A – Crack surface area

a – Laminate length; Beam length; Crack length

$\boldsymbol{A}$ – Transverse symmetry plane of the repair

a_0 – Initial crack length

A-A – Vertical symmetry line of the specimen

a_B – Repair length in bending

a_{eq} – Equivalent crack length

a_{TC} – Repair length in tension and compression

b – Laminate width; Beam width; Specimen width

$\boldsymbol{B}$ – Longitudinal symmetry plane of the repair

b_C – Cylinders width

$b\Delta a$ – Area of the new surface created by an increment of crack propagation

$\boldsymbol{C}$ – Laminate mid-thickness symmetry plane of the repair

C_0 – Constant of a polynomial fitting equation

C_1 – Constant of a polynomial fitting equation

C_2 – Constant of a polynomial fitting equation

C_3 – Constant of a polynomial fitting equation

$\mathbf{D}$ – Diagonal matrix containing the penalty/stiffness parameters

d – Hole diameter (three-dimensional repair); Gap between the laminates (two-dimensional repair)

$\boldsymbol{D}$ – Loading cylinder

d_1 – Characteristic distance for the patches alignment

d_2 – Characteristic distance for the patches alignment

d_3 – Characteristic distance for the patches alignment

d_C – Cylinders diameter

d_i – Penalty/Stiffness parameter in pure mode i

d_I – Penalty/Stiffness parameter in pure mode I

d_{II} – Penalty/Stiffness parameter in pure mode II

d_{III} – Penalty/Stiffness parameter in pure mode III

$\mathbf{E}$ – Diagonal matrix containing the damage parameters

e – Distance between the supporting cylinders and the laminate edges

$\boldsymbol{E}$ – Supporting cylinder

E – Young's modulus

E_{eq} – Equivalent Young's modulus

E_f – Corrected flexural Young's modulus

e_i – Damage parameter in pure mode i

e_I – Damage parameter in pure mode I

e_{II} – Damage parameter in pure mode II

e_{III} – Damage parameter in pure mode III

E_L – Young's modulus in direction L

E_R – Young's modulus in direction R

E_T – Young's modulus in direction T

E_x – Young's modulus in direction x

E_y – Young's modulus in direction y

E_z – Young's modulus in direction z

G – Shear modulus; Strain energy release rate (in elasticity)

G_c – Critical strain energy release rate or Fracture toughness (in elasticity)

G_i – Strain energy release rate in pure mode i (in elasticity)

G_{ic} – Critical strain energy release rate or Fracture toughness in pure mode i (in elasticity)

G_I – Strain energy release rate in pure mode I (in elasticity)

G_{Ic} – Critical strain energy release rate or Fracture toughness in pure mode I (in elasticity)

G_{II} – Strain energy release rate in pure mode II (in elasticity)

G_{IIc} – Critical strain energy release rate or Fracture toughness in pure mode II (in elasticity)

G_{III} – Strain energy release rate in pure mode III (in elasticity)

G_{IIIc} – Critical strain energy release rate or Fracture toughness in pure mode III (in elasticity)

G_{LR} – Shear modulus in the LR plane

G_{LT} – Shear modulus in the LT plane

G_{RT} – Shear modulus in the *RT* plane

G_{xy} – Shear modulus in the *xy* plane

G_{xz} – Shear modulus in the *xz* plane

G_{yz} – Shear modulus in the *yz* plane

h – Beam height

$\mathbf{I}$ – Identity matrix

J – Strain energy release rate (including plasticity)

J_c – Critical strain energy release rate or Fracture toughness (including plasticity)

J_i – Strain energy release rate in pure mode *i* (including plasticity)

J_{ic} – Critical strain energy release rate or Fracture toughness in pure mode *i* (including plasticity)

J_I – Strain energy release rate in pure mode I (including plasticity)

J_{Ic} – Critical strain energy release rate or Fracture toughness in pure mode I (including plasticity)

$J_{Ic\ avg}$ – Average value of the Critical strain energy release rate or Fracture toughness in pure mode I (including plasticity)

J_{II} – Strain energy release rate in pure mode II (including plasticity)

J_{IIc} – Critical strain energy release rate or Fracture toughness in pure mode II (including plasticity)

$J_{IIc\ avg}$ – Average value of the Critical strain energy release rate or Fracture toughness in pure mode II (including plasticity)

J_{III} – Strain energy release rate in pure mode III (including plasticity)

J_{IIIc} – Critical strain energy release rate or Fracture toughness in pure mode III (including plasticity)

K – Elastic stiffness; Stress intensity factor

K_c – Critical value of the stress intensity factor

L – Half-span length; Longitudinal direction in wood

l_1 – Node l_1 obtained from opening node 1

l_2 – Node l_2 obtained from opening node 1

L_C – Crack length

L_C' – Crack length projection along direction *L*

L_H – Half-span length

L_O – Overlap length

L_P – Patch length

L_{PR} – Distance between the beam and patch edges

LR – Longitudinal-radial propagation mode

L_S – Scarf length

LT – Longitudinal-tangential propagation mode

L_T – Total length

n – Direction *n* of the local coordinate system

P – Load

P_d – Load of patch debonding onset

P_{d0} – Load of patch debonding onset for the standard repair

P_m – Maximum load

P_{m0} – Maximum load of the repair of geometry S3 with initial properties; Maximum load of the repair without geometric changes

P-δ – Load-displacement

R – Radial direction in wood; Ratio between the descending and ascending lengths of the pure mode I trapezoidal law

RL – Radial-longitudinal propagation mode

RT – Radial-tangential propagation mode

S – Distance between the supporting cylinders

S' – Distance between the loading cylinders

t – Direction *t* of the local coordinate system

T – Tangential direction in wood

t_A – Adhesive thickness

t_H – Patch thickness

TL – Tangential-longitudinal propagation mode

t_P – Laminate thickness

TR – Tangential-radial propagation mode

U – Internal strain energy

w – Projection of the adhesive thickness in the direction *x*

W – Work of the external loads

w_P – Patch width

x – Direction *x* of the coordinate system

X_i – Load at the closed node *i* in the direction *x*

y – Direction *y* of the coordinate system

Y – Non-dimensional factor

Y_i – Load at the closed node i in the direction y

z – Direction z of the coordinate system

Γ – Adimensional factor

Δ – Crack length correction for crack tip rotation and deflexion

Δ_1 – Crack length correction to account for shear deformation

ΔE – Energy necessary to close the crack

Δu_l – Difference of displacement between nodes l_1 and l_2 in the direction x

Δv_l – Difference of displacement between nodes l_1 and l_2 in the direction y

α – Scarf angle

α_C – Cross-grain angle

β – Mixed mode ratio

β_i – Mixed mode ratio in pure mode i

β_I – Mixed-mode ratio in pure mode I

β_{II} – Mixed-mode ratio in pure mode II

β_{III} – Mixed-mode ratio in pure mode III

δ – Displacement

$\delta_{1,i}$ – Relative displacement at damage initiation in pure mode i

$\delta_{1,I}$ – Relative displacement at damage initiation in pure mode I

$\delta_{1,II}$ – Relative displacement at damage initiation in pure mode II

$\delta_{1,III}$ – Relative displacement at damage initiation in pure mode III

δ_{1m} – Equivalent mixed mode displacement at damage initiation

$\delta_{1m,i}$ – Equivalent displacement at damage initiation in pure mode i

$\delta_{1m,I}$ – Equivalent displacement at damage initiation in pure mode I

$\delta_{1m,II}$ – Equivalent displacement at damage initiation in pure mode II

$\delta_{1m,III}$ – Equivalent displacement at damage initiation in pure mode III

$\delta_{2,i}$ – Relative displacement at stress softening in pure mode i

$\delta_{2,I}$ – Relative displacement at stress softening in pure mode I

$\delta_{2,I\,avg}$ – Average value of the relative displacement at stress softening in pure mode I

$\delta_{2,II}$ – Relative displacement at stress softening in pure mode II

$\delta_{2,II\,avg}$ – Average value of the relative displacement at stress softening in pure mode II

$\delta_{2,III}$ – Relative displacement at stress softening in pure mode III

δ_{2m} – Equivalent mixed mode displacement at stress softening

$\delta_{2m,i}$ – Equivalent displacement at stress softening in pure mode i

$\delta_{2m,I}$ – Equivalent displacement at stress softening in pure mode I

$\delta_{2m,II}$ – Equivalent displacement at stress softening in pure mode II

$\delta_{2m,III}$ – Equivalent displacement at stress softening in pure mode III

δ_i – Current relative displacement in pure mode i

δ_I – Current relative displacement in pure mode I

δ_{II} – Current relative displacement in pure mode II

δ_{III} – Current relative displacement in pure mode III

δ_m – Maximum load displacement; Equivalent mixed mode displacement

$\delta_{o,i}$ – Relative displacement at damage initiation in pure mode i

$\delta_{o,I}$ – Relative displacement at damage initiation in pure mode I

$\delta_{o,II}$ – Relative displacement at damage initiation in pure mode II

$\delta_{o,III}$ – Relative displacement at damage initiation in pure mode III

δ_{om} – Equivalent mixed mode displacement at damage initiation

$\delta_{om,i}$ – Equivalent displacement at damage initiation in pure mode i

$\delta_{om,I}$ – Equivalent displacement at damage initiation in pure mode I

$\delta_{om,II}$ – Equivalent displacement at damage initiation in pure mode II

$\delta_{om,III}$ – Equivalent displacement at damage initiation in pure mode III

δ_p – Plateau displacement

$\boldsymbol{\delta}_\mathbf{r}$ – Relative displacements vector

$\delta_{u,i}$ – Relative displacement at complete failure in pure mode *i*

$\delta_{u,I}$ – Relative displacement at complete failure in pure mode I

$\delta_{u,I\,avg}$ – Average value of the relative displacement at complete failure in pure mode I

$\delta_{u,II}$ – Relative displacement at complete failure in pure mode I

$\delta_{u,II\,avg}$ – Average value of the relative displacement at complete failure in pure mode II

$\delta_{u,III}$ – Relative displacement at complete failure in pure mode I

δ_{um} – Equivalent mixed mode displacement at complete failure

$\delta_{um,i}$ – Equivalent displacement at complete failure in pure mode *i*

$\delta_{um,I}$ – Equivalent displacement at complete failure in pure mode I

$\delta_{um,II}$ – Equivalent displacement at complete failure in pure mode II

$\delta_{um,III}$ – Equivalent displacement at complete failure in pure mode III

ε – Strain

ν – Poisson's ratio

ν_{LR} – Poisson's ratio in the *LR* plane

ν_{LT} – Poisson's ratio in the *LT* plane

ν_{RT} – Poisson's ratio in the *RT* plane

ν_{xy} – Poisson's ratio in the *xy* plane

ν_{xz} – Poisson's ratio in the *xz* plane

ν_{yz} – Poisson's ratio in the *yz* plane

π – Constant of Pi

σ – Stress

$\boldsymbol{\sigma}$ – Stress vector

σ_i – Current stress in pure mode *i*

σ_I – Current stress in pure mode I

σ_{II} – Current stress in pure mode II

σ_{III} – Current stress in pure mode III

σ_n – Normal stresses in the direction *n*

σ_R – Remote applied stress

σ_u – Local strength

$\sigma_{u,i}$ – Local strength in pure mode *i*

$\sigma_{u,I}$ – Local strength in pure mode I

$\sigma_{u,I\,avg}$ – Average value of the local strength in pure mode I

$\sigma_{u,II}$ – Local strength in pure mode II

$\sigma_{u,II\,avg}$ – Average value of the local strength in pure mode II

$\sigma_{u,III}$ – Local strength in pure mode III

$\sigma_{um,i}$ – Equivalent local strength in pure mode *i*

$\sigma_{um,I}$ – Equivalent local strength in pure mode I

$\sigma_{um,II}$ – Equivalent local strength in pure mode II

$\sigma_{um,III}$ – Equivalent local strength in pure mode III

σ_x – Normal stresses in the direction *x*

$\sigma_{x\,avg}$ – Average value of normal stresses in the direction *x* (σ_x)

σ_y – Normal stresses in the direction *y*

σ-ε – Stress-strain

τ_{avg} – Average shear stress in the middle of the adhesive layer along the bond length (strap repairs) or scarf length (scarf repairs)

τ_{tn} – Shear stresses in the *tn* plane

τ_{xy} – Shear stresses in the *xy* plane

1. INTRODUCTION

High performance composites are being increasingly used in structures requiring high specific strength and stiffness. Automotive, marine, military, aeronautical and aerospace industries are the main fields of application of these materials. The widespread employment of carbon-epoxy materials in these high responsibility and severely loaded applications introduces an issue regarding the handling of these materials after damage. Repair of these structures should be evaluated, instead of their disposal, for cost saving and ecological purposes. Under this perspective, the availability of efficient repair methods is essential to restore the damaged structure to an acceptable level of functionality. The development and validation of accurate predictive tools for the repairs behaviour are also extremely important, allowing the reduction of costs and time associated to extensive experimentation. Fastened repairs present some disadvantages, such as the weight penalty and significant stress concentrations at localized regions of the composite structure, which can cause local overloads and premature damage initiation. Repair techniques with adhesives overcome these limitations. Actually, adhesively-bonded joints or repairs (in this work named as *assemblies*) enclose several advantages relatively to alternative joining methods. They present fewer sources of stress concentrations, behave well under fatigue loads and allow joining different materials. However, their applicability on structural applications is still limited.

Most of the design approaches are based on finite element modelling coupled with strength of materials criteria, which are clearly inappropriate in the presence of singularities. In fact, the singular regions habitually found in bonded assemblies render the strength predictions highly mesh dependent. Fracture mechanics methods can be used as an alternative, with the energetic-based approaches acquiring special relevancy relatively to the employment of stress intensity factors. Energetic analyses provide the fracture toughness measurement using non-local parameters such as the applied load and displacement. Fracture mechanics approaches require the existence of an initial flaw or crack length. Since in many structural applications the locus of damage initiation is not obvious, these techniques show a limited applicability. In summary, strength of materials techniques behave well at predicting the damage initiation locus, while fracture mechanics is clearly more suited for damage propagation. Cohesive Zone Modelling is an appealing alternative to these methods, overcoming their limitations and exploiting their advantages. These methodologies combine features from the strength of materials analyses to model damage initiation with fracture mechanics to deal with propagation. Thus, the consideration of initial defects in the structure is not required and mesh dependency problems are overcome. Nonetheless, Cohesive Zone Models still depend on the accurate measurement of the values of fracture toughness and on the previous knowledge of the probable crack propagation planes. **This thesis initiates with a state-of-the-art review on the different topics investigated, for a broader understanding of the issues discussed, allowing also a clear assessment of the contribution of this work to the current state of affairs**.

In this work, a mixed mode (I+II+III) trapezoidal Cohesive Zone Model to be included in Finite Element simulations was developed to simulate thin layers of ductile adhesives in bonded assemblies. For a faithful

reproduction of the behaviour of these adhesives, after the ascending region of the cohesive law, which simulates the adhesive elasticity, a constant strength plateau follows, corresponding to the development of plasticity in the adhesive layer. Finally, a descending region is introduced instead of an abrupt failure, to avoid numerical convergence difficulties. **The cohesive laws in pure modes I and II for the ductile adhesive used throughout this work were derived by an inverse methodology. This also applied to the interlaminar and intralaminar fracture characterization of the composite used in this work as damaged structure or patch**. For the three-dimensional simulations, the pure mode III cohesive parameters were equalled to the corresponding pure mode II values, as an approximation. The inverse technique can be applied in two steps. The values of fracture toughness are initially extracted from standardized Double Cantilever Beam (pure mode I) or End-Notched Flexure (pure mode II) tests. The fracture toughness is then used as an input parameter in numerical Double Cantilever Beam or End-Notched Flexure models. These models, having the measured dimensions of each tested specimen, include the respective pure mode cohesive law with the fracture toughness previously determined and typical values for the other cohesive parameters. These properties are determined performing a few numerical iterations until a good accuracy between the experimental and numerical load-displacement curves is obtained. In this work, material properties were regarded as independent of viscoelastic effects. Actually, based on literature results, neglecting of these issues does not compromise the accuracy of results for quasi-static loadings. **Experimental validation of the trapezoidal model was carried out initially with a parametric study of single-strap repairs on carbon-epoxy laminates, as a function of the overlap length and patch thickness.** In this first study, a different adhesive to the one characterized by the inverse method was employed. The cohesive properties of this adhesive in each pure mode were approximated to their bulk quantities, despite the known differences between adhesives as thin layers and as a bulk. **Following, the inverse methodology was applied to carbon-epoxy single-lap joints for different values of overlap length**. The cohesive laws derived in this work allowed the simulation of cohesive crack growth in the adhesive, and the fracture loads were compared to the experiments for model validation purposes.

The development and validation of the trapezoidal Cohesive Zone Model preceded a comprehensive experimental and numerical study on the repair of carbon-epoxy structures, using the strap and scarf techniques. The strap repair technique consists on drilling a hole to remove the damaged material, followed by the adhesive-bonding of circular patches on one side (single-strap) or both sides (double-strap) of the structure. These repairs can be regarded as permanent in lightly loaded and relatively thin structures. However, they are not viable for high responsibility structures, since they are always linked to peel and shear peak stress at the bond edges, arising from the differential straining effects between the structure and patches, which hampers their high efficiency. If a full or significant strength recovery is required, or if a flush surface is needed for aerodynamic or stealth reasons, a scarf repair should be used instead. The higher efficiency of this repair method, compared with the easy-execution strap repairs, is caused by the larger bond areas and the reduction of stress concentrations at the bond edges due to the adherend tapering effect. **A Section of this work experimentally validates the developed numerical methodology with a study on the fracture behaviour and geometric parameters optimization of repairs for thin carbon-epoxy laminates**. Single and double-strap, and also scarf repairs, were examined under tension, compression and bending loads. Particular emphasis was paid to the fracture mechanisms, elastic stiffness and failure load. In the numerical models, added to the possibility of fracture in the adhesive layer, interlaminar and intralaminar failures were also equated, to accurately reproduce the test results. The use of geometric changes in adhesively-bonded structural assemblies is widely documented in the literature, as a mean to increase their strength. This is justified by the reduction of peel and shear peak stresses at the damage

initiation regions of the structures or alterations of the failure mechanism emerging from these local modifications. **Owing to this importance, a purely numerical optimization study was performed for single and double-strap repairs on composite structures**. Some of the geometric modifications regarded to increase the repairs strength are addressed, such as patch outer and inner chamfering, laminate outer and inner chamfering, adhesive filleting at the patch edges and plug filling the repair hole with adhesive.

The last Section of this work performs an experimental and numerical evaluation of repair techniques for wood members damaged under static bending. Reinforcement and repairing techniques for large-scale wood structures are extensively documented in the literature, but only a few of these studies involve the adhesive-bonding technique. In recent years, the use of adhesively-bonded carbon-epoxy plates, which are already extensively employed in several high performance applications, is gradually gaining acceptance in the construction industry, especially in the area of structural strengthening and repair. Glass-epoxy composites are also considered economically competitive with the traditional reinforcement materials, such as steel or aluminium, while keeping an acceptable performance. Carbon-epoxy composites are still not used as extensively as glass-epoxy ones, even though recent studies showed that these two compare similarly in terms of stiffness and strength improvement as a function of the reinforcement cost. The few works concerning composite repairs of wood structures are limited to experimental studies that most of the times are not easily applicable in-situ. In addition, no accurate predictive tools are yet available to the designer for adhesively-bonded repairs of wood members, which would save on the time and costs associated to extensive experimentation, otherwise necessary to allow the widespread use of these techniques. **To exploit this important subject, the numerical methodology developed in this thesis was employed to study adhesively-bonded repairs of wood structures under static bending**. Repair techniques were proposed for three of the most common damage mechanisms in members under bending, i.e., compression failure, horizontal shear and cross-graining, aiming the full re-establishment of the beams undamaged strength. The numerical simulations included the possibility of wood failure in two propagation planes, in addition to interlaminar patch failure and cohesive failure of the adhesive layer.

2. STATE-OF-THE-ART REVIEW

This Section addresses the most popular joining and repair techniques using adhesives, focusing with more detail on works with *Carbon-Fibre Reinforced Plastic* (CFRP) laminates. These advanced materials have recently come to the fore owing to a set of interesting characteristics over the conventional engineering materials such as aluminium or steel. In fact, these high performance composites are being increasingly used in structures requiring high specific strength and stiffness such as in the automotive, marine, military, aeronautical and aerospace industries. Unidirectional CFRP composites are also ideal for reinforcement purposes, not changing significantly the structures stiffness, and are corrosion resistant. The disadvantages of these advanced materials lie on their elevated cost, lack of confidence on the use of available design criteria, which hold back designers on using these materials, and absence of yielding prior to failure (Gibson 1994, Campilho 2005, Hosseinzadeh et al. 2005, Botelho et al. 2006). Actually, the lack of plasticity characteristic of these materials does not allow the redistribution of stresses at the loci of stress concentrations, such as fastener holes or regions of fabrication-induced defects, requiring a deep knowledge for a safe design (Zweben 1994, Lee and Soutis 2008). In this review, special attention is paid to the experimental testing and numerical prediction of the mechanical behaviour of adhesively-bonded assemblies, using different bonding techniques (single and double-lap/strap and scarf). The stress distributions at the bonding region of these assemblies and strength prediction methodologies are described in more detail. Another Sub-Section describes the most important geometric changes applied to these assemblies strength improvement purposes. Strengthening and repair techniques of wood structures with composites are also included. In this work, a trapezoidal CZM was developed for the simulation of thin layers of ductile adhesives. Thus, the review initiates with a state-of-the-art description on *Cohesive Zone Models* (CZM's) developed with this purpose. The nomenclature used throughout this work on the different bonding techniques, considering a *Two-Dimensional* (2D) geometry, is clarified in Fig. 1. In the *Single-Lap* (SL), *Double-Lap* (DL) and scarf joints the adherends are bonded directly. In the *Single-Strap* (SS), *Double-Strap* (DS) and scarf repairs, a continuous plate is supposed to have sustained some sort of damage at an intermediate region.

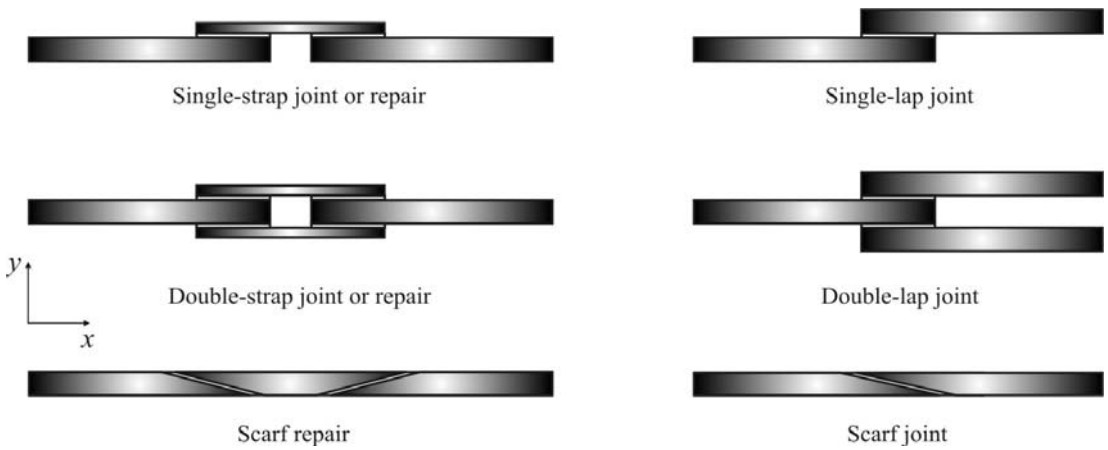

Fig. 1 – Nomenclature on the joining and repair techniques using adhesives (2D geometries).

The repair procedure involves the removal of the damaged material, creating a material discontinuity. The load transfer is assured by the use of patches, adhesively-bonded between the two discontinuity edges. The coordinate system *x*-*y* used in this work is plotted in Fig. 1. In bonded assemblies, the most important components of stress are shear, due to the differential straining of the adherends, and peel, caused by out-of-plane loading or different transverse deformation between the bonded components (Fitton and Broughton 2005). Stress concentrations, especially peel peak stresses, are important to consider when bonding composite materials that exhibit low through-thickness tensile properties (Hart-Smith 1995). In this work, through-thickness normal stresses are generally referred as σ_y stresses, specifying as σ_y peel stresses or σ_y compressive stresses if they are tensile or compressive, respectively. Shear stresses are designated as τ_{xy} stresses. Normal stresses in the laminate or beam length direction are addressed in this work as σ_x stresses. It should be stressed at this point that the 2D strap and scarf repairs of Fig. 1 are often used as an approximation of the corresponding *Three-Dimensional* (3D) repairs presented in Fig. 2 (Richardson et al. 1993, Soutis et al. 1999, Hu and Soutis 2000, Campilho et al. 2005). With this simplification, the cylindrical (strap repairs) or conical (scarf repairs) hole is replaced by a gap between the laminates.

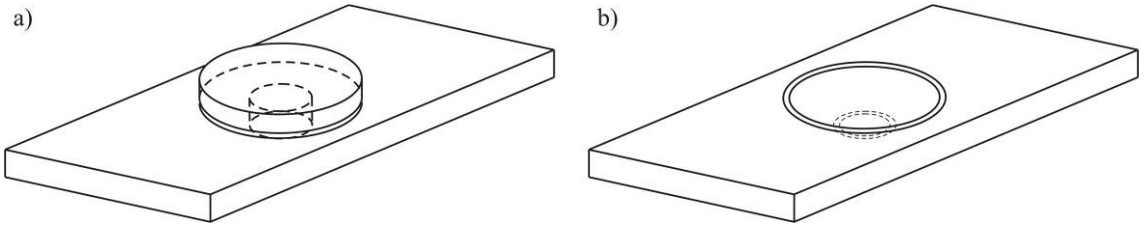

Fig. 2 –SS (a) and scarf (b) repairs (3D geometries).

It is known that the structural integrity of composite structures is usually determined by the strength and durability of their joints (Hart-Smith 1987, Chamis and Murthy 1991, Messler 1993). In fact, although complex polymer composite structures can be molded in single pieces, to simplify the manufacturing processes and to reduce the assembly costs, joining is often used (Hou and Liu 2003). On this issue, adhesive bonds of structures provide several advantages, compared to welding, riveting and bolting methods, such as reduction of stress concentrations, reduced weight penalty and easy manufacturing. However, the limited understanding of the behaviour of bonded assemblies over the life of structures (Karbhari and Shulley 1995, Colombi and Poggi 2006, Yuan and Xu 2008) and the lack of well-established failure criteria (Cole 1999, de Morais et al. 2007) hinder their prompt usage on industry applications. Different approaches were employed in the past to predict the mechanical behaviour of bonded assemblies. In the early stages of bonded structures analyses, beam-bending theoretical studies were popular (Volkersen 1938, Goland and Reissner 1944, Szépe 1966, Hart-Smith 1973a, Pirvics 1974, Thamm 1976, Allman 1977, Ojalvo and Eidinoff 1978, Chan and Sun 1980, Chen and Cheng 1983, Wu et al. 1997, Penado 1998, Tsai et al. 1998). These analytical approaches employed simplifying assumptions in terms of the structures geometry, loading, and boundary conditions, to formulate efficient closed-form elasticity solutions for the local fields in the adhesive region (Lai et al. 1996). The main advantage of analytical modelling is that each bonded structure configuration can be analyzed quickly, although with lot of embedded assumptions (Panigrahi and Pradhan 2007a). One of these consisted on assuming linear elastic adhesives (Erdogan and Ratwani 1971, Grimes 1971, Baker and Hatt 1973, Allman 1977, Johnson 1989), which is not consistent with their real behaviour. These models were able to calculate the strains and stresses, assuming additionally elastic adherends, allowing obtaining as well the distribution of the bending moment in the structure. In the computers age, *Finite Element Method* (FEM) codes to simulate the mechanical behaviour of structures were rapidly implemented,

providing a more accurate insight on this subject. In the FEM, each component of the adhesive joint is treated as a continuum and the geometry can be regarded as either a simplified 2D representation, or a full 3D model of the joint. Large displacements, such as those seen in the SL joints, can also be simulated, as well as thermal behaviour. FEM modelling also allows including in the analysis the materials plasticity, since FEM codes actually incorporate several complex material models. One of the first FEM works on bonded assemblies dates back to the 1970's when Wooley and Carver (1971) conducted a stress analysis on SL joints. The influence of material and geometric parameters on the structures behaviour was amongst the most relevant issues in these works (Adams and Peppiatt 1974, Bigwood and Crocombe 1989, Tsai and Morton 1994, Tsai and Morton 1995a). One of the most important conclusions of these studies regarded the high sensitivity of the assemblies strength to geometric details and loading conditions. **On the strength prediction of bonded assemblies, two different lines of analyses were developed: the strength of materials and fracture mechanics-based methods**.

The **strength of materials approach** is based on the evaluation of allowable stresses (Greenwood et al. 1969, Hart-Smith 1973a, Harris and Adams 1984, Bigwood and Crocombe 1990, Ikegami et al. 1990, Crocombe and Bigwood 1992) or strains (Crocombe and Adams 1982, Harris and Adams 1984, Lee and Lee 1992, Chai 1993, Salmon and Pocius 2004, Hua et al. 2006), by the beam-bending analyses or the FEM. The assemblies strength can be predicted comparing the respective equivalent stresses or strains at the critical regions, obtained by stress or strain-based criteria (e.g. the *Maximum Normal Stress Criterion*, MNSC, or the *Maximum Shear Strain Criterion*, MSSC), with the properties of the structure constituents. This applies to adhesively-bonded assemblies with or without an initial damage, and under a arbitrary loading (Panigrahi and Pradhan 2007a). Stress criteria have a main limitation when applied to the failure prediction of bonded assemblies. In fact, in these structures stress singularities arise at the end of the overlapping regions due to sharp corners (Qian and Akisanya 1999, Dragoni and Mauri 2000, Feih and Shercliff 2005). A stress singularity can be defined as a point where, according to a linear elastic analysis, an infinite value of stress appears. Evidence of this problem can be found in FEM analyses, when stresses at the singularity points increase with the mesh refinement and convergence is not attained. In conclusion, stress-based methods present mesh dependent predictions due to stress singularities (Panigrahi and Pradhan 2007a). To overcome this problem, the point stress or average stress methods can be used instead (Whitney and Nuismer 1974) to predict failure. In the point stress method, stresses are evaluated at a characteristic distance from the singularity point, whereas in the average stress method they are averaged over a length. Failure occurs when these stress values attain the respective material strength. These criteria can be viewed as semi-empirical, since the characteristic distance or length is determined from experimental data. Towse et al. (1997) used the strains at a given distance to the singularity to predict the tensile failure of DL joints. In this case, failure occurs when the strains in the neighbouring regions of the singularity reach the respective limiting value. Although the obtained results agreed with the experimental ones, it should be emphasized that the characteristic distance was determined experimentally, which limits its use in other types of joints. John et al. (1991) studied a DL joint with unidirectional composite adherends, considering that failure occurs when shear stresses attain a critical value at a normalized distance from the singularity point. However, this assumption implies that the critical distance varies as a function of the overlap length, which is not physically tolerable. The *Average Stress Criterion* (ASC) was used by Zhao (1991) to predict failure in bonded joints. The critical dimension used to evaluate the average of the maximum principal stress was considered equal to the adhesive thickness. However, Charalambides et al. (1997) demonstrated that, for DL joints, the point of maximum stress occurs out of the characteristic region. In summary, it can be affirmed that the point and the average stress criteria can provide accurate results but they depend markedly on the previous

determination of the characteristic distance, which is usually performed by experimental tests. Moreover, this distance cannot be promptly applied to joints with different materials and geometry. In fact, the lack of a physical meaning for this characteristic distance makes impossible the establishment of generic predictive tools of failure that can be straightforwardly applied to different types of loading, materials involved and assembly geometries.

The **fracture mechanics methods**, using *Linear-Elastic Fracture Mechanics* (LEFM), have become an accepted instrument to predict the strength of bonded assemblies if the adherends behave elastically up to failure (Anderson et al. 1988, Chai 1988, Fernlund et al. 1994, Papini et al. 1994, Tong 1996). However, for many adhesive/adherend combinations, plasticity in the adherends occurs prior to failure in the adhesive layer (Kim and Kim 1988, Lai and Dillard 1997, Kafkalidis and Thouless 2002), rendering the LEFM inappropriate to predict the assemblies strength. Using this approach, unlike what happens in the strength of materials-based approaches, an inherent defect in the material must be considered, supposedly induced during the fabrication process or in-service operation. In this case, the objective is to know if the defect can induce catastrophic failure or if, during the predicted structure life, it can propagate stably maintaining its dimensions inferior to the critical size. Since in many situations adhesively-bonded assemblies fail by progressive crack growth, with the maximum load exceeding the load of crack initiation (Malyshev and Salganik 1965, Mostovoy et al. 1971, Donaldson and Roy 1997, Roy et al. 1997, Bogdanovich and Yushanov 1999a, Campilho et al. 2007a), an ultimate failure criterion for these situations cannot avoid using a fracture mechanics-based analysis. Several authors applied these methodologies to the strength prediction of bonded assemblies. The majority of the proposed works are based on the concepts of strain energy release rate (G). It is usually assumed that damage propagation occurs when G at the crack front is equal to the critical strain energy release rate or fracture toughness (G_c), which is a material property. Kinloch (1987) refers that the energetic approach is advantageous relatively to the stress intensity factors method, since G has an important physical significance related to the energy absorption and, additionally, the stress intensity factors are not easily determinable, namely when the crack grows at or near to an interface. Ripling et al. (1963) also recommended the energetic approach instead of stress intensity factors, recognizing the non-homogeneity of bonded assemblies. However, it should be referred that the energetic approach has difficulties related to mixed mode crack propagation. In fact, in homogeneous and isotropic materials cracks tend to propagate under mode I (opening), perpendicularly to the direction of maximum principal stress, independently of the original crack orientation. However, in a bonded assembly, crack growth is restricted by the adherends, which typically leads to a mixed mode crack propagation (opening and shear). Under these circumstances, it is fundamental to use adequate energetic criteria for the prediction of crack propagation.

The limitations of the previous approaches can be overcome using **cohesive-zone modelling**, combining elements of strength and fracture approaches to derive the fracture loads (Tvergaard and Hutchinson 1992, Tvergaard and Hutchinson 1996, Wei and Hutchinson 1997, Wei and Hutchinson 1999, Yang et al. 1999, Yang et al. 2000, Cavalli and Thouless 2001, Yang and Thouless 2001, Campilho et al. 2005, Campilho et al. 2007a). The use of CZM's in fracture problems has become frequent in recent years. One of the most important advantages of CZM's is related to their ability to simulate onset and non-self-similar growth of damage. No initial crack is needed and damage propagation takes place without user intervention. They do not depend on an initial flaw, unlike conventional fracture mechanics approaches. Usually, CZM's are based on spring (Cui and Wisnom 1993, Lammerant and Verpoest 1996) or cohesive elements (Mi et al. 1998, Petrossian and Wisnom 1998, de Moura et al. 2000, Feraren and Jensen 2004), connecting plane or 3D solid elements of structures. Those elements are placed at the planes where damage is prone to occur, which, in several

applications, can be difficult to identify *a priori*. However, an important characteristic of bonded assemblies is that damage propagation is restricted to well defined planes, i.e., at or near the interfaces between the adhesive and the adherends, or inside the adhesive, which allows overcoming this limitation. CZM's are based on a softening relationship between stresses and relative displacements between the crack faces, thus simulating a gradual degradation of material properties. The shape of the softening laws can be adjusted to conform to the behaviour of the material or interface they are simulating. Thus, they can be adapted to simulate ductile adhesive layers, which can be modelled with trapezoidal laws (Campilho et al. 2008a, Campilho et al. 2009a). The areas under the traction-separation laws in each mode are equalled to the respective value of G_c of the adhesive layer or interface. Under pure mode, damage propagation occurs in a given integration point when the stresses are released in the respective traction-separation law. Under mixed mode, energetic criterions are often used to combine pure modes I and II (2D analyses) or I, II and III (3D analyses), thus simulating the typical mixed mode behaviour inherent to bonded assemblies. The complete P-δ curve and respective failure mode can be obtained with this methodology.

2.1. Cohesive zone models to simulate ductile adhesive layers

Several researchers studied damage onset and growth on adhesively-bonded structures. The majority of the works on this subject use triangular softening laws with a penalty function for the initial stiffness of the cohesive elements (Campilho et al. 2005, Liljedahl et al. 2006, Turon et al. 2007). With this methodology, the adhesive layer is simulated by solid finite elements including the adhesive plasticity, whilst the cohesive elements only simulate damage growth. The cohesive laws usually present an extremely high elastic stiffness, not influencing the structures stiffness. The cohesive elements can also be placed at different planes in the adhesive thickness, capturing the respective stress gradients. Recently, trapezoidal softening laws have been used to simulate the behaviour of ductile adhesive layers, replacing the solid elements habitually used to simulate their behaviour (Kafkalidis and Thouless 2002, Campilho et al. 2008a, Campilho et al. 2009a). The initial stiffness of the cohesive laws in each pure mode, unlike for the triangular laws, represents the adhesive layer stiffness in opening or shear. A plateau region follows, simulating the ductility of the adhesive. The decaying portion of the cohesive law is introduced for computational ease.

Yang et al. (1999) used a CZM to simulate a pure mode I fracture in adhesively-bonded joints, using the *Double Cantilever Beam* (DCB) specimen under a constant bending moment and the *T*-peel test. A trapezoidal softening law was employed to simulate the adhesive layer behaviour (Fig. 3). This law can be characterized by Γ_0, the work of separation per unit area of crack advance (equal to the area under the traction-separation curve), the peak stress supported by the bonding tractions, σ_c, and the two shape parameters, δ_1/δ_c and δ_2/δ_c.

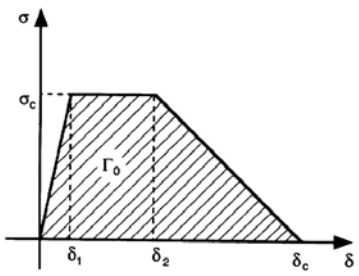

Fig. 3 – Trapezoidal traction-separation law in pure mode I used by Yang et al. (1999).

It was concluded that Γ_0 and σ_c are the dominant parameters in the numerical analyses, while the two shape parameters only present a minor influence on the results. These shape parameters were arbitrarily fixed at δ_1/δ_c=0.15 and δ_2/δ_c=0.5. Γ_0 and σ_c were determined using an inverse method, fitting the experimental and the numerical data of the DCB specimens. It was concluded that the cohesive law obtained could be used to predict the mechanical behaviour under pure mode I of different test geometries and loads.

The same authors considered an identical traction-separation law for elastic-plastic mode II crack growth modelling of a 0.4 mm thickness layer of a ductile adhesive (Yang et al. 2001). The objective of the work was to simulate the role played by the adhesive layer during the deformation and fracture of the joints. The *End-notched flexure* (ENF) test was considered in the analysis. To reduce friction effects between the cracked surfaces, a glass fibre with a diameter of 0.4 mm was inserted as a spacer between the adherends at the crack tip. In the numerical models, contact elements were used to simulate sliding between the supporting cylinders and the adherends, and between the glass fibre and the adherends. The fracture parameters were determined comparing the experimental and numerical data for one particular set of dimensions. Those parameters were then applied to ENF specimens with different dimensions, and the results were found to be in agreement with the tests. The interfacial toughness (Γ_{II0}) and cohesive strength (τ_c) in pure mode II were the main parameters in the traction-separation law (Fig. 4 a). δ_{t1}/δ_{tc} and δ_{t2}/δ_{tc} represent the two shape parameters.

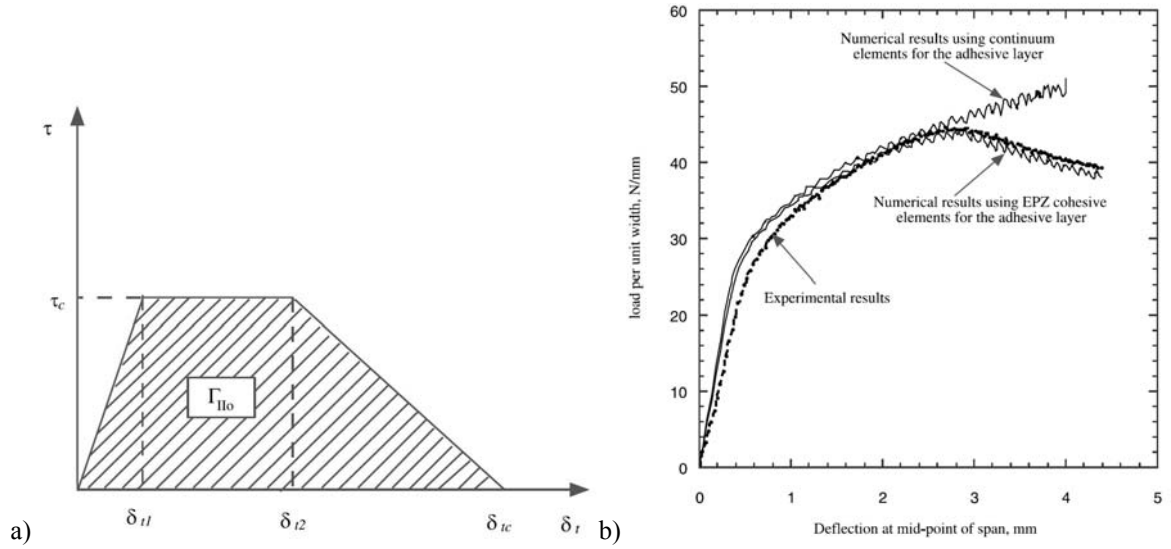

Fig. 4 – Traction-separation law in pure mode II (a) and load as a function of the mid-span deflection (b) (Yang et al. 2001).

Γ_{II0} and τ_c were predicted comparing the experimental and numerical data, while the two shape parameters, δ_{t1}/δ_{tc} and δ_{t2}/δ_{tc}, were arbitrarily equalled to 0.15 and 0.5, respectively, since it was observed numerically that they do not present a significant influence on the fracture process. τ_c was determined considering that in the ENF tests performed, the local strains at the crack tip were approximately 40%. Using the τ-γ experimental curve of the adhesive obtained by torsion tests of adhesively-bonded butt joints, the value of τ_c=35 MPa was obtained for a 40% strain and used in the subsequent analyses. The value of Γ_{II0} was determined by an inverse method, fitting the experimental and numerical P-δ curves for the same set of dimensions (Fig. 4 b). Results from a FEM calculation using only the continuum properties of the adhesive layer with no failure criterion were superimposed in Fig. 4 (b). It was found that such calculation captures the deformation behaviour of the specimen accurately until crack growth initiation, rendering the results invalid for crack

propagation. The obtained values of Γ_{II0} and τ_c were used to simulate fracture in specimens with different adherend thicknesses. An excellent correlation between the experimental and numerical analyses was found. Therefore, the proposed traction-separation law was considered appropriate for the particular thickness of adhesive and strain rate. The authors emphasized on the large difference of the cohesive-zone parameters for mode I and mode II fractures, justifying the use of mode dependent traction-separation relations to analyze the mixed mode fracture of bonded assemblies. This specific issue was also studied by the same authors (Yang and Thouless 2001).

Yang and Thouless (2001) simulated the mixed mode fracture of plastically deforming adhesive joints using a mode-dependent CZM to simulate the adhesive layer. Mode I and II fracture parameters obtained from previous works were combined with a mixed mode propagation criterion to provide quantitative predictions of the deformation and fracture load of bonded assemblies under mixed mode. The numerical calculations predicted accurately the failure loads for two geometries that undergo large plastic deformation in the adhesive layer prior to failure: asymmetric *T*-peel specimens and SL joints. Details of the deformed shapes, loads, displacements and crack propagation were well captured by the simulations. Modelling with mode-independent mixed mode CZM's was employed in the past to investigate fracture of bonded structures (Tvergaard and Hutchinson 1993, Tvergaard and Hutchinson 1996). This model involved a three-parameter traction-separation law with equal cohesive parameters in pure modes I and II. However, former results by Yang et al. (1999, 2001) showed a significant difference between the two modes, proving that a mode-independent model is not always appropriate. Therefore, the authors implemented an alternative mode-dependent CZM (Fig. 5). Mode I and II cohesive laws, previously developed for this adhesive in the works of Yang et al. (1999) and Yang et al. (2001), respectively, were used without modification with an energetic propagation criterion.

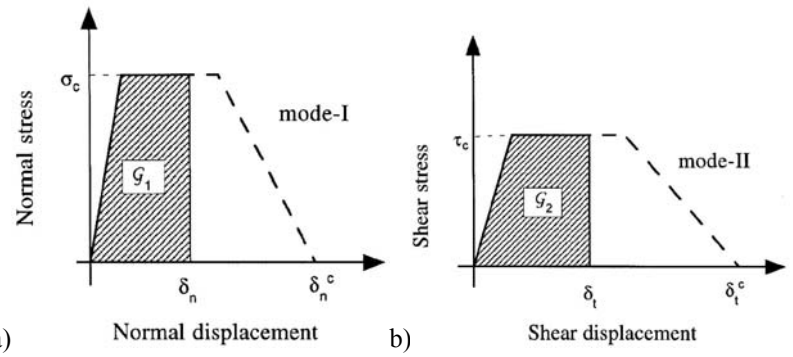

Fig. 5 – Pure mode I (a) and II (b) traction-separation laws (Yang and Thouless 2001, Kafkalidis and Thouless 2002).

In the proposed model, the total traction-separation work absorbed during fracture was divided into opening (mode I) and shear (mode II) components, G_I and G_{II} respectively. These two components can be calculated by integration of the respective traction-separation curve

$$G_I = \int_0^{\delta_n} \sigma(\delta_n) d\delta_n \qquad G_{II} = \int_0^{\delta_t} \tau(\delta_t) d\delta_t . \tag{1}$$

An energetic propagation criterion was defined to establish the critical values of G, G_I* and G_{II}*, at which separation of the CZM elements occurred (areas under the traction-separation laws integrated up to the current displacements; Fig. 5). The propagation criterion can be written as (Hutchinson and Suo 1992)

$$\frac{G_I^*}{\Gamma_{I0}} + \frac{G_{II}^*}{\Gamma_{II0}} = 1 , \tag{2}$$

in which Γ_{I0} and Γ_{II0}, representing the fracture toughness in each pure mode, are the total areas under the complete traction-separation laws. The numerical procedure included the following steps: the opening and shear displacements of the CZM were determined numerically using the FEM and G_I and G_{II} extracted from equation (1) at each increment of the analysis. When the propagation criterion (2) was satisfied at a determined integration point, the element opened, releasing its stresses and loading the adjacent point. The damage process initiated, leading to a gradual crack growth. Since experimentally both geometries evaluated undergo adhesive failures, pure mode II parameters from the work of Yang et al. (2001) were used, since in this work adhesive failures also occurred in the ENF specimens tested. However, the pure mode I parameters from the work of Yang et al. (1999) were not considered to be reliable, as they were obtained from cohesive failures. Consequently, the pure mode I parameters were determined with the wedge test on adhesively-bonded DCB specimens. Interfacial crack growth was induced placing a Teflon® strip prior to specimen curing. A slight asymmetry was then enough to keep the crack growing along the interface for the entire test. Values of 60 MPa and 1 kJ/m^2 for σ_c and Γ_{I0} were obtained, respectively, in contrast to the higher values of 100 MPa and 1.4 kJ/m^2 estimated in the work of Yang et al. (1999) for a cohesive failure. For the *T*-peel specimens, the numerical results showed a good agreement with the experiments, in terms of σ-δ curve, strains and rotations, extent of fracture and asymmetry of bending. For the SL joints, the numerical simulations predicted accurately the load-deformation behaviour of the joints, capturing the influence of the adherend thickness on the fracture loads and strains.

Kafkalidis and Thouless (2002) analysed aluminium SL joints under a tensile load using a trapezoidal CZM to simulate the adhesive layer, including plasticity. Plastic deformation of the adherends was also included in the simulations. Using cohesive parameters determined for a particular combination of materials, the numerical predictions showed an excellent agreement with the experiments. The traction-separation laws (Fig. 5), propagation criterion and analysis procedure were similar to the work of Yang and Thouless (2001). This numerical approach was validated by the comparison of the simulations with the test results, for several values of overlap length and adherend thickness.

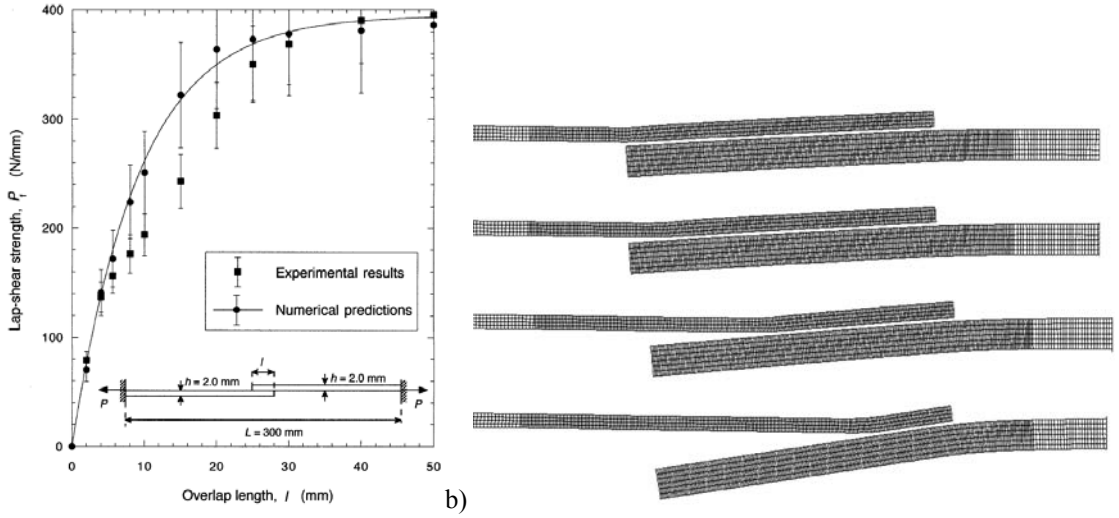

Fig. 6 – SL joint strength as a function of the overlap length for symmetric specimens (a) and numerical deformation sequence and crack growth in asymmetric SL joints (b) (Kafkalidis and Thouless 2002).

For both studies, an excellent correlation was obtained. The numerical models predicted accurately the failure loads, displacements and deformations of the joints. Fig. 6 (a) shows a comparison between the measured and numerically predicted peak loads for a series of symmetric SL joints with 2.0 mm thick aluminium adherends bonded with a 250 μm

thickness layer of the adhesive Ciba XD4600. The slight discrepancies on the predicted strengths that can be seen in Fig. 6 (a) were justified by the sensitivity of the joint behaviour to the boundary conditions. In fact, the experimental configuration results in a slight misalignment of the grips, which is not accounted for in the simulations. Fig. 6 (b) shows the numerical predictions for the sequence of deformation and crack growth in an asymmetric joint with a thickness ratio of two. This deformed configuration reflected accurately the experimental behaviour.

Li et al. (2005a) analysed the mode I fracture process of *Compact-Tension* (CT) and *Single-Edge Notched* (SEN) *Glass-Fibre Reinforced Plastic* (GFRP) specimens with randomly oriented fibres using a CZM. In this work, the cohesive law in pure mode I it simulating crack growth within the composite. Even though the CZM was not used to simulate an adhesive layer, it was included in this review to follow the authors investigation sequence, which afterwards used the laws developed in this work to simulate an adhesive layer/composite interface in pure mode I. A two-parameter model (Fig. 7 a) with a characteristic toughness (Γ) and strength (σ_b) was defined by an inverse data fitting procedure on CT specimens. The value of Γ was determined by fitting the decreasing portions of the experimental and numerical P-δ curves, corresponding to the crack growth region, because these regions are very sensitive indicators of Γ and relatively insensitive to σ_b (Γ=40±4 kJ/m^2). σ_b was then established by fitting the initial parts of the P-δ curves (σ_b=79±8 MPa). The obtained law was considered appropriate to predict the mechanical behaviour of specimens including an initial crack with non-negligible dimensions, since in these conditions the fracture process is ruled by the fibre-bridging strength. However, it was concluded that when the characteristic dimensions of the composite structure (e.g., the initial crack length or ligament length) are very small, such as in the SEN specimen, fracture onset occurs due to matrix cracking. Consequently, two separate processes occur: matrix cracking followed by fibre pull-out, with the toughness contribution emerging mainly from fibre pull-out. Thus, to model the SEN specimen, a three-parameter law was developed (Fig. 7 b). The peak strength corresponds to the matrix cohesive strength, while the following inflexion point simulates the onset of fibre bridging. The value of Γ was estimated following a similar procedure to the triangular law.

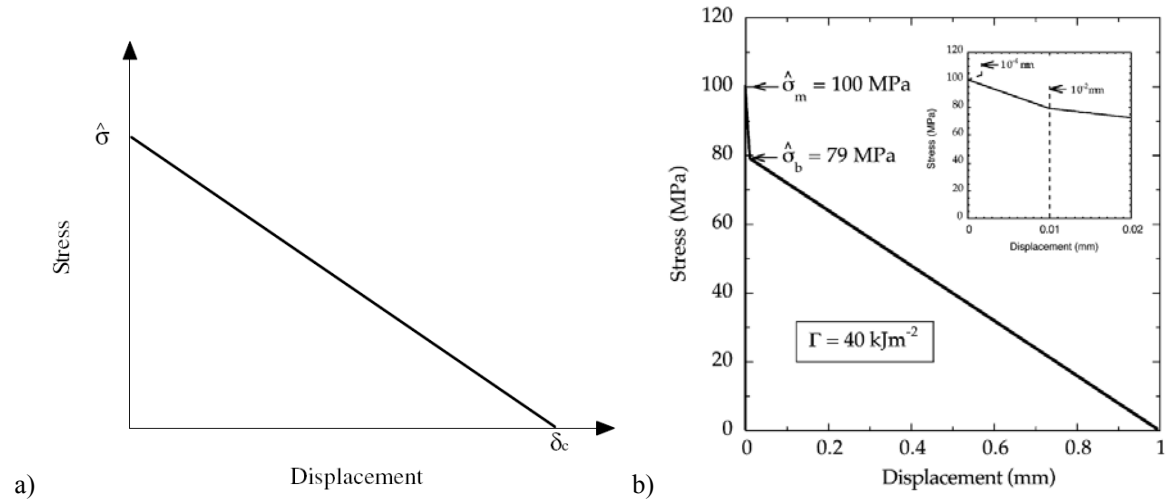

Fig. 7 – Two (a) and three-parameter (b) cohesive laws (Li et al. 2005a, Li et al. 2005b).

While the fibre pull-out strength, obtained from the CT specimens, was set at σ_b=79 MPa, the matrix-cracking strength (σ_m) was equalled to 100 MPa, the average strength in uniaxial tensile tests to the composite plate. The displacements corresponding to σ_b and σ_m were defined to model the elastic behaviour of the composite, followed by a relatively sudden drop in strength that would not cause numerical difficulties. This CZM successfully simulated the mechanical

behaviour of the SEN experiments. When this three-parameter CZM was employed to simulate the behaviour of the CT specimen, the results were similar to the ones based on the two-parameter CZM. The authors concluded that the three-parameter CZM was required when analyzing geometries with very small crack or ligament lengths.

Li et al. (2005b) considered two and three-parameter CZM's identical to Fig. 7, to numerically simulate the pure mode I fracture of adhesive layer/adherend interfaces in GFRP bonded joints, in which an interfacial failure was always observed in the experiments. The CZM elements were used to simulate the adhesive layer, considering interfacial properties. The mode I cohesive parameters of a bonded interface and their physical significance were investigated and the predictive capabilities of the model were assessed by predicting the failure mechanism of bonded joints. The cohesive parameters of the adhesive layer/adherend interface for the 2D triangular model (Fig. 7 a) were obtained in a previous work with DCB tests with interfacial crack propagation (Li et al. 2005a). The characteristic strength obtained with this procedure was associated to fibre bridging, observed during crack propagation in the DCB experiments. A three-parameter traction-separation law was used to capture the effect of initial interfacial cracking, followed by fibre pull-out (Fig. 7 b). Thus, a second strength parameter associated with the intrinsic cohesive strength of the interface was included in the CZM, which is distinct from the characteristic strength of the interface. The values of Γ and σ_b of the adhesive layer/adherend interface were retained from the two-parameter law. The value of σ_m was then determined by interfacial tensile specimens, matching the specimen numerical predictions based on this cohesive law to the experimental results. The numerical simulations including the three-parameter CZM fitted the experimental data of the interfacial tensile and DCB specimens (analogous results compared to the two-parameter law). However, it was emphasized that the two-parameter CZM may not accurately predict the strengths of bonded structures if the characteristic dimensions (such as flaw or ligament lengths) are considerably small.

In the investigation of Li et al. (2006a), a CZM approach was employed to simulate the mixed mode fracture of adhesively-bonded SL joints with randomly-oriented fibre GFRP adherends, assuming an interfacial failure at the adhesive layer/adherend interface. In the numerical simulations, experimentally determined softening laws with interfacial properties simulated the adhesive layer. The three-parameter mode I traction–separation law developed in the previous work of Li et al. (2005b) was used (Fig. 8a).

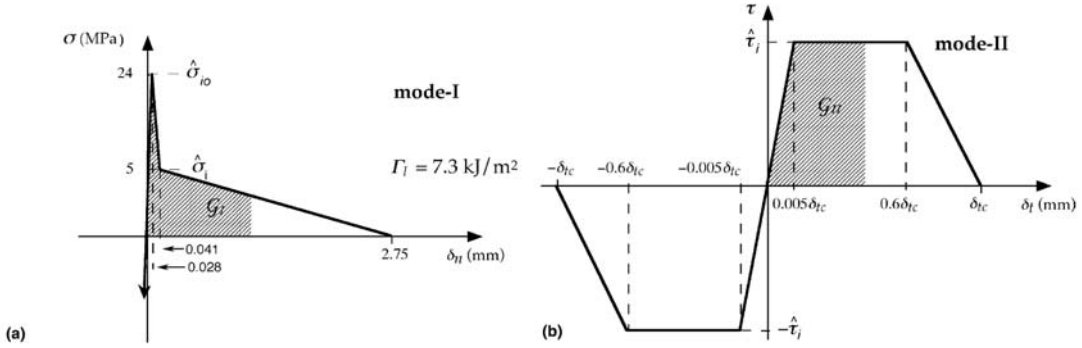

Fig. 8 - Traction–separation laws for pure mode I (a) and II (b) (Li et al. 2006a).

This law that was intended to simulate interfacial cracking followed by fibre pull-out (experimentally observed for mode I fracture), and the three important parameters that describe the law are the cohesive strength of the interface (σ_{i0}), the characteristic strength of the interface (σ_i) and the fracture toughness (Γ_i). The cohesive law in pure mode II was

determined with interfacial shear specimens and sandwich ENF specimens. The sandwich ENF specimens consisted on the typical ENF geometry, using the GFRP adherends, bonded on both faces to aluminium plates. This procedure was justified by the difficulty to keep stable interfacial crack propagation, as the composite arms failed after reduced crack growth. With this modification, the premature composite breaking was suppressed, equally to the effect of the GFRP modulus variability, since the sandwich equivalent stiffness is ruled by the stiffness of the aluminium plates. Under pure mode II, preliminary tests indicated that few fibres were pulled out during mode II fracture. Consequently, a two-parameter trapezoidal law (Yang and Thouless 2001) was chosen to simulate elastic/plastic behaviour of the adhesive layer/adherend interface in shear (Fig. 8b). The initial slope of the traction–separation law was chosen to simulate the shear stiffness of the adhesive layer, and the unloading slope was selected for computational ease, since experience showed that the precise details of the descending part of the curve does not significantly influence the results. The mode II parameters were obtained by comparison of the numerical P-δ curves with the experimental ones. The value of Γ_{II} was calculated matching the numerical predictions and the experimental results in the final ascending part of the curves (region ruled by Γ_{II}). The interfacial shear strength (τ_i) was after determined adjusting the maximum stress in the traction–separation law, until the complete P-δ curve was properly adjusted to the experimental data. The interfacial shear specimens also allowed obtaining the interfacial shear strength, assuming constant shear stress along the interface. An excellent correlation was found with the value of τ_i obtained by the fitting procedure. The propagation criterion of the work of Yang and Thouless (2001) was used. The softening laws were tested using sandwich SL joints, considering a similar arrangement to the sandwich ENF specimens. The numerical simulations showed stable crack propagation for approximately 8 mm before instantaneous failure, with crack propagation being accompanied by visible plastic deformation of the aluminium. The experimental results showed that, in all cases, the fracture of the sandwich specimens was purely interfacial, as assumed for the numerical simulations. The specimens showed stable crack growth for approximately 13 mm before catastrophic failure occurred. Experimental and numerical curves revealed an excellent agreement, including the strengths and failure mechanisms.

2.2. Adhesively-bonded assemblies

2.2.1. Numerical analysis

The numerical studies on adhesively-bonded assemblies use the FEM, either with 2D (plane-stress or plane-strain) or 3D analyses (Charalambides et al. 1998a, Rastogi et al. 1998, Soutis et al. 1999, Hu and Soutis 2000, Seo and Lee 2002, Achour et al. 2003, Campilho et al. 2005, Fernlund 2007). The majority of the 2D studies use plane-strain finite elements, because they capture more accurately the stress fields within the structures. A common bonded repair technique consists on drilling a hole in the damaged laminate to remove the damaged material, followed by adhesively-bonding one or two circular patches. These geometries are modelled most accurately with 3D FEM models (Oterkus et al. 2005, Liu and Wang 2007, Gong et al. 2007, Zemlyanova 2007, Campilho et al. 2008b). However, the SS and DS repairs in Fig. 1 can be considered as an approximation (Richardson et al. 1993, Hu and Soutis 2000, Campilho et al. 2005). This simplified geometry, predicting more or less accurately the stress fields of the 3D repair, is acceptable only for the optimization of geometric parameters influencing the repairs strength. However, it is widely regarded to underestimate the repair strength (Hu and Soutis 2000), since with this approach failure occurs when the adherend and patch (or patches) separate, either by fracture of the adhesive layer or within the structure or patch. As a result, the load-

supporting capability of the damaged structure after patch debonding is not taken into account on the repair strength prediction. Moreover, the 2D simplified geometry does not capture the typical 3D stress concentration effects found near the hole (Hu and Soutis 2000, Gonçalves et al. 2002).

2.2.1.1. Single and double-lap/strap assemblies

Single and double-lap/strap assemblies are the most common nowadays, due to their simplicity (Her 1999, Yeh and Tandjung 2005). However, a full strength recovery after repair is not attained, partly due to the significant shear stress concentrations at the overlap edges characteristic of these assemblies (Sheppard et al. 1998, Dvorak et al. 2001, Mahdi et al. 2003a, Oterkus et al. 2006, Quaresimin and Ricotta 2006a, da Silva and Adams 2007a) induced by the differential deformation of the adherends along the overlap (Volkersen 1938, Adams et al. 1997, Adams and Comyn 2000, Mahdi et al. 2003a). The considerable bending of the SL and SS geometries leads to peel stresses in the adhesive layer, increasing the mixed mode stress fields in the adhesive layer, reducing the strength of the assemblies (Mahdi et al. 2003a, Campilho et al. 2005, Oterkus et al. 2006, Pinto et al. 2008). Davis and Bond (1999) addressed the basic principles for adhesive bonds. Particular attention was paid to the SS repair technique, whose geometry and τ_{xy} stress distributions in the adhesive layer are presented in Fig. 9. The shear stress profile of Fig. 9 (b) applies to both tensile and compressive loads, with shear stresses peaking at the overlap edges. As a result, plasticity develops at this region, which then grows to the adhesive layer central region as the applied load further increases.

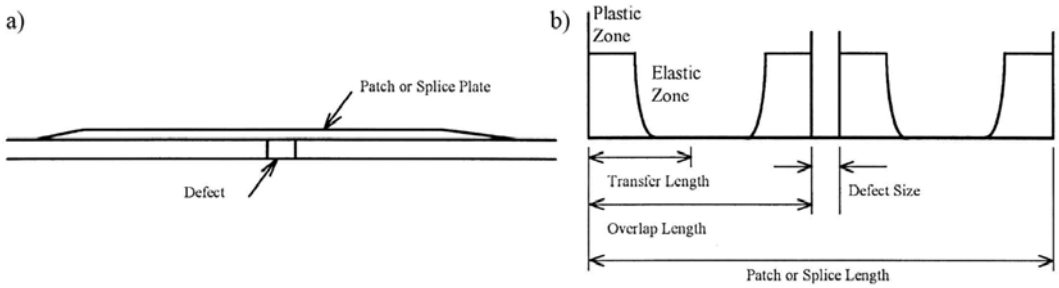

Fig. 9 – SS repair geometry (a) and shear stress distributions in the adhesive along the overlap (b) (Davis and Bond 1999).

An analytical model was developed by Mortensen and Thomsen (2002) to obtain the stress distributions on adhesively-bonded composite assemblies under a generic load. SL and DL, stepped and scarf joints were evaluated. The adherends were modelled as beams or wide plates in cylindrical bending and were considered as orthotropic laminates using the *Classical Laminate Plate Theory* (CLPT). Consequently, asymmetric and unbalanced composite adherends could be analysed with this procedure. Two different approaches were followed. In the first one, the adhesive layer was modelled as an elastic material, and in the second one, plasticity was incorporated. The constitutive equations used for the theoretical model were formulated as first order differential equations, solved numerically by direct integration. The results obtained with this formulation were compared with a FEM analysis. Fig. 10 compares stress distributions in the overlap region using linear (a) and non-linear (b) adhesive layer behaviours, considering the SL geometry and a tensile loading. σ_y, τ_{ax} (loading direction) and τ_{ay} (transverse direction) stress distributions were evaluated. It was concluded that the non-linear material behaviour of most adhesives influences the stress distributions in the adhesive layer. In fact, σ_y peel and τ_{ay} peak stresses at the overlap edges for the linear model smoothen as a result of the adhesive plasticization. Since most bonded assemblies show peak stresses at the overlap edges, it is not possible to avoid plasticization of the

adhesive. Consequently, the authors concluded that modelling adhesively-bonded joints using a linear idealization of the adhesive underestimates their strength. This is not applicable when brittle adhesives are used.

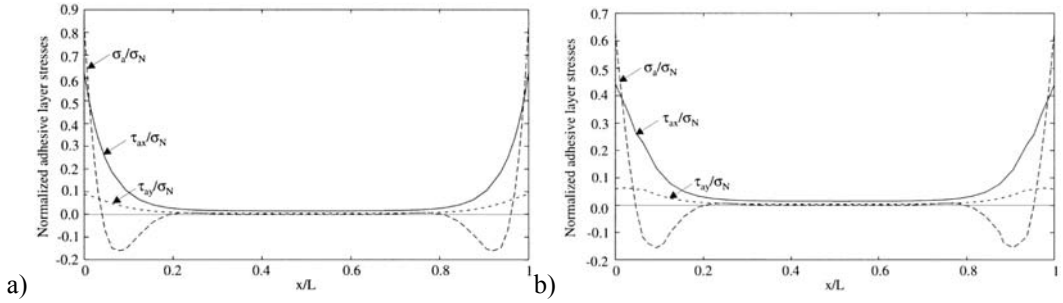

Fig. 10 – Stress distributions at the adhesive mid-thickness using linear (a) and non-linear (b) material behaviours for the adhesive layer (Mortensen and Thomsen 2002).

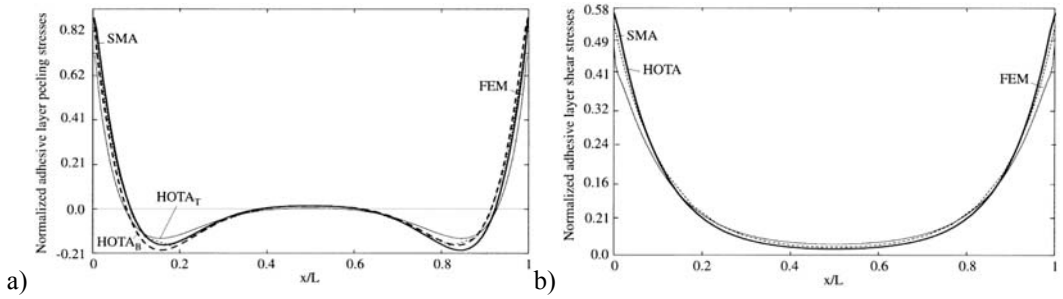

Fig. 11 – σ_y (a) and τ_{ay} (b) stress distributions at the adhesive mid-thickness (Mortensen and Thomsen 2002).

Fig. 11 compares σ_y (a) and τ_{ay} (b) stress distributions at the adhesive mid-thickness, normalized by the remote applied stress, for three different FEM approaches, considering a tensile loaded SL joint: a high order analytical model (HOTA – *High Order Theory Approach*) developed by Frostig et al. (1997) to capture the localized effects observed in sandwich beams, a model in which the adhesive layer is modelled by a system of tensile, compressive and shear springs (SMA – Spring Model Approach) and a conventional FEM model. The FEM analysis uses six and eight-node isoparametric 2D solid finite elements. The adhesive layer was modelled using eight elements through-thickness. Fillets were also considered at the overlap edges. For the σ_y stress distributions (Fig. 11 a), a distinction is made between upper (HOTAT) and lower (HOTAB) adhesive/laminate interfaces. A high agreement was found between the three approaches, even though slightly smaller peak stresses were obtained by the FEM.

Zou et al. (2004) carried out an explicit analytical analysis, complemented with a numerical 2D FEM analysis, of adhesively-bonded joints between *Fibre Reinforced Plastic* (FRP) and metallic adherends. Patch reinforced panels under tensile and bending loads, and SL and SS joints under a tensile load, were considered. The analytical solution developed was found to be applicable to most adhesively-bonded assemblies and boundary conditions. It is based on the CLPT, incorporating a constitutive model applicable to balanced composite joints under in and out-of-plane loadings. Value of adherend and adhesive thickness of 5 and 0.25 mm, respectively, were considered. Fig. 12 compares the analytical and numerical σ_y (a) and τ_{xy} (b) stress distributions in the adhesive layer for the SL joint with CFRP adherends, highlighting the acceptable correlation between both. σ_y peel peak stresses present similar magnitude. However, the analytical solution also predicts the existence of two σ_y compressive peak stresses adjacent to the tensile ones, which are not captured in the FEM simulations.

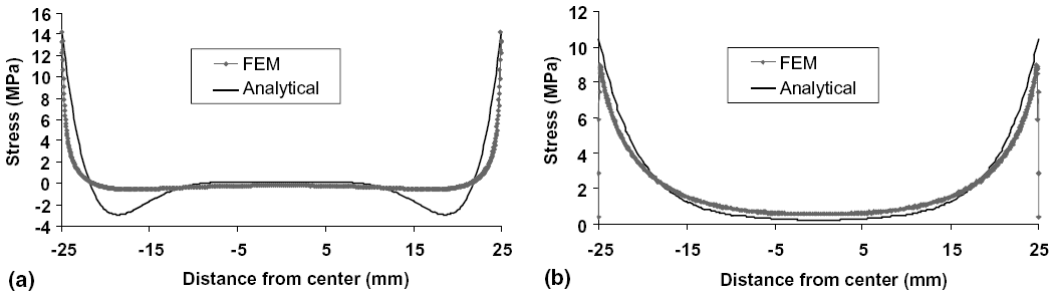

Fig. 12 – Analytical and numerical stress distributions in the adhesive layer (Zou et al. 2004).

Bogdanovich and Kizhakkethara (1999) presented a 3D FEM study of DS repairs with $[0]_{16}$ lay-up CFRP adherends under a tensile load. A method based on the sub-modelling approach available in ABAQUS® was used to predict the stress fields at the singularity regions. The method consisted on an initial global analysis of the structure (using a coarse mesh), followed by detailed analyses of the higher stressed regions. These analyses are carried out independently in several steps, such as the nodal displacements obtained in one step are used as external boundary conditions for the following one. Furthermore, in each step, the analysed volume is smaller and more refined than in the previous step. Consequently, if the region considered has a finite stress field, the model converges to the correct solution after a determined number of steps. On the other hand, if a stress singularity exists, the model does not converge. Some differences between stresses obtained by the traditional 3D model and the sub-modelling approach were observed. Fig. 13 presents a detail of σ_y stresses in the adhesive layer (a) and laminate (b) from a traditional 3D analysis and the sub-modelling method at the patch edges. σ_y peel peak stresses differ between the two methodologies, with the sub-modelling approach presenting a higher magnitude peak than the traditional 3D analysis.

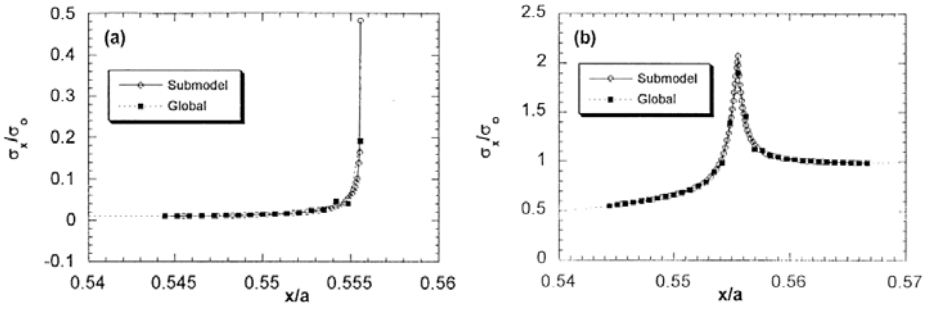

Fig. 13 – σ_y stresses in the adhesive layer (a) and laminate (b) (Bogdanovich and Kizhakkethara 1999).

Li et al. (1999) presented a 2D FEM analysis of SL joints with $[0/45/-45/0]_{2S}$ lay-up CFRP laminates under a tensile load, including non-linear geometric effects. Adhesive thicknesses of 0.13 mm (modelled by two and six finite elements through-thickness) and 0.26 mm (modelled by ten finite elements through-thickness) were considered. Results were compared with the work of Tsai and Morton (1995b). σ_y and τ_{xy} stress distributions in the adhesive and laminates were studied, together with the influence of several geometric and material parameters (e.g. adhesive thickness and Young's modulus) on these stresses. The ANSYS® software was used in the simulations, considering four-node quadrilateral isoparametric plane-strain solid finite elements. One element through-thickness for each ply was considered (the CFRP plies were modelled as orthotropic). Fig. 14 compares the strains at the overlap edge at the adhesive mid-thickness (joint with a 0.13 mm thickness adhesive layer and two elements through-thickness) with the results of Tsai and Morton (1995b) using the *Moiré Interferometry Method* (MIM). A good agreement was found, inclusively at the overlap edge, where significant gradients exist. It was emphasized that the slight differences observed are caused by the mesh and

boundary conditions. Fig. 15 represents σ_y and τ_{xy} stress distributions at the laminate/adhesive interface (a) and at the adhesive mid-thickness (b) for two different values of Young's modulus (E modulus) of the adhesive layer.

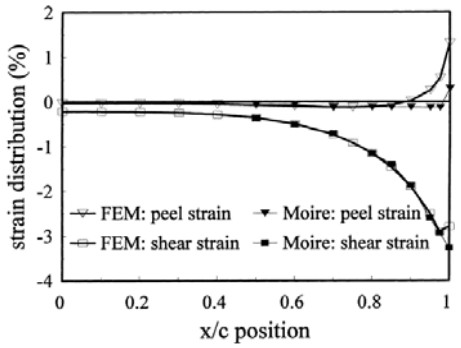

Fig. 14 – Experimental and numerical strains at the overlap edge at the adhesive mid-thickness (Li et al. 1999).

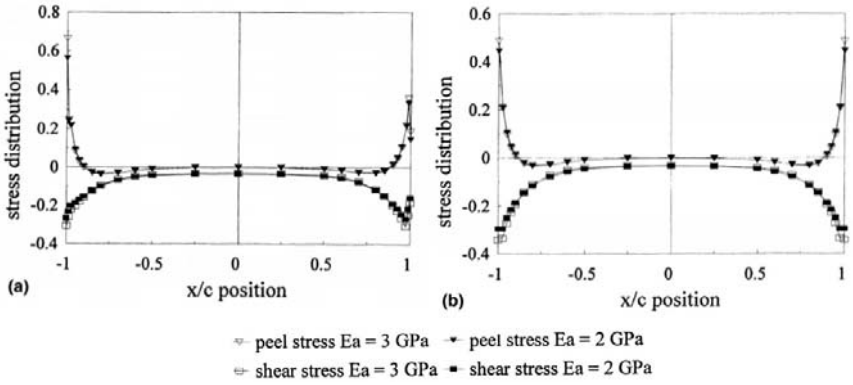

Fig. 15 – σ_y and τ_{xy} stresses at the laminate/adhesive interface (a) and at the adhesive mid-thickness (b) (Li et al. 1999).

σ_y and τ_{xy} stresses are normalized by the remote stress applied to the laminates (the ratio between the applied load and the laminates cross-sectional area). At the middle of the adhesive thickness (Fig. 15 b), these stresses are symmetric relatively to x/c=0. σ_y and τ_{xy} stress distributions peak at the overlap edges. At the laminate/adhesive interface (Fig. 15 a) a slight reduction on both peak stresses is observed at x/c=1. Higher values of E modulus slightly increase peak stresses, thus decreasing the joints strength. A similar study with an adhesive thickness of 0.26 mm also yielded higher magnitude peak stresses, consequently decreasing the joints strength.

An experimental and numerical comparison between bonded, bolted and bonded/bolted CFRP SS joints under a tensile load was carried out by Chan and Vedhagiri (2001). The FEM analysis used ANSYS® and 3D solid finite elements. For the bonded joints, the authors concluded that the joints strength greatly depends on several factors such as the laminates lay-up, surface preparation and the anisotropic nature of the materials. On the stress distributions, σ_x stresses were practically constant far from the overlap region. At the overlap, the load eccentricity of these joints creates a bending moment, increasing significantly σ_x stresses. σ_y and τ_{xy} stress distributions at the adhesive/laminate interfaces were approximately constant and nil at the central overlap region, peaking at its edges.

Ganesh and Choo (2002) addressed the influence of longitudinal E modulus grading in the adherends at the overlap region on the tensile stresses and displacements of SL and DL joints (Fig. 16) with CFRP adherends. Stress distributions at the adhesive mid-thickness were compared by the FEM for different E modulus grading schemes in the overlap and the standard joint (with a constant E modulus).

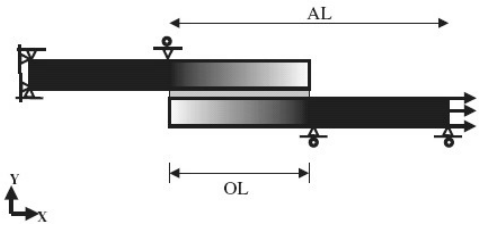

Fig. 16 – Longitudinal *E* modulus grading in a SL joint (Ganesh and Choo 2002, Boss et al. 2003).

E modulus grading was achieved varying the braid angle of the reinforcing fibres. σ_y and τ_{xy} stress distributions were obtained along the overlap at the middle of the adhesive thickness for three *E* modulus grading types. In all cases, τ_{xy} stresses peaked at the overlap edges, while the overlap central region was practically unloaded. The laminate stiffness reduction at the overlap edges caused a reduction of 20% on the τ_{xy} peak stresses in the adhesive near those regions and a slight increase at the overlap central region, while no significant changes were observed on σ_y stress distributions. σ_x peak stresses were also found in the adhesive for the standard joint at the overlap edges, while the overlap central region was practically unloaded. *E* modulus grading increased σ_x peak stresses along the entire overlap. The proposed technique was found valid, given that σ_y and especially τ_{xy} stresses, which rule fracture in these joints, diminished.

It is extremely important to account for the non-linear geometric effects when modelling numerically the behaviour of asymmetric assemblies such as SL joints, due to the adherends bending. Osnes and Andersen (2003) carried out a detailed FEM study about the influence of the non-linear geometric effects on stress distributions, reaction loads and displacements of SL joints with adhesive fillets at the overlap edges under a tensile load. CFRP, steel and CFRP-steel mixed joints were evaluated. The results were compared with classic analytical theories. For the CFRP adherends, $[0/90]_{2S}$ and $[90/0]_{2S}$ lay-ups with a 0.125 mm ply thickness were considered. The numerical analysis was carried out in ANSYS®, using four-node solid finite elements. Three elements were considered through-thickness for each ply, while the adhesive layer was modelled with four elements. It was concluded that, under an equal tensile displacement, the corresponding reaction load at the clamped edge is approximately 15% higher with a geometric non-linear analysis, resulting on a higher strength. Fig. 17 represents the transverse displacement (a) and the equivalent Von Mises stresses (b) at the fillet tip, considering linear and non-linear geometric analyses and $[0/90]_{2S}$ laminates. Between the linear and non-linear geometric analyses, an increasing difference was found with the applied load on the transverse displacement and equivalent Von Mises stresses at the fillet edge.

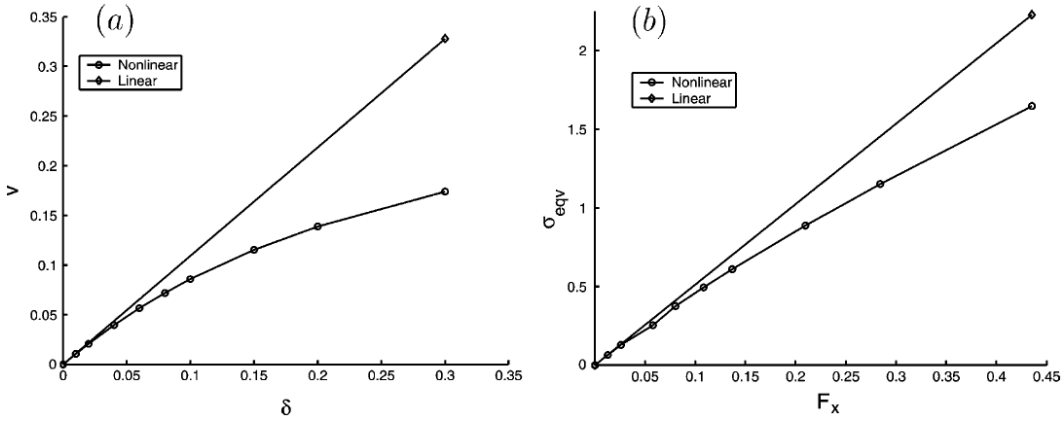

Fig. 17 – Transverse displacement (a) and Von Mises stresses (b) at the fillet tip (Osnes and Andersen 2003).

Displacements and stresses are smaller including the non-linear geometric effects in the analysis. Consequently, numerical analyses not including this effect will underestimate the joint strength. A similar study was accomplished on DL joints. However, identical results were obtained with both analyses, since these differences are only relevant when significant rotations of bodies occur (in this particular case due to load eccentricities).

Gonçalves et al. (2002) performed a FEM stress analysis of adhesively-bonded SL joints under a tensile load with isotropic adherends. The numerical models included material and geometric non-linearities, and employed hexahedral solid finite elements and developed cohesive elements. Cohesive elements allow the extraction of stresses at the adherend/adhesive interfaces and at the adhesive mid-thickness. The adherends and adhesive were modelled using four and three elements through-thickness, respectively. Fig. 18 shows stress distributions at the middle of the adhesive thickness. Stresses are plotted at several planes of the joint in the width direction (z=0 at the middle of the laminate width), and are normalized by the average shear stress at the adhesive mid-thickness. σ_x stresses peak at the overlap edges, at the longitudinal plane closest to the symmetry plane of the joint (z=0.176 mm). σ_x stresses are approximately constant along the joint width, diminishing significantly at the joint free edges (z=12.324 mm). σ_x and σ_z stresses present similar magnitude. σ_y stresses are the highest at the overlap edges. τ_{xy} stresses are practically insensitive to the longitudinal plane considered. The authors concluded that the stress distributions in a SL joint are 3D and that 2D models shall be used with caution. Pandey and Narasimhan (2001) obtained similar results. At the adherend/adhesive interfaces, σ_y and τ_{xy} stresses are practically constant along the joint width, diminishing at the free edges (z=12.324 mm). All stress components evaluated in this work were highest at the laminate/adhesive interfaces. Therefore, it was concluded that damage onset and growth occurs at or near those interfaces.

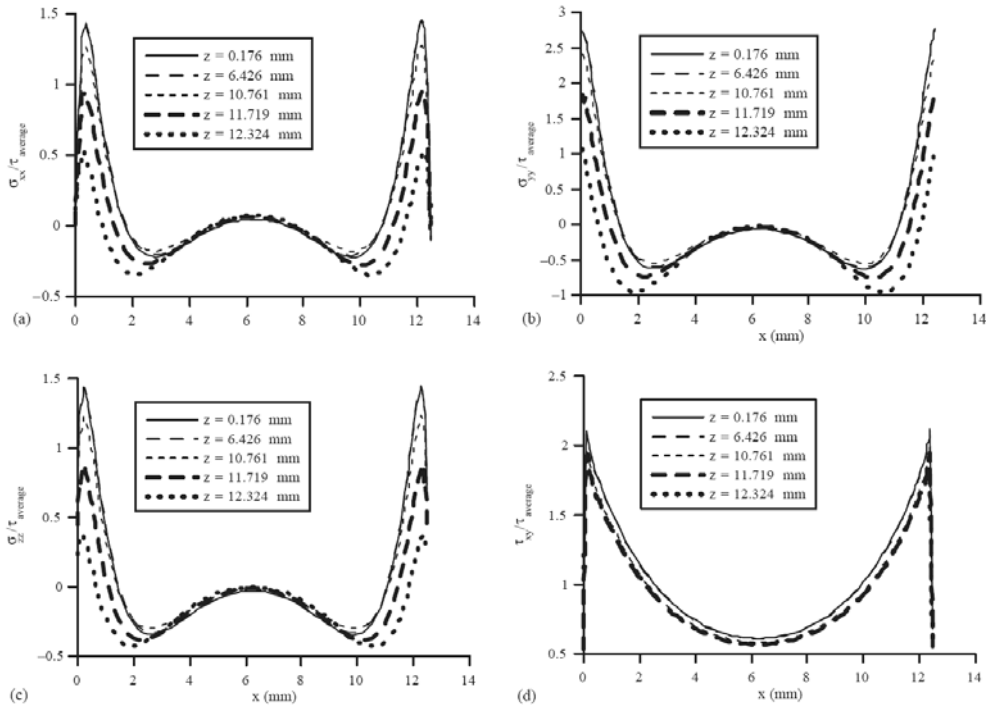

Fig. 18 – Stress distributions at the adhesive mid-thickness (Gonçalves et al. 2002).

The work of Magalhães et al. (2005) focus a 2D FEM analysis of adhesively-bonded SL composite joints with a $(0_4,90_4)_S$ lay-up. The model uses developed cohesive elements, compatible with the eight-node solid finite elements of

ABAQUS®. The cohesive elements were placed between the adhesive/laminate interfaces, at the middle of the adhesive thickness and between different oriented plies in the laminates. Cohesive elements allow obtaining the stress distributions at the interfaces between different materials and different oriented plies, which is not possible to accomplish using conventional solid finite elements. Stress distributions were plotted for GFRP, CFRP and GFRP-CFRP mixed joints. Fig. 19 details the overlap and planes for evaluation of stresses via cohesive elements. Fig. 20 (a) and (b) show σ_y and τ_{xy} stresses, respectively at the overlap for joints with CFRP adherends, normalized by the average shear stress at plane P4. σ_y peel and τ_{xy} peak stresses are generally observed at the overlap edges and are highest at planes P3 and P5, corresponding to the laminate/adhesive interfaces (stress singularity regions). It was stressed that a stress concentration effect exists along the adhesive thickness, although at a highly localized region, since far from the overlap edges the stress magnitudes are identical.

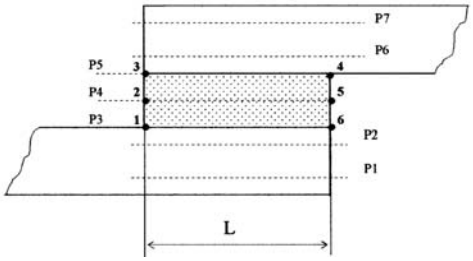

Fig. 19 – Detail of the model at the overlap and planes for the evaluation of stresses (Magalhães et al. 2005).

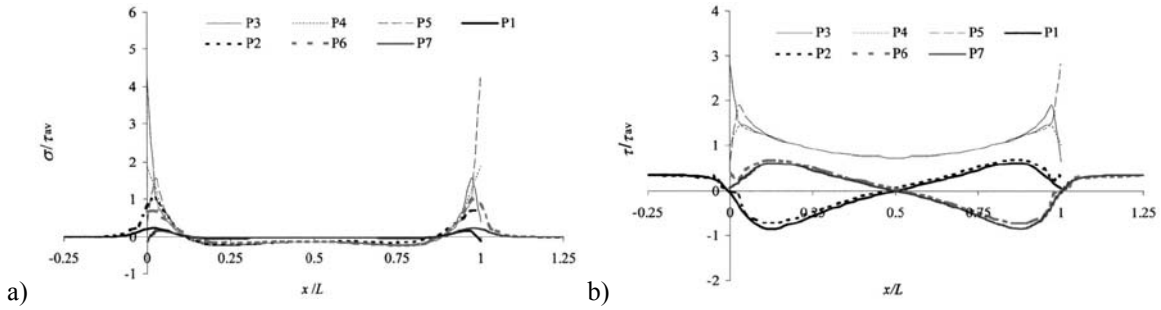

a) b)

Fig. 20 – σ_y (a) and τ_{xy} (b) stress distributions (Magalhães et al. 2005).

It was also concluded that damage onset is prone to occur at or near the laminate/adhesive interfaces, and that the stress singularities at planes P3 and P5 can explain adhesive failures, sometimes incorrectly related to a poor surface preparation. The mentioned stress concentrations at planes P3 and P5 can also justify damage growth near one of the laminates/adhesive interfaces instead of an intermediate region at the thickness of the adhesive layer. GFRP and mixed joints showed equivalent results, although with slight differences in the magnitude of peak stresses.

Soutis et al. (1999) studied, using 3D FEM models, the influence of several geometric parameters on the compressive strength of DS composite repairs (Fig. 21 a). A comparison was conducted between load-oriented normal stresses in the laminate for different patch thicknesses (Fig. 21 b). Stresses are normalized to the un-notched plate ones and are plotted at the symmetry line of the repair perpendicular to the applied load. A repaired specimen with the drilled hole filled with adhesive (plug filling technique) was also evaluated. Normal peak stresses near the hole diminished increasing the patch thickness. Plug filling leads to a significant reduction on normal peak stresses. The strength and locus of damage initiation of the geometries evaluated were predicted with the MNSC for the laminate microbuckling and the *Average Shear Stress Criterion* (ASSC) for the adhesive layer.

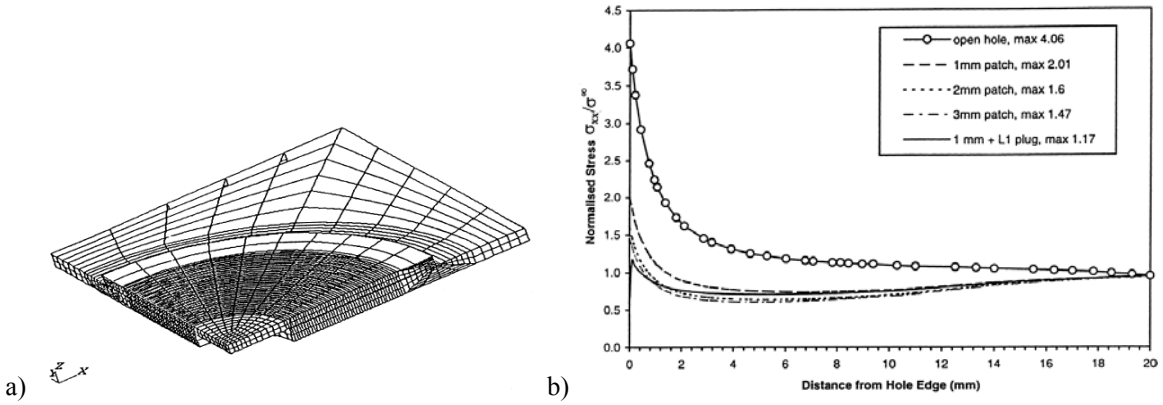

Fig. 21 – DS repair and mesh (a) and normalised load-oriented normal stresses (b) (Soutis et al. 1999).

Hu and Soutis (2000) addressed by the FEM the compressive behaviour of DS CFRP repairs with a centred-hole, bonded with circular patches. The repairs strength was evaluated with the MSSC for the adhesive layer failure (assuming an elastic-perfectly plastic behaviour). τ_{xy} peak stresses were observed at the adhesive mid-thickness at the overlap edges, causing the adhesive plasticity. Above a determined overlap length the repair strength remained practically constant (Fig. 22 a), since an unloaded central region of the overlap increased in extension with the overlap length. The influence of the patch stiffness on the repair strength was also assessed (Fig. 22 b). It was found that the patch/laminate stiffness optimal ratio was 0.5. The effect of the adhesive ultimate shear strain (Fig. 23 a) and shear strength (Fig. 23 b) on the repair strength was also studied.

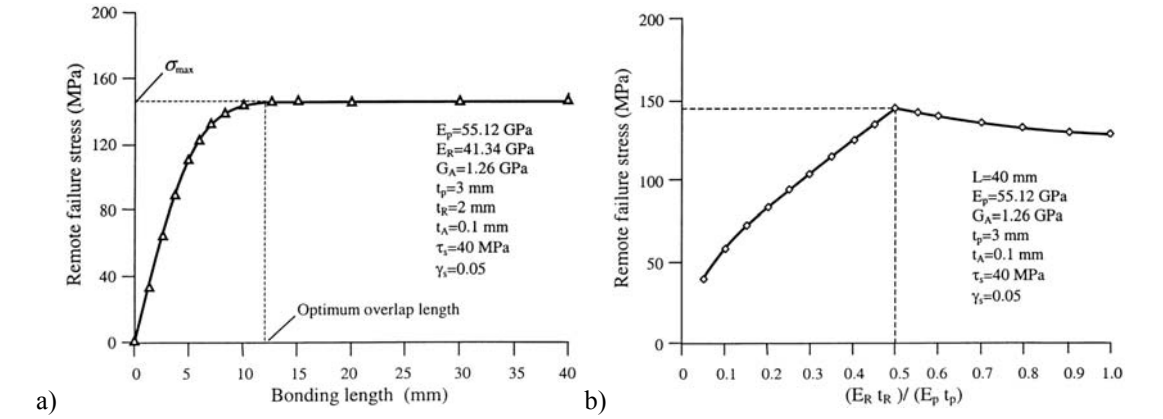

Fig. 22 – Repair strength as a function of the overlap length (a) and the patch/laminate stiffness ratio (b) (Hu and Soutis 2000).

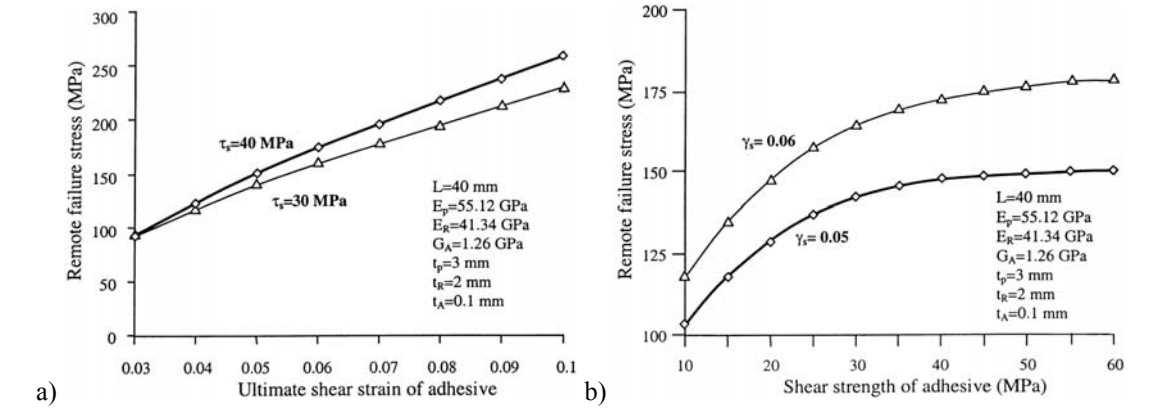

Fig. 23 – Repair strength as a function of the adhesive ultimate shear strain (a) and shear strength (b) (Hu and Soutis 2000).

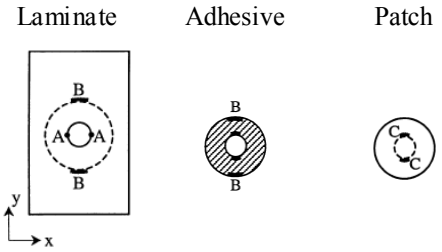

Fig. 24 – Stress critical regions of the repair (Hu and Soutis 2000).

The authors concluded that the adhesive failure strain has a bigger influence on the repair strength, compared to the adhesive failure shear strength. It was also underlined that to correctly evaluate stress distributions in the repairs and predict accurately their strength, a 3D analysis was necessary to capture the stress singularities near the drilled hole. Fig. 24 presents the stress critical regions of the 3D repair. In the laminate, load-oriented normal stresses are the most significant, peaking at region A (thin patches) or region B (thick patches). In the adhesive, shear stresses are highest, peaking at region B. Peel peak stresses in the adhesive layer were also captured by the numerical models, eventually leading to delaminations in the laminate or patch. In the patch, load-oriented normal stresses are the most significant, even though smaller than in the laminate, peaking at region C.

An experimental and numerical study on the tensile behaviour of SL GFRP joints was conducted by Reis et al. (2005), for overlap lengths of 15, 30, 45 and 60 mm. A 2D FEM analysis with eight-node plane-strain elements was carried out. σ_y and τ_{xy} stresses in the adhesive layer were found to be highest at the overlap edges, near the laminate/adhesive interfaces. It was found that σ_y and τ_{xy} peak stresses in the adherends at the overlap edges move towards the overlap central region as the applied load increases. The authors also concluded that a 30 mm overlap length joint is the best solution, since Von Mises peak stresses in the adhesive are the lowest of all overlap lengths.

Liu and Wang (2007) presented an experimental and numerical study on 3D DS repairs (Fig. 2 a) under a tensile load, using CFRP laminates and patches. A $[(0/90/\pm45/90/0)_2]_S$ lay-up was considered for the laminate, and several quasi-isotropic lay-ups were tested for the patches. An epoxy adhesive film with 0.12 mm thickness was used. The experimental part of this work will be discussed in Sub-Section 2.2.2.1. The numerical models were built in ANSYS® using twenty-node solid finite elements. The repairs strength was estimated combining the Tsai-Wu criterion (Tsai and Wu 1971) to predict fibre breakage and matrix cracking of the laminate and patches, the Ye delamination criterion (Ye 1988) to detect delamination between plies and the Maximum Shear Stress Criterion for the adhesive layer.

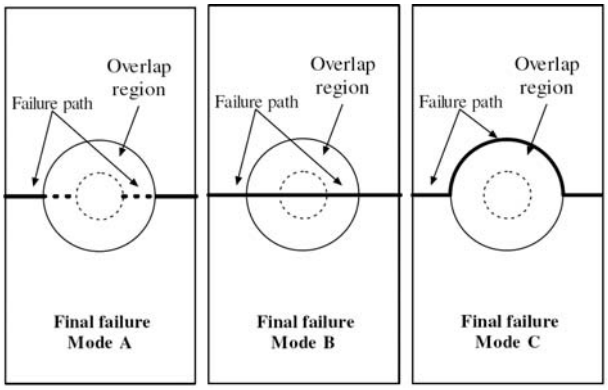

Fig. 25 – Failure modes of the repaired structures (Liu and Wang 2007).

A progressive damage model was implemented in which the element properties are degraded when the mentioned criteria are satisfied. In each load step, the failure criteria were applied to the structure. If any of the criteria was met at a given element, its elastic properties were diminished, simulating material degradation. The analysis then restarted without increment of load until no damage was found in that load step, or final failure of the structure was attained. Three failure mode possibilities were introduced (Fig. 25). Mode A failure initiates in the adhesive layer, leading to patch debonding. The laminates brake transversely near the hole, leading to catastrophic failure of the repair. The patches are left undamaged. In mode B failure, the patches fail to sustain the loads transmitted by the structure and split transversely. Almost simultaneously, the laminates fracture transversely. In mode C failure, the failure path follows the singularity regions at the patch edges, growing to the laminate as transverse cracks. Numerically, the influence of several geometric parameters on the repairs strength and failure mode was studied.

- ***Patch diameter:*** The strength increases approximately proportionally to the patch diameter, for the smaller values of this parameter. For the bigger values, the strength improvement gradually diminishes up to a strength plateau. The smaller patches fractured in mode A, due to the significant shear stresses in the adhesive layer, promoting patch debonding from the laminate prior to patch failure. Increasing the patch diameter causes a reduction on the adhesive layer stresses, and the ultimate stresses in the patch are attained before failure in the adhesive (mode B failure). For the bigger diameter patches, the adhesive is stronger than the laminate, leading to a mode C fracture.
- ***Patch thickness:*** An optimal patch thickness/laminate thickness ratio of 0.6 was obtained. The numerical simulations foresee that thin patches do not suppress crack propagation in the laminates effectively. At final failure, the patches present damaged regions (mode B failure). A higher patch thickness hinders this effect, increasing the repair strength. Extremely thick patches significantly increase stresses in the adhesive layer. Consequently, a premature failure in the adhesive is anticipated, leading to a mode A failure.
- ***Patch lay-up:*** Several quasi-isotropic lay-ups were tested and a small influence on the repairs strength was observed. However, different failure modes were captured.
- ***Adhesive thickness:*** An approximate 0.3 mm adhesive thickness was found to maximize the repairs strength. Smaller values render the adhesive layer too stiff and brittle, causing a premature debonding of the patches (mode A failure). Higher values relieve stresses in the adhesive, decreasing the load transmitted to the patches. As a result, the laminate has to bear the majority of the loads, failing prematurely (similar to mode B failure).

SS and DS repairs of unidirectional CFRP laminates under a tensile load were studied by Campilho et al. (2005). A 2D FEM analysis was carried out using plane-strain eight-node elements and a CZM for damage propagation. This work focused on the effect of the overlap length and the patch thickness on the stress distributions in the adhesive layer and the repaired strength. A numerical model using ABAQUS® and cohesive elements was used to perform the strength analysis and to evaluate the influence of the cohesive properties of the adhesive, and laminate/adhesive and adhesive/patch interfaces on the repaired strength and failure modes. σ_y and τ_{xy} stress distributions were plotted at five planes at the repair region: the interface between the two adherends plies closest to the adhesive, the adherend/adhesive interface, the middle of the adhesive, the adhesive/patch interface and the interface between the two patches plies closest to the adhesive. σ_y peel and τ_{xy} peak stresses were found at the overlap edges, highest at the laminate/adhesive and adhesive/patch interfaces. These results indicated that for identical properties at all planes, damage onset and growth occurs at the referred interfaces. The non-proportional relation of the repaired strength as a function of the

overlap length, for both SS (Fig. 26 a) and DS (Fig. 26 b) repairs, was justified by an increasing unloaded inner region in the adhesive layer with the overlap length. σ_C represents the repair strength (considering the laminate cross-sectional area), $\Delta\sigma_C$ its percentile variation and η the efficiency of the repair (compared to an undamaged laminate).

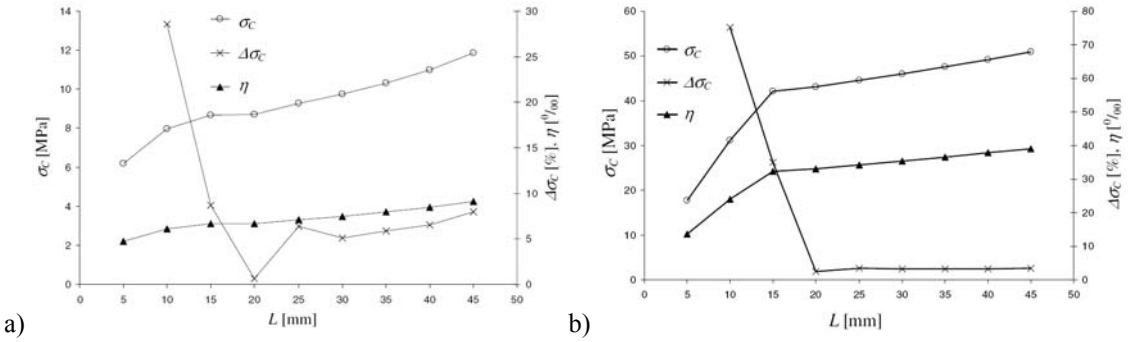

Fig. 26 – Strength as a function of the overlap length for the SS (a) and DS (b) repairs (Campilho et al. 2005).

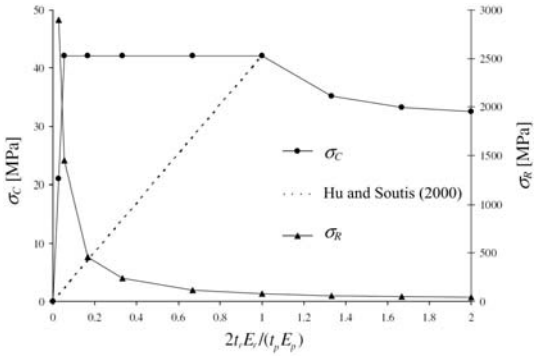

Fig. 27 – Strength as a function of the patch thickness for the SS repairs (Campilho et al. 2005).

Fig. 27 presents the SS repair strength as a function of the patch thickness, and the respective σ_x peak stresses in the patch (σ_R), comparing with the results of Hu and Soutis (2000). Above a determined patch thickness, the repair residual strength diminished, due to the increase of σ_y peel peak stresses at the overlap edges. The numerical simulations were consistent with the stress analyses, i.e., adhesive failure at the laminate/adhesive and adhesive/patch interfaces for both SS and DS repairs. It was found that the repairs fracture is ruled by the adhesive layer strengths.

2.2.1.2. Scarf assemblies

Oztelcan et al. (1997) presents a FEM study on repaired sandwich helicopter blades with GFRP faces and honeycomb core under a compressive load. Two repairing techniques were evaluated: SS (Fig. 28 a) and scarf (Fig. 28 b).

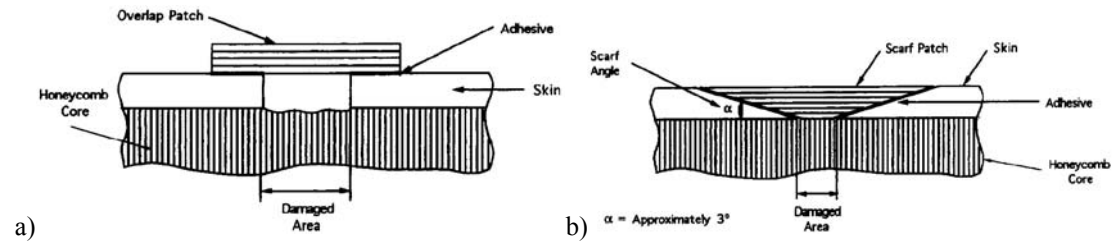

Fig. 28 – Repair techniques evaluated: SS (a) and scarf (b) repairs (Oztelcan et al. 1997).

The numerical models used eight-node reduced integration shell elements for the composite faces, available in ABAQUS®. However, since the honeycomb thickness is not constant, it was not possible to use shell elements conventionally. To overcome this problem, shell elements were placed vertically between the upper and lower composite faces, creating a 3D structure. The boundary conditions included clamping one of the model edges and applying a compressive displacement at the other. The analysis procedure initiated using a global model to identify the most stressed regions of the structure, and then a smaller local model was built for the critical region and only for the composite faces. This local model was subjected to the displacements obtained from the global model. A subroutine was developed for the adhesive layer elements, including a progressive damage model based on the *Maximum Stress Criterion* (MSC) to obtain the shear stress distributions in the adhesive layer. For the SS geometry, shear stress distributions presented a parabolic shape, symmetric relatively to the overlap central region, and peaking at the overlap edges. Increasing the compressive load, shear peak stresses moved towards the overlap inner region. The scarf repair used a 3º scarf angle and matching lay-ups for the laminate and patch. Triangular elements were used to model the laminate edges, patch and adhesive. Flatter shear stress distributions were obtained. Moreover, increasing the compressive load, the adhesive layer was kept uniformly loaded along all its length, resulting in a more efficient distribution of stresses, compared to the SS repairs.

Odi and Friend (2002) performed a comparative study of different FEM approaches to simulate the repair of composite laminated structures, exploring the advantages and identifying the problems associated to each one of these approaches, using a linear static analysis. The following approaches were considered: a traditional 2D simulation adapted to composite structures (Siener 1992), a 2D simulation using 3D shell elements (Bair et al. 1991) and a 3D simulation using solid finite elements (Soutis and Hu 1996, Soutis and Hu 1997). The Siener's model assumes a 2D plane-strain condition for each laminate ply. The laminate properties are determined using the CLPT, from the lay-ups and mechanical properties of an individual ply. The Bair's model, despite being regarded as a 2D model, is in fact a 3D one, since it uses shell elements. With this approach, the model is built using a combination of effective plies and dummy plies, these with an extremely low stiffness. The 3D simulation uses 3D solid isoparametric finite elements to model the laminates and the adhesive. Equivalent properties were used for these elements, obtained from the CLPT. Each laminate ply was modelled with one solid finite element through-thickness. A scarf repaired carbon/epoxy laminate with a $[0_2/\pm45/90/\pm45/0_2]_S$ lay-up under a tensile load was considered to compare the models. For the Siener's model, two distinct configurations were evaluated: a five step (Fig. 29 a) and a 3º scarf repair (Fig. 29 b). The Bair's model was simulated only using the five step scheme (Fig. 29 a), while the 3D model was modelled using a step configuration, with one step for each laminate ply (Fig. 29 c), to approximate real structures more accurately. The longitudinal displacements, σ_y and τ_{xy} stress distributions in the adhesive layer were compared between the three approaches.

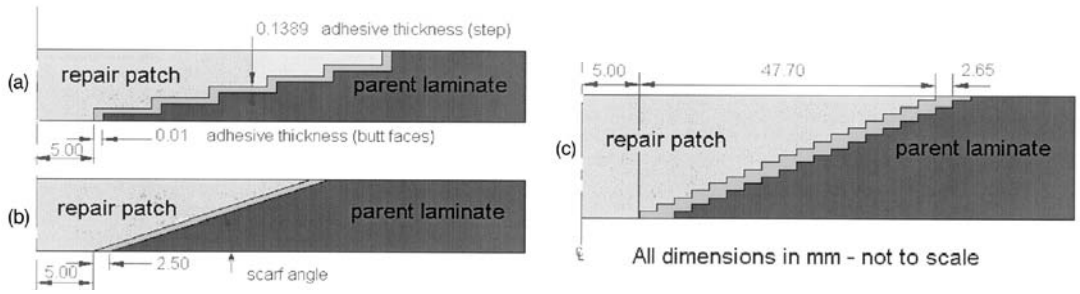

Fig. 29 – Repairing configurations (Odi and Friend 2002).

The repair longitudinal displacements at the symmetry line (Fig. 29) showed an almost perfect agreement between undamaged and repaired laminates with the three techniques. Fig. 30 plots τ_{xy} stress distributions in the adhesive layer for the stepped repair at the top step using the three approaches (a) and for the Siener's model using a 3º scarf angle (b).

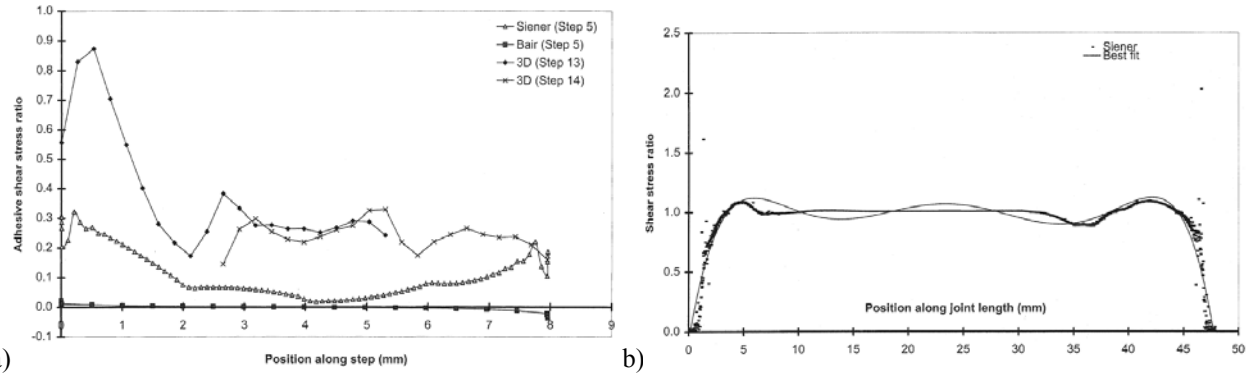

Fig. 30 – τ_{xy} stresses in the adhesive layer: stepped repair at the top step (a) and 3º scarf repair (b) (Odi and Friend 2002).

The five step repair (Fig. 30 a) shows a similarity between Siener's and 3D approaches. The small discrepancy is justified by different mesh refinements. The large divergence of the Bair's model is explained by the model idealization, leading to the extraction of stresses at a different plane. For the Siener's model (Fig. 30 b), τ_{xy} stresses in the adhesive layer are practically constant (Oztelcan et al. 1997), leading to an improved repair efficiency, since failure in the adhesive is prone to occur simultaneously in all its length.

Gunnion and Herszberg (2006) carried out a parametric 2D FEM study of CFRP scarf joints under tension. A linear material and geometric stress analysis was performed. A local coordinate system was built to extract shear and normal stresses in the middle of the adhesive thickness tangentially and normally to the scarf. Peel and shear peak stresses were evaluated for different combinations of material/geometric parameters: scarf angle, adhesive thickness, ply thickness, laminate thickness, over-laminate thickness and lay-up sequence. $[90/0]_{2S}$, $[0/90]_{2S}$, $[45/0/-45/90]_S$ and $[0]_8$ lay-ups were evaluated. It was also investigated the influence of laminate mismatching on normal and shear stresses in the adhesive layer. It was observed that the lay-up has a high influence on the stress distributions, since stresses are higher near the 0º plies. Using unidirectional laminates, shear stresses are almost constant and peel peak stresses are observed near the overlap edges. The influence of all parameters on peel and shear average and peak stresses is summarized in Table 1.

Table 1 – Influence of the evaluated parameters on peel and shear stresses (Gunnion and Herszberg 2006).

Parameter	***Average peel***	***Peak peel***	***Average shear***	***Peak shear***
Lay-up	No effect	Increases if 0º plies are on the outer surfaces	No effect	Decreases with more 0º plies. Increases with increasing distance between 0º plies across the scarf
Laminate thickness	No effect	Decreases with increasing laminate thickness	No effect	Decreases with increasing laminate thickness
Mismatched adherends	No effect	Slight increase or decrease, depending on lay-up	No effect	Slight increase or decrease, depending on lay-up
Adhesive thickness	No effect	Increases with increasing adhesive thickness	No effect	Increases with increasing adhesive thickness
Scarf angle	Increases with increasing scarf angle	Significantly decreases with increasing scarf angle	Decreases with increasing scarf angle	Slightly decreases with increasing scarf angle
Over-laminate	Decreases with increasing over-laminate stiffness	Significantly decreases with increasing over-laminate stiffness	Decreases with increasing over-laminate stiffness	Significantly decreases with increasing over-laminate stiffness
Allowing load by-pass of patch	Decreases with the presence of alternate load paths	Decreases with the presence of alternate load paths	Decreases with the presence of alternate load paths	Decreases with the presence of alternate load paths
Angle to the loading direction for a 3D circular patch	Decreases with increasing angle from loading direction	Decreases with increasing angle from loading direction	Decreases with increasing angle from loading direction	Decreases with increasing angle from loading direction

3D numerical models were built to compare stress distributions with 2D ones. $[90/0]_{2S}$ and $[0/90]_{2S}$ lay-ups were considered, which allowed modelling only one quarter of the joints, using symmetry conditions. Fig. 31 shows normal and shear stress distributions in the middle of the adhesive thickness at different vertical planes, corresponding to angles with the applied load from 0 to 90º. Increasing this angle, both peel and shear peak and average stresses decreased. Similar profiles to the 2D models were obtained. Therefore, the authors concluded that the 2D models are valid for parameter optimization. The most important conclusions concerned the relatively low dependence of adhesive stresses to mismatched adherend lay-ups and the dramatic reduction on peak stresses using an over-laminate covering the repair region. These results are in agreement with the failure load analyses of Myhre and Beck (1979) and Ahn and Springer (1998a), which reported significant strength improvements with this technique.

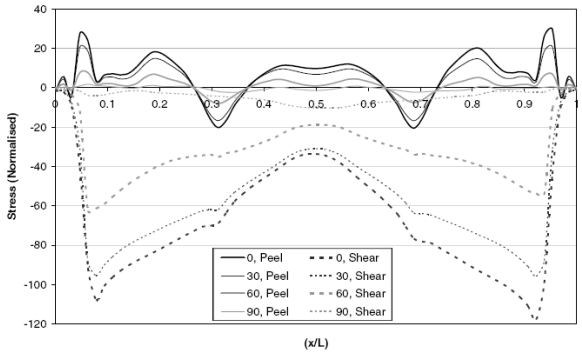

Fig. 31 – Normal and shear stresses at different planes at the adhesive mid-thickness (Gunnion and Herszberg 2006).

Harman and Wang (2006) proposed an analytical method to optimize the profile of aluminium and CFRP scarf joints between equal and different modulus adherends, aiming reducing peak stresses along the bond length. A FEM analysis was also performed to validate these results and to study the influence of the patch lay-up on adhesive stresses. A linear variation of the scarf angle along the bond length was considered to optimize the scarf profile. The optimization procedure focused on shear stresses, since for small scarf angles the joint strength is dominated by shear failure. A sensitivity study was conducted for several adherend moduli combination, to establish the scarf profile that minimized shear peak stresses. FEM simulations used a constant equivalent scarf angle. The following conclusions were drawn:

- ***Aluminium adherends and a linear scarf of 5º:*** shear stresses are more uniform using equal longitudinal E modulus for both adherends (E_1=E_2). Normalized shear peak stress values in the adhesive layer for dissimilar adherends approach the adherend modulus ratio of the laminates. It is possible to flatten shear stress distributions in joints with different modulus adherends using a variable scarf angle along the bond length. The authors concluded that higher E_1/E_2 ratios should correspond to higher $\alpha_{máx}/\alpha_{min}$ ratios (α represents the scarf angle), to ensure uniform shear stresses along the bond length.
- ***CFRP adherends with constant and varying scarf angles:*** shear stresses were obtained for E_1=E_2 and E_1=0.8E_2, analytically and with the FEM. Shear stresses in the adhesive peaked near the 0º load oriented plies. Using a linear variation of the scarf angle was not found to be effective, since shear peak stresses increased. The authors concluded that the optimization of CFRP scarf joints would be possible using a complex scarf profile in which the scarf angle would be reduced adjacent to the 0º plies, and then increased in areas adjacent to less stiff plies. However, this joint would be extremely difficult to manufacture, with likely pronounced stress concentrations due to small laminate misalignments.

Charalambides et al. (1998a) predicted by the FEM the tensile strength of adhesively-bonded CFRP scarf joints. Linear elastic and linear elastic-plastic laws were considered for the adhesive layer. The quasi-isotropic $[\pm 45/0/90]_{2S}$ lay-up was used for the laminates, with additional 0º plies overlapping the bonded region (Fig. 32). The joints strength was predicted for dry and conditioned (immersed in distilled water for varying periods) specimens. The mechanical properties of the adhesive and laminate were determined in both conditions. Two approaches were considered to model the laminates: the use of a homogeneous orthotropic idealization with equivalent properties, and a ply-by-ply modelling with individual properties. A 0.17 mm adhesive thickness was used. 2D numerical models with plane-strain eight-node rectangular and six-node triangular solid finite elements were built to simulate the joints behaviour. Three failure mechanisms were evaluated, consistent with previous experimental work: cohesive failure of the adhesive layer, failure originating from a delamination in the laminate near the overlapping ply (type A; Fig. 32 a) and tensile failure along the scarf repair (type B; Fig. 32 b). The numerical models included different failure criteria to account for these failure modes. Failure of the adhesive layer was simulated using the Raghava yield criterion (Raghava et al. 1973). Type A failure was investigated using a fracture mechanics-based criterion to predict the failure load. The procedure consisted on introducing in the numerical models a 2 mm crack on the experimental damage initiation locus, i.e., between the two laminate plies nearest the overlapping ply (Fig. 32 a). The value of G was calculated numerically using the J-integral method. The mode-mixity was evaluated using the *Virtual Crack Closure Technique* (VCCT). These values were compared with G_c in pure modes I and II, calculated using the DCB and *End-Loaded Split* (ELS) tests, respectively. The tensile failure of the laminate (type B failure) was predicted comparing the maximum normal stresses in the load direction in the 0º plies with the tensile strength of a unidirectional laminate. The experimental failure loads were predicted reasonably with the proposed methodologies.

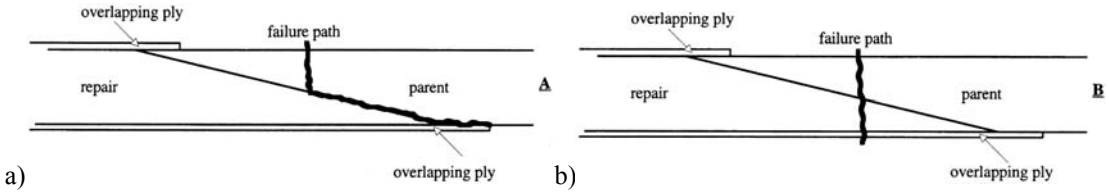

Fig. 32 – Failure paths evaluated, besides cohesive failure (Charalambides et al. 1998a).

Odi and Friend (2004) performed a 2D FEM study concerning scarf repairs with CFRP laminates and scarf angles of 1.1º, 1.9º, 3.0º, 6.2º and 9.0º. A $[0_2/\pm 45/90/\pm 45/0_2]_S$ lay-up and an adhesive thickness of 0.25 mm were considered. The tensile failure loads of the repairs were obtained with the Tsai-Wu and the MSC criteria for the laminates (Sandhu 1972) and the ASC for the adhesive layer (Soutis and Hu 1997, Odi 1998), and were compared with the experimental results of Adkins and Pipes (1988). The laminates were modelled ply-by-ply, allowing applying failure criteria developed specifically for composite laminates. Fig. 33 shows shear stress distributions in the adhesive layer, normalized by the remote applied stress. Fig. 33 (a) compares results of a traditional model (using equivalent elastic properties for the laminates) and the proposed methodology, for a 3º scarf angle, while Fig. 33 (b) equates the five scarf angles evaluated. The traditional approach leads to a practically uniform shear stress distribution. The improved approach captures the shear stress gradients along the bond length caused by the distinct plies compliance in the load direction. It was found that shear stresses are highest near the 0º plies. In addition, shear stresses in the adhesive layer increase with the scarf angle, diminishing the repair strength. It was observed that the failure load increased reducing the scarf angle. With a 1.1º scarf angle, a reduction of the failure load was observed numerically, due to elements

distortion. The comparison between the test results and simulations allowed concluding that the proposed methodology accurately predicted the failure load of these repairs.

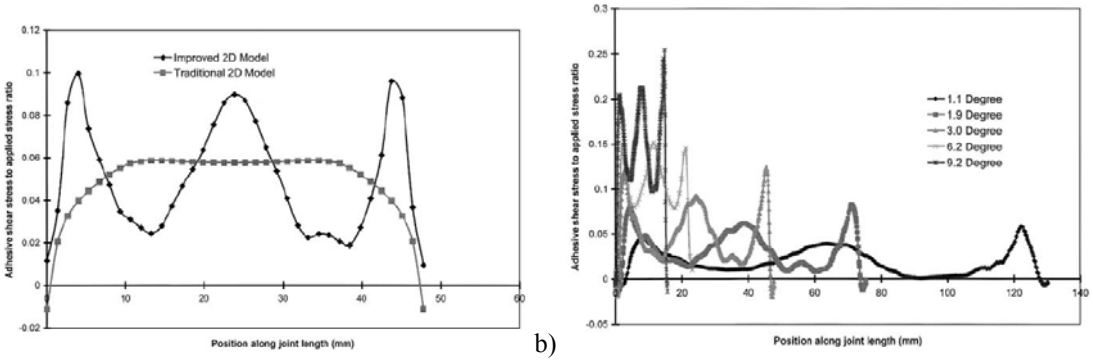

a) b)

Fig. 33 – Shear stresses in the adhesive for a 3º scarf repair (a) and comparison between five scarf angles (b) (Odi and Friend 2004).

A 2D study of tensile loaded scarf repairs with unidirectional CFRP adherends was presented by Campilho et al. (2007a). A non-linear material and geometric FEM analysis was performed, using plane-strain rectangular 8-node and triangular 6-node finite solid elements. A mixed mode CZM implemented within cohesive elements was used to extract σ_n and τ_{tn} stress distributions in the directions normal and tangent to the scarf, respectively, and also to simulate the gradual failure process of the repairs. Stresses were plotted in the middle of the adhesive layer, and in the laminate/adhesive and adhesive/patch interfaces. Flatter σ_n and τ_{tn} stress distributions were obtained compared to SS and DS geometries (Kinloch 1990, Tong et al. 1995, Adams et al. 1997, Campilho et al. 2005, Campilho et al. 2009a). Inclusively, for a 2º scarf angle, σ_n stresses are practically nil, compared to τ_{tn} stresses. Slight stress concentrations were observed at the overlap edges, but only in a very restrict region. The influence of the scarf angle on stresses in the middle of the adhesive layer and failure load was investigated, for scarf angles between 2 and 45º. σ_n stresses increased gradually with the scarf angle, with a similar magnitude to the shear ones for a 45º scarf angle (Fig. 34 a). Shear stresses, on the other hand, tend to flatten, becoming practically constant for a 45º angle (Fig. 34 b).

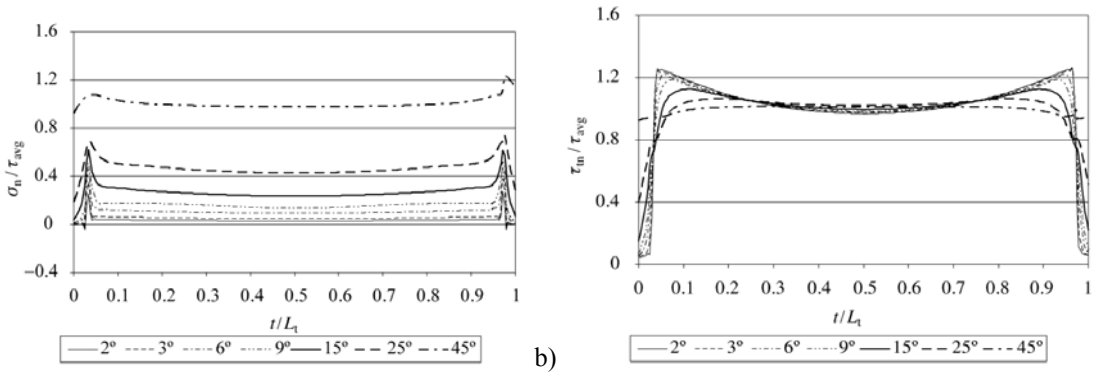

a) b)

Fig. 34 – σ_n (a) and τ_{tn} (b) stress distributions at the adhesive mid-thickness (Campilho et al. 2007a).

The repairs strength increased exponentially with the scarf angle reduction (Adkins and Pipes 1988, Odi and Friend 2004, Du et al. 2004, Objois et al. 2005, Campilho et al. 2007a, Wang and Gunnion 2008). An efficiency study was performed as a function of the laminates lay-up. Considering the better solution, i.e., the 2º scarf angle repair, a full strength recovery after repair was obtained for all the lay-ups, except the unidirectional laminate (47% of the undamaged laminate strength). Gradually smaller strengths were obtained increasing the scarf angle for all lay-ups. A

failure mechanisms analysis was also performed. An adhesive failure occurred with identical mechanical and fracture properties for the adhesive and laminate/adhesive and adhesive/patch interfaces. A cohesive failure was simulated reducing the cohesive mechanical and fracture properties of the adhesive. It was also concluded that the repairs strength depends almost exclusively on the strength properties. The low influence of the fracture properties is justified by the flat shear stress profiles, which rule the fracture of these joints, leading to an almost simultaneous softening onset for all cohesive elements and to a lesser influence of the adhesive and interfaces toughness.

2.2.1.3. Geometric changes

The work of Bogdanovich and Kizhakkethara (1999), concerning the behaviour of DS joints with unidirectional CFRP adherends under a tensile load, also focused numerically the effect of an adhesive fillet at the overlap edges. Fig. 35 (a) represents several tested configurations for the fillet, while Fig. 35 (b) shows the final solution adopted, using a curved fillet. The sub-modelling approach was used to obtain the stress distributions near the fillet. A 2D mesh was built (Fig. 35 b) using plane-stress 2D solid finite elements. Fig. 36 presents σ_y (a) and τ_{xy} (b) stress distributions in the adhesive layer, near the adhesive/adherend interface, with and without the fillet. A major reduction on σ_y peel and τ_{xy} peak stresses is observed using an adhesive fillet.

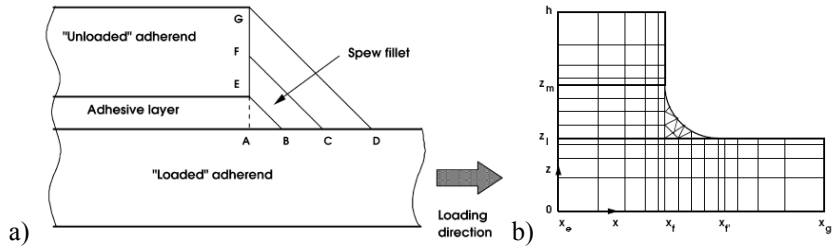

Fig. 35 – Tested fillet configurations (a) and final solution adopted (b) (Bogdanovich and Kizhakkethara 1999).

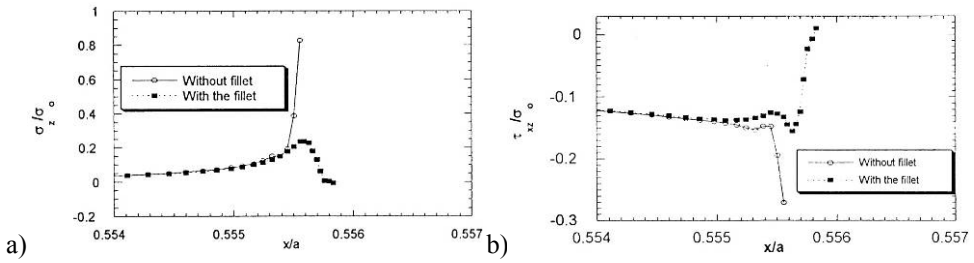

Fig. 36 – σ_y (a) and τ_{xy} (b) stress distributions (Bogdanovich and Kizhakkethara 1999).

Rispler et al. (2000) proposed a FEM optimization process of adhesively-bonded joints. Titanium and unidirectional CFRP reinforced tabs under a tensile load were considered in the analysis (Fig. 37). Four-node plane-strain solid finite elements were used. The optimization process consisted on determining the optimal shape of the adhesive fillet at the overlap edges, and was based on a FEM iterative procedure for the elements representing the adhesive. In each iteration, low stressed adhesive elements were removed from the model, and a new iteration initiated. This procedure was repeated until all the adhesive elements presented at least 20% of the maximum Von Mises stress of the entire structure. This methodology allowed obtaining flatter stress distributions in the adhesive layer along the bond length, eliminating the peak stresses usually found in these joints. Results showed that a 45º straight fillet accounting for all the tab

thickness was the optimal solution. Comparing this geometry with the initial one (Fig. 37), approximately 50 and 40% reductions were obtained on σ_y peel peak stresses in the adhesive and adherends, respectively (CFRP tabs and patches). Shear stresses in the adhesive layer and the assembly strength were not addressed in the analysis.

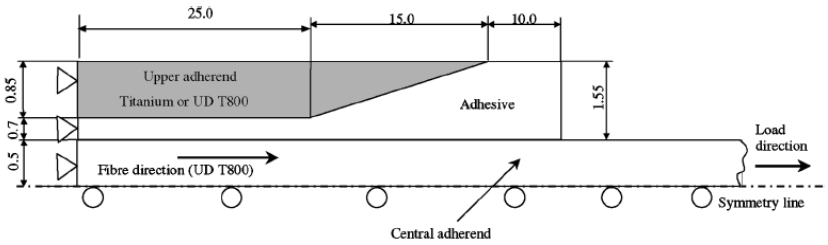

Fig. 37 – Geometry and boundary conditions of the reinforced tabs (Rispler et al. 2000).

Boss et al. (2003) extended the work of Ganesh and Choo (2002), analysing by the FEM the effect of laminate stiffness grading on the tensile stress distributions and strength of CFRP SL joints. The laminate stiffness grading was accomplished with two distinct approaches. In the first one, the laminates longitudinal E modulus was varied along its length (Fig. 16) by changing the braid angle of the fibres. Another technique consisted on chamfering the laminates at the overlap region (Fig. 38). Generally, stiffness grading led to a significant reduction on τ_{xy} peak stresses in the adhesive layer. Fig. 39 (a) and (b) compare σ_y and τ_{xy} stress distributions at the adhesive mid-thickness, respectively, for linear grading of the E modulus and laminate thickness, and the standard joint. In all cases, σ_y and τ_{xy} stresses were highest at the overlap edges. τ_{xy} peak stresses diminished using both optimization solutions. Oppositely, only the linear thickness grading effectively reduced σ_y peel peak stresses at the overlap edges.

Fig. 38 – Different chamfer shapes at the overlap region (Boss et al. 2003).

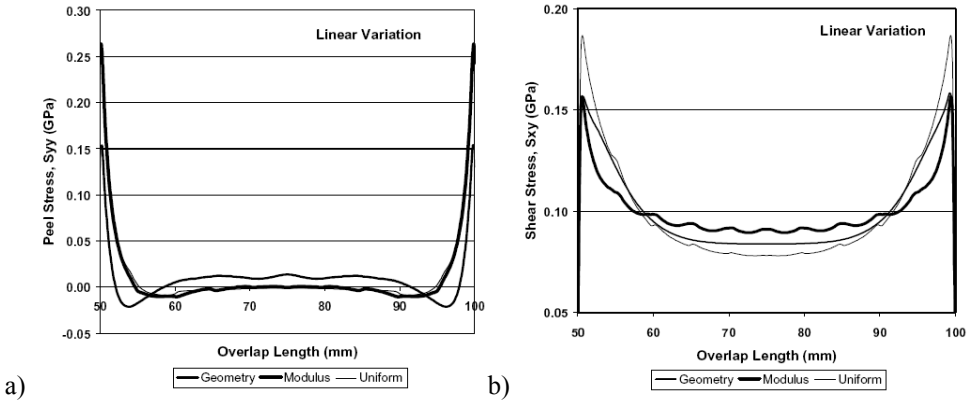

Fig. 39 – σ_y (a) and τ_{xy} (b) stress distributions at the adhesive mid-thickness (Boss et al 2003).

An innovating SL joint configuration was proposed by Ávila and Bueno (2004a, 2004b), consisting on a wavy geometry in the overlap region (Fig. 40). Sixteen plies E-glass/epoxy GFRP laminates, with the same number of yarns in the load and perpendicular directions, were used as adherends. Both experimental and FEM results allowed concluding that this improved configuration significantly increases the joints strength. The wavy-lap joint avoids the eccentricity of the

transmitted load, characteristic of the SL joints, developing σ_y compressive peak stresses at the overlap edges. Therefore, load transfer by the adhesive layer is more efficient, when compared to the flat SL joint, for which σ_y and τ_{xy} stresses peak at the overlap edges. Fig. 41 shows σ_y and τ_{xy} stress distributions at the middle of the adhesive thickness for standard SL joints (a) and wavy-lap joints (b).

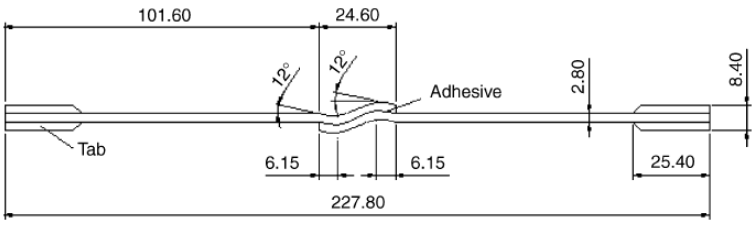

Fig. 40 –Wavy-lap geometry (Ávila and Bueno 2004a).

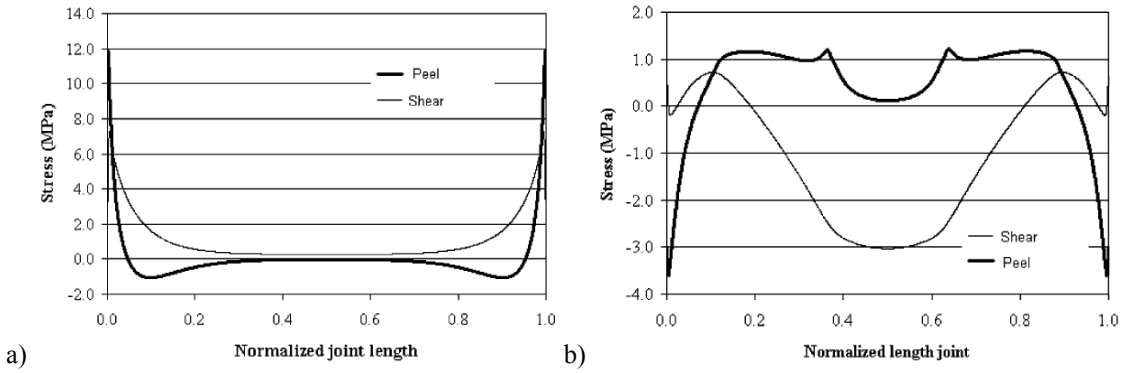

Fig. 41 – σ_y and τ_{xy} stress distributions in SL (a) and wavy-lap joints (b) (Ávila and Bueno 2004a).

The traditional σ_y and τ_{xy} stress profiles (Adams and Comyn 2000, Andruet et al. 2001, Li and Sullivan 2001, da Silva et al. 2009a) were obtained with the standard SL geometry (Fig. 41 a), peaking at the overlap edges. For the wavy-lap joints (Fig. 41 b), σ_y stresses were compressive at the overlap edges, although a peel region was identified at the overlap central region. τ_{xy} stress distributions are also highly influenced by this modification, with the wavy-lap joint suppressing τ_{xy} peak stresses at the overlap edges. These results show that the wavy-lap geometry increases the joint strength. Experimental testing was also accomplished.

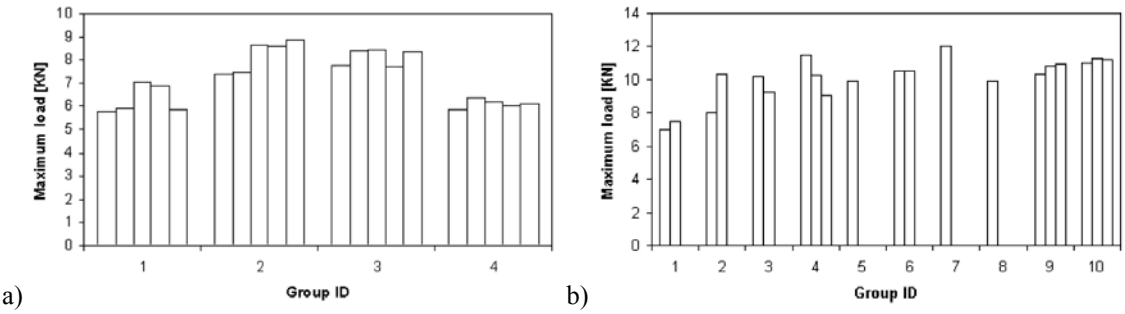

Fig. 42 – Maximum loads for the standard (a) and wavy-lap joints (b) (Ávila and Bueno 2004a).

Fig. 42 represents the maximum loads of the standard (a) and wavy (b) specimens. Groups two and three of the standard joints were bonded with a temperature of 28ºC and air humidity of 40%, while in groups one and four the air humidity was modified to 60%. Groups two and three showed a higher failure load, with the high levels of air humidity of the

other groups leading to a poor bonding. Only 75% of the wavy-lap specimens failed in the adhesive layer, while the other ones delaminated between the outer laminate plies. This was explained by the improved adhesive stress distributions, with the attainment of the laminate interlaminar strength and corresponding fracture prior to failure in the adhesive layer. An average 41% strength improvement to the SL joint was obtained with the wavy-lap configuration.

Tsai and Morton (1995b) carried out an experimental and FEM study on SL graphite-epoxy joints under tension, with and without a fillet at the overlap edges. The displacements fields were obtained with the MIM. Geometric linear and non-linear analyses were performed in ABAQUS®. Two solid finite elements were used through-thickness to simulate the adhesive layer and one element through-thickness was used for each laminate ply. The adhesive was modelled as an isotropic material, while the laminates were regarded as orthotropic. Experimental and numerical strains were compared at several loci in the joints, and a high agreement was found, considering the geometric non-linear FEM analysis. The linear geometric model overestimated the strains. Fig. 43 compares the experimental and FEM (geometric non-linear) results for the joints with and without fillet. Fig. 43 (a) compares the shear strains at the overlap edge. Fig. 43 (b) shows σ_y, σ_x and τ_{xy} stress distributions in the adhesive layer by the FEM. The experimental and numerical shear strains agreed reasonably. The joints with fillet showed a significant reduction of shear peak strains at the overlap edge. In addition, the fillet reduced peel and shear peak stresses at the overlap edge.

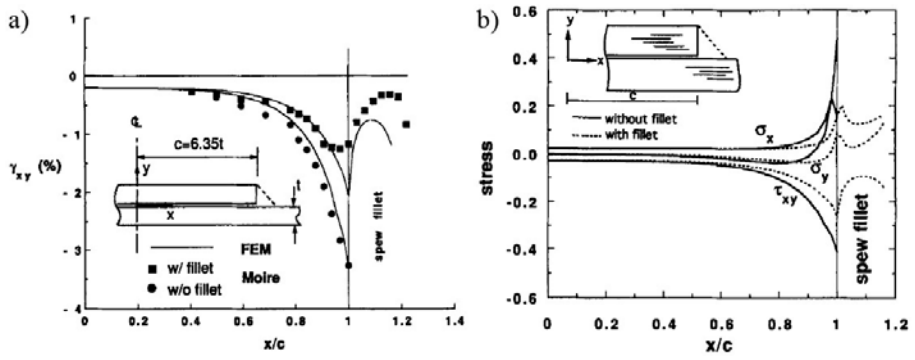

Fig. 43 – Experimental and numerical shear strains (a) and FEM stresses (b) at the overlap edge (Tsai and Morton 1995b).

Fessel et al. (2007) performed a 2D experimental and FEM analysis of steel SL joints under a tensile load. Wavy, improved wavy and reverse-bent geometries were evaluated (Fig. 44). The reverse bent geometry with out-of-plane substrates presented the best results in terms of stress distributions, since the maximum principal stresses in the adherends were located at their outer surface.

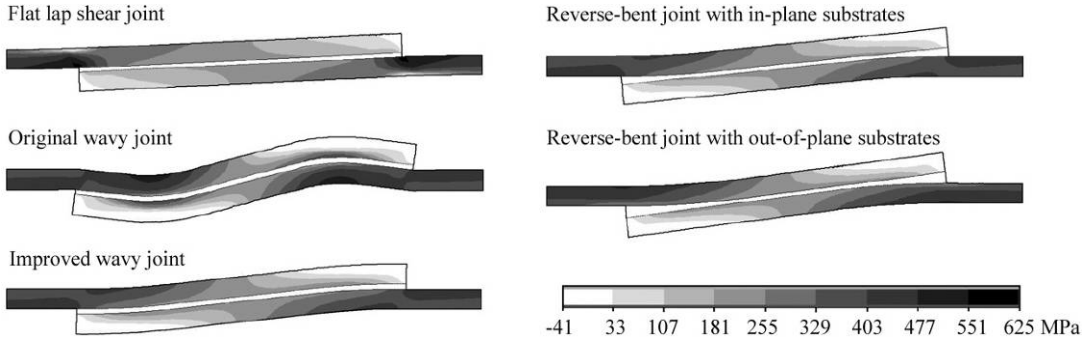

Fig. 44 – Principal stresses on different joint geometries (Fessel et al. 2007).

σ_y and τ_{xy} stresses are plotted in Fig. 45 (a). Results showed a major reduction of the σ_y peel and τ_{xy} peak stresses at the overlap edges for all modified geometries, comparing with the flat lap shear joint, especially for the reverse-bent geometry. The wavy and reverse-bent geometries were found to be particularly valuable for joints with FRP adherends, since σ_y peel stresses were highly reduced at the overlap edges, thus reducing the risk of delaminations. Several parameters were studied for the reverse-bent joint, such as the joint eccentricity and adhesive thickening size at the overlap edges. Aligned substrates (with zero eccentricity) led to the best results and a fillet with 15% the size of the overlap length maximized the joint strength. Experimentally, flat lap-shear and reverse-bent joints were tested considering three steels for the adherends and overlap lengths of 10 mm (Fig. 45 b) and 20 mm. Results showed strength improvements up to approximately 40%, depending on the adherends material and the overlap length.

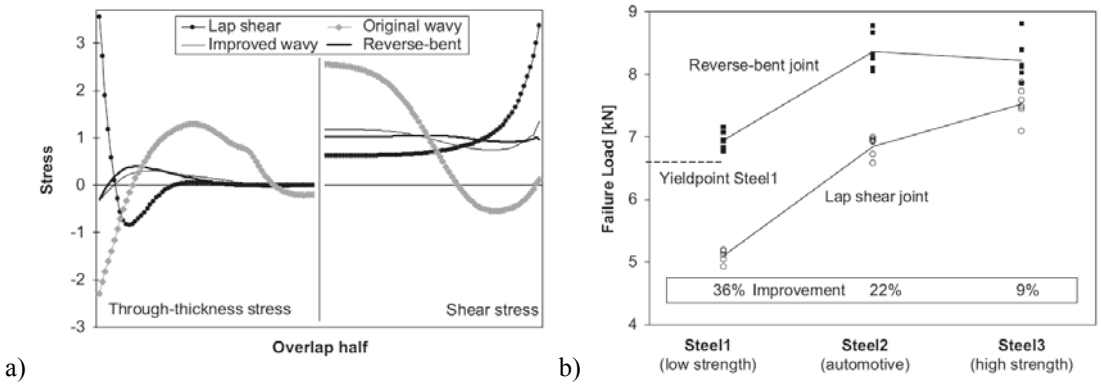

Fig. 45 – σ_y and τ_{xy} stresses (a) and failure load for an overlap length of 10 mm (b) (Fessel et al. 2007).

2.2.2. Experimental analysis

Experimental work on adhesively-bonded assemblies was extensively addressed, focusing on the failure loads and failure modes as a function of several geometric and material parameters (Kairouz and Matthews 1993, Charalambides et al. 1998b, Schubbe and Mall 1998, Baker et al. 1999, Bartholomeusz et al. 1999, Huang et al. 2000, Kayupov and Dzenis 2001, Berry and d'Almeida 2002, Kim et al. 2003, Qin and Dzenis 2003, Hamoush et al. 2005). It is also habitually used to validate theoretical and FEM models for the structures mechanical behaviour (Keller and Vallée 2005a, Vallée and Keller 2006, Xiao et al. 2004a, Xiao et al. 2004b), to validate failure criteria, comparing the experimental and numerical failure loads (Tong 1997, Tong et al. 1997, Sheppard et al. 1998, Shin and Lee 2003, Keller and Vallée 2005b), and also in the subject of CZM's applied to bonded structures, to evaluate their adequacy in predicting the failure loads and damage paths (Kafkalidis and Thouless 2002, Liljedahl et al. 2006, Campilho et al. 2008a, Campilho et al. 2009b). The next Sub-Section addresses some of the most prominent works on these subjects.

2.2.2.1. Single and double-lap/strap assemblies

Soutis et al. (1999) complemented their numerical work on 3D CFRP DS repairs under a compressive load (Fig. 21 a) with experimental testing. $[(\pm 45/0_2)_3]_S$ and $[(\pm 45/0/90)_3]_S$ lay-ups were considered and named L_1 and L_2, respectively. Damage initiation on all repairs occurred transversely at the hole, at lower loads than the undamaged laminates. The compressive strength of the repairs was normalised by the mean undamaged strength of the laminates, equal to 776.2 MPa and 571.1 MPa for lay-ups L_1 and L_2, respectively. No significant differences on the repairs strength was found for

the evaluated values of patch thickness. However, the damage process at the repaired region was different and failure initiation in the adhesive layer was prone to occur at lower loads for thicker patches. The residual strength of the repairs varied between 65% and 80% of the laminate undamaged strength, and was approximately 49% for the open-hole laminate (without using patches). An approximate 8% additional strength improvement was obtained repairing L_1 laminates with L_2 patches instead of L_1 ones, i.e., using patches more compliant in the load direction, compared to the laminates. Plugging the repair hole resulted on a strength improvement of approximately 20%. An approximate 90% strength recovery was achieved repairing a L_2 laminate with a 1 mm thick L_2 patch and plugging the repair.

Hu and Soutis (2000) completed their numerical work with an experimental evaluation of the failure modes and strength of CFRP DS repairs under compression (Fig. 46), to validate the numerical predictions. Damage initiated with adhesive plasticity and patch debonding at region B, which subsequently caused a significant increase of compressive stresses in the laminate at region A, leading to fibre microbuckling and delamination. Following, delamination propagated along the laminates width. Failure was attained when the buckling length reached a critical value of 2-3 mm.

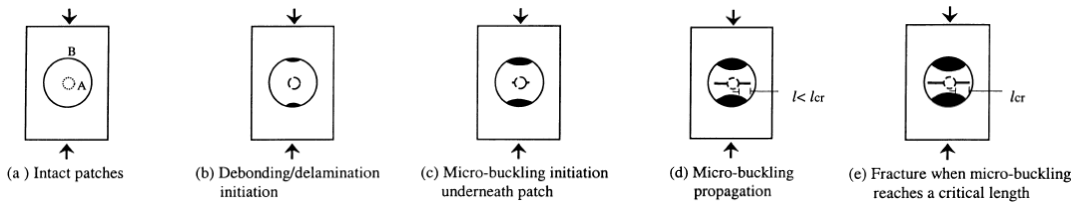

Fig. 46 – Experimental failure mode of a DS repair under compression (Hu and Soutis 2000).

The work of Reis et al. (2005), concerning SL GFRP joints under a tensile load, also included experimental testing. The shear stress-shear strain (τ_{xy}-γ) curves of the adhesive layer were obtained for overlap lengths of 15, 30, 45 and 60 mm (Fig. 47). The 30 mm overlap length joint presented the highest shear stiffness and strength. The failure strain was found to be identical between the overlap lengths evaluated. These results are consistent with the works of Jain and Mai (1999), Balkova et al. (2002), Kafkalidis and Thouless (2002), Keller and Vallée (2005b) and de Morais et al. (2007), where the joints strength increased at a decreasing rate with the overlap length.

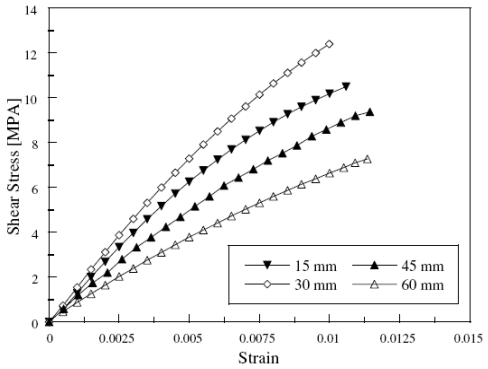

Fig. 47 - τ_{xy}-γ curves for different overlap lengths (Reis et al. 2005).

Kim et al. (2006) presented an experimental work on the tensile failure mode and strength of CFRP SL joints, using different techniques to bond the laminates (Fig. 48): co-curing the laminates with (a) and without adhesive layer (b), and adhesive bonding after curing the laminates without (c) and with fillet (d). The laminates consisted on carbon-

epoxy pre-preg with 0.155 mm ply thickness and a $(0)_{10}$ lay-up. The manufacturing procedure for the specimens co-cured with the adhesive consisted on positioning an adhesive film during the lay-up, followed by simultaneous curing of the entire set. Some parameters were studied, such as the contact pressure between the laminates during the adhesive curing (leading to different adhesive thicknesses), the bonding surfaces roughness, and the fillet shape and dimensions.

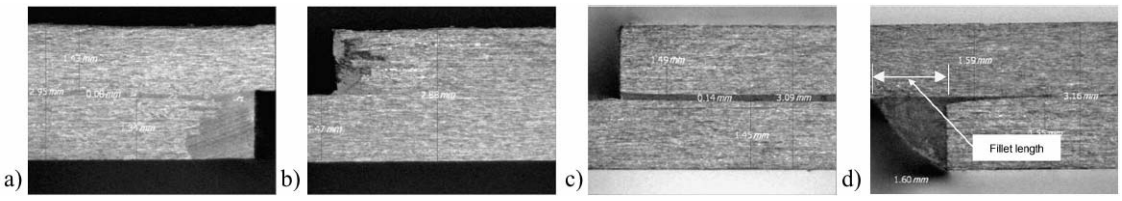

Fig. 48 – Different bonding solutions (Kim et al. 2006).

The mechanical properties of the adhesives used were obtained experimentally, and it was concluded that the adhesive film used for the co-cured specimens presented higher mechanical properties (approximately 50%) than the adhesive used for the other techniques. For the joints bonded after curing the laminates (Fig. 48 (c) and (d)), damage initiated in the adhesive at the overlap edges, growing slowly for 1 to 3 mm. Afterwards, the joints failed by abrupt crack growth. The failure surfaces revealed a mixed adhesive and cohesive failure, accompanied by fibre pull-out of the outer laminates plies (justified by the surfaces roughness, with higher values of roughness leading to a more significant fibre pull-out). For the co-cured specimens without adhesive film, an abrupt failure occurred at the interface between the laminates. An interlaminar failure was found for the co-cured specimens with an adhesive film, due to the higher strength properties of the adhesive film, compared to the laminate interlaminar strength.

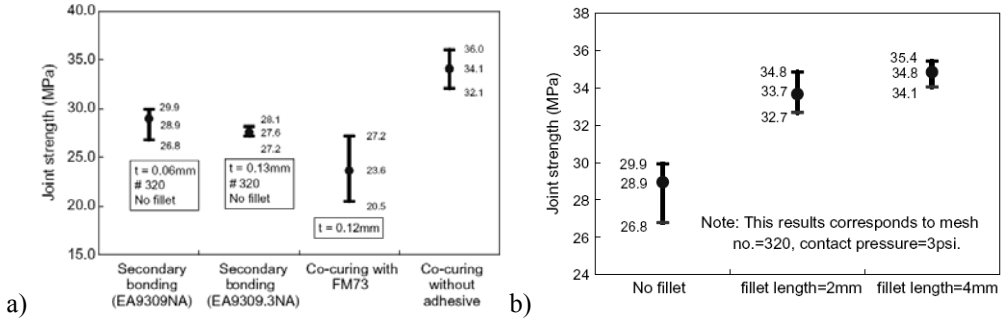

Fig. 49 – SL joints strength for secondary bonding with two adhesives and no fillet, and co-curing with and without adhesive (a) and for secondary bonding with and without fillet (b) (Kim et al. 2006).

The joints strength, regarded as the ratio between the failure load and the bonding area of each individual specimen, is presented in Fig. 49. The lowest failure load was obtained for the co-cured specimens with an adhesive film. The most efficient solutions were co-curing without adhesive (Fig. 49 a) and secondary bonding with a 4 mm length fillet (Fig. 49 b). Different studies showed that abrading the surfaces significantly improved the joint strength. On the other hand, increasing the adhesive thickness led to a reduction of the joints strength.

The work of Liu and Wang (2007) mentioned earlier, concerning 3D DS repairs (Fig. 2 a) under tension, also included experimental testing, varying the patches diameter and thickness, and the patches lay-up (Table 2). Mode A and mode B failure modes, described earlier in Sub-Section 2.2.1.1, were obtained experimentally (Fig. 50 (a) and Fig. 50 (b)), respectively). Fig. 50 (c) compares the experimental and numerical strengths.

Table 2 – Groups of specimens tested (Liu and Wang 2007).

Group	Patch diameter (mm)	Patch thickness (mm)	Patch lay-up	Experimental failure mode
1	40	0.35	[±45]	B
2	40	0.7	[0/±45/90]	A
3	50	0.875	[0_2/±45/90]	A

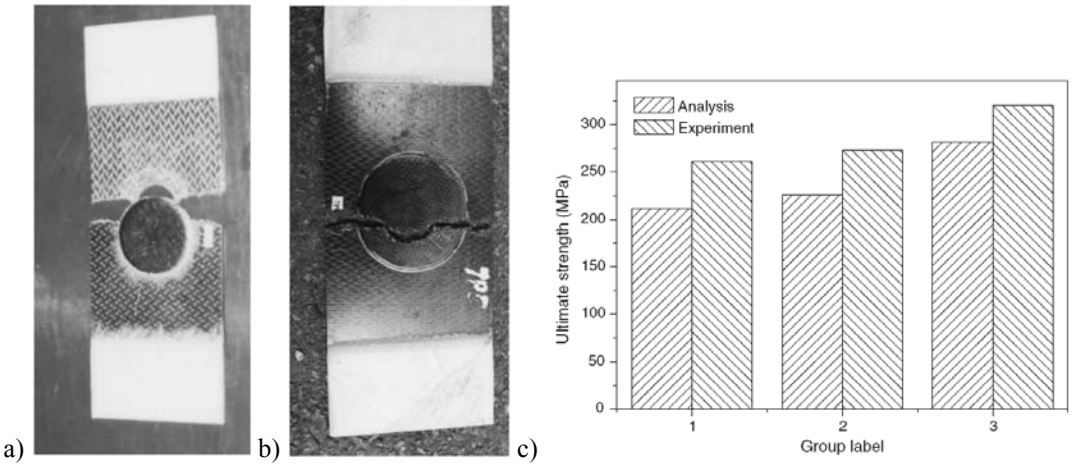

Fig. 50 – Mode A (a) and mode B (b) failures; experimental and numerical strengths (c) (Liu and Wang 2007).

Specimens from group 1 showed a mode B failure (Fig. 50 b), with transverse rupture of the patch and the laminate almost simultaneously. This behaviour was justified by the patches impossibility to prevent a premature crack growth in the laminate at the stress concentration regions, i.e., transversely near the hole. Concurrently, the patches cracked transversely, owing to their small thickness. Fracture for groups 2 and 3 initiated in adhesive layer, due to the significant stresses caused by the thicker patches. After losing the support of the patches, the laminate failed by transverse cracking initiating at the hole edges (mode A failure, Fig. 50 a). This behaviour is consistent with the numerical analysis described earlier. Evaluating both analyses, it is possible to conclude that for the material and geometric parameters evaluated, the failure mode is ruled by the patch thickness (recalling that numerically thick patches led to a mode A failure, with thin patches causing a mode B failure, similarly to the experiments). On the repair strengths, group 3 revealed the best results, which is justified by the larger diameter of the patches. Since groups 1 and 2 show identical strengths, it is concluded that this parameter, unlike the failure mode, is ruled by the patch diameter.

2.2.2.2. Scarf assemblies

The scarf repair technique was addressed by Found and Friend (1995) on $[0,45,0,-45]_S$ lay-up CFRP laminates repaired with a 3º scarf angle, considered a tensile load applied diagonally to the specimens (Fig. 51 a). Stresses and strains at several loci at the repair region were obtained with strain gauges adhesively-bonded to the structure. An additional 0º over-laminating ply was bonded at the larger surface of the embedded patch, assuring a more balanced load transfer. Fig. 51 (b) shows the load-strain plots at different regions. Test results showed a strength improvement of the damaged laminates from 24 to 62%, depending on the repair conditions (temperature and curing time of the patches). Additionally, for the loading applied, the repair strength was ruled by the laminate buckling, which was responsible for the patch debonding onset, leading to a catastrophic failure.

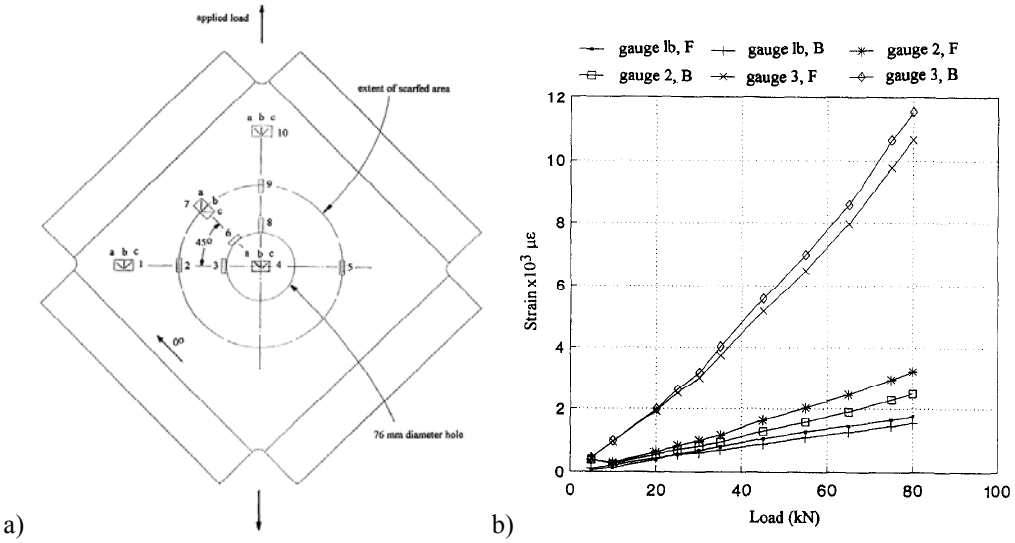

Fig. 51 – Strain gauges loci (a) and load-strain plots (b) (Found and Friend 1995).

Baker et al. (1999) also studied experimentally and by FEM simulations a scarf repair on a horizontal stabilator of a F/A-18 spacecraft composed by an aluminium honeycomb core and CFRP faces, tested under a bending load. Fig. 52 (a) schematically represents the repair technique, emphasising on the composite faces. The specimen geometry and loading conditions are shown in Fig. 52 (b).

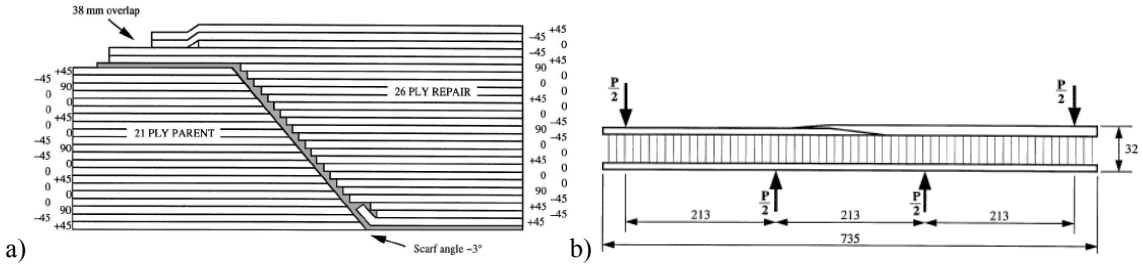

Fig. 52 – Schematic representation of the repair (a) and geometry (b) (Baker et al. 1999).

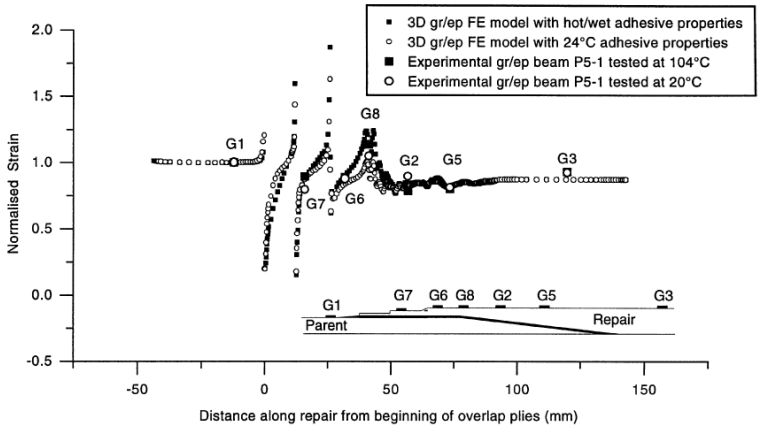

Fig. 53 –Experimental and numerical strains at different regions (Baker et al. 1999).

The specimens were tested at -40ºC, room temperature and 104ºC, in dry and wet conditions. Eight strain gauges were glued at several locations of the repaired surface of the structure (Fig. 53) to monitor the longitudinal strains during the test. The adhesive layer failure was cohesive for all test conditions. At 104ºC, the failure strains were reduced by 50%,

compared to the specimens tested at room temperature. Fig. 53 compares the experimental strains at eight different locations of the repair region with the FEM simulations, in the elastic stages of loading. Strains are normalized by the laminate strain at gauge G1, placed outside the repair region. The authors emphasized on the acceptable consistency between the test results and FEM simulations.

The work of Charalambides et al. (1998b) investigated experimentally the tensile performance of adhesively-bonded CFRP scarf joints with $[\pm 45/0/90]_{2S}$ quasi-isotropic lay-ups and 2º scarf angles under static and dynamic loads. The influence of extreme temperature and humidity was also assessed. The failure modes of these joints are presented in Fig. 54. Under a static load, a full recovery of the laminate undamaged strength was achieved (500 MPa). However, the failure mode varied according to the environmental conditions. In fact, under typical conditions (20ºC and dry) the joints failed in type A. Under high temperature and humidity for four months, a type B failure occurred. Under the same conditions for sixteen months, type A, B and C failures were noticed, with preponderance of type A and B failures. Under a dynamic load, the authors observed a strength reduction of approximately 50%, when compared to the static results. The failure mode was also highly dependent on the environmental conditions. In fact, under typical conditions, a type C failure was observed, while under high temperature and humidity for periods of four and sixteen months, type A, C and D failures were obtained, with prevalence of type A and C failures.

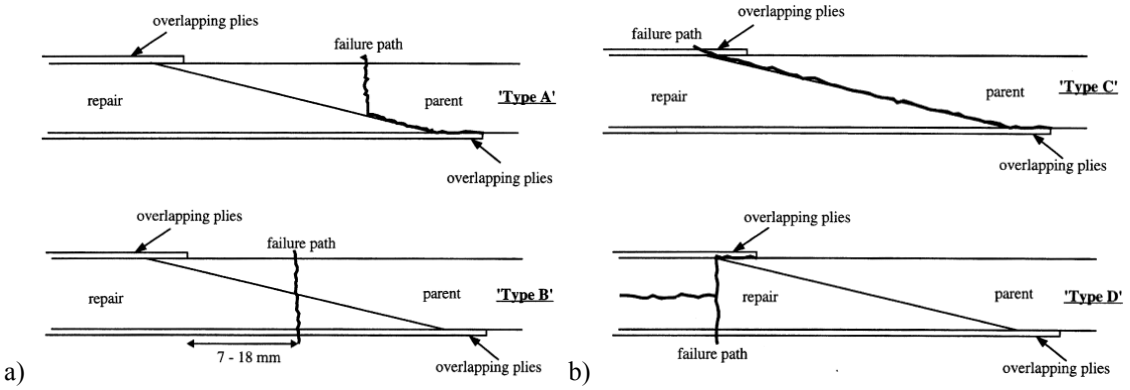

Fig. 54 – Experimental failure modes of the scarf joints (Charalambides et al. 1998b).

2.3. Strengthening and repair of wood structures with composites

Wood is amongst the oldest construction materials in the world and has been widely used to build large-scale structures like bridges, lightweight warehouses and residential buildings, railroad infrastructures and telephone poles (Akbiyik 2005, Radford et al. 2002). This material is available in most parts of the world, is a renewable natural resource, presents a natural and aesthetically pleasing appearance, has a notable resistance under both tension and compressive loads, which are nearly unique as specific properties (i.e., divided by its weight), and performs well under the influence of wind and especially earthquake loads. Additionally, wood structures present a high durability, as long as they undergo correct maintenance during their life, adding the possibility of the structures assembly under cold and wet conditions, without influence on the beams mechanical properties. Wood constructions can also sustain overloads for short periods and are easier to repair and rehabilitate because of their small specific weight. Fastened or bolted connections between wood elements usually present interesting damping characteristics, due to the high deformation capacity of wood, especially in the direction perpendicular to fibres (Ou and Weller 1986, Premrov et al. 2004a,

Premrov et al. 2004b, Akbiyik 2005, Borri et al. 2005, Akbiyik et al. 2007, Corradi and Borri 2007). However, without proper maintenance, wood deteriorates due to fungi and insects, and swelling and shrinkage caused by variations on ambient humidity. In fact, these dimensional variations warp and twist wood members, lowering their strength and introducing localized stress concentrations within the structures (Marshall 1998). The poor shear strength of wood in the direction parallel to grain and its reduced tensile strength in the perpendicular direction should not be disregarded as well (Triantafillou 1997, Borri et al. 2005, Akbiyik et al. 2007). **Several studies were published in the last decades about the reinforcement and repair of wood structures with aluminium/steel and composites**.

Reinforcement can be used for different purposes, such as increasing the load-carrying capacity of the structure, improving the safety margins, extending the service life or modification of the design codes (Ebeling 1990, Humphreys and Francey 2004, Akbiyik et al. 2007). However, since the tensile strength of wood beams in the grain direction is not much lower than its compressive strength, the applications of CFRP to reinforce wood are not as widespread as in masonry or especially in concrete structures (Premrov et al. 2004a). **Repairing** aims to restore the structures strength after damage due to aging and environmental degradation, poor initial design or construction, lack of maintenance or short duration episodes such as overloads and earthquakes (Triantafillou 1998a). Reinforcement or repairing are particularly interesting for large wood beams, since their replacement is becoming increasingly difficult, owing to the limited availability of large wood trunks. Three traditional repair methods are currently used for wood structures, excluding the members replacement (Wheeler and Hutchinson 1998): carpentry-joined repairs, consisting on the replacement of deteriorated wood portions by new ones with a pressure fit union to the structure (Ebeling 1990); mechanical methods, in which reinforced elements are bolted in position (Windorski et al. 1997, Soltis et al. 1998, Natterer 2002); and resin repairs, characterized by the damaged material removal and casting of resin as a filling material (Avent 1985, Avent 1986, Wheeler and Hutchinson 1998). Resin repairs have the advantages of avoiding dismantling of the structure and also in-situ application with little disruption to the historic fabric of buildings.

In recent years, composite materials, which are already extensively used in several high performance applications in the aerospace, automotive, marine and military industries (CFRP), as well as in house-hold and leisure appliances (GFRP), are gradually gaining acceptance in the construction industry, especially in the area of structural strengthening and repair. Moreover, in the last decades, seismic retrofit of concrete beams with CFRP strips has been extensively used, especially in earthquake prone areas (Triantafillou 1998a, Neale 2000). In fact, these materials offer an outstanding set of benefits, compared with conventional engineering materials (Triantafillou 1998a). Unidirectional composites are ideal for the reinforcement and repair of wood beams under tensile or bending loads without changing significantly the beams stiffness, are widely available in the form of thin pultruded elements of different shapes (e.g. Sika® CarboDur strips) with continuously decreasing costs, present a lighter weight than conventional materials, are corrosion resistant and are flexible, due to the small thickness necessary to guarantee the desired level of reinforcement or repair, which allows an easier transportation to the operation site. Moreover, wood is tolerant to large strains before failure, necessary to develop the characteristic high strength of composite materials (Humphreys and Francey 2004). GFRP composites are also economically competitive with the traditional reinforcement materials, such as steel or aluminium, while keeping an acceptable performance (Premrov et al. 2004a, Corradi and Borri 2007). CFRP composites are still not used as extensively as GFRP ones (Pirvu et al. 2004), even though a recent study by Dagher and Lindyberg (2000) showed that CFRP and GFRP materials compare similarly in terms of stiffness and strength improvement as a function of the reinforcement cost. This is caused by the higher value of longitudinal E modulus and lower strain to failure of CFRP

than GFRP materials. The disadvantages of these materials to reinforce or repair wood structures lie on their elevated cost, in the case of CFRP materials, difficulty to cost accurately non-standard projects, lack of widespread use and adequate experimentation, especially on antique wood elements, which hampers the confidence of designers on using these materials, absence of yielding prior to failure, higher degree of workmanship required than for traditional reinforcements, problems of joining and connections, and bonding issues between the FRP and wood, due to the dimensional changes of the wood elements caused by the moisture changes (Steiger 2002, Pirvu et al. 2004, Premrov et al. 2004a, Humphreys and Francey 2004, Corradi and Borri 2007). Other issues, such as the poor bonding on wood treated by preservatives and with unfilled splits or checks, and also the poor aesthetics of the repair, must be taken into account, regardless the reinforcement or repair material.

The study of wood structures reinforced with composites dates back to the 1980's and has been focused by several investigators since then (Fardis and Khalili 1981, Meier 1987, Rostasy 1987, Triantafillou and Plevris 1991, Plevris and Triantafillou 1992, Triantafillou and Deskovic 1992, Meier and Winistorfer 1995, Triantafillou 1997, Qiao et al. 1998, Gentile et al. 2000, Johns and Lacroix 2000, Svecova and Eden 2004, Borri et al. 2005). Oppositely, on the repair of wood structures with composites, only a few studies were published in the last decades (Radford et al. 2002, Ehsani et al. 2004, Akbiyik 2005, Lopez-Anido et al. 2003, Lopez-Anido et al. 2005, Akbiyik et al. 2007, Lamanna et al. 2007, Alam et al. 2009). Moreover, most of the techniques proposed were not specifically developed for in-situ application and require the damaged members dismantlement, making them less appealing (Radford et al. 2002). These techniques involve adding a bolted or fastened member in parallel, stitch bolting, inserting steel or fibreglass dowels, post-tensioning the member, epoxy filling approaches, bonding of thin FRP plates on the beam exposed faces and wrapping the beams with composites at the damaged region (Triantafillou 1998b). The wrapping technique can only be applied with full access to the damaged portion of the beam, implying that in many cases the removal of the damaged member is required. However, this approach grants a considerable strength increase without changing the stiffness considerably. In the plate bonding repairs the FRP sheets shall be bonded with the fibres aligned with the principal stress direction, e.g. longitudinally at the tension face of a wood member under bending (Bakis et al. 2002). **The repair of a wood member can be performed due to natural defects, deterioration or in-service damage**.

Natural defects in wood reduce its strength and durability. The most common types of defects are knots, splits, checks, wanes, shakes, heart checks and natural decay. Knots are circular material discontinuities that reduce the strength of wood members (Fig. 55 a). These defects are more detrimental to the tensile strength than the compressive strength of wood beams, since under tension they are prone to induce cracks. As a result, if a wood beam with knots is to be used under bending, it is advisable to leave the knots in the compression regions (Bodig and Jayne 1982). Splits represent cracks in the length direction across the annual rings, which extend to the inner regions of the beam (Fig. 55 b), and severely weaken the wood beams (Rammer 1999, Falk et al. 2000, Green et al. 2001, Akbiyik et al. 2007). Checks are similar phenomena, but occurring locally at the beam edges with a random orientation (Christy et al. 2005, Fig. 56 a). Splitting and checking are amongst the most common defects found in exposed wood bridge members and wood columns, and can result from swelling and shrinkage arising from changes on the moisture contents in the surrounding environment (Rammer and McLean 1996, Rammer et al. 1998, Akbiyik et al. 2007). Because of these defects, unprotected crack surfaces emerge, neutralizing the benefits of eventual superficial treatments applied to the wood members. Fig. 56 (b) and (c) represent schematically wanes and shakes, respectively. Wanes are wood voids on the sharp edges of wood members (Lee et al. 2003a), whereas shakes represent lengthwise discontinuities between rings

(Akbiyik et al. 2007). Finally, heart checks, extending deep in the wood, show up in wood members due to differences in tangential and radial shrinkage (Green et al. 2001, Fig. 56 d).

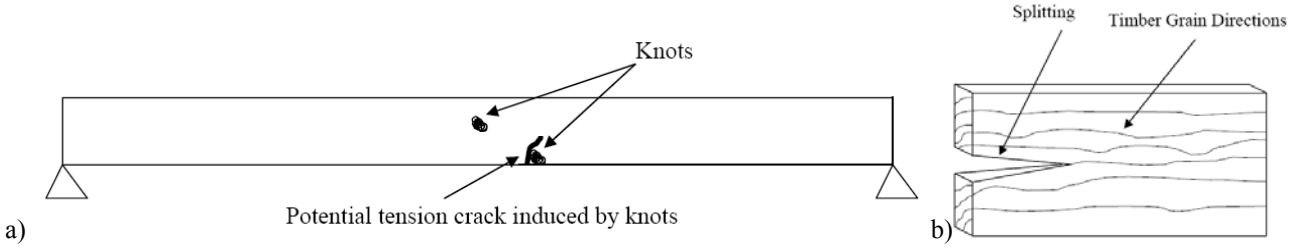

Fig. 55 – Natural defects in wood: knots (a) and splits (b) (Akbiyik 2005).

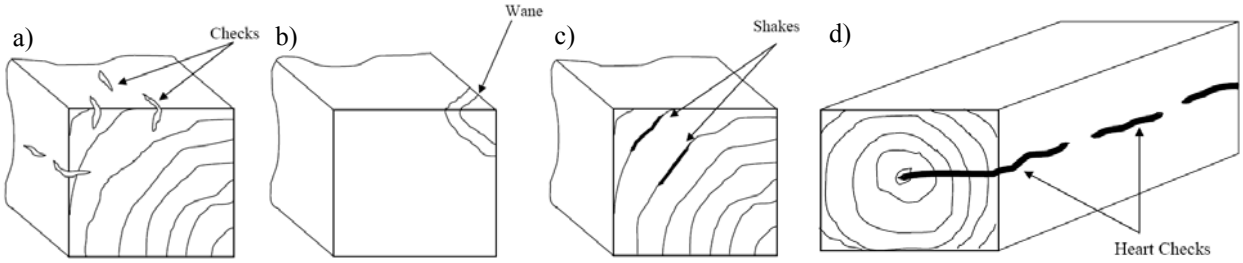

Fig. 56 – Natural defects in wood: checks (a), wanes (b), shakes (c) and heart checks (d) (Akbiyik 2005).

Deterioration or decay of wood members is mainly caused by bacteria, moisture, fungi and insects, leading to a decrease on hardness, stiffness and strength of wood members, breaking down the internal structure of wood (Watt and Swallow 1996, Radford et al. 2002, Akbiyik 2005). Deterioration can be stopped by treating the wood exposed surfaces with fungicides and pesticides (Richardson 1995). **In-service damage** of wood can occur in different ways, e.g. fatigue, overloads, earthquakes, human intervention, adverse environmental conditions or aging. In this review, the most common failure modes under static bending will be described (Fig. 57). These are simple tension and compression, cross-grain tension and horizontal shear (Akbiyik 2005, Akbiyik et al. 2007, Lamanna et al. 2007).

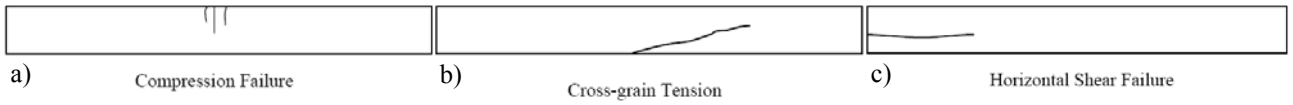

Fig. 57 – Most common failures under static bending: compression failure (a), cross-grain tension (b) and horizontal shear (c) (Akbiyik 2005, Akbiyik et al. 2007, Lamanna et al. 2007).

Compression failure is a typical failure mode in low-density wood (Alam et al. 2009, Campilho et al. 2009c). Moreover, it can also occur in beams under bending reinforced in the tension face, since the reinforcement strips change the location of the neutral axis, providing a larger cross-section to bear the compressive stresses (Chajes et al. 1995, Davalos et al. 1999, Bakis et al. 2002, Humphreys and Francey 2004). Tension failure is similar, but is more likely to occur in high-density wood. Wood members usually fail by cross-grain tension when their fibres are not perfectly aligned with the beam major axis. This occurs when trees that have grown spirally or with a pronounced taper are cut for lumber. Cross-graining drastically reduces the tensile strength of wood, typically leading to abrupt and early bending failures (Zandbergs and Smith 1988, Winandy 1994, Green et al. 1999, de Lorenzis et al. 2005). Horizontal shear failure develops near the neutral plane of the wood beam, and normally initiates from checks and shakes acting as planes of weakness for shear failure (Bodig and Jayne 1982, Akbiyik 2005). Wood members showing sharp changes in growth ring density or extremely low humidity contents are more likely to fail by horizontal shear (Bodig and Jayne

1993). Vertical shear failure, which consists on a cross-sectional transverse fracture of the wood member, has also been reported in timber beams (Itagaki et al. 2003), although not being frequent.

Several studies were published on the reinforcement of wood beams with composites. One of the pioneering works on this subject was carried out by Theakston (1965), which addressed the reinforcement of wood members with resin-impregnated GFRP plates bonded with an epoxy adhesive. Experimental tests showed a 39% increase of the bending strength. Spaun (1981) chose *E*-glass fibre rovings to reinforce the wood beams, because of their reduced cost, and a phenol-resorcinol adhesive to bond the reinforcement. A significant increase of the unreinforced beam tensile strength was attained, in proportion to the fibre-volume fraction of the *E*-glass reinforcement. Leichti et al. (1993) reported on the installation of aramid fibre reinforced glulam members for a pedestrian bridge in Oregon. Tingley (1994) described a method of reinforcing glulam timber using aramid fibre and glass-reinforced laminates. The work of Borri et al. (2005) is a comprehensive study concerning the reinforcement of wood beams with CFRP laminates. The *Four-Point Bending* (4PB) test configuration was used to characterize the stiffness, ductility and strength of the reinforced beams. Unreinforced beams were also tested to evaluate the effectiveness of the strengthening interventions. Unidirectional carbon reinforcing fabrics embedded in an epoxy resin were used as reinforcement. Fig. 58 illustrates the evaluated reinforcement schemes, consisting on adhesively-bonding two (Fig. 58 a) or three (Fig. 58 b) CFRP plies at the tension face of the beams, bonding two pairs of CFRP plies laterally to the tension face of the beams (Fig. 58 c), and strengthening with one (Fig. 58 d) or two (Fig. 58 e) CFRP bars bonded to the wood tension face using epoxy resin. Pre-stressed reinforcements using the schemes presented in Fig. 58 (a) and (b) were also evaluated. The pre-stressing technique consisted on the application of a 30 mm displacement at the beams mid-span, followed by adhesively-bonding of the CFRP laminates in the compression face and curing under this deformed configuration. With this procedure, an increase on the stiffness properties of the wood beams was achieved, since the CFRP strips were already tensioned in the beams unloaded condition.

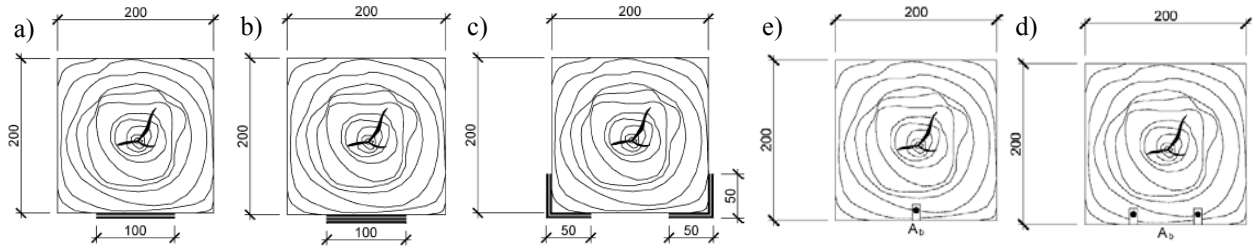

Fig. 58 – Wood beam reinforcement schemes (Borri et al. 2005).

The experiments showed that reinforcing with CFRP sheets in the tension face (Fig. 58 (a) and (b)) significantly increases the bending characteristics of the beams. Using three sheets of CFRP (Fig. 58 b) resulted on a 60% increase of the beams flexural strength. Oppositely, reinforcement with CFRP bars led to a poor strength improvement. The sole advantage of this reinforcement technique is related to its aesthetics, since the CFRP bars are inserted in the wood beam, therefore not visible. Regardless the reinforcement method, failure always occurred within the wood beams, with an adhesion failure between the CFRP and wood taking place only afterwards. The stiffness improvements due to the reinforcements were not significant, with maximum values of 30% for the pre-stressing technique on the CFRP sheets. A developed numerical procedure, based on the Bazan-Buchanan law, allowed a fairly accurate estimation of the failure loads of the reinforced beams. Oppositely to the reinforcement studies, not many works were carried out in recent years on the repair of wood structures with composites. The M.Sc. Thesis of Akbiyik (2005), whose major findings were

afterwards published (Akbiyik et al. 2007), focused on the repair of large-scale wood beams with horizontal checking and splitting along their length. A preliminary survey allowed defining the five most important types of damage in wood beams (Fig. 59). Type 1 damage corresponds to internal deterioration. Type 2 damage is a full width splitting in the tension face. This damage mechanism, also referred as cross-grain tension, is caused by small grain misalignments with the beam length direction (angles below 15º). The third damage type is side or corner damage or full width vertical splits. Horizontal splitting approximately at the mid-height of the beam corresponds to type 4 damage. This is the most common damage mechanism in bridge structures, which often extends to the entire beam length. This damage emerges from shear stresses and severely reduces the strength of wood members. Finally, any type of damage near the face of the pier cap, such as deterioration, side damage, crushing or splitting is included in type 5.

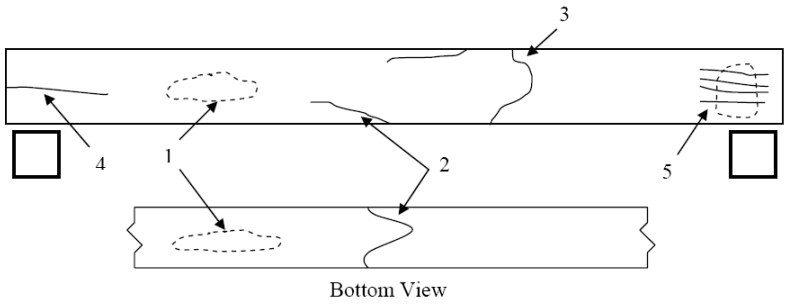

Fig. 59 – Most common damage types in wood beams (Akbiyik 2005, Akbiyik et al. 2007).

Several repair solutions were tested on beams damaged with horizontal splits (type 4 damage, Fig. 59). These consisted on using long hex bolts and lag-screws securing the top and bottom halves of the wood beam at several positions along its length, with different spacings and orientations (Fig. 60 (a) and (b)). The feasibility and effectiveness of attaching plywood and GFRP plates to the side faces of the beams with lag screws was also investigated (Fig. 60 c). The GFRP plates were composed of several plies of continuous strand *E*-glass mats, with a total thickness of 6.4 mm. Three beams (B1, B2 and B3) with checks along the length (Fig. 56 a) were tested in 4PB up to failure, occurring by horizontal shear damage (type 4 damage, Fig. 59). Another three beams (B4, B5 and B6) already showing evidence of horizontal shear damage were also included in the analysis.

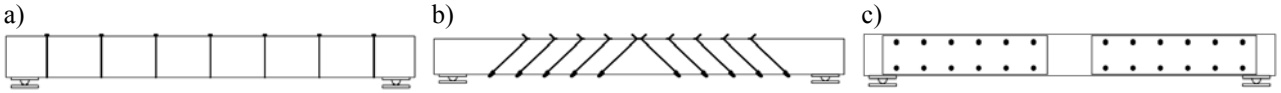

Fig. 60 – Repair methods tested in the wood beams fractured by horizontal shear (Akbiyik 2005, Akbiyik et al. 2007).

The six beams were then repaired by the methods described to ascertain the effectiveness of each repair technique, compared to the horizontal shear fractured condition. Fig. 61 (a) illustrates the analysis procedure for beam B1, which was repaired using hex bolts transversely over the entire beam length with spacings of 610 mm (Fig. 60 a). Fig. 61 (b) summarizes the repair effectiveness for all specimens tested. The best results were obtained with beam B2, repaired with lag screws at 45º to the beam transverse direction (Fig. 60 b), and with beams B3 and B6, repaired using GFRP side plates (Fig. 60 c). Poor results (effectiveness≈15%) were obtained for beams B4 (repaired with lag screws transversely over the entire length of the beam) and B5 (using plywood plates instead of GFRP ones in a scheme similar to Fig. 60 c). For beams B1 and B2, the hex bolts and lag screws were found to be effective. Between beams B3, B5 and B6, repaired with side plates, using GFRP plates was more effective, due to the higher stiffness of the plates. In fact, the

GFRP plates prevented horizontal sliding, increasing the beams stiffness. After testing, no visible damage was found in the GFRP plates, except minor bearing damage where the lag screws were installed.

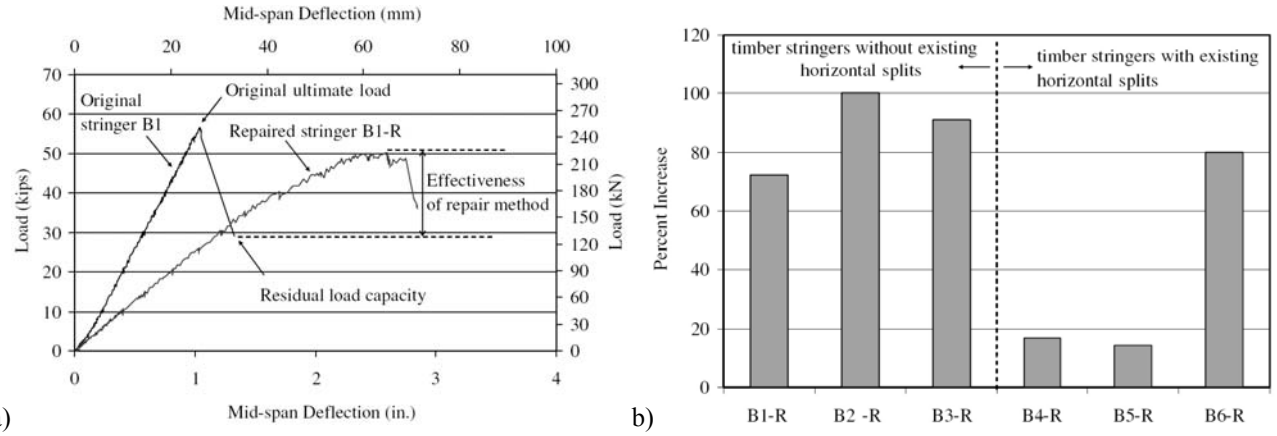

Fig. 61 –Calculation of the repair method effectiveness for beam B1 (a) and percentile increase of the residual load capacity (b) (Akbiyik 2005, Akbiyik et al. 2007).

The use of dowel-type connectors, or shear spikes, was also suggested as a mean for repairing timber. Radford et al. (2002) tested this technique in low aspect ratio wood beams, representative of railroad bridge span members, damaged by a longitudinal crack along their length. The repair procedure aimed restoring the beams shear properties, adhesively-bonding steel nails or fibreglass pultruded rods transversely in the beams (Fig. 62). GFRP rods were chosen due to their strength, low cost, and compatibility to the wood members. The repair procedure consisted on drilling holes in the damaged beams, followed by insertion of the rods pre-impregnated with the adhesive. The adhesive improved the load transfer between the wood and rods, preventing water contamination and filling eventual gaps in the wood member, already existing in the beams or caused by the repair procedure. Since the rods are fully inserted in the timber, the aesthetics are only marginally affected. The proposed concept was validated with scale tests, and the influence of the rods number and loci on the repairs behaviour was evaluated. The repairs stiffness and strength were determined under *Three-Point Bending* (3PB). The configurations tested are shown in Fig. 62. Configuration R1 consisted on two rows of rods, near the load cylinder. Configurations R2 to R6 incrementally add one rod on each side towards the beam edges.

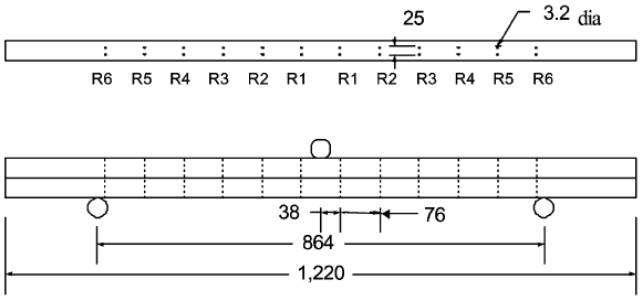

Fig. 62 – Repair geometry, dimensions in mm (Radford et al. 2002).

The beams stiffness was evaluated for the six repair configurations (Fig. 62), pointing towards an increasing stiffness trend as a function of the number of rods, with both steel and GFRP rods. However, the GFRP rods showed higher values, compared to the steel nails. It was also concluded that repairing with GFRP rods was an effective method to restore the undamaged strength of the beams. Adhesively-bonding the beams with epoxy adhesive was also evaluated,

and a full recovery of the undamaged beams strength was similarly attained. However, repairing solely with adhesive was found to be less desirable than adhesively-bonding GFRP rods, which showed twice as large failure strain values.

The work of Lopez-Anido et al. (2003, 2005) addressed a repair methodology for decayed underwater wood piles in waterfront facilities, using GFRP shells and a grouting material. Two mechanisms of load transfer to the GFRP shells were also discussed and a step-by-step procedure for field installation was described with detail. The proposed wood pile repair method (Fig. 63 (a) and (b)) consisted on a GFRP encasement that enclosed the deteriorated portion of the pile. The shells were fabricated with a longitudinal slit (Fig. 63 a), allowing their opening for installation in-situ. Depending on the deterioration of the wood pile to be repaired, several shells can be overlapped. Nonetheless, as least two shells should be applied. The slits in each cylindrical shell are out of phase (Fig. 63 a), to avoid weak regions in the shield. Additionally, the region between the GFRP shield and the wood pile was filled with a grouting material that, although not providing a structural bond, creates interlocking (friction) between both. The proposed lay-up for the composite shield consisted on three inner plies of unidirectional GFRP with the fibres aligned in the pile longitudinal direction, another ply oriented transversely and two outer plies of *E*-glass chopped strand mat with random orientation. The composite shield is to be assembled and bonded in-situ from these individual shells, which are bonded individually with an underwater curing adhesive after they are placed in position.

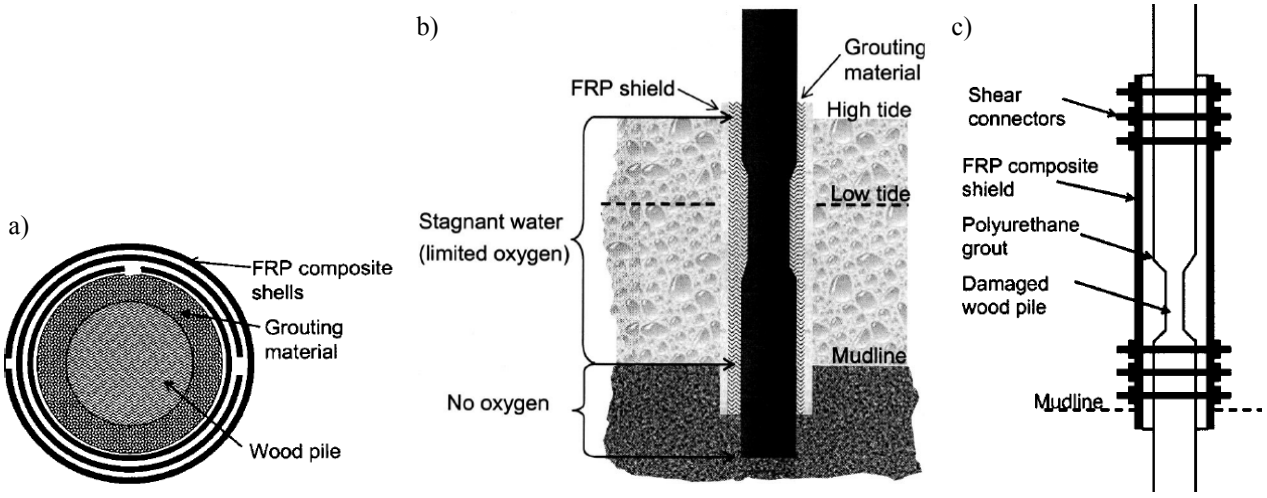

Fig. 63 – Repair method: section view (a), longitudinal view (b) and with shear connectors (c) (Lopez-Anido et al. 2005).

Two different types of grouting materials were evaluated: cement-based structural grout and expanding polyurethane chemical grout. Shear connectors (steel threaded rods) were also evaluated to transfer loads between the GFRP shield and the wood pile (Fig. 63 c). Although no repairs were performed in-situ, the feasibility of the repair methodology proposed was demonstrated in the laboratory with full-size specimens. Damage in the wood piles was simulated reducing the cross-sectional area of the pile. The specimens were subjected to two types of experiments: push out tests by compression loading to characterize the interface response (wood/grout/shear connector/FRP composite) and bending tests to characterize the overall structural response. It was found that, when a polyurethane grout was employed, shear connectors were required to effectively deviate loads to the GFRP shield and restore the piles strength. For the cement-based grout, metal shear connectors were not necessary.

Alam et al. (2009) studied repair strategies for wood beams damaged in the laboratory under bending to simulate structural damage. The repairs used bonded-in reinforcements of steel or composite pultruded rods with a rectangular section adhesively-bonded to the wood member. Pultruded bars of CFRP, GFRP and FULCRUM (commercial designation of a glass fibre reinforced polyurethane) were evaluated. The repair technique proposed consisted on straightening the artificially damaged wood members, followed by routing of grooves in their tension and compression faces and adhesively-bonding the reinforcement with an epoxy adhesive (rotafix® CB10TSS). Three different repair configurations were evaluated: strengthening at the compression face, at the tension face, and both. The repairs were tested under 4PB and their stiffness and strength compared to the undamaged beam values. Since wood properties are known to significantly vary between specimens, a simple procedure was used to assure the accuracy of the comparative results between the repaired and undamaged members. For each specimen, a vertically laminated spruce beam was cut in two halves. One of these was tested, to assess the stiffness and strength of the undamaged wood member. The other halve was damaged and repaired afterwards, and the results compared with the corresponding undamaged beam. This allowed the measurement of the flexural properties unique to each beam, for a direct comparison with the same beam following mechanical repair. The test results showed that, between the different reinforcement materials, the steel bars yielded the higher values of flexural modulus of the repaired beams, which was expected due to the higher value of *E* modulus than the pultruded rods. For all the materials used as reinforcement, repair on both tension and compression faces of the beams led to a higher stiffness, while repairing only at the compression face gave the worst results.

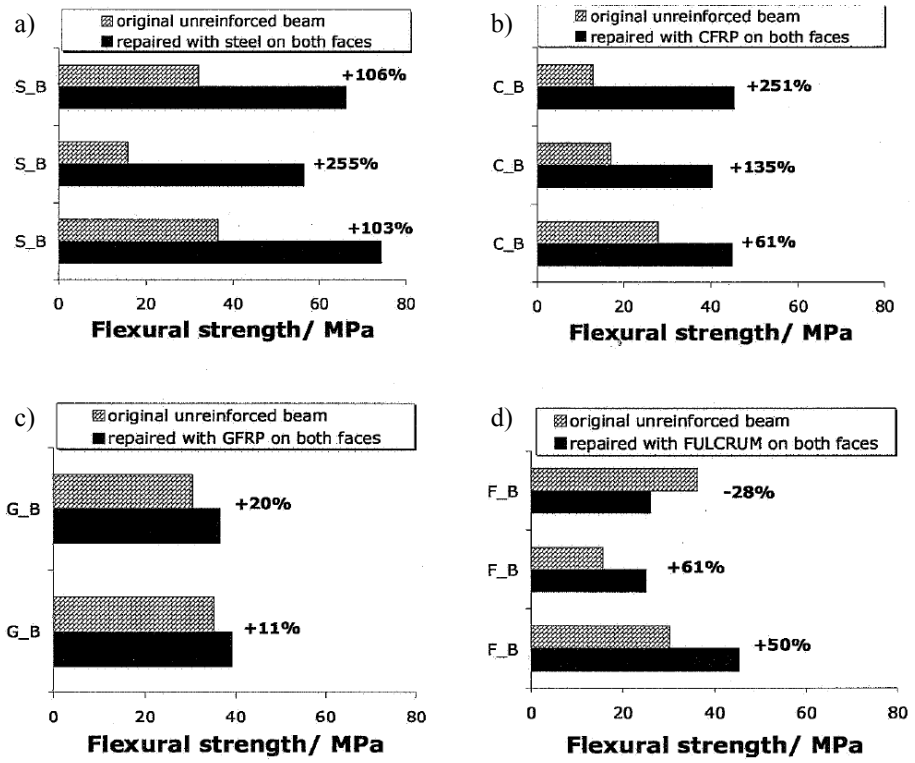

Fig. 64 – Flexural strength of the beams repaired in both faces as a function of the reinforcement material (Alam et al. 2009).

Fig. 64 compares the flexural strength of undamaged beams with the beams repaired at both tension and compression faces, for the reinforcements of steel (a), CFRP (b), GFRP (c) and FULCRUM (d). The trends obtained for the flexural strength are similar to the stiffness analysis. Thus, independently of the reinforcement material, the repairs strength increased from repairing in the compression face to the repair on both faces. On all cases, fracture initiated on the tensile face of the beam. Repairing solely in the compression face leads to a strength improvement that is not caused by

restraint of crack propagation, which occurs mostly at the tension region of the beams, but due to the added compressive strength and stiffness of the reinforcing material. Repairing the tensile face with the same volume fraction of reinforcement restrains crack propagation and increases the strength, due to the higher tensile strength of the reinforcement material. Repairing on both faces doubles the volume fraction of reinforcement and constrains crack propagation on both faces. The authors concluded that, in general, repairing on both faces of the wood member was the best solution, yielding the best stiffness and strengths results. However, the other two configurations also restored the undamaged strength in some of the beams tested. Comparing the different reinforcement materials, steel led to the best results on the stiffness, while in terms of flexural strength it was similar to the CFRP composite, with both these materials leading to the bigger improvements.

2.4. Concluding remarks

This review was intended to highlight the state-of-the-art on the different topics developed in this thesis, for a broader knowledge and an easier understanding of the issues discussed, allowing also a clear assessment of the contribution of this work to the current state of affairs. Particular attention was paid to the most solid assumptions and investigation tendencies followed during the last decades on each topic. **The review initiated with some works on the use of trapezoidal cohesive laws in FEM simulations to model thin layers of ductile adhesives**. These works were the basis of the trapezoidal CZM developed in this thesis. The subject of cohesive laws with a strength plateau was introduced recently, with the first simulations using identical cohesive laws for tension and shear. However, this assumption was not found to be adequate for thin adhesive layers, which are significantly tougher in shear than peel. In all the investigations described in this review, the cohesive laws in each pure mode were determined experimentally for the respective mode of loading. In most cases, the cohesive laws in pure modes I and II were characterized by DCB and ENF tests, respectively. These laws were often applied to different test geometries for model validation purposes, with accurate predictions of the experimental P-δ curves up to fracture. The adhesive layer thickness was always kept constant, owing to the mechanical properties variation of adhesive layers with this parameter. The results obtained were thus promising, opening a good perspective for the work addressed here.

The mechanical behaviour and characteristics of adhesively-bonded lap, strap and scarf assemblies were subsequently described, with special attention to composite structures. A consensus was achieved amongst researchers on the difficulty of 2D FEM models to simulate accurately 3D repairs, resulting on an underestimation of the assemblies strength. This was mainly due to the laminates ability to bear loads after patch failure, which is not accounted for with 2D models. Besides, 2D models are not able to capture 3D stress effects near the notch. In most of the works, stress distributions in the adhesive layer constituted the basis for discussion and interpretation of results. Peel and shear stresses in these geometries were generally highest at the overlap edges. Whilst peel peak stresses are mainly caused by load eccentricities, leading to the adherends and/or patches flexure, shear peak stresses arise from the differential deformation of the adherends and patches along the overlap length. These peak stresses justified damage initiation at the overlap edges. Assemblies bonded with ductile adhesives, tolerating plasticity at these regions with the consequent increase of stresses towards the lightly loaded inner regions of the overlap before fracture, were less affected by this impairing characteristic of bonded assemblies. Stress concentration effects in the adhesive layer were also found towards the interfaces with the adherends or patches, which can justify cohesive failure near these interfaces, sometimes regarded as adhesive failures by visual inspection. Some investigators developed analytical theories for the

prediction of stresses or strains, with good comparative results with FEM or experimental methods. On the strength of the assemblies, different researchers concur that above a determined value of overlap length, no significant improvement is attained, due to the increasing dimensions of the unloaded inner region of the bond. The optimal value of the overlap length depends on parameters such as the dimensions, and also strength and fracture properties of the different constituents of the assembly. Accounting for the patch thickness, owing to the increase on peel peak stresses at the overlap edges of these assemblies for thicker patches, over a determined value of patch thickness the structure strength diminished. On scarf bonds, it was found that employing equivalent elastic properties for composite laminates with differently oriented plies masks peel and shear peak stresses in the adhesive, arising from the different compliance between plies. Thus, this simplification should not be equated for strength prediction purposes. Ply-by-ply modelling, used by others, captures these localized effects, yielding accurate strength predictions using stress or strain-based criteria, or even CZM's. Unidirectional laminates or isotropic adherends led to flat stress distributions, due to the adherend tapering effect at the overlap edges. The use of a few over-laminating plies covering the repair region was unanimously considered to significantly increase the assemblies strength. The scarf angle is the most significant geometric parameter on scarf assemblies, with a direct influence on the bond length and magnitude of peel stresses. In fact, whilst for small scarf angle shear stresses govern fracture, for larger values, peel and shear stresses display similar magnitudes. Different experimental and numerical studies showed an exponential increase of strength with the reduction of the scarf angle, due to the increase of bond area and reduction of peel stresses. For a small value of scarf angle, a modification of the failure mechanism takes place, from a bond failure to a tensile fracture of the adherends.

Various geometric modifications for bonded assemblies were also discussed, employed to increase the assemblies strength characteristics by a modification of the stress fields or alteration of the failure mechanisms. One of the most popular techniques is filleting at the overlap edges. Different fillet shapes and dimensions were tested, always accompanied by a reduction of peel and shear peak stresses due to a redistribution of loads at the overlap edges. The MIM was also used to compare stress distributions at the overlap edges in joints with and without fillet. Chamfering the adherends at the overlap region was also focused, as a mean to reduce the adherends differential straining, thus promoting more constant stress distributions in the adhesive layer. This led to a corresponding strength improvement. Wavy shapes of the adherends at the overlap region avoided the eccentricity of the transmitted load that, in addition to the suppression of peel and shear peak stresses at the overlap edges, led to a significant strength improvement. Reverse-bent geometries were also proposed to eliminate the eccentricity of SL joints, with satisfactory results.

Some of the most relevant works documented in the literature on reinforcement and repair procedures with composites for wood structures were finally described. The most common types of damage observed in large-scale wood structures were initially characterized, allowing the definition of the damage types to be repaired in the final part of this thesis, with the respective testing and numerical modelling. An extensive literature research allowed concluding that, under static bending, compression failure, horizontal shear and cross-graining are amongst the most important fracture mechanisms. Since it is not within the scope of this thesis to reinforce wood members, only one work on reinforcement was discussed, to give an overall idea of the reinforcement schemes recently employed. Thus, a comprehensive study was selected, which focused on several reinforcement techniques and also pre-stressing of the reinforcement, allowing an additional increase of the beams stiffness by tensioning the reinforcement strips at the beams unloaded configuration. A few works regarding the repair of wood members with composites were afterwards described, two of which addressed repair methodologies for horizontal shear damage. One of these approaches

employed fastening composite plates to the lateral faces of the damaged beams, to obstruct the sliding between the cracked arms. In the other study, cylindrical composite rods were glued transversely in the beams along their full height with the same purpose. Both techniques were effective in increasing the beams residual strength, with the composite reinforcements yielding a superior performance than conventional engineering materials such as plywood for the lateral faces reinforcements or steel for the bonded rods. Yet, between the two solutions, the bonding rods method had the advantage of not compromising the aesthetics. A less conventional approach for repairing wood consisted on straightening damaged wood trusses, followed by the routing of longitudinal grooves, allowing the insertion of bonded reinforcements for the restraint of damage propagation in the existing cracks. Another study focused on the repair of deteriorated underwater piles, using a composite encasement to protect the weakened portion of the pile and deviate loads from that region, using a filling grout solely or combined with shear connectors. All these studies drawn attention to the known variability in the elastic and strength properties of wood, with one of them proposing a simple mean to alternatively evaluate the stiffness and strength properties of damaged wood members, reducing the influence of the wood properties variability. To this end, large beams were cut in two halves, with one of them being damaged in the laboratory. The damaged beam was repaired and the strength improvement evaluated to the respective undamaged half. It should be emphasized that no studies were found in the literature regarding adhesively-bonded repairs to wood members, oppositely to the reinforcement of undamaged beams, for which a few studies exist not only with composites, but also with metal plates. This reinforces the importance of the study carried out in this thesis, for the feasibility assessment of adhesively-bonded repairs to restore wood structures, and also to provide an alternative to the extensive experimentation usually required for the implementation of these techniques.

3. FRACTURE APPROACHES FOR STRENGTH PREDICTION

It is known that the traditional fracture mechanics-based criteria for strength prediction present some disadvantages. Actually, they depend on the definition of an initial flaw and characteristic length. However, in many structural applications, the damage initiation locus is not obvious, neither the length of damage is easy to ascertain. On the other hand, fracture mechanics has already demonstrated its suitability in modelling crack propagation. CZM's overcome these limitations and exploit the advantages of fracture mechanics. These methodologies combine features from strength of materials to model damage initiation with fracture mechanics to deal with damage propagation. Thus, it is not necessary to induce an initial defect and mesh dependency problems are overcome. In this Section, the most habitually used LEFM techniques to simulate damage propagation in engineering structures are initially described. **A triangular CZM used in this work is subsequently formulated. A new CZM with a trapezoidal shape is also developed to simulate a thin layer of ductile adhesives such as the Araldite® 2015, which will be used throughout this work**. The trapezoidal CZM will be used as a replacement of the solid finite elements usually employed to simulate the adhesive layer in bonded assemblies. **The definition of the pure mode I and II cohesive laws of this adhesive by an inverse data fitting method is also described. Finally, the developed CZM will be validated with experiments**.

3.1. Linear Elastic Fracture Mechanics

Oppositely to the strength of materials-based criteria, the fracture mechanics-based approaches assume the presence of an inherent defect in the structure to be examined, induced during the fabrication process or sustained under in-service operation. Under these conditions, the emergent question is whether the defects can induce catastrophic failure or if, during the predicted structure lifetime, they can propagate stably keeping their dimensions inferior to the critical size. There are two types of fracture mechanics criteria, which can be based either on stress intensity factors or on energetic concepts. The **stress intensity factor** (K) is defined as

$$K = Y\sigma_{\mathrm{R}}\sqrt{\pi a}\,, \tag{3}$$

where Y is a non-dimensional factor depending on the geometry and load distribution, σ_{R} the remote applied stress and a the crack length. It is assumed that crack propagation occurs when K attains its critical value (K_{c})

$$K_{\mathrm{c}} = \sigma_{\mathrm{u}}\sqrt{\pi a}\,, \tag{4}$$

with σ_{u} representing the strength of the material. The **energetic criterion** is based on the assumption that crack growth will occur when the energy available at the crack tip due to the applied load (G – strain energy release rate), overcomes the critical strain energy release rate (G_{c}), which is a material property. It should be emphasized that G and G_{c} do not account for the plasticity of materials. G is given by the expression

$$G = \frac{dW}{dA} - \frac{dU}{dA}\,. \tag{5}$$

W is the work of the external loads, U the internal strain energy and A the crack surface area. G and K are intrinsically related. In fact, Irwin (1957), demonstrated that in plane-stress

$$G = \frac{K^2}{E} \tag{6}$$

and in plane-strain

$$G = \frac{K^2\left(1-\upsilon^2\right)}{E}, \tag{7}$$

where E and υ are the Young's modulus and Poisson's ratio, respectively. These relationships are also valid for the respective critical values (G_c and K_c). Crack growth can develop under three modes (Fig. 65). Mode I represents an opening mode, while modes II and III are the shear modes. In most structures, the applied load creates a combination of modes at the crack tip, which implies the use of a mixed mode criterion to simulate damage propagation.

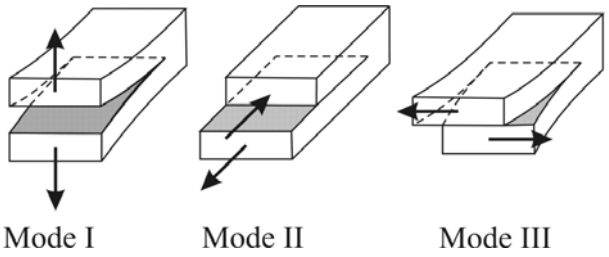

Fig. 65 – Modes of crack propagation in structures.

Under these circumstances, it is fundamental to use adequate energetic criteria, which are generally in the form of

$$\left(\frac{G_I}{G_{Ic}}\right)^A + \left(\frac{G_{II}}{G_{IIc}}\right)^B + \left(\frac{G_{III}}{G_{IIIc}}\right)^C = 1, \tag{8}$$

with G_{Ic}, G_{IIc} and G_{IIIc} being the values of G_c in pure modes I, II and III, respectively. The linear energetic criterion (A=B=C=1) and the quadratic one (A=B=C=2) are the most used. One of the most popular methods based on fracture mechanics is the VCCT. This method allows obtaining the values of G at the crack tip, based on the assumption that, when a crack grows, the energy released is equal to the work required to close the crack to its initial length before propagation (Krueger 2002). In the diagram of Fig. 66, the crack grows from the node l to node i. The method can be applied by two different ways, the first one consisting in two steps. In a first run, whilst node l is closed, its loads in mode I and mode II are registered. In a second run, applying the same load to the structure, node l is opened, originating nodes l_1 and l_2. The relative displacements between these nodes in the respective directions are also determined.

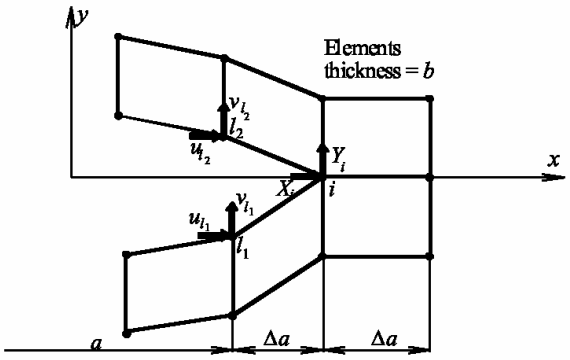

Fig. 66 – Schematic representation of the crack tip in 2D for the application of the VCCT.

However, these quantities can be extracted in a sole run. In this case, it is necessary to use a refined mesh, to assure the condition of self-similar crack propagation. The energy necessary to close the crack (ΔE) is obtained by multiplying the loads at node i by the relative displacements between nodes l_1 and l_2

$$\Delta E = \frac{1}{2}\left(X_i \, \Delta u_l + Y_i \, \Delta v_l \right), \tag{9}$$

where X_i, Y_i represent the loads at the closed node i and Δu_l, Δv_l the difference of displacements between nodes l_1 and l_2. The values of G can then be calculated by the product of the relative displacements at the opened point (nodes l_1 and l_2) with the loads at the closed point (node i)

$$G_{\mathrm{I}} = \frac{1}{2b\Delta a} Y_i \Delta v_l \;\; ; \;\; G_{\mathrm{II}} = \frac{1}{2b\Delta a} X_i \Delta u_l \,, \tag{10}$$

being $b\Delta a$ the area of the new surface created by an increment of crack propagation (Fig. 66). Using the energetic criterion expressed by equation (8) in 2D (neglecting the mode III term), propagation will occur when the values of G_{I} and G_{II} obtained from equation (10) satisfy the criterion. The method can also be easily applied in 3D problems, where G_{III} can be obtained by the same procedure.

It should be noted that the use of fracture mechanics criteria depends on the existence of some kind of defect, which is usually simulated as a pre-crack. The initial cracks are artificially introduced and intend to simulate damage or defects sustained during the fabrication process or in-service operation. Thus, it can be affirmed that fracture mechanics-based criteria are more adequate for damage growth rather than initiation. In fact, these criteria present some difficulties for the onset of damage, such as the initial crack length and its locus.

3.2. Cohesive zone models

CZM's were largely employed in the last decades to simulate crack initiation and propagation in delaminations, and also cohesive and interfacial failure problems. Weighed against the conventional fracture mechanics approaches, CZM's are generally preferred in presence of a quasi-brittle behaviour, i.e., with a non-negligible *Fracture Process Zone* (FPZ) and gradual reduction of tractions from a peak value to zero (Alfano 2006). Whilst the first works on CZM's date back to the 1960's, with the contributions of Dugdale (1960) and Barenblatt (1962), several shapes for the cohesive laws were afterwards developed to meet the requirements of specific materials. These include triangular (Hilleborg et al. 1976, Mi et al. 1997, Mi et al. 1998, Alfano and Crisfield 2001, Campilho et al. 2008c, de Moura et al. 2009a), linear-parabolic (Allix et al. 1995, Allix and Corigliano 1996, Champaney and Valoroso 2001), polynomial (Needleman 1987, Chen et al. 1999, Chen 2002), exponential (Needleman 1990, Chandra et al. 2002, Xu and Needleman 1994) and trapezoidal laws (Tvergaard and Hutchinson 1992, Tvergaard and Hutchinson 1993). CZM's, implemented within cohesive elements, allow the establishment of traction-separation laws between coincident but unconnected nodes in the numerical simulations of engineering structures. CZM's simulate damage initiation, which occurs in a given node when the local strength of the material is attained. Following, softening initiates, leading to damage growth when the stresses in that node are completely released. Damage growth is ruled by energetic criteria. With this methodology, the complete numerical characterization of the structures behaviour up to failure is obtained. A previously developed mixed mode I+II+II triangular CZM used in this work will be presented (de Moura et al. 1997, de Moura et al. 2000, Gonçalves et al. 2000, Gonçalves et al. 2002, Gonçalves et al. 2003, de Moura et al. 2004, Campilho et al. 2005). A newly developed trapezoidal mixed mode I+II CZM suited for ductile adhesives will also be formulated

and initially validated with experimental results of SS repairs, for different values of overlap length and patch thickness, and SL joints with different overlap lengths. A trapezoidal mixed mode I+II+III CZM was also developed for the simulation of 3D problems. An extensive validation of the developed models will be carried out throughout this thesis for different repair techniques, materials and loadings.

3.2.1. Triangular cohesive zone model

Several researchers focused on the strength prediction of bonded assemblies, including the numerical simulation of damage onset and growth. Charalambides et al. (1998a) calculated the values of G for crack interlaminar growth in scarf joints using the J-integral method. Three possible failure types of the joints were analysed to predict the failure paths and loads. The agreement between the experiments and predictions on the failure paths and loads was found to be good. Pradhan et al. (1994) analysed adhesively-bonded joints using the FEM, computing the value of G for debonding initiation. Paired nodes were generated on the interfaces and released one after another sequentially, modelling gradual crack growth. Bogdanovich and Yushanov (1999b) presented a new development of a 3D variational stress/strain and progressive failure analysis of adhesive composite joints. The progressive failure analysis used the values of G to predict different scenarios of cohesive, adhesive or interlaminar crack growth. Gonçalves et al. (2003) used cohesive elements including a triangular mixed mode CZM to simulate progressive debonding in adhesively-bonded SL joints. It was concluded that the model can accurately predict the joints mechanical behaviour and failure load.

The triangular mixed mode I+II+III CZM based on zero thickness cohesive elements is initially presented. Two versions are currently implemented: the 8 and 18-nodes cohesive elements, compatible with the 8 and 27-nodes 3D hexahedral solid elements of ABAQUS®, respectively. The mixed mode I+II version of this model, with 6 nodes, can be derived assuming a few simplification hypotheses. In the model description, guidelines will be included on how to obtain the governing equations of the mixed mode I+II model. The CZM can be defined in terms of pure modes (mode I-opening or modes II and III-shear), or the mixed mode (combination of the pure modes) expected in most structural applications. For the pure mode model, the constitutive equation can be defined in two different ways (Fig. 67) between the stresses ($\boldsymbol{\sigma}$) and relative displacements ($\boldsymbol{\delta}_\mathbf{r}$) between homologous points.

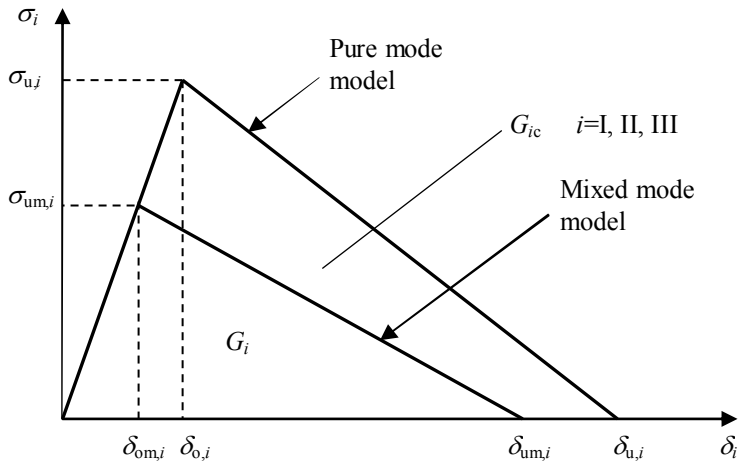

Fig. 67 – The triangular softening law in pure mode and mixed mode.

Before damage starts to grow

$$\boldsymbol{\sigma} = \mathbf{D}\boldsymbol{\delta}_{\mathbf{r}}, \tag{11}$$

where **D** is the diagonal matrix containing the penalty parameters in each pure mode (d_i i=I, II, III). The chosen values for the penalty parameter must be quite high not to affect the structures stiffness and prevent interpenetration of the element faces. Following extensive studies (de Moura et al. 1997, Gonçalves et al. 2000), it was found that d_i=10^6 N/mm^3 was the optimal value for an accurate convergence and minimization of numerical problems during the non-linear procedure. After the local strength ($\sigma_{\mathrm{u},i}$) is attained, the material undergoes damage, softening linearly up to failure. This is simulated by the energy being released in a cohesive zone ahead of the crack tip. This region (FPZ), is where the material undergoes softening damage by different ways (Pereira and de Morais 2003), e.g. micro-cracking, extensive plasticity and fibre bridging (if applicable). Numerically, this is implemented by a damage parameter whose values vary from zero (undamaged) to unity (complete loss of stiffness) as the material deteriorates. The respective constitutive relationship writes

$$\boldsymbol{\sigma} = \left(\mathbf{I} - \mathbf{E}\right)\mathbf{D}\boldsymbol{\delta}_{\mathbf{r}}, \tag{12}$$

with **I** representing the identity matrix and **E** a diagonal matrix containing the damage parameters e_i

$$e_i = \frac{\delta_{\mathrm{u},i}\left(\delta_i - \delta_{\mathrm{o},i}\right)}{\delta_i\left(\delta_{\mathrm{u},i} - \delta_{\mathrm{o},i}\right)}. \tag{13}$$

$\delta_{\mathrm{o},i}$ is the displacement corresponding to the onset of damage and δ_i the current relative displacement. The maximum relative displacement $\delta_{\mathrm{u},i}$, for which complete failure occurs is obtained by equating the area under the softening curve to the respective value of $G_{i\mathrm{c}}$

$$G_{i\mathrm{c}} = \frac{1}{2}\sigma_{\mathrm{u},i}\delta_{\mathrm{u},i}. \tag{14}$$

In structures, failure is more likely to occur under a mixed mode load. Therefore, this formulation includes a mixed mode CZM, which is an extension of the pure mode model described above (Fig. 67). Damage initiation is predicted using the quadratic stress criterion

$$\begin{aligned} &\left(\frac{\sigma_{\mathrm{I}}}{\sigma_{\mathrm{u,I}}}\right)^2 + \left(\frac{\sigma_{\mathrm{II}}}{\sigma_{\mathrm{u,II}}}\right)^2 + \left(\frac{\sigma_{\mathrm{III}}}{\sigma_{\mathrm{u,III}}}\right)^2 = 1 \quad \text{if} \quad \sigma_{\mathrm{I}} > 0 \\ &\left(\frac{\sigma_{\mathrm{II}}}{\sigma_{\mathrm{u,II}}}\right)^2 + \left(\frac{\sigma_{\mathrm{III}}}{\sigma_{\mathrm{u,III}}}\right)^2 = 1 \qquad \text{if} \quad \sigma_{\mathrm{I}} \le 0 \end{aligned}, \tag{15}$$

where $\sigma_{\mathrm{u,I}}$, $\sigma_{\mathrm{u,II}}$ and $\sigma_{\mathrm{u,III}}$ represent the local strengths in each pure mode, and it is assumed that normal compressive stress do not induce damage. Considering (11), the first equation (15) can be rewritten as

$$\left(\frac{\delta_{\mathrm{om,I}}}{\delta_{\mathrm{o,I}}}\right)^2 + \left(\frac{\delta_{\mathrm{om,II}}}{\delta_{\mathrm{o,II}}}\right)^2 + \left(\frac{\delta_{\mathrm{om,III}}}{\delta_{\mathrm{o,III}}}\right)^2 = 1 \tag{16}$$

being $\delta_{\mathrm{om},i}$ (i=I, II, III) the mixed mode relative displacements at damage initiation, corresponding to the critical mixed mode local strengths $\sigma_{\mathrm{um},i}$ (Fig. 67). In the last two equations, to derive the equations for mixed mode I+II, the mode III terms should be considered equal to zero. On the following equations, this simplification involves assuming

$$\delta_{\mathrm{III}} = \delta_{\mathrm{o,III}} = \delta_{\mathrm{u,III}} = 0; \quad \beta_i = \beta = \frac{\delta_{\mathrm{II}}}{\delta_{\mathrm{I}}}. \tag{17}$$

Combining an equivalent mixed mode displacement (δ_{m})

$$\delta_{\mathrm{m}} = \sqrt{\delta_{\mathrm{I}}^{\,2} + \delta_{\mathrm{II}}^{\,2} + \delta_{\mathrm{III}}^{\,2}} \tag{18}$$

and the mixed mode ratio (β_i)

$$\beta_i = \frac{\delta_i}{\delta_{\mathrm{I}}} \tag{19}$$

with equation (16), it is obtained

$$\delta_{\mathrm{om}} = \delta_{\mathrm{o,I}}\delta_{\mathrm{o,II}}\delta_{\mathrm{o,III}}\sqrt{\frac{1+\beta_{\mathrm{II}}^{\,2}+\beta_{\mathrm{III}}^{\,2}}{\left(\delta_{\mathrm{o,II}}\delta_{\mathrm{o,III}}\right)^2+\left(\beta_{\mathrm{II}}\delta_{\mathrm{o,I}}\delta_{\mathrm{o,III}}\right)^2+\left(\beta_{\mathrm{III}}\delta_{\mathrm{o,I}}\delta_{\mathrm{o,II}}\right)^2}}\,, \tag{20}$$

which represents the relative displacement in mixed mode at the onset of the softening process. The mixed mode I+II equations can be written as (using equation (17))

$$\delta_{\mathrm{om}} = \delta_{\mathrm{o,I}}\delta_{\mathrm{o,II}}\sqrt{\frac{1+\beta^2}{\delta_{\mathrm{o,II}}^{\,2}+\beta^2\delta_{\mathrm{o,I}}^{\,2}}}. \tag{21}$$

The mixed mode damage propagation is simulated considering the linear fracture energetic criterion (the mixed mode I+II model eliminates the mode III term)

$$\frac{G_{\mathrm{I}}}{G_{\mathrm{Ic}}}+\frac{G_{\mathrm{II}}}{G_{\mathrm{IIc}}}+\frac{G_{\mathrm{III}}}{G_{\mathrm{IIIc}}}=1 \tag{22}$$

The value of G_i at complete failure can be obtained from the area of the minor triangle of Fig. 67

$$G_i = \frac{1}{2}\sigma_{\mathrm{um},i}\delta_{\mathrm{um},i}\,, \tag{23}$$

being $\delta_{\mathrm{um},i}$ (i=I, II, III) the relative displacement in each mode for complete failure. Considering equations (11), (18) and (19), the energies (equations (14) and (23)) can be written as functions of the relative displacements. Substituting in (22) it can be shown that

$$\delta_{\mathrm{um}} = \frac{1+\beta_{\mathrm{II}}^{\,2}+\beta_{\mathrm{III}}^{\,2}}{\delta_{\mathrm{om}}}\left[\frac{1}{\delta_{\mathrm{o,I}}\delta_{\mathrm{u,I}}}+\frac{\beta_{\mathrm{II}}^{\,2}}{\delta_{\mathrm{o,II}}\delta_{\mathrm{u,II}}}+\frac{\beta_{\mathrm{III}}^{\,2}}{\delta_{\mathrm{o,III}}\delta_{\mathrm{u,III}}}\right]^{-1} \tag{24}$$

which corresponds to the mixed mode displacement at failure. Simplifying equation (24) with (17), the mixed mode I+II equations corresponding to damage growth can be defined as

$$\delta_{\mathrm{um}} = \frac{1+\beta^2}{\delta_{\mathrm{om}}}\left[\frac{1}{\delta_{\mathrm{o,I}}\delta_{\mathrm{u,I}}}+\frac{\beta^2}{\delta_{\mathrm{o,II}}\delta_{\mathrm{u,II}}}\right]^{-1} \tag{25}$$

The equivalent displacements (equations (18), (21) and (25)) are used in equation (13) to define the damage parameter.

3.2.2. Trapezoidal cohesive zone model

Triangular CZM's were extensively applied to bonded assemblies in the past (de Moura et al. 1997, Chen 2002, Campilho et al. 2005, Valoroso and Champaney 2006). However, when ductile adhesives are used, it is more adequate to employ trapezoidal softening laws including the adhesive plasticity. The employment of such laws is vital to model accurately the behaviour of bonded structures, especially when extremely stiff components are bonded, due to the practically absence of differential deformation effects in these components (Alfano 2006, Pinto et al. 2009). This yields the structural response predominantly dependent on the shape of the cohesive laws chosen for the adhesive layer, since the adhesive is similarly loaded along the bond length. One of the first studies with trapezoidal laws included a mixed

mode CZM (Tvergaard and Hutchinson 1993, 1996) to study interfacial fracture of bi-material systems. This involved three-parameter traction-separation laws with a mode-independent intrinsic toughness of the interface. However, the experimental results of Yang et al. (1999) and Yang et al. (2001) showed a significant difference between the adhesive fracture toughness in the two modes, which indicated that a mode-independent model is not always appropriate. Yang et al. (1999) used a CZM to study the coupling between interface fracture and plastic strain of the adherends. For the adhesive, a traction-separation law including plasticity was used. The model was validated performing *T*-peel tests on adhesively-bonded aluminium DCB specimens. The same authors (Yang et al. 2001) considered an identical traction-separation law for elastic-plastic mode II crack growth modelling. Adhesively-bonded ENF specimens under a bending load, and undergoing extensive plastic strain accompanying failure, were used to validate the model. The main fracture parameters were determined comparing experimental and numerical results for one particular geometry, and then applied to a different geometry. The proposed traction-separation law was found appropriate for the particular thickness of the adhesive and the respective strain rate. Yang and Thouless (2001) simulated the mixed mode fracture of plastically deforming adhesive joints using a mode-dependent CZM. Mode I and mode II fracture laws obtained from previous works (Yang et al. 1999, Yang et al. 2001) were combined with a mixed mode failure criterion to provide quantitative predictions of the deformation and fracture of *T*-peel specimens and SL joints. A linear toughness criterion (Hutchinson and Suo 1992) was used to access complete failure of the CZM elements and subsequent crack growth. Kafkalidis and Thouless (2002) performed a FEM analysis of SL joints using a cohesive-zone approach that included the plastic strain of the adhesive. This model allowed the influence of the geometry to be considered, and included in the analysis the plastic deformation of the adherends. Using cohesive-zone parameters determined for the particular combination of materials used, the numerical predictions showed excellent agreement with the experimental observations. The traction-separation law, failure criterion and model parameters were consistent with the work of Yang and Thouless (2001). Li et al. (2005a) used a CZM previously developed by Li et al. (2005b) on adhesively-bonded joints to validate two and three-parameter laws. Using this method, the strengths and deformations were accurately described, as well as the transition between failure of the composite and failure of the interface. The CT test was used to determine the properties of the traction-separation laws. The results obtained with the three-parameter CZM presented a good agreement with the experimental data. Li et al. (2006a) used a CZM approach to model the mixed mode fracture of adhesively-bonded GFRP SL joints. A three-parameter cohesive law was employed for mode I (Li et al. 2005a), and a two-parameter law was used for mode II (Yang and Thouless 2001). A three-parameter mode I traction–separation law was equated for mode I to allow the simulation of interfacial cracking followed by fibre pull-out (experimentally observed for mode I fracture). On the other hand, preliminary mode II tests indicated that only few fibres were pulled out during mode II fracture. Consequently, a simple two-parameter traction-separation law was chosen to simulate the elastic/plastic behaviour of the adhesive under mode II. The experimental and numerical results revealed an excellent agreement, including the strengths and failure mechanisms.

A mixed mode I+II+III CZM with trapezoidal traction-separation laws was implemented within cohesive elements to fully simulate the behaviour of ductile adhesive layers, replacing the solid elements traditionally used to this end. To reproduce the tensile and shear behaviour of ductile adhesives, trapezoidal laws between stresses (σ) and relative displacements (δ_r) between homologous points of the cohesive elements with zero thickness were employed in each pure mode (Fig. 68). These types of laws are regarded to accurately reproduce the behaviour of thin ductile adhesive layers in mode I (Andersson and Stigh 2004) and mode II (Hogberg and Stigh 2006, Leffler et al. 2007). The constitutive relationship before damage onset is

$$\boldsymbol{\sigma} = \mathbf{D}\boldsymbol{\delta}_{\mathbf{r}}, \tag{26}$$

where **D** is a stiffness diagonal matrix defined later in this work. Considering the pure mode model, after $\delta_{1,i}$ the material softens progressively or, in other words, undergoes damage. Numerically, this is implemented by a damage parameter whose values vary from zero (undamaged) to unity (complete loss of stiffness) as the material deteriorates.

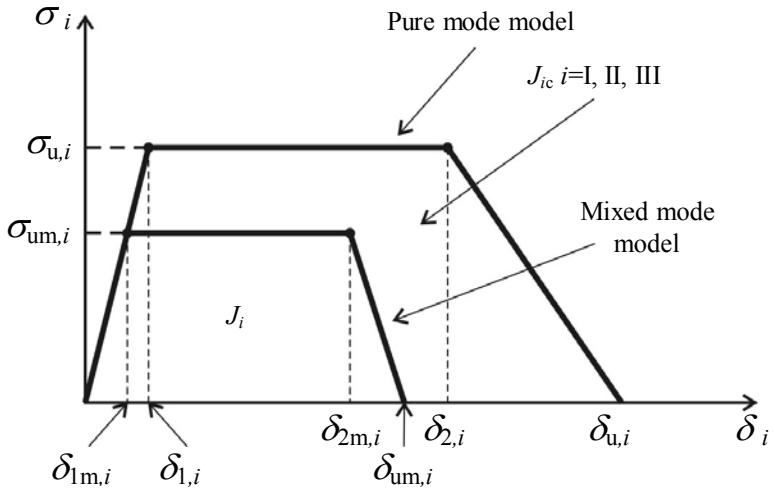

Fig. 68 – The trapezoidal softening law in pure mode and mixed mode.

The softening relationship can be written as

$$\boldsymbol{\sigma} = (\mathbf{I} - \mathbf{E})\mathbf{D}\boldsymbol{\delta}_{\mathbf{r}}. \tag{27}$$

I is the identity matrix and **E** is a diagonal matrix containing, on the position corresponding to mode i (i=I, II, III), the damage parameter (e_i). In the plateau region the damage parameter can be defined as

$$e_i = 1 - \frac{\delta_{1,i}}{\delta_i} \tag{28}$$

and, in the stress softening part of the curve

$$e_i = 1 - \frac{\delta_{1,i}\left(\delta_{u,i} - \delta_i\right)}{\delta_i\left(\delta_{u,i} - \delta_{2,i}\right)}. \tag{29}$$

The maximum relative displacement, $\delta_{u,i}$, at which complete failure occurs, is obtained by equating the area under the softening curve to the respective critical strain energy release rate (J_{ic})

$$J_{ic} = \frac{\sigma_{u,i}}{2}\left(\delta_{2,i} - \delta_{1,i} + \delta_{u,i}\right). \tag{30}$$

Since the plasticity of the adhesive is accounted for in these analyses, the strain energy release rate and the respective critical value are addressed as J_i and J_{ic}, respectively, instead of G_i and G_{ic}. Also in this formulation, a mixed mode CZM is included (Fig. 68). Damage onset is predicted using the quadratic stress criterion

$$\begin{aligned} &\left(\frac{\sigma_{\mathrm{I}}}{\sigma_{u,\mathrm{I}}}\right)^2 + \left(\frac{\sigma_{\mathrm{II}}}{\sigma_{u,\mathrm{II}}}\right)^2 + \left(\frac{\sigma_{\mathrm{III}}}{\sigma_{u,\mathrm{III}}}\right)^2 = 1 \quad \text{if} \quad \sigma_{\mathrm{I}} > 0 \\ &\left(\frac{\sigma_{\mathrm{II}}}{\sigma_{u,\mathrm{II}}}\right)^2 + \left(\frac{\sigma_{\mathrm{III}}}{\sigma_{u,\mathrm{III}}}\right)^2 = 1 \qquad \text{if} \quad \sigma_{\mathrm{I}} \le 0 \end{aligned}, \tag{31}$$

σ_i (i=I, II, III) representing the stresses in each pure mode. It is assumed that normal compressive stresses do not induce damage. Considering equation (26), the first equation (31) can be rewritten as a function of the relative displacements

$$\left(\frac{\delta_{1\mathrm{m,I}}}{\delta_{1,\mathrm{I}}}\right)^2+\left(\frac{\delta_{1\mathrm{m,II}}}{\delta_{1,\mathrm{II}}}\right)^2+\left(\frac{\delta_{1\mathrm{m,III}}}{\delta_{1,\mathrm{III}}}\right)^2=1 \tag{32}$$

where $\delta_{1\mathrm{m},i}$ (i=I, II, III) are the relative displacements corresponding to damage initiation. In the last two equations, to derive the mixed mode I+II equations, the mode III terms should be considered equal to zero. In the following equations, this simplification involves assuming

$$\delta_{\mathrm{III}}=\delta_{\mathrm{o,III}}=\delta_{\mathrm{u,III}}=0;\quad \beta_i=\beta=\frac{\delta_{\mathrm{II}}}{\delta_{\mathrm{I}}} \tag{33}$$

Defining an equivalent mixed mode displacement (δ_{m})

$$\delta_{\mathrm{m}}=\sqrt{\delta_{\mathrm{I}}^2+\delta_{\mathrm{II}}^2+\delta_{\mathrm{III}}^2} \tag{34}$$

and mixed mode ratios (β_i, i=I, II, III)

$$\beta_i=\frac{\delta_i}{\delta_{\mathrm{I}}}, \tag{35}$$

the mixed mode relative displacement at the onset of the softening process ($\delta_{1\mathrm{m}}$) can be obtained combining equations (32), (34) and (35)

$$\delta_{1\mathrm{m}}=\sqrt{\frac{1+\beta_{\mathrm{II}}^2+\beta_{\mathrm{III}}^2}{\frac{1}{\delta_{1,\mathrm{I}}^2}+\frac{\beta_{\mathrm{II}}^2}{\delta_{1,\mathrm{II}}^2}+\frac{\beta_{\mathrm{III}}^2}{\delta_{1,\mathrm{III}}^2}}} \tag{36}$$

Assuming (33) to yield the mixed mode I+II equation

$$\delta_{1\mathrm{m}}=\delta_{1,\mathrm{I}}\delta_{1,\mathrm{II}}\sqrt{\frac{1+\beta_{\mathrm{II}}^2}{\delta_{1,\mathrm{II}}^2+\beta_{\mathrm{II}}^2\delta_{1,\mathrm{I}}^2}} \tag{37}$$

Stress softening onset ($\delta_{2,i}$) was predicted using a criterion similar to (31), leading to

$$\left(\frac{\delta_{2\mathrm{m,I}}}{\delta_{2,\mathrm{I}}}\right)^2+\left(\frac{\delta_{2\mathrm{m,II}}}{\delta_{2,\mathrm{II}}}\right)^2+\left(\frac{\delta_{2\mathrm{m,III}}}{\delta_{2,\mathrm{III}}}\right)^2=1 \tag{38}$$

The mixed mode relative displacement at the onset of the stress softening process ($\delta_{2\mathrm{m}}$) can be obtained identically to the calculation of $\delta_{1\mathrm{m}}$

$$\delta_{2\mathrm{m}}=\sqrt{\frac{1+\beta_{\mathrm{II}}^2+\beta_{\mathrm{III}}^2}{\frac{1}{\delta_{2,\mathrm{I}}^2}+\frac{\beta_{\mathrm{II}}^2}{\delta_{2,\mathrm{II}}^2}+\frac{\beta_{\mathrm{III}}^2}{\delta_{2,\mathrm{III}}^2}}}\,. \tag{39}$$

The mixed mode I+II equation, according to (33), can be defined as

$$\delta_{2\mathrm{m}}=\delta_{2,\mathrm{I}}\delta_{2,\mathrm{II}}\sqrt{\frac{1+\beta_{\mathrm{II}}^2}{\delta_{2,\mathrm{II}}^2+\beta_{\mathrm{II}}^2\delta_{2,\mathrm{I}}^2}}\,. \tag{40}$$

Crack growth was simulated by the linear energetic criterion

$$\frac{J_{\mathrm{I}}}{J_{\mathrm{Ic}}}+\frac{J_{\mathrm{II}}}{J_{\mathrm{IIc}}}+\frac{J_{\mathrm{III}}}{J_{\mathrm{IIIc}}}=1\,. \tag{41}$$

When equation (41) is satisfied, damage growth occurs and stresses are completely released, with the exception of normal compressive ones. The energy released in each mode at complete failure can be obtained from the area of the minor trapezoid of Fig. 68

$$J_i = \frac{\sigma_{\mathrm{um},i}}{2}\left(\delta_{2\mathrm{m},i} - \delta_{1\mathrm{m},i} + \delta_{\mathrm{um},i}\right). \tag{42}$$

Combining equations (34), (35), (41) and (42) it can be written

$$\delta_{\mathrm{um}} = \frac{2(1+\beta_{\mathrm{II}}{}^2+\beta_{\mathrm{III}}{}^2)J_{\mathrm{Ic}}J_{\mathrm{IIc}}J_{\mathrm{IIIc}} - \delta_{1\mathrm{m}}\left(\delta_{2\mathrm{m}}-\delta_{1\mathrm{m}}\right)\left(d_{\mathrm{I}}J_{\mathrm{IIc}}J_{\mathrm{IIIc}} + d_{\mathrm{II}}\beta_{\mathrm{II}}{}^2J_{\mathrm{Ic}}J_{\mathrm{IIIc}} + d_{\mathrm{III}}\beta_{\mathrm{III}}{}^2J_{\mathrm{Ic}}J_{\mathrm{IIc}}\right)}{\delta_{1\mathrm{m}}\left(d_{\mathrm{I}}J_{\mathrm{IIc}}J_{\mathrm{IIIc}} + d_{\mathrm{II}}\beta_{\mathrm{II}}{}^2J_{\mathrm{Ic}}J_{\mathrm{IIIc}} + d_{\mathrm{III}}\beta_{\mathrm{III}}{}^2J_{\mathrm{Ic}}J_{\mathrm{IIc}}\right)}. \tag{43}$$

The corresponding mixed mode I+II equation, according to (33), is given by

$$\delta_{\mathrm{um}} = \frac{2(1+\beta^2)J_{\mathrm{Ic}}J_{\mathrm{IIc}} - \delta_{1\mathrm{m}}\left(\delta_{2\mathrm{m}}-\delta_{1\mathrm{m}}\right)\left(d_{\mathrm{I}}J_{\mathrm{IIc}} + d_{\mathrm{II}}\beta^2J_{\mathrm{Ic}}\right)}{\delta_{1\mathrm{m}}\left(d_{\mathrm{I}}J_{\mathrm{IIc}} + d_{\mathrm{II}}\beta^2J_{\mathrm{Ic}}\right)}, \tag{44}$$

which corresponds to the mixed mode ultimate relative displacement. The equivalent displacements ($\delta_{1\mathrm{m}}$, $\delta_{2\mathrm{m}}$ and δ_{um}) are used in equations (28) or (29) to define e_i and simulate material degradation.

3.2.2.1. Cohesive parameters

The trapezoidal laws in pure modes I and II of a 0.2 mm thickness adhesive layer of Araldite® 2015, used in this work, are following characterized. **The pure mode III cohesive law, used for 3D models, was equalled to the pure mode II one as an approximation**. In bonded assemblies, adhesives are in the form of thin layers and consequently behave differently relatively to adhesives as a bulk material (Andersson and Stigh 2004). In fact, the strain constraining effect of the adherends in the bonded assemblies and the respective typical mixed mode crack propagation justify this assumption (Andersson and Stigh 2004, Hogberg and Stigh 2006, Leffler et al. 2007). Actually, in bulk materials cracks tend to grow perpendicularly to the direction of maximum principal stress. In thin layers, cracks are forced to follow the bond length path. These scaling issues will be discussed with more detail in Sub-Section 4.2. To account for this difference, the cohesive laws of the adhesive layer were determined using an inverse data fitting method on fracture characterization tests, applied individually for each tested specimen (Campilho et al. 2008d, Campilho et al. 2009a). **Particular attention was paid to match as possible the adherend thickness and lay-up between these fracture characterization tests and the bonded assemblies to be simulated, since the cohesive parameters of the adhesive layer are known to depend on the adherends restraining to the adhesive layer**. In fact, Pardoen et al. (2005) performed a parametric study on the effect of the adherends thickness on the values of J_{Ic}, using the *Tapered Double Cantilever Beam* (TDCB) and CT fracture tests. It was shown that the increased bending of thin adherends promoted plasticity in the adhesive layer, greatly increasing J_{Ic}. Actually, the bending of thin adherents is associated with large root rotation and substantial shear stresses, which tend to promote plastic yielding in the adhesive, increasing plastic strains as well. Additionally, extra plastic dissipation associated with the bending of the adhesive layer develops around the crack tip. In this work, since the adhesive layer is fully modelled using the trapezoidal cohesive laws, these should reproduce the adhesive layer stiffness up to $\sigma_{\mathrm{u},i}$. This is accounted for in the stiffness parameters (d_i, i=I, II, III) included in the matrix **D** of equations (26) and (27), which are defined as the ratio between the E or shear (G) modulus and t_{A}. The DCB and ENF tests were used to characterize the adhesive Araldite® 2015 as a 0.2 mm thickness layer under pure modes I and mode II, respectively. These tests were initially used to obtain the respective value of J_{ic}, using a proper data reduction scheme, while the other cohesive parameters ($\sigma_{\mathrm{u},i}$ and $\delta_{2,i}$) were estimated using an inverse data fitting

method. Using this technique, the value of J_{ic}, which corresponds to the plateau value of the respective *R*-curve, is used as an input parameter in numerical DCB or ENF models. These models, presenting the same dimensions of each tested specimen, also include the respective pure mode cohesive law with the value of J_{ic} previously determined and typical values for $\sigma_{u,i}$ and $\delta_{2,i}$. A few numerical iterations must be performed until a good accuracy between the experimental and numerical load-displacement (P-δ) curves is obtained. A detailed description of this methodology is presented in the works of de Moura et al. (2008a, 2008b, 2009b). The following Sub-Sections describe the determination of the cohesive laws of a thin adhesive layer of the adhesive Araldite® 2015 in pure modes I and II following the inverse procedure. The specimens manufacturing and testing procedures are formerly addressed.

3.2.2.1.1. Specimens preparation

The specimens consisted on unidirectional laminates of CFRP cut from bulk laminates, produced by hand lay-up and cured in a hot plates press at *Faculdade de Engenharia da Universidade do Porto* (FEUP). The bulk laminates with dimensions of 400 mm x 400 mm were fabricated from a unidirectional 0º lay-up of sixteen plies of carbon/epoxy pre-preg (SEAL® Texipreg HS 160 RM) with 0.15 mm of ply thickness. This material was selected for the laminates and patches employed throughout this work, only varying the lay-ups and thickness. The laminate manufacturing process involves the following steps:

1. Unfreezing the pre-preg (stored in the freezer at -18ºC) for at least one hour.
2. Cutting the pre-preg in squares of 400 mm x 400 mm.
3. Stacking the laminate by hand lay-up, respecting the pre-defined sequence. In this procedure the plies are piled one at a time, after heating to promote an easier adhesion (Fig. 69 a), followed by the application of pressure on all the surface area with a small scraper (Fig. 69 b).

a)  b) 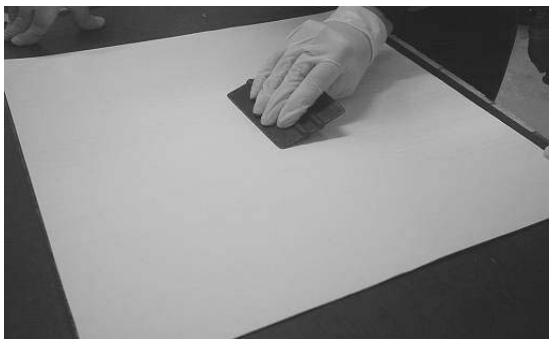

Fig. 69 – Heating the plies (a) and application of pressure (b) during the hand lay-up procedure.

4. Following the sixteen plies lay-up, the laminate is sealed with a Teflon® film to prevent contamination of the press during the curing procedure (Fig. 70 a). Sealing was completed with adhesive tape (Fig. 70 b). To provide a 2.4 mm thickness, spacing bars were used along the entire plate perimeter.
5. The laminate is cured in a hot plates press (Fig. 71 (a) and (b)) under the defined thermal cycle recommended by the material supplier (Fig. 72), under a pressure of 4 bar.
6. The laminate is removed from the press when the temperature reaches approximately 50ºC after cooling down from a one hour period at 130ºC.

a) 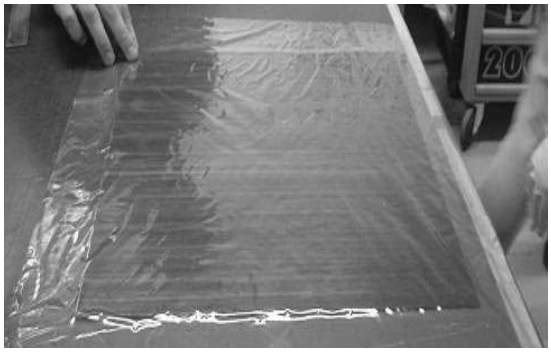 b) 

Fig. 70 – Laminate sealing with Teflon® film (a) and sealing with high-temperature adhesive tape (b).

a)  b) 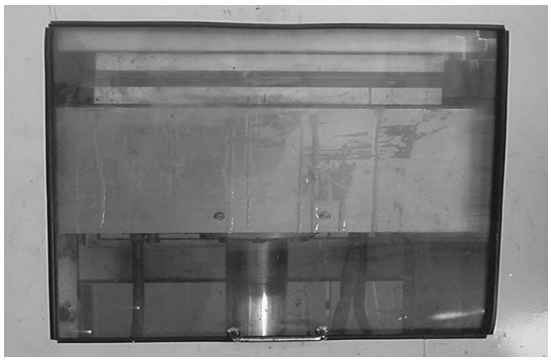

Fig. 71 – Laminate inside the press (a) and during curing (b).

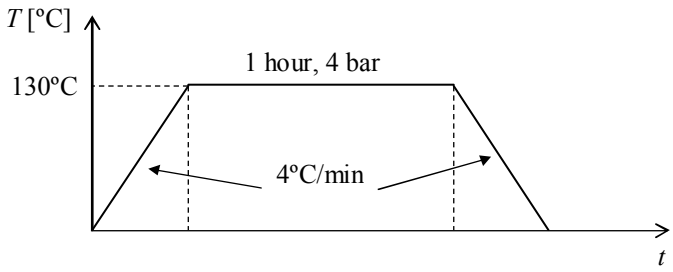

Fig. 72 – Thermal cycle applied to the laminate.

It is worth mentioning that a variation of the laminate properties in the thickness direction usually occurs due to an inevitable uneven curing cycle and thermal residual stresses. However, only small deviations are expected due to the reduced thickness of the laminates used in this work (Joh et al. 1993, Ersoy and Vardar 2000). After removal from the press, the laminate was cut into small specimens using a diamond disc cutting machine, and edge finishing was carried out manually with 120 grit sandpaper to remove the loose fibres and smoothen the sharp edges. Thickness and width measurement of the specimens was accomplished at several regions in the specimens length using a digital micrometer with a 1 μm precision. The specimens were grouped in pairs, matching their width as possible. Bonding was performed manually, following the procedure described below:

1. Abrasion of the bonding surfaces with 220 grit sandpaper until complete removal of their glossy outer surface.
2. Placement of the lower adherend in a wooden board to guarantee its flatness, followed by the introduction of 0.2 mm calibrated stainless steel spacers between the laminates on the edges of the bonding area, to guarantee the desired 0.2 mm adhesive thickness. The spacers were secured in position with cyanoacrylate glue. An

additional spacer was inserted at the pre-crack region, ensuring a perfect alignment of the lower and upper adherends along all the specimens length (Fig. 73 a).

3. Pouring of the adhesive in thin wires with the manufacturer mixing nozzle, covering the entire bonding area.
4. Application of the upper adherend and application of pressure with three grips on top of the spacers (Fig. 73 a).
5. Application of grips vertically at the edges of the bonding area (Fig. 73 (a) and (b)), assuring the correct width alignment between the lower and upper adherends.
6. Curing at room temperature for at least two hours before removing the grips.

a) 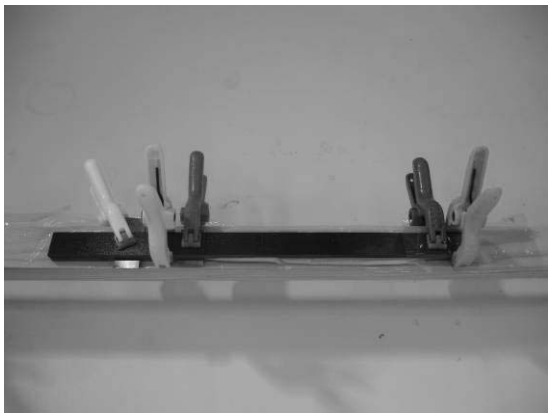 b) 

Fig. 73 – Pressure application with grips (a) and detail of the vertical grips (b).

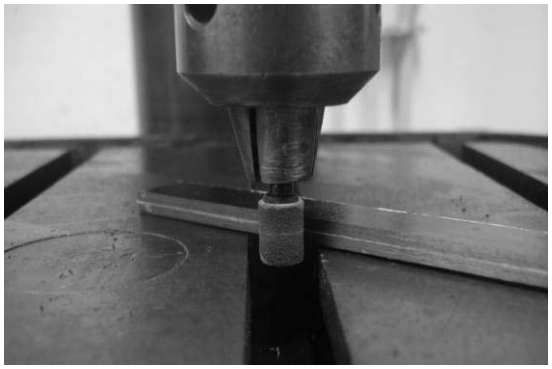

Fig. 74 – Finishing of a specimen in a drilling machine with a spiral band.

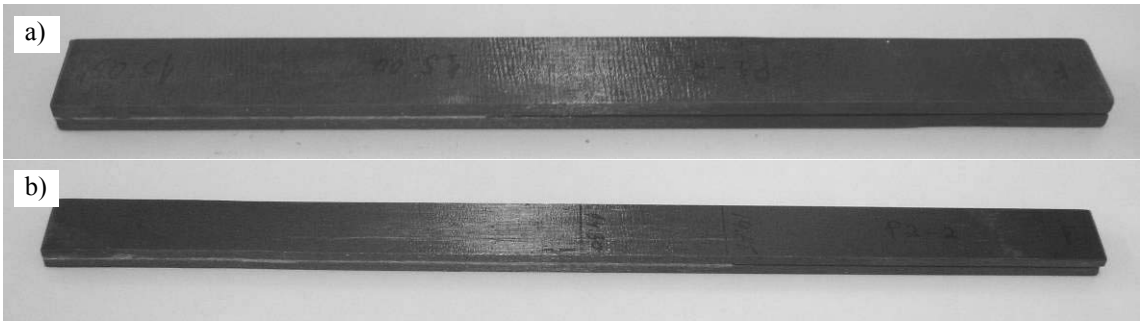

Fig. 75 – DCB (a) and ENF (b) specimens after finishing.

The excess of adhesive at the specimens edges was removed in a drilling machine with a *High Speed Steel* (HSS) end-mill, and finishing was performed with an abrasive 60 grit spiral band mounted on an expandable drum (Fig. 74). Fig. 75 shows a DCB (a) and ENF (b) specimen after finishing. Following, the specimens side faces were painted with

correction fluid and a scale was glued in one of the adherends, allowing for the crack length measurement during the test (Fig. 76). Stainless steel piano hinges were glued manually to the DCB specimens with the adhesive Araldite® 420, to apply the mode I loading. This adhesive was chosen due to its high strength and toughness. Fig. 77 shows the piano hinges glued to a DCB specimen (a) and a detail of the fillet at a hinge edge (b). Three piano hinges were used to determine experimentally Δ, a crack length correction for crack length rotation and deflexion. This issue will be addressed further in this Section, at the time of the data reduction schemes description for the determination of J_{Ic}.

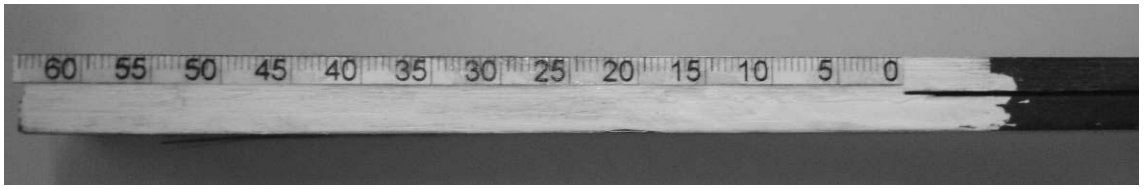

Fig. 76 – DCB specimen painted with correction fluid and with a scale.

a)  b) 

Fig. 77 – DCB specimen with glued piano hinges (a) and fillet detail (b).

3.2.2.1.2. Pure mode I (DCB specimen)

Several investigators addressed the determination of J_{Ic} of thin adhesive layers in bonded assemblies. Recently, CZM's have been used to simulate damage onset and growth in these structures, to accurately predict the fracture behaviour of bonded assemblies. Blackman et al. (2003) used a CZM approach on TDCB and peel tests under mode I load including two parameters, G_c and σ_{max}, to study the fracture of adhesively-bonded joints. A polynomial traction-separation law was considered, and special attention was paid to the physical significance of σ_{max}. It was concluded that the specimens compliance and G_c depend on the value of σ_{max} until a relatively high value of this parameter, when the dependence significantly diminished. Andersson and Stigh (2004) used an inverse method to determine the cohesive parameters of a ductile adhesive layer in a DCB specimen. The results showed that the stress-relative displacement relationship can be divided in three parts. Initially the stress increases proportionally to the elongation (linear elastic behaviour of the adhesive layer), until a limit stress is achieved. A plateau region follows, corresponding to the development of plasticity in the adhesive. The curve ends with a parabolic softening region. A similar softening law was employed by Tvergaard and Hutchinson (1993, 1996) and Yang et al. (1999, 2001). The majority of adhesively-bonded assemblies fracture characterization under pure mode I is performed using the DCB specimen (Andersson and Stigh 2004, Bader et al. 2000, Ducept et al. 2000, Nairn 2000, Hojo et al. 2006). The main advantages of this test method include its simplicity

and the possibility to obtain J_{Ic} mathematically using the beam theory (Yoshihara 2007). However, some issues must be taken into account to accurately measure this quantity. In fact, unstable crack propagation was experimentally detected by Bader et al. (2000) and Ducept et al. (2000), which hinders a clear crack length monitoring during the test. On other cases, in the DCB test of adhesively-bonded assemblies, the crack tip may not be clearly visible depending on the adhesive. This can induce non-negligible errors on the derivative of the compliance ($C=\delta/P$) relatively to the crack length (a) used in the *Compliance Calibration Method* (CCM). On the other hand, the energy dissipated at the FPZ can be large, namely when ductile adhesives are used (de Moura 2006). This implies that beam theory-based methods without any corrections will underestimate J_{Ic}. The *Compliance-Based Beam Method* (CBBM) based on the crack equivalent concept was recently developed (de Moura et al. 2008a, de Moura et al. 2008b), and accounts for the FPZ effects. In this method, J_{Ic} is extracted directly from the specimens compliance. Similar approaches were proposed in the works of Tamuzs et al. (2003) and Biel and Stigh (2008) for the DCB specimen.

3.2.2.1.2.1. Experimental work

The pure mode I cohesive law of the adhesive Araldite® 2015 as a thin layer was characterized with the DCB test. The geometry of the DCB specimens is shown in Fig. 78 (total length L_T=120 mm, initial crack length a_0=45 mm, laminate thickness t_P=2.4 mm, width b=15 mm and adhesive thickness t_A=0.2 mm). Unidirectional 0º lay-ups of carbon/epoxy pre-preg (SEAL® Texipreg HS 160 RM) with 16 plies were used as adherends, whose ply elastic properties are presented in Table 3. **Throughout this work, the CFRP components were always modelled as elastic orthotropic, owing to their brittle nature (Lin and Jen 1999), being employed CZM's for the composite interlaminar, intralaminar and fibre fractures whenever the experimental results show evidence of these phenomena**.

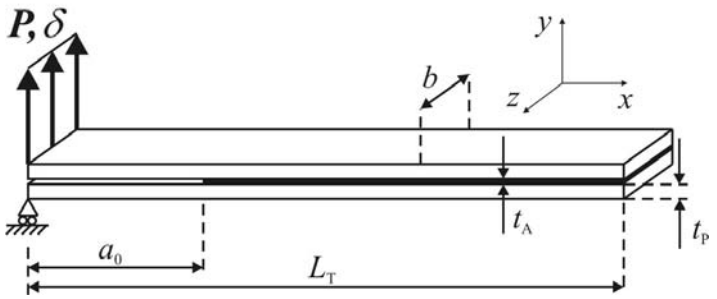

Fig. 78 – Schematic representation of the DCB test.

Table 3 – CFRP components elastic orthotropic properties for a unidirectional ply aligned in the x direction (Campilho et al. 2005).

E_x=1.09E+05 MPa	ν_{xy}=0.342	G_{xy}=4315 MPa
E_y=8819 MPa	ν_{xz}=0.342	G_{xz}=4315 MPa
E_z=8819 MPa	ν_{yz}=0.380	G_{yz}=3200 MPa

The elastic properties of the adhesive, E and G moduli, were measured experimentally (Lee and Kong 2000, Marques and da Silva 2008) in bulk tensile and TAST tests, respectively (E=1850 MPa, G=680 MPa). The bonding process included manual abrasion with 220 grit sandpaper and cleaning with acetone to increase the adhesion and avoid adhesive failures (Zimmerman and Liu 1995, Campilho et al. 2008a). After adhesively-bonding the laminates, the specimens were left to cure at room temperature for at least one week before testing. Five specimens were tested at

Instituto de Engenharia Mecânica e Gestão Industrial (INEGI) at room temperature and under displacement control (2 mm/min) in an Instron® 4208 electro-mechanical testing machine equipped with a 1 kN load cell. Fig. 79 (a) shows the experimental setup. The P-δ curve was registered during the test. Pictures were recorded during the specimens testing with 5 s intervals using a 10 MPixel digital camera. This procedure allows the measurement of a during crack growth to collect the P-δ-a parameters at several instants during the tests. This was performed correlating the time elapsed since the beginning of each test between the P-δ curve and each picture (the testing time of each P-δ curve point is defined accurately by the absolute displacement and the established loading rate). Fig. 79 (b) gives an example of a picture recorded during testing, allowing the crack length measurement. Cohesive propagations were obtained for all specimens, which is essential for the characterization of the adhesive layer cohesive properties (Campilho et al. 2008a).

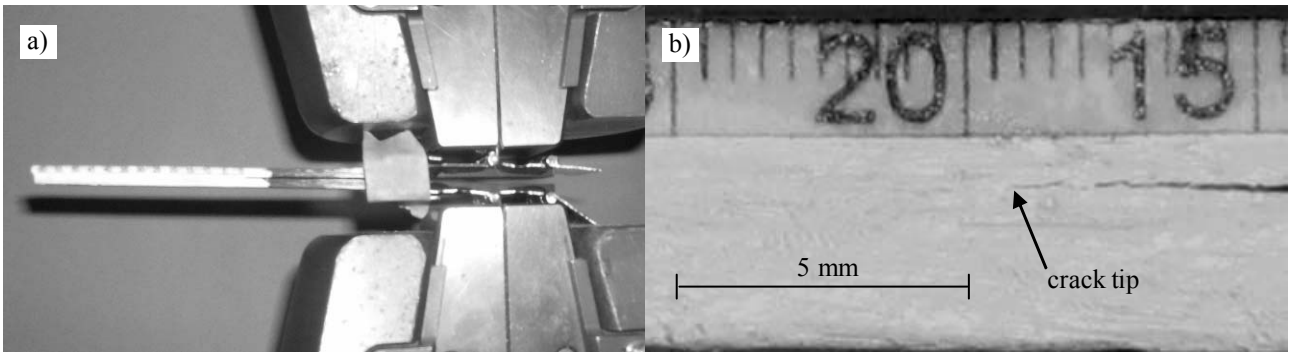

Fig. 79 – Experimental setup (a) and experimental crack length measurement during propagation (b).

3.2.2.1.2.2. Data reduction schemes

Different methods were employed to evaluate J_{Ic}. The CCM is based on the Irwin-Kies equation (Trantina 1972, Kanninen and Popelar 1985)

$$J_{Ic} = \frac{P^2}{2b}\frac{dC}{da}. \tag{45}$$

Cubic polynomials (C=C_3a_3+C_2a_2+C_1a+C_0) are used to fit the C=f(a) curves. Beam theories were also used to measure J_{Ic}. The *Direct Beam Theory* (DBT), based on elementary beam theory, gives (Ding 1999)

$$J_{Ic} = \frac{12a^2P^2}{b^2t_p{}^3E_x}, \tag{46}$$

E_x representing the Young's modulus of the adherends in the longitudinal direction. By the *Corrected Beam Theory* (CBT), J_{Ic} is obtained using (Robinson and Das 2004)

$$J_{Ic} = \frac{3P\delta}{2b\left(a+|\Delta|\right)}, \tag{47}$$

where Δ is the crack length correction for crack tip rotation and deflection mentioned in the experimental procedure. In fact, in the beam theory it is assumed that each arm of the DCB specimen is a clamped beam with the length equal to the value of a, which does not reflect the real conditions of the DCB test. Δ corrects the value of a for the crack tip rotation and deflection of the specimen arms, being determined by a linear regression of $C^{1/3}$=f(a). This can be performed by slightly loading the specimen with three different initial crack lengths to define the $C^{1/3}$=f(a) linear regression. The value of Δ is extracted from $C^{1/3}$=0 (de Moura et al. 2008b). The CBBM was recently developed (de

Moura et al. 2008a, de Moura et al. 2008b) and is based on the crack equivalent concept, depending only on the specimen's compliance during the test. J_{Ic} can be obtained by the following expression

$$J_{Ic} = \frac{6P^2}{b^2 t_P}\left(\frac{2a_{eq}^2}{t_P^2 E_f} + \frac{1}{5G_{xy}}\right). \quad (48)$$

a_{eq} is an equivalent crack length obtained from the experimental compliance and accounting for the FPZ at the crack tip, E_f is a corrected flexural modulus to account for all phenomena affecting the P-δ curve, such as stress concentrations at the crack tip and stiffness variability between specimens, and G_{xy} is the shear modulus in the xy plane.

3.2.2.1.2.3. Experimental results

J_{Ic} was evaluated by the four methods described in Sub-Section 3.2.2.1.2.2. Fig. 80 shows the experimental R-curves for one tested specimen. A correspondence was established between a_{eq} and a using the applied displacement, to plot the CBBM R-curve as a function of a instead of a_{eq}. Table 4 presents the J_{IIc} results of all specimens, including the average values and standard deviation. Similar results were obtained by the CBT and CBBM. The CCM results show slight divergent values, explained by polynomial fitting difficulties (Hug et al. 2006, de Moura et al. 2008b). The DBT presents a smaller value of J_{Ic} for all tested specimens. In fact, this method does not include crack length corrections to account for root rotation and shear effects, which explains the underestimated results. **The average value of the CBBM is chosen to define the value of J_{Ic} of a t_A=0.2 mm layer of the adhesive Araldite® 2015 (J_{Ic}=0.43 N/mm)**.

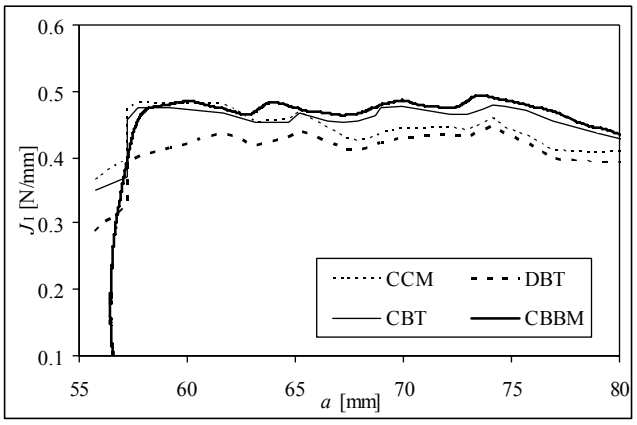

Fig. 80 – Experimental R-curves obtained by different methods.

Table 4 – J_{Ic} (N/mm) values of the five specimens obtained by different methods.

Specimen	CCM	DBT	CBT	CBBM
1	0.40	0.37	0.45	0.44
2	0.39	0.36	0.42	0.42
3	0.43	0.29	0.44	0.40
4	0.33	0.36	0.40	0.41
5	0.46	0.42	0.45	0.46
Avg. J_{Ic}	0.40	0.36	0.43	0.43
St. Dev.	0.04	0.04	0.02	0.02

3.2.2.1.2.4. Numerical analysis

The trapezoidal mixed mode CZM presented in Sub-Section 3.2.2 was used to simulate the behaviour of a t_A=0.2 mm adhesive layer of Araldite® 2015 in pure mode I. An inverse data fitting method was employed to ascertain the cohesive law in mode I. The numerical approach is also applied to ascertain the suitability of the data reduction schemes tested to obtain J_{Ic}, comparing the input value of J_{Ic} with the values provided by the different methods. In the inverse methodology, the CBBM values of J_{Ic}, which correspond to the plateau values of the *R*-curve, are initially considered as an input parameter in the numerical approach, which includes the trapezoidal mixed mode CZM to simulate damage initiation and growth, with typical values for $\sigma_{u,I}$ and $\delta_{2,I}$. In the following step, some numerical iterations are performed, until a good accuracy between the experimental and numerical P-δ curves is attained (Fig. 81), thus defining the values of $\sigma_{u,I}$ and $\delta_{2,I}$. The deformed shape of the DCB specimen during damage propagation and the applied boundary and loading conditions are shown in Fig. 82.

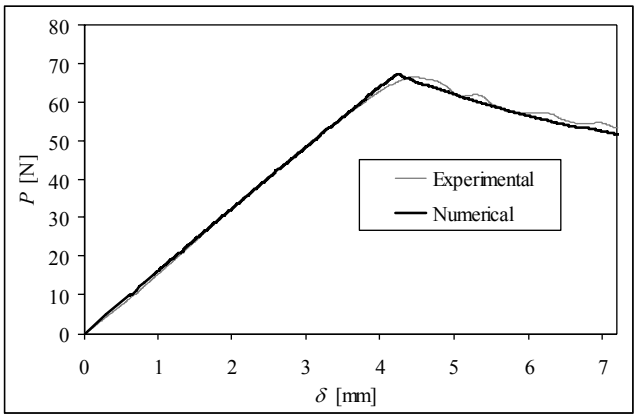

Fig. 81 –Experimental and numerical P-δ curves comparison.

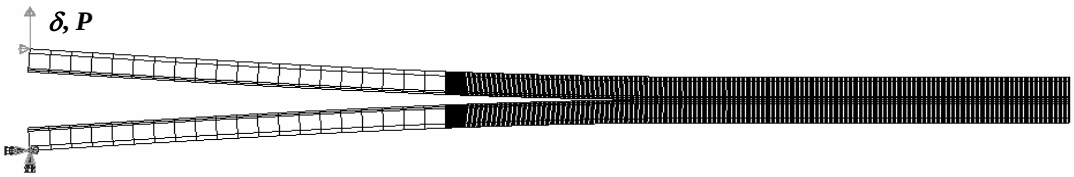

Fig. 82 – Deformed shape of the DCB specimen during propagation, with boundary and loading conditions.

The specimen arms were modelled with plane-strain 8-node quadrilateral solid finite elements (CPE8 from ABAQUS®) and the adhesive was modelled with 6-node cohesive elements, including the trapezoidal mixed mode CZM. Four solid finite elements were used through-thickness in each arm, with a more refined mesh near the adhesive region and the respective outer surface (Trantina 1972, Daghyani et al. 1996). In the damage propagation region a more refined mesh was used, considering 0.15 mm length elements. The applied boundary conditions consisted on clamping the lower edge node of the lower arm, and applying a vertical displacement and horizontally restraining the upper edge node of the upper arm (Fig. 82). $\sigma_{u,I}$ was not found to greatly influence the P-δ curve (Fig. 83 a). Consequently, $\sigma_{u,I}$ was fixed at 23 MPa, which is the average value of all the specimens tested. The influence of $\delta_{2,I}$ on the P-δ curve was also assessed. *R* represents the ratio between the descending and ascending lengths of the pure mode I trapezoidal law (Fig. 68)

$$R = \frac{\delta_{u,I} - \delta_{2,I}}{\delta_{1,I}}. \quad (49)$$

Since this parameter practically did not influence the P-δ curve for $0.5 \leq R \leq 2$, R=1 was defined. This analysis shows that a unique solution is not achieved with the inverse methodology for the pure mode I cohesive law of the adhesive, since $\sigma_{u,I}$ and $\delta_{2,I}$ practically do not affect the numerical P-δ curve, which is ruled by the value of J_{Ic}. Despite constituting a limitation, this detail was not found to endanger the accuracy of the predictions, as will be discussed in the validations performed in Section 3 and throughout this thesis. Fig. 83 (b) presents the average cohesive law and respective cohesive parameters ($J_{Ic\ avg}$, $\sigma_{u,I\ avg}$ and $\delta_{2,I\ avg}$), and the trapezoidal laws range obtained fitting the P-δ curves of the five specimens tested. **The average values obtained will be used in this work to characterize the pure mode I behaviour of a t_A=0.2 mm adhesive layer of Araldite® 2015 on all tested geometries**.

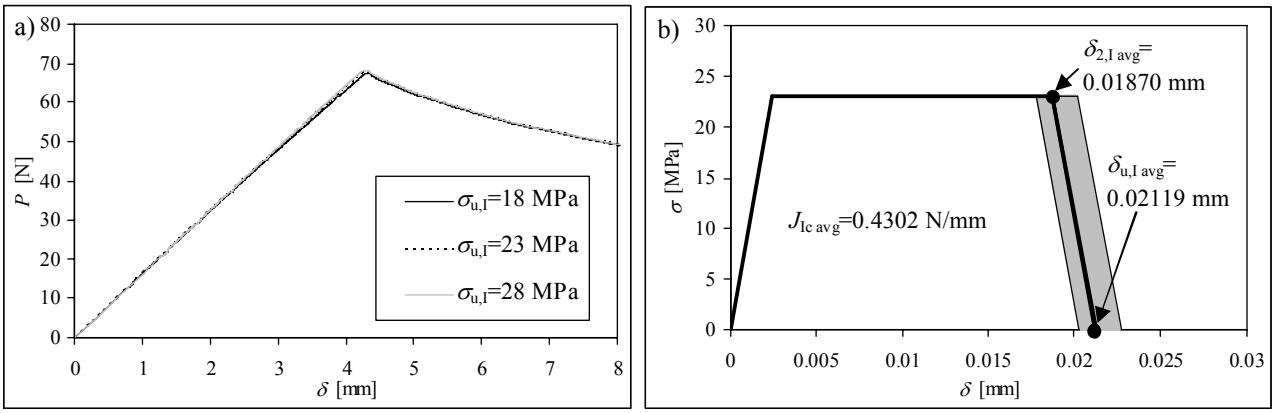

Fig. 83 – Influence of $\sigma_{u,I}$ on the P-δ curve (a) and cohesive laws range in pure mode I (b).

3.2.2.1.2.5. Comparison between the experimental and numerical results

The suitability of the data reduction schemes used to measure accurately J_{Ic} was evaluated by numerical simulations of the DCB test, comparing the input values of J_{Ic} with the values extracted by each method. The numerical P-δ-a parameters were collected to obtain the respective R-curves. Fig. 84 (a) shows the numerical R-curves for one specimen.

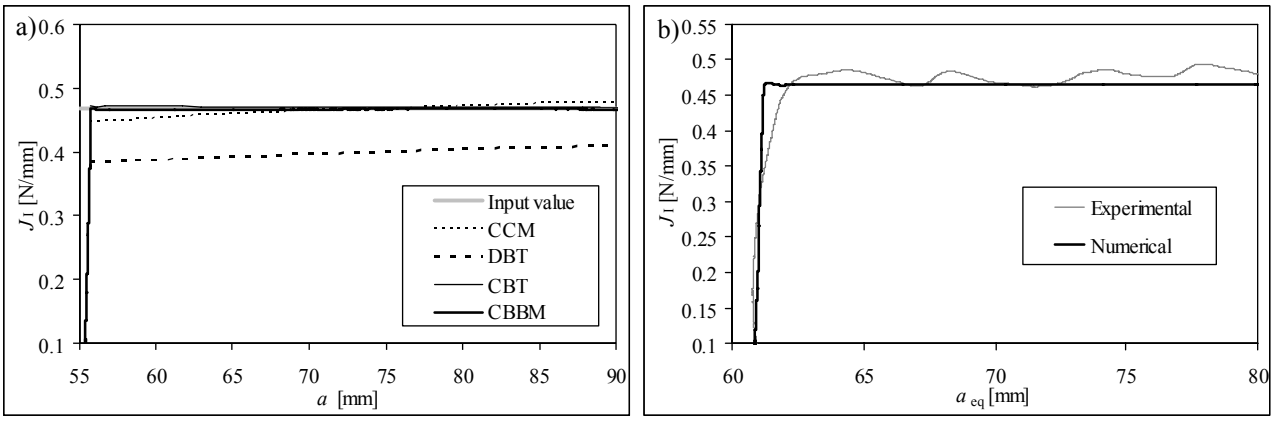

Fig. 84 – Numerical R-curves by different methods (a) and experimental and numerical CBBM R-curves (b).

The CBBM and CBT provide the most accurate results, when compared to the input value. A comparison between the experimental and numerical *R*-curves using the CBBM is presented in Fig. 84 (b), for the same specimen of Fig. 81, after the fitting procedure. Table 5 presents the global results of J_{Ic} predicted by the several methods, the respective error relatively to the input value and the average error based on absolute error values for each method. The CBBM yields the best results, with an average error of 0.5%. The CBT also agrees with the input value of J_{Ic}. An error of 5.6% was obtained using the CCM, due to polynomial fitting difficulties (Hug et al. 2006, de Moura et al. 2008b). The larger differences were attained with the DBT, whose J_{Ic} predictions were 14.9% lower than the input ones. **In conclusion, it was found that the CBBM, used to obtain the value of J_{Ic}, is an accurate method to this end**.

Table 5 – Input and predicted J_{Ic} [N/mm] values by the four methods.

Specimen	Input	CCM	Err. [%]	DBT	Err. [%]	CBT	Err. [%]	CBBM	Err. [%]
1	0.444	0.420	-5.4	0.375	-15.5	0.448	1.0	0.442	-0.5
2	0.420	0.442	5.3	0.355	-15.6	0.422	0.5	0.416	-0.9
3	0.415	0.452	9.0	0.352	-15.1	0.423	2.0	0.413	-0.5
4	0.406	0.373	-8.2	0.348	-14.3	0.410	0.9	0.405	-0.3
5	0.468	0.469	0.2	0.402	-14.1	0.472	0.8	0.466	-0.3
Avg. Error [%]			5.6		14.9		1.0		0.5

3.2.2.1.3. Pure mode II (ENF specimen)

Fracture characterization of adhesively-bonded assemblies under pure mode I has been extensively studied by several authors. However, mode II is still not well addressed owing to some inherent features of the most popular tests: ENF, ELS and *Four-Point End-Notched Flexure* (4ENF). The ELS test involves clamping one of the specimen edges, constituting a source of variability and increasing the complexity of data reduction (Blackman et al. 2005). On the other hand, the 4ENF test requires a complex setup and presents some problems related to large friction effects (Schuecker and Davidson 2000). Therefore, the ENF appears to be the most suitable test for mode II fracture characterization of adhesively-bonded assemblies (Davidson et al. 1996, Blackman et al. 2006, Leffler et al. 2007). However, problems related to unstable crack growth and to crack monitoring during propagation are yet not well solved. In fact, in mode II fracture characterization tests, the crack tends to close due to the applied load, which hinders a clear visualization of its tip. In addition, the classical data reduction schemes, based on beam theory analysis and compliance calibration, require crack monitoring during propagation. Moreover, added to these factors a quite extensive FPZ develops ahead of the crack tip for ductile adhesives. This non-negligible FPZ affects the measurement of J_{IIc}. Consequently, its influence should be taken into account, which does not occur when the real value of a is used in the selected data reduction scheme. To overcome these limitations, a new data reduction scheme based on the crack equivalent concept and depending only on the specimen compliance is also used to evaluate J_{IIc}.

3.2.2.1.3.1. Experimental work

The ENF test was used to characterize in pure mode II a t_A=0.2 mm adhesive layer of Araldite® 2015. Fig. 85 shows the geometry of the ENF specimens. The following dimensions were considered: half-span length L_H=100 mm, initial crack

length a_0=70 mm, laminate thickness t_P=2.4 mm, width b=15 mm and adhesive thickness t_A=0.2 mm. The value of a_0 was equalled to 70% of L_H, to provide a stable crack growth (Carlsson et al. 1986). The same unidirectional 0º lay-ups of carbon/epoxy pre-preg (SEAL® Texipreg HS 160 RM) with 16 plies and 0.15 mm ply thickness were used as adherends (whose ply elastic properties are described in Table 3). The determination of the adhesive elastic properties was discussed in Sub-Section 3.2.2.1.2.1. The bonding surfaces were abraded manually with sandpaper and cleaned with acetone prior to bonding, to avoid adhesive failures (Zimmerman and Liu 1995, Campilho et al. 2008a). Assembly was achieved pressing the laminates with grips and curing at room temperature for at least one week before testing. Five specimens were tested at INEGI in an Instron® 4208 electro-mechanical testing machine equipped with a 1 kN load cell, at room temperature under displacement control (2 mm/min), registering the P-δ curve during the test. Fig. 86 (a) shows the experimental setup. In pure mode II fracture tests, crack length monitoring during propagation is very difficult to perform, as the crack grows without a clear opening (Blackman et al. 2005, de Moura et al. 2006a). Nevertheless, the crack length was monitored by taking photos during the tests with 5 s intervals using a 10 MPixel digital camera (Fig. 86 b). For an improved crack tip visualization, the specimens were painted with correction fluid. These procedures aid to the reduction of reading errors made by visual inspection during the tests. The experimental values of P-δ-a as a function of time were obtained. The testing time of each P-δ data point was calculated from the current value of δ and the loading rate. The correspondence to the values of a was established knowing the testing time of each picture.

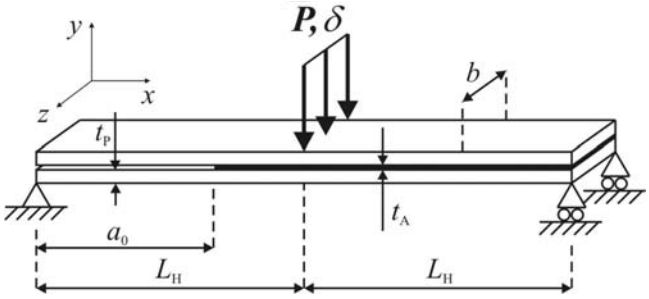

Fig. 85 – Schematic representation of the ENF test.

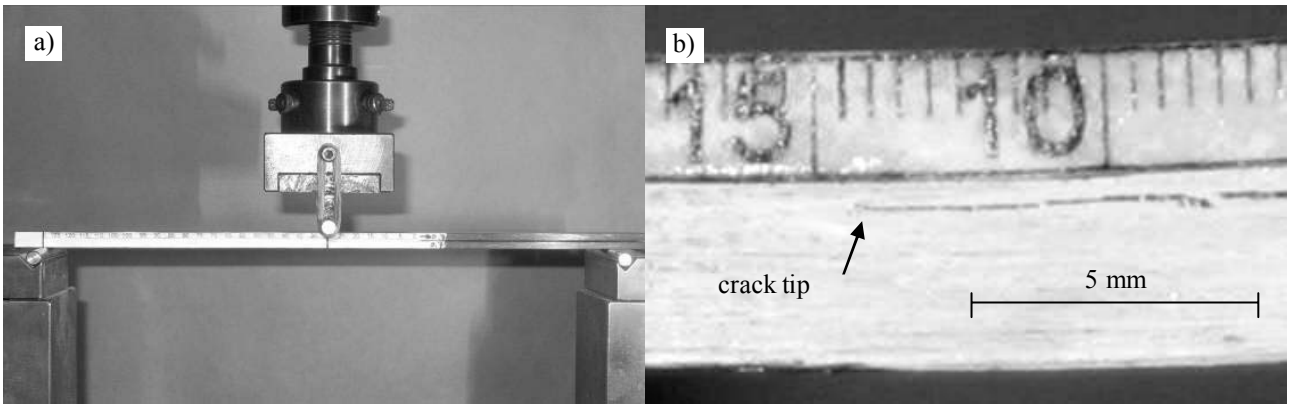

Fig. 86 – Experimental setup (a) and experimental crack length measurement during propagation (b).

3.2.2.1.3.2. Data reduction schemes

The classical data reduction schemes to obtain J_{IIc} are usually based on compliance calibration or beam theories. The CCM is based on the Irwin-Kies equation (Trantina 1972, Kanninen and Popelar 1985)

$$J_{\mathrm{IIc}} = \frac{P^2}{2b}\frac{dC}{da}. \tag{50}$$

Cubic polynomials ($C=C_1a^3+C_0$) were used to fit the $C=\mathrm{f}(a)$ curves, leading to

$$J_{\mathrm{IIc}} = \frac{3P^2C_1\,a^2}{2b} \tag{51}$$

For the ENF test, the DBT was not employed, due to a large expected disparity of the J_{IIc} values, arising from the absence of corrections. The CBT proposed by Wang and Williams (1992) leads to

$$J_{\mathrm{IIc}} = \frac{9(a+0.42\Delta_1)^2P^2}{16b^2E_{\mathrm{x}}{t_{\mathrm{P}}}^3}, \tag{52}$$

where Δ_1 is a crack length correction to account for shear deformation

$$\Delta_1 = h\sqrt{\frac{E_{\mathrm{x}}}{11G_{\mathrm{xy}}}\left[3-2\left(\frac{\Gamma}{1+\Gamma}\right)^2\right]} \tag{53}$$

with

$$\Gamma = 1.18\frac{\sqrt{E_{\mathrm{x}}E_{\mathrm{y}}}}{G_{\mathrm{xy}}}. \tag{54}$$

The CBBM was also developed for the ENF specimen (de Moura et al. 2008a, de Moura et al. 2009b), allowing obtaining J_{IIc} only using the experimental compliance, giving

$$J_{\mathrm{IIc}} = \frac{9P^2a_{\mathrm{eq}}^2}{16b^2E_{\mathrm{f}}{t_{\mathrm{P}}}^3}, \tag{55}$$

where a_{eq} is directly obtained from the P-δ curve and accounts for the FPZ effects at the crack tip.

3.2.2.1.3.3. Experimental results

The experimental P-δ-a parameters were used to obtain J_{IIc} as a function of a for the CCM and the CBT. The crack length correction Δ_1 used in the CBT (equation (53)) was calculated individually for each specimen, taking into account the E modulus variation between specimens, giving an average value of 4.706 mm. The complete CBBM R-curves were determined from the respective experimental P-δ curves and equation (55).

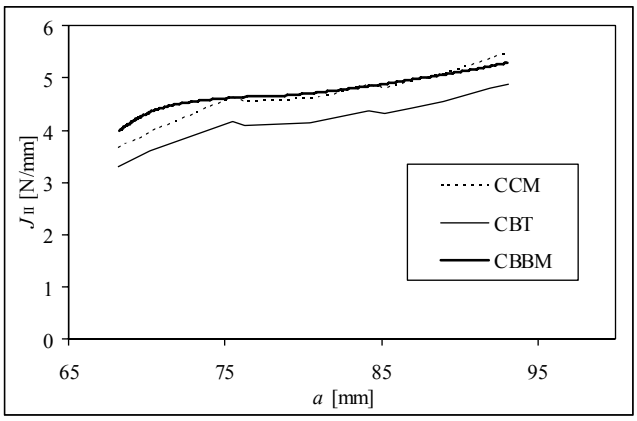

Fig. 87 – Experimental R-curves obtained by different methods.

A comparison between the three methods is presented in Fig. 87 for one of the specimens tested. Equally to the pure mode I analysis, a correspondence between a_{eq} and a using the applied displacement was applied, to plot the CBBM R-curve as a function of a. The global results of all specimens are summarized in Table 6. Fig. 87 shows, for the three data reduction schemes, a short plateau region followed by an increasing trend of J_{II}=f(a), especially when the crack approaches the loading cylinder. This effect is justified by the large FPZ of this adhesive, due to its high value of J_{IIc}. In fact, the quite large FPZ quickly attains the loading cylinder, where compressive stresses oppose to crack growth. The CCM and the CBBM behave identically, whilst the CBT underestimates J_{IIc} (de Moura 2006). Analysing the average results of all specimens (Table 6), J_{IIc} is slightly higher for the CBBM than the CBT. **The value of J_{IIc} for the Araldite® 2015 cohesive law in pure mode II was equalled to the average value of the CBBM (J_{IIc}=4.70 N/mm)**.

Table 6 – J_{IIc} [N/mm] values of the five specimens obtained by different methods.

Specimen	CCM	CBT	CBBM
1	4.71	4.7	4.94
2	4.87	4.87	5.13
3	4.81	4.09	4.82
4	4.15	4.27	4.28
5	4.44	4.09	4.32
Avg. J_{IIc}	4.60	4.40	4.70
St. Dev.	0.27	0.32	0.34

3.2.2.1.3.4. Numerical analysis

A numerical analysis was performed to characterize the trapezoidal cohesive law in pure mode II of a t_A=0.2 mm adhesive layer of Araldite® 2015. A similar data fitting procedure to the pure mode I law was followed (Sub-Section 3.2.2.1.2.4). The resulting law was then used to ascertain the accuracy of the three data reduction schemes employed to extract the values of J_{IIc}. This assessment is based on the comparison between the J_{IIc} values input in the numerical models with the values provided by the three methods, calculated from the P-δ-a data obtained from those analyses. The CBBM values of J_{IIc} for each one of the five specimens tested were employed in the inverse method. These values, corresponding to the plateau value of the respective R-curves (Table 6), were used as inputs in the numerical models. The remaining cohesive parameters ($\sigma_{u,II}$ and $\delta_{2,II}$) were estimated by the inverse method, fitting the experimental and numerical P-δ curves of each specimen. Fig. 88 (a) shows the experimental and numerical P-δ curves for one tested specimen after the fitting procedure. Fig. 89 shows the deformed shape of the ENF specimen during crack propagation, and the respective boundary and loading conditions. The specimen arms were modelled with plane-strain 8-node quadrilateral solid finite elements (CPE8 from the ABAQUS® library). The adhesive layer was simulated with six-node cohesive elements compatible with the ABAQUS® elements, including the trapezoidal mixed mode CZM. Each specimen arm was modelled by eight solid finite elements through-thickness. A more refined mesh was considered at the propagation region and near the cylinders (Daghyani et al. 1996). The boundary conditions consisted on clamping the supporting cylinders in the x and y directions and restraining the loading cylinder in the x direction. The lowest node at the specimen mid-section was also restrained in the direction x. Fig. 88 (b) shows the average pure mode II cohesive law and respective values of J_{IIc}, $\sigma_{u,II}$ and $\delta_{2,II}$, and the trapezoidal cohesive laws range obtained fitting the five

experimental P-δ curves. The manual fitting allowed a clear insight on the influence of the cohesive parameters on the numerical P-δ curves profile. J_{IIc}, which is the input value in the numerical simulations, mainly influences the peak load value. Higher values of $\sigma_{u,II}$ increase the peak load, and the specimen stiffness up to the peak load, leading to a more abrupt post-peak load reduction. Finally, $\delta_{2,II}$ plays an important role on the roundness of the P-δ curve near the peak value. This indicates that a unique solution for the pure mode II cohesive law of the adhesive is guaranteed by this methodology. **The average values of the pure mode II cohesive law will be used in this work to simulate the t_A=0.2 mm adhesive layer of Araldite® 2015 on all tested geometries**.

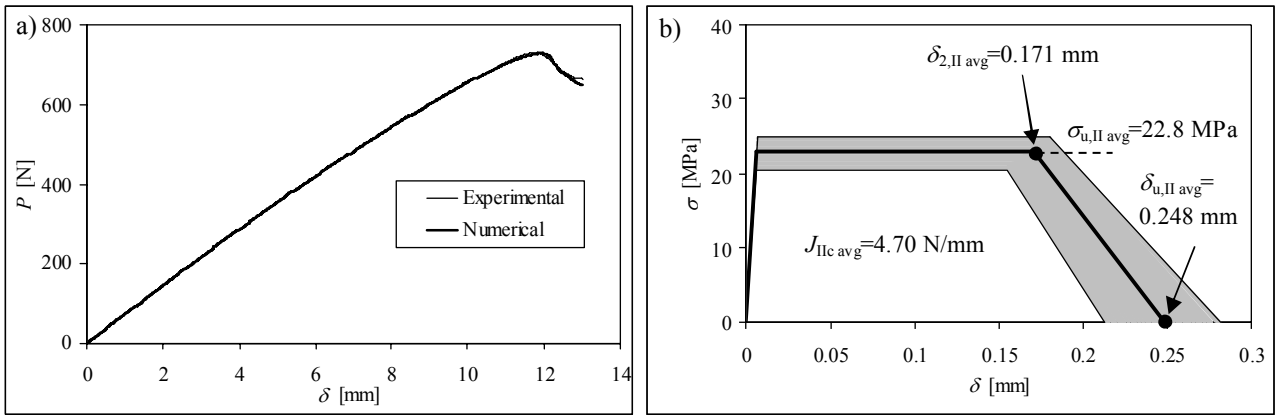

Fig. 88 – Experimental and numerical P-δ curves comparison (a) and cohesive laws range in pure mode II (b).

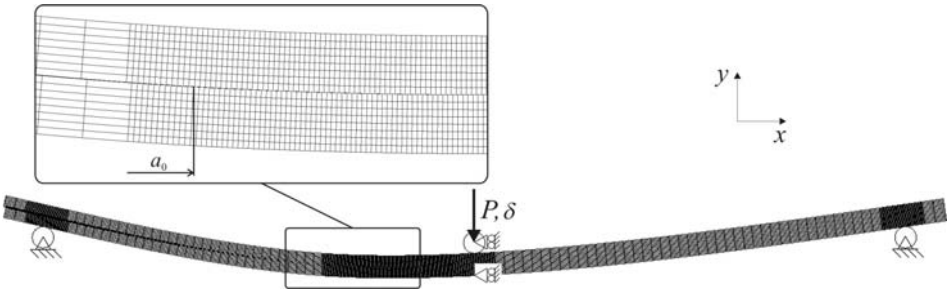

Fig. 89 – Deformed shape of the ENF specimen during propagation, with boundary and loading conditions.

3.2.2.1.3.5. Comparison between the experimental and numerical results

A numerical study was performed to assess the adequacy of the three data reduction schemes to measure accurately J_{IIc}, in an attempt to reproduce the input value of J_{IIc}. To accomplish this study, the numerical P-δ-a parameters were collected during crack propagation, allowing obtaining the values of J_{IIc} for each method. Fig. 90 (a) shows the results for one specimen. Accurate results were obtained with the CCM and especially the CBBM. The CBT underestimated the input J_{IIc}. Moreover, it should be emphasized that the CCM also requires the crack length measurement during the propagation stage which, even using an optical method, is prone to introduce additional errors. On the other hand, using the CBBM, the complete R-curve is extracted from the P-δ data. Fig. 90 (b) compares the experimental and numerical R-curves using the CBBM, for the same specimen of Fig. 88 (a), after the fitting procedure. The initial part of the curve (before the J_{II} plateau) does not correspond to crack propagation, but to the FPZ. In fact, since a_{eq} includes the FPZ effects, the FPZ development is also accounted for in the J_{II}=f(a_{eq}) plot. Crack growth only initiates at the beginning of

the plateau. A summary of the J_{IIc} values predicted by the three data reduction schemes for the five specimens is presented in Table 7. Accurate predictions were achieved with the CBBM (average error of 0.6%) and the CCM (average error of 2.9%). However, the CBT showed a large discrepancy, underestimating the input value of J_{IIc} by 24.9%. This difference is not consistent with the test results, since the experimental J_{IIc} values provided by the three methods were in close agreement. As observed in Fig. 91, the experimental and numerical offset on the value of a is practically independent of C. This attests the inaccuracy in the experimental identification of the crack tip. Probably, the FPZ damage ahead of the crack tip induces material deformation originating some local slip, which fractures the correction fluid layer used to track the evolution of a during the test. This yielded a bigger value of a than the effective one by a constant amount, during the process of self-similar propagation with a pronounced FPZ at the crack tip.

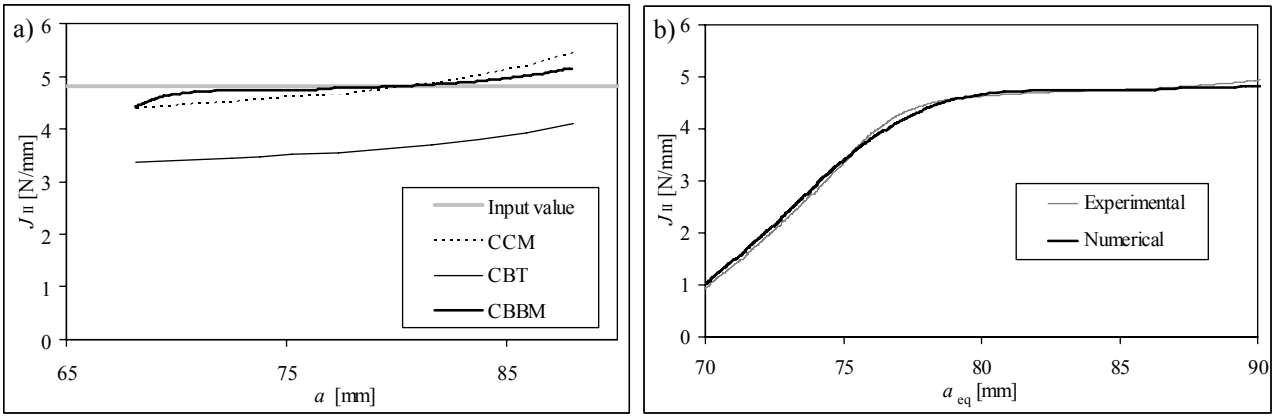

Fig. 90 – Numerical R-curves by different methods (a) and experimental and numerical CBBM R-curves (b).

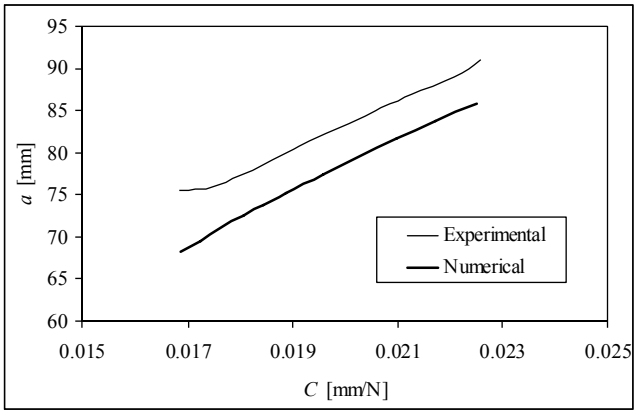

Fig. 91 – Experimental and numerical crack length as a function of the specimen compliance.

Table 7 – Input and predicted J_{IIc} [N/mm] values by the three methods.

Specimen	Input	CCM	Err. [%]	DBT	Err. [%]	CBT	Err. [%]
1	4.94	4.74	-4.0	3.73	-24.5	4.89	-0.9
2	5.13	5.05	-1.6	3.84	-25.1	5.07	-1.1
3	4.82	4.76	-1.2	3.62	-24.9	4.80	-0.5
4	4.28	4.10	-4.2	3.24	-24.3	4.26	-0.4
5	4.32	4.17	-3.5	3.21	-25.7	4.31	-0.2
Avg. Error [%]			2.9		24.9		0.6

3.2.2.1.4. Summary of the results

Table 8 summarizes the cohesive parameters obtained, which will be used in this work to simulate a t_A=0.2 mm adhesive layer of Araldite® 2015 in all the repairs tested in this thesis. On the other hand, as will be detailed further in this work, the experimental failure modes for some of the repair techniques studied also included regions of interlaminar and transverse intralaminar failures. Consequently, the respective cohesive laws were also obtained experimentally using a similar inverse data fitting procedure (Table 9). However, it should be emphasized that, in these situations, a traditional penalty function method was used (de Moura et al. 1997) for the initial ascending part of the cohesive laws (considering d_i=10^6 N/mm^3 in the matrix **D** of equations (26) and (27)), since the cohesive elements in these cases simulate a zero thickness interface instead of a finite thickness layer. Moreover, triangular shape laws were used ($\delta_{2,i}$=$\delta_{1,i}$ in Fig. 68), due to the brittle nature of these interfaces (Lee and Soutis 2008). A detailed description of the interlaminar and intralaminar characterization of the CFRP used in this work is not presented here, due to the similitude to the adhesive characterization, despite having been published recently (Campilho et al. 2009d, de Moura et al. 2009c). Table 9 also includes the cohesive parameters used to simulate a tensile fibre failure. This failure option will be introduced in some of the numerical models of the repairs, although it was not observed in the experiments. The fibre properties were not obtained experimentally; they were estimated from typical values in the literature for the material in question (Campilho et al. 2008a, Campilho et al. 2009a).

Table 8 – Cohesive parameters of a t_A=0.2 mm adhesive layer of Araldite® 2015 in pure modes I and II.

	Pure mode I	Pure mode II
Elastic modulus [GPa]	1850	680
$\sigma_{u,i}$ [MPa]	23.0	22.8
J_i [N/mm]	0.43	4.70
$\delta_{1,i}$ [mm]	0.0025	0.0067
$\delta_{2,i}$ [mm]	0.01870	0.171
$\delta_{u,i}$ [mm]	0.02119	0.248

Table 9 – Cohesive parameters for CFRP interlaminar, intralaminar and fibre failures in pure modes I and II (Campilho et al. 2009a).

	Interlaminar		Intralaminar		Fibre	
Pure mode	I	II	I	II	I	II
d_i [N/mm^3]	10^6	10^6	10^6	10^6	10^6	10^6
$\sigma_{u,i}$ [MPa]	25.0	13.5	42.6	39.3	750	100
J_i [N/mm]	0.33	0.79	0.54	0.93	20	4
$\delta_{1,i}$=$\delta_{2,i}$ [mm]	$2.5*10^{-5}$	$1.4*10^{-5}$	$4.3*10^{-5}$	$3.9*10^{-5}$	$7.5*10^{-4}$	$1.0*10^{-4}$
$\delta_{u,i}$ [mm]	$2.6*10^{-2}$	0.117	$2.5*10^{-2}$	$4.7*10^{-2}$	$5.3*10^{-2}$	$8.0*10^{-2}$

3.2.3. Validation of the trapezoidal cohesive zone model

This Sub-Section aims the validation of the developed trapezoidal CZM with experiments. The tensile behaviour of adhesively-bonded CFRP SS repairs is initially considered to this end, using experimental results from a previous study

(Campilho 2005). The failure mode, equivalent stiffness and failure load of the repairs were evaluated for different values of overlap length and patch thickness. The ductile adhesive Araldite® 420 was used. An initial elastic stress analysis was performed to identify the critical regions of the repairs and probable fracture paths. The trapezoidal CZM was used to predict the failure modes and repair strengths. **In this initial study, the cohesive parameters were estimated from the bulk adhesive properties, based on justified assumptions. Previous published works assuming adhesive bulk properties for the cohesive parameters, with acceptable results, support this course of action (Gonçalves et al. 2003, Campilho 2005)**. A second study is presented regarding the tensile behaviour of SL joints with CFRP adherends, bonded with the ductile adhesive Araldite® 2015. In this analysis, the cohesive laws in pure modes I and II determined in Section 3 for this particular adhesive will be employed. The validation of the inverse methodology for the characterization of materials is accomplished with a parametric study for different values of L_O.

3.2.3.1. Single-strap repairs

The trapezoidal mixed mode CZM presented in Sub-Section 3.2.2 was used in this validation to simulate a t_A=0.2 mm layer of the ductile adhesive Araldite® 420 in adhesively-bonded SS repairs. As mentioned earlier, the strain constraining effects of thin adhesive layers between adherends lead to a different behaviour than adhesives as a bulk (Andersson and Stigh 2004, Hogberg and Stigh 2006, Leffler et al. 2007). However, an initial validation of this model will be performed assuming the adhesive bulk quantities for the cohesive parameters in pure modes I and II. The stiffness matrix (**D**) components (d_i, i=I, II) in equations (26) and (27) are obtained from the ratio between the E or G modulus of this adhesive and t_A. The parameters to be defined for the trapezoidal law are $\sigma_{u,i}$, $\delta_{2,i}$ and J_{ic}. Andersson and Stigh (2004) used an inverse method to obtain the cohesive properties of an adhesive layer in mode I using the DCB test. The authors concluded that $\sigma_{u,I}$ is of the same order of magnitude of the tensile strength measured in bulk tests. However, they also concluded that this statement is not valid concerning the fracture strain of the adhesive. On the other hand, Yang et al. (1999) demonstrated, after a series of analyses, that the parameters $\delta_{1,i}$ and $\delta_{2,i}$ do not significantly influence the numerical results. Therefore, in the present work, the values of $\delta_{u,i}$ and $\delta_{2,i}$ were obtained from the stress-strain (σ-ε) curve of the bulk adhesive (Fig. 92), assumed as elastic-perfectly plastic. $\sigma_{u,I}$ was defined as the bulk strength of the adhesive and $\delta_{2,I}$ was calculated from the product of the fracture strain with t_A. The first inflexion point ($\delta_{1,I}$) was defined from the values of E modulus and $\sigma_{u,I}$. The value of $\sigma_{u,II}$ was estimated applying the Von Mises yield criterion to $\sigma_{u,I}$. Owing to its less influence on the results (Yang et al. 1999), $\delta_{2,II}$ was defined considering that stress softening occurs under a similar slope to mode I (Carlberger and Stigh 2007). In fact, the length of the damage zone, which is intrinsically associated to the plateau size in the trapezoidal law, is substantially larger in shear than in peel (Andersson and Biel 2006), which supports the chosen course of action. Nonetheless, a sensitivity analysis will be presented in Sub-Section 3.2.3.1.3.4 to study the influence of $\delta_{2,i}$ of the adhesive on the failure path and load. Typical ductile adhesive properties for the value of J_{ic} were considered. The cohesive parameters of the adhesive in pure modes I and II are listed in Table 10 (Campilho et al. 2005, Campilho et al. 2007a).

In the experiments, regions of intralaminar and fibre failures also occurred. Consequently, cohesive elements were also employed to simulate these failures (Table 9 details the respective cohesive properties). In the particular case of fibre properties, it was found that $\sigma_{u,I}$ has a significant influence on the crack onset locus. Since its value was determined by an inverse method, a sensitivity analysis was performed (Sub-Section 3.2.3.1.3.4) to study the influence of this

parameter on the failure path and load. The value of J_{Ic} was established to promote immediate failure after $\sigma_{u,I}$ is reached, since the composite has a brittle behaviour under mode I in the fibres direction.

Table 10 – Cohesive parameters of the adhesive Araldite® 420 in pure modes I and II.

	Pure mode I	Pure mode II
Elastic moduli [GPa]	1850	680
$\sigma_{u,i}$ [MPa]	40.0	23.1
J_i [N/mm]	0.6	1.2
$\delta_{1,i}$ [mm]	$4.3*10^{-3}$	$6.8*10^{-3}$
$\delta_{2,i}$ [mm]	0.013	0.052
$\delta_{u,i}$ [mm]	$2.1*10^{-2}$	$5.9*10^{-2}$

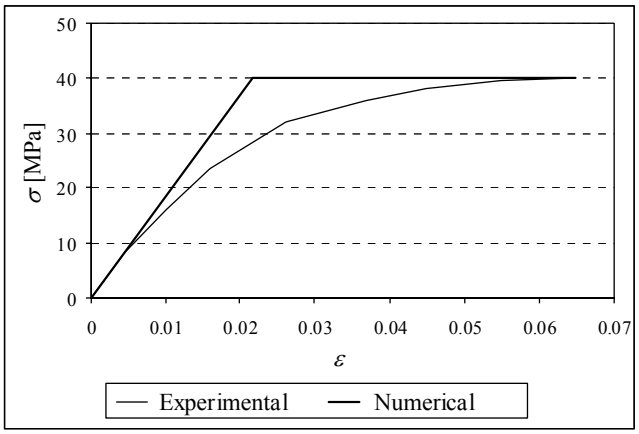

Fig. 92 – σ-ε curve of the adhesive Araldite® 420 and numerical approximation.

3.2.3.1.1. Experimental work

The geometry of the SS repairs is presented in Fig. 93. The *Inner Edge of the Overlap* (IEO) and *Outer Edge of the Overlap* (OEO) are identified in the figure. The laminates and patches were manufactured considering unidirectional 0º lay-ups of carbon/epoxy pre-preg (SEAL® Texipreg HS 160 RM) with 16 plies and 0.15 mm of ply thickness, whose ply elastic properties are presented in Table 3.

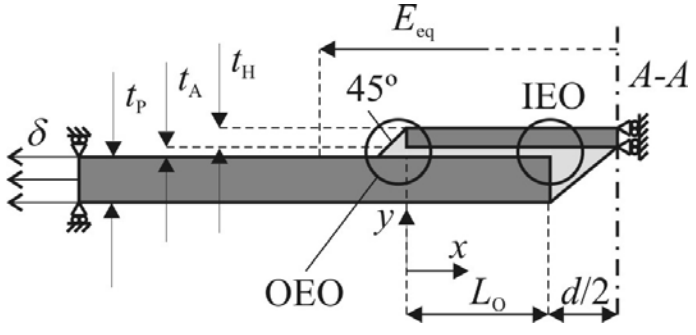

Fig. 93 – SS repair geometry.

Bonding consisted on manual abrasion of the bonding surfaces with 220 grit sandpaper and cleaning with compressed air, to avoid adhesive failures, followed by assembly and holding with contact pressure, and curing at room temperature. The initial dimensions of the repairs are listed in Table 11. A parametric study on the overlap length (L_O=5, 10, 15 and 20 mm) and patch thicknesses (t_H=0.6, 1.2, 1.8 and 2.4 mm) was performed. Table 12 characterizes the geometries tested, as a function of L_O and t_H, as well as the experimental and numerical types of failure (to be characterized later).

Table 11 – Laminates, patches and adhesive dimensions.

Laminates	Patches	Adhesive
Width b=15 mm	Thickness t_H=1.2 mm	Thickness t_A=0.2 mm
Thickness t_P=2.4 mm	Overlap length L_O=15 mm	
Spacing between laminates d=5 mm		

Table 12 –Geometries evaluated and respective failure modes.

Specimen	L_O [mm]	t_H [mm]	Failure type	Specimen	L_O [mm]	t_H [mm]	Failure type
S1	5	1.2	A	S5	15	0.6	A
S2	10	1.2	A	S6	15	1.2	A
S3	15	1.2	A	S7	15	1.8	A
S4	20	1.2	A	S8	15	2.4	B

Three specimens were tested for each geometry. Adhesive fillets at the overlap edges were used, comprising all the values of t_P and t_H (see Fig. 93 for shape and dimensions). Adhesive fillets are widely regarded to increase the efficiency of bonded assemblies, as peel peak stresses are reduced (Kim et al. 2006, Rispler et al. 2000). The specimens were tested at INEGI under tension using an Instron® 4208 electro-mechanical testing machine equipped with a 5 kN load cell, at room temperature and under displacement control (0.5 mm/min). The experimental setup is presented in Fig. 94. The longitudinal strains were measured using a 50 mm length strain gauge. Intralaminar failures in the laminate and patch were observed experimentally. These occurred at an average distance of 0.05 mm from the laminate/adhesive and adhesive/patch interfaces. The failure mechanisms will be discussed in more detail in Sub-Section 3.2.3.1.3.2.

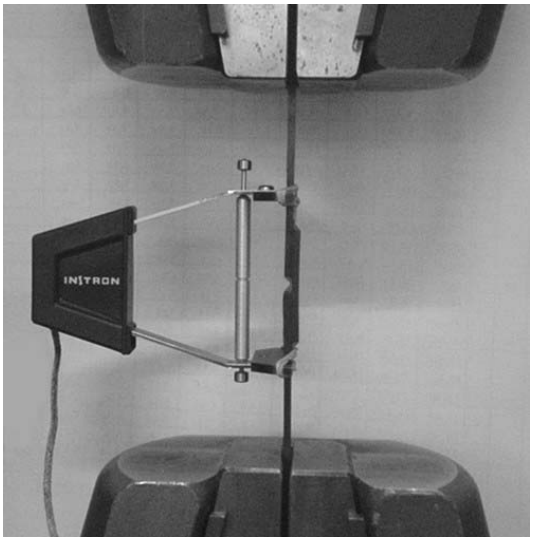

Fig. 94 – Experimental setup in the testing machine.

3.2.3.1.2. Numerical analysis

A non-linear material and geometric numerical analysis was performed, using plane-strain rectangular 8-node and triangular 6-node solid finite elements available in ABAQUS®. Fig. 95 details the mesh at the overlap region. Eight elements were used through-thickness for the laminates and the patches. Vertical symmetry conditions were used at the middle of the specimen (line *A-A* in Fig. 93 and Fig. 96) and a tensile displacement was applied at the edge of the model. The cohesive elements were introduced at several planes in the model (Fig. 96) to simulate crack onset and growth, to account for the different failure modes likely to occur. These included failure in the adhesive (plane P2) and intralaminar failures of the laminate (plane P1) or patch (plane P3). In view of the possible failure modes likely to occur (intralaminar, in the adhesive and fibre failure), three different sets of cohesive properties were considered (Table 9 and Table 10). Three locations of fibre rupture were considered (Fig. 96): in the laminate at the OEO, in the patch at the IEO, and in the patch at the symmetry line *A-A* (thick marks in Fig. 96). Several options were included for damage onset (locations 1, 2, 3 and 4 in Fig. 96), damage growth (planes P1, P2 and P3 in Fig. 96) and final failure (locations 5, 6, 7 and 8 in Fig. 96). Vertical cohesive elements allow fillets separation from the laminate and patch (respectively locations 4 and 8 in Fig. 96), and the alteration of the crack path between planes P1, P2 and P3 at the IEO and OEO.

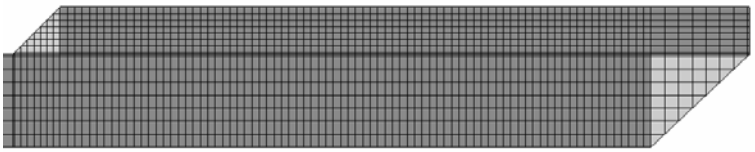

Fig. 95 – Detail of the mesh for model S3.

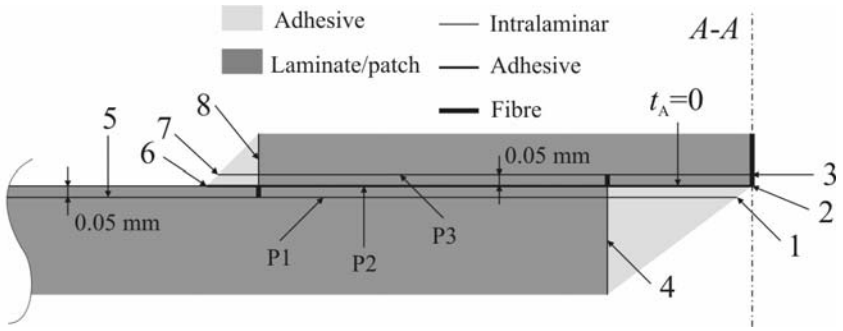

Fig. 96 – Cohesive elements loci in the SS repairs.

3.2.3.1.3. Results

3.2.3.1.3.1. Stress analysis

An elastic stress analysis was conducted for a clear insight on the influence of σ_y and τ_{xy} stresses on the crack onset locus, and to justify the planes selected for the cohesive elements. Stresses are normalized by τ_{avg}, the average shear stress along the overlap for geometry S3 at plane P2 (Fig. 96). Two additional failure loci, corresponding to the interlaminar interface between the two plies of the laminate and patch closest to the adhesive layer (planes L1 and L2, respectively), were considered in the stress analysis. These failure paths were placed at 0.15 mm from the adhesive, and

were included in the analysis to justify the use of cohesive elements only at 0.05 mm from the adhesive (intralaminar failures experimentally observed). Fig. 97 (a) and (b) present σ_y and τ_{xy} stress distributions, respectively, for geometry S3 at planes L1, P1, P2, P3 and L2. Typical profiles for these kinds of assemblies (Campilho et al. 2005, Cheng et al. 2007) were obtained. τ_{xy} stresses at planes L1 and L2 are remarkably lower at the crack onset region (IEO and symmetry line *A-A*), comparing with planes P1 and P2. Moreover, τ_{xy} stresses at planes L1 and L2 at the symmetry line *A-A* are practically nil. **Thus, planes L1 and L2 were not considered as critical failure regions and, consequently, cohesive elements were not introduced at those planes**.

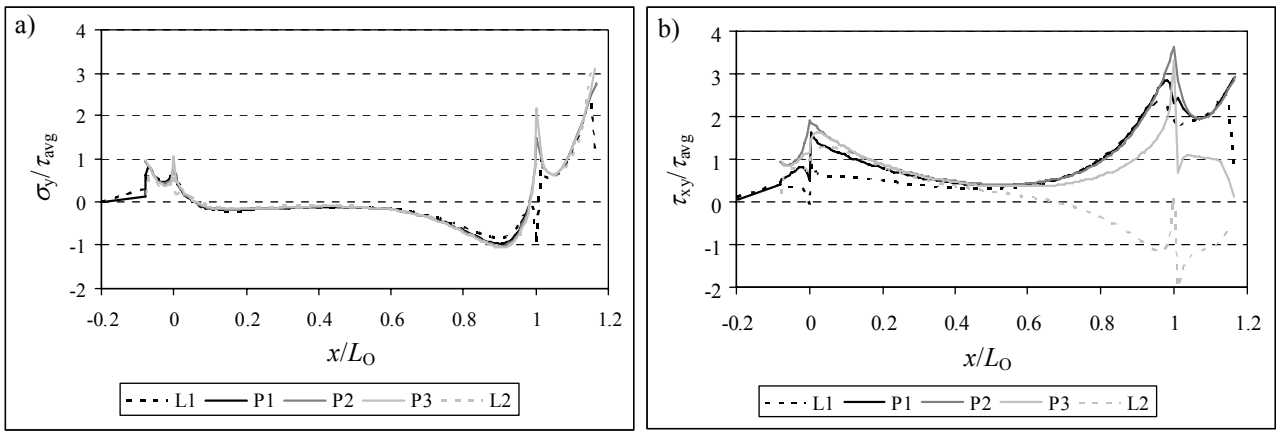

Fig. 97 – σ_y (a) and τ_{xy} (b) stress distributions at planes L1, P1, P2, P3 and L2 for geometry S3.

3.2.3.1.3.2. Failure modes

The initial comparison between the experiments and FEM simulations concerns the failure modes. Experimentally, two distinct ones were observed: type A and type B (Table 12). Type A failure represents an intralaminar failure of the patch (Fig. 98 a). This failure initiates with fibre rupture at line *A-A* between locations 2 and 3, followed by crack growth along plane P3 (Fig. 96). Type B failure is a combination of intralaminar failure of the laminate and patch (Fig. 98 b). In this case, fracture initiates within the inner fillet with no patch fibres rupture (location 1 in Fig. 96) and then grows as an intralaminar failure of the laminate and patch along planes P1 and P3. Final failure occurs at the OEO, at the vertical fillet/patch interface (location 8 in Fig. 96), for type A and B failures.

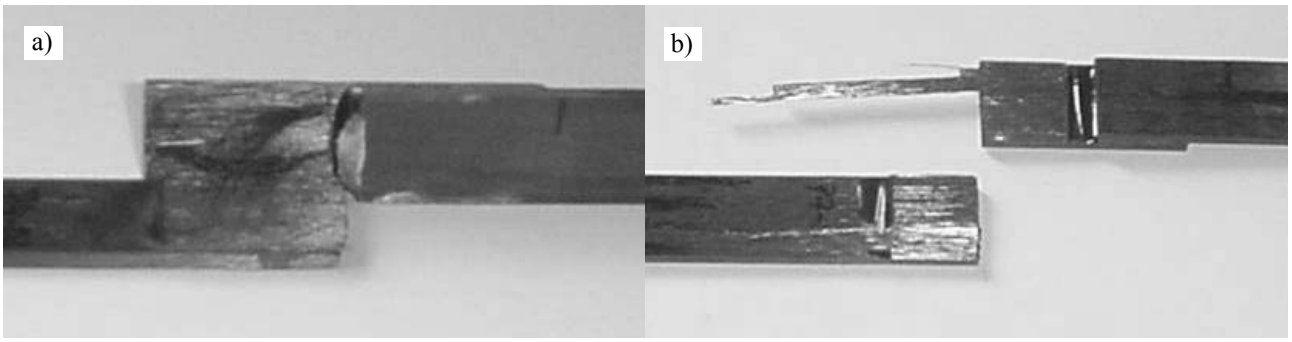

Fig. 98 – Type A (a) and type B (b) experimental failures.

These failures are prone to occur with FRP adherends, depending on the adhesive used, due to a typically smaller composite interlaminar strength than the adhesive (Renton and Vinson 1975a, Adams 1989, Long 1991, Campilho et al. 2007b, Panigrahi and Pradhan 2007b, Kim et al. 2008a). Type B failure was observed only for the three specimens of geometry S8 (t_H=2.4 mm). An intralaminar failure of the patch with patch fibres rupture (type A failure) was observed for all specimens of the other geometries (S1 to S7).

The experimental crack onset loci and growth paths until complete fracture were captured by the simulations. In fact, models ranging from S1 to S7 presented a type A failure, while model S8 presented a failure similar to type B already described, with intralaminar failure only of the patch. However, before failure, the cohesive elements of both interfaces P1 and P3 presented similar magnitude of the stresses in the respective cohesive elements, proving that both failures are prone to occur. Fig. 99 (a) represents the numerical type A damage onset for geometry S3. Damage initiates with a tensile fibres rupture at line *A-A* between locations 2 and 3 (Fig. 96). Subsequently, crack grows along plane P3. Fig. 99 (b) shows the numerical type B damage initiation for geometry S8. Crack initiates at location 1, propagating as an intralaminar patch failure along plane P3. Type A and B numerical final failures are presented in Fig. 100 (a) and (b), respectively, for the same geometries. For both failures, damage grows along plane P3 from the IEO to the OEO. The outer fillet/patch vertical interface (location 8) fractured completely for both type A and B failures. These numerical results are consistent with the experimental crack onset loci and growth paths until complete failure.

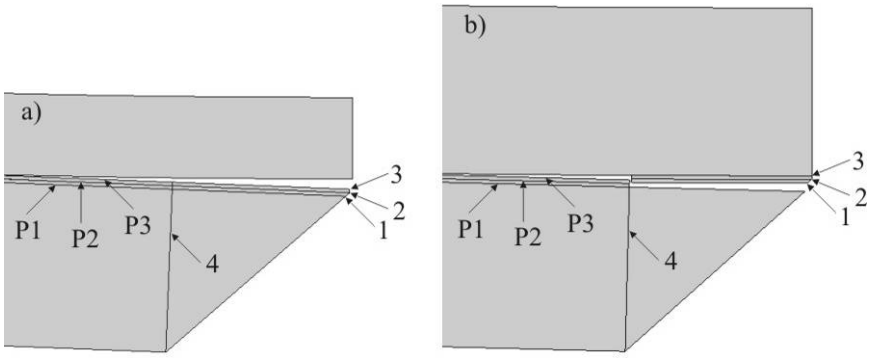

Fig. 99 – Type A (a) and type B (b) numerical damage initiations.

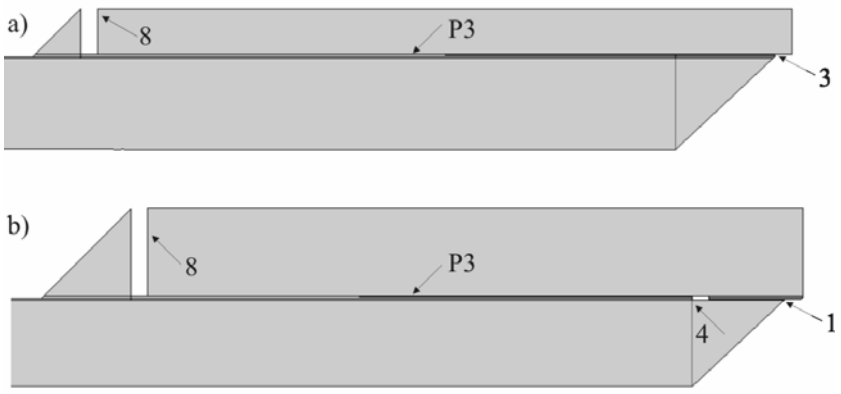

Fig. 100 – Type A (a) and type B (b) numerical final failures.

Fig. 101 presents the cross-sectional tensile stresses (σ_x) in the patch at the symmetry line *A-A* for the values of t_H tested, normalized by the average stress in the patch at line *A-A* for geometry S3 (σ_{avg}). The type A failure onset, characterized by fibres rupture at line *A-A*, is justified by the patch longitudinal stiffness, associated to the asymmetry of loading, which causes σ_x stresses of significant magnitude in the fibre cohesive elements located between locations 2 and 3 (Fig. 96), enough to induce a tensile patch failure prior to damage initiation in the adhesive. The modification of failure path for the highest value of t_H is related to the reduction of σ_x stresses in the patch at the symmetry line *A-A*. In fact, since t_H increases, the load is distributed over a larger area. For the t_H=2.4 mm specimens, σ_x peak stresses are not enough to induce fibres rupture in the patch, and damage initiates within the inner adhesive fillet (location 1 in Fig. 96).

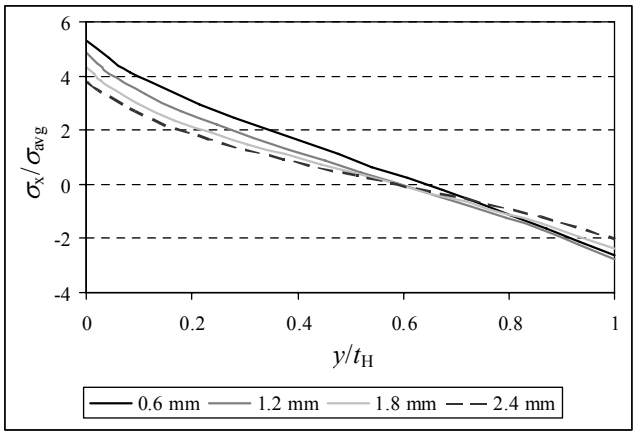

Fig. 101 – σ_x stress distributions at line *A-A* as a function of t_H.

3.2.3.1.3.3. Summary of the results

The experimental and numerical *P-δ* curves for geometry S5 are presented in Fig. 102 (a). A good agreement was found, in terms of stiffness and failure load/displacement. A similar consistency was attained with the other geometries.

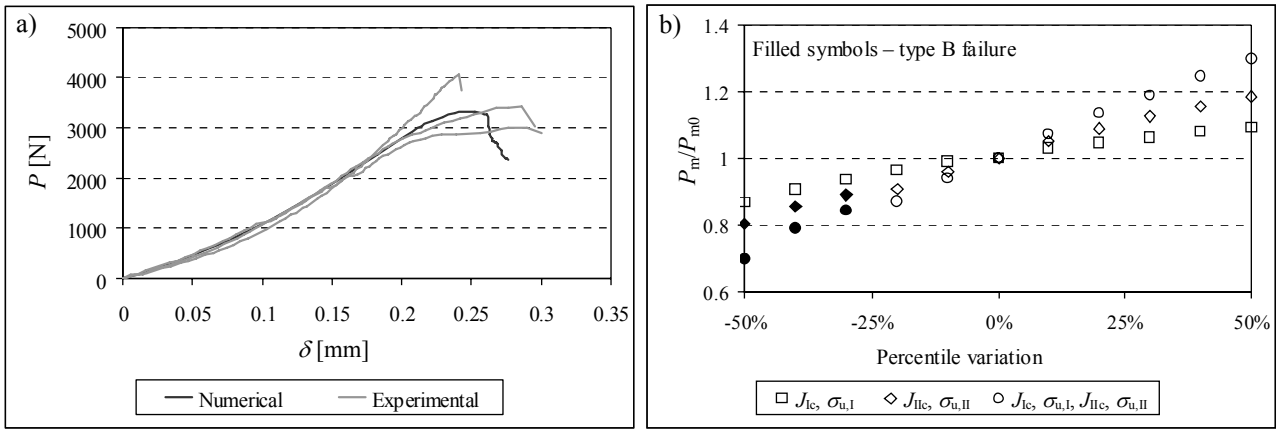

Fig. 102 – *P-δ* curves for geometry S5 (a) and P_m as a function of the intralaminar properties (b).

A comparison between the experiments and simulations was also performed on the equivalent longitudinal *E* modulus (E_{eq}) and maximum load (P_m) of the repairs, as a function of the values of L_O and t_H presented in Table 12. E_{eq} denotes for the equivalent stiffness of the repair along 50 mm at the repair region (Fig. 93). This length represents the effective

span of the strain gauge used (Fig. 94), being considered as an approximation of the repair stiffness. P_m represents the maximum load sustained by the specimens. Fig. 103 (a) and Fig. 104 (a) show E_{eq} and P_m, respectively, as a function of L_O. Fig. 103 (b) and Fig. 104 (b) present the same quantities as a function of t_H. The standard deviation of the experimental results is included in the graphs.

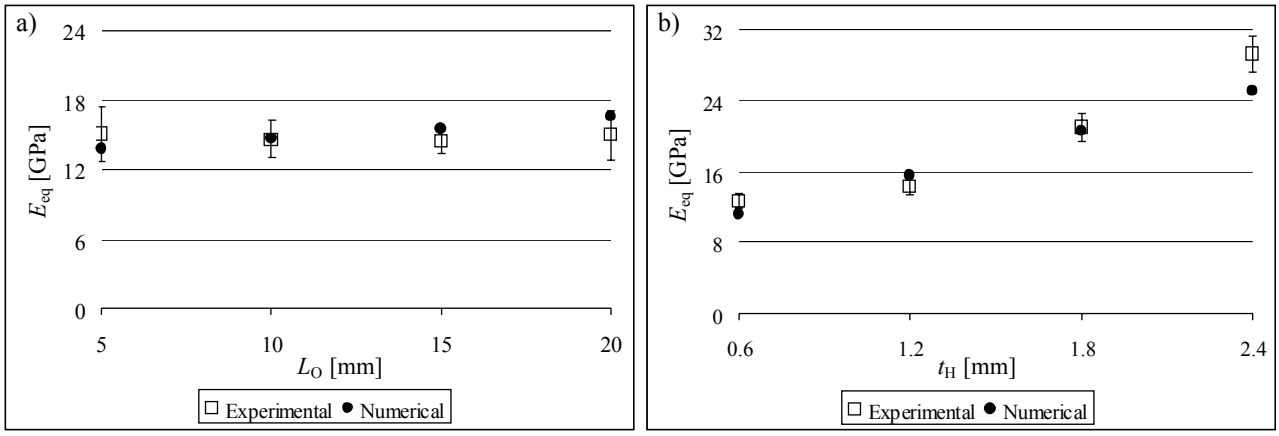

Fig. 103 – E_{eq} as a function of L_O (a) and E_{eq} as a function of t_H (b).

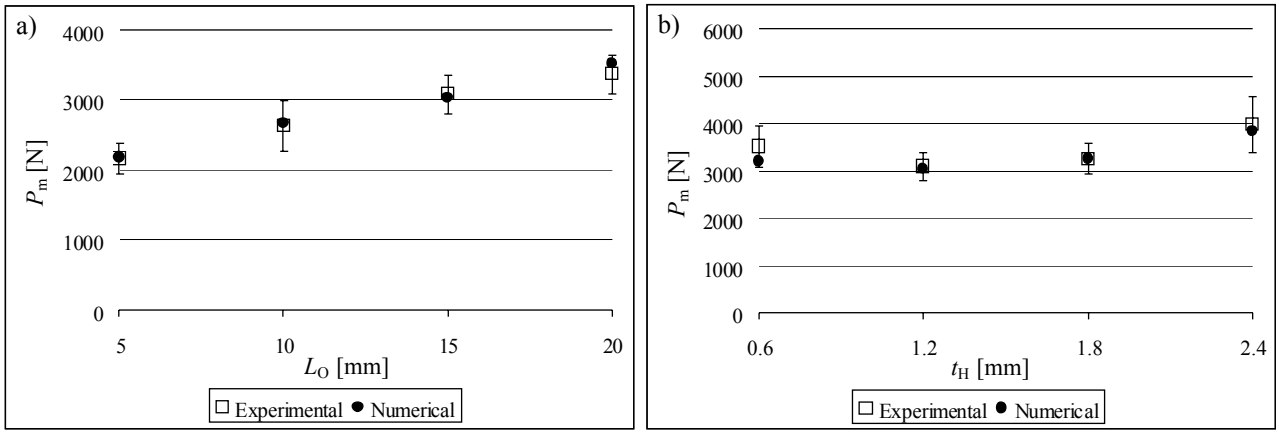

Fig. 104 – P_m as a function of L_O (a) and P_m as a function of t_H (b).

The numerical results in Fig. 103 (a) show a slight increasing trend of E_{eq} as a function of L_O, which is not clearly observed in the experiments. This is probably due to small variations of the adhesive thickness, since the repair stiffness depends almost exclusively of the adhesive deformation. Fig. 104 (a) shows accurate P_m predictions as a function of L_O, with P_m increasing approximately linearly as a function of L_O (Campilho et al. 2005, Hu and Soutis 2000). The increase of the adhesive resistant shear area justifies this behaviour, although τ_{xy} peak stresses also increase in magnitude with L_O (Campilho et al. 2005). However, P_m is not proportional to the bond area, due to an increasingly unloaded overlap inner region with the increase of L_O (Campilho 2005, Campilho et al. 2005, Kim et al. 2008a). The value of t_H shows a significant influence on E_{eq} (Fig. 103 b), with higher values of t_H leading to stiffer repairs. This is explained by the reduction of the repair flexure with t_H (Campilho et al. 2005). Fig. 104 (b) shows a minor reduction of P_m with the increase of t_H from 0.6 to 1.2 mm that can be explained by higher magnitude σ_y peel and τ_{xy} peak stresses at the overlap inner region (Campilho et al. 2005, Campilho 2008a). However, from t_H=1.2 mm this effect is surmounted by the reduction of σ_x stresses in the patch, increasing P_m. For t_H=2.4 mm, the alteration of the failure mode from a patch tensile fracture to failure within the adhesive fillet also justifies the increasing tendency of P_m for this geometry. The

uncharacteristic behaviour documented for $P_m=f(t_H)$ emerges from the existence of different failure mechanisms. Using weaker adhesives, a failure in the adhesive region is expected, with P_m always decreasing with t_H (Hu and Soutis 2000, Campilho et al. 2005). Overall, the experimental and simulations show an acceptable correlation.

3.2.3.1.3.4. Sensitivity analyses

Sensitivity analyses were performed on the cohesive parameters that play a significant role in the repairs fracture and were not measured with experiments. Geometry S3 was considered to assess the influence of $\delta_{2,i}$ of the adhesive on the failure path and load, considering its range of possible values (from 0%, corresponding to $\delta_{2,i}=\delta_{1,i}$ and a triangular law, to 100%, corresponding to $\delta_{2,i}=\delta_{u,i}$ and an abrupt failure when $\delta_{2,i}$ is reached). This study was accomplished for $\delta_{2,1}$ and $\delta_{2,2}$ separately and simultaneously (using the same percentile range of values). No difference was found in the original failure mode and value of P_m, which is easily justified by the occurrence of intralaminar failures.

The influence of intralaminar mode I (J_{Ic} and $\sigma_{u,I}$), mode II (J_{IIc} and $\sigma_{u,II}$) and overall (J_{Ic}, $\sigma_{u,I}$, J_{IIc} and $\sigma_{u,II}$) properties on the failure path and P_m was also examined. Values ranging from -50% to +50% of the initial ones considered in this analysis (Table 9) were considered. Fig. 102 (b) presents the evolution of P_m with the intralaminar properties. The results are normalized by P_m for the repair of geometry S3 with initial properties (P_{m0}). P_m increased with each group of properties. As expected, mode II properties have a higher effect on P_m, since the repair is primarily loaded in shear (Campilho et al. 2005, Campilho et al. 2008a). On the failure modes, a modification to type B was attained reducing 30% or more mode II and overall properties (filled symbols in Fig. 102 b). This is justified by the strength reduction at plane P1, causing a premature failure at this plane, before attaining $\sigma_{u,I}$ for the fibre cohesive elements at line *A-A*. For the tensile fibre failure, $\sigma_{u,I}$ is the most influent cohesive parameter for damage onset. An analysis was conducted for $500<\sigma_{u,I}<1000$ MPa, allowing an evaluation of the influence of this quantity on the failure path and value of P_m. Between 500 MPa$<\sigma_{u,I}<$710 MPa no modification of the failure mechanism was detected (type A). Actually, the lower values used for $\sigma_{u,I}$ reinforce the fibre failure at locations 2 and 3 (Fig. 96) prior to damage initiation and growth at location 1. In the interval of 710 MPa$<\sigma_{u,I}<$792 MPa a type B failure was observed only for geometry S8, as occurred experimentally. The increase of $\sigma_{u,I}$ for the fibre cohesive elements at locations 2 and 3 (Fig. 96) justifies this modification, leading to damage initiation at location 1 before $\sigma_{u,I}$ for the fibre cohesive elements is reached. Between 792 MPa$<\sigma_{u,I}<$827 MPa, a type B failure was also observed for geometry S7, which does not correspond to the experiments. For $\sigma_{u,I}>827$ MPa, the other geometries also present a type B failure, which deviates even more to the experimental observations. In the range of $\sigma_{u,I}$ values studied, no difference was observed on P_m. Owing to these results, an average value of the interval 710 MPa$<\sigma_{u,I}<$792 MPa was selected ($\sigma_{u,I}=750$ MPa).

In this Sub-Section, a developed trapezoidal mixed mode CZM to simulate ductile adhesive layers in bonded assemblies was validated. This approach was applied on tensile loaded SS CFRP repairs, accounting for different values of L_O and t_H. The model performance was evaluated comparing the experiments with FEM predictions, in terms of failure path, E_{eq} and P_m. On E_{eq} and P_m, a good correspondence was found for the values of L_O and t_H evaluated. Only for E_{eq} as a function of L_O a small deviation was detected, attributed to manufacturing issues of the repairs. The experimentally observed failure modes were also reproduced in the numerical analysis, in terms of failure onset and progression path until failure. **It is thereby concluded that the presented model and bulk assumption for the cohesive elements can**

be applied to predict the value of P_m and failure path of assemblies bonded with ductile adhesives, with satisfactory results. However, for a more accurate characterization of materials or interfaces and guarantee of reliable results, an inverse method should be used instead (Yang et al. 1999, Yang et al. 2001, Kafkalidis and Thouless 2002, Campilho et al. 2009a).

3.2.3.2. Single-lap joints

Following the study of Sub-Section 3.2.3.1, considering as an approximation the adhesive bulk properties for the cohesive parameters, another validation is presented (de Moura et al. 2009d), concerning the tensile behaviour of SL joints with unidirectional CFRP adherends, adhesively-bonded with the ductile adhesive Araldite® 2015. Values of L_O between 10 and 80 mm were evaluated. In this validation, the cohesive laws determined in Sub-Sections 3.2.2.1.2 (pure mode I) and 3.2.2.1.3 (pure mode II) by an inverse data fitting methodology were employed to simulate the t_A=0.2 mm adhesive layer. As discussed previously, the CZM laws obtained with the inverse method are specific for the combination of adherend and adhesive used, as well as the respective value of t_A. Thus, the same adherends (unidirectional CFRP), adhesive (Araldite® 2015) and value of t_A (0.2 mm) of the inverse characterization procedure were considered. Apart from the calculation of the cohesive parameters, the value of t_A is also included in the formulation, in the stiffness matrix (**D**) components (d_i, i=I, II) in equations (26) and (27). Indeed, t_A is incorporated in the values of d_i, obtained by the ratio between the E or G modulus and t_A. In the experiments conducted, the joints fractured entirely cohesively in the adhesive layer for all values of L_O analysed, without visible damage or plasticization of the CFRP adherends. As a result, the use of cohesive elements to simulate damage initiation and propagation was only equated for the cohesive fracture of the adhesive layer.

3.2.3.2.1. Experimental work

Fig. 105 shows the geometry of the SL joints, and Table 13 the dimensions used. The material and fabrication procedure of the adherends were already described in Sub-Section 3.2.2.1.1 (corresponding to unidirectional pre-preg Texipreg HS 160 RM from SEAL® with 16 plies and 0.15 mm of ply thickness).

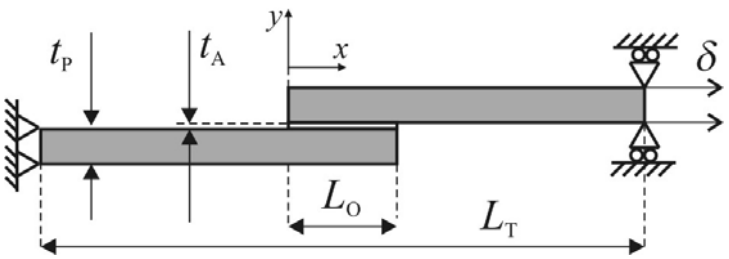

Fig. 105 – SL joint geometry.

Table 13 – SL joint dimensions.

Adherends		Adhesive
Width b=15 mm	Total length L_T=240 mm	Thickness t_A=0.2 mm
Thickness t_P=2.4 mm	Overlap length L_O=10-80 mm	

Table 3 shows the elastic orthotropic properties of a unidirectional ply. Surface preparation involved manual abrasion with 220 grit sandpaper, followed by wiping with acetone, to assure a strong bond and avoid adhesive failures (Zimmerman and Liu 1995, Campilho et al. 2008a). The adherends alignment and bonding was carried out manually following the guidelines of Sub-Section 3.2.2.1.1 (Fig. 106). Initially, the specimens were cut from bulk plates with a diamond disc cutting machine, followed by smoothing of the rough edges with 120 grit sandpaper. The desired value of t_A was achieved placing a dummy adherend and a 0.2 mm spacer under the upper adherend (Fig. 106), jointly with the application of pressure with grips. At this stage, the lower adherend was also fixed with grips. The correct alignment of the joints was adjusted visually with a sheet of paper under the joints, outlining their edges. The value of t_P of all the adherends was measured individually at three locations in the adherends length and the respective average was calculated, to match the values of t_P of the lower and dummy adherends as possible, minimizing the scattering on t_A. The adherends and tabs bonding was simultaneous, which did not guarantee the correct value of t_A for the leftmost tab in Fig. 106. However, this was not deemed to be relevant, since the tabs do not require a structural bond, aiming only the specimens alignment in the testing machine.

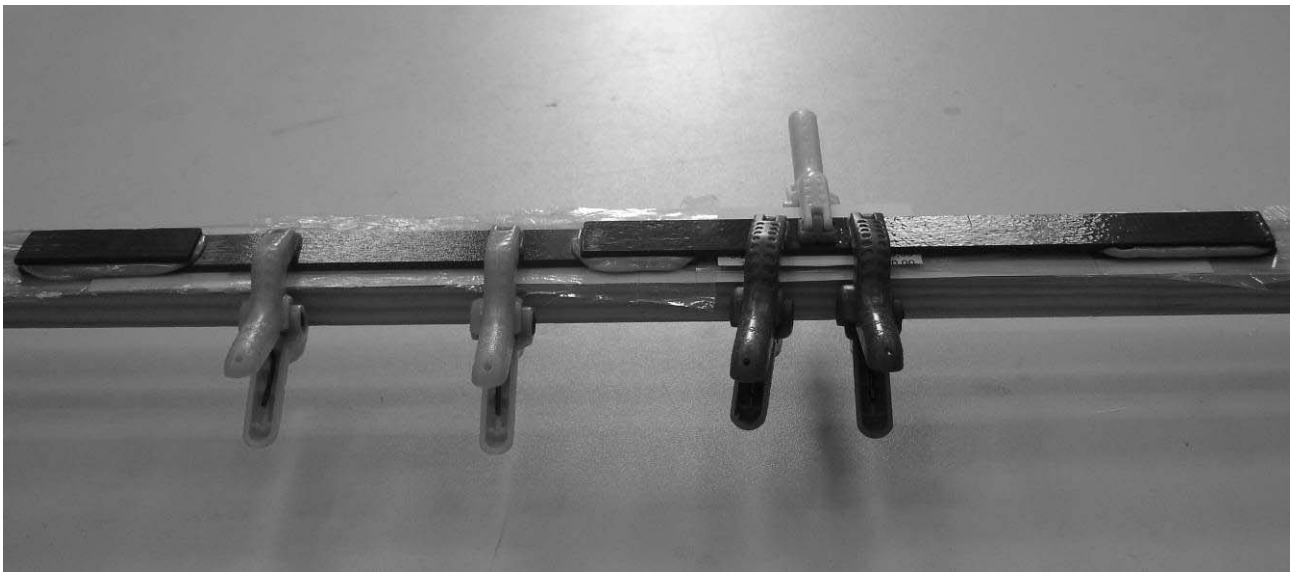

Fig. 106 – Specimens bonding procedure.

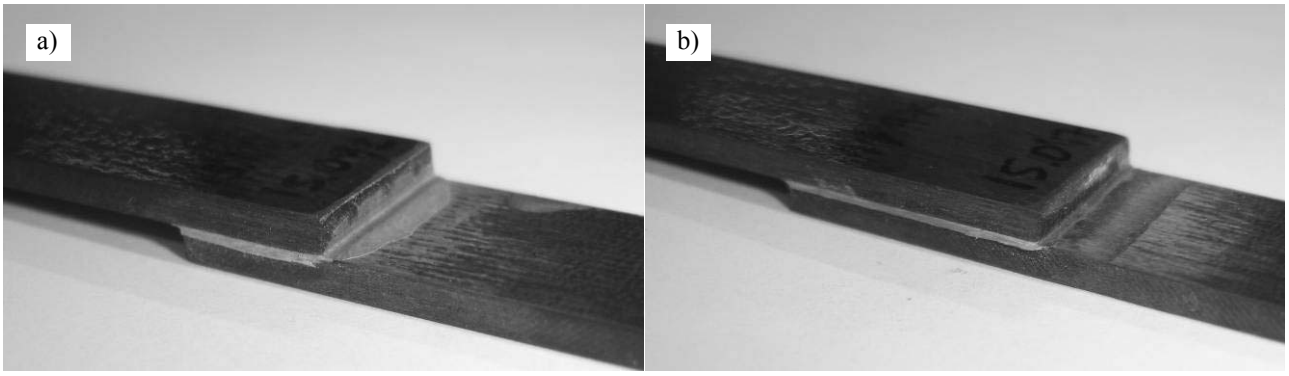

Fig. 107 – L_O=10 mm (a) and L_O=20 mm specimens after finishing.

After bonding, the specimens were left to cure at room temperature for at least two hours before removing the grips. The adhesive excess removal followed the procedure of Sub-Section 3.2.2.1.1 (Fig. 74), to produce specimens with square-edges (Fig. 107). Eight different values of L_O were evaluated (10, 20, 30, 40, 50, 60, 70 and 80 mm). The tensile

tests were performed at least one week after bonding at INEGI with an Instron® 4208 electro-mechanical testing machine with a 100 kN load cell, at room temperature and under displacement control (0.5 mm/min). The testing machine grips displacement was considered to build the P-δ curves. Fig. 108 shows a L_O=40 mm specimen in the beginning (a) and during the test (b). For each value of L_O, six specimens were tested, with at least four valid results.

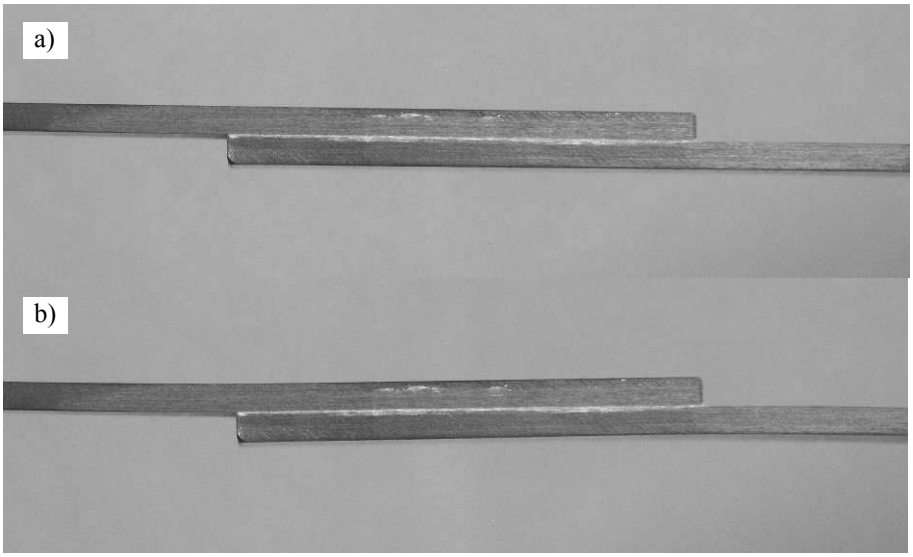

Fig. 108 – L_O=40 mm specimen in the beginning (a) and during the test (b).

3.2.3.2.2. Numerical analysis

The numerical simulations were carried out in ABAQUS®, using rectangular plane-strain 8-node solid finite elements. The mesh refinement is shown in Fig. 109 for a L_O=40 mm specimen. Four solid elements were used in the adherends thickness directions and 160 elements along the overlap, without bias effects. Outside the overlap, a coarser mesh was employed, since stresses are approximately constant in the length direction at these regions (Campilho 2005).

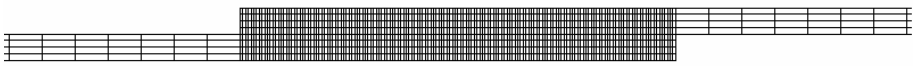

Fig. 109 – Detail of the mesh for the L_O=40 mm model.

The SL joint was modelled without symmetry conditions. The boundary conditions consisted on clamping one of the joint edges, while the other one was vertically restrained and subjected to a tensile displacement (Fig. 105), to reproduce the testing conditions (Goyal et al. 2008, Radice and Vinson 2008). The cohesive elements were only used to simulate a cohesive failure of the adhesive layer, since all experimental fractures corresponded to this mechanism. Being this the first validation to the inverse material characterization methodology, different combinations of the cohesive laws in pure modes I and II for the adhesive Araldite® 2015 were tested, for a critical perception of the influence of the cohesive data scattering on the strength predictions. The average cohesive laws (which will be employed throughout this work and whose parameters are summarized in Table 8), as well as the minimum and maximum cohesive laws, will

be used. Thus, the numerical values of P_m also include deviation, with the average value corresponding to the average cohesive laws, and the minimum and maximum values relating to the respective cohesive parameters.

3.2.3.2.3. Results

3.2.3.2.3.1. Stress analysis

The SL joints analysis begins with an elastic representation of σ_y and τ_{xy} stress fields at the overlap region for the L_O=10 mm joint and corresponding distributions in the adhesive layer, for an easier and comprehensive understanding of the joints mechanical behaviour. The stress distributions were extracted from the cohesive elements stresses, representing the adhesive stresses as a whole without accounting for the known thickness gradients (Gonçalves et al. 2002, Campilho et al. 2005, Magalhães et al. 2005). Fig. 110 initially shows the deformed configuration, for a tensile displacement of 0.2 μm and displacements magnification of 2000x. These values are also used in the subsequent figures in this Sub-Section. Fig. 111 illustrates σ_x stresses at the overlap region.

Fig. 110 – Deformed configuration of the SL joint under a tensile load.

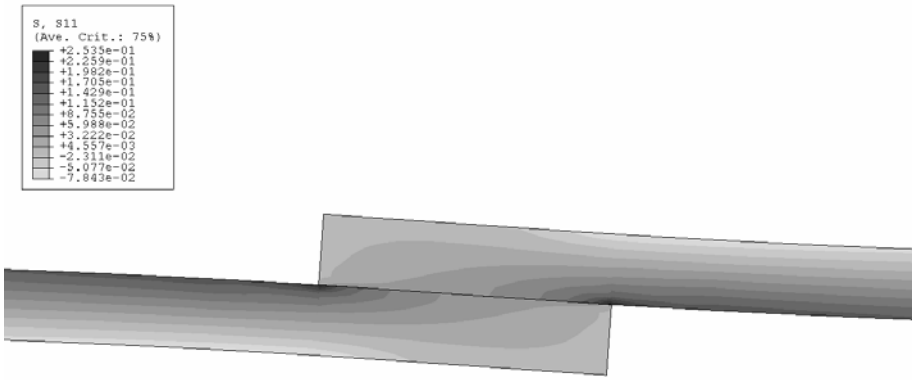

Fig. 111 – σ_x stresses at the overlap region.

The load eccentricity owing to the offset of the adherends is a distinctive feature of SL joints, causing a bending moment that reflects on the adherends transverse flexure (Heslehurst 1999, Pires et al. 2003, Apalak and Gunes 2005, Apalak and Gunes 2007). This happening, which is also responsible for σ_y stresses peaking at the overlap edges and consequent weakening of the joints, causes σ_x stress gradients in the thickness direction. σ_x stresses also increase in magnitude towards the bond, where tensile σ_x stresses due to the axial and bending efforts sum (Campilho 2005). Along the overlap, σ_x stresses in each one of the adherends diminish towards the respective adherend edge, due to the reduction of shear transfer length contributing to the axial loads within the adherend. Outside the overlap region, σ_x stresses are approximately constant in the length direction. Fig. 112 and Fig. 113 report on the σ_y and τ_{xy} stress fields,

respectively, at the overlap region. The plots of σ_y and τ_{xy} stress distributions in the adhesive layer as a function of L_O are presented in Fig. 114 and Fig. 115, respectively. A normalization procedure was carried out, dividing σ_y and τ_{xy} stresses by τ_{avg}, the average shear stress along the overlap for the respective value of L_O.

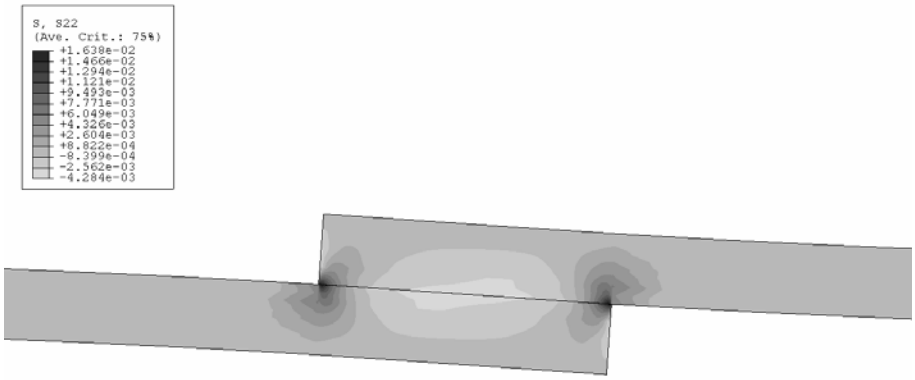

Fig. 112 – σ_y stresses at the repair region.

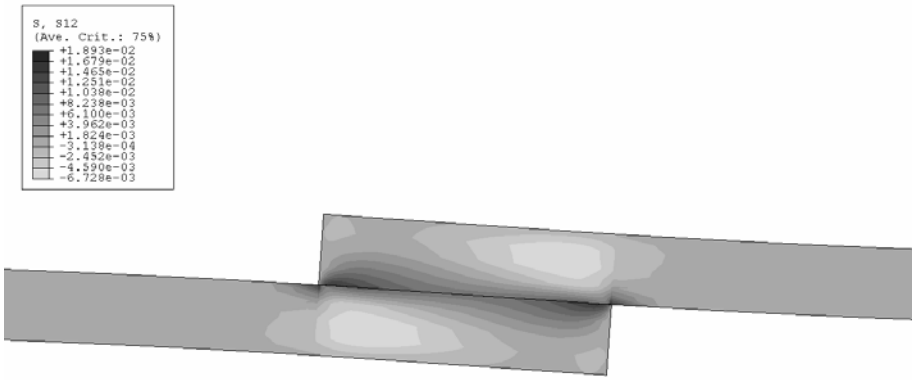

Fig. 113 – τ_{xy} stresses at the repair region.

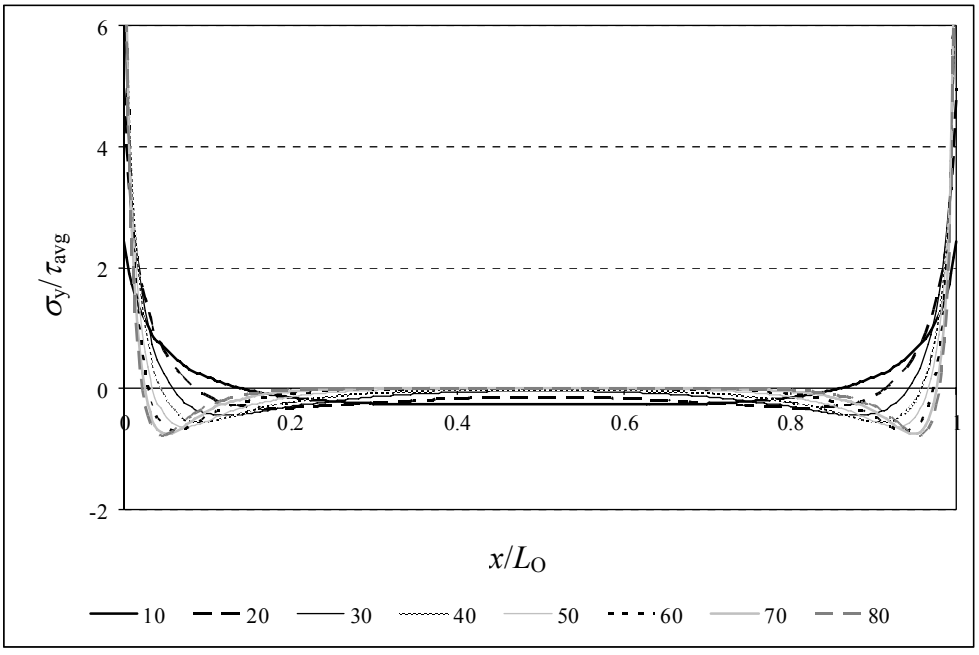

Fig. 114 – σ_y stress distributions in the adhesive layer as a function of L_O.

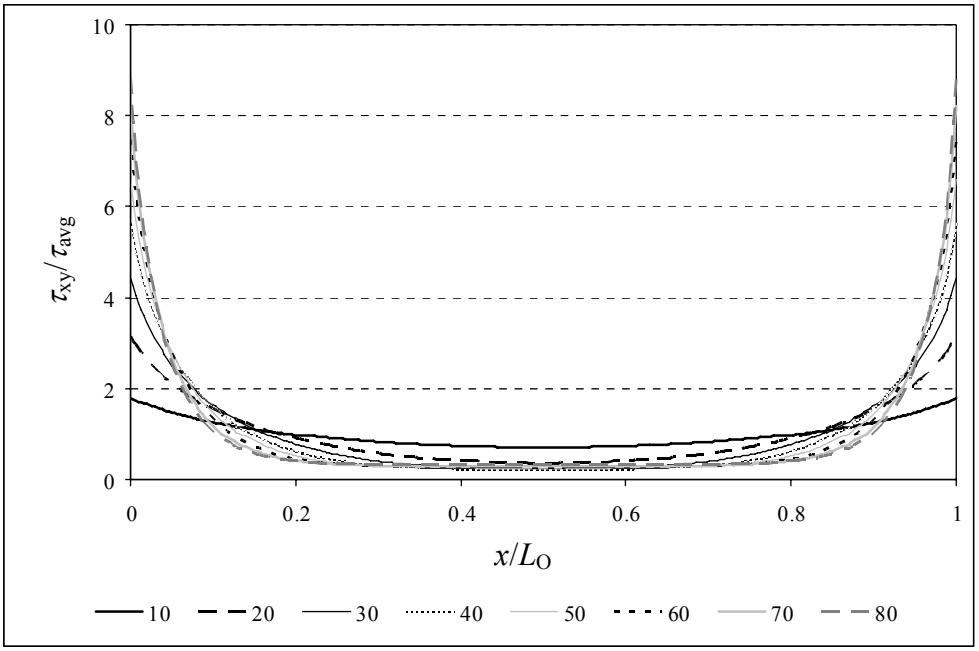

Fig. 115 – τ_{xy} stress distributions in the adhesive layer as a function of L_O.

The widely documented stress profiles for these kinds of joints were obtained (Shin et al. 2003, Cognard et al. 2006, Kilic et al. 2006). Thus, σ_y stress singularities build up at the overlap edges at a very restricted region, owing to the square-edge geometry (Towse et al. 1999, Penado 2000, Wang and Rose 2000, Radice and Vinson 2006, Taib et al. 2006a). At the inner overlap region, these stresses are compressive, although much smaller in magnitude than τ_{avg}. The classic shape of σ_y peel stresses increasing towards the overlap edges from compressive inner regions is mainly due to the already discussed asymmetry of loading, yielding the transverse flexure of the joints (Ferreira et al. 2005, Pinto et al. 2009). In fact, the adherends opposed curvature results on a separation at the overlap edges and compression in-between. It is also common knowledge that this effect is more noticeable with lower stiffness adherends, which undergo larger flexure (Schroeder 1990, Narasimhan et al. 2004, Pinto et al. 2009). σ_y singularities are usually regarded to significantly diminish the strength of adhesive layers, constituting one of the main factors for damage initiation at the overlap edges (Campilho et al. 2005, Campilho et al. 2009b). For layered composites, σ_y peel stresses can also initiate delaminations between plies, emerging from the lower interlaminar strength of composites than the cohesive properties of most structural adhesives (Renton and Vinson 1975a, Adams 1989, Long 1991, Campilho et al. 2007b, Panigrahi and Pradhan 2007b, Kim et al. 2008a). The parametric study on L_O (Fig. 114) revealed that σ_y stresses always peak at the overlap edges, although concentrating in smaller normalized regions with the increase of L_O. Bigger values of L_O give rise to σ_y compressive stresses near the peel singularities, of increasing magnitude with L_O. Concurrently, σ_y compressive stresses at the inner region of the overlap diminish in magnitude. This tendency alone is prone to reduce the peel effects at the overlap edges or hinder crack propagation after localized damage at the square-edges (Campilho et al. 2005), justifying sometimes the attainment of P_m after crack initiation (Campilho et al. 2007a). τ_{xy} stresses are also consistent with the reported tendencies for SL joints, with a smaller load bearing potential at the overlap inner region and peaking towards the overlap edges (Vable and Maddi 2006, Luo and Tong 2007). This is caused by the differential deformation of each one of the adherends along the overlap. In fact, the adherends are increasingly loaded from their free overlap edge towards the other overlap edge. As a result of this gradient, the practically unloaded free edges of each adherend slide relatively to the matching regions of the other adherend that endure high longitudinal deformations,

causing τ_{xy} peak stresses at those regions (Volkersen 1938, Adams et al. 1997, Zou et al. 2004, Campilho et al. 2005). At the central region of the overlap these effects are cancelled, with τ_{xy} stresses developing solely by the tensile pulling of the specimen. It can be easily concluded from this assumption that stiffer adherends such as CFRP laminates yield smaller τ_{xy} gradients along the overlap, due to the reduction of the differential straining effects (Renton and Vinson 1975b, Pinto et al. 2009). τ_{xy} peak stresses also aid to damage initiation in SL joints at the overlap edges, impairing the strength of SL joints more severely for brittle adhesives, which do not allow plasticization at the overlap edges (da Silva and Lopes 2009, Grant et al. 2009). Oppositely, ductile adhesives consent the redistribution of stresses at these regions while the inner region of the overlap is gradually put under loads, masking the stress grading effects to an extent depending on the adhesive allowable ductility, and increasing the joints strength accordingly (Davis and Bond 1999, Campilho 2005, da Silva et al. 2009b). Whilst τ_{xy} stress gradients are not important for small values of L_O (Fig. 115), they gradually increase with this quantity, owing the increasing gradient of longitudinal strains in the adherends caused by the bigger bonding areas and loads. This is regarded in the literature as the main justification for a strength improvement of SL joints with L_O at a decreasing rate, eventually leading to a strength plateau (Adams et al. 1997, Jain and Mai 1999, Hu and Soutis 2000, Campilho 2005, Reis et al. 2005). However, it is expected that for CFRP adherends this reduction is smaller than for less stiff adherends (Pinto et al. 2009). In other situations, the strength plateau is not related to stresses, corresponding instead to a modification of the failure mechanism, from a cohesive failure of the adhesive layer to a cross-sectional tensile fracture of the adherends (Chan and Sun 1980, John et al. 1991, Ahn and Springer 1998a). This can be caused by extremely big values of L_O or reduced tensile strength of the adherends. As a final observation, the comparative analysis of σ_y (Fig. 114) and τ_{xy} (Fig. 115) stress distributions also allows the perception of why adhesive bonds should be loaded in shear rather than peel. In fact, under shear loads, the applied loads are spread by larger areas than under peel loads, resulting on smaller peak stresses (Adams et al. 1997). Obviously, this effect is more noticeable for the smaller values of L_O. Additionally, due to the significantly larger fracture toughness of adhesives in shear than peel (Yang et al. 1999, Yang et al. 2001, Campilho et al. 2009a), the stress redistribution effect in bonded assemblies induced by the adhesive plasticity is much more substantial under shear.

3.2.3.2.3.2. Failure modes

All the joints tested experienced a cohesive failure of the adhesive layer, showing the suitability of the surface preparation technique. Fig. 116 shows examples of a cohesive failure for L_O=20 mm (a) and 80 mm (b) SL joints.

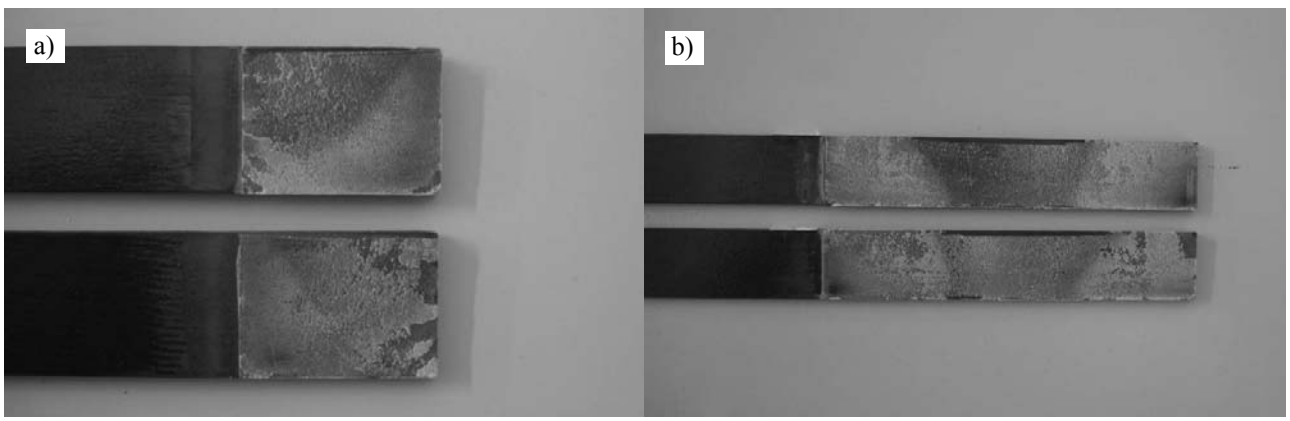

Fig. 116 – Experimental cohesive failure of the adhesive layer for a L_O=20 mm (a) and 80 mm (b) joint.

The FEM simulations followed an identical behaviour, since failure was only equated in the adhesive, as referred in Sub-Section 3.2.3.2.2 (Fig. 117 shows two examples of cohesive failures). Failure can be confirmed by the adherends sliding (the transitions between different meshes pertain to the overlap edges in both adherends).

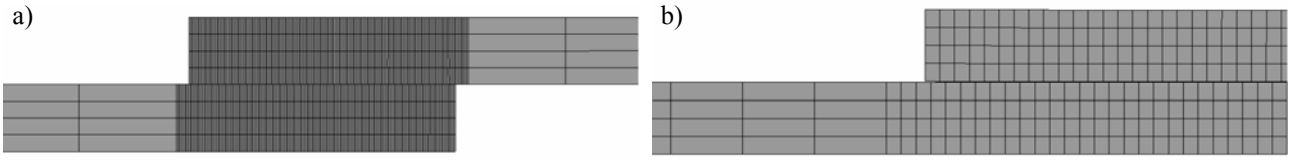

Fig. 117 – Numerical cohesive failure of the adhesive layer for a L_O=10 mm (a) and 80 mm (b) joint.

3.2.3.2.3.3. Summary of the results

Fig. 118 compares, as an example, the experimental and numerical P-δ curves for the L_O=50 mm joints. The two numerical curves correspond to the minimum and maximum cohesive laws (logically yielding the smaller and bigger values of P_m, respectively). The good agreement on the values of elastic stiffness (K) and P_m, which was also obtained for the other values of L_O, is emphasized. K is defined as the P/δ quotient in the initial part of the P-δ curve. The numerical limit values for P_m also concur reasonably with the experimental scattering. Table 14 summarizes, for each value of L_O, the average values of P_m and respective standard deviation (experimental) or range, i.e., difference between P_m for the average and minimum/maximum cohesive laws for the adhesive layer (numerical). The error, calculated as the relative difference between the experimental and numerical average values, normalized by the experimental average value, allows a more critical evaluation of the divergence evolution between both with L_O.

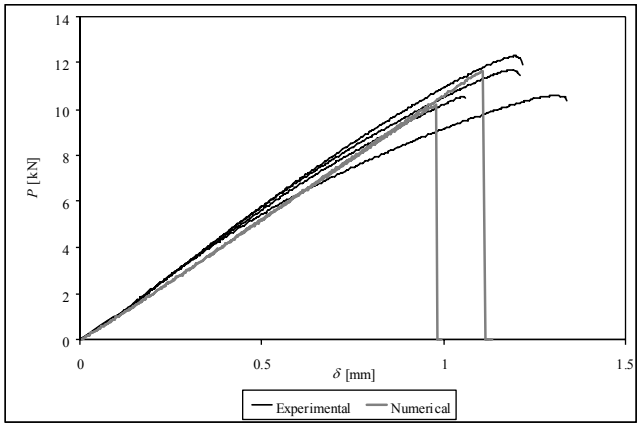

Fig. 118 – Experimental and numerical P-δ curves comparison for the L_O=50 mm SL joints.

In this Sub-Section, the results of K and P_m, including the standard deviation of the experiments, are also presented graphically as a function of L_O (Fig. 119). The range is also included for the numerical values of P_m, using a thicker line for a clear distinction to the experimental deviation. K showed numerically a proportional improvement with L_O, explained by a parallel increase on the bond area, which was also found in the tests despite an under prediction for the smaller values of L_O. Equally to the previous study on SS repairs, small variations of the adhesive layer thickness resulting from the joints fabrication could be blamed for this deviation. However, this does not seem plausible on account of the bonding technique described (Fig. 106). Whilst no definitive conclusions can be presented for this

variation, different adhesive batches or laminate curing conditions/pre-preg aging can be on the origins of such difference (which would influence the adhesive or laminates stiffness, respectively). However, at the time of analysis of these results, it was not possible to keep track of such fabrication issues, which would be interesting to investigate.

Table 14 – Experimental and numerical values of P_m for the SL joints.

	Experimental P_m [N]		Numerical P_m [N]		Error [%]
L_O (mm)	Average	St. Dev.	Average	Range	
10	2781	213	3506	229	26.1
20	5050	358	6490	306	28.5
30	7184	309	7940	393	10.5
40	8780	650	9439	481	7.5
50	11330	754	10881	561	-4.0
60	12376	2035	12053	617	-2.6
70	13215	1043	13203	663	-0.1
80	16005	1655	14037	690	-12.3

P_m increased at a decreasing rate with L_O (Hu and Soutis 2000, Campilho et al. 2005, Kim et al. 2008a), although without a strength plateau up to the maximum value of L_O evaluated. This was caused by the combination of two factors: the tensile strength of the laminates was not attained for the values of L_O tested, and the ductility of the adhesive allowed a progressively larger redistribution of stresses in the adhesive layer up to the largest value of L_O, initiating from the overlap edges (Fig. 114 and Fig. 115). In fact, since fracture of all the joints was abrupt, only with a negligible crack growth before P_m for the bigger values of L_O, it can be concluded that the adhesive plasticity always held up crack initiation at the overlap edges up to P_m, keeping these regions at the plateau strength while stresses increased at the inner regions. The numerical values of P_m are accurate for L_O values from 30 to 80 mm, being worse for the L_O=10 and 20 mm SL joints, for which P_m was especially overestimated. Kafkalidis and Thouless (2002) also obtained differences close to 30% between the experimental and numerical average strengths for L_O=10 and 20 mm in SL joints with aluminium adherends. It was theorized that such errors could be related to a misalignment of the grips during testing, which is more influent for the smaller values of L_O. In this study, the differences of K for these values of L_O occurring from a smaller experimental longitudinal E modulus of the adherends are another possible explanation. Actually, this would cause a larger differential straining (Renton and Vinson 1975b, Pinto et al. 2009), weakening the joints.

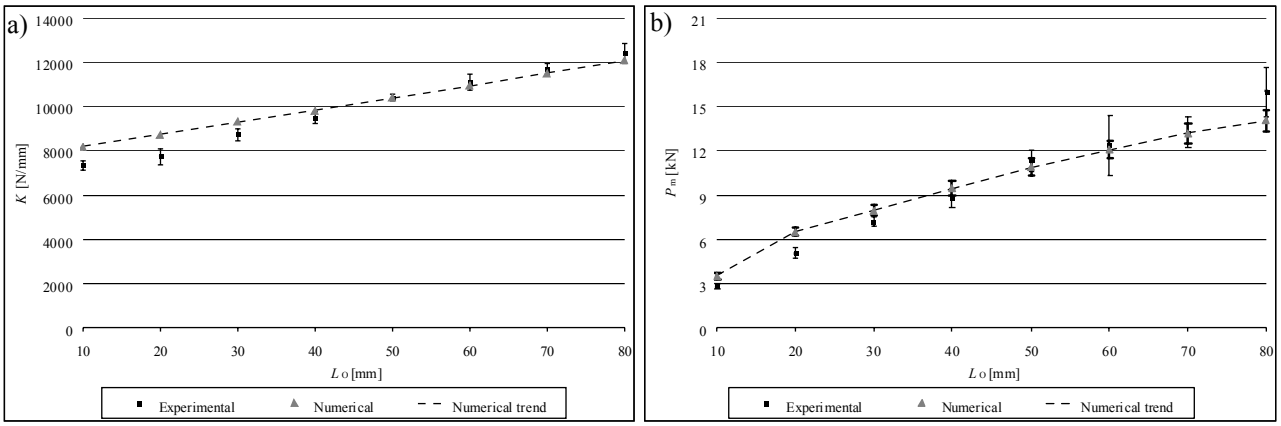

Fig. 119 – K as a function of L_O (a) and P_m as a function of L_O (b).

A distinctive feature of CZM's weighed against the traditional approaches is the ability to model the evolution of damage and crack growth. The two continuous curves of Fig. 120 represent the variation of P (up to P_m) as a function of the damage length for the L_O=10 and 80 mm joints (limit values studied). These curves relate the increase of P to a progressive softening of the adhesive layer, occurring from the overlap edges towards its inner region (Fig. 114 and Fig. 115). As expected, for the bigger values of L_O, this process initiates for smaller P/P_m ratios, due to the higher stress gradients. The dotted curve in Fig. 120 represents crack growth for the L_O=80 mm joint. No crack initiation was visible before P_m for the L_O=10 mm joint. The non-existence or diminished crack growth up to P_m supports the absence of a strength plateau in Fig. 119 (b), testifying an increasing redistribution of stresses in the adhesive layer with L_O up to P_m, while the adhesive at the overlap edges still adds to the joints strength.

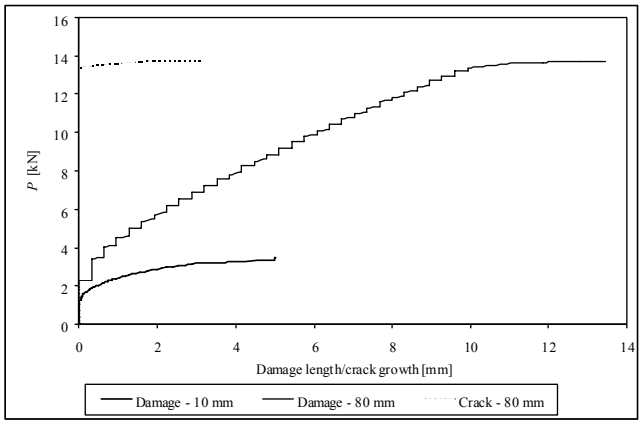

Fig. 120 – Numerical curves of P versus damage or crack length for the L_O=10 and 80 mm SL joints.

The first validation of the proposed inverse data fitting and strength prediction methodology for bonded assemblies was performed with tensile tests on SL joints with CFRP adherends and the adhesive previously characterized in Sub-Section 3.2.2.1. Different values of L_O were tested, to assess the applicability of this methodology under different mode-mixities and load conditions for the adhesive layer. In general, the K and P_m predictions were accurate. The best P_m predictions were obtained for values of L_O between 40 and 70 mm, while this value was largely overestimated for the two smaller values of L_O tested (10 and 20 mm). Two hypotheses for this difference were discussed. The overall results obtained encourage the use of CZM's and the inverse material characterization technique to predict the fracture behaviour of bonded assemblies. However, it should be noted that the results presented here were obtained for a very specific set of material properties, geometry and value of t_A. Therefore, more studies are needed to validate the model under different loadings and geometries, to expand the use of this methodology to all sorts of bonds (either joints or repairs) prone to be found in structural applications.

4. REPAIR OF COMPOSITE STRUCTURES

Adhesively-bonded repairs in engineering applications are gaining acceptance over the traditional repair techniques, such as riveting or mechanical fastening. Several authors addressed adhesively-bonded repair techniques on composite structures (Myhre 1981, Myhre and Kiger 1981, Stone 1985, Deaton 1987, Hall et al. 1988, Ong and Shen 1991, Ahn et al. 1996, Hu and Soutis 2000, Campilho et al. 2005, Chu and Ahn 2005, Campilho et al. 2007a, Liu and Wang 2007, Campilho et al. 2008b). Such repairs benefit from a reduction of weight, easy conformance to complex shapes, capability of fluid sealing and joining of dissimilar materials, prevention of corrosion, less stress concentrations, preservation of the fibres continuity (FRP adherends), improved fatigue behaviour, vibration damping, enhanced electrical insulation capabilities, easier inspection using non destructive techniques, in situ application and reduction of the maintenance costs (Vinson and Sierakowski 1987, Mallick 1988, Tsai et al. 1995, Olia and Rossettos 1996, Zimmerman and Liu 1996, Mehrkam and Cochran 1997, Davis and Bond 1999, Fredell et al. 1999, Ashcroft et al. 2000, Bahei-El-Din and Dvorak 2001, Reis et al. 2005, Papanikos et al. 2005, Radice and Vinson 2006, Savage 2007, Campilho et al. 2008a). On the other hand, bonded components cannot be separated easily or without damage, added to the prospect of residual stresses arising from different thermal expansion coefficients between the adherends and adhesive. In addition, the lower resistance to high temperature or fire and higher susceptibility to degrade in severe environments than steel rivets or fasteners should not be disregarded (Ferreira et al. 2005). Moreover, in most cases, moderate fatigue stress levels in bonded assemblies lead to failure initiation in the adhesive (Renton and Vinson 1975b, Renton and Vinson 1975c). There are mainly two repair techniques for composite structures, referred to as strap (SS or DS) and scarf repairs (Ahn and Springer 1998a). The SS repair technique consists on drilling a hole in the laminate to remove the damaged material, followed by bonding of a circular patch on one of the laminate faces, concentric with the hole. DS repairs use two patches (on both laminate faces). Scarf repairs are executed drilling a conical hole in the laminate to remove the damage, and adhesively-bonding a patch with the complementary shape.

The optimization of the most significant geometric parameters of adhesively-bonded CFRP repairs is one of the main goals of this work, concurrently to the validation with experiments of the FEM methodology developed in Section 3 using ABAQUS® and the trapezoidal CZM to simulate the adhesive layer. SS, DS and scarf repair techniques were analysed to repair a $[0_2,90_2,0_2,90_2]_S$ lay-up CFRP laminate under tensile, compression and bending (4PB) loads. This Section structure is as follows: initially, the laminate and adhesive properties will be presented. The analysis procedure will be briefly described. Subsequently, the analysis is divided in two Sub-Sections with a similar structure, corresponding to the strap and scarf repair techniques evaluated. Each Sub-Section begins with a brief review highlighting some of the most relevant works on the subject. The problem statement is then presented, including the repair description, characteristics and geometry. The numerical methodology is discussed in a separate Sub-Section, followed by the experimental procedure, detailing the repair manufacturing and the test method. Subsequently, a stress analysis in the elastic stages of loading is presented, allowing locating critical stress regions and

potential damage onset locations. The failure analysis succeeds this study, including an experimental and numerical comparison between the repairs failure modes, K and P_m. Different parameters may be equated, depending on the characteristics of each repair technique or loading.

4.1. Material properties

CFRP laminates and patches were used (the elastic orthotropic properties of a unidirectional ply are presented in Table 3, Sub-Section 3.2.3.1.1). The properties indices are consistent with the coordinate systems presented in the following Sub-Sections to characterize each repair geometry, with a 0º ply aligned in the x direction. The epoxy adhesive Araldite® 2015 was used, whose cohesive laws were previously characterized in Section 3 by an inverse data fitting method. The respective cohesive parameters in pure modes I and II are presented in Table 8. Throughout Section 4, t_A=0.2 mm will be used, which corresponds to the value of t_A defined in the characterization procedure. For the stress analysis carried out in this Section, the adhesive representative solid elements were modelled as elastic materials, with the values of E and G modulus defined in Sub-Section 3.2.2.1.2 for the particular adhesive used.

4.2. Procedure

The analysis procedure for the three repair methods evaluated in this Section initiates with an elastic stress analysis in several planes in the thickness direction. These include the laminate/adhesive interfaces, the middle of the adhesive, and between plies in the laminate or patches (only for the SS and DS repairs). This allows a clear perception of the critically stressed regions and the potential loci of damage onset. In this stage of the analysis, the adhesive layer is modelled as an elastic material by the traditional solid finite elements of ABAQUS®. The triangular cohesive elements presented in Sub-Section 3.2.1 were introduced in the numerical models at several planes with an initial high stiffness (d_i=10^6 N/mm^3 in equations (11) and (12)), allowing the accurate extraction of stresses at selected thickness planes. The solid elements are not suitable to this end because stresses are calculated at the Gauss integration points, rendering them inappropriate to obtain stresses at the interfaces between different constituents and between composite plies (Campilho 2005). This analysis methodology allows obtaining the normal and shear stress distributions in the adhesive layer, laminate and patches, capturing the stress gradients in the adhesive thickness direction. In the subsequent failure analysis, the adhesive layer is modelled with the developed trapezoidal CZM, thus replacing the solid finite elements used in the stress analysis. Experimental and numerical comparisons on the failure modes, K and P_m will be performed. Additional parameters will be analysed according to the specificities of each repair technique and loading configuration.

At this stage, a small discussion on scale effects is introduced, which applies to all the repair studies in this thesis, comprising Sections 4, 5 and 6. This subject gains a crucial importance in this work, since scaled repair geometries of small dimensions were always used to test the different repair solutions and to validate the numerical methodology developed to predict the behaviour of adhesively-bonded assemblies. Scaling effects in composites design have become an important issue in recent years. Nowadays, a substantial amount of full size component testing is still currently required to qualify a composite aerospace, which could be avoided if more information was available on scale effects for composites (Lee and Soutis 2008). For a broader understanding of these phenomena, different investigators examined these effects in composites under tensile, compressive and bending loads

(Haberle 1991, Wisnom 1991a, Wisnom 1991b, Kellas and Morton 1992, Jackson et al. 1992, Daniel and Hsiao 1999, Davis and Petton 1999, Lavoie et al. 2000). In this work, scale effects are particularly evident for the repair of wood beams, which usually are part of large-scale structures. The obvious reasons of material cost reduction, specimens handling, and restrictions to the size of the CFRP plates manufacturing equipment and of the testing machines equipment, led to the use of small dimensions specimens. **In the tested repair geometries, it is not guaranteed that the failure mechanisms are identical and the scaled specimens strength is in exact proportion to the dimensions of the full-size repair, due to the known scale effects in layered composite materials, and also accounting for the typically different behaviour of adhesive layers depending on their thickness constraints (de Moura et al. 2008a, de Moura et al. 2008b, de Moura et al. 2009b). This simplification does not compromise the objectives of this thesis to validate the numerical methodology proposed to predict the behaviour of bonded assemblies and optimize the main geometric parameters of each technique, rather than reproducing faithfully real-size structures**. The influence of the materials or geometries size scaling on the repairs behaviour was not addressed either, despite the importance of such study for the confidence on the performance prediction of large dimension structures based on the properties of small models. The thickness effects for both the CFRP laminates and patches, and the adhesive layer, are particularly relevant in the repair geometries examined in this work.

For layered composite materials, in-plane scaling and thickness scaling can be distinguished. In-plane scaling emerges for instance in fastened assemblies. For these structures, the literature reports that the bearing strength of the laminate near the holes increases with the plate dimensions (Jackson et al. 1992, Bazant et al. 1996, Wang et al. 1996). Thickness scaling also plays an important role in composite size scaling (Chang et al. 1990, Gurvich and Byron 1995, Hsial et al. 1995, Ireman 1998), being more complicated to deal with than in-plane scaling since both material properties and geometrical parameters are involved. As an example, the study of Hou and Liu (2003) reported on a modification of the failure mode in bolted DL composite joints from bearing failure near the hole for thin adherends to cross-section failure for thick adherends. This was caused by a larger thickness constraining with thicker adherends, diminishing fibre microbuckling and delamination on the origin of the bearing damage. Lee and Soutis (2008) published a comprehensive study on the most significant geometric variables showing scaling dependence in unnotched and open-hole CFRP laminates under buckling restrained compression. Thickness scaling was more evident at a ply-level (increasing the plies thickness) than at a sub-laminate level (increasing the number of plies of a pre-defined sequence). A bigger thickness for the unnotched unidirectional specimens gradually diminished the compressive strength due to an increase of stress concentrations near the tabs, ply waviness and void content (Lee and Soutis 2005, Lee and Soutis 2007). In-plane scale effects (scaling concurrently the width and length, while keeping the hole diameter/width or length ratio) were also detected in notched multi-directional laminates, with a reduction of strength with the dimensions. This difference was associated with an overall distribution of stresses dependent on the hole size, despite the stress concentration factor at the hole being kept constant.

Thickness scaling effects of adhesive layers in bonded assemblies are also substantial, with the value of t_A significantly influencing the structures strength. Therefore, a good understanding of the fracture of adhesive bonds and associated thickness and boundary effects is essential for the design, construction and maintenance of structures bonded with adhesives (Duan et al. 2004). It is common knowledge that the mechanical properties of adhesives as a thin layer, such as the values of σ_u and J_c, vary with t_A and surrounding material characteristics, diverging also to the adhesive bulk properties (Andersson and Stigh 2004). In fact, in an adhesive bond between two high-modulus and non-yielding

adherends, the FPZ and respective height and extension are naturally confined by t_A, developing differently than in a bulk adhesive. Actually, the adhesive layer properties largely depend on the degree of constraint to deformations around the crack tip (Andersson and Stigh 2004, Hogberg and Stigh 2006, Leffler et al. 2007). Additionally, in bonded assemblies the adhesive is typically weaker and more compliant than the components to be joined. As a result, failure is often cohesive in the adhesive layer, which results on a mixed mode crack propagation (Campilho 2005). Oppositely, in bulk adhesives cracks tend to grow perpendicularly to the direction of maximum principal stress (Chai 1992), which constitutes another difference between these two scenarios. Kinloch and Shaw (1981) examined the fracture behaviour of rubber-modified epoxy adhesive layers in TDCB specimens with mild steel adherends. The effects of temperature, loading rate, adherends thickness and t_A on J_{Ic} were reported. J_{Ic} depended mainly on the adherends thickness and t_A. The adherends thickness effect became stable from 25 mm. Different studies reported on a obvious dependence of J_c of adhesive layers in bonded assemblies with t_A, specimen geometry and stiffness of the adherends (Bascom et al. 1975, Bascom and Cottingham 1976, Chai 1986, Hunston et al. 1989, Bell and Kinloch 1997, Lee et al. 2003b, Lee et al. 2004). Typically, the value of J_c of a thin adhesive layer increases with t_A up to a peak value, bigger than the bulk quantity (Kinloch 1987, Chai 1988, Crews et al. 1988). After, J_c decreases with t_A up to a plateau value, corresponding to J_c of the bulk adhesive (Bascom and Cottingham 1976, Hunston et al. 1989, Ikeda et al. 2000, Duan et al. 2002, Duan et al. 2003). This tendency is consistent with the works of Yan et al. (2001a, 2001b), which studied the influence of t_A on the fracture properties of DCB and CT joints with aluminium adherends and a rubber-modified epoxy adhesive. Using a large deformation FEM technique and the peak loads measured in the experiments, the critical value of the *J*-integral was calculated for different values of t_A. Gardon (1963) carried out peel tests considering cellophane adherends and an acrylic adhesive with varying values of t_A, having reported that the peeling strength, which was regarded as proportional to J_{Ic}, monotonically decreased with the reduction of t_A from its optimal value. Duan et al. (2004) addressed the thickness effect of adhesive layers in bonded assemblies adapting the Boundary Effect Model (Hu and Whitmann 1992) and the Essential Work of Fracture Model (Cotterell and Reddell 1977, Mai and Cotterell 1980). Results showed that the FPZ height and extension variation is closely related to the changes on J_c. These values greatly diminished when the crack-tip approached the back-face boundary of a specimen, because of the constraint to the FPZ development. For bonded joints, a linear relationship between the values of t_A and J_c was established up to a peak value of J_c, due to the FPZ restraint between the adherends. Above this value of t_A, J_c diminished up to the bulk value. The theoretical predictions were consistent with test results from the literature. Lee et al. (2004) examined the effect of t_A of a rubber-modified epoxy adhesive layer on J_{Ic} using the CT specimen with aluminium adherends, being found the previously reported evolution for the J_{Ic}-t_A curve. The reduction of J_{Ic} below the optimal value of t_A (0.3 mm) was substantiated by the small extension of the allowable damage zone around the crack tip. In fact, the main crack kinked directly into an interface damage zone, with coalescence of voids. For bigger values of t_A, an interface damage zone developed in the vicinity of the interface with the metal adherend, judged to have a considerable influence on the value of J_{Ic}. This was due to a stress-shielding effect, which consisted on the reduction of stresses around the crack tip due to energy dissipation at the interface region. This effect was cancelled for the bigger values of t_A, giving values of J_{Ic} equivalent to the bulk adhesive. Biel (2005) emphasized on the bigger values of J_c near the optimal value of t_A than as a bulk. This was due to the predominantly state of prescribed deformation at the region where the crack can propagate, which enlarges the FPZ. Actually, with a tough engineering adhesive, near the optimal value of t_A the FPZ typically extends several times larger than the value of t_A, and substantially longer than in bulk adhesives, resulting on bigger values of J_c. An identical interpretation for this behaviour can be found in the work of Pardoen et al. (2005). The earlier works of Daghyani et al. (1995a, 1995b) attributed this decrease in J_{Ic} with t_A up to the bulk value to a transition of the

fracture process from a cohesive failure to an apparent adhesive failure at the adherend/adhesive interface. However, this assumption does not sound reasonable, given that adhesive failures are regarded to result from an inadequate surface preparation (Campilho et al. 2008a). Moreover, using magnification techniques, many adhesive failures are found be actually cohesive, occurring very near to the interface (Gonçalves et al. 2002). This is a very strong scenario to be considered, owing to the typical concentration of the adhesive layer stresses towards the interfaces with the increase of t_A (Ojalvo and Eidinoff 1978, Sawa and Uchida 1997, Gleich et al. 2001a).

4.3. Strap repairs

Different techniques were used in the past to predict the mechanical behaviour of adhesively-bonded repairs of isotropic or orthotropic composite structures using the strap repair technique. Analytical studies (Ahn and Springer 1998b, Nishino and Aoki 2006, Romilly and Clark 2008), experimental strain-based methods (Hamoush et al. 2005) and numerical works using the FEM (Soutis et al. 1999, Hu and Soutis 2000, Campilho 2005, Campilho et al. 2005, Kaye and Heller 2006) are the most common methodologies of analysis. Numerically, the repairs strength can be predicted using adequate stress or strain-based criteria for the adhesive layer, damaged structure and patches (Papanikos et al. 2005, Liu and Wang 2007). However, since these repair techniques often lead to stress concentrations or even singularities, these criteria are highly mesh dependent. Alternatively, CZM's coupled to FEM models can be used to simulate the behaviour of adhesively-bonded repairs (Campilho 2005, Campilho et al. 2005, Campilho et al. 2008a, Campilho et al. 2008b, Campilho et al. 2009b), simulating fracture of the adhesive layer and, in the case of layered composites, between plies, to simulate delaminations, intralaminar or fibre fractures. This methodology has the advantages of its mesh independency, since damage growth is ruled by energetic criteria, and the possibility to characterize the behaviour of structures up to failure. Mahdi et al. (2003b, 2003c) used 2D and quasi 3D FEM models to predict the performance of undamaged and repaired (overlap and scarf) sandwich beams, under 4PB. The beams consisted on a honeycomb core adhesively-bonded to CFRP faces. The 2D model simulated the repairs behaviour accurately and was considered suitable to qualitatively design the repair patches. The DS repair technique on CFRP laminates was studied by Liu and Wang (2007) for a tensile loading. The FEM simulations using ANSYS® were able to predict the repair strength, using the Tsai-Wu criterion to predict fibre and matrix cracking of the laminate and patches, the Ye delamination criterion to detect delamination between plies and the Maximum Shear Stress Criterion for the adhesive layer. A repair optimization was performed by studying the influence of the patch diameter, thickness and lay-up, as well as the adhesive thickness, on the strength and failure mode of the repairs. This methodology was compared with experiments, with a good correlation between both. Soutis et al. (1999) evaluated by the FEM the influence of several geometric parameters on the compressive strength of DS composite repairs, addressing also a repaired specimen with the drilled hole filled with adhesive (plug filling). The strength and locus of damage initiation of the repairs were predicted with the MNSC for the microbuckling in the laminate and the ASSC for the adhesive layer failure. Hu and Soutis (2000) simulated numerically, using the FEM, the mechanical behaviour of compression loaded DS composite CFRP repairs. The repairs strength was evaluated with the MSSC for the prediction of a cohesive failure in the adhesive layer. Above a determined value of overlap length, the repair strength remained practically constant, due to the appearance of an unloaded central region of the overlap of increasing dimensions. Campilho et al. (2005) addressed SS and DS repairs on unidirectional CFRP laminates under a tensile load. A 2D FEM analysis was used as an approximation to the 3D geometry of these repairs, for parameter optimization purposes. The numerical analysis used ABAQUS® and plane-strain eight-node elements, including a triangular CZM to simulate damage initiation and growth.

This work focused on the effect of the overlap length and the patch thickness on the stress distributions in the adhesive layer and the residual strength of the repairs. One of the main findings pertained to the non-proportional strength improvement of the repairs as a function of the overlap length, since above a critical value, the strength improvement was minimal. The same authors (Campilho et al. 2008a) evaluated the tensile behaviour of 2D SS repairs on CFRP laminates for different overlap lengths and patch thicknesses. A FEM methodology including a CZM with a trapezoidal shape in pure modes I and II was used to simulate a ductile adhesive layer, and was validated with experiments. Accurate predictions were found for the failure modes, K and P_m, which allowed the authors to assume that the developed cohesive model was adequate to simulate the mechanical behaviour of repairs bonded with ductile adhesives.

The compressive behaviour of these structures must also be taken into account during the design process (Yurgartis 1987, Budiansky and Fleck 1993). In fact, different failure mechanisms arise under compression, such as fibre microbuckling, for buckling restrained structures (Lessard and Chang 1991, Lankford 1997, Berbinau et al. 1999, Lee and Soutis 2008), or global buckling of the assembly between clamping points, if no transverse restriction exists (Eryigit et al. 2009). Fibres microbuckling comes from the compliant materials used as matrix, whilst global buckling is justified by the slenderness of elements, depending on their cross-section, elastic properties, and boundary and loading conditions. When loaded along its length, a slender member initially deforms in pure compression. At a certain level of applied load, elastic instability leads to a transverse deflexion of the beam accompanied by cross-sectional rotation along the axis of smaller second moment of inertia. This phenomenon is known as lateral buckling, and the corresponding load the critical buckling load (Eryigit et al. 2009). Owing to these fracture mechanisms, the compressive strength of CFRP laminates is lower than the tensile one (Tsuji and Kubomura 1992, Suemasu et al. 2006), implying that bonded assemblies under bending are more likely to fail in compression than tension. This also applies to repaired sandwich structures with composite faces, which would more easily fail in the compression face (Ramantani et al. 2009). The mentioned failure mechanisms under compression lead to a completely different behaviour of composite structures, with the accurate assessment of the stability limit states showing a particular importance in their design. This justified the attention paid to the development of theoretical and computational methods for the buckling analysis of slender elements, with particular attention to thin-walled composite panels (Svensson 1985, Thevendran and Shanmugam 1992, Haengsoo et al. 1994). With this purpose, analytical approaches based on the Vlasov theory were applied to conventional (Bleich 1952, Chajes 1952, Wang et al. 2004) and composite structures (Lee et al. 2002, Sapkas and Kollar 2002). Bauld and Tzeng (1984) applied a Vlasov-based analytical solution for thin-walled fibre-reinforced beams with an open-hole. A linear theory was developed for the determination of stresses and deflexions, followed by a non-linear theory, suitable for limit point stability analyses of the global buckling modes. The critical buckling load predictions focused on different loads, boundary conditions and laminate lay-ups. Other investigators (Brooks and Turvey 1995, Turvey 1996a, Lee et al. 2002) studied the buckling behaviour of I-beam composite sections. Lee and Kim (2001) developed an analytical approach accounting for the torsional buckling of I-section composite beams. The proposed model predicted accurately the buckling loads and modes for different geometries. A few closed-form solutions were also developed for the critical buckling loads of slender structures (Anderson and Trahair 1972, Pi and Trahair 1992, Trahair 1993, Mohri et al. 2002). Composite structures with a rectangular section, including thin plates, are widely used in the most varied applications, and some works reported on these geometries. The experimental measurement and analytical prediction of the lateral torsional buckling loads of composite wood beams with a rectangular section were addressed by Hindman et al. (2005). Turvey (1996b) experimentally determined the lateral buckling loads of rectangular cross-section pultruded GFRP cantilever beams loaded on one of their edges at the

centroid of the cross-section. Hodges and Peters (2001) developed an analytical technique for the torsional buckling load of composite beams with a rectangular section and I-beams, applying an asymptotic method and considering various refinements of previously published results, including the Vlasov effect, elastic coupling, load offset from the centroid and in-plane lateral deflexion. An FEM static and dynamic buckling stability study of laminated composite cantilever beams with rectangular sections under a longitudinal edge load was published by Karaagaç et al. (2007), which compared the results obtained with the theoretical analysis of Tai (2004), with promising results. The work of Finn et al. (1992) consisted on one of the few studies found in the literature concerning the behaviour of composite repairs under buckling compression. The authors estimated experimentally the effectiveness of strap and plug repairs on the compressive strength of CFRP laminates without global buckling restraining. It was found that, under uniaxial compression, the applied load increased until the buckling load, representing the load at which the repair global buckling between grips initiated. A plateau region followed in the P-δ curve, corresponding to the buckling development, at an approximate constant load. Failure occurred after a determined displacement. Plugging the laminate, i.e., cutting the damaged zone and replacing with a plug was not found to be effective. Similarly, the strap repair results indicated that for the damaged laminates used in the tests, no significant improvement of the compressive strength was attained. As a result, the recommended course of action was not to repair the damaged laminates.

The **SS repair technique** is firstly characterized. The repair procedure is carried out after the laminate undergoes damage at an intermediate section, for instance due to microbuckling or low-velocity impact, causing fibre rupture or delamination between plies. The damage is subsequently removed by drilling a hole at the damaged region, and a circular patch is adhesively-bonded on one of the laminate faces, concentric with the drilled hole (Fig. 121 a).

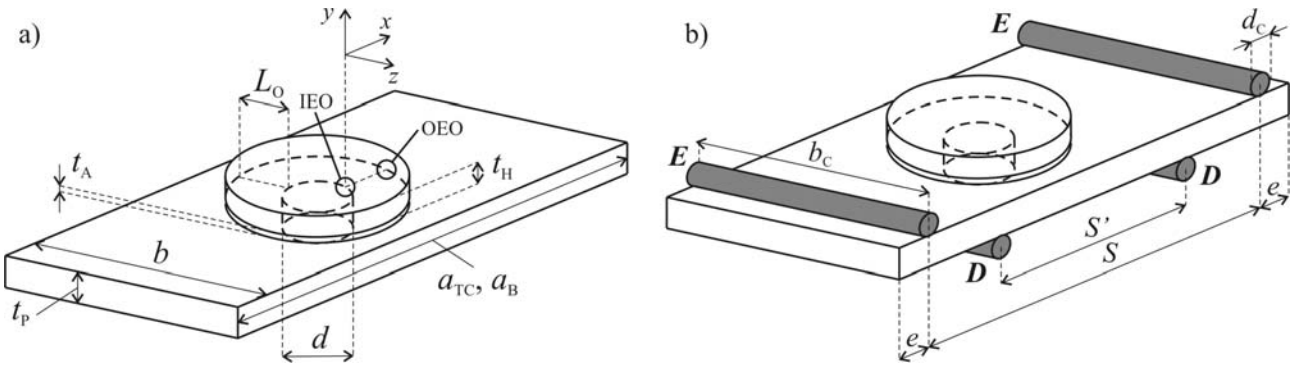

Fig. 121 – SS repair geometry and characteristic dimensions (a) and test configuration under 4PB (b).

The IEO and OEO are defined in Fig. 121 (a). This repair technique, which is representative of typical repairs found in many structural applications (Zhang and Keller 2008), was studied by Hu et al. (1997). In the investigation by these authors, it was concluded that peel and shear stresses peak near the central hole, leading to delaminations between plies. SS repairs are characterized by an easy execution and eccentricity of the transmitted load, which leads to a significant flexure at the repair region and consequent peel peak stresses at the overlap edges (Li et al. 1999, Osnes and Andersen 2003, Campilho et al. 2005, Radice and Vinson 2006, Luo and Tong 2007). These, added to the shear peak stresses developing at the same regions due to the differential straining of the repair constituents (Volkersen 1938, Adams et al. 1997, Zou et al. 2004, Campilho et al. 2005), justify the small efficiency of SS repairs. Consequently, this repair technique is usually not used as a permanent repair, nor in highly stressed or high responsibility structures (Hu and Soutis 2000, Owens and Sullivan 2000a, Owens and Sullivan 2000b, Campilho et al. 2005). In these cases, both SS and

DS repairs are regarded as temporary, aiming to restore the strength required to permit operation only until a permanent repair can be performed (Soutis et al. 1999).

The **DS repair technique** is based on the same geometry (Fig. 121 a). However, two patches are bonded concentric with the drilled hole, one on each face of the damaged laminate. DS repairs are more efficient than the SS repair, due to the duplication of the adhesive shear area and the elimination of the laminate flexure, since it is under symmetric loads (Hu and Soutis 2000, Campilho 2005, Campilho et al. 2005). This reduces σ_y peel peak stresses and significantly enhances the repair strength (Fernlund et al. 1994, Tong et al. 1995, Campilho et al. 2005). Therefore, τ_{xy} stresses also become flatter along the bond length (Kinloch 1990, Adams et al. 1997, Campilho et al. 2005). Still, some bending occurs in the patches, giving rise to σ_y peel peak stresses in the adhesive layer at the OEO, and σ_y compressive stresses at the IEO (Volkersen 1965, Adams and Peppiatt 1974, Adams et al. 1997, Kinloch 1990, Campilho et al. 2005). This repair procedure may not be straightforward to execute, depending on the available access to both laminate faces (Osnes and Andersen 2003). In this situation, partial disassembly of the structure may be required. An alternative to the SS and DS repair techniques, used in the past by some investigators (Kocher and Cross 1972, O'Neill 1982, Tan and Tsai 1987, Lee and Mall 1989), consists on reinforcing the hole with a circular shape material, either adhesively-bonded or pressure-fit. However, experimental observations under tension and compression showed, as a rule, a small strength improvement to the open-hole condition.

The characteristic dimensions of the repair are the laminate length (a_{TC} or a_B) and respective width (b), the overlap length (L_O), defined as the radial overlap between the hole and the patch, the laminate thickness (t_P), the adhesive layer thickness (t_A), the patch thickness (t_H) and the hole diameter (d). Two different laminate lengths were considered: a_{TC} (tensile and compressive loads) and a_B (bending load), with $a_{TC}<a_B$. The distinction was considered to guarantee that under a bending load the dimension of a is sufficiently large to ensure that the loading cylinders do not interfere with the repair region. The 4PB configuration was chosen, to assure a constant bending moment at the repair region. For the subsequent analyses, the following *initial dimensions* were considered for the SS and DS repairs [mm]: a_{TC}=70, a_B=150, b=50, L_O=10, t_P=2.4, t_A=0.2, t_H=1.2 and d=10. t_P and t_H correspond to sixteen and eight plies for the laminate and patch, respectively. Ply unit thickness is 0.15 mm. $[0_2, 90_2, 0_2, 90_2]_S$ and $[0_2, 90_2]_S$ lay-ups were used for the laminate and patches, respectively, for all SS and DS repairs, except for the parametric study on t_H. Fig. 121 (b) shows the testing configuration under bending, in which ***D*** and ***E*** represent the loading and supporting cylinders, respectively (S=130 mm, S'=60 mm, d_C=5 mm and b_C=70 mm). The distance between the supporting cylinders and the laminate edges (e) is 10 mm. **A parametric study will be performed on the values of L_O, t_H and t_A. This study will comprise the following values: L_O (2.5, 5, 7.5, 10, 12.5, 15 and 17.5 mm), t_H (0.6, 1.2, 1.8 and 2.4 mm) and t_A (0.1, 0.2 and 0.3 mm). The chosen t_H values correspond, by the same order, to $[0,90]_S$, $[0_2,90_2]_S$, $[0_2,90_2,0_2]_S$ and $[0_2,90_2,0_2,90_2]_S$ lay-ups. For each one of these repairs, the other parameters are the ones designated as the *initial dimensions*. It should be emphasized that the study on t_A consisted only on a stress analysis**.

4.3.1. Numerical work

The SS and DS repairs were numerically modelled in ABAQUS® with 3D models. Twenty-seven-node solid finite elements were used for the stress analysis, while eight-node reduced integration solid finite elements were considered for the failure analysis, to reduce the computational effort necessary to run the models. These elements are compatible

with the cohesive elements. Non-linear material (for the adhesive) and geometric analyses were performed. Including the non-linear geometric effects is extremely important, especially for the SS repairs, since a considerable flexure is observed (Fernlund et al. 1994, Mortensen and Thomsen 2002, Osnes and Andersen 2003, Das et al. 2008). In fact, a linear geometric analysis will underestimate the SS repairs strength, since higher strains and peak stresses will be extracted from the simulations, comparing with a non-linear geometric analysis (Tsai and Morton 1995b, Mortensen and Thomsen 2002, Osnes and Andersen 2003). On the other hand, for the DS repairs, no significant differences are expected, since flexure for these repairs is minimal. Cohesive elements were placed in the numerical models at seven different planes in the repair thickness direction for the SS and DS repairs (Fig. 122), to obtain σ_y and τ_{xy} stress distributions at the potential damage onset loci (Adams et al. 1986, Campilho et al. 2005, Magalhães et al. 2005, Kim et al. 2006, Taib et al. 2006b, Campilho et al. 2008a, Goyal et al. 2008). They were introduced in the laminate between the second and third plies closest to the adhesive (P1) and between the two laminate plies closest to the adhesive (P2), at the laminate/adhesive interface (P3), at the middle of the adhesive (P4), at the adhesive/patch interface (P5) and in the patch between the two plies closest to the adhesive (P6) and between the second and third plies closest to the adhesive (P7). Planes P1 and P7 represent the interfaces between the 0º and 90º sets of plies closest to the adhesive. The use of cohesive elements allowed an accurate characterization of σ_y and τ_{xy} stress distributions at the mentioned planes, in contrast to the ABAQUS® continuum elements, in which stresses are evaluated at the Gauss integration points. Both stress extraction methods yield similar results along the bond length. However, stresses at the singularity regions and at the plies boundaries are described more accurately with cohesive elements (Gonçalves et al. 2002, Campilho 2005, Campilho et al. 2005, Magalhães et al. 2005, de Moura et al. 2006b, Campilho et al. 2008b).

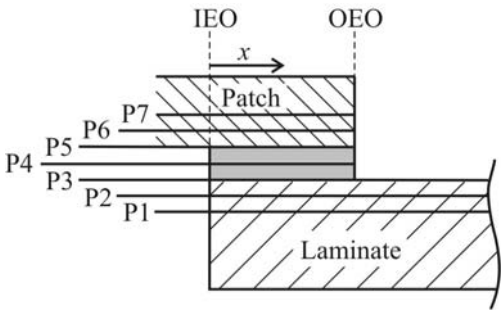

Fig. 122 – Cohesive elements planes in the SS and DS numerical models.

Fig. 123 (a) shows the symmetry conditions used for the SS numerical models, under a tensile or compressive load. DS repairs were modelled using only half the laminate thickness (through-thickness restraining was applied at the middle of the laminate thickness – plane ***C*** in Fig. 123a). Thus, only 1/8 of the model was considered. The symmetry conditions for the SS and DS numerical models in bending are presented in Fig. 123 (b).

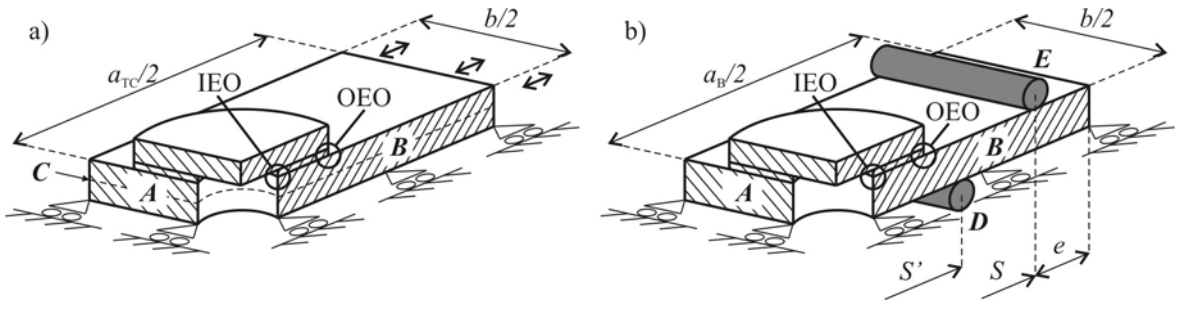

Fig. 123 – Symmetry conditions for the numerical models under tensile or compressive (a) and bending (b) loads.

The mesh detail at the repair region is presented in Fig. 124 for the SS repair. Eight elements through-thickness were used for the laminate and five elements were employed for the patches, while the adhesive thickness was modelled by two elements. For the DS repair, only five elements were used in the laminate owing to the additional symmetry conditions (Fig. 123 a). The mesh was built using one element through-thickness for each two adjacent equally oriented plies, except near the adhesive, where one element was used per ply because of the planes selected for the evaluation of stresses. The four plies at the middle of the laminate were modelled using only one element through-thickness. Thirty elements were applied along the overlap and for ¼ of the patch in the circumferential direction. Bias effects were used, to ensure a more refined mesh where stress gradients are known to be greater (Wang and Rose 1997, Lang and Mallick 1999, Cheikh et al. 2001, Lazzarin et al. 2002, Yang et al. 2004, Ferreira et al. 2005, Luo and Tong 2007). Fig. 125 shows the repair mesh used in the failure analysis. The failure analyses concerning the SS and DS repairs included cohesive elements with trapezoidal laws to simulate the adhesive layer (Section 3.2.2.1). As referred previously, these elements replace the solid finite elements usually employed to simulate the adhesive layer.

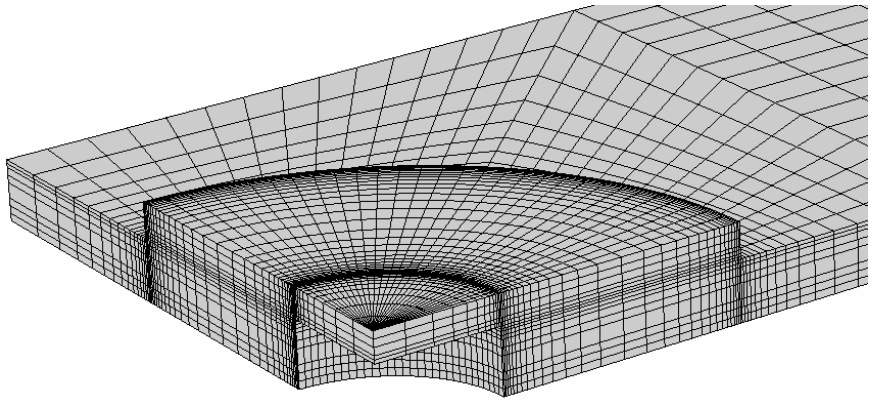

Fig. 124 – Detail of the mesh at the overlap region (SS repair).

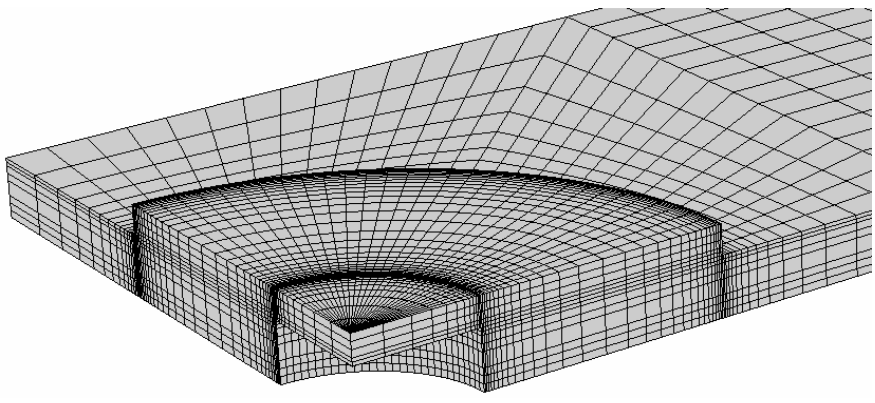

Fig. 125 – Detail of the mesh for the failure analysis at the overlap region (SS repair).

4.3.2. Experimental work

4.3.2.1. Specimens preparation

The specimens were manufactured from bulk plates with different lay-ups for the laminates and patches (Section 3.2.2.1.1 details the manufacturing procedure of a bulk plate by hand lay-up). The specimens cutting also followed a

similar procedure. Subsequent preparation included three main steps: drilling the *d*=10 mm hole in the middle of the laminate, machining the patches from pre-cut squares and adhesive bonding the patches.

Hole drilling

The *d*=10 mm holes were executed at *Instituto Superior de Engenharia do Porto* (ISEP) in a GAMBIN^{SA} 1m conventional milling machine using solid carbide Guhring 1149 drills with a 10 mm diameter and an h8 tolerance. These drills were chosen due to their special application to fibre-reinforced materials. In fact, they possess a sickle-form design of the cutting edges, which pre-stresses the fibres in the direction of pull and separates them in the direction of thrust, resulting on a clean cut with a smooth surface, with a corresponding minimization of delaminations near the hole edges. A vertical feed of 14 μm/rev was used in the drilling operation, considering a 1800 *Revolutions Per Minute* (RPM) drill rotational speed (Durão 2005). The following figures detail the specimens alignment technique and drilling.

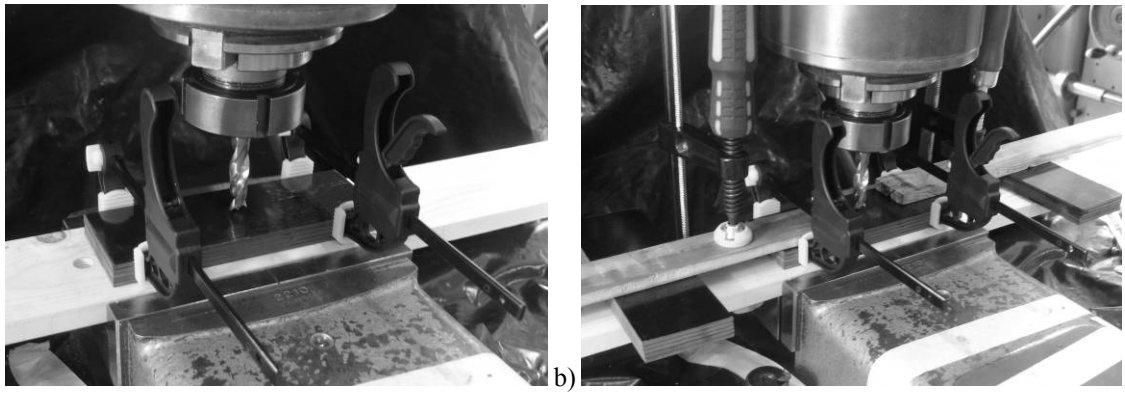

a) b)

Fig. 126 – Specimens alignment with grips (a) and fixing to the screw-vice (b).

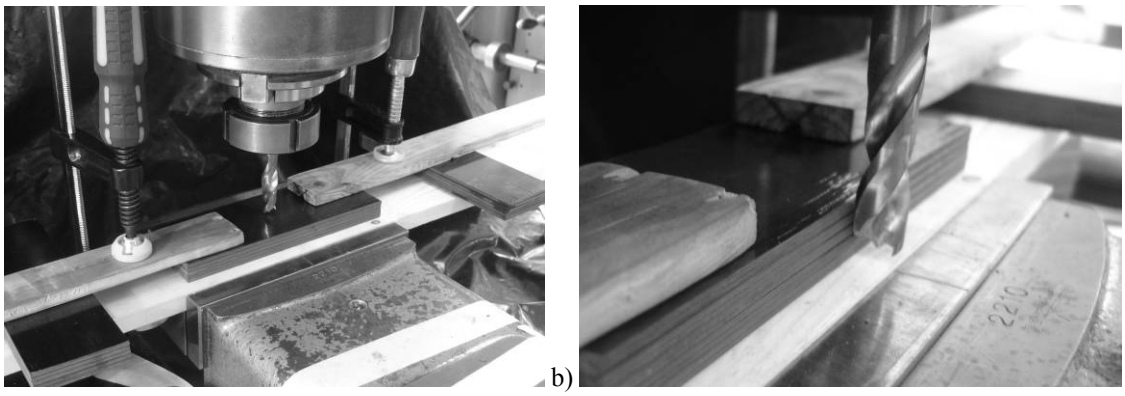

a) b)

Fig. 127 – Specimens fixed to the screw-vice (a) and position measurement (b).

Initially, a wood bar was secured in the vice (Fig. 126 a), working as sacrifice material at the drill exit to a group of five piled specimens. The specimens were aligned with grips on both directions (Fig. 126 (a) shows the width alignment). After this operation, these were compressed to the sacrifice bar with grips and wood bars at opposite edges (Fig. 126 b). Fig. 127 (a) shows the entire set after removal of the alignment grips, with the drill in place for the drilling operation. The drill positioning at the laminates centre was performed assessing its position at the specimens edges in the width and length directions using the milling machine digital position reader (precision of 5 μm). Fig. 127 (b) represents the drill position measurement in the width direction. The specimens centre was estimated by the average of the width and length edges coordinates. Fig. 128 (a) and (b) show different stages of the drilling operation. Each drill executed forty

holes (eight sets of specimens in groups of five) before replacement. With this procedure, no delaminations were visually detected at the hole region. The value of d of all the drilled holes was measured with a digital calliper (10 μm precision), giving values between 9.98 mm (new drill) and 9.95 mm (worn drill).

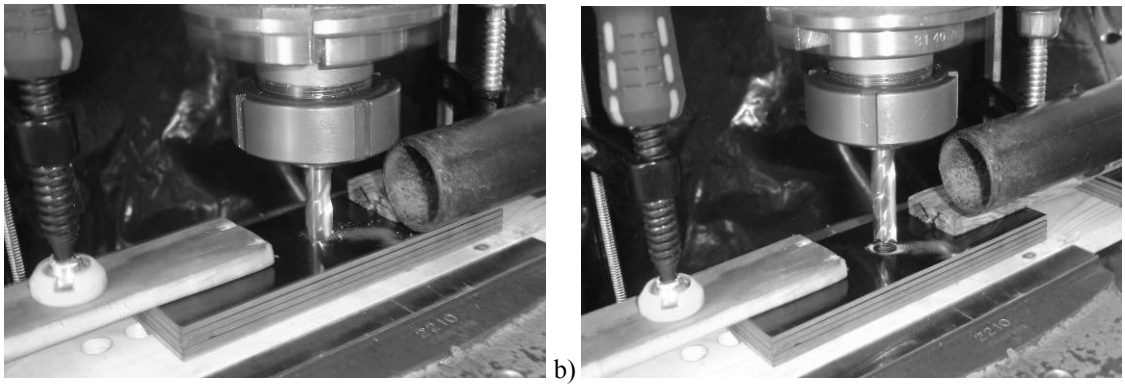

Fig. 128 – Specimens during the hole drilling operation (a) and after drilling (b).

Machining the patches

The circular patches were manufactured at ISEP in an EFI Cadete conventional turning lathe, using *Cubic Boron Nitride* (CBN) inserts from SECO (ref. VBMT 110204). The patches were fabricated from bulk plates, initially cut in squares with slightly higher dimensions than the final patch diameter. At this stage, a straight line was marked in the patches, allowing for a subsequent correct alignment of the patches with the laminate. A rough circular shape was obtained for each patch individually using a grinding wheel, to simplify the turning operation. The machining setup in the turning lathe is presented in Fig. 129 and Fig. 130, for a set of 30 mm diameter (corresponding to L_O=10 mm) and t_H=1.2 mm patches. Steel cylinders were machined with a diameter 0.1 mm smaller than the patches diameter to firmly tighten the set of patches between the lathe spindles. The chosen diameter for the cylinders assured a perfect edge finishing of the adjacent patches. The number of patches machined simultaneously depended on t_H, to make up a total machining thickness of approximately 15 mm. Machining was executed in both directions with a manual feed at a rotational speed of 1800 RPM, with an incremental depth feed of 0.2 mm per run. Measurements were performed when the patches diameter approached the final diameter. After the final diameter was reached, six more runs were executed with no further depth feeding, to avoid elliptical shape patches. This would otherwise occur due to the different material removal rate along the patches perimeter, due to the orthotropic nature of these materials.

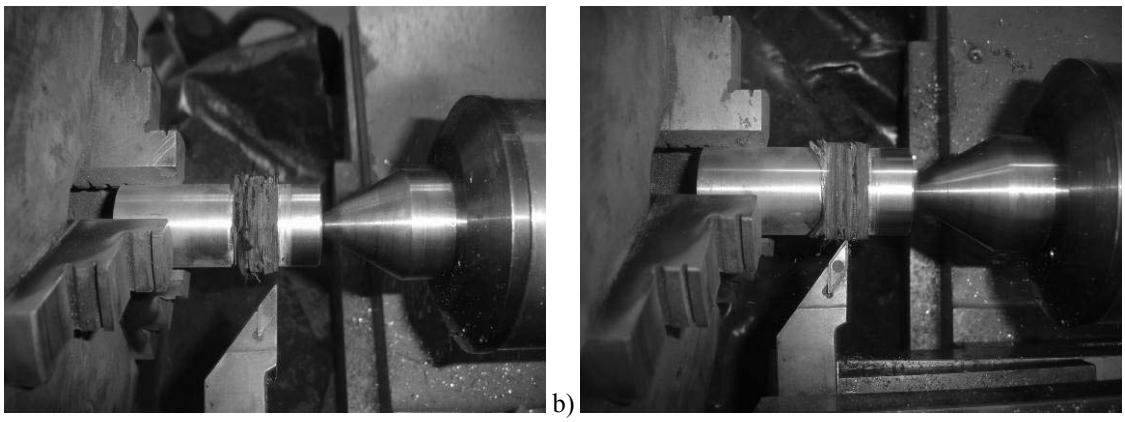

Fig. 129 – Set of patches tightened in the device (a) and during the machining process (b).

Fig. 129 (a) shows a set of patches tightened in the turning lathe prepared for the machining process. Fig. 129 (b) and Fig. 130 (a) exemplify the machining process at two different stages. In Fig. 130 (b) the procedure is completed.

a) 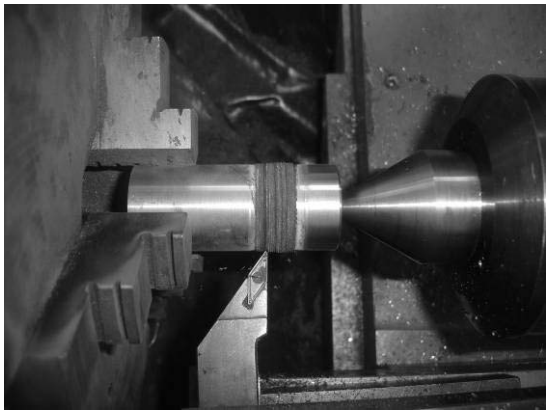 b) 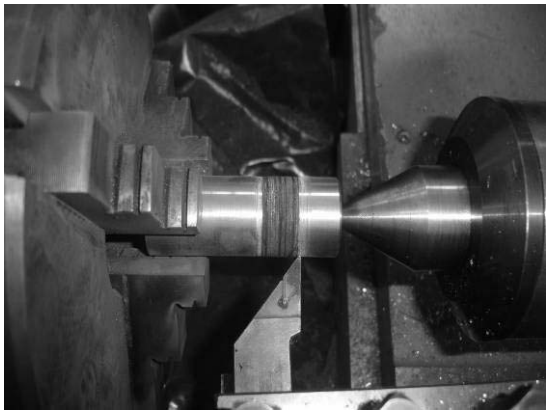

Fig. 130 – Set of patches during the machining process (a) and after machining (b).

Adhesive bonding the patches

The patches were bonded to the laminates using a manual positioning method. Initially, the laminates and patches were abraded with 220 grit sandpaper and cleaned with acetone, to avoid adhesive failures (Zimmerman and Liu 1995, Campilho et al. 2008a). To guarantee a uniform value of t_A on all the bond area, a fishing line with a diameter of 0.2 mm was used. The correct alignment of the patches lay-up was achieved using the straight line previously marked in the patches. To align the patch and certify the concentricity between the patch and the laminate hole, several markings were placed in the laminate (Fig. 131 a). The bonding procedure involved the following steps:

1. Drawing a line at the specimens mid-width, allowing for the posterior patch lay-up alignment, and engraving two marks at a distance d_1=5 mm to the patch edges.
2. Engraving two marks at points 2 (Fig. 131 a) at a distance d_1=5 mm to the patch edges.
3. Engraving marks at points 3 (Fig. 131 a) at 45º to the specimen longitudinal axis and at a distance d_2=1 mm to the patch edges.
4. Introducing the 0.2 mm diameter fishing lines at the positions showed in Fig. 131 (a), secured with adhesive tape. The distance d_3=2 mm, corresponding to the length under the patch, allows supporting the patch and obtaining the desired value of t_A, with the minimal disturbance to the adhesive layer.

a) 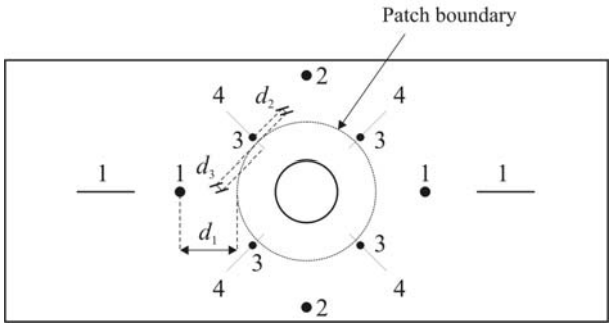

b) 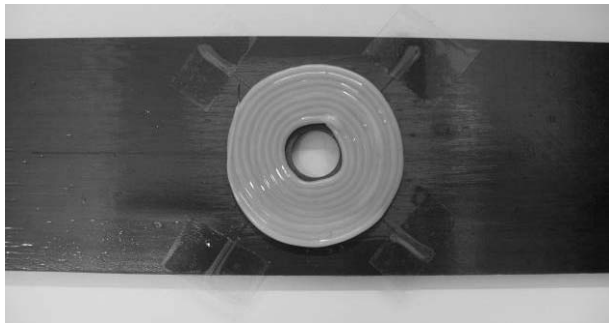

Fig. 131 – Scheme of the patch positioning system (a) and adhesive poured in the specimen in spiral (b).

5. Pouring the adhesive at the bond region in a spiral, as shown in Fig. 131 (b) for a L_O=15 mm repair. A small region without adhesive is left near the hole (IEO) and at the outer contour (OEO), to minimize the adhesive excess when it spreads due to the pressure applied on the patch.
6. Pressing the patch to the laminate until it touches the fishing lines (Fig. 132 a). The lay-up alignment, using the lines drawn in the laminate and patch, is performed visually at this stage. The concentricity between the laminate hole and the patch is also performed roughly, using the marks 1 and 2 at a 5 mm distance to the patch edges (Fig. 131 a) and a digital calliper with a precision of 10 μm.
7. Placing the repair on a wooden board and pressing it using two plastic grips (Fig. 132 b). The grips were placed very carefully to avoid the patch slipping and consequent misalignment.

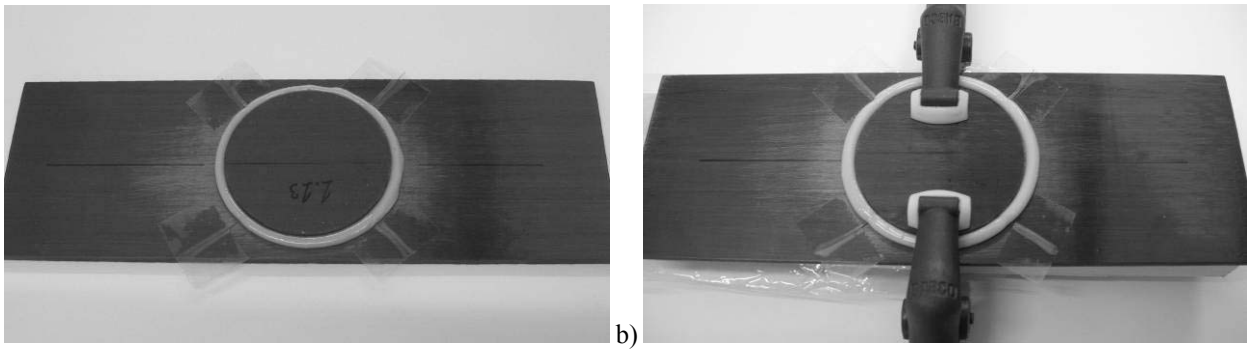

a) b)

Fig. 132 – Repair after the patch placement (a) and application of pressure using grips (b).

8. The adhesive is left to cure during approximately one hour. After this period, the adhesive is still not cured, allowing the manual removal of the fishing lines and the adhesive excess, but has the enough consistency to avoid t_A variations. The adhesive excess is removed with a sharp blade.
9. Finally, the patch is accurately checked for the lay-up alignment and concentricity with the laminate hole. The lay-up alignment is performed with a ruler and the marks on the laminate and patch. The concentricity is attained with the digital calliper, measuring the distance d_1 (Fig. 131 a) from marks 1 and 2 to the patch outer edge, and readjusting the patch before testing until it is perfectly aligned. The repair is then left to cure at room temperature for at least one week. The values of t_A were measured individually for all the repairs at several positions using a 1 μm precision micrometer knowing the individual values of t_P and t_H for each bonded set, and very accurate values for t_A were obtained (0.20 mm<t_A<0.22 mm). The final look of the repair is presented in Fig. 133 for two values of L_O.

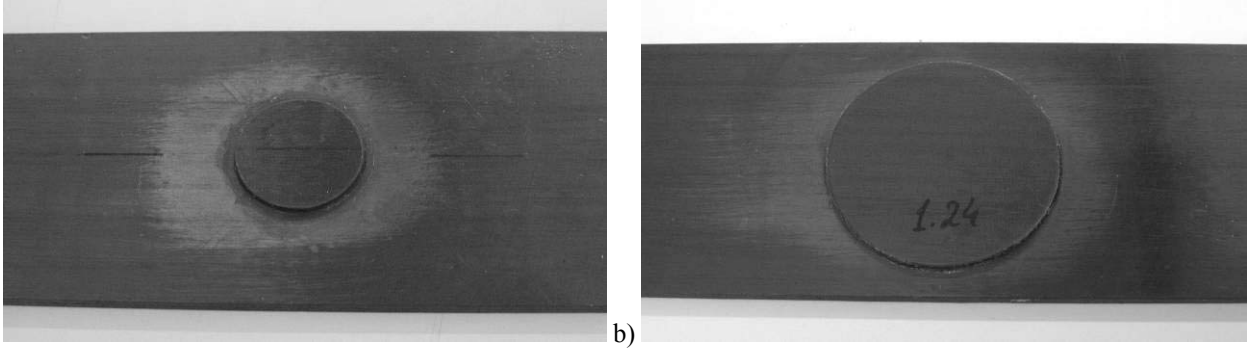

a) b)

Fig. 133 – Final look of a L_O=5 mm (a) and L_O=15 mm (b) repair.

4.3.2.2. Specimens testing

Different testing machines and conditions were used for the tensile, compressive and bending loads. The next Sub-Sections describe the equipment, testing procedure and conditions of the experimental tests conducted.

4.3.2.2.1. Tensile load

The SS and DS repairs were tested in tension at *Universidade de Trás-os-Montes e Alto Douro* (UTAD). A hydraulic testing machine (Instron® 8801) equipped with a 100kN load cell was used to this end. The repairs were tested at room temperature and under displacement control (0.5 mm/min). To avoid slipping between the repairs and the testing machine grips, 40 grit sandpaper was employed. The grips displacement was used to extract the P-δ curves. A sample rate of 5 points per second was considered in the tests. **Pictures were taken with 5 s intervals to fully characterize the damage evolution of the repairs up to failure**. **This procedure was applied to all repair configurations in Section 4. For all the SS and DS repair geometries, three specimens were tested. Whenever one or more results of a given testing condition was not considered valid, due to testing or manufacturing inaccuracies, or also evident deviation to the other results of the same geometry, additional tests were made to guarantee three valid results**. The experimental setup in the testing machine is presented in Fig. 134 for a t_H=2.4 mm SS repair. Fig. 134 (a) consists on a close-up of the repair, while Fig. 134 (b) shows the repair secured in the grips.

a) 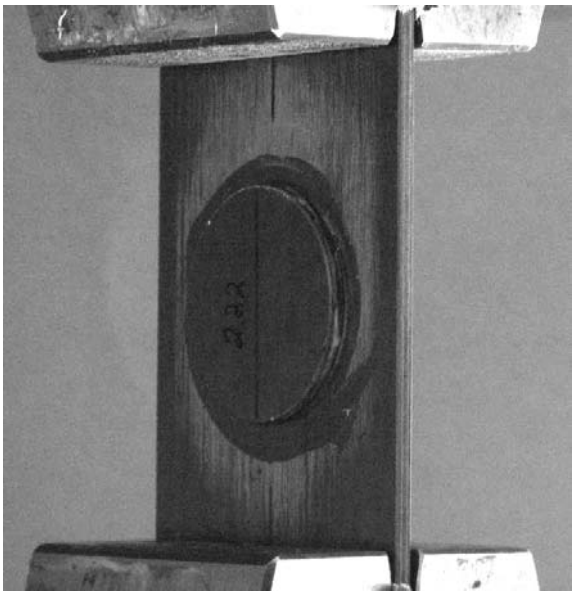 b) 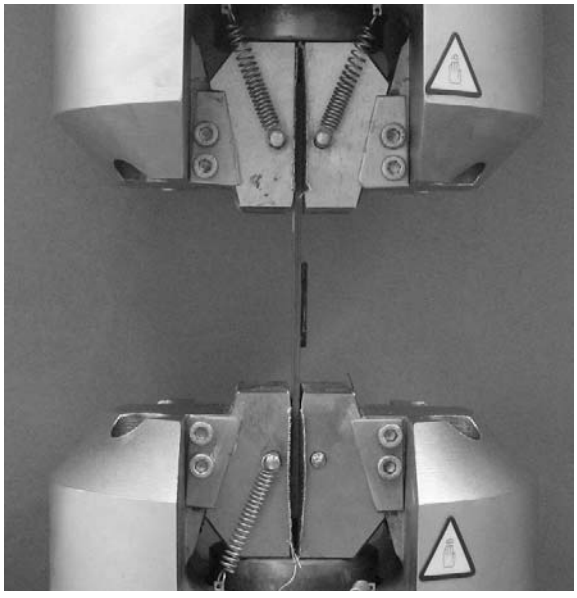

Fig. 134 – Experimental setup in the testing machine (tensile load, t_H=2.4 mm SS repair).

4.3.2.2.2. Compressive load

Under compression, the SS and DS repairs were also tested at UTAD. The testing machine and setup were similar to the tensile load (Section 4.3.2.2.1, Fig. 134). Additionally, the same testing velocity and sample rate were used.

4.3.2.2.3. Bending load

The bending tests to the SS and DS repairs were carried out at the UTAD facilities in an Instron® 5848 electro-mechanical Microtester equipped with a 2kN load cell. The tests were performed at room temperature and under displacement control with a cross-head speed of 2 mm/min, using a sample rate of 5 points per second. The P-δ curves were built on the assumption that the loading cylinders displacement is equal to the cross-head displacement, i.e., neglecting the bending device flexure. The 4PB tests were performed on a built aluminium device, which consisted on two reinforced beams supporting four towers, used to hold the loading and supporting pins (Fig. 135). The pins length was 70 mm, to comprise the repairs value of b=50 mm, and were grinded for a smooth sliding of the repairs during the tests. The towers width was only 15 mm, since these were adapted from an existing device. However, for the loads involved (maximum of 1000 N per pin), no flexure of the pins was detected. Fig. 135 (a) shows the experimental setup for a L_O=5 mm DS repair, while Fig. 135 (b) and (c) present the detail of the loading and supporting cylinders in the beginning and during the test, respectively.

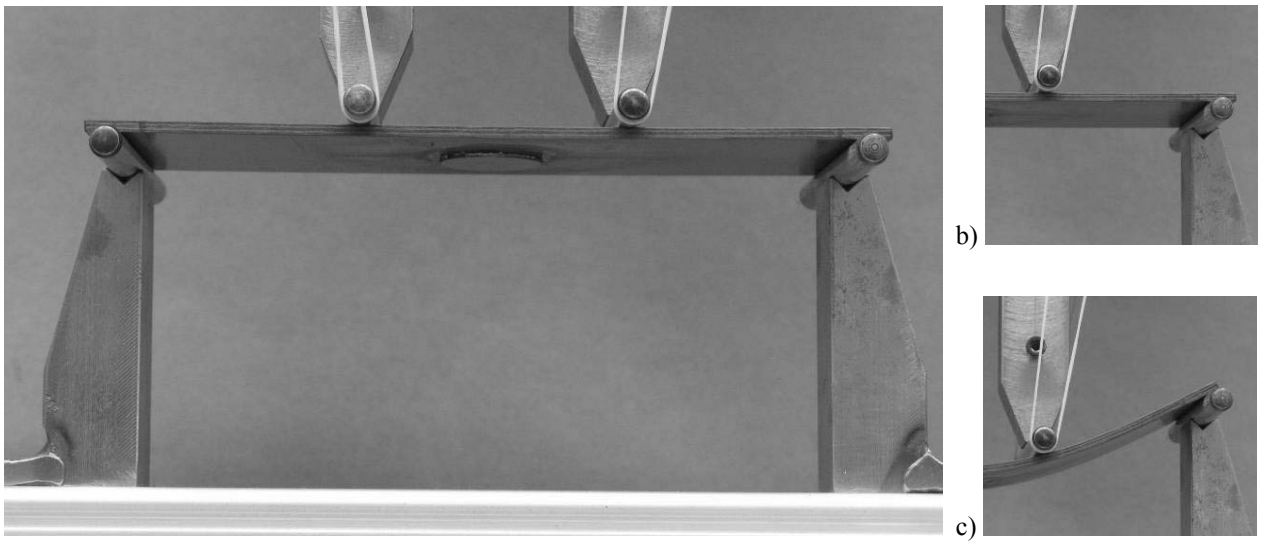

Fig. 135 – Experimental setup in the testing machine (bending load, L_O=5 mm DS repair).

4.3.3. Tensile load

The tensile characteristics of the strap repairs are initially evaluated. A stress analysis is primarily presented, to allow an insightful understanding of the effect of some geometric parameters on the distributions of stresses and repairs strength. A failure analysis follows, including the description of the failure modes and summary of the results.

4.3.3.1. Stress analysis

4.3.3.1.1. Single-strap repairs

Fig. 136 exemplifies the deformed configuration of the SS repair under a tensile displacement of 0.2 μm (applying a 10000x enhancement to the displacements). **The mentioned displacement and magnification are used throughout**

Section 4 for the SS, DS and scarf repair configurations under tensile and compressive loads, including all deformed configuration and stress distributions figures, to allow a direct comparison between the three repair techniques. σ_y and τ_{xy} stress fields at the adhesive region are shown in Fig. 137, to allow an evaluation of the repair critical regions. **The patch is removed, for a clear visualization of the adhesive layer stresses. This is applied throughout Section 4 for the corresponding figures**. It was found that σ_y and τ_{xy} stresses are critical near the symmetry plane ***B*** (Campilho et al. 2008b). Consequently, the following stress analysis will focus on the stress distributions only at this plane. Fig. 138 shows σ_x stresses at the repair region.

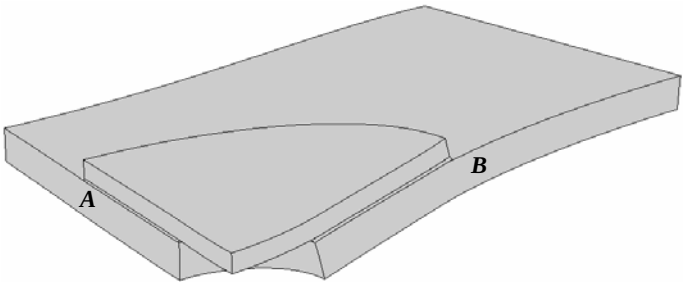

Fig. 136 – Deformed configuration of the SS repair under a tensile load.

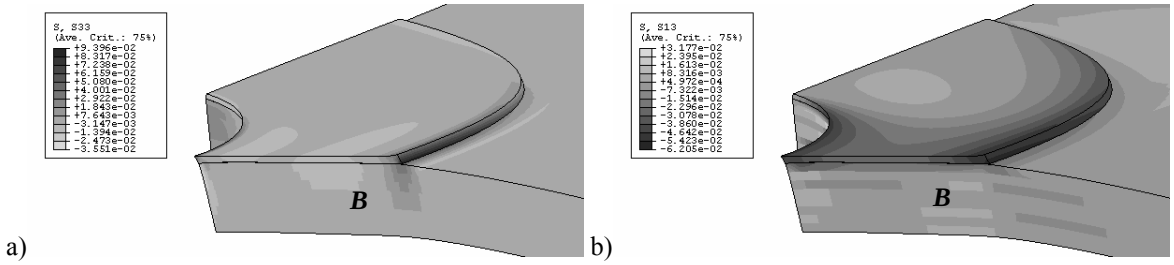

a) b)

Fig. 137 – σ_y (a) and τ_{xy} (b) stresses at the repair region.

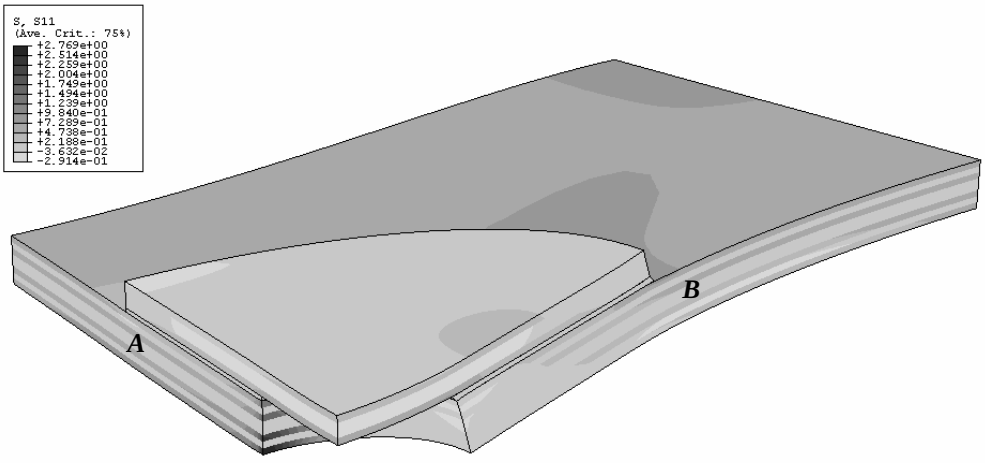

Fig. 138 – σ_x stresses at the repair region.

Under a tensile load, the SS repair undergoes significant flexure, which is justified by the eccentricity of the loads transmitted to the laminate due to the repair asymmetry (Campilho 2005, Campilho et al. 2005, Campilho et al. 2008b). This causes σ_x stress concentrations at the unrepaired face of the laminate at plane ***A*** near the hole. At this region σ_x tensile stresses, due to the specimen pulling, add to flexure ones (Fig. 138; Campilho 2005, Campilho et al. 2009b). σ_x

stresses are also generally higher for 0º, i.e., load oriented plies, due to their higher stiffness in the load direction (Fig. 138). The following figures plot σ_y stresses (Fig. 139), σ_y stress distributions at three planes at the repair region (Fig. 141 a), τ_{xy} stresses (Fig. 140) and τ_{xy} stress distributions at three planes at the repair region (Fig. 141 b). Planes P3, P4 and P5 are evaluated, respectively at the laminate/adhesive interface, at the middle of the adhesive and at the adhesive/patch interface (Fig. 122). **Throughout Section 4, x/L_O represents the overlap normalized distance from the IEO (Fig. 121 and Fig. 122). σ_y and τ_{xy} stress distributions are always normalized by the τ_{avg}, the average shear stress along the bond length at the middle of the adhesive (plane P4 in Fig. 122). This procedure is applied for all stress distributions in Section 4**.

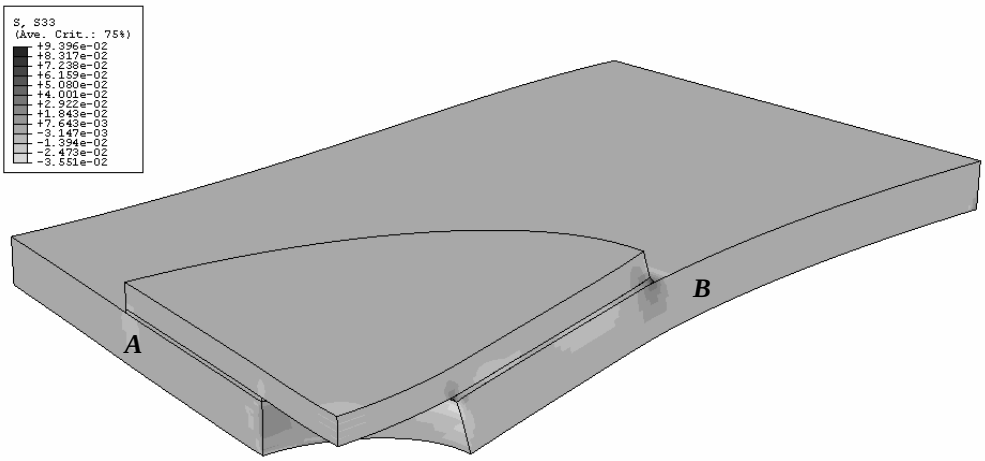

Fig. 139 – σ_y stresses at the repair region.

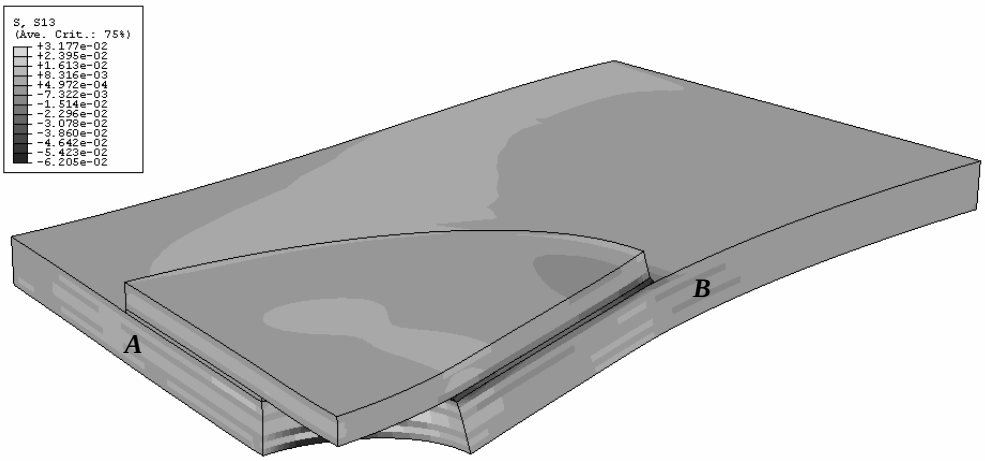

Fig. 140 – τ_{xy} stresses at the repair region.

The stress distributions are typical for these repairs (Campilho 2005, Campilho et al. 2005, Campilho et al. 2007c, da Silva and Adams 2007a, da Silva and Adams 2007b). Actually, σ_y peel peak stresses developed locally at the overlap edges, showing singularities at the overlap edges (Towse et al. 1999, Penado 2000, Wang and Rose 2000, Campilho 2005, Campilho et al. 2005, Radice and Vinson 2006, Taib et al. 2006a), in contrast with σ_y compressive stresses at the overlap inner region, negligible when compared to τ_{avg}. The singularities are located at the IEO, at the laminate/adhesive interface (plane P3, Fig. 122), and at the OEO, at the adhesive/patch interface (plane P5, Fig. 122).

τ_{xy} stresses are identical between the three planes, peaking at the overlap edges from a lightly loaded inner region (Radice and Vinson 2006, Taib et al. 2006a, Campilho et al. 2007c). This is caused by the differential deformation between the laminate and patch along the overlap (Volkersen 1938, Adams et al. 1997, Adams and Comyn 2000, Mahdi et al. 2003a). At plane P3, the τ_{xy} stress singularities are located at the OEO, while at plane P5 they develop at the IEO.

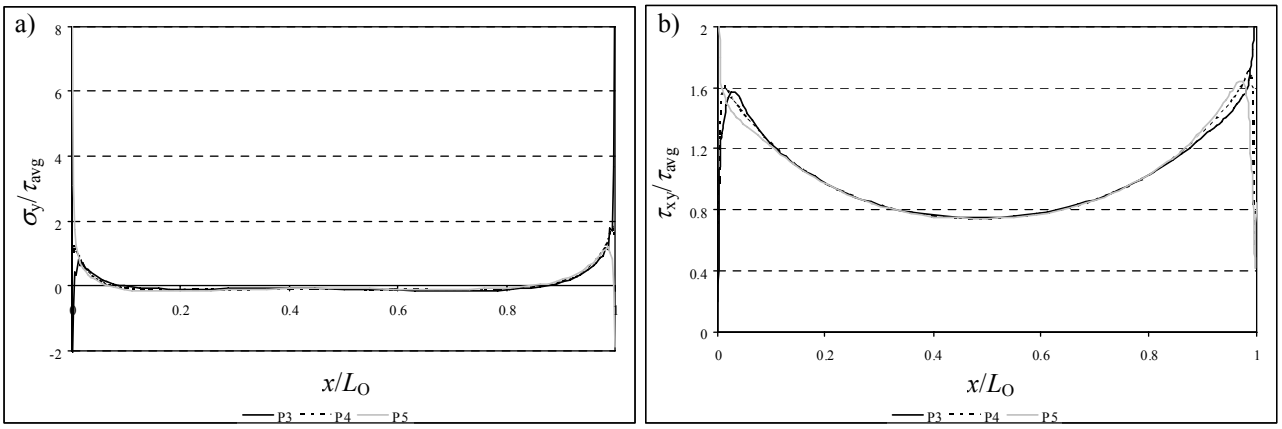

Fig. 141 – Normalized σ_y (a) and τ_{xy} (b) stress distributions at the repair region.

The following figures pertain to σ_y (Fig. 142) and τ_{xy} (Fig. 143) stress distributions at seven planes in the repair thickness (Fig. 122). σ_y peel stresses always peak towards the overlap edges disregarding the plane considered, being significantly smaller in the laminate and patch (Kim et al. 2008b). σ_y compressive peak stresses are also observed at planes P1, P2 and P3 (IEO) and P5, P6 and P7 (OEO). τ_{xy} stresses are highest and identical in magnitude at planes P3, P4 and P5. In the laminate and patch, τ_{xy} stresses progressively diminish outside the overlap ($x/L_O<0$ and $x/L_O>1$). Additionally, in the laminate (planes P1 and P2) shear stresses are higher at the overlap inner region ($0<x/L_O<0.5$), while in the patch (planes P6 and P7) τ_{xy} stresses are higher at the overlap outer region ($0.5<x/L_O<1$). The opposite regions in the laminate and patch exhibit lower τ_{xy} stresses and higher σ_y stresses.

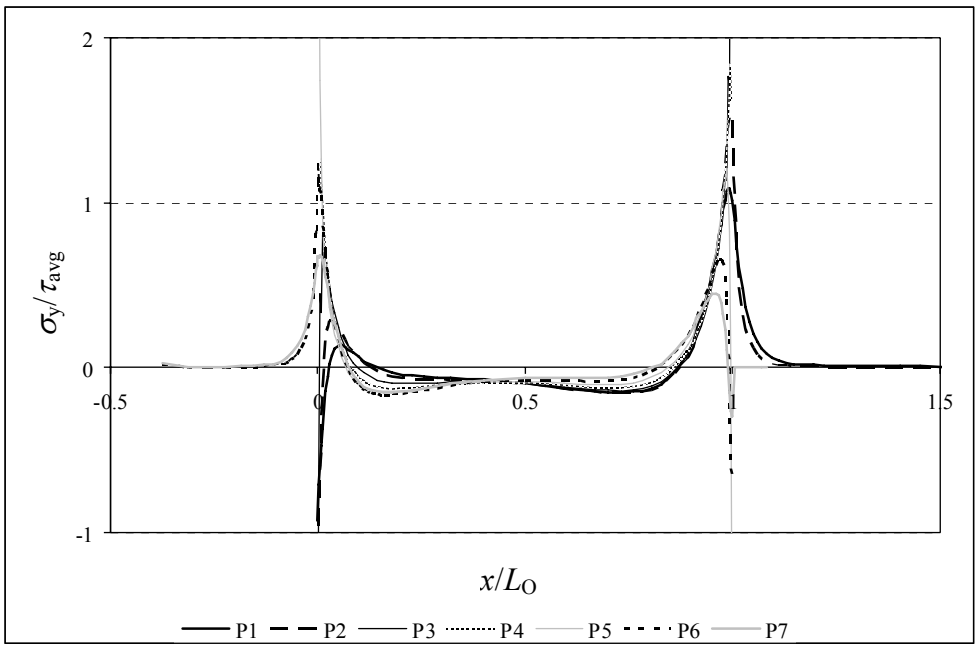

Fig. 142 – Normalized σ_y stress distributions at seven planes in the repair.

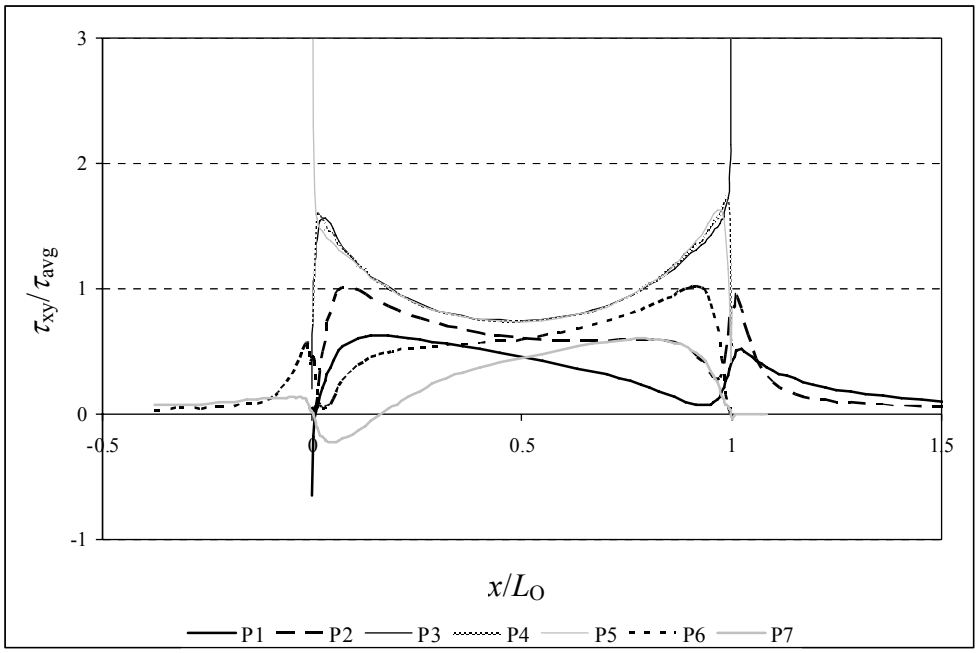

Fig. 143 – Normalized τ_{xy} stress distributions at seven planes in the repair.

The presented results point in the direction of probable damage onset at or near the stress singularities (plane P3 at the OEO and plane P5 at the IEO), progressing along or near these planes to the overlap inner region (Gonçalves et al. 2002, Campilho 2005, Campilho et al. 2005).

4.3.3.1.1.1. Overlap length

σ_y and τ_{xy} stress distributions are plotted at planes P3, P4 and P5, respectively the laminate/adhesive interface, the middle of the adhesive and the adhesive/patch interface (Fig. 122). Fig. 144 corresponds to plane P3 (laminate/adhesive interface), Fig. 145 to plane P4 (middle of the adhesive) and Fig. 146 to plane P5 (adhesive/patch interface). **σ_y and τ_{xy} stress distributions are normalized by τ_{avg}, the average shear stress along the overlap at plane P4, for the respective repair. This procedure is applied to all L_O studies on SS and DS repairs**.

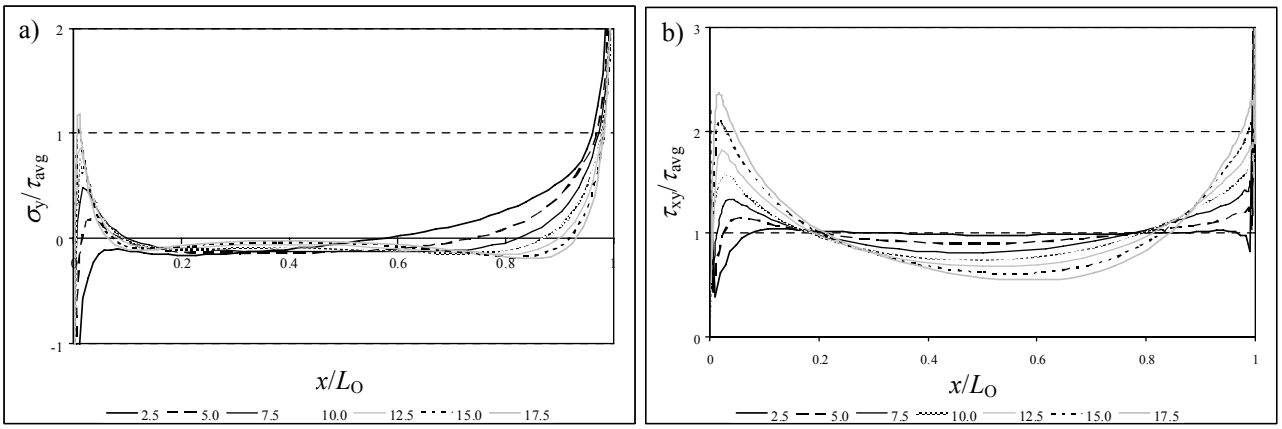

Fig. 144 – Normalized σ_y (a) and τ_{xy} (b) stress distributions at the laminate/adhesive interface (P3) as a function of L_O.

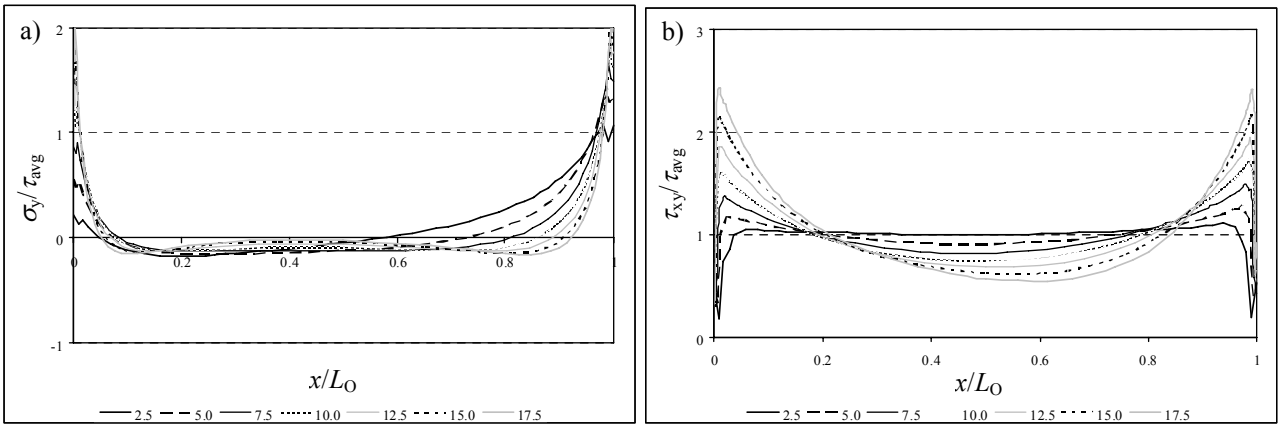

Fig. 145 – Normalized σ_y (a) and τ_{xy} (b) stress distributions at the middle of the adhesive (P4) as a function of L_O.

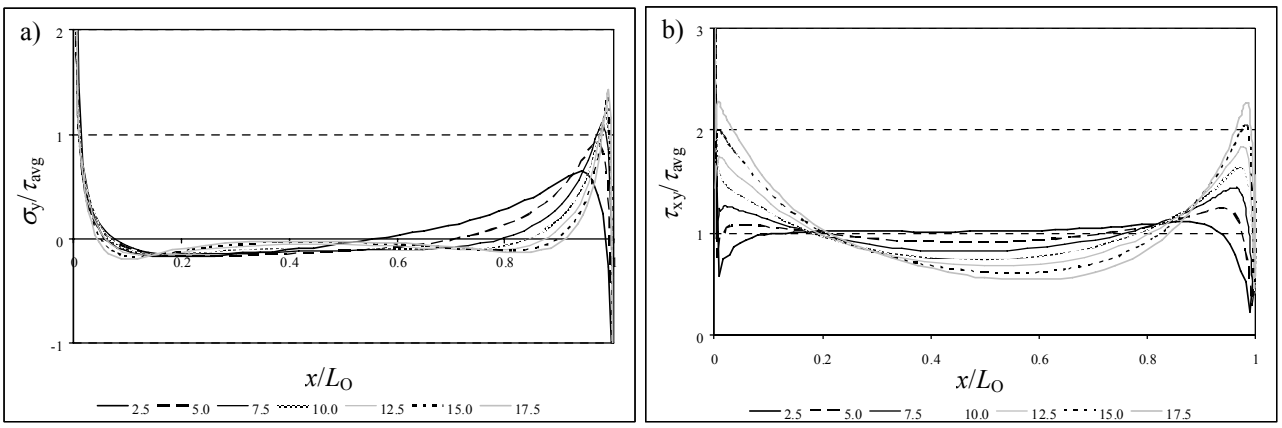

Fig. 146 – Normalized σ_y (a) and τ_{xy} (b) stress distributions at the adhesive/patch interface (P5) as a function of L_O.

As a rule, σ_y peel stresses peak at the overlap edges from a compressive inner region of small magnitude. At the middle of the adhesive (plane P4) two tensile peaks are observed at the overlap edges for all values of L_O. These are higher in magnitude at the OEO, increasing with L_O. σ_y peel peak stresses at the IEO also increase in magnitude with this parameter. The stress singularity loci are consistent with the results of Fig. 142 and Fig. 143. τ_{xy} stresses are identical in the bond length at the three planes under analysis disregarding the value of L_O, peaking at the overlap edges. τ_{xy} peak stresses at the overlap edges increase in magnitude with L_O, from a flat stress distribution for L_O=2.5 mm. Stress singularities at planes P3 (OEO) and P5 (IEO) are captured by the numerical models. Presumably, the repairs strength will not increase proportionally with L_O, since σ_y and τ_{xy} stress gradients towards the overlap edges increase with this parameter, impairing the repairs strength averaged to the bond area (Czamocki and Piekarski 1986, Hu and Soutis 2000, Kafkalidis and Thouless 2002, da Silva et al. 2004, Campilho et al. 2005, Reis et al. 2005, Murillo et al. 2007).

4.3.3.1.1.2. Patch thickness

Fig. 147 plots σ_y and τ_{xy} stress distributions at plane P3 (laminate/adhesive interface), Fig. 148 at plane P4 (middle of the adhesive) and Fig. 149 at plane P5 (adhesive/patch interface). **σ_y and τ_{xy} stress distributions are normalized by τ_{avg}, the average shear stress for the t_H=1.2 mm repair in the bond length at plane P4. This procedure is applied to all t_H studies in Section 4 (all loads, SS and DS configurations)**.

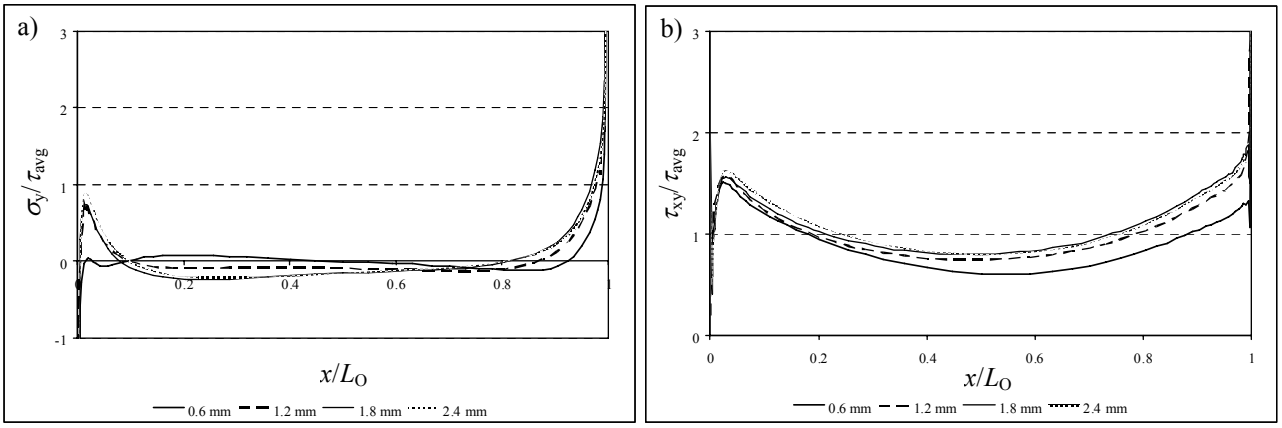

Fig. 147 – Normalized σ_y (a) and τ_{xy} (b) stress distributions at the laminate/adhesive interface (P3) as a function of t_H.

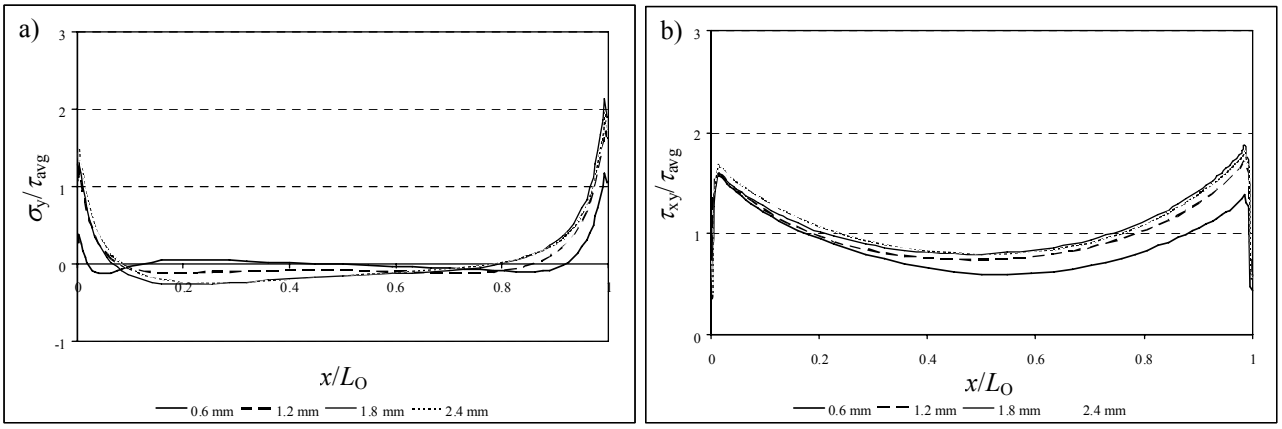

Fig. 148 – Normalized σ_y (a) and τ_{xy} (b) stress distributions at the middle of the adhesive (P4) as a function of t_H.

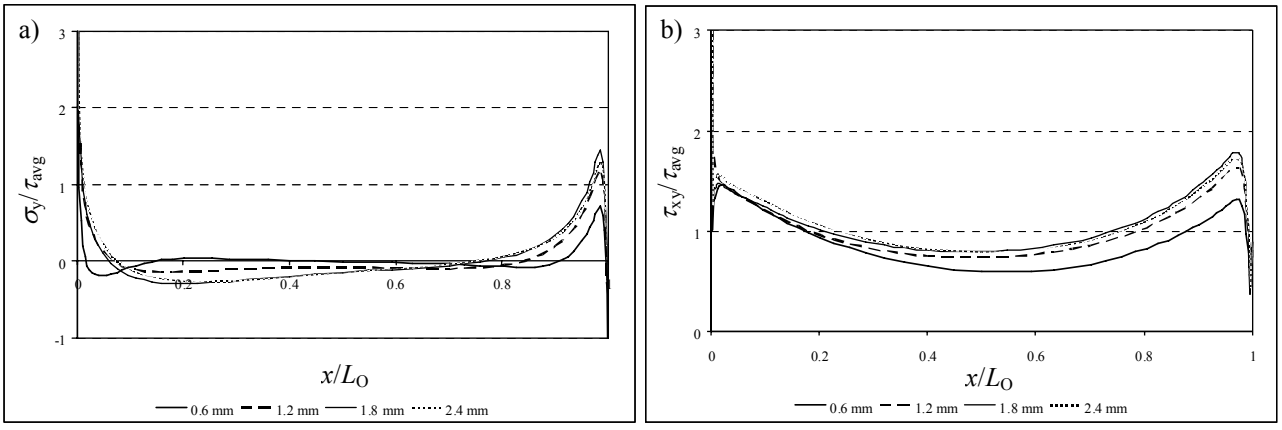

Fig. 149 – Normalized σ_y (a) and τ_{xy} (b) stress distributions at the adhesive/patch interface (P5) as a function of t_H.

σ_y stresses are usually small in magnitude and compressive at the overlap central region, except for the t_H=0.6 mm repair. For all values of t_H, σ_y peel stresses peak at the overlap edges. Stress singularities are captured at planes P3 (OEO) and P5 (IEO). Based on this analysis, the lowest value of t_H evaluated is recommended, since σ_y peel peak stresses at the overlap edges are minimized (Campilho 2005, Campilho et al. 2005). In fact, at plane P3 no σ_y peel peak stresses subsist at the IEO (Fig. 147), at plane P4 these are smaller in magnitude at both overlap edges, comparing with the remaining t_H repairs (Fig. 148), and at plane P5 these stresses are also smaller at the OEO (Fig. 149). τ_{xy} stress

distributions present a similar profile, regardless the value of t_H. Stress singularities were found at planes P3 (OEO) and P5 (IEO). Smaller magnitude shear stresses are observed for the t_H=0.6 mm repair, with a gradually increasing difference from the IEO towards the OEO. This is caused by the bigger load transmission capabilities for the thicker patches (Campilho 2005, Campilho et al. 2005). For the other repairs, τ_{xy} stress distributions are similar. Numerically, it is possible to say that the smallest value of t_H is preferable, since σ_y and τ_{xy} peak stresses at the overlap edges are smaller in magnitude (Soutis et al. 1999, Hu and Soutis 2000, Campilho et al. 2005). However, a patch premature tensile failure can occur, depending on its strength.

4.3.3.1.1.3. Adhesive thickness

Fig. 150 represents σ_y and τ_{xy} stress distributions at plane P3 (laminate/adhesive interface), Fig. 151 at plane P4 (middle of the adhesive) and Fig. 152 at plane P5 (adhesive/patch interface). **σ_y and τ_{xy} stress distributions are normalized by τ_{avg}, the average shear stress for the t_A=0.2 mm repair along the overlap at plane P4. This procedure is applied to all t_A analyses in Section 4**. Bigger values of t_A reduce the σ_y peak stresses at the overlap edges, except at the two stress singularity regions (plane P3 at the OEO and plane P5 at the IEO). σ_y stresses at the overlap central region are similar, regardless the value of t_A. τ_{xy} stresses are highly influenced by the value of t_A, with τ_{xy} peak stresses diminishing progressively at the overlap edges with this quantity (Her 1999). Singularities exist at the same regions to σ_y stresses.

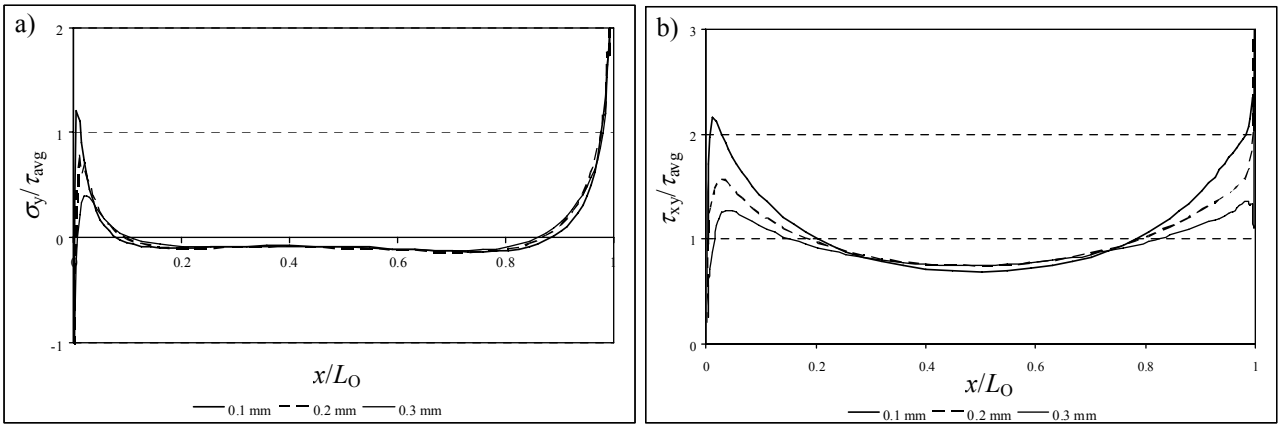

Fig. 150 – Normalized σ_y (a) and τ_{xy} (b) stress distributions at the laminate/adhesive interface (P3) as a function of t_A.

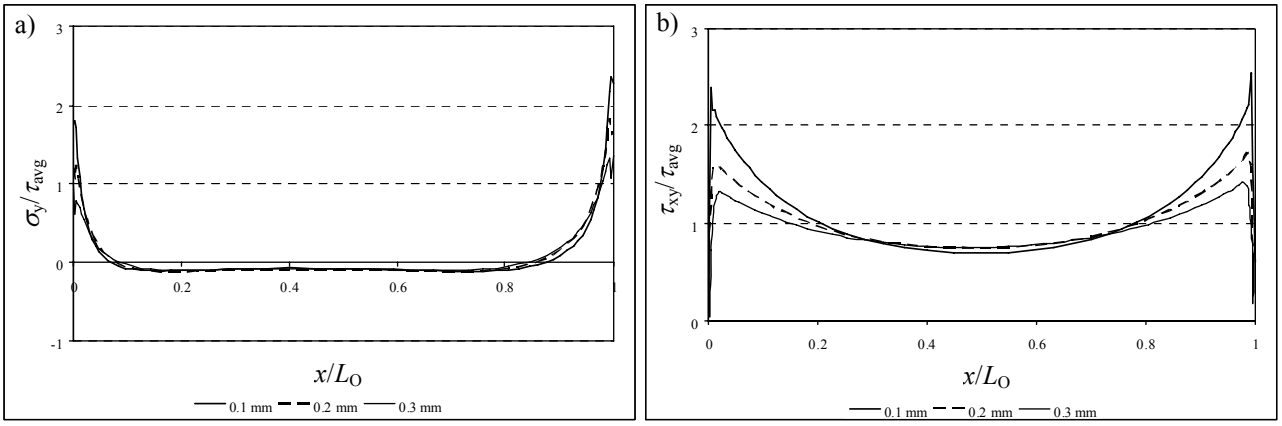

Fig. 151 – Normalized σ_y (a) and τ_{xy} (b) stress distributions at the middle of the adhesive (P4) as a function of t_A.

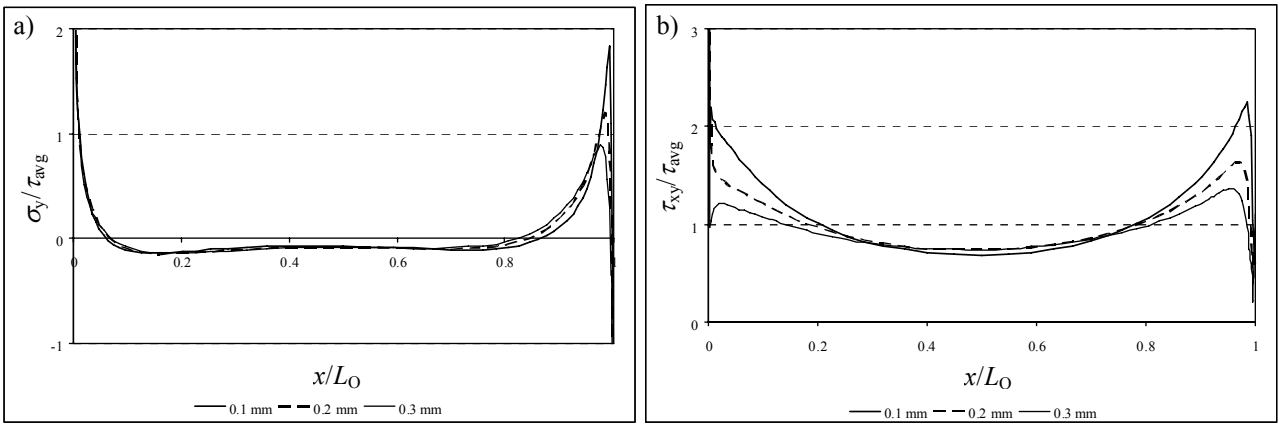

Fig. 152 – Normalized σ_y (a) and τ_{xy} (b) stress distributions at the adhesive/patch interface (P5) as a function of t_A.

Elastic analyses, such as the one presented here, thus foresee an increasing strength of the repairs with t_A, since peel and shear peak stresses in the adhesive layer diminish (Volkersen 1938, Goland and Reissner 1944, Volkersen 1965, Bigwood and Crocombe 1990, Tsai et al. 1998). However, experiments showed that the optimal value of t_A in bonded assemblies is approximately 0.1-0.2 mm, and that smaller or higher values reduce the assemblies strength (Objois et al. 1999, Gleich et al. 2001a, Van Tooren et al. 2004). This effect was addressed by Vallée et al. (2006a, 2006b) on DL joints between GFRP pultruded profiles with thick adhesive layers. A decreasing strength was obtained with t_A (from 5 to 35 mm). Crocombe and Moult (1987) and Crocombe (1989) showed for SL joints using a global yield criterion that the joint strength decreases with t_A, despite the corresponding peak stresses reduction. This was justified by a faster yielding with thicker bond lines. Van Tooren et al. (2004) predicted a strength reduction with t_A using a stress singularity model on SL joints with aluminium adherends under tension. The interfacial shear stresses increase with t_A is a hypothesis defended by some investigators (Ojalvo and Eidinoff 1978, Sawa and Uchida 1997, Gleich et al. 2001a), although it is not well accepted in the scientific community. Adams and Peppiatt (1974) argued that a higher number of porosities and micro-cracks are the only features not incorporated in the theoretical models that can justify the mentioned strength decreasing trend with t_A. Other authors (Mahdi et al. 2003a) argue that extremely small values of t_A lead to a brittle behaviour of the adhesive layer or do not guarantee proper wetting of the bonded surfaces, reducing the assemblies strength. **In all stress analyses performed in this work concerning t_A and the corresponding results discussion, the mentioned reduction of strength for values of t_A smaller or higher than the optimal value, as well as the adhesive thickness scaling effects discussed in Sub-Section 4.2, were not taken into account. In fact, conclusions were drawn based exclusively on the elastic stress distributions, which may lead to different results than the ones highlighted in this discussion**.

4.3.3.1.2. Double-strap repairs

The deformed shape of the DS repair under a tensile load is presented in Fig. 153. Fig. 154 (a) and (b) show σ_y and τ_{xy} stress distributions at the adhesive region, respectively. Equally to the stress fields for the SS repairs (Fig. 137), it can be concluded that σ_y and τ_{xy} stresses peak near the symmetry plane ***B***, gradually diminishing in magnitude with the distance to this plane. Owing to this behaviour, the following stress analysis will focus only on this plane. Fig. 155 corresponds to σ_x stresses at the repair region.

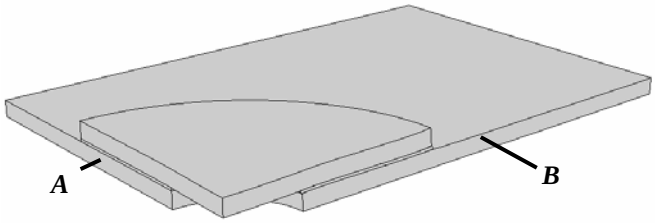

Fig. 153 – Deformed configuration of the DS repair under a tensile load.

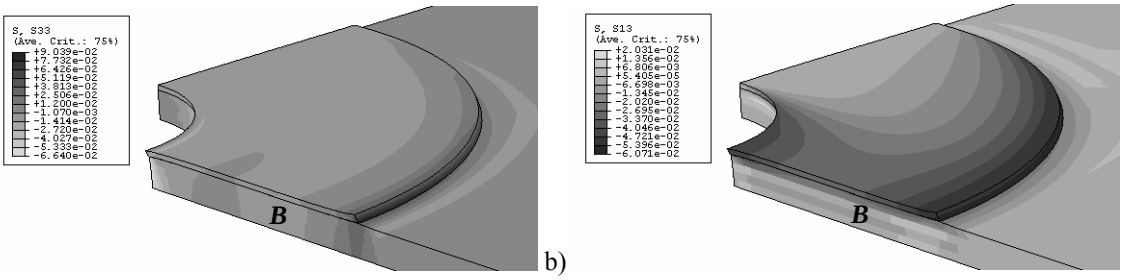

a) b)

Fig. 154 – σ_y (a) and τ_{xy} (b) stresses at the repair region.

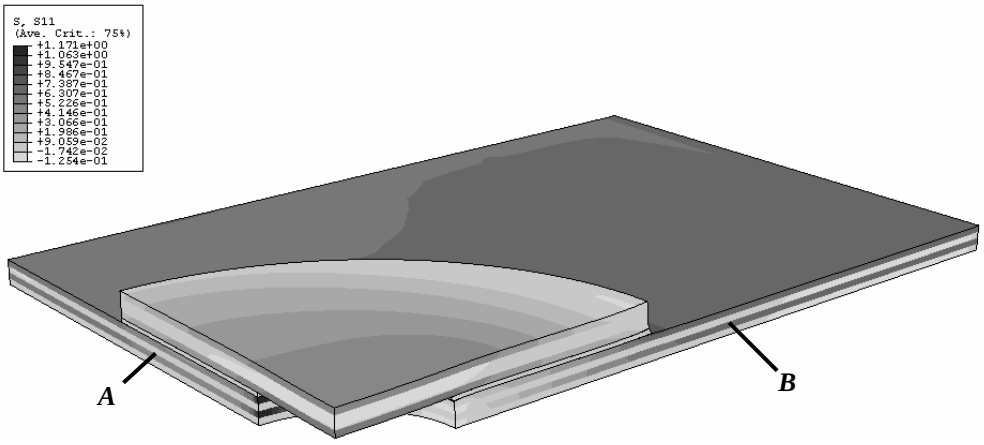

Fig. 155 – σ_x stresses at the repair region.

The transverse laminate flexure characteristic of the SS repairs under tension, due to the eccentricity of the transmitted loads (Fig. 136), is eliminated with the DS repair technique. This can be justified by the symmetry of the loads applied to the laminate (Campilho 2005, Campilho et al. 2005, Campilho et al. 2008b, de Castro and Keller 2008a). However, the patches are still under flexure, leading to σ_y peel peak stresses in the laminate (Campilho 2005). σ_x stresses (Fig. 155) are highest in magnitude within the laminate in the 0º plies, due to their higher stiffness in the load direction than the transversely oriented plies. These stresses peak at the cross-sectional symmetry plane ***A***, near the drilled hole. Comparing with the corresponding results of the SS repair (Fig. 138), an approximate 58% reduction on the σ_x peak stresses is attained for the same value of δ. This difference is caused by the suppression of the laminates flexure (Xiao et al. 2004a, Campilho et al. 2005). Fig. 156 and Fig. 158 (a) show σ_y stresses and σ_y stress distributions at planes P3, P4 and P5, respectively. Fig. 157 and Fig. 158 (b) present τ_{xy} stresses and τ_{xy} stress distributions, by the respective order, at the same planes. The laminate/adhesive interface (P3), the middle of the adhesive (P4) and the adhesive/patch interface (P5) were evaluated (Fig. 122).

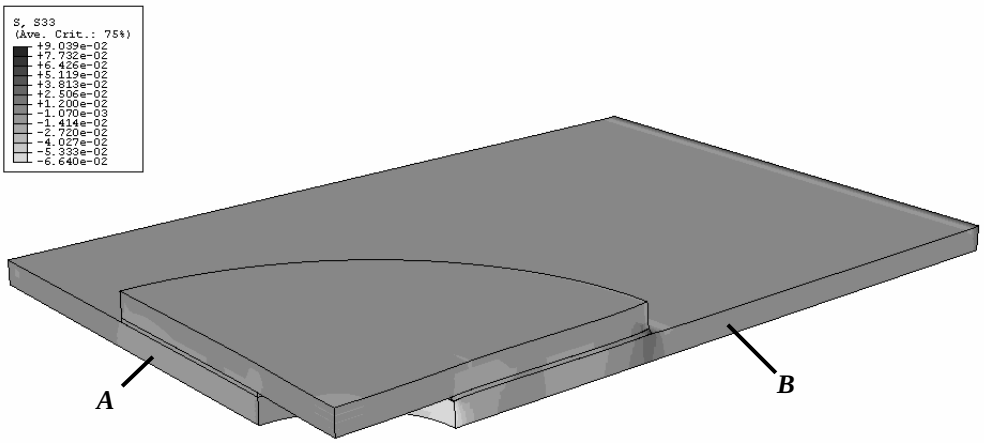

Fig. 156 – σ_y stresses at the repair region.

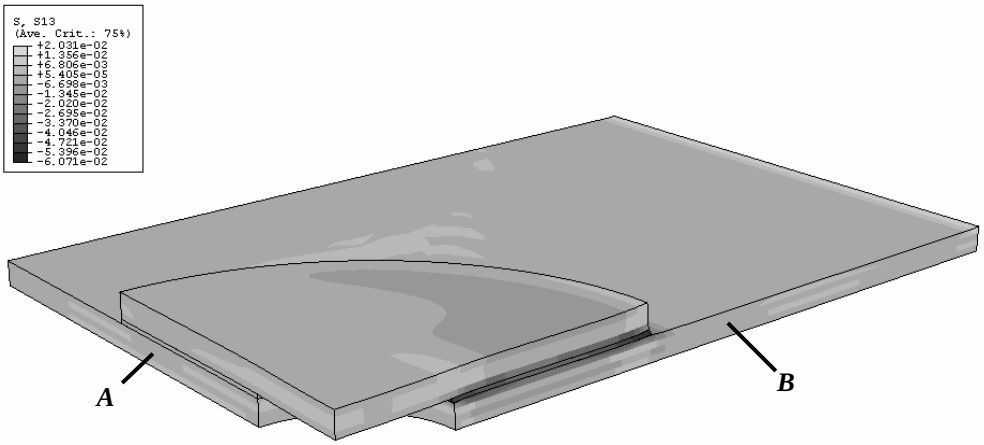

Fig. 157 – τ_{xy} stresses at the repair region.

σ_y stresses are practically nil at the overlap central region, comparing with τ_{avg}. On the other hand, σ_y peel stresses peak at the overlap edges (Campilho et al. 2008b). At the middle of the adhesive (plane P4), a moderate magnitude peak develops at the OEO, while at the IEO σ_y stresses are approximately nil. At the laminate/adhesive interface (plane P3), σ_y stresses are compressive at the IEO with a singularity at x/L_O=0, while at the OEO a tensile singularity is present. At the adhesive/patch interface (plane P5), a σ_y stress singularity is identified at the IEO. σ_y peak stresses at the adhesive region (OEO) are only slightly smaller in magnitude than the corresponding SS ones (Fig. 156 compared to Fig. 139). However, the σ_y peel region at the IEO, observed for the SS repair, is eliminated (Fig. 156 compared to Fig. 139; Xiao et al. 2004a, Campilho et al. 2005). τ_{xy} stresses peak at the overlap edges, with stress singularities at the OEO (plane P3) and IEO (plane P5) (Vallée et al. 2006a, Vallée et al. 2006b, de Castro and Keller 2008b). However, τ_{xy} stress gradients are smaller, compared to the SS repair, especially towards the IEO (Fig. 158 (b) compared to Fig. 141 (b)). This is due to a larger longitudinal deformation of the laminate near the IEO emerging from the use of two patches, which diminishes the differential deformation effects along the bond length (Campilho 2005). Comparing τ_{xy} stresses at the repair region (Fig. 157) with the SS ones (Fig. 140), slightly smaller peak values develop in the adhesive layer using the DS repair technique, under an equal value of δ.

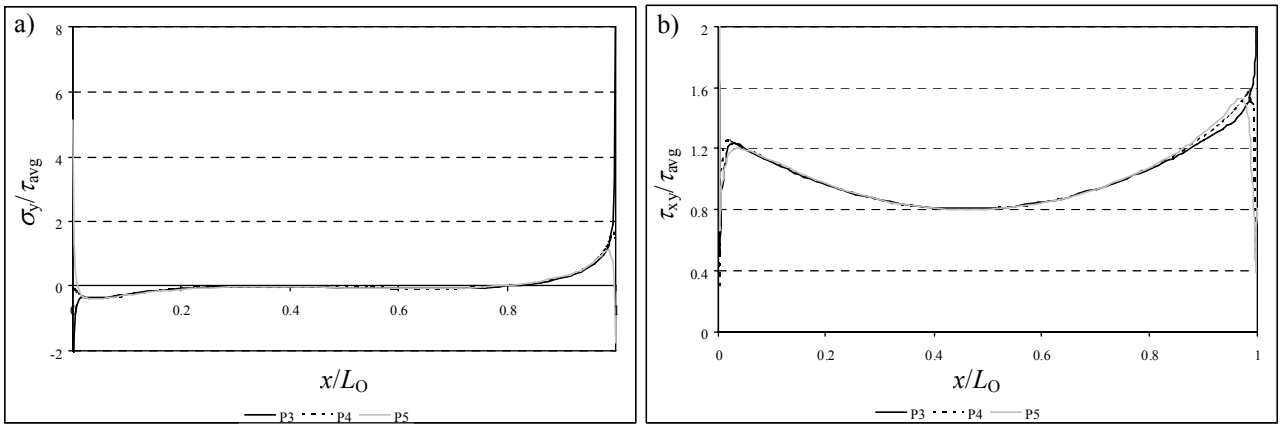

Fig. 158 – Normalized σ_y (a) and τ_{xy} (b) stress distributions at the repair region.

Fig. 159 and Fig. 160 plot σ_y and τ_{xy} stress distributions, respectively, at seven planes (Fig. 122). σ_y peel peak stresses, potentially leading to delaminations, subsist at the OEO, similarly to the SS repairs. These are smaller in magnitude in the laminate and highest at plane P3, with a stress singularity at x/L_O=1 (Vallée et al. 2006a, Vallée et al. 2006b). On the other hand, at the IEO, σ_y peak stresses are mainly compressive. Tensile peaks were only found in the patch and at the stress singularity (plane P5). The existence of σ_y compressive peak stresses at the IEO is caused by the patches flexure, which is not accompanied by the laminate (Campilho et al. 2008b). This constitutes an advantage to the SS repair, showing σ_y peel peak stresses at both overlap edges (Fig. 142). τ_{xy} stresses, equally to SS ones (Fig. 143), are highest in magnitude and similar at planes P3, P4 and P5 (Vallée et al. 2006a, Vallée et al. 2006b). In the laminate (planes P1 and P2), τ_{xy} stresses are higher at the overlap inner region, while in the patch (planes P6 and P7) these are higher at the overlap outer region. It is concluded from these results that damage initiation is likely to occur at or near the stress singularity regions located at the IEO (plane P5) and at the OEO (plane P3) (Campilho 2005, Campilho et al. 2005).

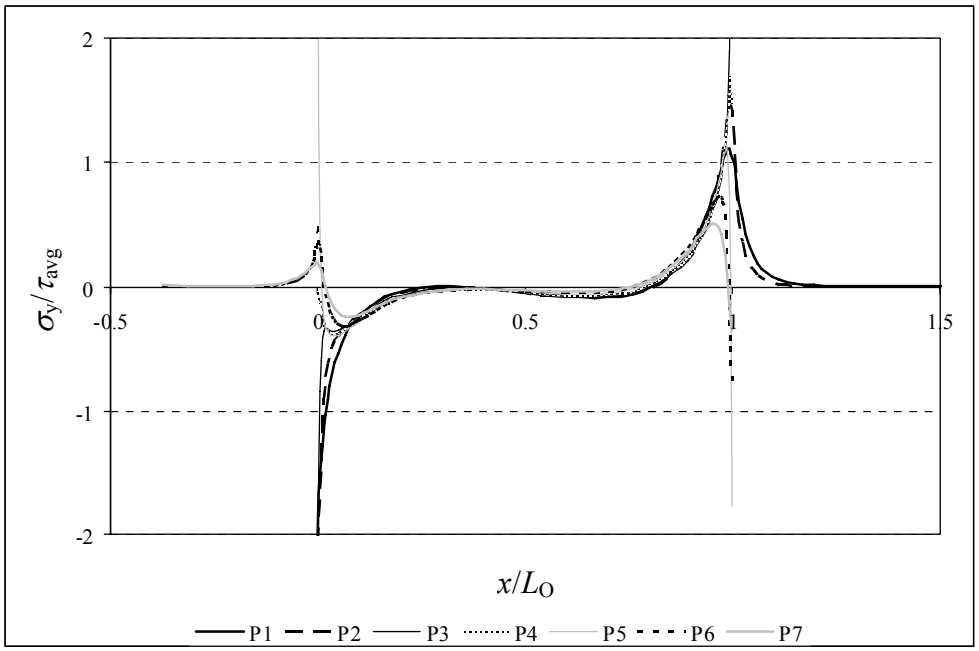

Fig. 159 – Normalized σ_y stress distributions at seven planes in the repair.

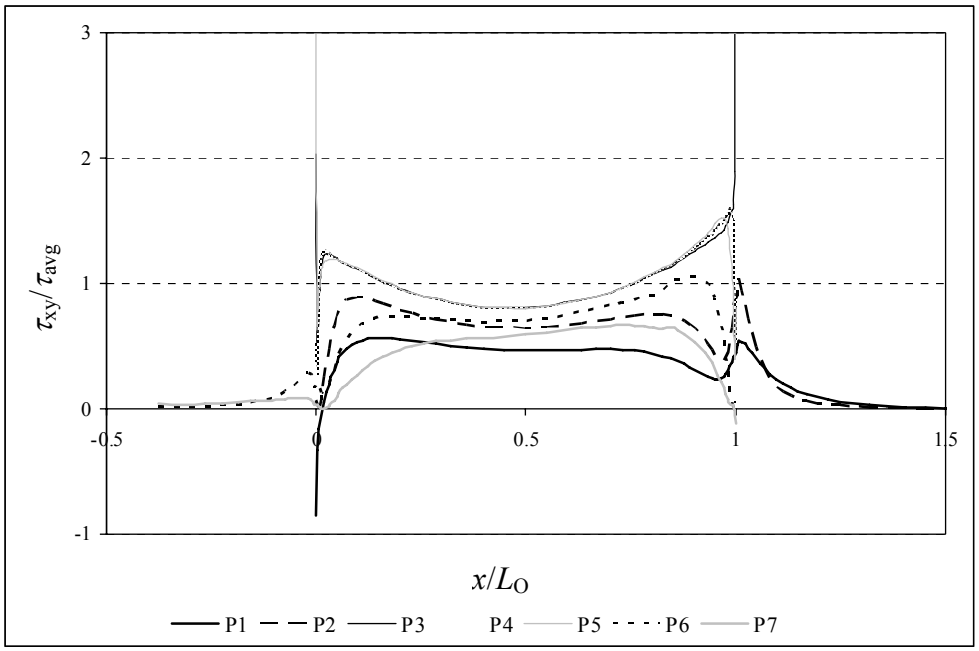

Fig. 160 – Normalized τ_{xy} stress distributions at seven planes in the repair.

4.3.3.1.2.1. Overlap length

σ_y and τ_{xy} stress distributions are plotted at planes P3, P4 and P5, respectively the laminate/adhesive interface, the middle of the adhesive and the adhesive/patch interface (Fig. 122). Fig. 161 corresponds to plane P3 (laminate/adhesive interface), Fig. 162 to plane P4 (middle of the adhesive) and Fig. 163 to plane P5 (adhesive/patch interface).

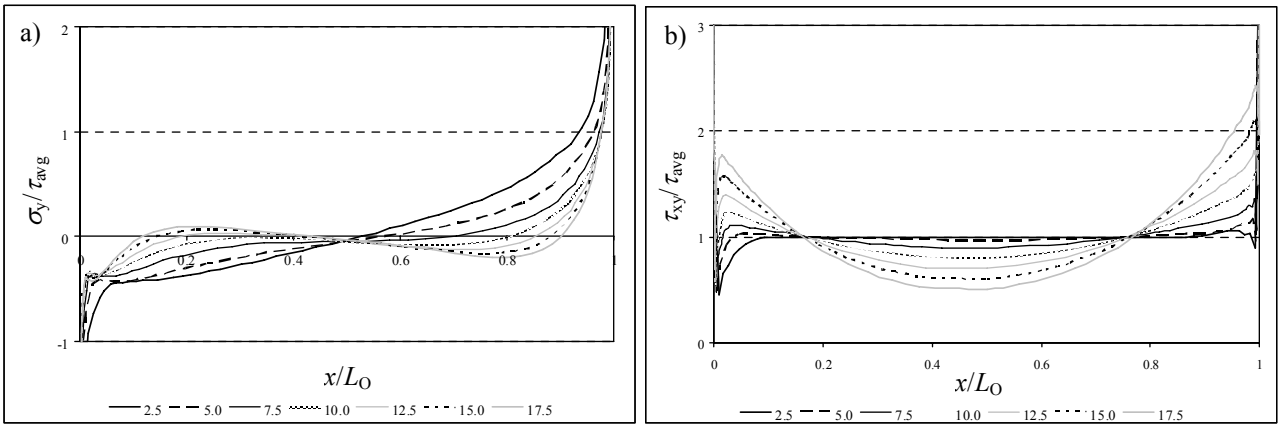

Fig. 161 – Normalized σ_y (a) and τ_{xy} (b) stress distributions at the laminate/adhesive interface (P3) as a function of L_O.

The figures show similar σ_y stress distributions to the SS ones under tension at the overlap outer region, with peel peaks concentrating near x/L_O=1 (Fig. 144 (a), Fig. 145 (a) and Fig. 146 (a)). However, oppositely to the SS repairs, σ_y peak stresses are compressive at the overlap inner region, with the stress singularities at plane P3 (OEO) and P5 (IEO) leading to tensile discontinuities (Campilho 2005, Campilho et al. 2005, Campilho et al. 2008b). At the OEO, pronounced σ_y peel peak stresses or singularities may be responsible for delaminations. At the middle of the adhesive (plane P4), σ_y compressive peak stresses develop at the IEO, opposing to the peel ones at the OEO. σ_y stresses at the

overlap central region tend to become nil L_O, with corresponding bigger gradients towards the overlap edges. At the laminate/adhesive interface (plane P3) the stress singularity at the OEO is common to all values of L_O. At the IEO, σ_y peak stresses are compressive, showing a significant magnitude. At the adhesive/patch interface (plane P5), a σ_y peel singularity region exists at the IEO. At the opposite edge, σ_y peel peak stresses increase in magnitude with L_O.

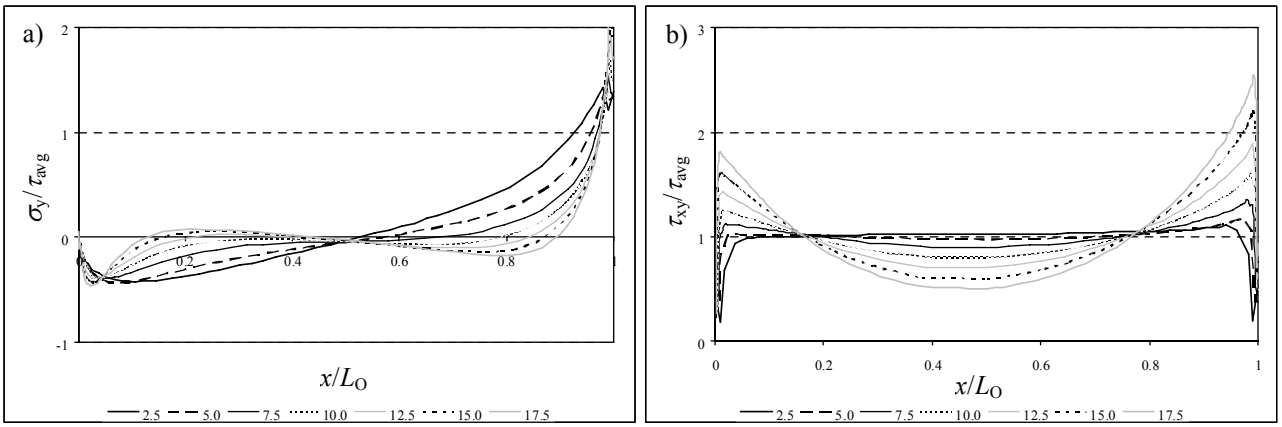

Fig. 162 – Normalized σ_y (a) and τ_{xy} (b) stress distributions at the middle of the adhesive (P4) as a function of L_O.

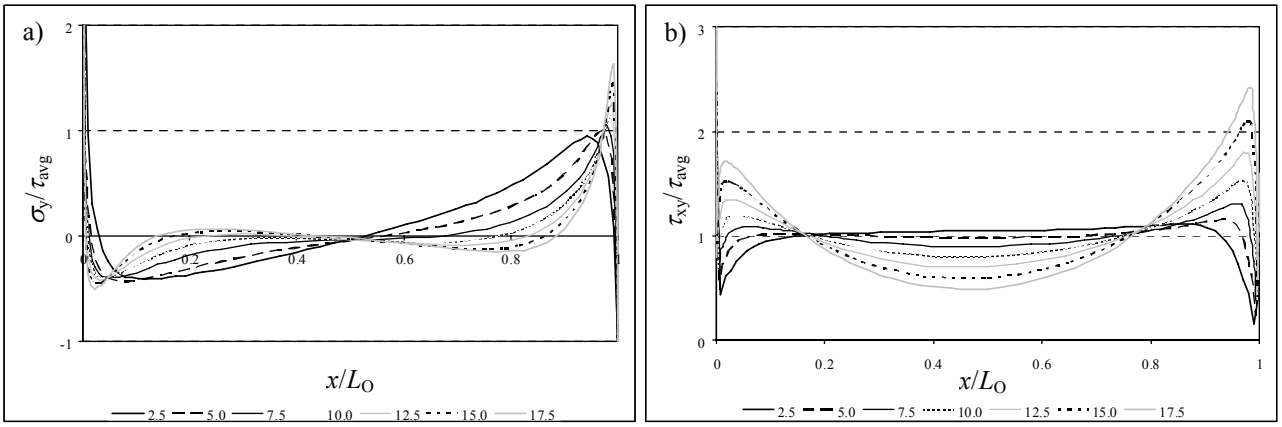

Fig. 163 – Normalized σ_y (a) and τ_{xy} (b) stress distributions at the adhesive/patch interface (P5) as a function of L_O.

τ_{xy} stress distributions are identical between the three planes. Normally, smaller values of L_O lead to flatter profiles, with bigger values gradually increasing shear peak stresses at the overlap edges (Vallée et al. 2006a, Vallée et al. 2006b). These present a higher magnitude at the OEO than the SS repairs (Fig. 144 (b), Fig. 145 (b) and Fig. 146 (b)). The smaller τ_{xy} gradients at the overlap inner region, compared to the SS repairs, are caused by a larger longitudinal deformation of the laminate near the IEO, reducing the differential straining with the patches (Campilho 2005). Stress singularities were captured for all values of L_O at planes P3 (OEO) and P5 (IEO). Equally to the SS repairs, probably the repairs strength do not increase in exact proportion to L_O, since σ_y peel and τ_{xy} peak stresses at the overlap edges increase with L_O. Enhanced σ_y stress distributions are attained with the DS repair over the SS repair, since σ_y compressive peak stresses at the IEO hinder delaminations at this region. Moreover, τ_{xy} peak stresses are smaller in magnitude at the IEO. The influence of L_O on the strength of DL joints between GFRP pultruded profiles was studied by Vallée et al. (2006a, 2006b). The authors concluded that the joints strength increases proportionally with L_O. However, a bigger increase on the damage initiation load was observed for the smaller values of L_O, which is in agreement with the stress analysis presented in this Sub-Section.

4.3.3.1.2.2. Patch thickness

σ_y and τ_{xy} stress distributions are plotted at planes P3, P4 and P5. Fig. 164 relates to plane P3 (laminate/adhesive interface), Fig. 165 to plane P4 (middle of the adhesive) and Fig. 166 to plane P5 (adhesive/patch interface).

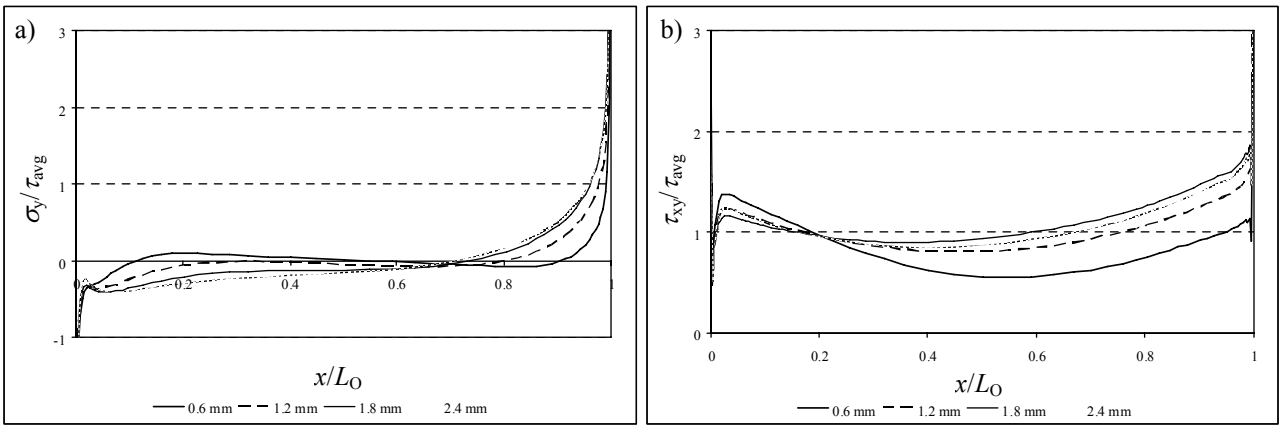

Fig. 164 – Normalized σ_y (a) and τ_{xy} (b) stress distributions at the laminate/adhesive interface (P3) as a function of t_H.

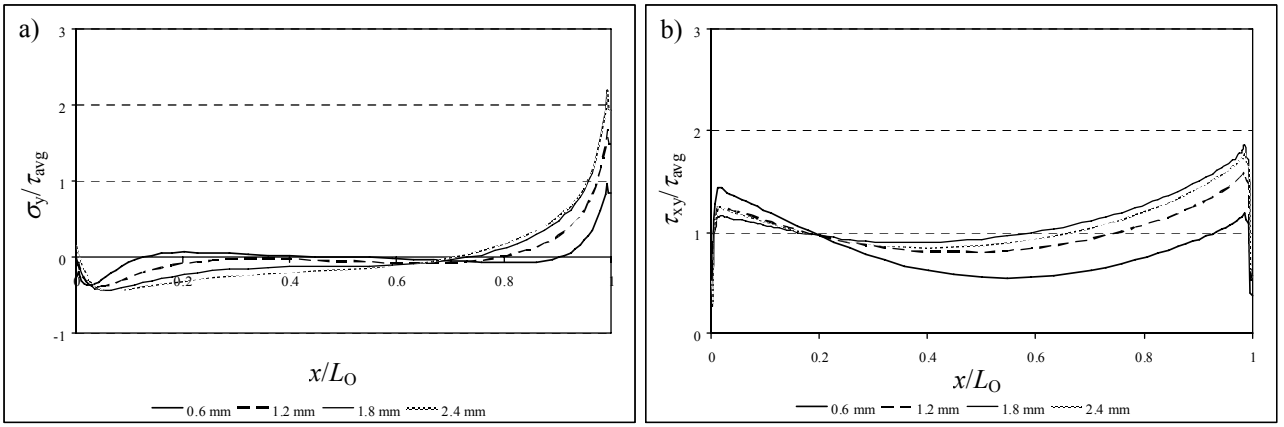

Fig. 165 – Normalized σ_y (a) and τ_{xy} (b) stress distributions at the middle of the adhesive (P4) as a function of t_H.

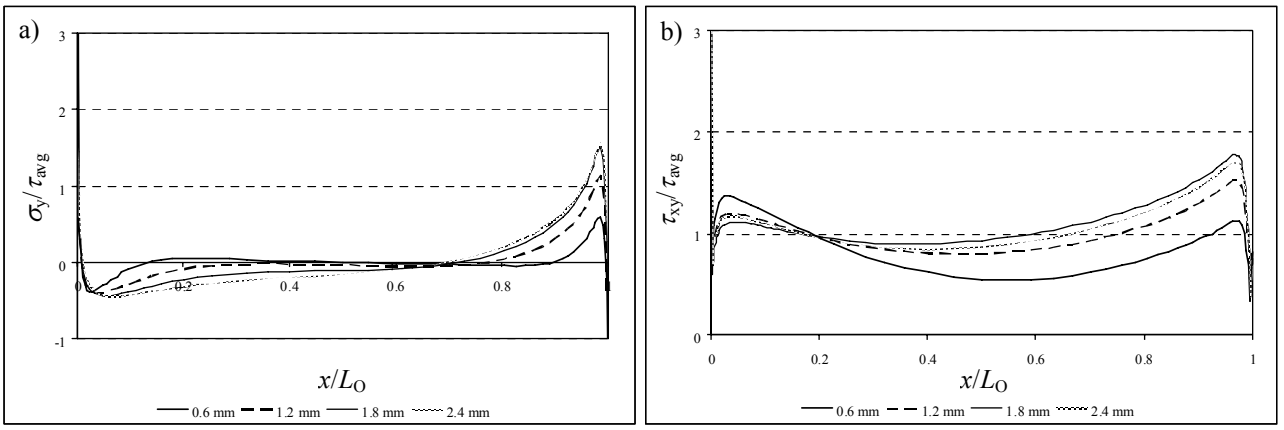

Fig. 166 – Normalized σ_y (a) and τ_{xy} (b) stress distributions at the adhesive/patch interface (P5) as a function of t_H.

σ_y stresses are compressive and small in magnitude at the overlap central region (only the t_H=0.6 mm repair shows a minor peel region), peaking at the overlap edges. The singular regions loci are consistent with the previous analyses, i.e., at planes P3 (OEO) and P5 (IEO). σ_x compressive peak stresses at the IEO contrast with σ_y tensile ones for the SS repairs (Fig. 147 (a), Fig. 148 (a) and Fig. 149 (a)). On the other hand, equally to the SS repairs, the smallest value of t_H shows to be the best solution, as σ_y stresses are almost nil at the overlap central region and are markedly smaller at the OEO, at planes P4 and P5. From t_H=1.8 mm the influence of t_H on σ_y appears to wane (Campilho 2005, Campilho et al. 2005). τ_{xy} stress distributions are identical between all values of t_H. Only for t_H=0.6 mm, τ_{xy} stresses are smaller in magnitude at the three planes at the OEO and higher at the IEO. This agrees with the SS repairs tendency (Fig. 147 (b), Fig. 148 (b) and Fig. 149 (b)). The justification for the smaller magnitude of τ_{xy} peak stresses at the IEO was given in the previous Sub-Section (4.3.3.1.2.1). In view of these results, the smallest value of t_H is recommended, since σ_y peel and τ_{xy} peak stresses are smaller in magnitude at the OEO, where σ_y peel peak stresses add to τ_{xy} ones. However, possible patch failure shall be accounted for, depending on the materials strength properties.

4.3.3.1.2.3. Adhesive thickness

σ_y and τ_{xy} stress distributions are plotted at planes P3, P4 and P5. Fig. 167 corresponds to plane P3 (laminate/adhesive interface), Fig. 168 to plane P4 (middle of the adhesive) and Fig. 169 to plane P5 (adhesive/patch interface).

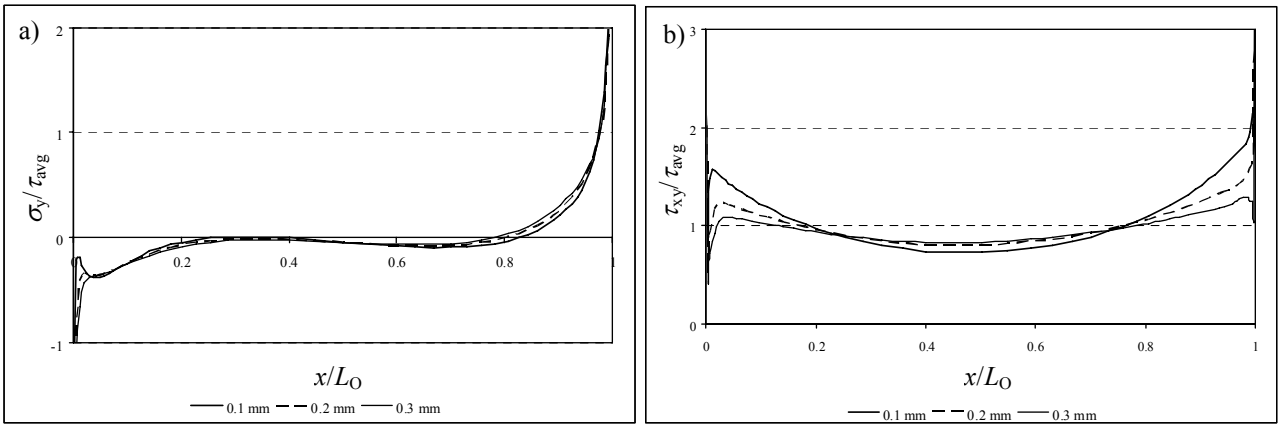

Fig. 167 – Normalized σ_y (a) and τ_{xy} (b) stress distributions at the laminate/adhesive interface (P3) as a function of t_A.

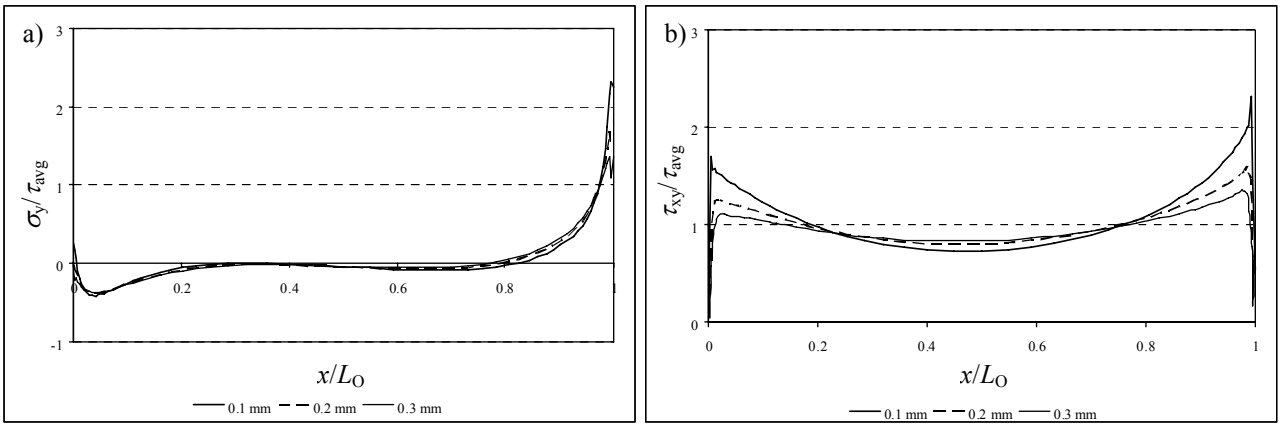

Fig. 168 – Normalized σ_y (a) and τ_{xy} (b) stress distributions at the middle of the adhesive (P4) as a function of t_A.

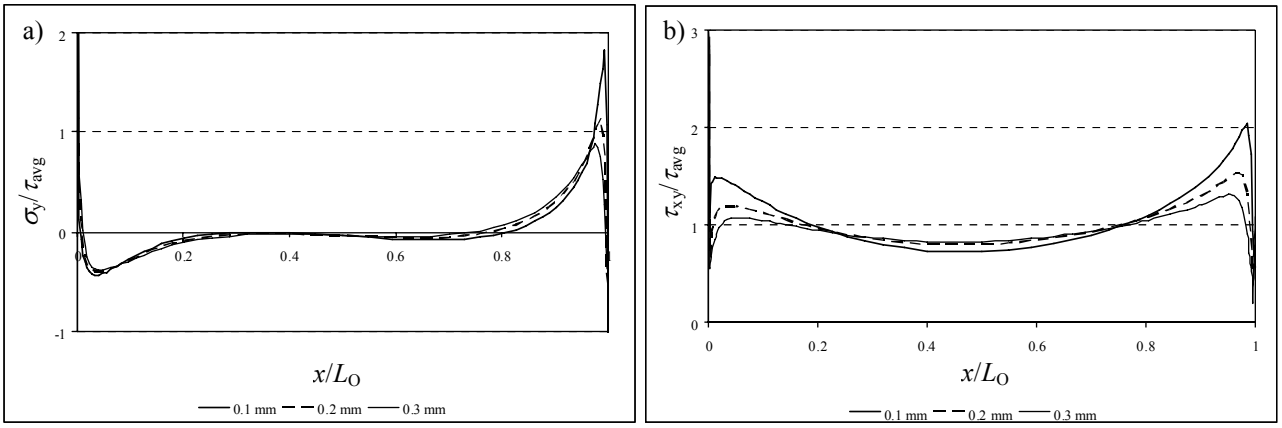

Fig. 169 – Normalized σ_y (a) and τ_{xy} (b) stress distributions at the adhesive/patch interface (P5) as a function of t_A.

σ_y and τ_{xy} stress distributions as a function of t_A followed the tendency of the SS repairs (Fig. 150, Fig. 151 and Fig. 152). Thus, σ_y peak stresses at the overlap edges diminished with t_A, especially at the OEO. At the overlap central region, no significant different difference was detected for the values of t_A evaluated. A σ_y compressive peak at the IEO is the only difference worth noticing compared to the SS repairs (Fig. 150 (a), Fig. 151 (a) and Fig. 152 (a)), whose implications were previously discussed. τ_{xy} peak stresses diminish at the overlap edges with t_A, giving flatter shear stress distributions at the three planes than the corresponding SS repairs (Fig. 150 (b), Fig. 151 (b) and Fig. 152 (b)). These results are consistent with the FEM analyses of Vallée et al. (2006a, 2006b) and Her (1999) on DL joints. The stress singularities at planes P3 (OEO) and P5 (IEO) agree with the previous studies. These numerical results indicate that bigger values of t_A increase the repairs strength, since σ_y peel and τ_{xy} peak stress diminish at the overlap edges, where damage initiation is prone to occur.

4.3.3.2. Failure analysis

4.3.3.2.1. Mechanical behaviour

The SS and DS repairs failure analysis follows the stress analysis performed. It will be divided into the mechanical behaviour characterization up to failure and the summary of the results. This applies throughout Section 4. **The open-hole laminate was also studied in all strap repairs studies, for an assessment of the strength improvement of the proposed repair techniques**. The tensile behaviour of this notched geometry, emerging from the removal of a damaged portion of the structure or introduced for assembly purposes, was comprehensively studied in the past (Awerbuch and Madhukar 1985, Lee and Mall 1989). **The undamaged laminate was not examined in none of the studies in Section 4**, despite the interest of such analysis for comparison purposes, since the main objective to be fulfilled in this Section is related to the validation of the FEM prediction methodology and parameter optimization. The expectable impossibility to attain the undamaged strength of the laminates, due to the differences in the mechanical properties between the CFRP and the adhesive (Campilho 2005, Campilho et al. 2005), also helped to this choice.

- In the open-hole specimens, damage initiated by tensile failure accompanied by delamination between differently oriented plies at the hole edges near the symmetry plane ***A*** (Fig. 123). This is justified by significant

tensile (Fig. 155) and interlaminar stress concentrations arising at this region when using layered composites with different ply orientations (Iarve 1996, Iarve and Pagano 2001). However, this highly localized damage showed only a negligible influence on the repairs stiffness. P_m related to the onset of axial splitting at the two superficial 0º plies at both laminate faces. This damage mechanism initiated at the hole edges at plane ***A*** and propagated up to the testing machine grips (Fig. 170 a), growing along plane ***A*** towards the specimens lateral edges (Fig. 170 b), causing a gradual decrease on P. Shortly after, the laminate failed transversely at plane ***A***, at one of the hole sides. **The influence of the adhesively-bonded patches on the tensile mechanical behaviour and strength of the repairs consisted on their ability to modify the displacement corresponding to the initiation of axial splitting. In fact, some repairs experienced a premature axial splitting event in the repaired face of the laminate, causing a reduction on P_m. Other repair geometries, retarding this fracture mechanism in the repaired face of the laminate, led to an increase on P_m.**

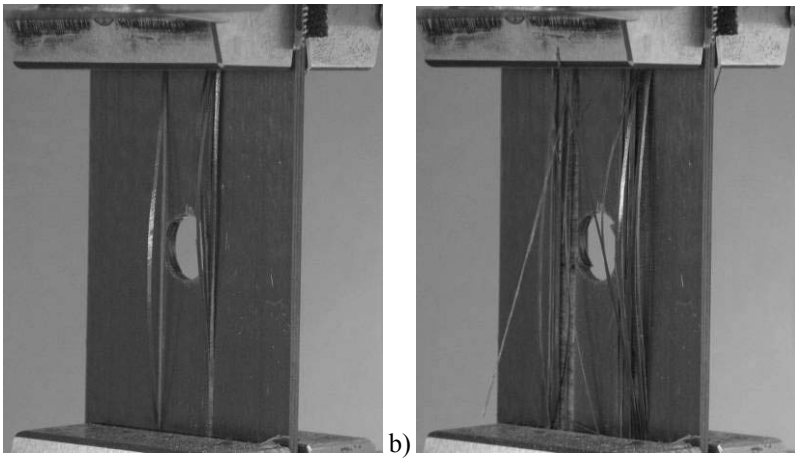

a) b)

Fig. 170 – Damage growth in an open-hole laminate.

- The L_O=5 mm SS repair experienced a premature axial splitting and corresponding patch debonding in the repaired face of the laminate initiating at the OEO (Fig. 121 a), which corresponded to P_m (Fig. 171 a). Axial splitting in the unrepaired face occurred only after this event, subsequently to P_m (Fig. 171 b). Final failure was related to a transverse fracture near the symmetry plane ***A*** (Fig. 171 c). The introduction, due to the repair procedure, of higher magnitude τ_{xy} peak stresses at the hole region for the smaller values of L_O (Campilho 2005, Campilho et al. 2005, Campilho et al. 2008b) justifies the premature axial splitting observed only in the L_O =5 mm SS repairs. Moreover, for the smaller values of L_O, these higher magnitude stresses extend to the entire overlap, opposed to the bigger L_O values (Fig. 144 (b), Fig. 145 (b) and Fig. 146 (b)), which helps to this difference. Owing to the premature axial splitting, a P_m reduction to the open-hole laminate is expected.
- For the L_O=10 and 15 mm SS repairs, patch debonding occurred approximately simultaneously or after axial splitting in the unrepaired face. Fig. 172 shows the evolution of damage in a L_O =15 mm SS repair. For this repair, damage initiated in the unrepaired face of the composite with minor axial splitting (Fig. 172 a). At this stage, the adhesive layer presented only a localized damage at the OEO. Fig. 172 (b) shows the repair in a more advanced stage, showing extensive damage in the adhesive layer and some evidence of axial splitting in the repaired laminate face. P_m corresponded to a complete patch debonding simultaneously with transverse failure and extensive axial splitting in both repaired and unrepaired faces of the laminate (Fig. 172 c).

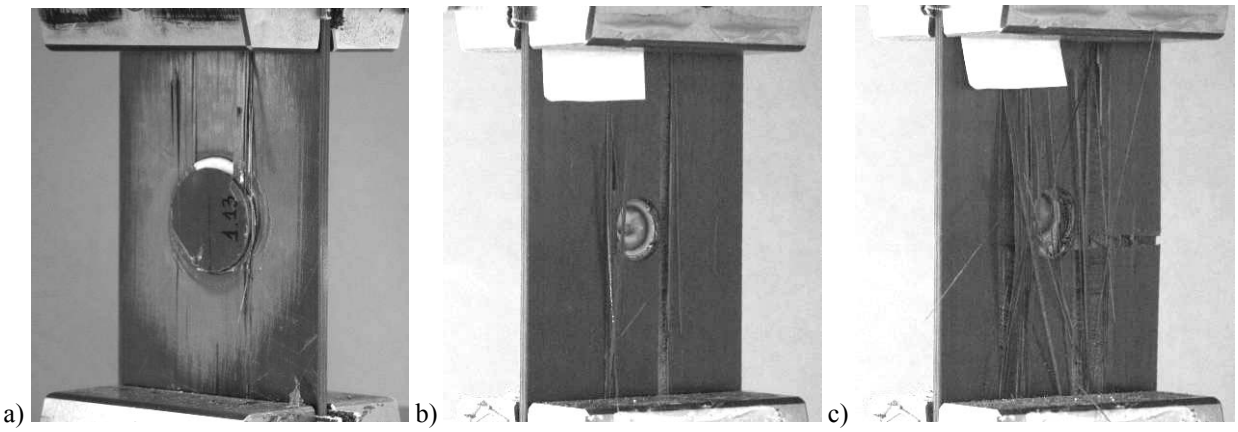

Fig. 171 – Damage growth in a L_O=5 mm SS repair.

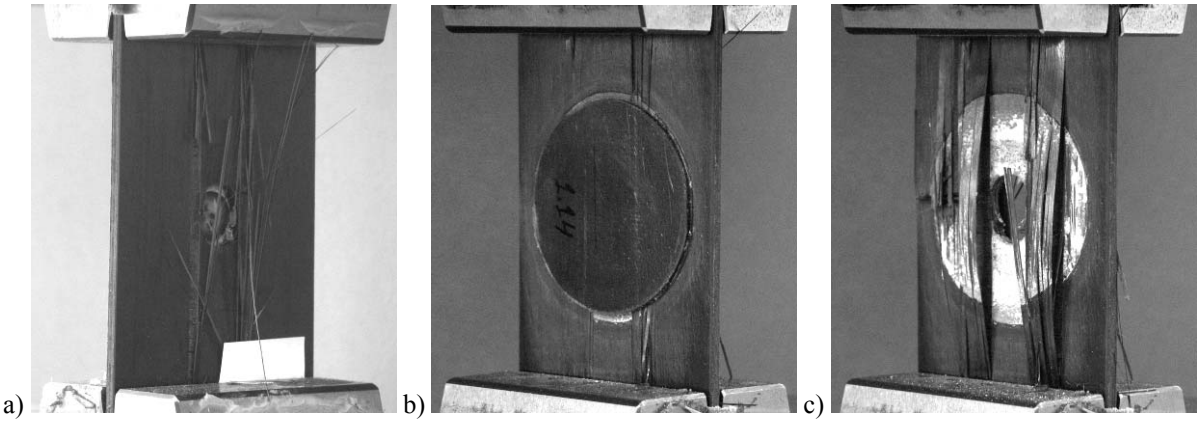

Fig. 172 – Damage growth in a L_O=15 mm SS repair.

- The L_O =5 mm DS repairs exhibited a similar premature debonding of the two patches with axial splitting, compared to the open-hole laminate. Equally to the equivalent SS repair, a strength reduction is expected.
- In DS repairs with bigger patches a premature patch debonding was not detected, which is likely to increase P_m. The justification presented for the SS repairs is also valid in this case (Fig. 161 (b), Fig. 162 (b) and Fig. 163 (b) show the corresponding τ_{xy} stress distributions).
- Conversely to L_O, t_H does not have influence on the failure mode for both SS and DS repairs. In fact, for all values of t_H the adhesive layer debonded concurrently with axial splitting in the unrepaired face. The relatively small influence of t_H on the stress distributions in the adhesive layer is pointed out to clarify this behaviour (Fig. 147, Fig. 148 and Fig. 149 for the SS repairs and Fig. 164, Fig. 165 and Fig. 166 for the DS repairs).

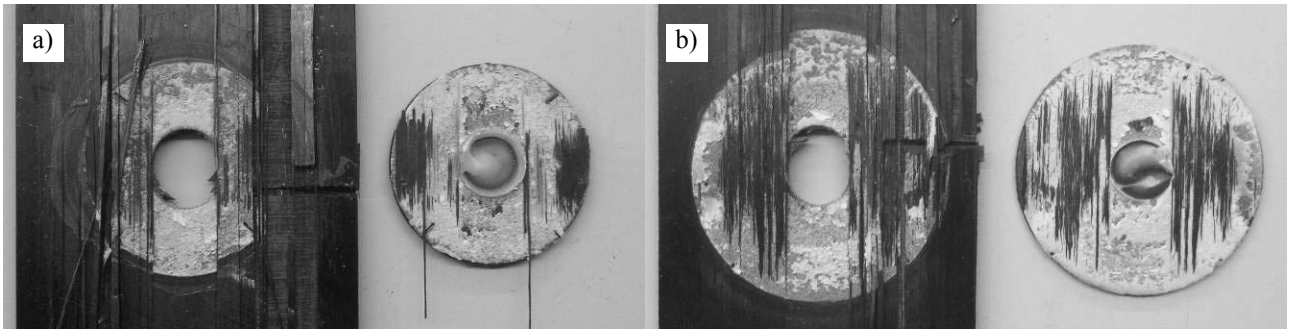

Fig. 173 – Cohesive failure of the adhesive layer for a t_H=2.4 mm SS repair (a) and L_O=15 mm DS repair (b).

In all the repair configurations tested, fractures were predominantly cohesive in the adhesive layer. Fig. 173 shows cohesive failures of the adhesive layer for two of these configurations. **The FEM simulations were used to estimate the patch debonding load. Thus, they will be only used for a better understanding of the repairs behaviour. This approach was adopted due to the impossibility to simulate with CZM's the axial splitting of the laminate, which ruled fracture behaviour in the repairs, as already discussed**. Fig. 174 (a) and (b) show the instants of patch debonding for the L_O=5 and 15 mm SS repairs, respectively. In the first case, this occurred for a smaller value of P than axial splitting onset and P_m for the open-hole laminate. Oppositely, for the L_O=15 mm DS repairs, patch debonding occurred only after axial splitting in the open-hole laminate.

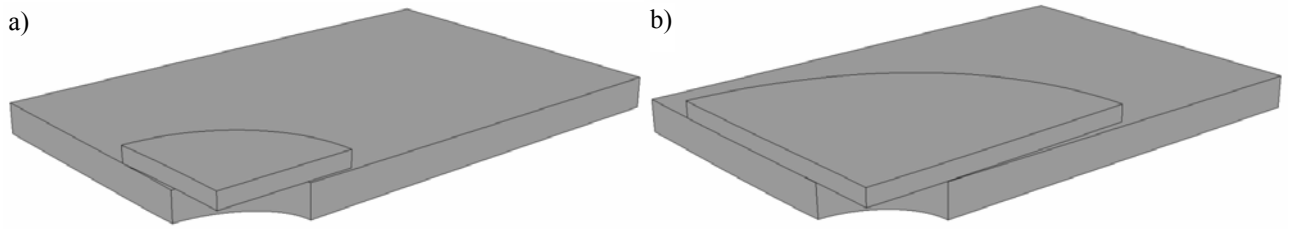

Fig. 174 – Numerical patch debonding for the L_O=5 mm (a) and L_O=15 mm (b) SS repairs.

- Fig. 175 compares the experimental and numerical P-δ curves for the L_O=5 mm SS and DS repairs (the circle marks on the numerical curves represent the prediction of patch debonding). For both repairs, the patch debonding prediction corresponded to a smaller value of P than the average value of P_m for the open-hole laminate (86.90 kN). This behaviour agrees with the experimental observations. Since premature patch debonding was accompanied by the initiation of axial splitting in the respective laminate face, corresponding to P_m, a strength reduction was observed.

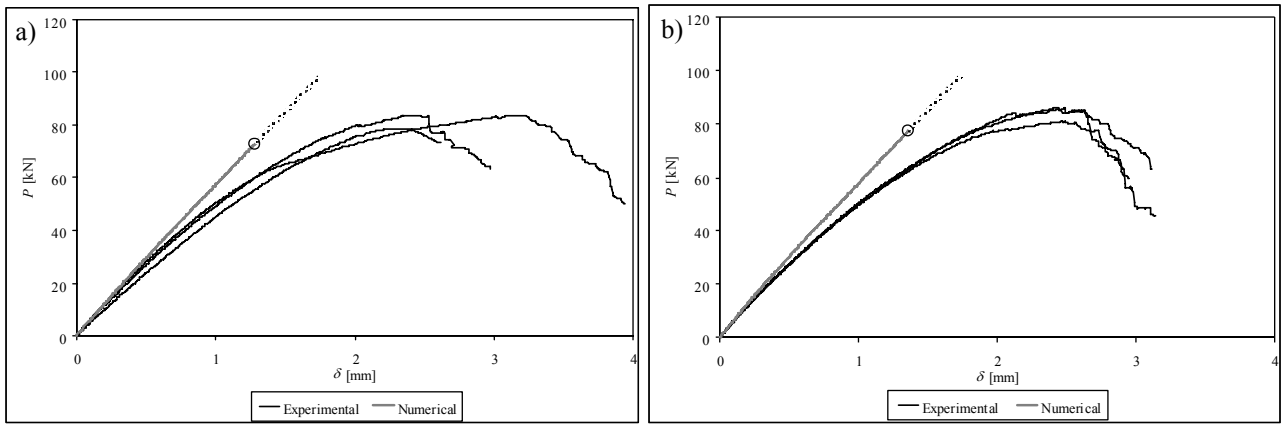

Fig. 175 – Experimental and numerical P-δ curves comparison for the L_O=5 mm SS (a) and DS (b) repairs.

- The P-δ curves for the L_O=15 mm SS and DS repairs are presented in Fig. 176 (a) and (b), respectively. Patch debonding values of P=93.78 kN (SS repairs) and 99.00 kN (DS repairs) were predicted. Experimentally, a strength improvement to the open-hole laminate was attained, which corroborated the FEM results. It should be emphasized that the gradually increasing difference between the experimental and numerical stiffness up to P_m is caused by an unavoidable slipping of the repairs in the testing machine grips, due to the magnitude of the loads involved, not representing the brittle nature of the composite, which rules the repairs stiffness.

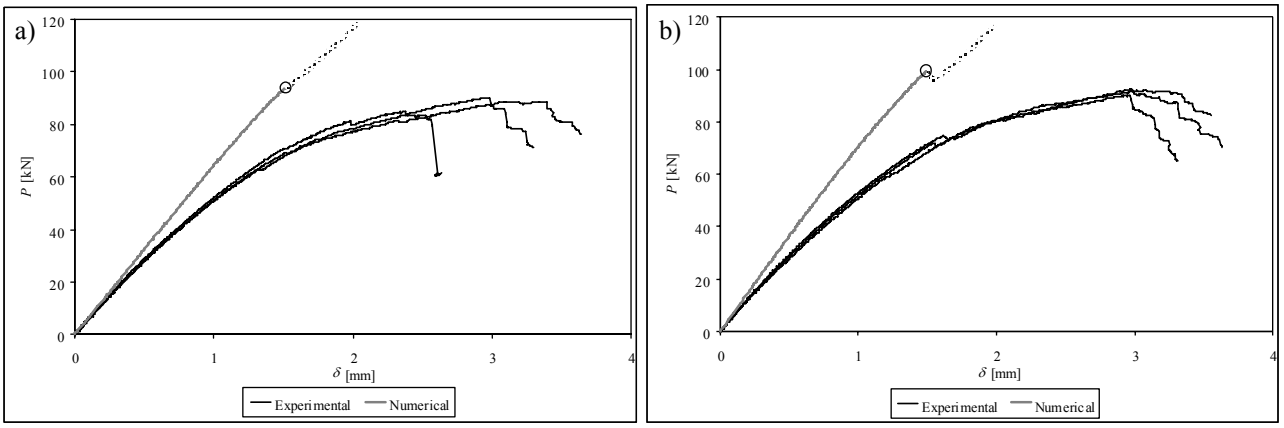

Fig. 176 – Experimental and numerical P-δ curves comparison for the L_O=15 mm SS (a) and DS (b) repairs.

4.3.3.2.2. Summary of the results

The following figures outline the values of K of the SS and DS repairs as a function of L_O (Fig. 177 a) and t_H (Fig. 177 b), and the values of P_m as a function of L_O and t_H (Fig. 178 (a) and (b), respectively), including the standard deviation of the experiments. **The numerical values of P_m correspond to the patch debonding load instead of the maximum load sustained by the repairs, and will be only used for an easier interpretation of the test results**. A good correlation was found between the experiments and the numerical simulations for the values of K as a function of L_O and t_H. K showed an increasing trend with the value of L_O, for both SS and DS repairs, caused by the corresponding increase of the adhesive shear area (Campilho et al. 2008b, Campilho et al. 2009e). The DS repairs also presented bigger values of K than the corresponding SS repairs, due to the suppression of the laminate flexure and duplication of the adhesive shear area (Campilho et al. 2008b). On the other hand, no significant variation of K was found for the SS repairs as a function of t_H. The DS repairs displayed a slight increasing tendency of K with the value of t_H, approaching a constant value for the bigger t_H values.

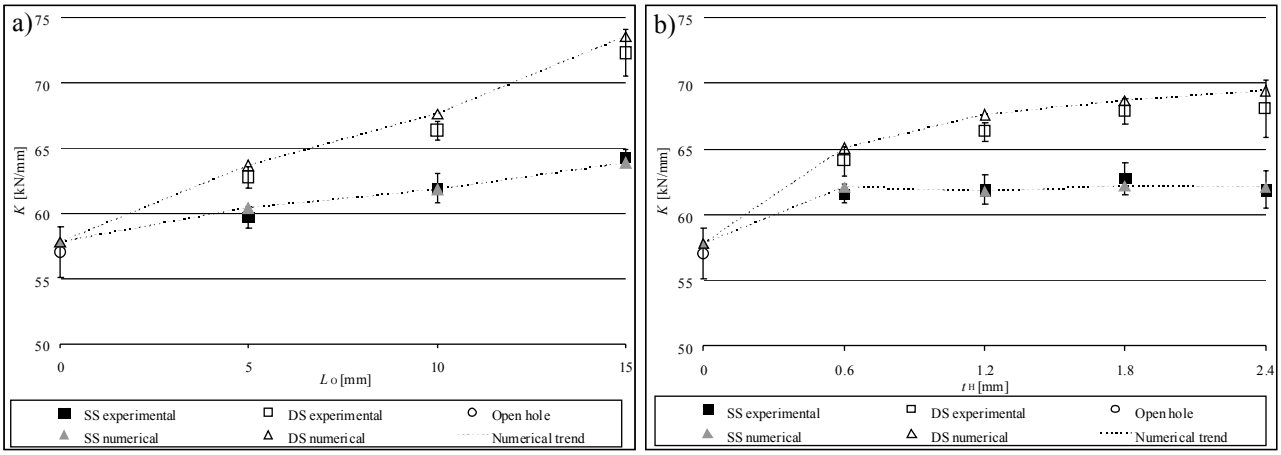

Fig. 177 – K as a function of L_O (a) and K as a function of t_H (b).

Numerically, the values of P_m (corresponding to patch debonding) were qualitatively consistent with the experimental observations, i.e., for the L_O=5 mm SS and DS repairs, patch debonding occurred at smaller values of P than the value of P_m for the open-hole laminate. This behaviour justified the experimentally observed premature patch debonding with

axial splitting in the repaired face of the laminate (Fig. 171 a). Consequently, P_m is smaller than for the open-hole laminate. For the bigger values of L_O evaluated, patch debonding occurred at similar or higher values of P_m than the open-hole laminate, justifying a gradual P_m increase with L_O. The results of Fig. 178 (a) show a benefit in repairing the open-hole laminate with the L_O=10 and 15 mm DS repair configurations. It can be ascertained from Fig. 178 (b) that t_H practically does not influence P_m for the SS repairs. Using a t_H=0.6 mm patch, P_m slightly diminishes from the open-hole laminate value. No definitive conclusions were drawn about this behaviour. In fact, similarly to the repairs with higher values of t_H, patch debonded for a similar value of P to the open-hole laminate. Using the DS repair, an identical increase of P_m is observed for all values of t_H evaluated, compared to the equivalent SS repairs. The reduced influence of this parameter on the repairs strength is justified by the patch failure occurring approximately simultaneously to axial splitting in the unrepaired face of the laminate. In the numerical analyses, P_m was practically insensitive to t_H, even though a slight decreasing trend was observed as a function of t_H for both SS and DS repairs, due to a corresponding increase of the patch stiffness. This led to higher σ_y peel and τ_{xy} peak stresses at the OEO (Fig. 164, Fig. 165 and Fig. 166), causing a reduction on the numerical value of P_m. These simulations corroborate the experimental results concerning the small influence of t_H on P_m.

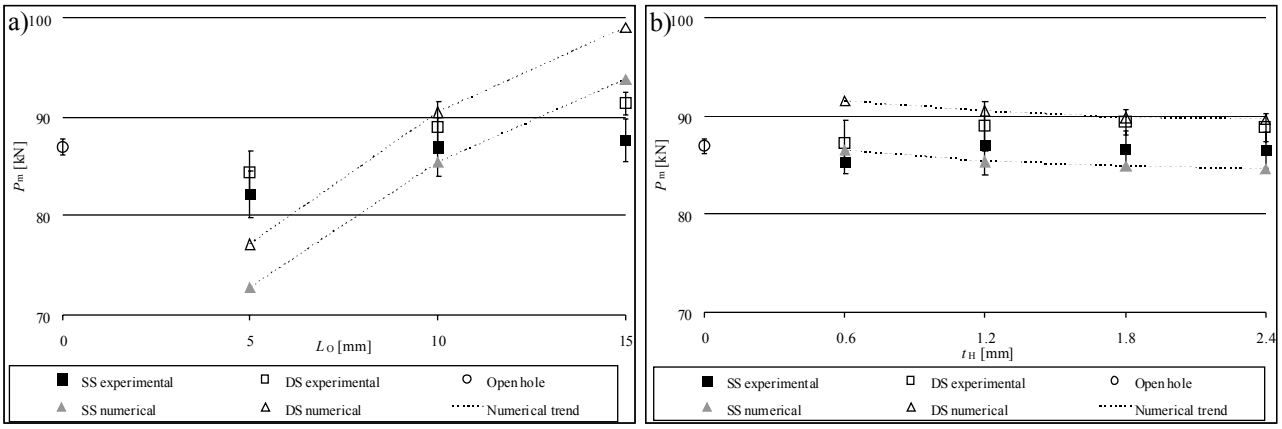

Fig. 178 – P_m as a function of L_O (a) and P_m as a function of t_H (b).

Based on the presented results, the L_O=15 mm DS repair is recommended, since it attains the highest value of P_m. Between the different values of t_H evaluated for the SS and DS repairs, the t_H=1.2 mm DS repair is the best solution, since it leads to a smaller aerodynamic disturbance and weight penalty of the repaired structure, compared to the thicker patches which exhibit a similar strength. However, for the value of L_O used in this analysis (10 mm), no major strength difference was found, compared to the open-hole laminate, which could eventually occur with different values of L_O.

4.3.4. Compressive load

Following the tensile study on SS repairs, another scenario likely to occur in composite structures is addressed. It consists on the compressive behaviour without restraining to global buckling between the testing machine grips. The structure of this analysis is identical to the previous one, i.e., with a stress analysis preceding the characterization of the fracture mechanisms and summary of the most important parameters.

4.3.4.1. Stress analysis

4.3.4.1.1. Single-strap repairs

Fig. 179 shows the repair deformed configuration. σ_y and τ_{xy} stress distributions are plotted at the adhesive region in Fig. 180 (a) and (b), respectively, to assess the critical regions of the repairs. Equally to the tensile load (Fig. 137), σ_y and τ_{xy} stresses are highest at the overlap edges near the symmetry plane ***B***, diminishing progressively with the distance to this plane. The stress analysis carried out for these repairs will thus focus on this plane. Compared the tensile load (Fig. 137), σ_y and τ_{xy} stress fields are similar at the repair region, despite the fact that σ_y stresses are antisymmetric to the tensile ones, thus being generally compressive. σ_x stresses at the repair region are presented in Fig. 181.

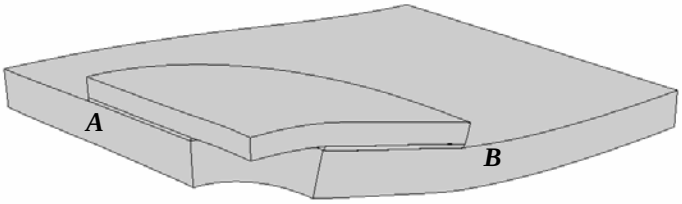

Fig. 179 – Deformed configuration of the SS repair under a compressive load.

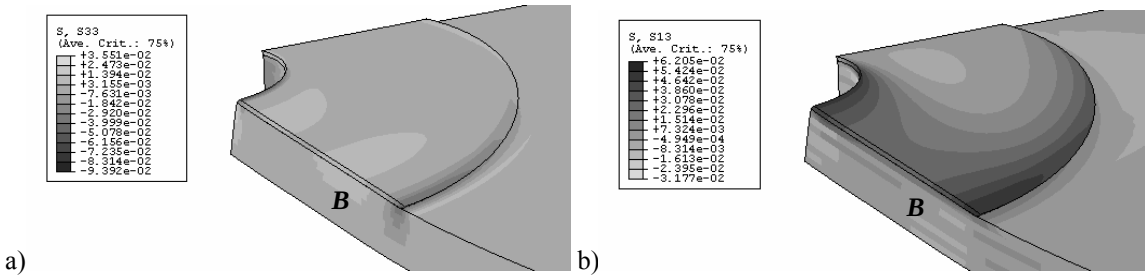

a) b)

Fig. 180 – σ_y (a) and τ_{xy} (b) stresses at the repair region.

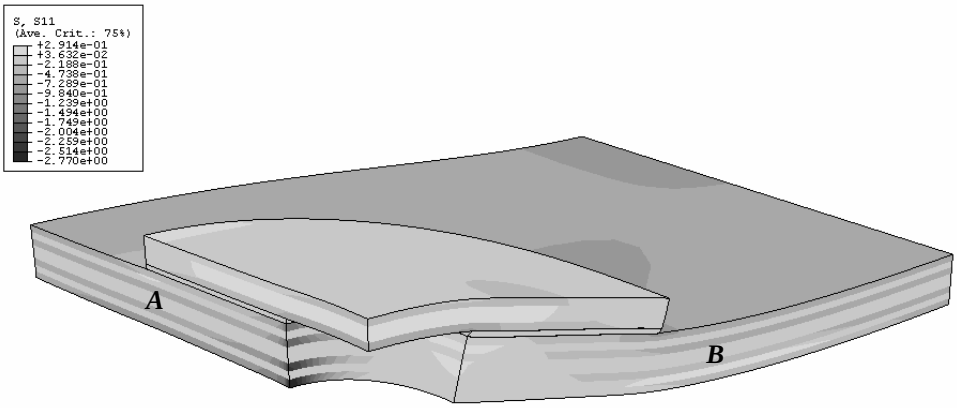

Fig. 181 – σ_x stresses at the repair region.

Under compression, the repairs bending develops in the opposite transverse direction compared to the repairs under tension (Fig. 136), due to the inversion of the connection loads between the laminate and patch (Campilho 2005). σ_x stress field and respective magnitude at the repair region (Fig. 181) is identical to the tensile one (Fig. 138). σ_x stresses are highest in magnitude in the laminate at the cross-sectional symmetry plane ***A***. The following figures present σ_y stresses (Fig. 182), σ_y stress distributions at three planes at the repair region (Fig. 184 a), τ_{xy} stresses (Fig. 183) and τ_{xy} stress distributions at three planes at the repair region (Fig. 184 b).

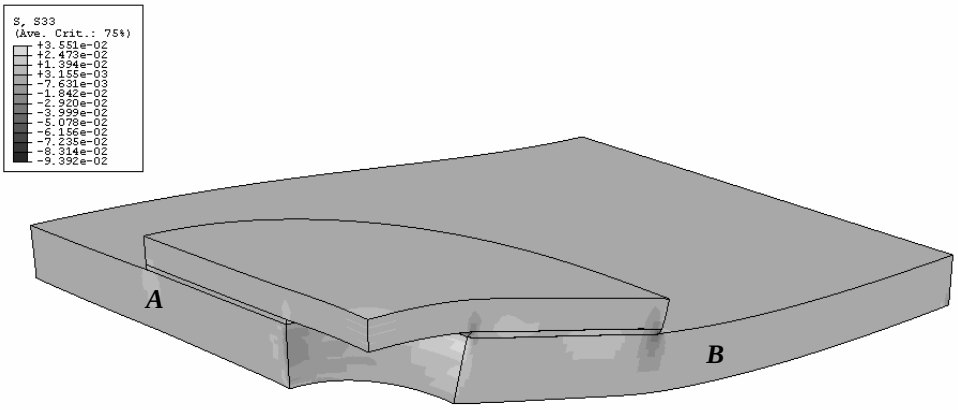

Fig. 182 – σ_y stresses at the repair region.

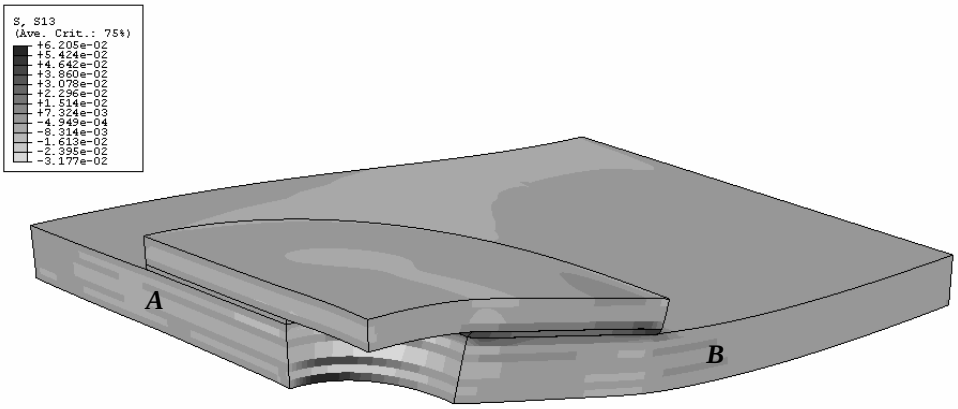

Fig. 183 – τ_{xy} stresses at the repair region.

σ_y stresses (Fig. 182 and Fig. 184 a) are antisymmetric in the entire repair compared to the tensile ones (Fig. 139 and Fig. 141 a). Thus, σ_y compressive stresses peak at the overlap edges, which constitutes an advantage to the tensile load, since σ_y peel peak stresses are prone to induce delaminations in the laminate or patch (Campilho 2005, Campilho et al. 2005, Campilho et al. 2008b). Singularities are captured by the numerical models at the repair discontinuities (plane P3 at the OEO and plane P5 at the IEO). At plane P4, moderate σ_y compressive peaks exist (similar magnitude to τ_{avg}). τ_{xy} stresses in the repair and the respective distributions at the three planes (Fig. 183 and Fig. 184 b) are equal to the tensile ones (Fig. 140 and Fig. 141 b). Thus, they reveal a similar profile in the three planes considered, peaking at the overlap edges due to the differential deformation effects. τ_{xy} stress singularities exist at the same locations as σ_y stresses.

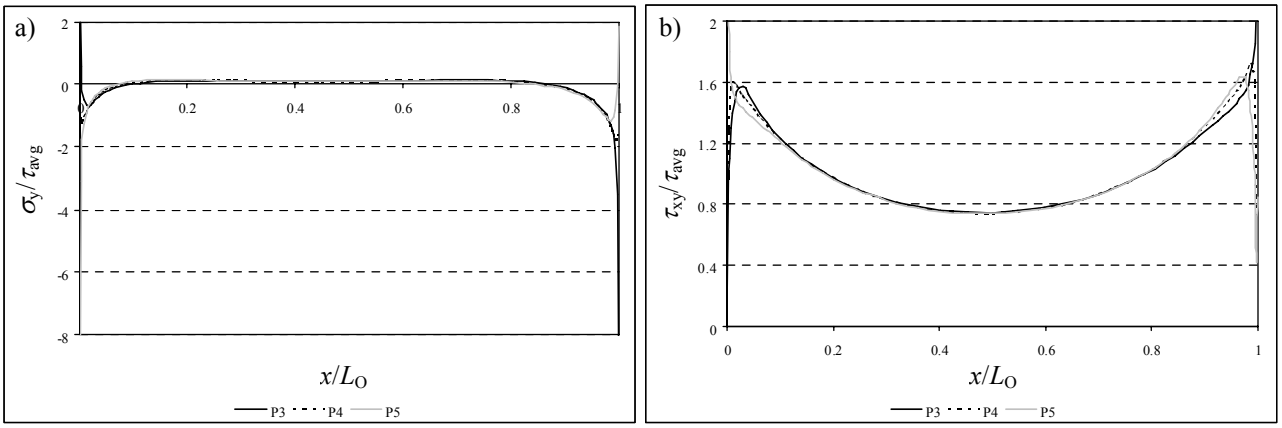

Fig. 184 – Normalized σ_y (a) and τ_{xy} (b) stress distributions at the repair region.

σ_y and τ_{xy} stress distributions at the seven planes in the repair described in Fig. 122 are shown in Fig. 185 and Fig. 186, respectively. The same conclusions to the tensile stresses can be drawn (Fig. 142 and Fig. 143). Actually, the highest σ_y peel peak stresses develop at the stress singularities (plane P3 at the OEO and plane P5 at the IEO), diminishing in the laminate and patch. σ_y compressive peak stresses at the overlap edges prevent the occurrence of delaminations at those regions. τ_{xy} stress distributions are identical to the tensile ones (Fig. 143). Thus, they are highest and similar at planes P3, P4 and P5, diminishing progressively in the laminate and patch with the distance to the bond edges. The results presented in this Sub-Section indicate that damage initiates at or near the singularity regions (OEO at plane P3 and IEO at plane P5). **Due to the documented relations between σ_y and τ_{xy} stresses under tension and compression, the stress distributions under compression loads will be omitted in all the following analyses in Section 4 concerning the optimization of the geometric parameters**.

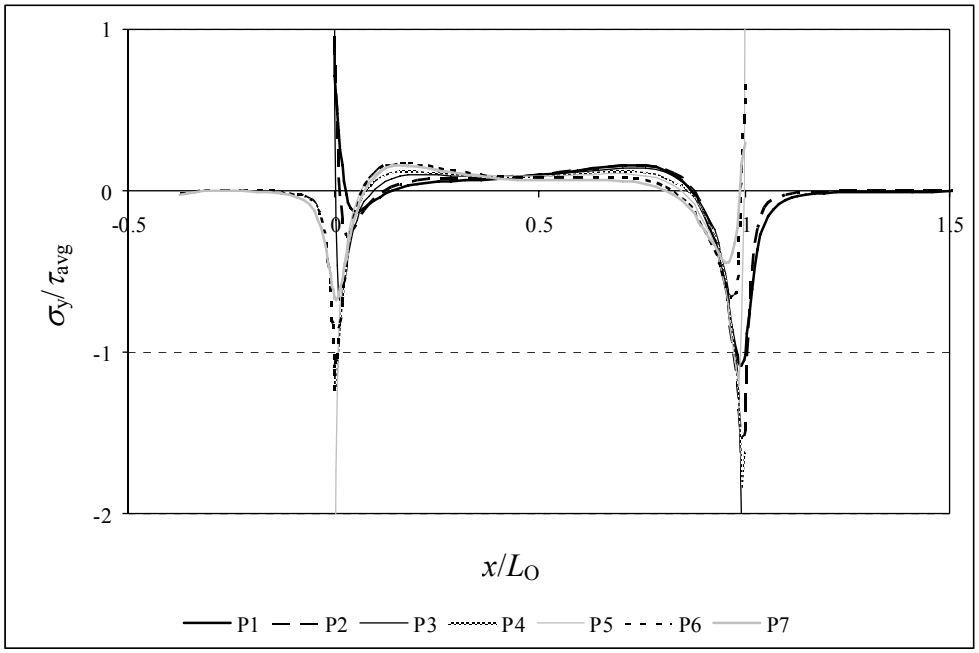

Fig. 185 – Normalized σ_y stress distributions at seven planes in the repair.

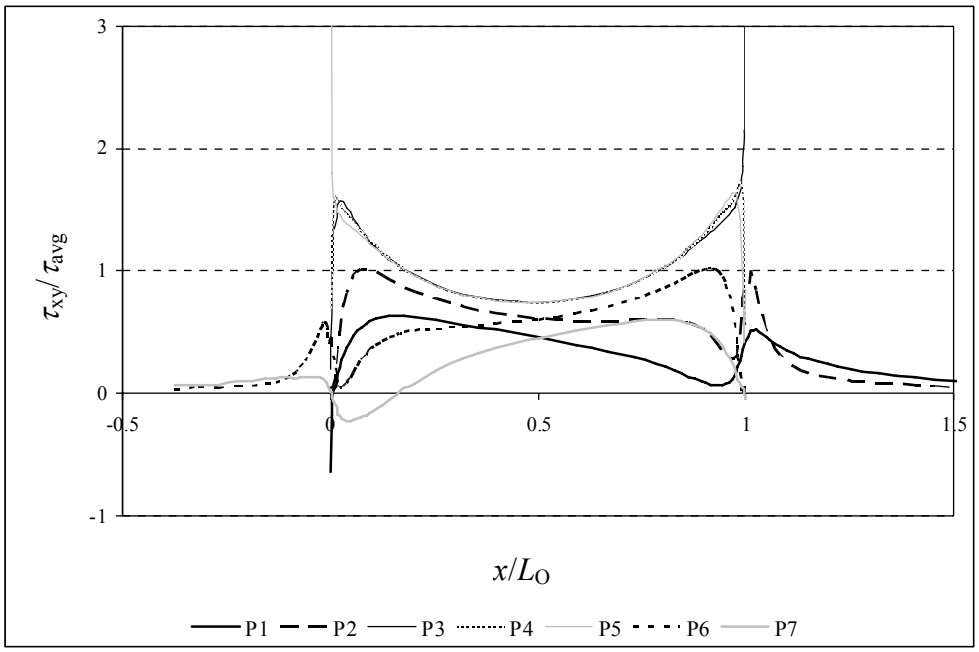

Fig. 186 – Normalized τ_{xy} stress distributions at seven planes in the repair.

4.3.4.1.1.1. Overlap length

σ_y stress distributions at planes P3, P4 and P5 are antisymmetric to the tensile ones (Fig. 144 (a), Fig. 145 (a) and Fig. 146 (a), respectively). τ_{xy} stress distributions are equal to the tensile ones (Fig. 144 (b), Fig. 145 (b) and Fig. 146 (b) at planes P3, P4 and P5, respectively). σ_y stress distributions develop compressive regions at the IEO and OEO of increasing extension and magnitude with the increase of L_O. Under these conditions, the chances of delamination in the laminate or patch diminish (Lazzarin et al. 2002, Campilho et al. 2005, da Silva et al. 2006, Kim et al. 2006). τ_{xy} stress distributions show increasing magnitude peaks at the overlap edges with the increase of L_O, equally to the tensile stress distributions. This elastic stress analysis indicates that probably P_m does not increase proportionally with L_O.

4.3.4.1.1.2. Patch thickness

Fig. 147 (a), Fig. 148 (a) and Fig. 149 (a) show σ_y stress distributions under tension at planes P3, P4 and P5, respectively. Under a compressive load, antisymmetric distributions shall be considered. τ_{xy} stress distributions are equal to the tensile load ones (Fig. 147 (b), Fig. 148 (b) and Fig. 149 (b)). Bigger values of t_H lead to a peel region of increasing dimensions at the overlap central region and σ_y compressive peak stresses of bigger extension and magnitude at the overlap edges. Since σ_y peak stresses at the overlap edges are compressive, these are not expected to greatly influence the repairs behaviour. However, bigger values of t_H also increase τ_{xy} peak stresses at the OEO, which are known to reduce the repairs strength (Soutis et al. 1999, Hu and Soutis 2000, Campilho et al. 2005). Thus, the smallest value of t_H is recommended based on this analysis.

4.3.4.1.1.3. Adhesive thickness

σ_y stress distributions are antisymmetric to the tensile load ones (Fig. 150 (a), Fig. 151 (a) and Fig. 152 (a) at planes P3, P4 and P5, respectively), while equal τ_{xy} stress distributions to tensile ones were obtained (Fig. 150 (b), Fig. 151 (b) and Fig. 152 (b), respectively). Thus, σ_y compressive peak stresses at the overlap edges diminish with t_A. Also, τ_{xy} peak stresses diminish in magnitude with t_A. Since σ_y stresses are compressive at the overlap edges, no significant influence of t_A on P_m is expected. On the other hand, the τ_{xy} peak stresses reduction at the same regions likely increases P_m.

4.3.4.1.2. Double-strap repairs

Fig. 187 illustrates the DS repair deformed configuration under a compressive load. σ_y and τ_{xy} stresses at the adhesive region are presented in Fig. 188 (a) and (b), respectively. Equally to the previous analyses, σ_y and τ_{xy} stresses are highest near the symmetry plane ***B*** at the overlap edges. Owing to this fact, the stress analysis in this Sub-Section will be centred only on plane ***B***. Comparing with the DS repairs under a tensile load (Fig. 154), a similar τ_{xy} stress field was obtained. σ_y stresses are antisymmetric, thus presenting a compressive peak at the OEO. σ_y compressive peak stresses slightly diminish at the overlap edges, comparing with the equivalent compressive loaded repair (Fig. 180 a). On the other hand, no significant difference was found on the magnitude of τ_{xy} peak stresses (Fig. 180 b). σ_x stresses at the repair region are presented in Fig. 189.

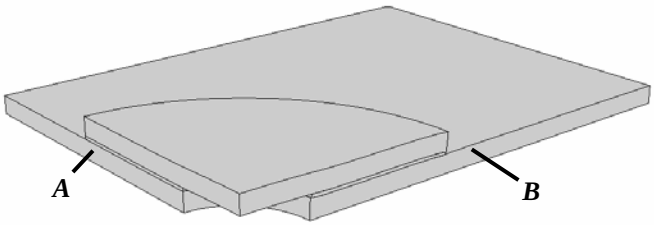

Fig. 187 – Deformed configuration of the DS repair under a compressive load.

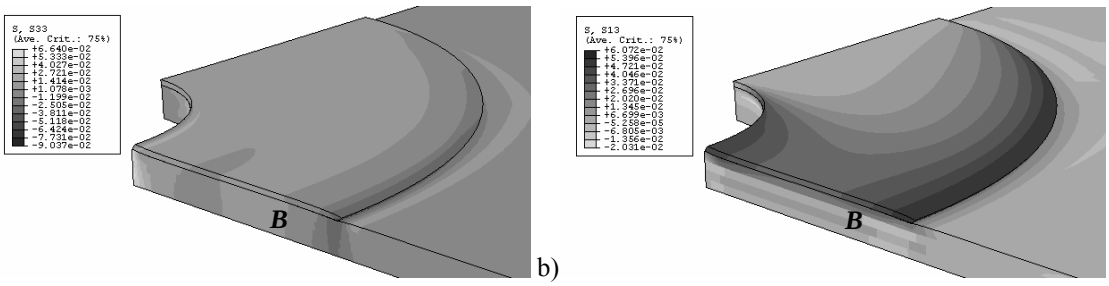

a) b)

Fig. 188 – σ_y (a) and τ_{xy} (b) stresses at the repair region.

The laminate flexure is suppressed with this repair technique, due to the symmetry of the transmitted loads (Campilho 2005, Campilho et al. 2005, Campilho et al. 2008b). However, the patches flexure, caused by the eccentricity of the loads transmitted to the patch, results on σ_y peak stresses at the IEO (tensile stresses) and at the OEO (compressive stresses). σ_x stresses are antisymmetric to the DS repair stresses under tension (Fig. 155). Oppositely, a significant

reduction on σ_x tensile stresses in the patch and compressive ones in the laminate is attained from the SS repair under compression (Fig. 181), justified by the elimination of the laminate flexure of the DS repairs.

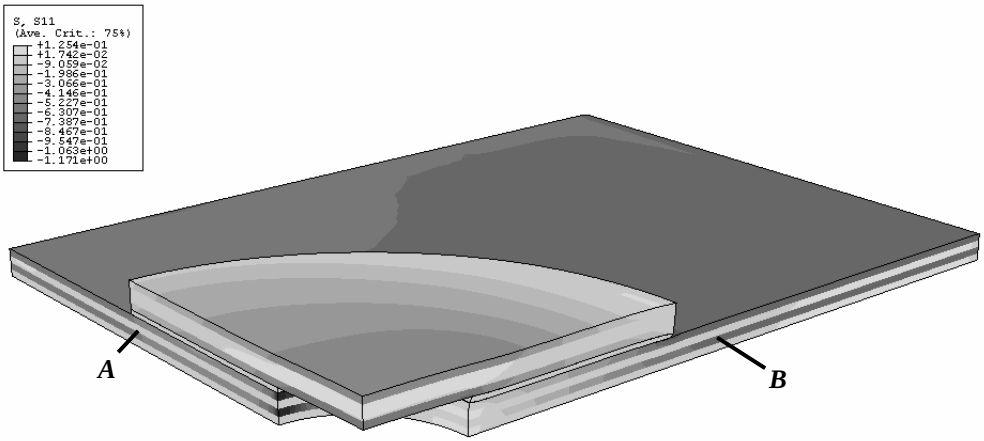

Fig. 189 – σ_x stresses at the repair region.

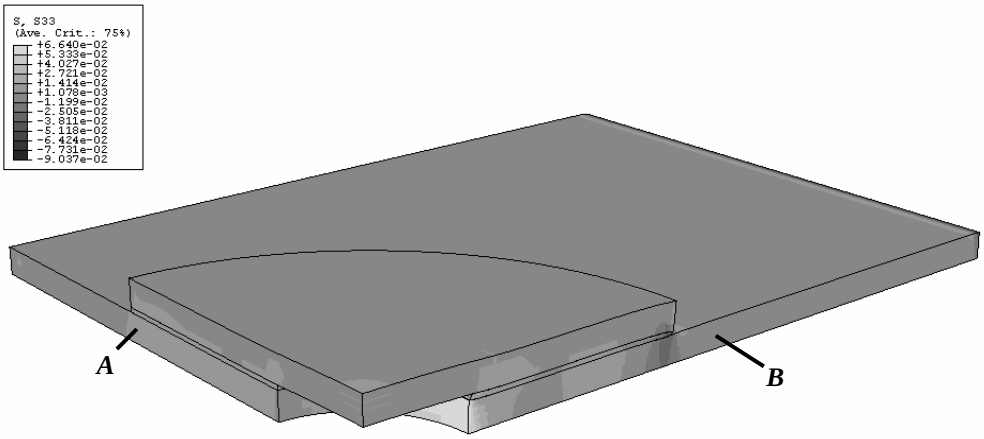

Fig. 190 – σ_y stresses at the repair region.

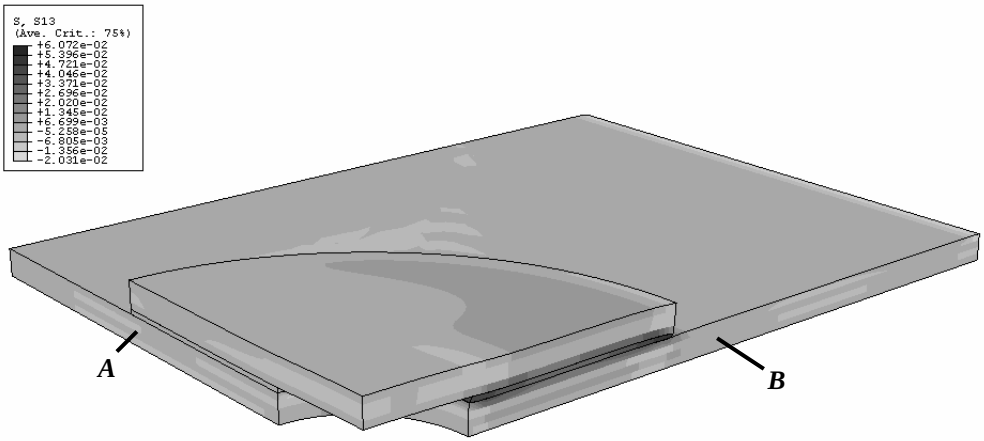

Fig. 191 – τ_{xy} stresses at the repair region.

σ_y stresses at the repair region are plotted in Fig. 190 and the respective stress distributions at planes P3, P4 and P5 are plotted in Fig. 192 (a). τ_{xy} stresses are presented in Fig. 191 and τ_{xy} stress distributions in Fig. 192 (b). σ_y stress

distributions are antisymmetric to the DS repair under tension (Fig. 158 a). Hence, they are nearly nil at the overlap central region, peaking at the overlap edges. At the middle of the adhesive (plane P4) σ_y compressive stresses peak at the OEO, while at the IEO negligible σ_y peak stresses develop. At planes P3 and P5, σ_y singularities exist at the overlap edges. This agrees with the SS repair under compression (Fig. 184 a), although SS repairs also exhibit moderate σ_y compressive peak stresses at the IEO at the three planes (Fig. 184 a). σ_y compressive peak stresses at the adhesive region (OEO) are similar in magnitude to the SS repair under a similar compressive displacement (Fig. 190 compared to Fig. 182). τ_{xy} stresses are equal to the DS repair ones under a tensile load (Fig. 158 b), thus peaking at the overlap edges. τ_{xy} stress profiles are identical between the three planes. Stress singularities were identified at planes P3 (OEO) and P5 (IEO). τ_{xy} stress distributions are flatter than the SS repair ones under compression (Fig. 184 b), which is caused by a smaller differential straining between the laminate and patches (Campilho 2005). Comparing τ_{xy} stresses magnitude in the adhesive layer at the repair region (Fig. 191) with the SS ones under the same loading (Fig. 182), approximate but slightly smaller peak values are obtained at the overlap edges.

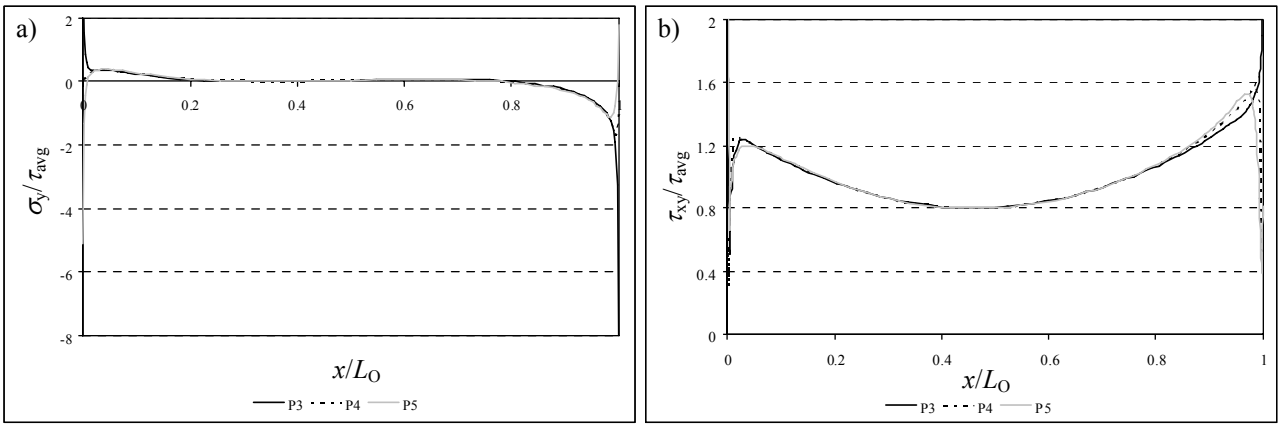

Fig. 192 – Normalized σ_y (a) and τ_{xy} (b) stress distributions at the repair region.

Fig. 193 and Fig. 194 plot σ_y and τ_{xy} stress distributions, respectively, at seven planes in the repair (Fig. 122). σ_y stresses are antisymmetric to the tensile load ones (Fig. 159). As a result, σ_y peel peak stresses develop at the IEO, while σ_y compressive ones concentrate in the direction of the OEO. Delaminations are particularly prone to occur in the laminate (IEO) at planes P1 and P2. At the OEO, σ_y compressive peak stresses in the laminate and patches prevent this occurrence. Improved σ_y stress distributions were obtained for the SS repairs under compression (Fig. 185), since peak stresses concentrate at a more restricted region. τ_{xy} stress profiles are identical to the tensile ones (Fig. 160). Accordingly to the behaviour of σ_y stresses, τ_{xy} stresses are higher and similar at planes P3, P4 and P5, peaking at the overlap edges. More uniform τ_{xy} stress distributions were obtained at the IEO, comparing with the corresponding SS repair (Fig. 186). Equally, in the laminate (planes P1 and P2), τ_{xy} stresses are higher in magnitude at the overlap inner region. In the patch (planes P6 and P7), τ_{xy} stresses are higher at the opposite region. In view of this behaviour, damage initiation is prone to occur at the IEO at or near the laminate/adhesive interface (plane P3), due to the σ_y peel stress singularities observed at this region, which add to the τ_{xy} peak stresses.

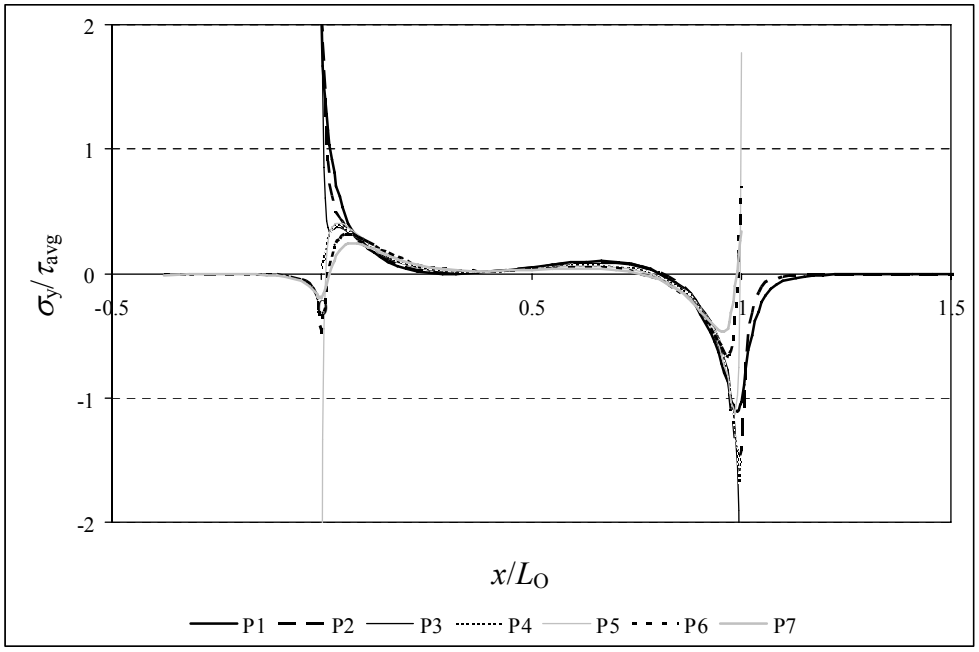

Fig. 193 – Normalized σ_y stress distributions at seven planes in the repair.

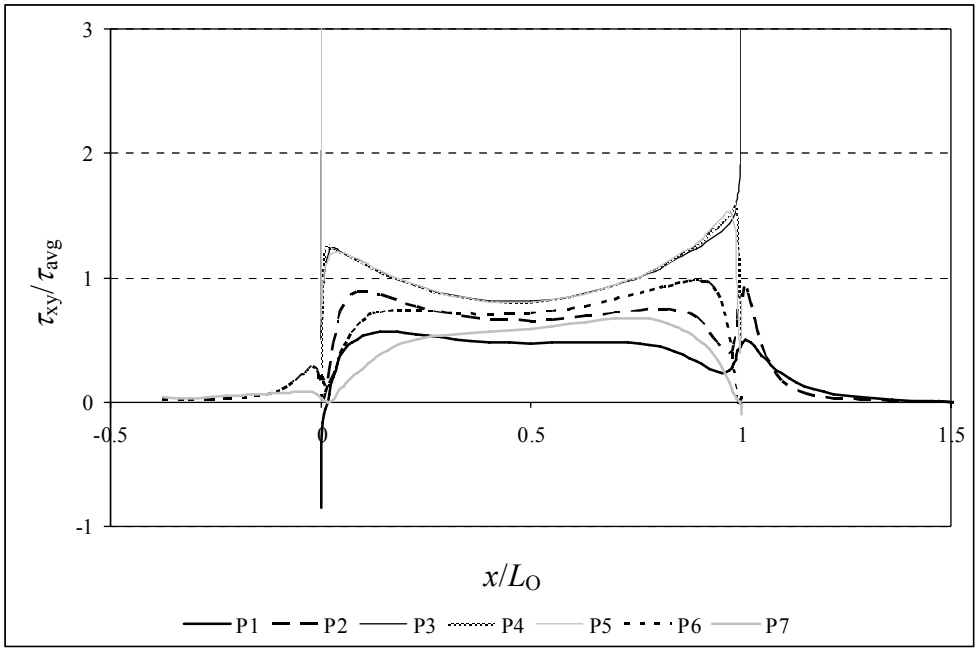

Fig. 194 – Normalized τ_{xy} stress distributions at seven planes in the repair.

4.3.4.1.2.1. Overlap length

Fig. 161 (a), Fig. 162 (a) and Fig. 163 (a) represent σ_y stress distributions at planes P3, P4 and P5, respectively, for the DS repairs under tension. Under a compressive load, antisymmetric distributions shall be considered. Oppositely, τ_{xy} stress profiles are equal to the tensile ones (Fig. 161 (b), Fig. 162 (b) and Fig. 163 (b) at planes P3, P4 and P5, respectively). Planes P3 (OEO) and P5 (IEO) are regions of σ_y singular behaviour. At the IEO, σ_y peel stresses peak at plane P3. At the OEO, σ_y peak stresses are compressive. σ_y peel peak stresses at the IEO and σ_y compressive ones at the OEO diminish with L_O. Equally to the tensile loaded SS repairs, τ_{xy} stress gradients towards the overlap edges increase

with L_O, suggesting a strength improvement at a decreasing rate with L_O. However, the corresponding increased bending stiffness of the repairs may increase the buckling strength, leading to different results.

4.3.4.1.2.2. Patch thickness

σ_y stress distributions are antisymmetric to the tensile load ones (Fig. 164 (a), Fig. 165 (a) and Fig. 166 (a) at planes P3, P4 and P5, respectively). τ_{xy} stresses are presented in Fig. 164 (b), Fig. 165 (b) and Fig. 166 (b) at the same planes. σ_y peel stresses at the IEO increase in magnitude with t_H, which may induce damage prematurely at this region for the bigger values of t_H and consequently reduce the repairs strength. Oppositely, σ_y compressive peak stresses of increasing magnitude with t_H show up at the OEO. τ_{xy} peak stresses also increase in magnitude with t_H at the overlap outer region. Since σ_y peel and τ_{xy} peak stresses increase with t_H (σ_y peel peak stresses at the overlap inner region and τ_{xy} peak stresses at the overlap outer region), the bigger values of t_H are considered to weaken the repairs.

4.3.4.1.2.3. Adhesive thickness

σ_y stresses at planes P3, P4 and P5 are antisymmetric to the tensile load ones (Fig. 167 (a), Fig. 168 (a) and Fig. 169 (a), respectively). Fig. 167 (b), Fig. 168 (b) and Fig. 169 (b) present τ_{xy} stresses at the same planes. No significant differences exist in σ_y stress distributions. However, these become slightly more compressive at the overlap outer region, despite the reduction of τ_{xy} peak stresses with t_A at the OEO at planes P4 and P5. τ_{xy} stresses become flatter increasing t_A, which is prone to increase the value of P_m.

4.3.4.2. Failure analysis

4.3.4.2.1. Mechanical behaviour

The open-hole laminate was also evaluated under compression, for comparison purposes. The buckling behaviour of this notched configuration is extensively documented in the literature, due to its practical importance, including in bolted or riveted structures (Lee and Soutis 2008). Moreover, the need for hole drilling can emerge in composite structures, emphasizing on the importance of their notched strength evaluation. The critical buckling load of slender structures depends on many factors, such as the dimensions, locations and number of holes (Eryigit et al. 2009). Some investigations are available about lateral buckling in open-hole isotropic plates (Uenoya and Redwood 1978, Shanmugam and Thevendran 1992). Lawson et al. (2006) examined the lateral buckling behaviour of I-section composite beams with openings under uniform distributed transverse loads, using both FEM and experimental studies. Soutis et al. (2002) and Lee and Soutis (2005) reported an increase of the compressive strength of this notched configuration decreasing the hole diameter. However, uncertainties still exist about the failure mechanisms for FRP structures, because of the different damages possible to occur (Andrews et al. 1993, Lee and Hyer 1993, Ireman and Eriksson 1997, Nguyen 1997). In the compressive tests described in this work, conversely to the tensile load, the damage mechanisms significantly varied, depending on the selected values of L_O and t_H. Additionally, these damage mechanisms were found to highly influence the value of P_m.

The global buckling and damage mechanisms observed during the tests will be initially characterized:

- **Global buckling of the repairs**. Corresponds to buckling between the testing machine grips. Fig. 195 (a) shows an open-hole laminate under global buckling, indicating the laminate tension and compression faces.
- **Compression failure in the laminate**. Damage in the laminate face under compression, being characterized by compressive failure of the two superficial 0º plies at plane ***A*** (Fig. 123), accompanied by a very localized vertical matrix cracking at the hole edges (Lee and Soutis 2008). Damage propagated to the adjacent plies, leading also to delaminations between differently oriented plies (Suemasu et al. 2006). Fig. 195 (b), related to a t_H=2.4 mm SS repair, allows the visualization of this damage mechanism.
- **Laminate failure outside the repair region**. Failure in the laminate outside the repair region, with no visible damage in the patches. This failure mode is illustrated in Fig. 195 (c), pertaining to a L_O=15 mm DS repair.

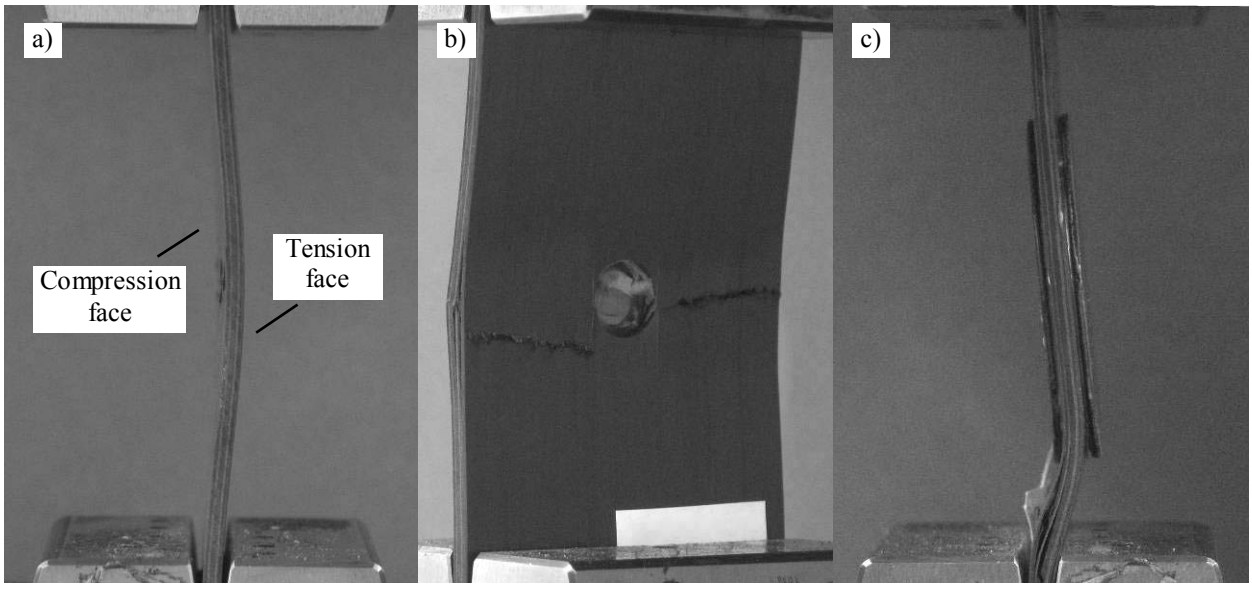

Fig. 195 – Global bucking (a), laminate compression failure (b) and laminate failure outside the repair region (c).

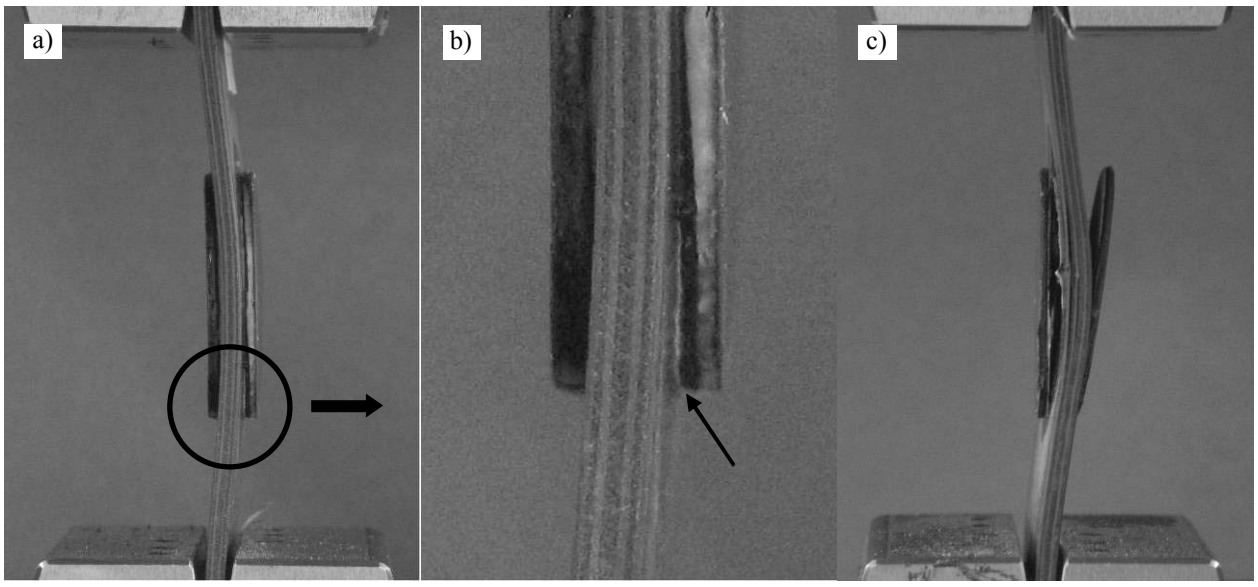

Fig. 196 – Partial patch debonding (a), detail of the patch partial debonding (b) and patch debonding (c).

- **Partial patch debonding**. Consists on a highly localized cohesive fracture of the adhesive layer at the OEO near plane ***B*** (Fig. 123). Fig. 196 (a) shows a t_H=1.8 mm DS repair with a partially debonded outer patch at the OEO, while Fig. 196 (b) presents the respective detail at the OEO.
- **Patch debonding**. Corresponds to a cohesive failure of the adhesive layer initiating at the OEO near plane ***B*** (Fig. 123) at one of the repair faces, propagating towards the IEO. Fig. 196 (c) represents a L_O=10 mm DS repair after debonding of the two patches. Fig. 197 shows cohesive failures for a L_O=5 mm SS repair (a) and for a t_H=2.4 mm DS repair in the compression face (b).

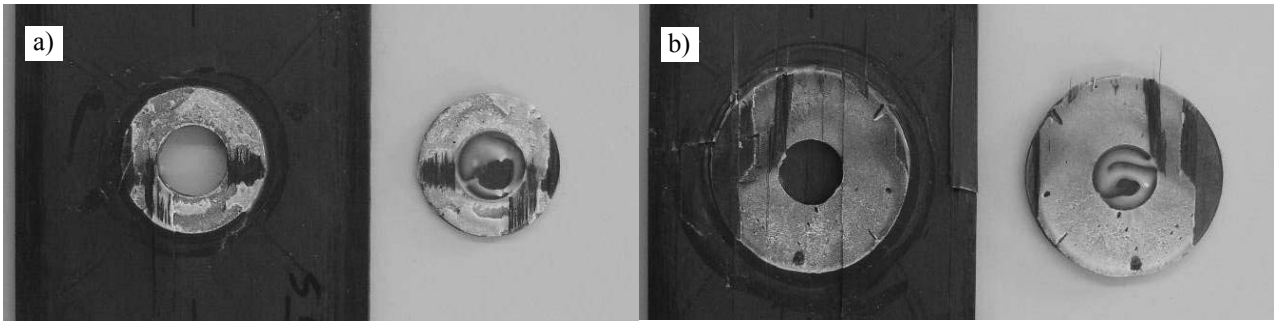

Fig. 197 – Cohesive failures for a L_O=5 mm SS repair (a) and t_H=2.4 mm DS repair in the compression face (b).

Table 15 and Table 16 summarize the damage mechanisms that rule the value of P_m as a function of L_O and t_H, respectively. **In some cases, designated by the dashed lines, damage occurred in two separate stages. However, P_m always corresponded to the first damage stage**.

Table 15 – Failure modes of the repairs as a function of L_O.

L_O	5 mm	10 mm	15 mm
SS repairs	Patch debonding and compression failure	Patch debonding and compression failure	Compression failure --- Patch debonding
DS repairs	Patch debonding and compression failure	Partial patch debonding --- Patch debonding and compression failure	Laminate failure outside the repair region

- For the open-hole laminate, failure was abrupt by compression failure (Fig. 195 b).
- The L_O=5 and 10 mm SS repairs failed simultaneously by patch debonding (Fig. 196 c) and compression failure (Fig. 195 b).
- Using a L_O=15 mm SS repair, P_m corresponded to compression failure (Fig. 195 b). Patch debonding (Fig. 196 c) occurred only after this event.
- The L_O=5 mm repair experienced a similar failure mode to the corresponding SS repair, i.e., failing concurrently by patch debonding (Fig. 196 c) and compression failure (Fig. 195 b).
- For the L_O=10 mm DS repair, P_m is ruled by partial patch debonding (Fig. 196 (a) and (b)), while the final failure of the repair occurs by patch debonding (Fig. 196 c) and compression failure (Fig. 195 b).

- With a L_O=15 mm repair, due to the higher stiffness and strength at the hole region, failure occurs in the laminate outside the repair region (Fig. 195 c).

The reported failure mode modification with L_O for both SS and DS repairs is justified by the larger adhesive shear area and consequent higher flexure capabilities of the patch before debonding. Also, the growth with L_O of an intermediate unloaded shear region helps to this behaviour (Fig. 144 (b), Fig. 145 (b) and Fig. 146 (b) for the SS repairs; Fig. 161 (b), Fig. 162 (b) and Fig. 163 (b) for the DS repairs).

Table 16 – Failure modes of the repairs as a function of t_H.

t_H	0.6 mm	1.2 mm	1.8 mm	2.4 mm
SS repairs	Compression failure	Patch debonding and compression failure	Patch debonding and compression failure	Partial patch debonding Patch debonding and compression failure
DS repairs	Partial patch debonding Compression failure	Partial patch debonding Patch debonding and compression failure	Partial patch debonding Patch debonding and compression failure	Partial patch debonding Patch debonding and compression failure

- Analysing the effect of t_H, it is noticed that for a t_H=0.6 mm SS repair, P_m is related to compression failure (Fig. 195 b), while the patch remained intact. This behaviour is explained by the bigger patch flexibility, leading to smaller magnitude σ_y and τ_{xy} peak stresses in the adhesive layer (Fig. 147, Fig. 148 and Fig. 149 show these distributions for a tensile load; under compression σ_y stresses are antisymmetric).
- Simultaneous patch debonding (Fig. 196 c) and compression failure (Fig. 195 b) occur with the t_H=1.2 and 1.8 mm SS repairs.
- The t_H=2.4 mm repair fails by partial debonding of the patch (Fig. 196 (a) and (b)). This is caused by the patch bigger stiffness, which causes a premature partial debonding at the OEO.
- For the DS repairs, t_H has a smaller influence on P_m. In fact, P_m is ruled by a partial patch debonding event for all values of t_H (Fig. 196 (a) and (b)). Final failure occurs by patch debonding (Fig. 196 c) and compression failure (Fig. 195 b), except for the t_H=0.6 mm repair, where no patch debonding was detected at failure. This is caused by the higher flexibility of the patches and consequent smaller magnitude of σ_y and τ_{xy} peak stresses in the adhesive layer (Fig. 164, Fig. 165 and Fig. 166 correspond to the DS repairs under a tensile load; under compression σ_y stresses are antisymmetric).

Summarizing the results, for the majority of the repair geometries the value of P_m was related to a patch debonding event. Only for the L_O=15 mm SS and DS repairs, and for the t_H=0.6 mm SS repair, the value of P_m is governed by the laminate strength.

Since compression failure ruled the value of P_m for some of the repair geometries, a stress-based criterion was used to predict numerically this occurrence. This procedure consisted on obtaining experimentally the average value of δ leading to compression failure in the laminate for the open-hole laminates. Following, with the corresponding numerical model, the average value of σ_x ($\sigma_{x\,avg}$) at the two superficial 0º plies in the compression face of the laminate

at plane ***A*** (Fig. 123) was obtained for the same value of δ. In the repaired geometries, the value of $\sigma_{x\,avg}$ was used to assess compression failure. This criterion is justified by an experimental practically simultaneous compression failure in these two plies. The numerical models thus included cohesive elements only to simulate the adhesive layer behaviour. It should be emphasized that, using this numerical methodology, patch debonding was found to rule the value of P_m on all repair geometries, except the ones mentioned earlier for the experiments (Table 15 and Table 16), for which a compression failure in the laminate governed P_m. Fig. 198 presents the patch debonding event for the L_O=15 mm (a) and t_H=2.4 mm (b) SS repairs. In the first case, patch debonding occurred after $\sigma_{x\,avg}$ was reached, while for the t_H=2.4 mm SS repair the opposite situation occurred. The following figures exemplify these different behaviours. Fig. 199 and Fig. 200 compare the experimental and numerical P-δ curves for the L_O=15 mm and t_H=2.4 mm SS and DS repairs, respectively. An increasing deviation of stiffness with δ was noticed for all repairs between the experiments and numerical simulations. This was caused by a minor slipping of the repairs in the testing machine grips, leading to an experimental reduction of stiffness during the tests that is not representative of the real behaviour of the composite.

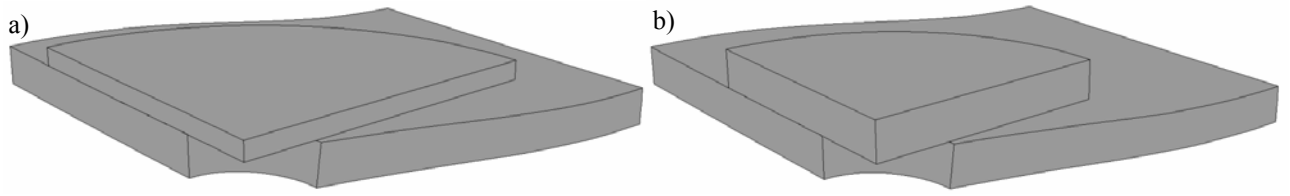

Fig. 198 – Numerical patch debonding for the L_O=15 mm (a) and t_H=2.4 mm (b) SS repairs.

- For the L_O=15 mm SS repairs, the value of P_m was ruled by compression failure (Table 15, Fig. 195 b). This causes the minor drop on P_m observed in the experimental P-δ curves of Fig. 199 (a). The final drop on P_m relates to patch debonding and complete failure at plane ***A*** (Fig. 123). Numerically, the abrupt drop on P at δ≈0.80 mm corresponds to patch debonding. This occurred after the predicted compression failure (the circle marks in each numerical P-δ curve correspond to the compression failure prediction). Therefore, it can be concluded that the experimental behaviour was correctly simulated using the proposed FEM methodology.

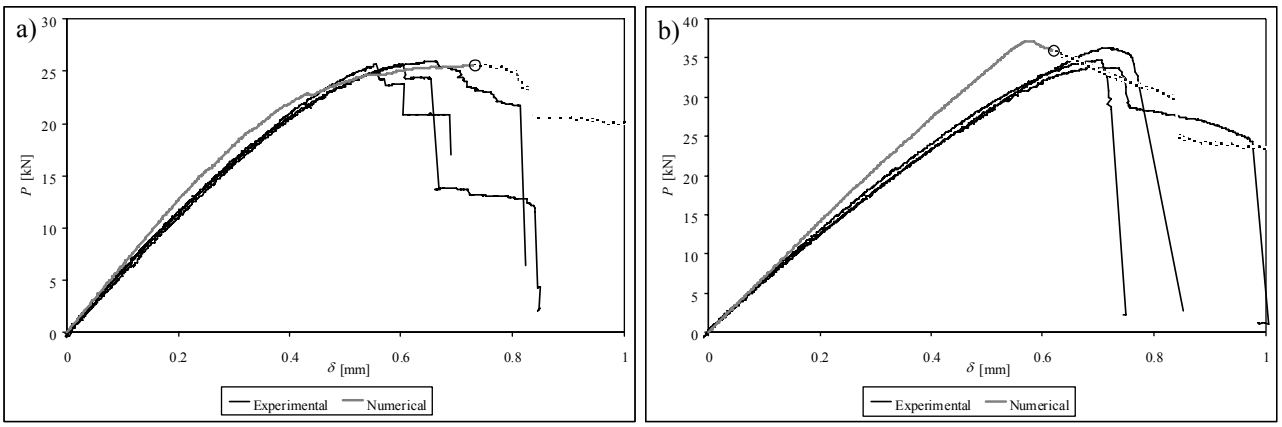

Fig. 199 – Experimental and numerical P-δ curves comparison for the L_O=15 mm SS (a) and DS (b) repairs.

- Considering the equivalent DS repair (Fig. 199 b), the drop on P_m of the experimental P-δ curves occurs due to laminate failure outside the repair region (Table 15, Fig. 195 c). In one of the specimens, this failure occurred

in two stages. The numerical approximation shows a value of P_m of identical magnitude, and compression failure in the laminate occurring after this value. Patch debonding occurs after these two events ($\delta \approx 0.82$ mm), which is consistent with the experiments. However, it should be mentioned that in this case the proposed stress criterion is not adequate, since the laminate failure occurred mostly by delamination between differently oriented plies (Fig. 195 c) instead of compression failure (Fig. 195 b).

The opposite behaviour, which is representative of the majority of the geometries evaluated, is presented in Fig. 200 (a) and (b) for the t_H=2.4 mm SS and DS repairs, respectively.

- For the t_H=2.4 mm SS repairs, the experimental P-δ curves show the drop on P_m due to partial patch debonding (Table 16, Fig. 196 (a) and (b)). A small plateau followed, prior to complete failure, relating to patch debonding (Fig. 196 c) and compression failure of the laminate (Fig. 195 b). This behaviour was accurately captured by the FEM simulation. In fact, patch debonding (corresponding to the drop on P_m at $\delta \approx 0.55$ mm) and a plateau occurred prior to σ_{xavg}.
- For the t_H=2.4 mm DS repair, P_m was ruled by the repair buckling. A partial patch debonding event (Table 16, Fig. 196 (a) and (b)) and a very small plateau region followed, prior to complete failure by patch debonding (Fig. 196 c) and compression failure (Fig. 195 b). This behaviour was obtained numerically, with P_m related to the onset of global buckling (Fig. 195 a) and the abrupt drop at $\delta \approx 0.60$ mm corresponding to partial patch debonding and compression failure. The estimated compression failure occurs only after P_m and patch debonding, which is consistent with the experimental observations.

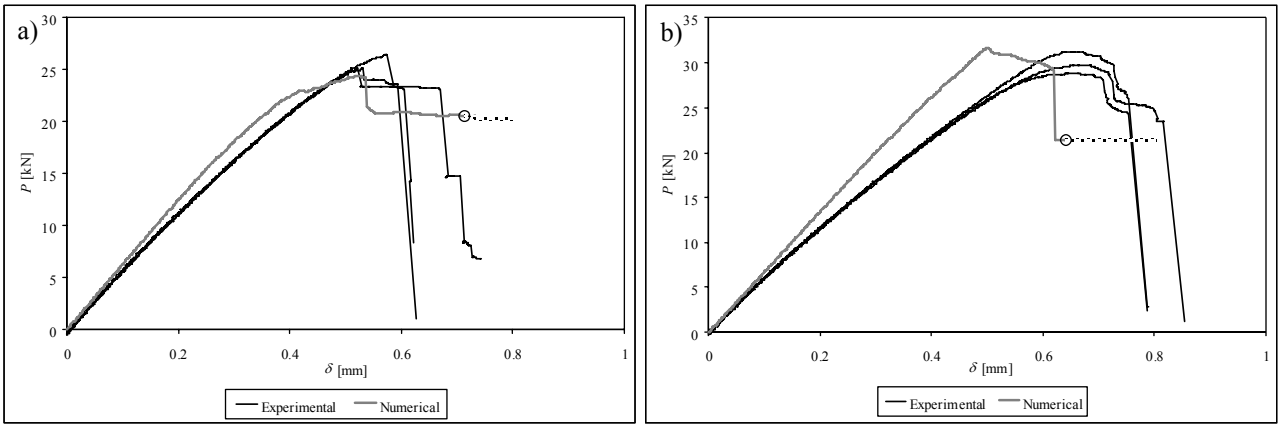

Fig. 200 – Experimental and numerical P-δ curves comparison for the t_H=2.4 mm SS (a) and DS (b) repairs.

4.3.4.2.2. Summary of the results

The summary of the experimental and numerical results of K (Fig. 201) and P_m (Fig. 202) as a function of L_O and t_H is presented, including the standard deviation of the experiments. A good agreement was found on K, as a function of the two geometric parameters evaluated. The gradual increase on K as a function of L_O (Fig. 201 a), for both SS and DS repairs is explained by the progressive increase of the adhesive shear area. This also explains the higher values of K obtained for the DS repairs. On the other hand, t_H influences K up to 1.8 mm for both SS and DS repairs, above which K remains practically constant (Fig. 201 b). This behaviour can be justified in light of the σ_y and τ_{xy} distributions in the

adhesive layer. Fig. 147, Fig. 148 and Fig. 149 show these distributions for a SS repair under a tensile load, while Fig. 164, Fig. 165 and Fig. 166 correspond to a DS repair under a tensile load (under compression, σ_y stresses are antisymmetric). In fact, under an equal compressive displacement, σ_y and τ_{xy} stresses magnitude in the adhesive layer, which rule the load transfer to the patch, increased up to the t_H=1.8 mm repair, remaining similar for t_H=2.4 mm.

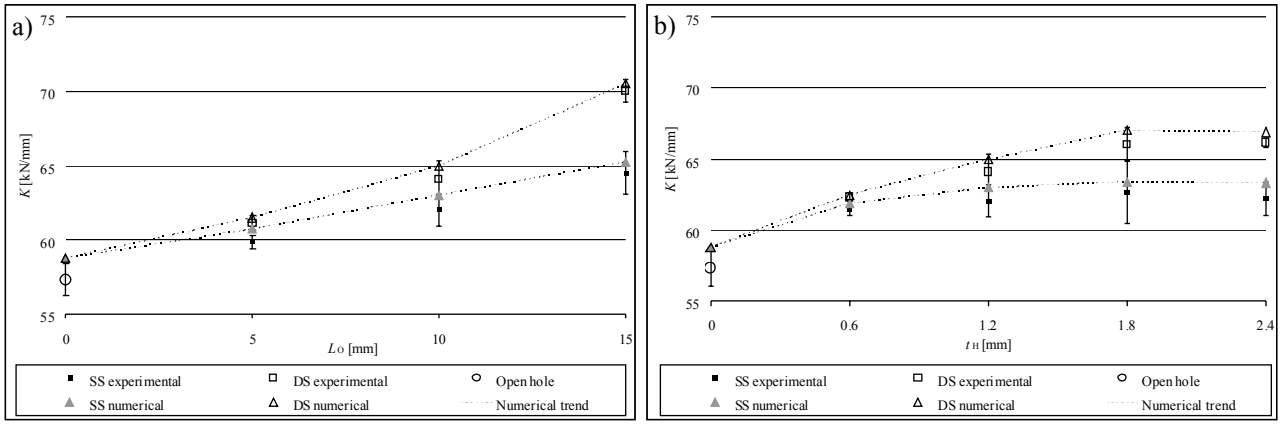

Fig. 201 – K as a function of L_O (a) and K as a function of t_H (b).

Evaluating P_m, a similar trend to K is expected, since the maximum load of structures under pure compression (corresponding to the initiation of global buckling) is generally ruled by their stiffness (Timoshenko and Gere 1961, Helms et al. 2003). The characteristic dimensions of structures are also known to greatly influence P_m. In fact, Eryigit et al. (2009) reported on the critical buckling loads of thin GFRP laminates with a circular hole at different locations, among which equally to this work, i.e., at the middle of the laminate. For this geometry, the buckling load significantly diminished increasing the length between grips. A moderate reduction was also found increasing the hole diameter. Oppositely, the mechanical properties of the materials involved typically only influence the failure displacement (Fig. 199 (b) and Fig. 200 (b) represent an example of this behaviour). However, in this particular situation, premature patch debonding and compression failure, prior to the repairs global buckling, must be checked. Actually, some of the geometries tested showed a premature patch debonding before global buckling (Table 15 and Table 16), of which the L_O=15 mm SS repairs are an example (Fig. 199 a). On the other hand, the t_H=2.4 mm SS repairs failed by compression prior to global buckling (Fig. 200 a). Apart from these exceptions, on all the other repair geometries P_m was ruled by the value of K, and a plateau was observed (Fig. 199 (b) and Fig. 200 (b)). Based on these assumptions, commonly similar tendencies to K were observed on P_m. In fact, P_m gradually increased as a function of L_O for both SS and DS repairs. No significant differences exist between the L_O=5 mm SS and DS repairs, oppositely to the bigger L_O repairs. It should be emphasized that the numerical prediction for the L_O=15 mm DS repair corresponds to a criterion (compression failure in the laminate, Fig. 195 b) that was not consistent with the experimental failure mode, as mentioned earlier (laminate failure outside the repair region, Fig. 195 c). The value of t_H has a bigger influence on P_m for the smaller values of t_H. A significant and similar difference exists between the SS and DS repairs. Overall, a good correspondence was found between the experiments and numerical predictions on the fracture behaviour of these repairs under a compressive load. **This study shows that the L_O=15 mm DS repair gives the best results. Good results are also attained with the L_O=10 mm and 1.2<t_H<2.4 mm DS repairs, and also the L_O=15 mm SS repairs. On the other hand, the analysis carried out shows a small benefit in repairing the damaged laminate with the L_O=5 mm SS and DS repair configuration, and with the L_O=10 mm SS repairs.**

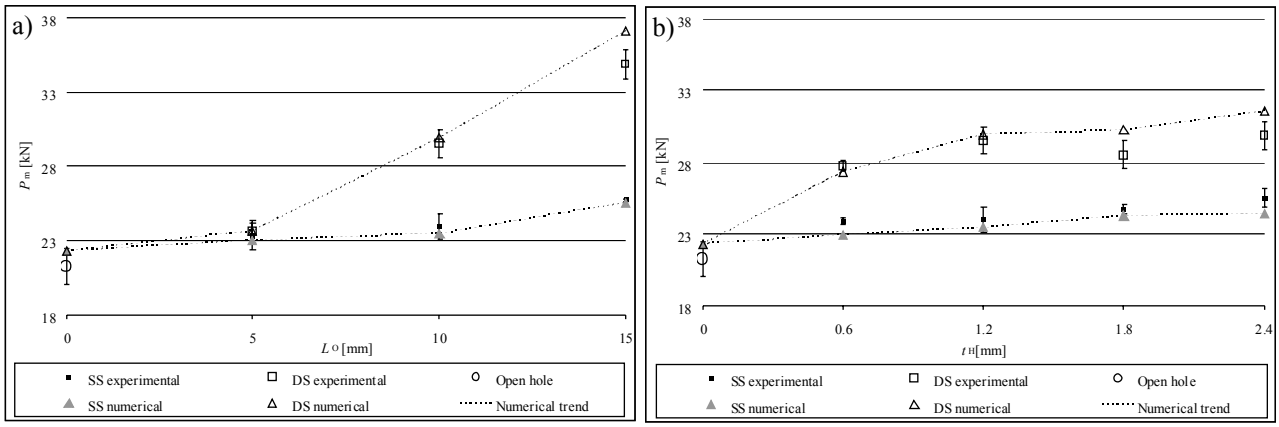

Fig. 202 – P_m as a function of L_O (a) and P_m as a function of t_H (b).

4.3.5. Bending load

As a final assessment on the fracture behaviour and model validation with strap repairs, the bending characteristics are examined. The stress analysis precedes the fracture mechanisms description and summary of the results.

4.3.5.1. Stress analysis

4.3.5.1.1. Single-strap repairs

The deformed configuration of the SS repair under a bending load is presented in Fig. 203, for a loading cylinder value of δ of 0.3 mm (applying an enhancement to the displacements of 20x). **This value of δ and magnification are applied throughout Section 4 for the SS, DS and scarf repairs under bending, including all deformed configuration and stress distributions figures, allowing a direct comparison between the different techniques.** σ_y and τ_{xy} stresses are plotted at the adhesive region in Fig. 204 (a) and (b), respectively. Similarly to the tensile and compressive loaded repairs (Fig. 137 and Fig. 180, respectively), σ_y and τ_{xy} stresses are highest in magnitude near the symmetry plane ***B***, decreasing progressively with the distance to this plane. As a result, the following stress analysis will focus on this plane only. Fig. 205 shows the σ_x stresses at the repair region.

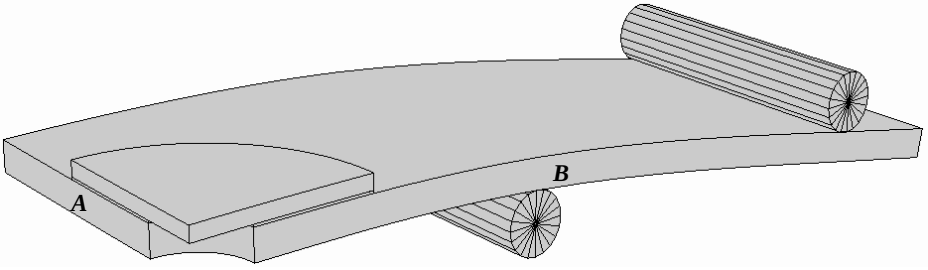

Fig. 203 – Deformed configuration of the SS repair under a bending load.

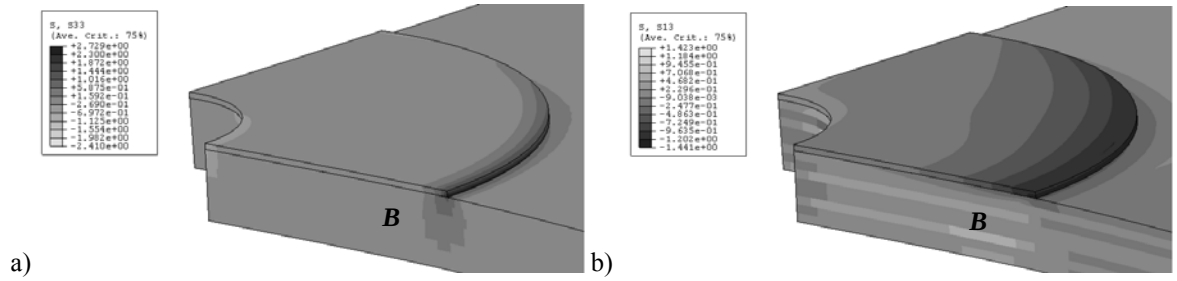

a) b)

Fig. 204 – σ_y (a) and τ_{xy} (b) stresses at the repair region.

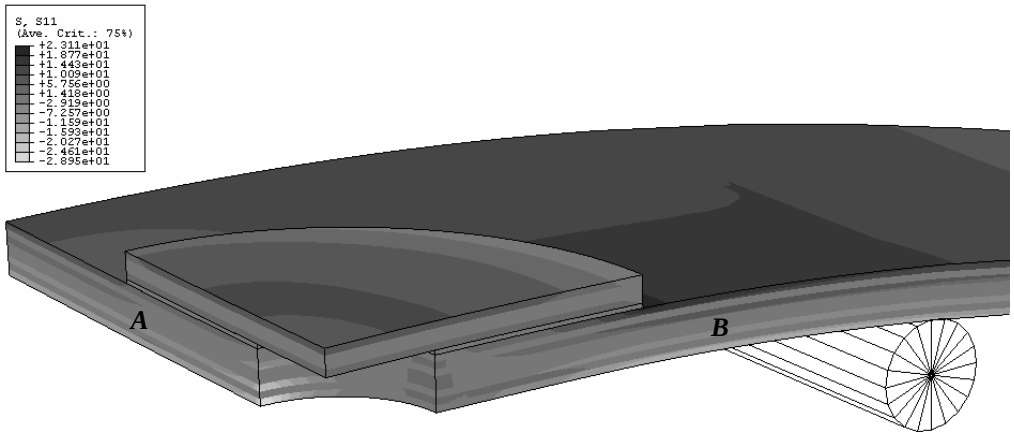

Fig. 205 – σ_x stresses at the repair region.

σ_x compressive stresses (Fig. 205) peak near the laminate hole at plane ***A***, whilst the highest magnitude tensile ones are located in the laminate at the outer surface plies, near the OEO. Apart from these regions and in the patch, σ_x stresses are approximately constant in the laminate between the loading cylinders, owing to an equally constant bending moment at that region. This opposes to the tensile (Fig. 138) and compression load (Fig. 181) SS repairs behaviour, for which σ_x stresses concentrate near the laminate hole at plane ***A***. The following figures show σ_y stresses (Fig. 206), σ_y stress distributions at three planes at the repair region (Fig. 208 a), τ_{xy} stresses (Fig. 207) and τ_{xy} stress distributions at three planes at the repair region (Fig. 208 b). Planes P3, P4 and P5 are considered in Fig. 208 (a) and (b).

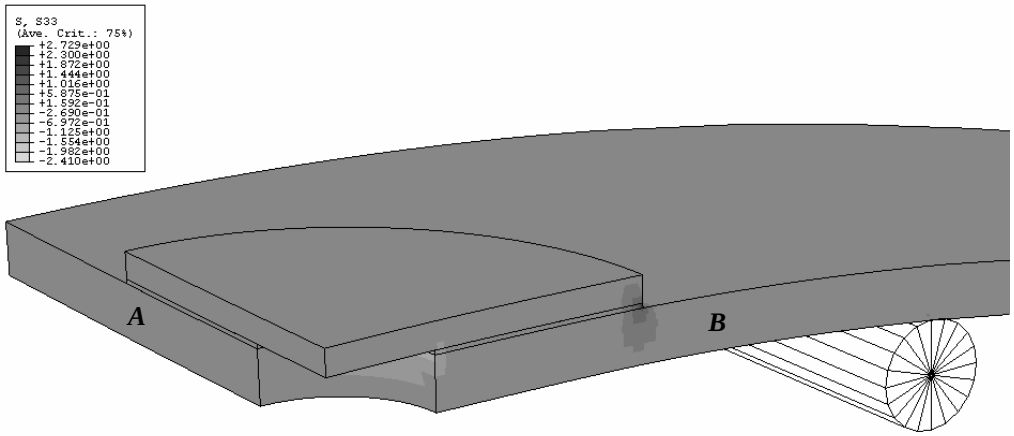

Fig. 206 – σ_y stresses at the repair region.

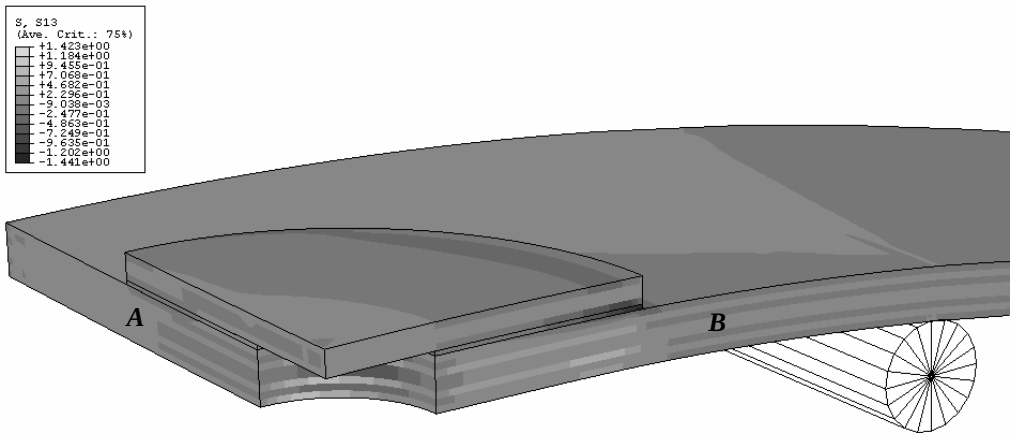

Fig. 207 – τ_{xy} stresses at the repair region.

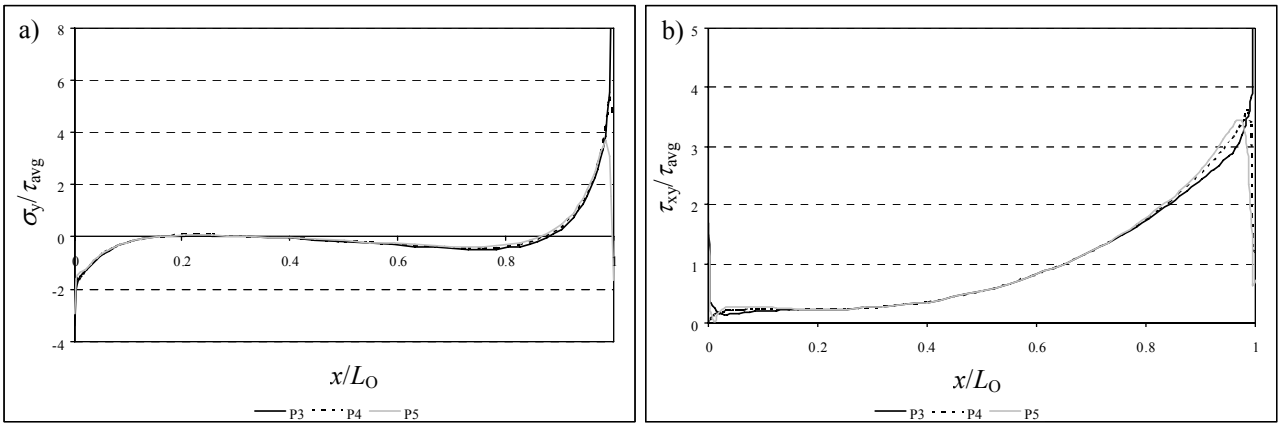

Fig. 208 – Normalized σ_y (a) and τ_{xy} (b) stress distributions at the repair region.

σ_y stresses are similar along the overlap at the three planes. In the overlap central region, σ_y stresses are practically nil. σ_y compressive stresses peak at the IEO, while at the OEO the highly pronounced peel peak stresses are caused by the repair bending (Dedale et al. 1981). These are highest at plane P3 (stress singularity region) and lowest at plane P5, which opposes to the SS repairs behaviour under tension (Fig. 141 a) and compression (Fig. 184 a), for which σ_y peel and compressive peaks, respectively, were observed at the overlap edges. τ_{xy} stresses also behave similarly at the three planes. τ_{xy} stresses are lower at the IEO and gradually increase towards the OEO (Dedale et al. 1981), conversely to the tension (Fig. 141 b) and compression load (Fig. 184 b) repairs, for which τ_{xy} peak stresses develop at the overlap edges from a lightly loaded inner region. A τ_{xy} stress singularity is observed at the OEO (plane P3).

Fig. 209 and Fig. 210 represent σ_y and τ_{xy} stress distributions, respectively, at seven planes in the repair (Fig. 122). Overall, σ_y stresses present the previously discussed behaviour at the seven planes, with a compressive peak at the IEO and a tensile one at the OEO. At planes P1 and P2 (laminate) and P6 and P7 (patch), σ_y peak stresses are smaller than in the adhesive layer, diminishing outside the overlap region ($x/L_O<0$ and $x/L_O>1$). τ_{xy} stresses are highest at the OEO at planes P3, P4 and P5. At planes P1 and P2 (laminate) and P6 and P7 (patch), τ_{xy} stresses tend to become nil outside the overlap region. The documented stress variations between the seven planes are consistent to the tensile (Fig. 142 and Fig. 143) and compressive loads (Fig. 185 and Fig. 186). These results show that damage is prone to initiate at or near

the stress singularity at the OEO, since σ_y peel and τ_{xy} stresses peak at this region, progressing to the overlap central region as the applied load increases (Olia and Rossetos 1996).

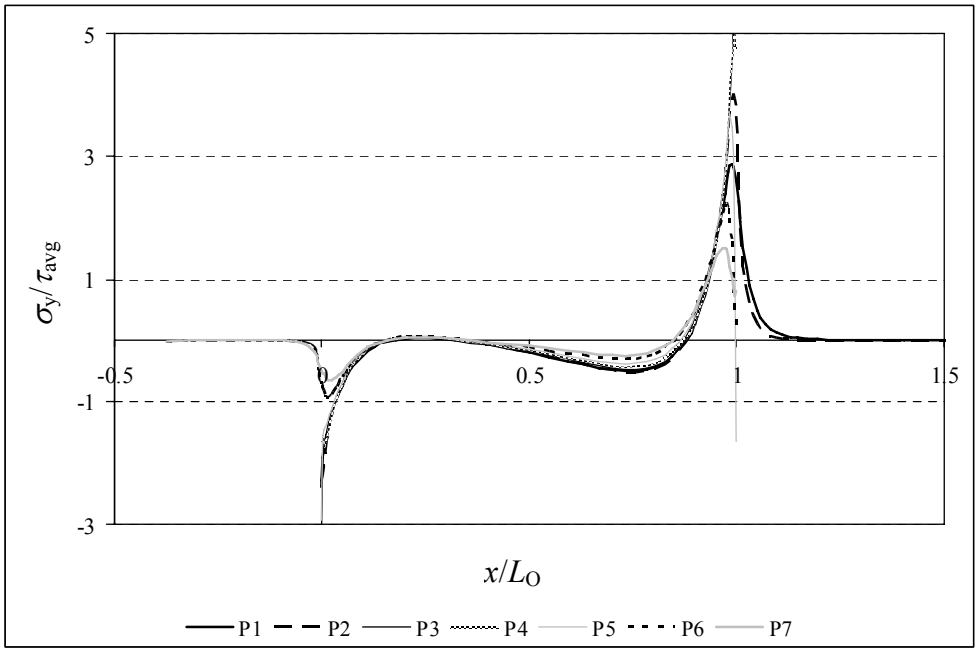

Fig. 209 – Normalized σ_y stress distributions at seven planes at the repair region.

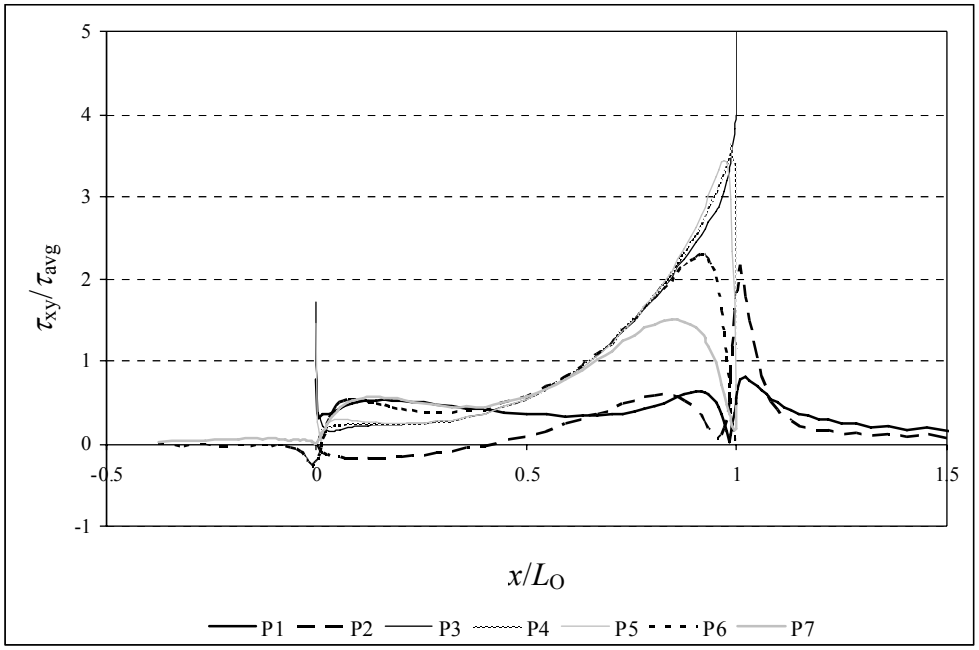

Fig. 210 – Normalized τ_{xy} stress distributions at seven planes at the repair region.

4.3.5.1.1.1. Overlap length

σ_y and τ_{xy} stress distributions are plotted at planes P3, P4 and P5. Fig. 211 corresponds to plane P3 (laminate/adhesive interface), Fig. 212 to plane P4 (middle of the adhesive) and Fig. 213 to plane P5 (adhesive/patch interface).

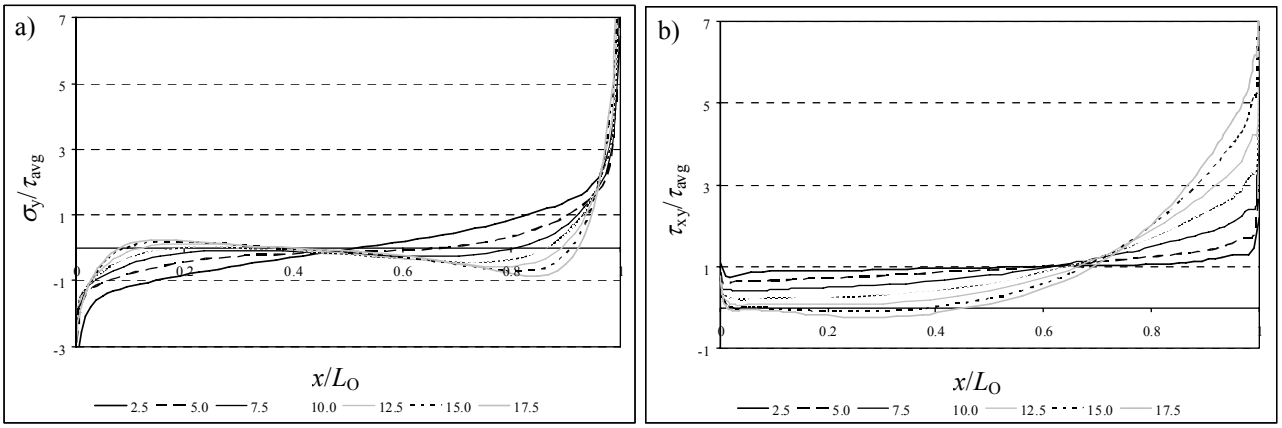

Fig. 211 – Normalized σ_y (a) and τ_{xy} (b) stress distributions at the laminate/adhesive interface (P3) as a function of L_O.

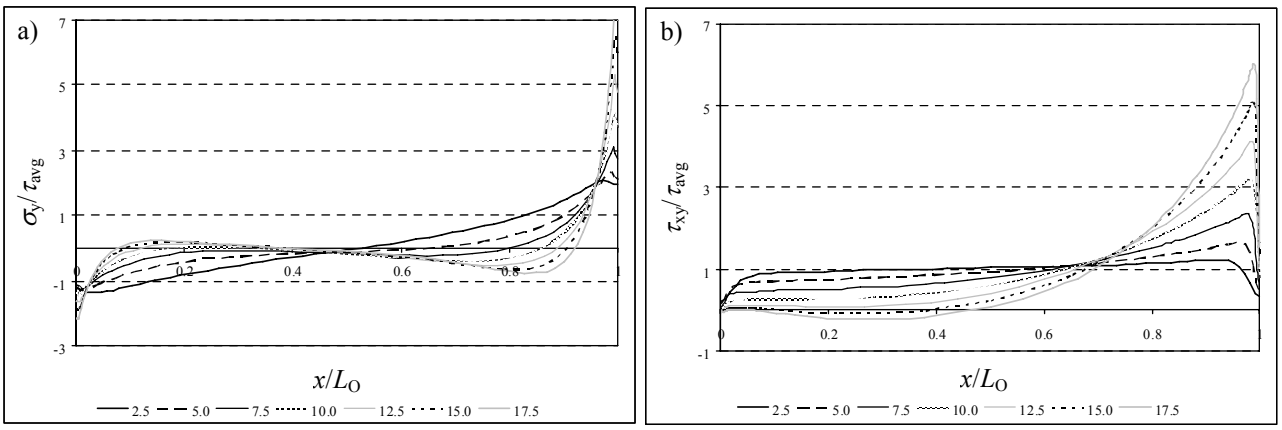

Fig. 212 – Normalized σ_y (a) and τ_{xy} (b) stress distributions at the middle of the adhesive (P4) as a function of L_O.

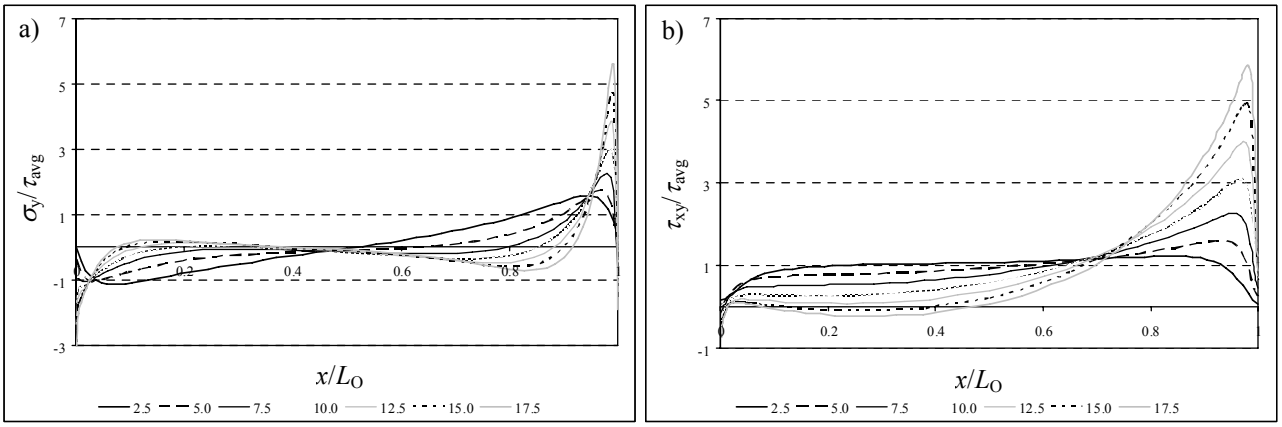

Fig. 213 – Normalized σ_y (a) and τ_{xy} (b) stress distributions at the adhesive/patch interface (P5) as a function of L_O.

σ_y stresses are as a rule smaller than τ_{avg}, except at the overlap edges, where σ_y peel stresses peak at the OEO for the bigger values of L_O. In opposition to these, σ_y compressive peak stresses exist at the IEO. At the middle of the adhesive (plane P4), moderate σ_y compressive peak stresses develop at the IEO, while at the OEO σ_y stresses are tractive. Both increase in magnitude with L_O. Furthermore, for the smaller values of L_O, σ_y stresses are compressive at the overlap inner region and tractive at the overlap outer region, although smaller than τ_{avg}. Increasing L_O reverses this behaviour. At the laminate/adhesive interface (plane P3), σ_y peak stresses become more pronounced, especially the one at the

OEO, due to the discontinuity at x/L_O=1. At the adhesive/patch interface (plane P5), σ_y peel peak stresses at the OEO are the smallest between the three planes, reaching approximately six times the value of τ_{avg} for the L_O=17.5 mm repair. τ_{xy} stresses peak at the OEO, being approximately constant at the overlap inner region. τ_{xy} stress distributions are similar between the three planes. For L_O=2.5 mm, τ_{xy} stresses are practically constant along the overlap, increasing their gradient towards the OEO with the value of L_O. Moderately compressive τ_{xy} peak stresses develop at plane P5 (IEO), growing with L_O. Similar tendencies were attained for the tensile and compressive load SS repairs, with increasing stress gradients towards the overlap edges. Fig. 144, Fig. 145 and Fig. 146 show the stress distributions for a tensile load. Under compression, antisymmetric σ_y stress distributions shall be considered. Equally to the tensile and compressive load scenarios, the repair strength is not prone to increase proportionally with L_O, since σ_y peel and τ_{xy} peak stresses at the OEO increase in magnitude with this quantity.

4.3.5.1.1.2. Patch thickness

σ_y stress distributions are plotted in Fig. 214 (a), Fig. 215 (a) and Fig. 216 (a). Fig. 214 (b), Fig. 215 (b) and Fig. 216 (b) relate to τ_{xy} stress distributions (with (a), (b) and (c) corresponding to planes P3, P4 and P5, respectively).

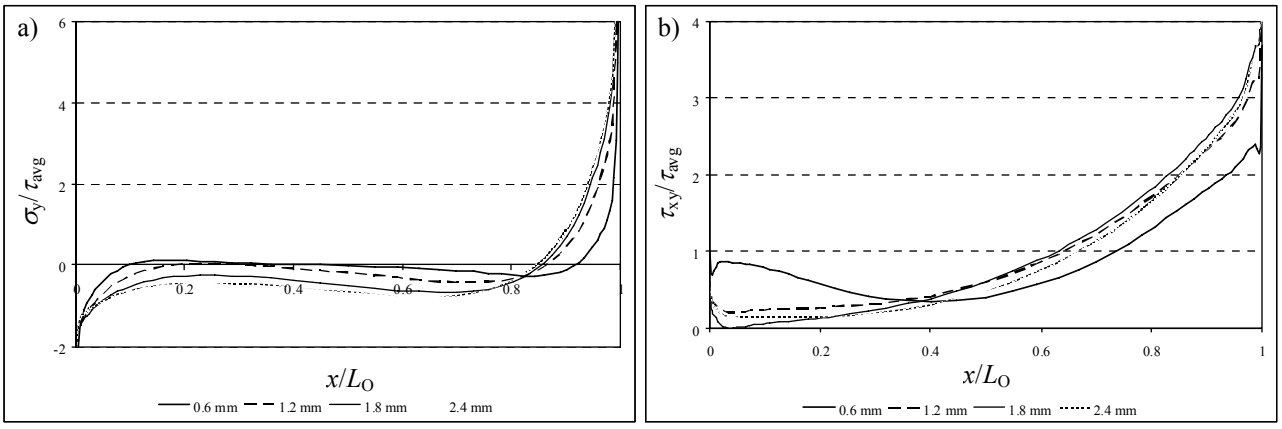

Fig. 214 – Normalized σ_y (a) and τ_{xy} (b) stress distributions at the laminate/adhesive interface (P3) as a function of t_H.

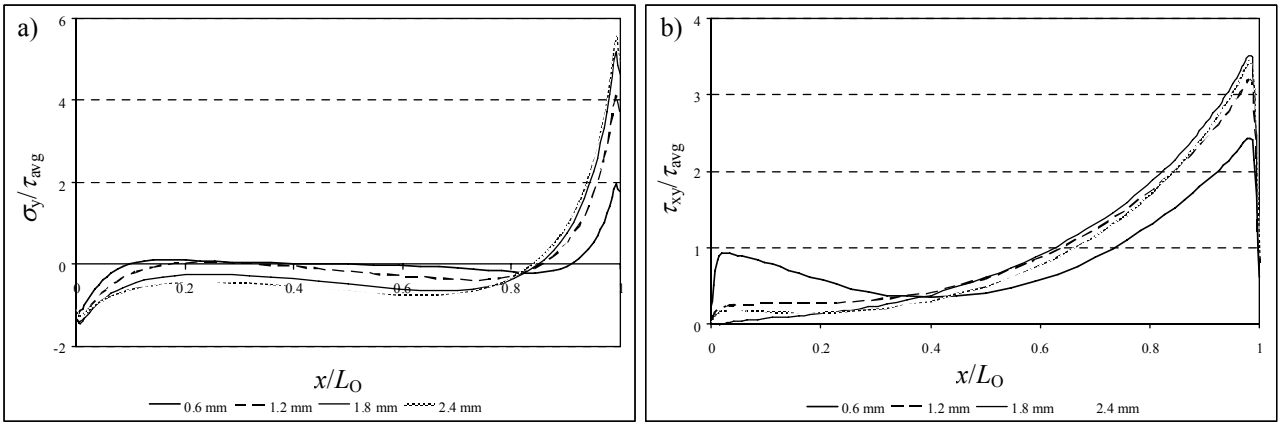

Fig. 215 – Normalized σ_y (a) and τ_{xy} (b) stress distributions at the middle of the adhesive (P4) as a function of t_H.

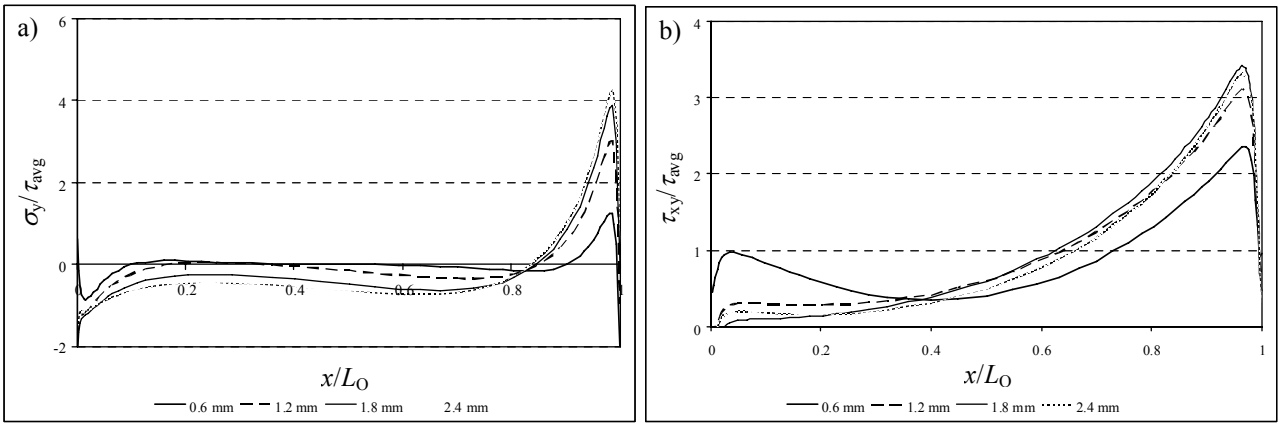

Fig. 216 – Normalized σ_y (a) and τ_{xy} (b) stress distributions at the adhesive/patch interface (P5) as a function of t_H.

σ_y stresses are mostly compressive at the overlap central region. Despite the value of t_H, σ_y stresses invariably peak in the direction of the overlap edges. The laminate flexure justifies the σ_y compressive peak stresses at the IEO and the σ_y peel peak ones at the OEO, both increasing with t_H. This modification is desirable at the IEO, but increases the odds of patch debonding at the OEO. σ_y peel peak stresses at the OEO gradually diminish from plane P3 (stress singularity region) to plane P5. Planes P3 and P5 contain a singularity at the IEO. τ_{xy} stress distributions for the t_H=0.6 mm repair exhibit moderate peaks at both overlap edges. For the other values of t_H, τ_{xy} stresses become almost nil at the IEO, showing a higher magnitude at the OEO. Similarly to σ_y stresses, τ_{xy} peak stresses at the OEO diminish from plane P3 (stress singularity region) to plane P5. Also for the SS repairs under tensile and compressive loads (Fig. 147, Fig. 148 and Fig. 149) σ_y and τ_{xy} peak stresses at the overlap edges increased in magnitude with t_H. These results point towards the use of a t_H=0.6 mm patch, since both σ_y and τ_{xy} peak stresses at the OEO are smaller in magnitude. Higher values of t_H may lead to a premature patch debonding at this region.

4.3.5.1.1.3. Adhesive thickness

Fig. 217, Fig. 218 and Fig. 219 show σ_y and τ_{xy} stress distributions at planes P3 (laminate/adhesive interface), P4 (middle of the adhesive) and P5 (adhesive/patch interface), respectively.

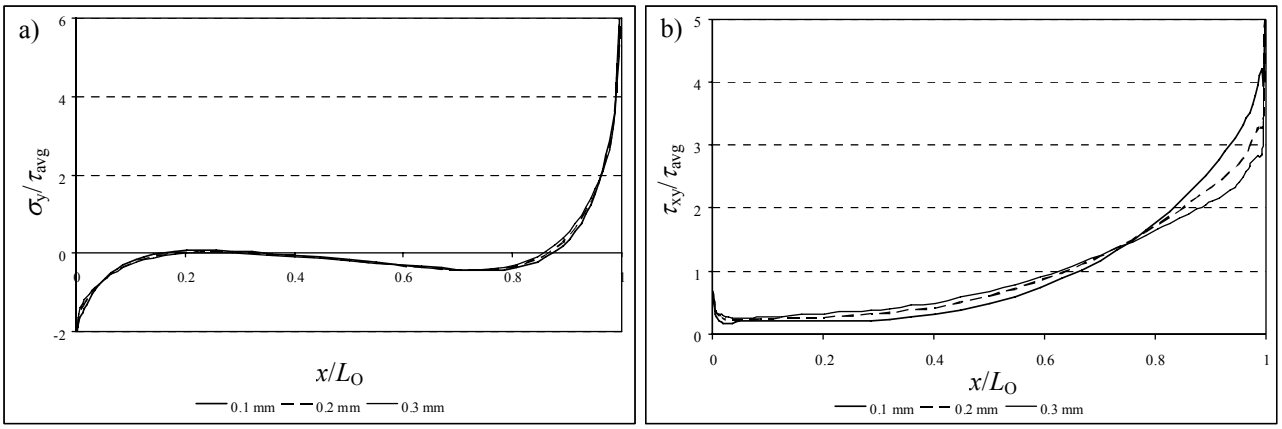

Fig. 217 – Normalized σ_y (a) and τ_{xy} (b) stress distributions at the laminate/adhesive interface (P3) as a function of t_A.

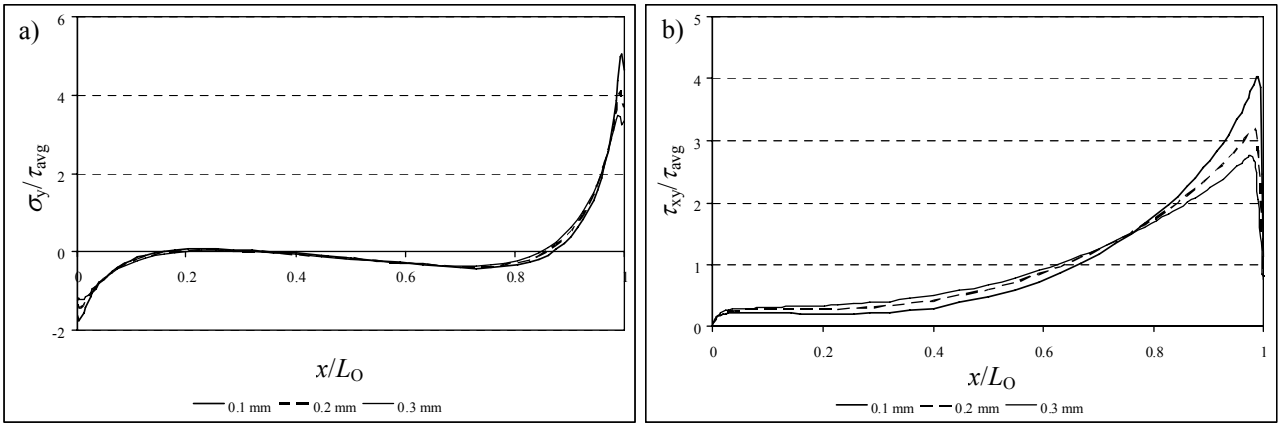

Fig. 218 – Normalized σ_y (a) and τ_{xy} (b) stress distributions at the middle of the adhesive (P4) as a function of t_A.

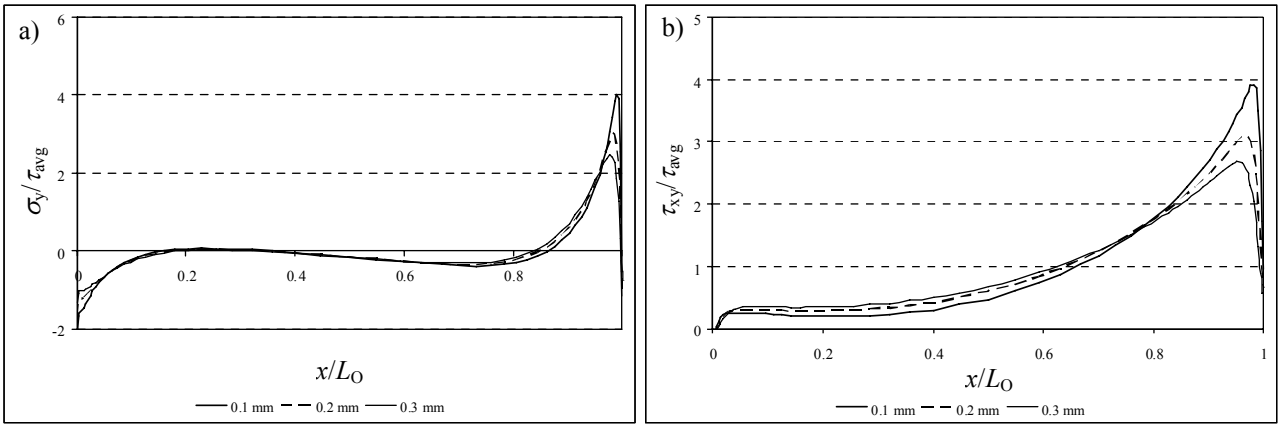

Fig. 219 – Normalized σ_y (a) and τ_{xy} (b) stress distributions at the adhesive/patch interface (P5) as a function of t_A.

σ_y stress distributions are similar along L_O, for all the values of t_A, except from the peak stresses at the overlap edges. Actually, a slight reduction of the σ_y peel peak stresses is attained by increasing the value of t_A. Furthermore, at the OEO σ_y stresses diminish with t_A, which reduces the odds of delamination in the laminate and patches. At the laminate/adhesive interface (plane P3), stress singularities develop at both overlap edges. τ_{xy} stresses also revealed a significant reduction in magnitude at the OEO with t_A. Moreover, between the three planes, the only significant difference on τ_{xy} stresses occurs at plane P3 (OEO), locus of a stress singularity. The reduction trend on τ_{xy} peak stresses with t_A is consistent with the tensile and compressive analyses (Fig. 150, Fig. 151 and Fig. 152 show σ_y and τ_{xy} stress distributions for the SS repairs under a tensile load). It should be emphasized that a slight strength improvement of the repairs with the value of t_A is expected based exclusively on this analysis.

4.3.5.1.2. Double-strap repairs

Fig. 220 shows the repair deformed configuration under a bending load. Fig. 221 (a) and (b) present σ_y and τ_{xy} stresses, respectively, in the inner and outer adhesive layers. σ_y and τ_{xy} stresses are highest near the symmetry plane ***B***, following the behaviour of the SS and DS repairs previously studied under all loads, and diminish gradually with the distance to this plane. As a result, the following stress analysis will focus on this plane. The stress fields are equivalent to the SS repairs under bending (Fig. 180). The loci of stress concentrations also agreed with the tensile (Fig. 154) and

compression loaded (Fig. 188) DS repairs. However, τ_{xy} peak stresses at the IEO are suppressed under bending. σ_x stresses are plotted at the repair region in Fig. 222.

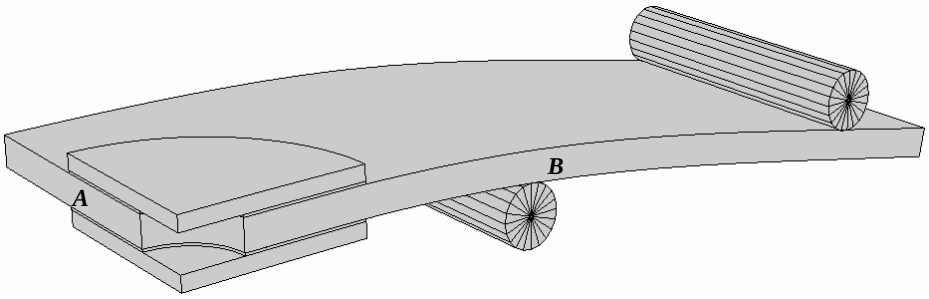

Fig. 220 – Deformed configuration of the DS repair under a bending load.

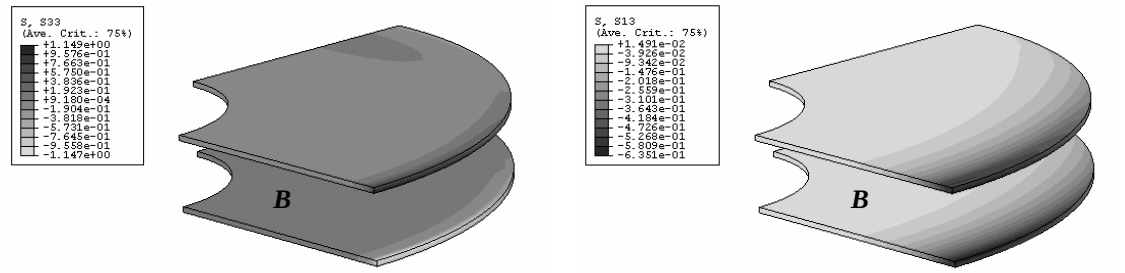

a) b)

Fig. 221 – σ_y (a) and τ_{xy} (b) stresses at the repair region.

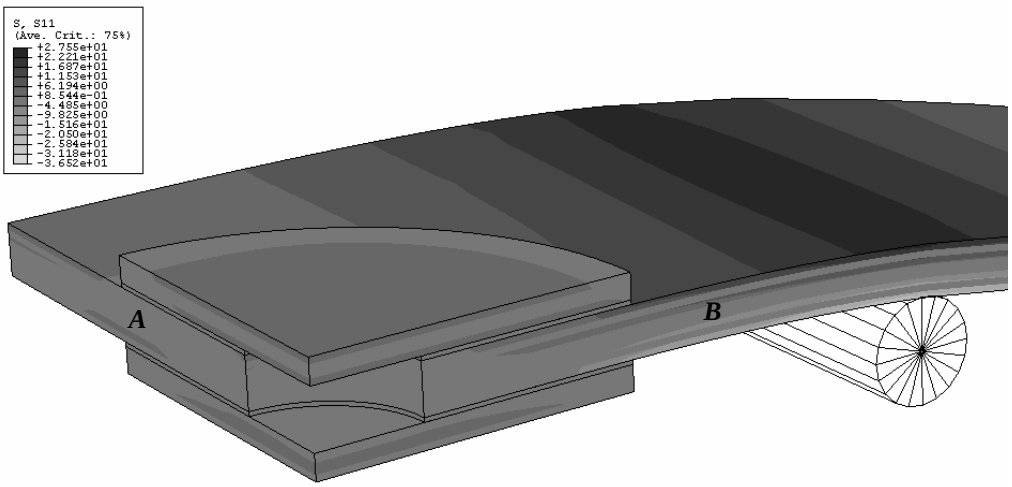

Fig. 222 – σ_x stresses at the repair region.

The σ_x compressive peak stresses at the symmetry plane ***A*** characteristic of SS repairs (Fig. 205) are eliminated with the DS repair technique (Fig. 222). This also applies to the σ_x stress fields for the tensile (Fig. 155) and compressive loaded (Fig. 189) DS repairs. Moreover, in contrast to the SS repairs under bending (Fig. 205) for which σ_x stresses peak near the overlap edges (plane ***B***), σ_x stresses are highest in the vicinity of the loading cylinder. σ_x tensile and compressive stresses are 19.2% and 26.2% higher than the corresponding SS ones, respectively, since the higher degree of reinforcement for this repair technique overloads the region near the loading cylinders (Fig. 222 compared to Fig. 205). σ_y stresses and σ_y stress distributions at three planes (planes P3, P4 and P5, Fig. 122) are plotted in Fig. 223 and Fig.

225 (a), respectively. Fig. 224 and Fig. 225 (b) present τ_{xy} stresses and τ_{xy} stress distributions at the same planes. The stress distributions concern the outer adhesive layer only, since σ_y stresses are antisymmetric between the two adhesive layers (Fig. 223), while shear stresses are identical (Fig. 224).

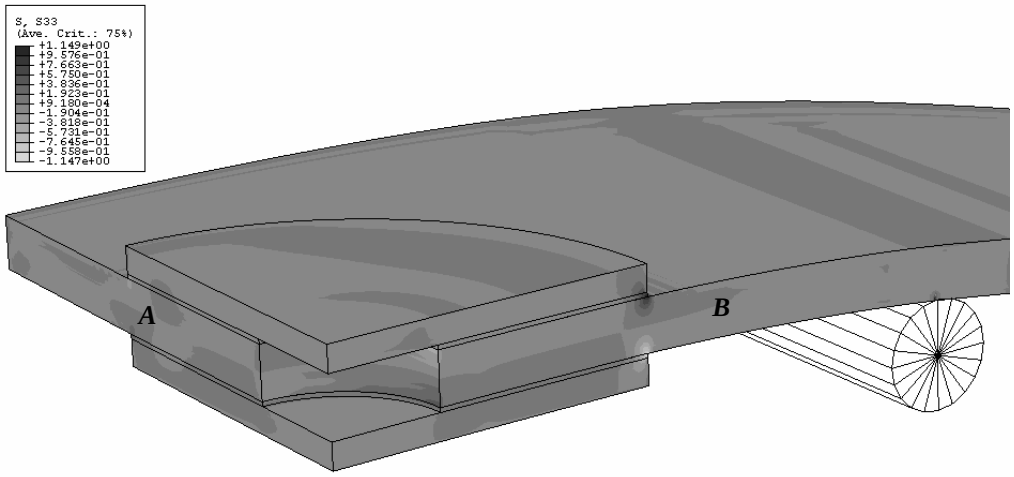

Fig. 223 – σ_y stresses at the repair region.

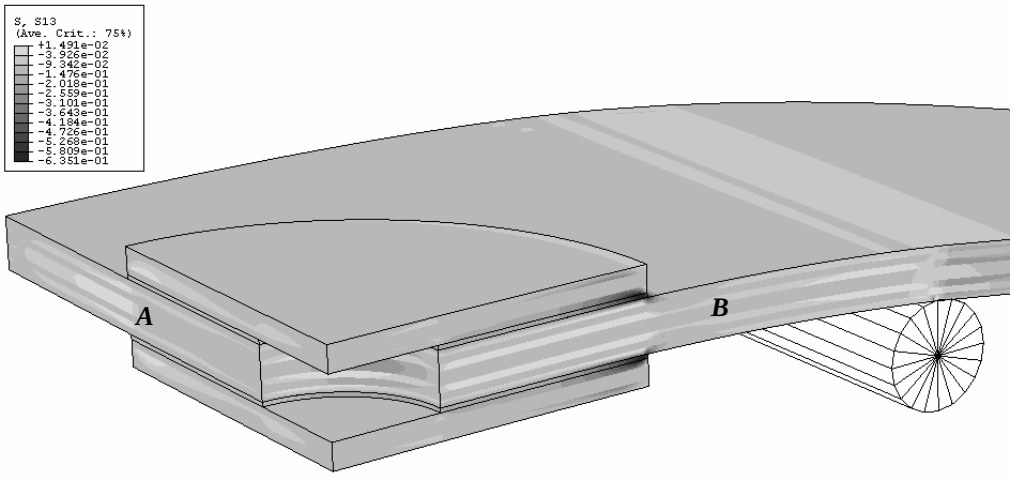

Fig. 224 – τ_{xy} stresses at the repair region.

The obtained σ_y stress profiles are identical to the SS ones under bending (Fig. 208 a). In addition, no significant difference exists between the three planes. Thus, σ_y stresses are negligible at the overlap central region, presenting a compressive peak at the IEO and a pronounced tensile one at the OEO, which diminishes from plane P3 to plane P5 (Dedale et al. 1981). At the inner adhesive layer σ_y stresses are antisymmetric to the ones presented in Fig. 225 (this is visible in Fig. 223), pointing towards damage onset at the outer patch. τ_{xy} stress distributions are also similar between planes P3, P4 and P5, showing identical profiles to the SS repairs under bending (Fig. 208 b). τ_{xy} stresses are reduced at the IEO, increasing gradually until peaking at the OEO (Dedale et al. 1981). The discontinuity at the OEO justifies the singularity at plane P3 (x/L_O=1). Compared to the equivalent SS repair, a higher magnitude normalized tensile peak develops at the OEO, owing to a reduction of stresses at the inner overlap region. Oppositely to the bending loading, the DS repairs under tension (Fig. 158) and compression (Fig. 192) reveal σ_y peak stresses at both overlap edges.

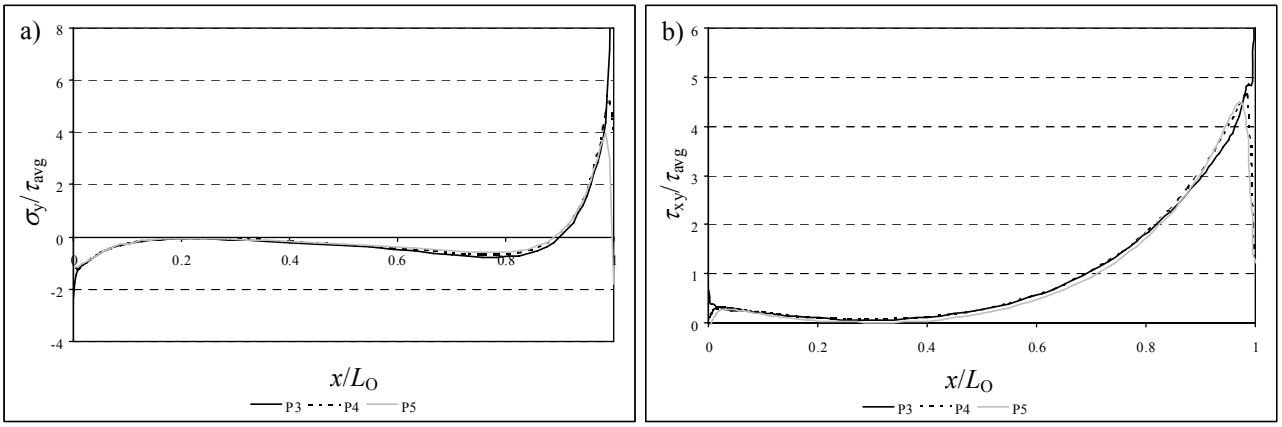

Fig. 225 – Normalized σ_y (a) and τ_{xy} (b) stress distributions at the repair region.

σ_y and τ_{xy} stress distributions are plotted in Fig. 226 and Fig. 227, respectively, at the seven planes of Fig. 122. σ_y stress distributions are similar to the SS ones (Fig. 209). σ_y peel peak stresses at the OEO and σ_y compressive ones at the IEO are higher at planes P3, P4 and P5. In the laminate and patch, σ_y stresses diminish outside the overlap region ($x/L_O<0$ and $x/L_O>1$). τ_{xy} stresses also compare reasonably to the SS repair ones (Fig. 210), with higher magnitude tensile peaks at the OEO at planes P3, P4 and P5. However, at planes P2 and especially P1 in the laminate, τ_{xy} stresses at the overlap central region are higher compared to the other considered locations. This behaviour, observed by comparing Fig. 224 and Fig. 207, is justified by the increase of the transmitted load through the laminate at the overlap region (caused by using two patches). Globally, the stress gradients between the seven planes follow the tensile (Fig. 159 and Fig. 160) and compressive (Fig. 193 and Fig. 194) DS results. Nevertheless, oppositely to these loadings, τ_{xy} stresses at planes P1 and P2 for the DS repair under bending are higher in magnitude than in the outer adhesive layer. This stress analysis indicates that damage will probably initiate in the adhesive layer at or near plane P3 at the OEO, since σ_y peel and τ_{xy} stress singularities develop at this region. The antisymmetry of σ_y stresses at the OEO between the outer an inner adhesive layers aids to damage initiation at the outer adhesive layer.

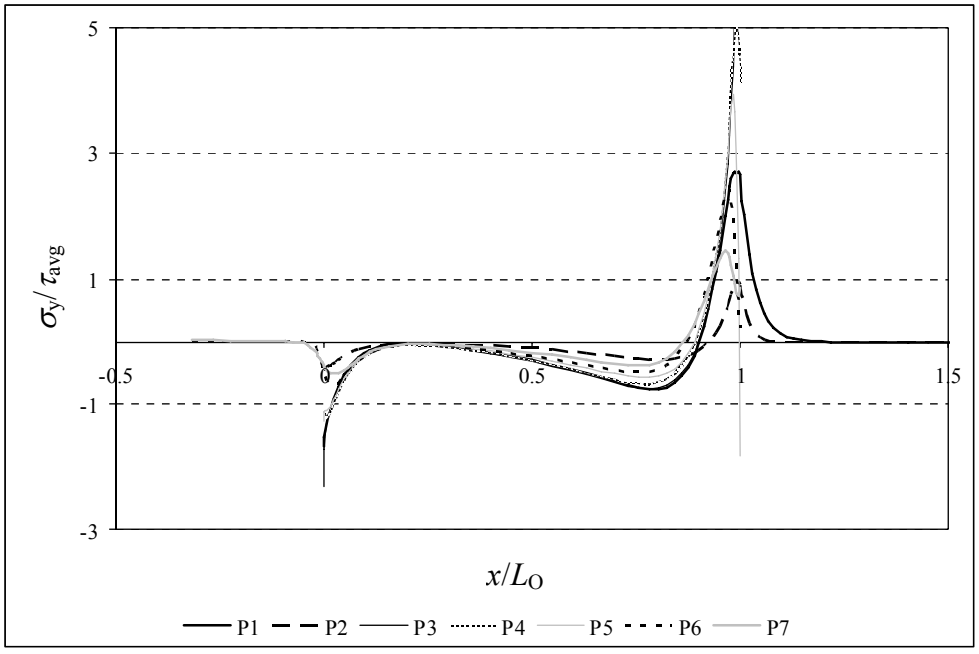

Fig. 226 – Normalized σ_y stress distributions at seven planes in the repair.

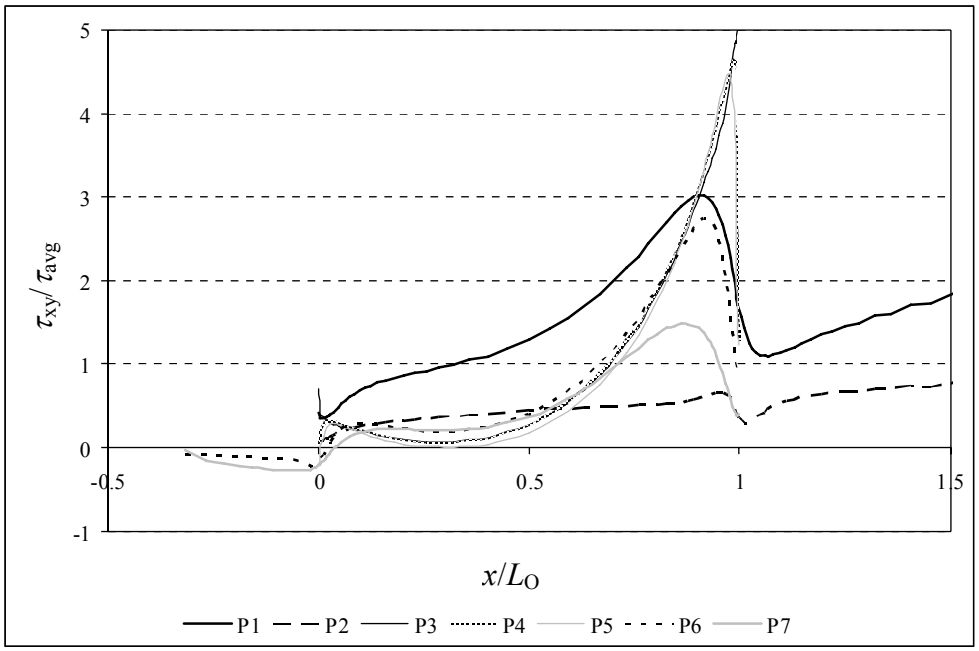

Fig. 227 – Normalized τ_{xy} stress distributions at seven planes in the repair.

4.3.5.1.2.1. Overlap length

σ_y and τ_{xy} stress distributions are plotted at planes P3, P4 and P5. Fig. 228 corresponds to plane P3 (laminate/adhesive interface), Fig. 229 to plane P4 (middle of the adhesive) and Fig. 230 to plane P5 (adhesive/patch interface).

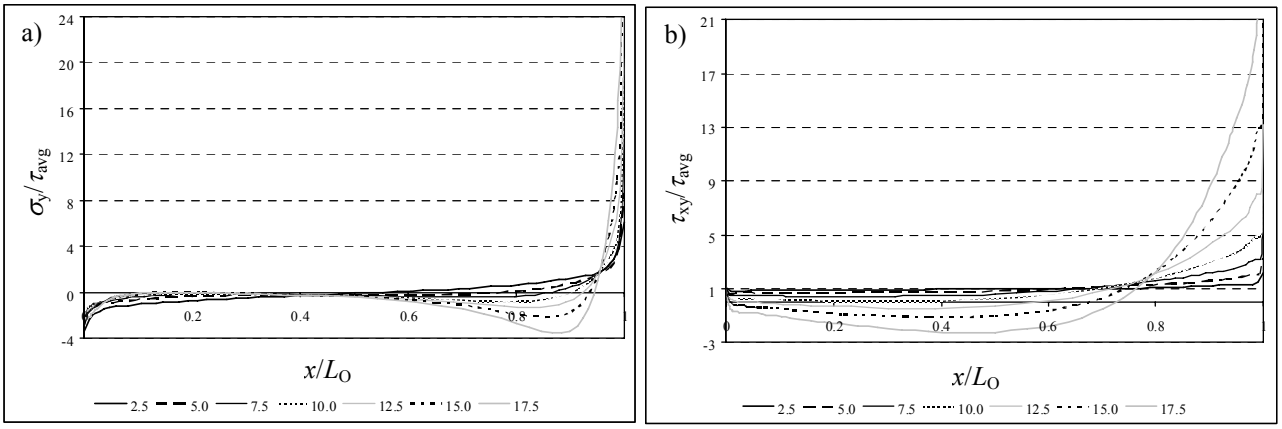

Fig. 228 – Normalized σ_y (a) and τ_{xy} (b) stress distributions at the laminate/adhesive interface (P3) as a function of L_O.

Similarly to the SS repairs (Fig. 211, Fig. 212 and Fig. 213), σ_y stresses are smaller in magnitude than τ_{avg}, except at the overlap edges, where pronounced peaks are observed. At the OEO, σ_y peel peak stresses increase in magnitude with L_O. At the overlap outer region, compressive regions develop for the bigger values of L_O. σ_y compressive peak stresses of smaller magnitude are registered at the IEO. Between the three planes, σ_y peel peak stresses at the OEO diminish in magnitude from plane P3 (stress singularity at x/L_O=1) to plane P5. σ_y peak stresses at the overlap edges are identical in magnitude to the SS ones under bending (Fig. 211 (a), Fig. 212 (a) and Fig. 213 (a)). However, the compression portion at the overlap outer region, for the bigger values of L_O, is larger for the DS repairs.

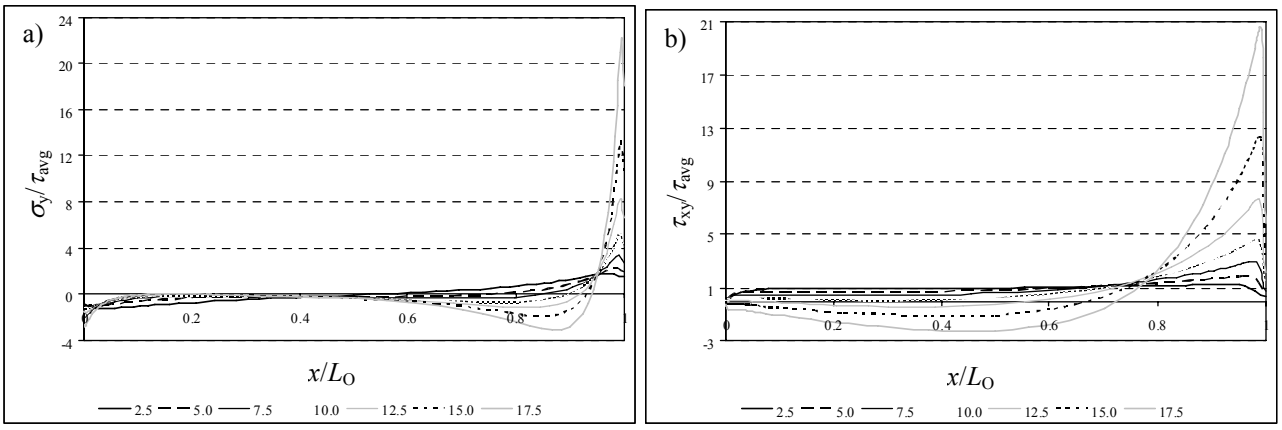

Fig. 229 – Normalized σ_y (a) and τ_{xy} (b) stress distributions at the middle of the adhesive (P4) as a function of L_O.

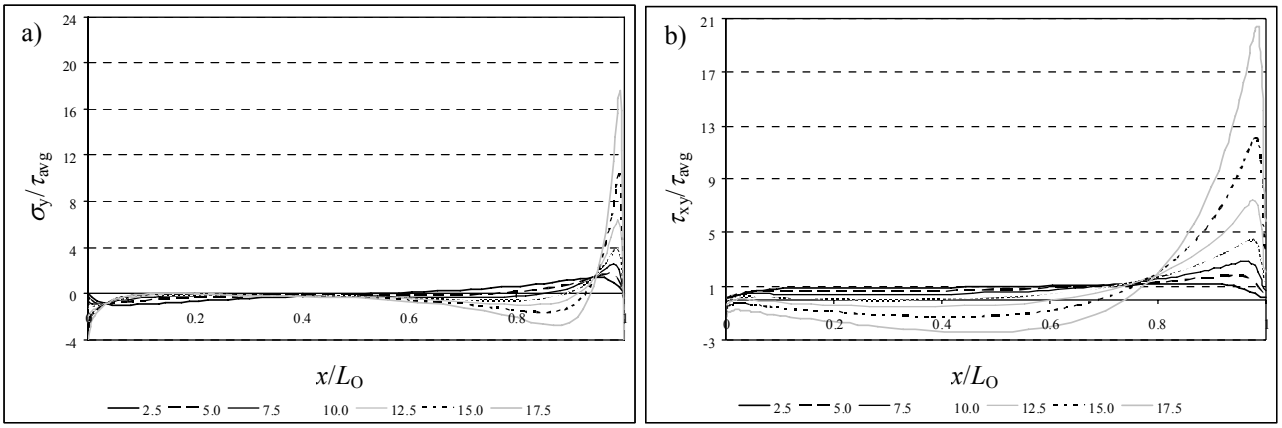

Fig. 230 – Normalized σ_y (a) and τ_{xy} (b) stress distributions at the adhesive/patch interface (P5) as a function of L_O.

τ_{xy} stresses peak at the OEO and are approximately constant at the overlap inner region. τ_{xy} stress distributions are similar between the three planes, with the exception of a stress singularity at plane P3 (OEO). Identically to the SS repairs under bending (Fig. 211 (b), Fig. 212 (b) and Fig. 213 (b)), whilst τ_{xy} stress profiles are more uniform for L_O=2.5 mm, the increase of L_O gives rise to τ_{xy} peak stresses of increasing magnitude at the OEO. Apart from slightly different stress distributions than the DS repairs under tension (Fig. 161, Fig. 162 and Fig. 163) or compression (antisymmetric σ_y stresses and equal τ_{xy} stresses to the tensile ones), an identical tendency was found. In fact, also for the tensile and compressive loadings, σ_y and τ_{xy} peak stresses increased in magnitude with L_O. The results presented here indicate that the repairs strength probably is not proportional to L_O, since σ_y peel and τ_{xy} peak stresses at the OEO increase in magnitude with this quantity, which may induce a premature damage at this region for the bigger values of L_O.

4.3.5.1.2.2. Patch thickness

σ_y and τ_{xy} stress distributions are plotted in Fig. 231, Fig. 232 and Fig. 233, corresponding to planes P3 (laminate/adhesive interface), P4 (middle of the adhesive) and P5 (adhesive/patch interface), respectively.

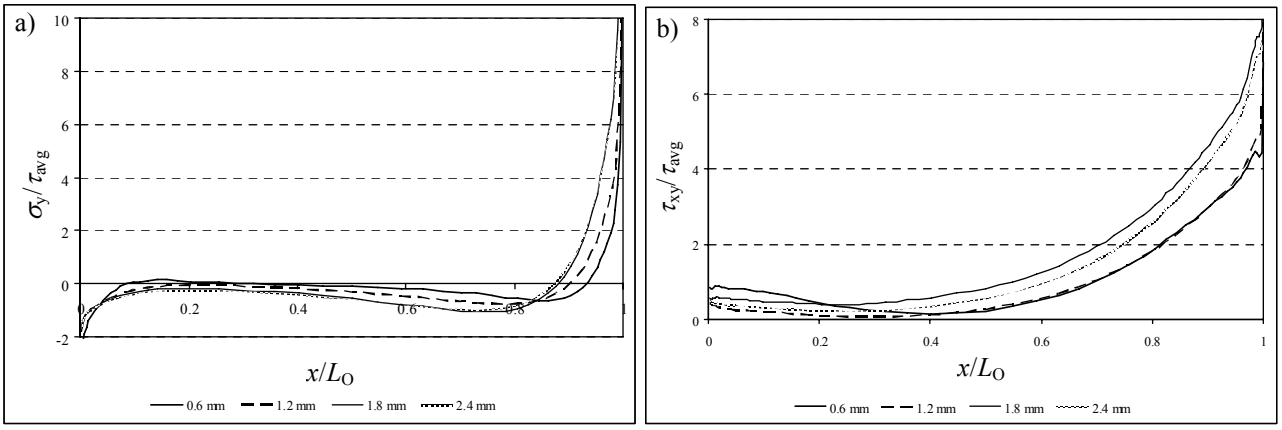

Fig. 231 – Normalized σ_y (a) and τ_{xy} (b) stress distributions at the laminate/adhesive interface (P3) as a function of t_H.

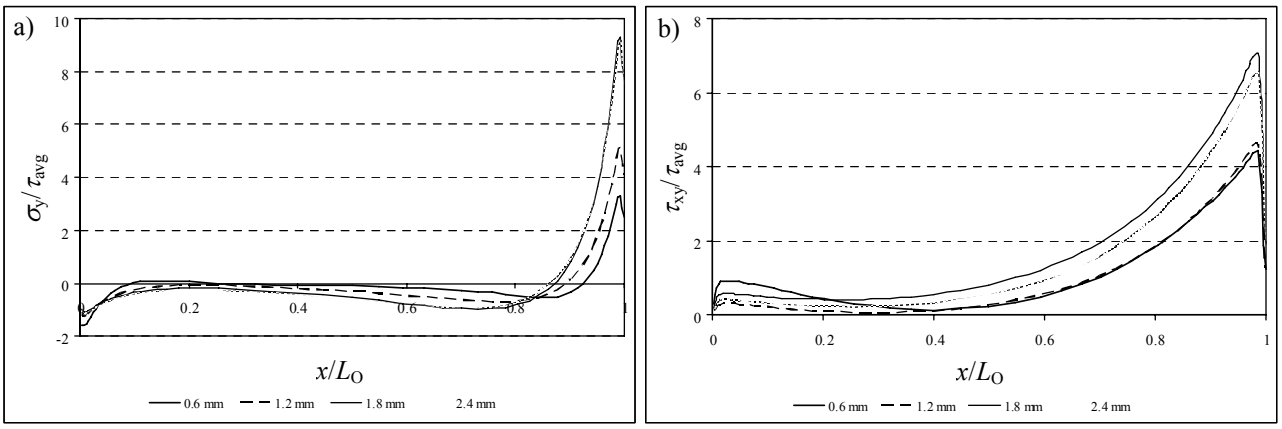

Fig. 232 – Normalized σ_y (a) and τ_{xy} (b) stress distributions at the middle of the adhesive (P4) as a function of t_H.

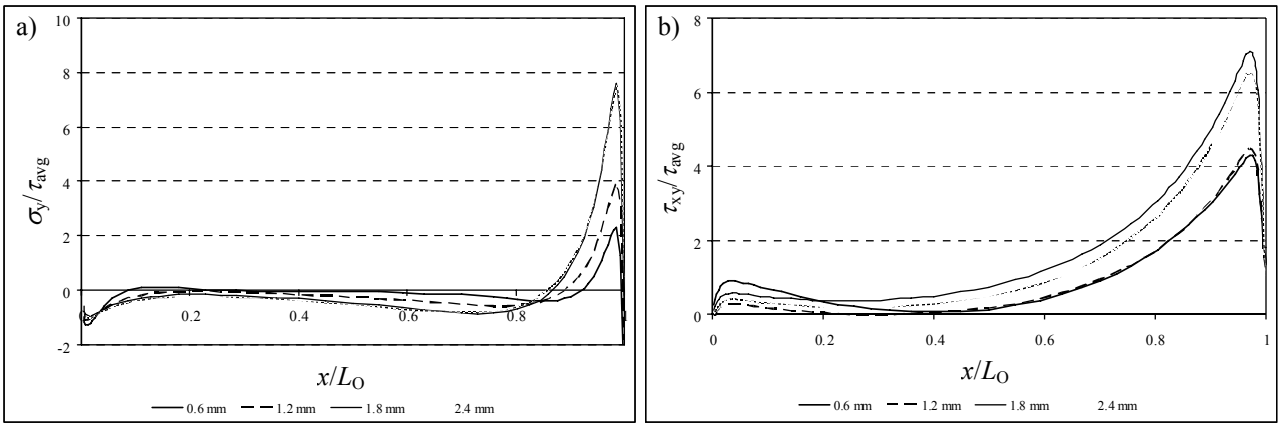

Fig. 233 – Normalized σ_y (a) and τ_{xy} (b) stress distributions at the adhesive/patch interface (P5) as a function of t_H.

σ_y stress distributions are identical to the SS repairs profiles under bending (Fig. 214 (a), Fig. 215 (a), Fig. 216 (a)). Thus, they reveal a minor concentration of compressive stresses at the IEO. σ_y peel peak stresses at the OEO also increase in magnitude with t_H. Conversely, for the DS repairs, σ_y peel peak stresses at the OEO are higher in magnitude and are limited to a more restricted region. Equally to the SS repairs, t_H=1.8 mm and 2.4 mm distributions are indistinguishable. σ_y peak stresses at the overlap edges diminish from plane P3 to plane P5. These results show that thicker patches are prone to induce delaminations in the laminate or outer patch. τ_{xy} stresses also showed similar

profiles to the SS repairs (Fig. 214 (b), Fig. 215 (b), Fig. 216 (b)). However, τ_{xy} stresses for the DS repairs are practically nil at the overlap central region, while τ_{xy} peak stresses at the OEO are higher in magnitude. τ_{xy} peak stresses also diminish from plane P3 to plane P5. σ_y and especially τ_{xy} stresses differ to the DS repair ones under tension and compression (Fig. 164, Fig. 165 and Fig. 166 for the tensile load). Despite this fact, also for these loadings, the bigger values of t_H showed to be prejudicial, leading to higher magnitude peak stresses at the OEO. Therefore, the 0.6 and 1.2 mm values of t_H are recommended based on this stress analysis instead of the bigger values, which are likely to induce premature failure at the OEO due to the correspondingly higher magnitude of stresses.

4.3.5.1.2.3. Adhesive thickness

Fig. 217, Fig. 218 and Fig. 219 show σ_y and τ_{xy} stress distributions at planes P3 (laminate/adhesive interface), P4 (middle of the adhesive) and P5 (adhesive/patch interface), respectively.

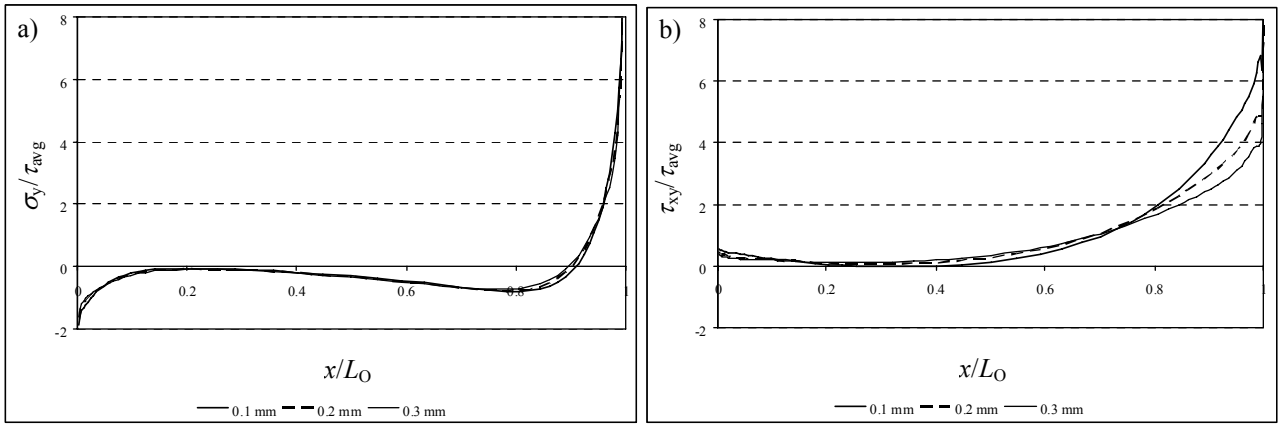

Fig. 234 – Normalized σ_y (a) and τ_{xy} (b) stress distributions at the laminate/adhesive interface (P3) as a function of t_A.

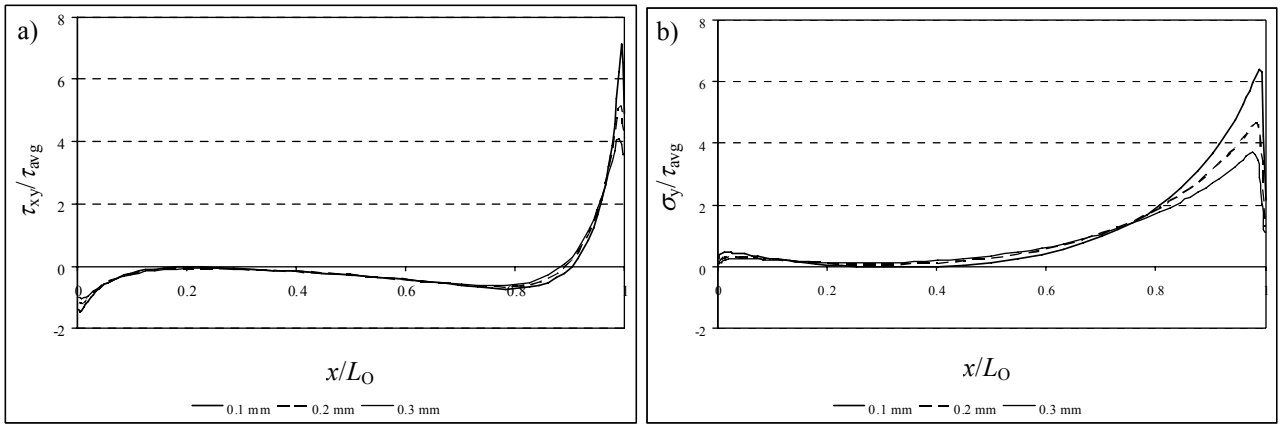

Fig. 235 – Normalized σ_y (a) and τ_{xy} (b) stress distributions at the middle of the adhesive (P4) as a function of t_A.

σ_y stress distributions are identical to the SS repairs under bending (Fig. 217 (a), Fig. 218 (a) and Fig. 219 (a)), although with higher magnitude peaks at the OEO. Owing to this similarity, σ_y stresses are also practically nil at the overlap central region, peaking at the overlap edges (compressive at the IEO and tensile at the OEO). The value of t_A mainly affects σ_y stresses at the OEO, with bigger values reducing σ_y peel peak stresses. On the other hand, at the overlap

central region and at the IEO, t_A has a minor influence. At the laminate/adhesive interface (plane P3), σ_y a stress singularity exists at the overlap edges. In agreement with the previous analyses, these stresses diminish in magnitude at the overlap edges from plane P3 to plane P5.

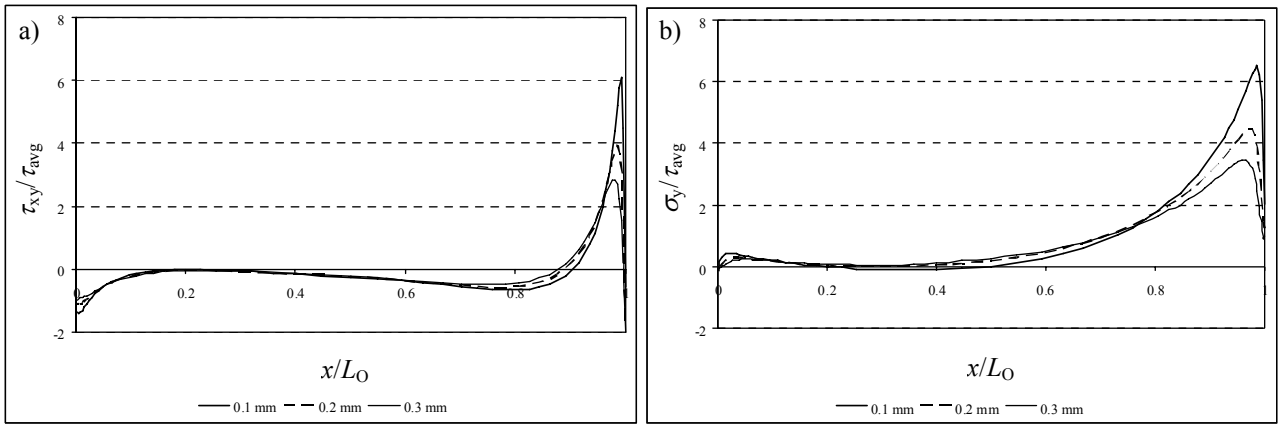

Fig. 236 – Normalized σ_y (a) and τ_{xy} (b) stress distributions at the adhesive/patch interface (P5) as a function of t_A.

τ_{xy} stress distributions are similar to the SS ones under a bending load (Fig. 217 (b), Fig. 218 (b) and Fig. 219 (b)). These are negligible at the overlap inner region, increasing progressively from $x/L_O \approx 0.5$ towards the OEO. Equally to σ_y stresses, the value of t_A only affects τ_{xy} stresses at the OEO, with τ_{xy} peak stresses diminishing with t_A. These stresses also become smaller from the stress singularity region (plane P3) to plane P5. Identical peak stresses reduction trends with t_A are observed for the corresponding tension and compression profiles (Fig. 167, Fig. 168 and Fig. 169 show tensile stresses). The documented tendency points towards an increasing strength of the repairs with t_A.

4.3.5.2. Failure analysis

4.3.5.2.1. Mechanical behaviour

The bending tests showed that the failure modes and value of P_m are ruled by patch debonding. In fact, a premature patch debonding occurred prior to damage initiation in the laminate for some repair geometries, leading to a value of P_m similar to the open-hole laminate. For the remaining repair geometries, patch debonding initiated simultaneously or after damage in laminate, increasing P_m. The experimental damage mechanisms under bending are initially characterized, prior to the description of the failure modes.

- **Partial compression failure in the laminate**. Fracture in the laminate face under compression, consisting on a compressive failure of the two superficial 0º plies near plane ***A*** (Fig. 123) on one of the hole sides. No delamination between plies was detected accompanying this event. Fig. 237 (a) shows an open-hole laminate during the test, after a partial compression failure.
- **Compression failure in the laminate with delamination**. This damage mechanism is similar to the previous one, but extends to all the laminate width. Delaminations between differently oriented plies near the hole region are identified simultaneously to the transverse failure. The previously mentioned damage mechanism

ends up invariably with this scenario. In this case, damage in the laminate occurs in two steps. Fig. 237 (b) corresponds to the same specimen of Fig. 237 (a). After a partial compression failure, this specimen failed concurrently by compression and delamination between the loading cylinders.

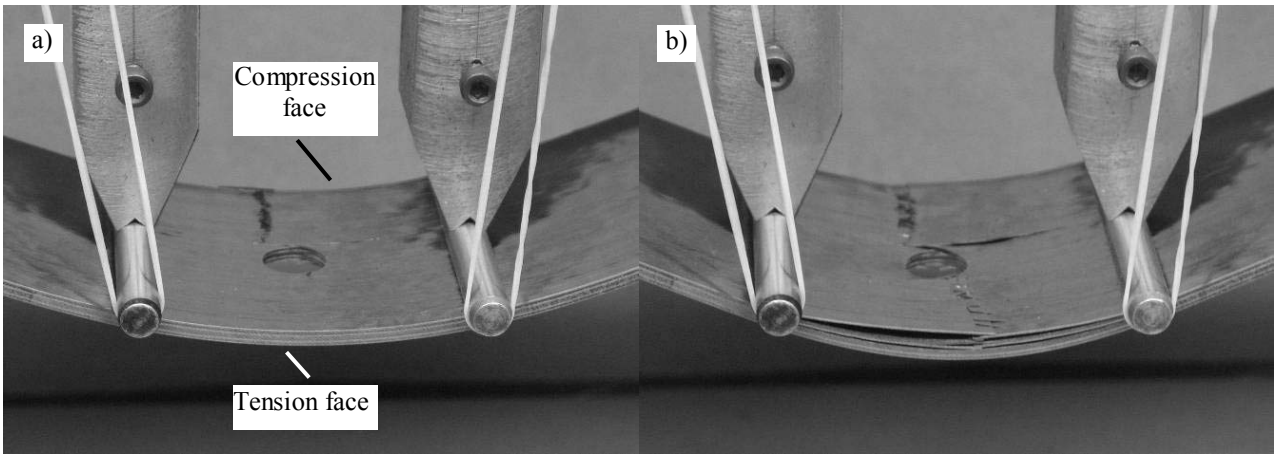

Fig. 237 – Partial compression failure (a) and compression failure with delamination (b) for an open-hole laminate.

- **Outer patch partial debonding**. In some of the geometries, a partial cohesive failure of the outer patch adhesive layer at the OEO (plane ***B***, Fig. 123) occurred prior to damage in the laminate, leading to a minor stiffness reduction of the repair. Fig. 238 (a) and (b) pertain to a L_O=10 mm DS repair.

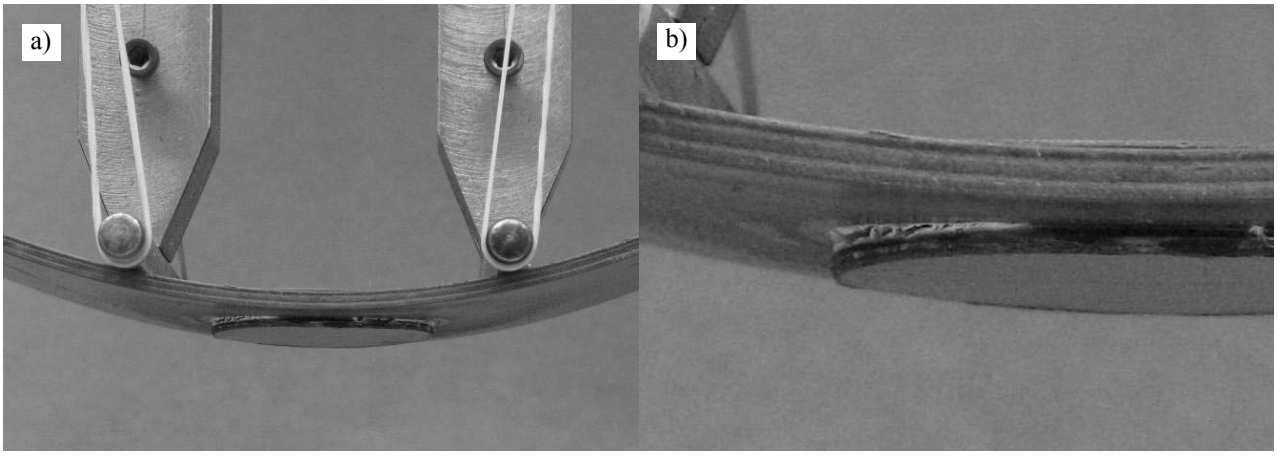

Fig. 238 –Outer patch partial debonding (a) and respective detail (b) for a L_O=10 mm DS repair.

- **Outer patch debonding**. Consists on a cohesive failure of the outer patch adhesive layer, leading to an almost complete debonding of the patch. After this event, a SS repair behaves similarly to an open-hole laminate. Fig. 239 (a) represents a t_H=1.8 mm SS repair after outer patch debonding.
- **Inner patch debonding**. This event always occurred simultaneously or after outer patch debonding, consisting on patch debonding at the compression face of a DS repair. The example of Fig. 239 (b) concerns a L_O=5 mm DS repair which initially suffered an outer patch debonding and, at a more advanced load stage, experienced debonding of the inner patch.
- **Simultaneous patch, compression and delamination failure**. Under these circumstances, no damage in the specimens was detected until P_m was reached (except outer patch partial debonding in some cases). At that

stage the patch (SS repairs) or patches (DS repairs) debonded simultaneously with a compression failure with delamination in the laminate. Fig. 240 refers to a L_O=10 mm DS repair after this occurrence.

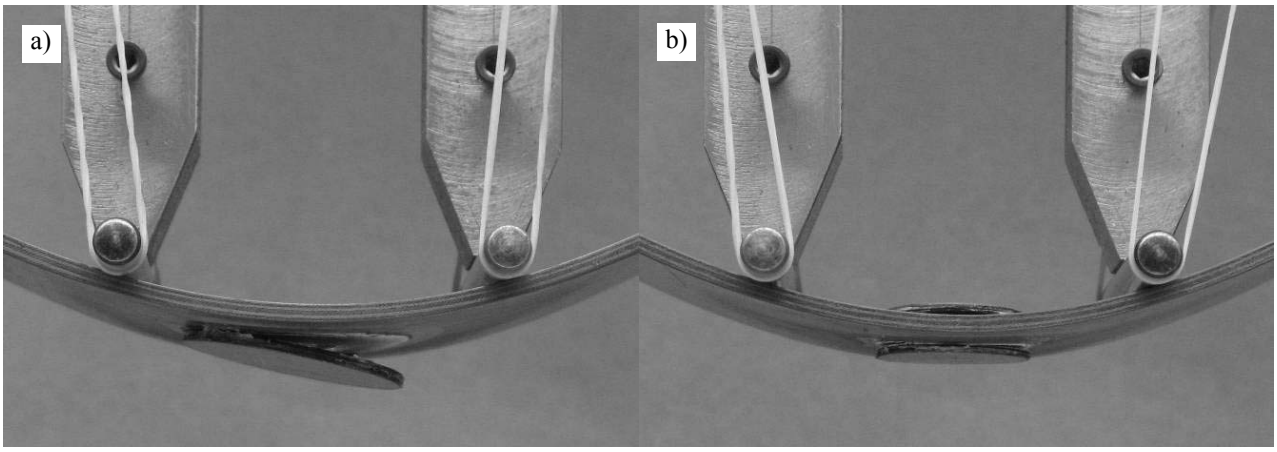

Fig. 239 –Outer patch debonding for a t_H=1.8 mm SS repair (a) and inner patch debonding for a L_O=5 mm DS repair (b).

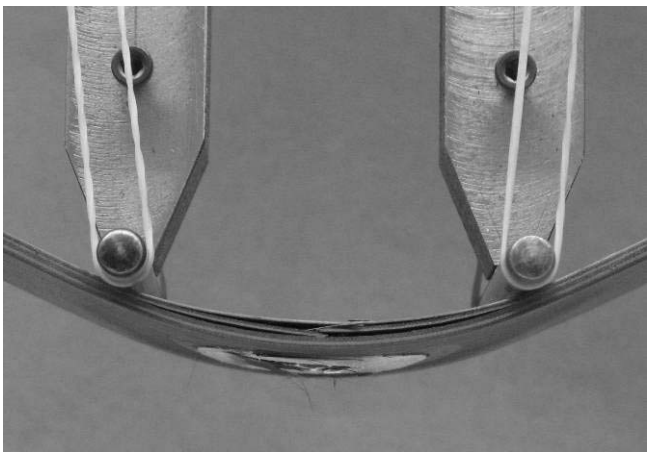

Fig. 240 – Simultaneous patch, compression and delamination failure for a L_O=10 mm DS repair.

On all patch debonding episodes, failure was essentially cohesive in the adhesive layer. Fig. 241 shows two examples of cohesive failures for a L_O=10 mm (a) and a t_H=1.8 mm (b) SS repair.

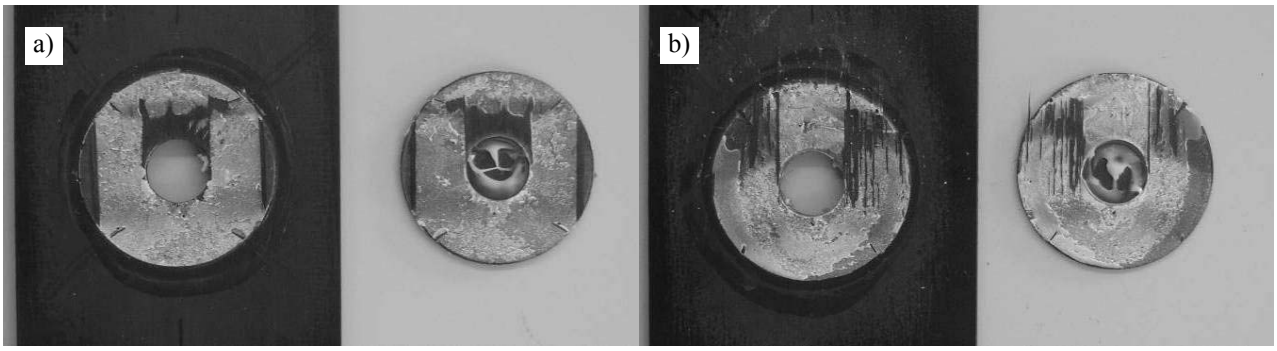

Fig. 241 – Cohesive failure of the adhesive layer for a L_O=10 mm (a) and t_H=1.8 mm (b) SS repair.

The damage mechanisms of the repairs are summarized in Table 17 and Table 18 as a function of the values of L_O and t_H, respectively. **In the cases where two damage mechanisms are mentioned for a given repair geometry**

(separated by the dashed lines), the first damage mechanism corresponds only to a drop of the repair stiffness, with the second damage mechanism corresponding to P_m. Additionally, despite compression failure with delamination being mentioned in some of the repair geometries as the mechanism leading to P_m, indeed for some specimens this event occurred in two steps (Fig. 237 (a) and (b)).

Table 17 – Failure modes of the repairs as a function of L_O.

L_O	5 mm	10 mm	15 mm
SS repairs	Outer patch debonding Compression failure with delamination	Outer patch debonding Compression failure with delamination	Outer patch debonding Compression failure with delamination
DS repairs	Outer patch partial debonding, outer patch debonding and inner patch debonding Compression failure with delamination	Outer patch partial debonding Patch debonding and compression failure with delamination	Patch debonding and compression failure with delamination

- The open-hole laminates failed by compression with delamination (Fig. 237 b), after a predominantly elastic behaviour up to P_m.
- The SS repairs behaved similarly for all the values of L_O (Table 17), with a premature outer patch debonding event (Fig. 239 a) occurring at a significantly lower load than the value of P_m for the open-hole laminate. Moreover, this occurred at gradually smaller values of P with L_O, which can be explained by a corresponding increase of the σ_y peel and τ_{xy} peak stresses at the particular region (OEO) where partial patch debonding initiates (Fig. 211, Fig. 212 and Fig. 213). Owing to this behaviour, values of P_m similar to the open-hole laminate ones are expected, since failure occurs by compression failure with delamination (Fig. 237 b) after patch debonding.
- For the L_O=5 mm DS repair, three premature damage events were observed by the following order: outer patch partial debonding (Fig. 238 (a) and (b)), outer patch debonding (Fig. 239 a) and inner patch debonding (Fig. 239 b). P_m corresponds to compression failure with delamination, identified only at a higher value of P. An approximate open-hole P_m value is thus expected.
- The L_O=10 mm DS repair showed an outer patch partial debonding (Fig. 238 (a) and (b)) as the only damage mechanism prior to P_m, which occurs by simultaneous patch debonding and compression failure with delamination (Fig. 240). The modification of the failure mode is caused by the larger adhesive area, which increases the bending capabilities of the patches prior to debonding. The simultaneous patch and compression failure will probably increase P_m, compared to the open-hole laminate.
- For the L_O=15 mm DS repair, no premature damage mechanisms were observed experimentally prior to P_m, which corresponded to a simultaneous debonding of the two patches and compression failure with delamination (Fig. 240). This different behaviour of the DS repairs with L_O superimposes to the increase of the peak stresses at the OEO with L_O (Fig. 228, Fig. 229 and Fig. 230), since it depends on stresses along the entire overlap region (oppositely to the patch partial debonding, which depends on the peak stresses at the OEO).

- The same behaviour was identified for the SS repairs, regardless the value of t_H. In fact, in all cases damage initiated with outer patch debonding (Fig. 239 a), while P_m corresponded to compression failure with delamination (Fig. 237 b), equally to the open-hole laminate. The experimental observations showed that the premature patch debonding corresponded to gradually smaller loads as t_H increased (average values of approximately 1700N, 1500N, 1000N and 800N for the t_H=0.6, 1.2, 1.8 and 2.4 mm repairs, by the respective order). This is caused by the increase on patch stiffness and corresponding higher magnitude of σ_y peak stresses at the OEO and τ_{xy} ones at the overlap outer region (Fig. 214, Fig. 215 and Fig. 216). Due to the premature patch debonding, no P_m improvement is expected, compared to the open-hole laminate.

On the other hand, t_H significantly influences the failure mode of the DS repairs.

Table 18 – Failure modes of the repairs as a function of t_H.

t_H	0.6 mm	1.2 mm	1.8 mm	2.4 mm
SS repairs	Outer patch debonding Compression failure with delamination	Outer patch debonding Compression failure with delamination	Outer patch debonding Compression failure with delamination	Outer patch debonding Compression failure with delamination
DS repairs	Compression failure with delamination	Outer patch partial debonding Patch debonding and compression failure with delamination	Outer patch partial debonding Patch debonding and compression failure with delamination	Outer patch partial debonding

- No patch debonding was observed for the t_H=0.6 mm DS repair up to P_m. This can be justified by the bigger patch flexibility, which leads to smaller magnitude σ_y peak stresses at the OEO and τ_{xy} ones at the overlap outer region (Fig. 231, Fig. 232 and Fig. 233).
- For both t_H=1.2 and 1.8 mm DS repairs, initially the outer patch partially debonded (Fig. 238 (a) and (b)). P_m corresponds to simultaneous patch debonding and compression failure with delamination (Fig. 240).
- For the biggest value of t_H (2.4 mm), P_m is governed by outer patch partial debonding (Fig. 238 (a) and (b)). Due to the bigger patch stiffness, the outer patch debonds completely just after this occurrence (Fig. 239 a), followed by compression failure with delamination (Fig. 240). Equally to the SS repairs, the outer patch debonding events were identified for gradually smaller values of P with L_O (Table 18), due to the increase of peak stresses at the OEO with t_H (Fig. 231, Fig. 232 and Fig. 233).

It should be emphasized that, for all the DS repairs, outer patch debonding always occurred before or simultaneously to inner patch debonding. The observed σ_y peel peak stresses at the OEO for the outer patch, opposed to the σ_y compressive ones for the inner patch, justify this behaviour (Fig. 228, Fig. 229 and Fig. 230 show stresses at the outer patch was a function of L_O; Fig. 231, Fig. 232 and Fig. 233 correspond to t_H).

To predict numerically a compression failure with delamination under bending, a similar procedure to the one described in Sub-Section 4.3.4.2.1 will be used. Therefore, the experimental average value of δ for the open-hole

laminates tested leading to compression failure was firstly calculated. This value was then used to estimate numerically the respective value of $\sigma_{x\,avg}$ at the two superficial 0º plies in the laminate face under compression. In the numerical models simulating the different repair geometries, compression failure was considered to occur when $\sigma_{x\,avg}$ in the mentioned plies was attained. This methodology was followed due to an experimentally observed simultaneous failure in these plies, even though in some cases on only half of the repairs width (Fig. 237 (a) and (b)). With this approach, the numerical simulations showed a good correspondence with the experimental behaviour of the repairs described in Table 17 and Table 18. In fact, numerically a premature outer patch debonding event occurred for practically all the geometries tested. The t_H=0.6 mm DS repair is the exception to this behaviour. The L_O=15 mm DS repair, which experimentally failed simultaneously by patch debonding and compression failure in the laminate with delamination without previous visible damage (Fig. 240), in the numerical simulations showed a premature outer patch partial debonding at the OEO. However, this occurred near P_m.

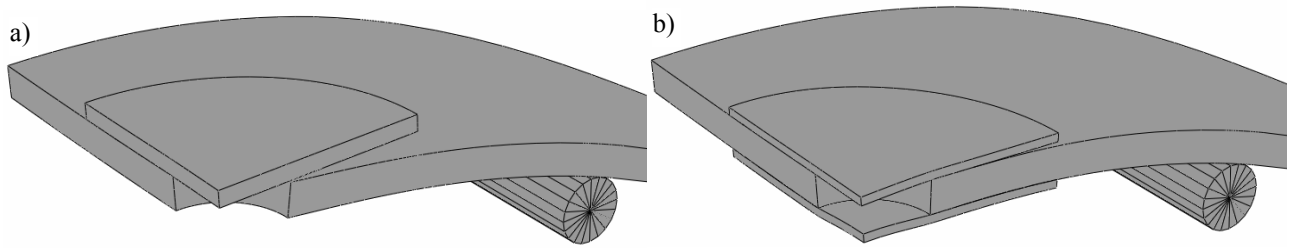

Fig. 242 – Deformed configuration of the L_O=10 mm SS (a) and t_H=0.6 mm DS (b) repairs.

Fig. 242 shows the deformed configuration of the L_O=10 mm SS (a) and t_H=0.6 mm DS repairs (b), at the predicted compression failure, calculated from $\sigma_{x\,avg}$. For the L_O=10 mm SS repair, a premature outer patch debonding event had already took place (Table 17). For the t_H=0.6 mm DS repair, the patches are still intact when P_m is attained. These results agree with the experimental observations. Fig. 243 compares the experimental and numerical P-δ curves for the t_H=0.6 mm (a) and L_O=10 mm (b) DS repairs.

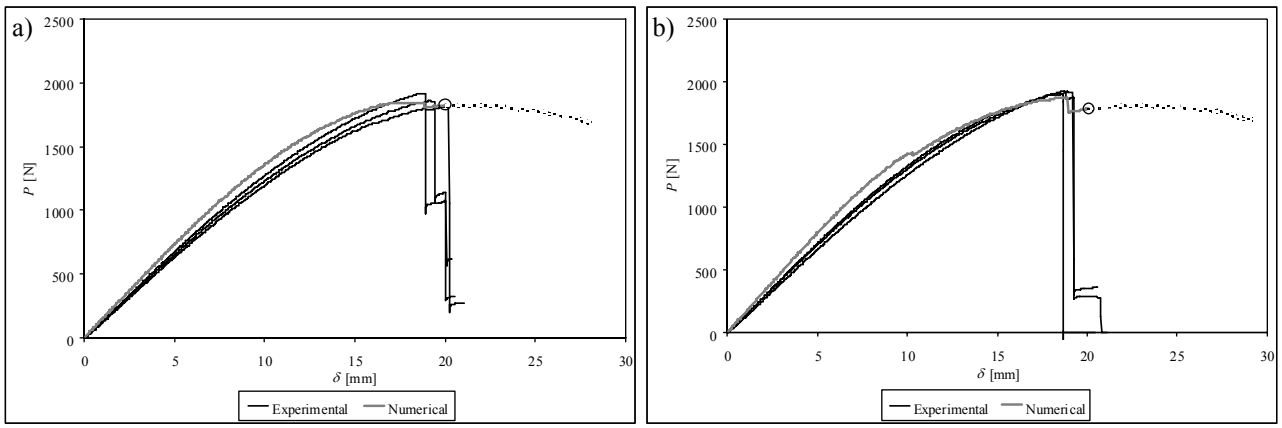

Fig. 243 – Experimental and numerical P-δ curves comparison for the t_H=0.6 mm (a) and L_O=10 mm (b) DS repairs.

- The experimental P-δ curves of the t_H=0.6 mm DS repairs (Fig. 243 a) show a smooth increase of P up to failure. P_m corresponded to compression failure with delamination, with only minor damage in the adhesive layer at this stage (Table 18). This behaviour, oppositely to the other repair geometries, in which the adhesive failed prior to $\sigma_{x\,avg}$, occurred due to the bigger flexibility of the patches. The numerical P-δ curve shows an

accurate prediction (the circle marks in the numerical P-δ curves correspond to the compression failure prediction). However, for this repair geometry, numerically the outer patch partially debonded before the compression failure prediction (Fig. 242 b). This contradicts the experimental observations and can be identified in Fig. 243 (a) as a drop of P near P_m.

In all of the repair geometries tested, the numerical patch debonding events took place slightly before the respective experimental observation. Under a bending load, the OEO is the critical stress region where damage is prone to initiate (Fig. 208, SS repairs and Fig. 225, DS repairs). Consequently, it is expected that the minor adhesive excess at the OEO during the repairs manufacture slightly increases the experimental values of *P* corresponding to patch debonding, due to a reduction of stresses at this particular region (Apalak and Engin 2004, Andreassi et al. 2007, Deng and Lee 2008).

- The numerical P-δ curve for the L_O=10 mm SS repair also agreed with the respective experiments (Fig. 243 b). Numerically, the outer patch partial debonding event preceding P_m occurred more abruptly at $\delta \approx 10$ mm. In the experiments, this occurred gradually and for slightly bigger values of displacement. Experimentally, P_m occurred due to compression failure with delamination for the three specimens tested (Table 17). In the numerical simulation, the outer patch debonded before the compression failure prediction.
- The experimental and numerical P-δ curves for the t_H=1.8 mm and t_H=2.4 mm SS repairs are presented in Fig. 244 (a) and (b), respectively. An analogous behaviour is acknowledged for these two geometries, with a premature outer patch debonding prior to P_m (Table 18). However, for the t_H=2.4 mm SS repair this event occurred for smaller values of P, due to a correspondingly higher patch stiffness. In both repairs of Fig. 244, the numerical patch debonding occurred prior to the experiments. P_m occurred by compression failure with delamination (Fig. 237 b), equally to the open-hole laminate. Under these circumstances, values of P_m similar to the open-hole laminate are expected.

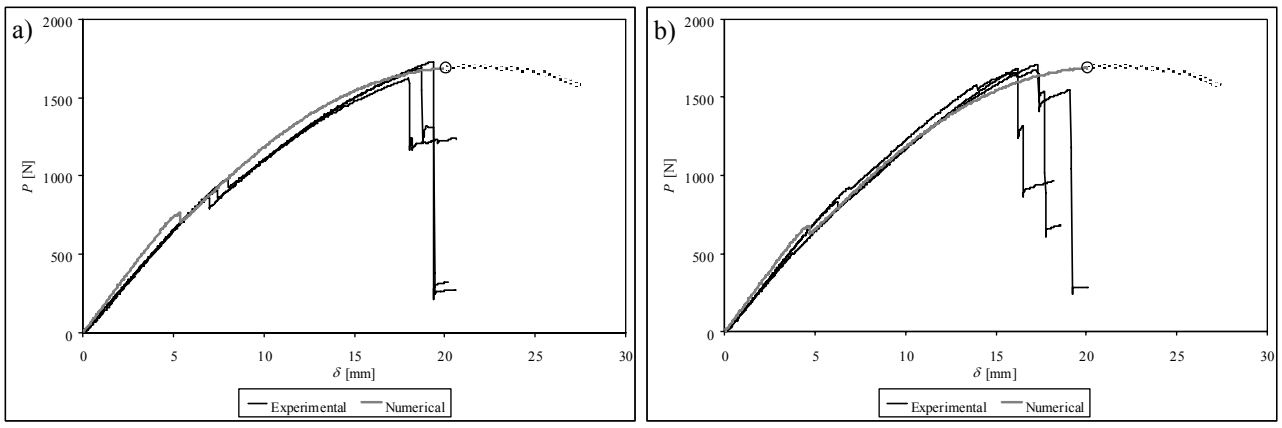

Fig. 244 – Experimental and numerical P-δ curves comparison for the t_H=1.8 mm (a) and t_H=2.4 mm (b) SS repairs.

It should be emphasized that the stiffness deviation up to P_m between the experimental and numerical P-δ curves of Fig. 243 and Fig. 244 is caused by an initially higher compliance of the experimental curves, due to the adjustment of the testing device (Fig. 135). Owing to this fact, in the evaluation of the experimental values of K, which will be presented further in this work, this initial part of the curves was neglected.

4.3.5.2.2. Summary of the results

The comparison between the experimental and numerical values of K and P_m is presented in Fig. 245 and Fig. 246, respectively, as a function of L_O and t_H. The standard deviation of the average experimental values for each quantity is also presented. It was found that L_O greatly influences K, for both SS and DS repairs (Fig. 245 a). Indeed, K gradually increases with L_O. DS repairs present also an increasing difference to the corresponding SS repairs with L_O. This tendency was expected, due to the increase of the cross-sectional area and second moment of inertia of the repairs with L_O, which govern the bending stiffness of structures (Olia and Rossetos 1996). This also applies to the difference between the SS and DS repairs. The enlargement of the region stiffened by the patches also contributes to the increasing tendency of K for the SS repairs. The value of t_H shows a fading effect on K as t_H increases, which can be interpreted in light of the transmitted loads by the adhesive layer, attaining a constant magnitude for the bigger values of t_H (Fig. 214, Fig. 215 and Fig. 216 show this trend for the SS repairs, while Fig. 231, Fig. 232 and Fig. 233 pertain to the DS repairs). In addition, a similar difference on K is identified between the equivalent SS and DS repairs. The results of Fig. 245 globally show an accurate numerical prediction of K for the values of L_O and t_H evaluated.

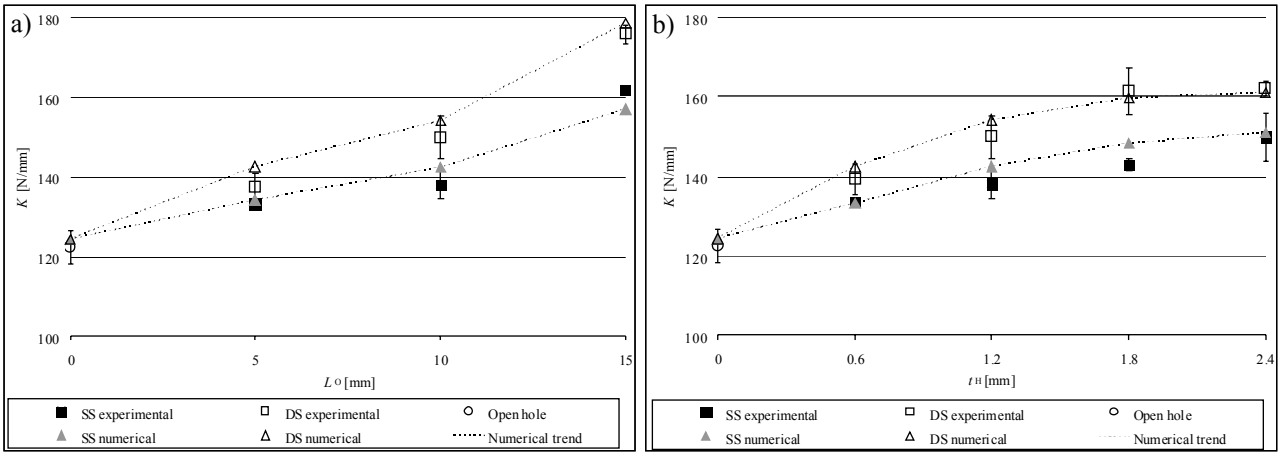

Fig. 245 – K as a function of L_O (a) and K as a function of t_H (b).

Fig. 246, concerning the evolution of P_m with L_O and t_H, shows that the SS repairs are always ineffective, disregarding the geometry, since they present values of P_m similar to the open-hole laminate. This was expected, since for all SS repairs outer patch debonding took place at smaller loads than the value of P_m for the open-hole laminate (Table 17 and Table 18). On the other hand, a completely different behaviour was observed for the DS repairs. In fact, an increasing trend of P_m was found as a function of L_O, starting from the L_O=5 mm repair (Fig. 246 a). For this repair, an identical value of P_m to the SS repairs was attained, since both outer and inner patches debonded prior to P_m (Table 17), leading to an approximate open-hole value of P_m. For the bigger L_O DS repairs, P_m corresponded to simultaneous patch debonding and compression failure with delamination events (Table 17). As a result, an increasing trend of P_m with L_O was observed. The value of t_H showed a smaller effect on P_m, with the t_H=0.6 and 2.4 mm DS repairs presenting slightly smaller values than the ones in-between. For the t_H=0.6 mm DS repair, this difference can be explained by the patches inability to reduce efficiently the laminate bending at its inner region, due to their bigger flexibility. This also justifies the repair failure without patch debonding (Table 18). For the t_H=2.4 mm DS repair, the smaller value of P_m is caused by an alteration of the failure mechanism (Table 18). In fact, P_m no longer corresponds to simultaneous patch debonding and compression failure with delamination (Fig. 240), observed for the t_H=1.2 and 1.8 mm DS repairs. Instead, it

corresponds to premature outer patch partial debonding (Fig. 238 (a) and (b)), due to the bigger patch stiffness. Regarding the two geometric parameters studied, the numerical simulations captured the experimental trends of the repairs, even though a small underprediction was observed for the DS repairs. **This analysis shows that the SS repairs are ineffective for the values of L_O and t_H studied. The L_O=15 mm DS repair is the best solution. An intermediate value of P_m between this and the open-hole laminate was obtained for the L_O=10 mm and all t_H values DS repairs**.

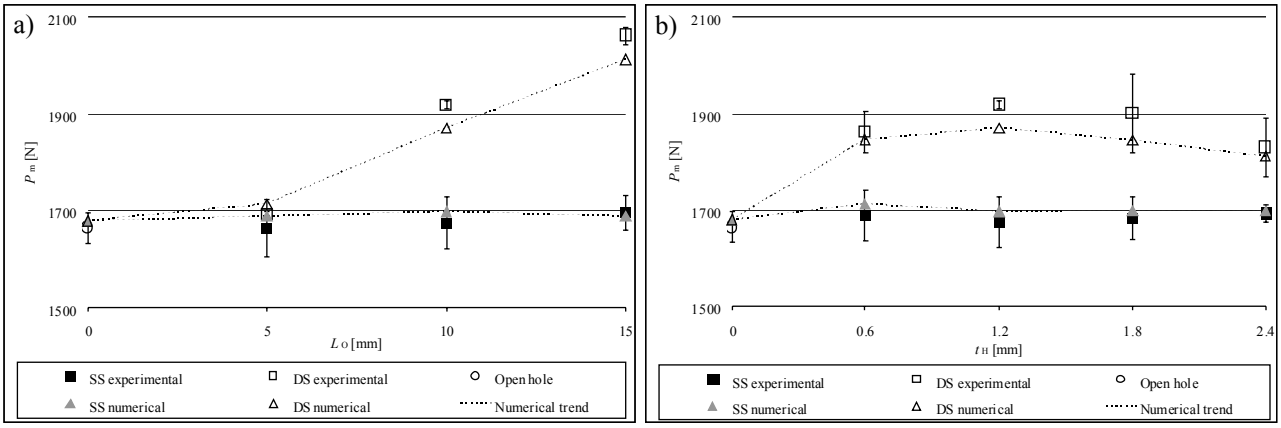

Fig. 246 – P_m as a function of L_O (a) and P_m as a function of t_H (b).

4.4. Scarf repairs

Various approaches have been employed to study the stress fields and predict the tensile strength of scarf assemblies. A few analytical works exist on this subject (Lubkin 1957, Erdogan and Ratwani 1971, Helms et al. 1996, Mortensen and Thomsen 1997, Gleich et al. 2000), but these are often limited to displacement and stress analyses, and do not account for different oriented plies of the adherends. Moreover, it is not possible to capture the stress gradients along the adhesive thickness. The work of Ahn and Springer (1998b) is an exception, adapting the failure models of Hart-Smith (1973b, 1981) to take into account each individual ply of the composite. Strain-based methods are a valid option to monitor damage progression in scarf repaired structures (Baker et al. 2004, Fredrickson et al. 2008). Baker et al. (1999) analysed the bending behaviour of a scarf repaired honeycomb sandwich aircraft structure with CFRP faces, using extensometry. Strain gauges were glued on the repair region to ascertain the most stressed regions and the failure strains of the repairs, under different conditions. The results were compared with FEM simulations, with a good agreement between both. Found and Friend (1995) used the same technique on CFRP scarf repairs under tension to detect buckling onset and corresponding patch debonding, leading to catastrophic failure. Other authors (Objois et al. 2000, Objois et al. 2005) used extensometry and acoustic emission to determine the thresholds for the initiation of the first micro-cracks and for the flaw propagation on the adhesive layer of mild steel scarf joints. A strain-based health assessment method for a scarf repaired sandwich structure with CFRP faces under a tensile load is presented by Li et al. (2006b). The technique is based on relative strain measurements using Bragg grating sensors. Debonding onset in the scarf was detected by a differential strain approach, using two sensors whose strain differential increased with the debond length. A critical value was set to alert for the necessity of a repair procedure. In the last decades, owing to the increase in computational power, the FEM has become a powerful tool to obtain the stress fields and predict failure of these assemblies, using adequate failure criteria (Das et al. 2005, Das et al. 2006). In tension, experimental and FEM studies showed an exponentially increasing strength with the reduction of the scarf angle, due to the corresponding increase on

the bond area (Hart-Smith 1973b, Kim et al. 1995, Ahn and Springer 1998a, Du et al. 2004, Campilho et al. 2007a, Wang and Gunnion 2008, Campilho et al. 2009a). On the failure modes of these assemblies, it was found that scarf angles below a value near 2º led to laminate tension failures, while bigger angles yielded failures in the adhesive layer (Adkins and Pipes 1988, Kumar et al. 2006, Campilho et al. 2009a). Oztelcan et al. (1997) studied by the FEM SL and scarf repairs on honeycomb sandwich structures under a compressive load. The scarf repair led to a more uniform shear stress distribution in the adhesive layer, which was considered to increase the repair strength. Charalambides et al. (1998b) tested experimentally scarf repairs with a 2º angle. Four distinct failure modes were identified, depending on the temperature and moisture conditions, as well as the type of load (static or dynamic). The same authors (Charalambides et al. 1998a) performed a 2D FEM analysis to simulate different failure modes in scarf repairs. The failure loads were compared with previously published experimental work. Harman and Wang (2006) developed an analytical solution, validated by the FEM, to optimize the shape of scarf joints between adherends with dissimilar longitudinal E modulus, using a linear variation of the scarf angle. Aluminium and CFRP joints under a tensile load were considered. Analytical and numerical shear stress distributions in the adhesive were in good agreement. Gunnion and Herszberg (2006) developed a parametric FEM model to analyse stress distributions in the adhesive layer at the mid-thickness of CFRP scarf repairs under tension. 2D and 3D geometric and material linear analyses were performed. The scarf angle, adhesive thickness, number of plies and lay-up were investigated. The most relevant conclusions of this work related to the low dependence of the adhesive layer stresses to mismatched adherend lay-ups and a major reduction on peak stresses using a few over-laminating plies covering the full length of the repair. Odi and Friend (2002) compared the stress distributions between three different FEM approaches to simulate stepped and 3º CFRP scarf repairs under tension. For the scarf repairs, shear stresses in the adhesive are practically constant, leading to a high efficiency of the repair, as the adhesive fails simultaneously at all the bond length. Odi and Friend (2004) performed a 2D FEM stress and failure analysis of tensile loaded scarf repairs, using scarf angles ranging from 1.1 to 9.2º. A quasi-isotropic $[0_2/\pm45/90/\pm45/0_2]_S$ lay-up was considered. The numerical model captured the shear stress variations along the bond length arising from different ply orientations. The numerical failure loads were obtained using different failure criteria for the laminates and the ASSC for the adhesive. The most accurate laminate failure predictions were obtained with the MSC, agreeing with the experimental ones presented in the work of Adkins and Pipes (1988) for the same materials and geometry. An experimental and numerical study regarding the tensile strength of CFRP scarf joints is presented by Kumar et al. (2006). Experimentally, two different failure modes were identified: fibre fracture and pull-out, for scarf angles below 2º, and shear failure in the adhesive layer with negligible fibre fracture, for scarf angles above 2º. The FEM failure loads for the scarf angle evaluated were estimated with the Hashin-Lee criterion for the adherends. A good correlation to the experiments was found. Tzetzis and Hogg (2008) used the vacuum-assisted resin infusion repair methodology to manufacture GFRP scarf repairs. The tensile strength and failure mode were studied for scarf angles between 2.8 and 5.8º. The experimental strengths were compared with FEM predictions using different failure criteria. The Tsai-Wu criterion for the adherends yielded the best results for the entire range of scarf angles studied. Even though the presented numerical methodologies have a significant usefulness in predicting the failure loads and identify damage onset locations, they cannot account for the progressive damage evolution and identify failure paths, as CZM's are able to (Tvergaard and Hutchinson 1993, Tvergaard and Hutchinson 1996, Wei and Hutchinson 1997, Campilho et al. 2008a, Yang et al. 2008). In addition, in these assemblies, a significant difference exists between damage initiation and ultimate loads, due to the peel and shear peak stresses developing at bond edges (Campilho et al. 2007a). Thus, CZM's implemented within FEM models are a more accurate tool to predict the failure path and strength of adhesively-bonded assemblies. Campilho et al. (2007a) numerically studied the tensile strength and failure modes of

unidirectional CFRP scarf repairs using a triangular CZM, for scarf angles from 2 to 45º. The authors concluded that the model successfully predicted the strength and failure modes in these repairs, and also that the adhesive fracture properties present a smaller influence on the repairs strength than the mechanical ones.

Also for scarf assemblies, a few studies focused on the global or localized buckling effects under longitudinal compression. Kumar et al. (2005) evaluated the compression behaviour of adhesively-bonded CFRP scarf joints, focusing on the influence of the scarf angle on the joints strength and failure mode. Aluminium tabs were glued on both the joint faces between the testing machine grips to prevent the global buckling of the specimens. Under these conditions and below 3º scarf angles, the specimens failed by fibre microbuckling, while for bigger scarf angles, failure occurred predominantly by shear in the adhesive layer. A slight increase on the failure strength was observed with the reduction of the scarf angle. On the other hand, if no restraining to the global buckling of the assembly exists, a completely different behaviour is expected. Helms et al. (2003) developed an analytical model based on the Ritz Method to simulate the buckling behaviour of adhesively-bonded GFRP scarf joints under pure compression. The scarf angle, and the adhesive layer thickness and stiffness were the parameters studied. FEM analyses were performed to validate the analytical model. The results showed that the buckling strength is practically insensitive to the scarf angle for the bigger scarf angles. Below a determined scarf angle, the bucking load decreases abruptly. For these small angles, increasing the adhesive layer stiffness or reducing its thickness are both valid options to oppose to this behaviour.

The scarf repair is the last technique evaluated in this Section (Fig. 247 a). The repair procedure consists on the damaged material removal by drilling of a conical hole with a pre-determined angle. The patch can be applied using two procedures: adhesively-bonding a conical patch with the complementary shape of the laminate (Helms et al. 2003, Kumar et al. 2006, Campilho et al. 2009a), or filling the scarfed hole with increasing diameter pre-preg plies, followed by simultaneous curing with the adhesive, in the autoclave or using a vacuum-bag (Robson et al. 1992, Sherwin 1999, Tzetzis and Hogg 2008). These procedures also apply to the 2D repair approximation (Fig. 247 b). Comparing with strap repairs, scarf repairs have the advantages of a higher efficiency and the absence of aerodynamic disturbance. Therefore, they are often used as a permanent repair, since they usually restore the undamaged strength of the laminate (Mortensen and Thomsen 1997, Kumar et al. 2005, Das et al. 2008, Wang and Gunnion 2008). The high efficiency is caused by the elimination of the significant joint eccentricities of strap repairs, which act as stress raisers along the loading paths (Campilho et al. 2007a, Fredrickson et al. 2008, Kumar et al. 2006). Moreover, stress distributions along the bond length are more uniform, due to the tapering effect at the scarf edges (Campilho et al. 2009a). The scarf repair technique has become particularly important in the last decades, due to the increasing use of sandwich panels in aircraft structures (Tomblin et al. 2004, Das et al. 2008). However, these repairs are more difficult to execute due to their geometry, which reflects on higher costs. In addition, they need a large repair area, since relatively small angles are necessary to restore the undamaged laminates strength (Kumar et al. 2005, Campilho et al. 2007a, Wang and Gunnion 2008). Fig. 247 (a) shows the 3D scarf repair geometry and characteristic dimensions. The *Outer Edge of the Scarf* (OES) and *Inner Edge of the Scarf* (IES) loci are identified in the figure. **In this work, only 2D scarf repairs (Fig. 247 b) will be considered in the experiments to validate the FEM technique proposed for bonded assemblies. The author made this choice, as an approximation of the 3D scarf repairs (Fig. 247 a), due to the complexity of these geometries, arising from the manufacture procedure. However, a stress analysis under tension with 3D models will be performed, allowing a comparison with the SS and DS repairs stress distributions, and to ascertain the suitability of the 2D approximation to study this 3D repair geometry**.

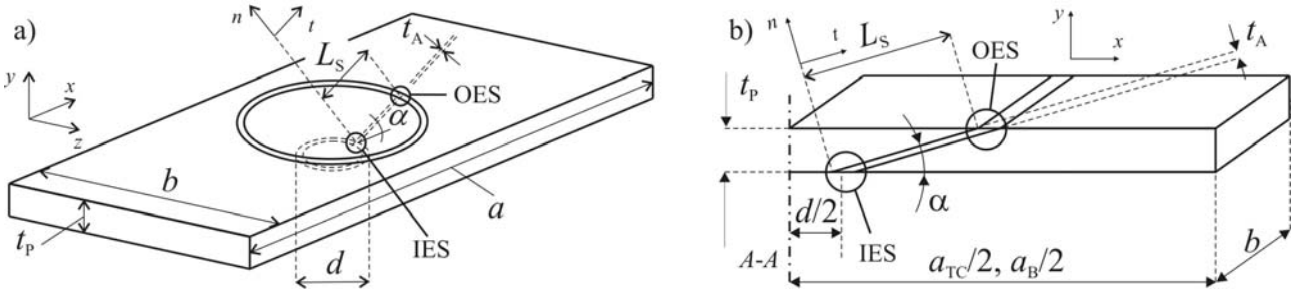

Fig. 247 – Scarf repair geometry and dimensions: 3D (a) and 2D (b) repair.

The characteristic dimensions of the 3D scarf repair are the laminate length (a) and width (b), the scarf angle (α), the laminate thickness (t_P), the adhesive layer thickness (t_A) and the hole diameter (d). The parameter α can be defined as the angle between the scarf and the horizontal plane. The scarf length (L_S) is intrinsically related to the chosen values of α and t_P. The following dimensions were considered for the numerical stress analysis under tension [mm]: a=70, b=50, α=9º, t_P=2.4, t_A=0.2, and d=10. Sixteen plies and $[0_2,90_2,0_2,90_2]_S$ lay-up laminates and patches were used in this analysis (considering a 0.15 mm ply unit thickness). Even though it is known that small angles are necessary for the repair to work in the preferential shear plane and to achieve a reasonable bond area, necessary to an efficient repair (Gacoin et al. 2007, Campilho et al. 2007a), scarf angles up to 45º, which may be imposed due to restrictions to the repair dimensions, were also analysed.

On the other hand, seven scarf angles, varying from 2 to 45º, will be analysed with 2D numerical models (Fig. 247 b). For these, a distinction was performed between the laminates length for tensile and compressive loads (a_{TC}) and a bending load (a_B), to ensure that the value of a_B is sufficiently large for the loading cylinders not to interfere with the repair region. For this 2D approximation, different *initial dimensions* were considered [mm]: a_{TC}=170, a_B=270, b=15, α=9º, t_P=2.4, t_A=0.2, and d=10. In this case, d represents the gap between the laminates. The same lay-up for the laminates and patch was used, compared to the 3D repair. Under a bending load, a similar setup to the SS and DS repairs was considered (4PB, Fig. 121 b), with S=250 mm, S'=150 mm, d_c=5 mm and b_c=15 mm. The distance between the supporting cylinders and the laminate edges (e) is 10 mm. **In the 2D study, comprising different values of α, the remaining geometric parameters were kept equal to the *initial dimensions***.

4.4.1. Numerical work

The scarf repairs were simulated numerically in ABAQUS® with 2D (plane-strain) and 3D models. Analogous modelling guidelines to the SS and DS repairs were followed (Sub-Section 4.3.1). The cohesive elements, used to extract the stress distributions along the bond length, were introduced in the 2D and 3D numerical models at three planes (Fig. 248): at the laminate/adhesive interface (P1), at the middle of the adhesive thickness (P2) and at the adhesive/patch interface (P3). Cohesive elements allow the extraction of stresses at these planes in the directions tangent and normal to the scarf (coordinate system t-n in Fig. 248). The ABAQUS® solid finite elements, which evaluate stresses at the Gauss points and, additionally, in the coordinate system x-y (Fig. 248), are not adequate for these geometries (Gunnion and Herszberg 2006, Campilho et al. 2007a, Wang and Gunnion 2008).

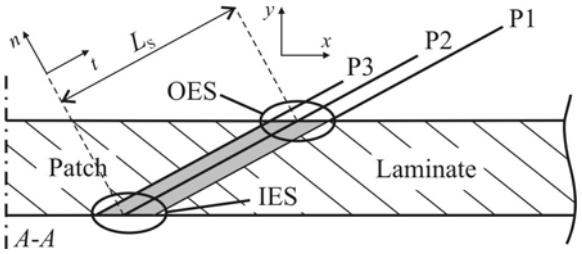

Fig. 248 – Cohesive elements loci in the scarf numerical models.

Equal symmetry conditions to the strap repairs were considered for the 3D scarf repair under tension (Fig. 123 a). Thus, only ¼ of the laminate was modelled. For the 2D models under all load configurations, vertical symmetry was applied at the middle of the repair (line *A-A* in Fig. 247 b), which allowed modelling only half of the repair. Fig. 249 shows the mesh of the α=9º 3D repair at the repair region (a) and a detail at the IES (b). Six and eight-node solid finite elements from ABAQUS® were used. The mesh is more refined at the scarf region, in the adhesive and in the laminate and patch, with forty elements along L_S, to ensure a more refined mesh where stress concentrations are known to exist (Odi and Friend 2004, Campilho et al. 2007a, Wang and Gunnion 2008). Four elements were used in the adhesive thickness direction, while thirty elements were considered for ¼ of the patch in the circumferential direction. At the scarf region, each group of two adjacent equally oriented plies was modelled using five solid elements (Fig. 249 b). Mesh coarsening was applied to reduce the number of elements outside the repair region. The scarf slope was built using six-node triangular elements (Fig. 249 b). The hexahedral elements simulating the adhesive layer were oriented perpendicularly to the scarf surfaces, to avoid distortions at this critical region (Campilho et al. 2007a). No bias effects were applied in neither of the scarf numerical models.

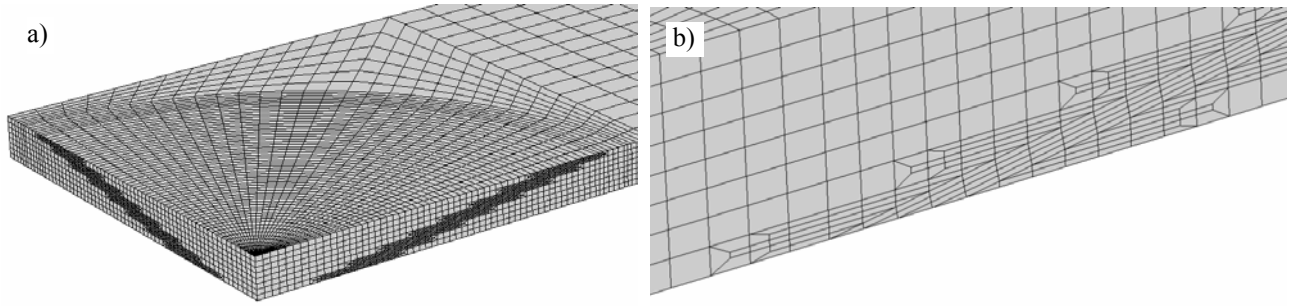

Fig. 249 – Detail of the mesh at the scarf region (a) and at the IES (b) (3D repair).

The following figures (Fig. 250 and Fig. 251) pertain to the 2D repairs (α=9º) mesh for stress analysis. These models were built with 2D eight-node quadrilateral and six node triangular solid elements. A more refined mesh than the corresponding 3D model was considered, since 2D models are less demanding in terms of computational power. Thus, eighty elements were used along L_S, while the adhesive layer was modelled with six elements through-thickness. In addition, at the repair region, ten elements modelled each set of two adjacent equally oriented plies (Fig. 251). Similarly, mesh coarsening was applied to reduce the number of elements outside the scarf region. The mesh of the α=9º repair employed in the failure analysis is shown in Fig. 252. As mentioned earlier, the failure analyses were performed with cohesive elements including trapezoidal laws to simulate the adhesive layer (Section 3.2.2.1), thus replacing the solid finite elements usually employed to this end.

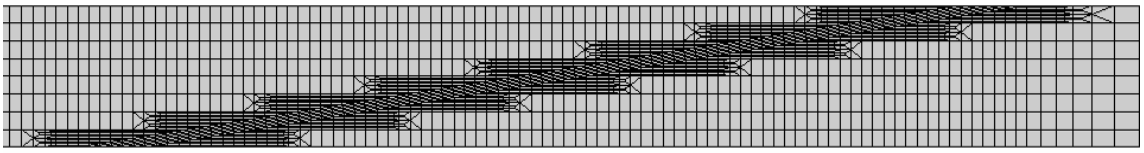

Fig. 250 – Detail of the mesh at the scarf region (2D repair).

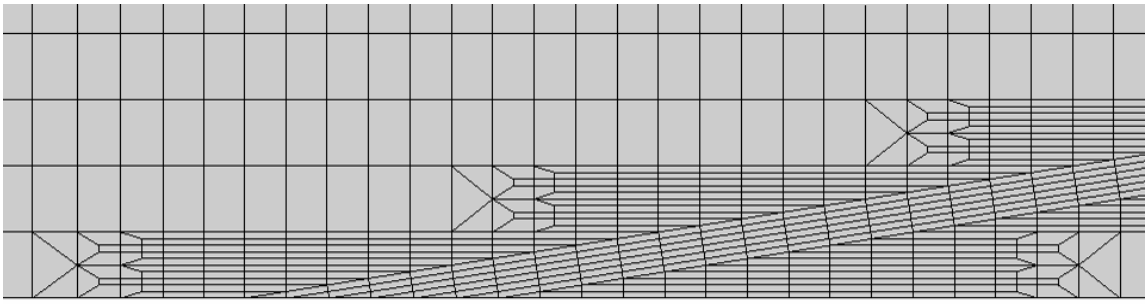

Fig. 251 – Detail of the mesh at the IES (2D repair).

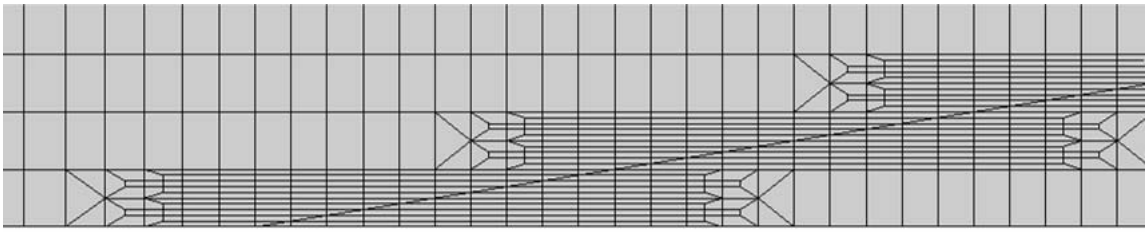

Fig. 252 – Detail of the mesh for the failure analysis at the IES (2D repair).

The cohesive elements loci for the failure analyses are identified in Fig. 253. The adhesive layer elements were introduced along the bond length. However, in the experiments regions of interlaminar and transverse intralaminar failures were also observed at the scarf region. To account for this behaviour, interlaminar finite elements were positioned between differently oriented plies, while intralaminar elements were placed vertically in the 90º plies to simulate an intralaminar matrix cracking. Additionally, cohesive elements with fibre properties were introduced vertically in the 0º plies to simulate a tensile fibre failure, even though this was not observed experimentally.

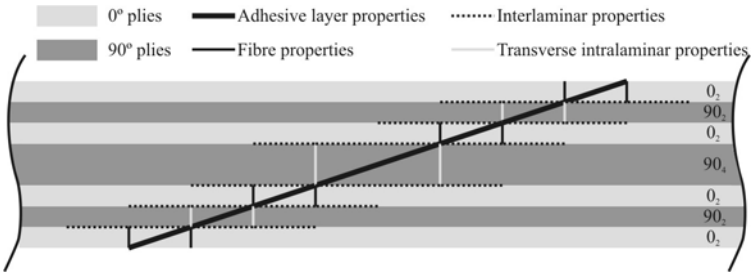

Fig. 253 – Cohesive elements loci with different laws in the numerical models.

For the interlaminar, intralaminar and fibre elements, a traditional penalty function method was used (de Moura et al. 1997) for the initial ascending part of the cohesive laws (considering d_i=10^6 N/mm^3 in equations (26) and (27)), since the cohesive elements in these cases simulate a zero thickness interface instead of a thin layer. Moreover, triangular shape laws were used, due to the brittle nature of these interfaces (Lee and Soutis 2008). The cohesive parameters to

simulate the mentioned failures were introduced earlier in this work (Table 8). At this stage it is emphasized that, since the repair dimensions differ between the 2D and 3D models, the stress fields of these repairs under an equal displacement (described in the beginning of Sub-Section 4.3.3.1.1), are not directly comparable.

4.4.2. Experimental work

4.4.2.1. Specimens preparation

The scarf repairs were fabricated from $[0_2,90_2,0_2,90_2]_S$ lay-up bulk plates. Details on the manufacturing and cutting procedures are presented in Sub-Section 3.2.2.1.1. The specimens cutting also followed a similar procedure. The scarf angles of the laminates and patches were machined at ISEP with 60 grit vitrified mounted points from FAST GRINDER^{TM} in a GAMBIN^{SA} 1m conventional milling machine. The work of Ahn and Springer (1998a) showed, using adhesively-bonded CFRP scarf repairs under tension, that grit sizes from 60 to 400 did not have influence on the repairs behaviour, provided that cohesive failures of the adhesive layer occur. For the grinding operation, the specimens were tightened in a screw-vice between stainless steel bars, to avoid the specimens flexure during the grinding operation.

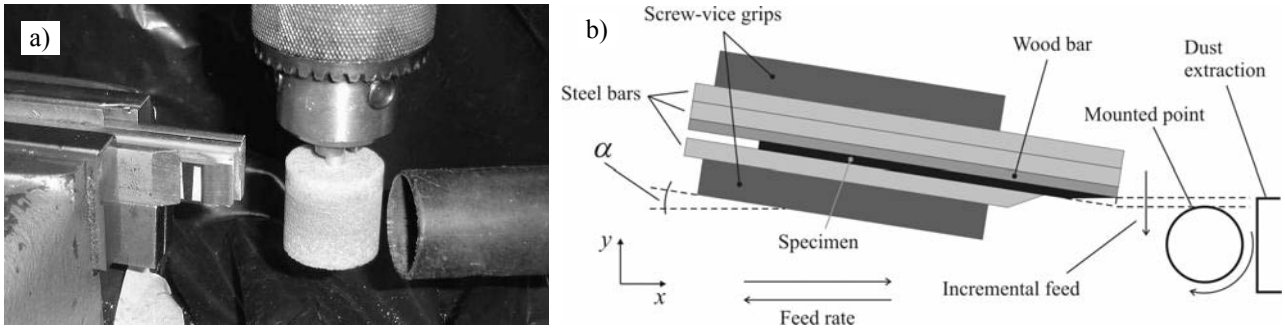

Fig. 254 – Grinding of a α=15º angle in a milling machine (a) and scheme of the grinding process (b).

Fig. 254 (a) and (b) show a specimen pressed between a chamfered steel bar and a set of three bars. This set of bars consisted on a wooden bar adjacent to the specimen, working as a sacrifice material, and two steel bars to prevent the specimen flexure during the grinding operation. Fig. 254 also shows the dust extraction system, using a house-hold vacuum cleaner with the nozzle near the grinding tool and working at full power during the grinding operation. Fig. 254 (b) allows a better understanding of the grinding process. Initially the screw-vice was rotated by an amount equal to the desired value of α. The mounted point was fixed, rotating at a constant speed of 1800 RPM, while the vice moved along the x axis in both directions alternately with a feed rate of 250 mm/min, grinding the specimen. An incremental feed along the y axis of 0.1 mm per run was employed until the scarf slope was complete. Subsequently, at least six more runs were carried out with no additional incremental feed to ensure a flat grinded surface. This step was extremely important to prevent a wavy scarf surface, which would otherwise result from the grinding process due to the higher material removal rate in the transversely oriented (90º) plies. Fig. 255 shows α=2º laminates after the grinding operation. After finishing of the grinding process, a slight bending of the α=2º and α=3º laminates and patches was detected visually at the scarf tips. This was due to introduction of thermal residual stresses in the bulk plates during the respective curing cycle (Fredrickson et al. 2008, Campilho et al. 2009a), added to the smaller stiffness and bigger length of the scarfed region for the smaller values of α.

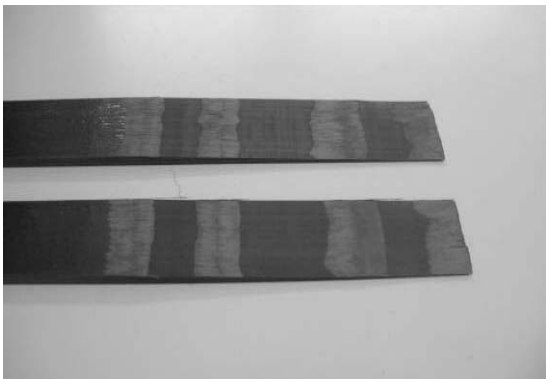

Fig. 255 – Laminates after the grinding operation (α=2º).

Following, all specimens edges were abraded manually with a 220 grit sandpaper to remove the loose fibres. The grinding operation assured the removal of the composite glossy surface and adequate roughness for a strong bond. Surface preparation prior to bonding was completed cleaning the grinded surfaces with compressed air, followed by wiping with acetone, to avoid adhesive failures (Zimmerman and Liu 1995, Campilho et al. 2008a). The repairs were bonded in a especially designed device that guarantees a perfect alignment of the laminates and patches to be bonded in both thickness and width directions (Fig. 256).

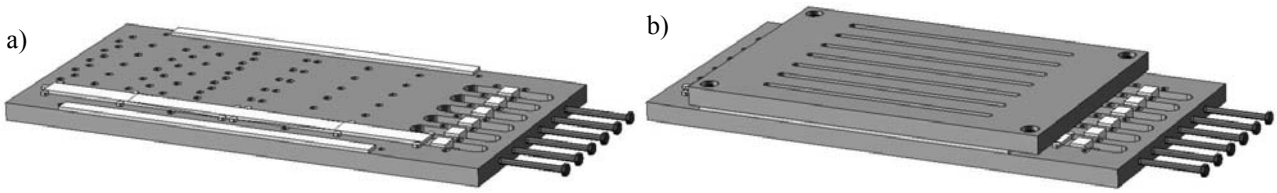

Fig. 256 – Schematic representation of the bonding device without (a) and with the upper plate (b).

This device consists on two steel plates. The lower plate aligns the repairs in the width direction with cylindrical pins placed along the repairs length. The upper plate is positioned after application of the adhesive and placement of the patch to compress the repairs between the two plates, assuring their alignment in the thickness direction. The defined value of t_A was achieved with a differential length technique, measuring with a digital calliper (precision of 10 μm) the repairs total length before and after the adhesive application. The screw-driven pressure devices showed in Fig. 256 were used to this end. The complete procedure will be following described step-by-step. Fig. 257 (a) shows the bonding procedure for a set of six α=9º repairs. The width alignment with pins can also be visualized in this figure. The bonding procedure consisted on pouring the adhesive in thin cords and perpendicularly to the laminates length on the two laminates of each repair, using original Araldite® mixing nozzles.

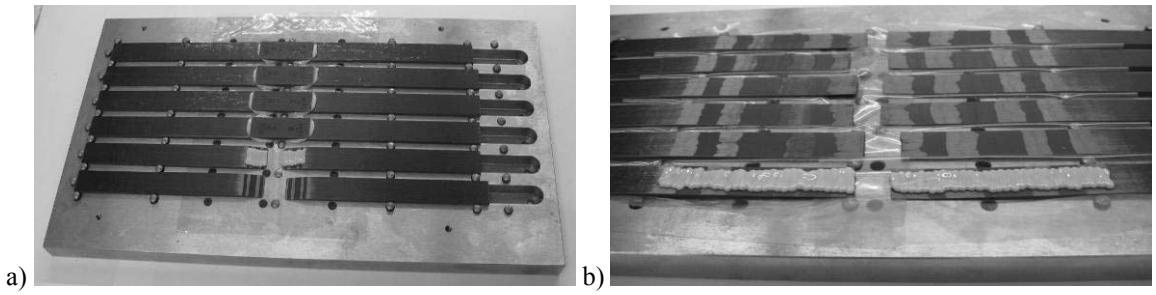

Fig. 257 – Pouring of adhesive in the specimens: α=9º (a) and α=2º (b) repairs.

Following, the patch was applied. During this operation, each patch was positioned immediately after pouring the adhesive on the respective laminates, to assure a strong bond. Before the alignment of the laminate, a 25 μm thickness Teflon® sheet was placed under the repairs to prevent the plates contamination and avoid the need for cleaning after bonding a set of repairs. A detail of the laminates after pouring of the adhesive is presented in Fig. 257 (b) for a α=2º repair. After pouring the adhesive, the patches were placed in position. Fig. 258 (a) shows a detail at the bond region of a α=2º repair after the patch application, while Fig. 258 (b) presents all the six specimens of this geometry. The chosen value of t_A was achieved using two different procedures, depending on the value of α.

- **α=2, 3 and 6º.** The total length of each repair was measured without adhesive and the scarf faces pressed to each other with the specimens in the bonding device and the upper plate compressing the repairs. The pressure devices were used at this stage to compress the laminates to the patch and eliminate possible gaps between them. The final length of each repair was then calculated individually adding $2w$ to the measured length. w represents the projection of t_A in the x direction (Fig. 247 b), given by expression (56). The pressure devices were adjusted accordingly and the laminates placed in the lower plate. After pouring the adhesive in the laminates and applying the patches, these were aligned with the laminates in the width direction and the distance w measured with a digital calliper at both patch edges to centre the patch between the laminates.

$$w = \frac{t_A}{\cos(\alpha).\tan(\alpha)} \tag{56}$$

- **α=9, 15, 25 and 45º.** For these bigger values of α, the measurement of w at the patch edges was not feasible, since the very small values of w were difficult to measure accurately using a calliper. Under these conditions, the laminates were also positioned with the pressure devices adjusted to the calculated total length of each repair. However, after pouring the adhesive, the patches were centred manually between the laminates. This task was accomplished by inserting the patches carefully between the two laminates, until they were roughly aligned. Following, they were shaken in the length direction with a gradually decreasing load, based on the assumption that equilibrium is attained for equal values of t_A between the two adhesive layers. In fact, a gradually increasing adhesive flow resistance is expected in each direction for the approaching adhesive layer with the reduction of t_A, which allowed using this simplified technique. After bonding and removal of the adhesive excess at the repairs lateral faces, the accuracy of this technique was certified by visual inspection.

a) 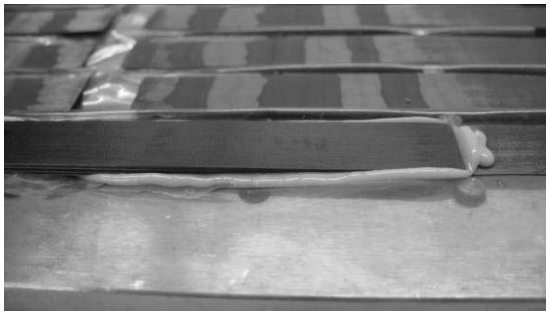 b) 

Fig. 258 – Patch application (a) and set of repairs after the patches application (b) for α=2º repairs.

The patches were also visually checked for their width alignment. After the alignment procedure, the adhesive excess at the OES (Fig. 258) was removed carefully with a razor blade. This was performed to avoid spreading of adhesive to the patches and laminates faces, which would difficult the repairs thickness alignment and the upper plate flatness. The

adhesive excess at the repairs lateral faces (Fig. 258) was not removed to achieve a uniform bond along the repairs width, being removed only after curing. The repairs were covered with a Teflon® sheet and steel bars placed at both sides of the set of repairs (Fig. 259 a). These bars, presenting a slightly bigger thickness than the repairs, were used to ensure that the repairs do not loose the alignment when the upper plate is lowered to apply the pressure. Finally, the upper plate was placed on top of the steel bars (not contacting with the repairs) and aligned with the four screws. The steel bars were carefully removed while the upper plate was lowered to apply the pressure to the specimens (Fig. 259 b). All specimens were cured at room temperature during at least twelve hours prior to removal from the device. The repairs were then left to cure at room temperature for at least one week before testing.

a) 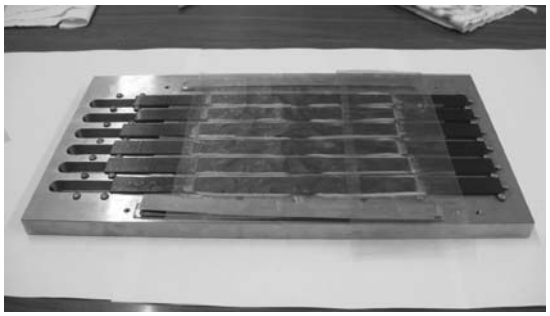 b) 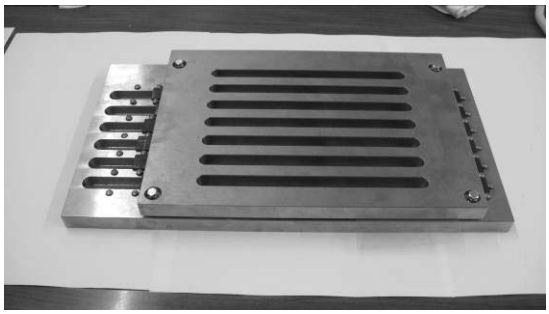

Fig. 259 – Covering of the repairs with a Teflon® sheet (a) and mould after positioning of the upper plate (b).

The adhesive excess at the lateral faces of the repairs was removed in a drilling machine with a HSS end-mill, followed by finishing with an abrasive 60 grit spiral wound band mounted on an expandable drum (Sub-Section 3.2.2.1.1, Fig. 74). Fig. 260 shows the final look of α=3º (a) and α=6º (b) repairs at the bond region after the accomplishment of these operations. In all the repairs, the values of t_A were measured individually in FEUP using a digital microscope equipped with 1 μm precision micrometers. Slightly bigger values of t_A were consistently measured for all the repairs (0.23 mm<t_A<0.27 mm), due to the inevitable rounding of the scarf edges, emerging from the abrading operation. However, only a negligible deviation was identified between the two adhesive layers of each repair, showing that the methods used to guarantee the desired value of t_A are adequate.

a)  b) 

Fig. 260 – Final look of α=3º (a) and α=6º (b) repairs at the bond region.

4.4.2.2. Specimens testing

The specimens were tested with different testing machines and conditions, according to the characteristic features of each loading. The following Sub-Sections describe the procedure for the tensile, compressive and bending loads.

4.4.2.2.1. Tensile load

The repairs were tested under tension at UTAD using an Instron® 1125 electro-mechanical testing machine equipped with a 100kN load cell. The tests were performed at room temperature under displacement control (0.5 mm/min). The displacement was recorded using two *Linear Variable Differential Transformers* (LVDT's) and their average displacement was considered to build the P-δ curves. A sample rate of 5 points per second was used in the tests. **Under all loads evaluated, six specimens were tested for each value of α, always guaranteeing at least four valid results**. Fig. 261 illustrates the experimental setup of the repairs in the testing machine. Fig. 261 (a) shows a 9º scarf angle specimen fixed in the testing machine, showing the holding device of the LVDT's. A detail of the LVDT coupling blocks at the repair edges is presented in Fig. 261 (b) and (c).

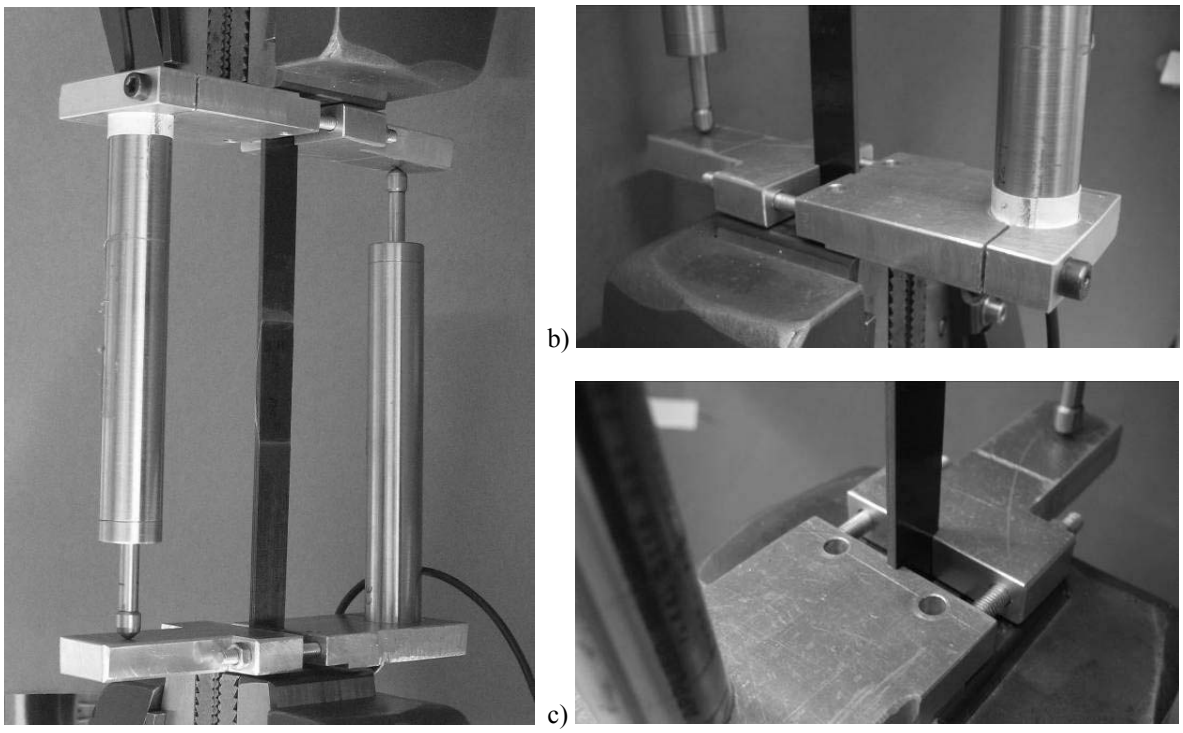

Fig. 261 – Experimental setup in the testing machine (tensile load, α=9º repair).

4.4.2.2.2. Compressive load

The compression tests were also performed at UTAD with an Instron® 8801 hydraulic testing machine equipped with a 100kN load cell. This equipment was found to be particularly suited to this loading, since the robust fixing system between the grips and machine or loading cylinder is essential to prevent the grips misalignment under load, which is imperative for an accurate characterization of the buckling behaviour of the repairs. The specimens were tested at room temperature under displacement control (0.5 mm/min). The experimental P-δ curves were built using the load cell measurements and the grips displacement, with a sample rate of 5 points per second. The LVDT's were not used in these tests due to the expected buckling of the repairs. Fig. 262 (a) shows the experimental setup in the testing machine. Fig. 262 (b) details a specimen pressed between the grips using six sheets of sandpaper. This was used to prevent the repairs slipping and interaction with the grips during buckling (Fig. 262 c).

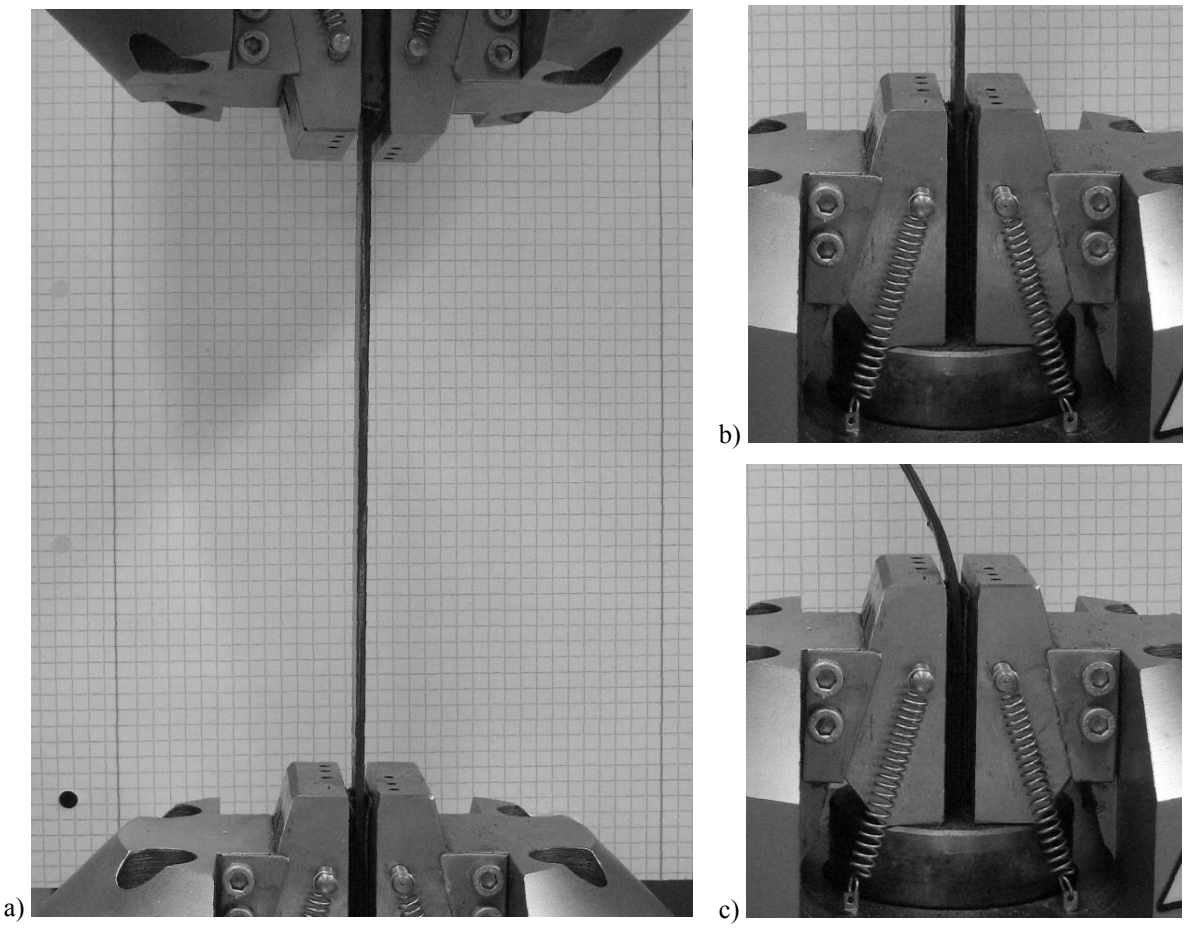

Fig. 262 – Experimental setup in the testing machine (compressive load, α=2º repair).

4.4.2.2.3. Bending load

Under bending, the repairs were tested at UTAD with an Instron® 5848 electro-mechanical Microtester equipped with a 2kN load cell. A constant velocity was applied (2 mm/min) during the tests, accomplished at room temperature.

Fig. 263 – Experimental setup in the testing machine (bending load, α=2º repair).

A sample rate of 5 points per second was selected. The grips displacement was used to extract the values of δ during the tests and build the P-δ curves. A testing device was built to perform the 4PB tests (Fig. 263 a), involving two reinforced aluminium beams to hold the loading and supporting cylinders. It also allowed the cylinders span adjustment by the grooves routed along the beams length, which guided the aluminium towers used to hold the cylinders. Fig. 263 (b) and (c) detail the loading and supporting system at one of the repair edges in the beginning and during the test, respectively.

4.4.3. Tensile load

The scarf repairs study follows the guidelines of Sub-Section 4.3, i.e., evaluating the tensile, compressive and bending fractures of the repairs. The tensile analysis initially compares 2D and 3D stress fields, for an assessment of the suitability of 2D models to simulate this typically 3D geometry. The failure mechanisms are subsequently described and the most important parameters summarized.

4.4.3.1. Stress analysis

The deformed configuration of the 3D repair under tension is presented in Fig. 264. Fig. 265 (a) and (b) show σ_y and τ_{xy} stress fields at the adhesive region in the coordinate system x-y (aligned with the laminate edges), to justify considering only plane ***B*** in the following stress analysis. In fact, Fig. 265 shows that σ_y and τ_{xy} stresses are critical at this region. σ_x stresses are shown in Fig. 266 at the scarf region.

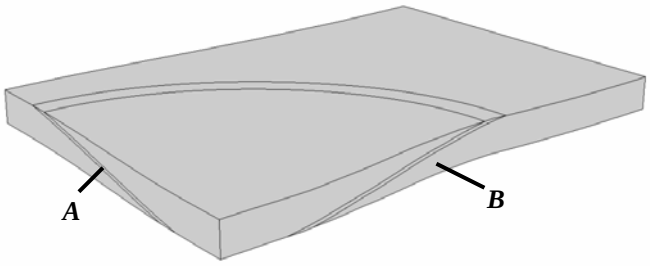

Fig. 264 – Deformed configuration of the scarf repair under a tensile load (3D repair).

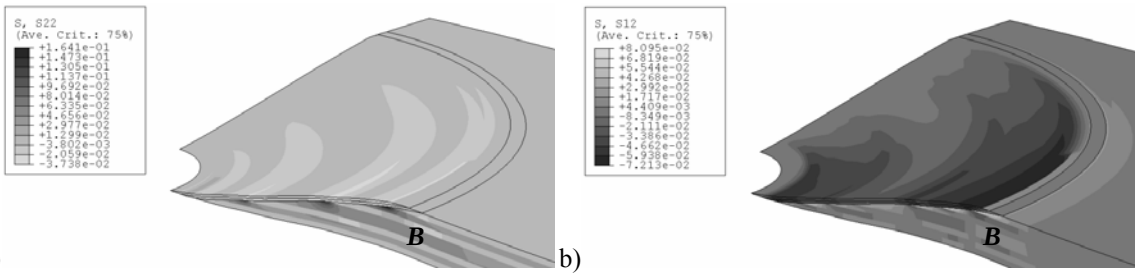

a) b)

Fig. 265 – σ_y (a) and τ_{xy} (b) stresses at the repair region (3D repair).

Scarf repairs are characterized by a smaller flexure at the repair region than the SS repairs under tension (Fig. 136), since the load eccentricities are minimized with this geometry (Kumar et al. 2006, Campilho et al. 2007a, Fredrickson et al. 2008). Moreover, due to the tapering effect at the scarf edges unique to this repair, stress gradients along the bond length edges are minimal (Tzetzis and Hogg 2008). This fact also justifies a 55% reduction of the σ_x peak stresses in the

laminate at the repair region, comparing with the corresponding SS repair (Fig. 266 compared to Fig. 138). On the other hand, compared to the DS repair under tension (Fig. 155), whose symmetry eliminates the laminate flexure, a 7% increase on σ_x peak stresses was identified. However, it should be emphasized that these peak stresses were detected only at a very restricted region (at the IES and OES). Apart from these regions, σ_x stresses are also smaller than the DS repair ones. Moreover, σ_x stresses are practically uniform in the laminate thickness direction, in contrast to the DS (Fig. 155) and especially the SS (Fig. 138) repairs under tension. However, equally to these configurations, σ_x stresses are much higher in the load-oriented plies, due to their higher stiffness in the load direction.

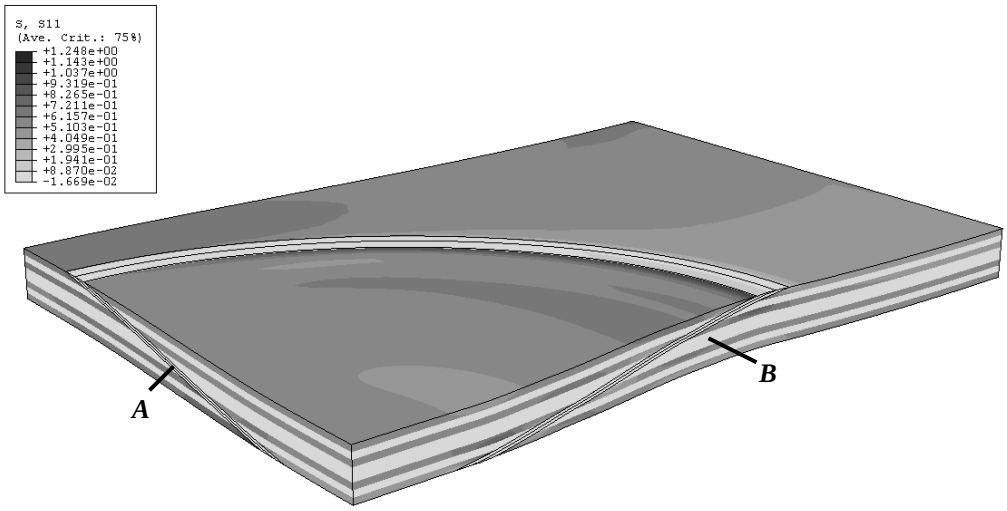

Fig. 266 – σ_x stresses at the repair region (3D repair).

Fig. 267 shows σ_y stresses in the repair, Fig. 269 (a) σ_n stress distributions at three planes at the repair region, Fig. 268 τ_{xy} stresses and Fig. 269 (b) τ_{tn} stress distributions at three planes at the repair region. The planes evaluated (schematically represented in Fig. 248) are the laminate/adhesive interface (plane P1), the middle of the adhesive thickness (plane P2) and the adhesive/patch interface (plane P3).

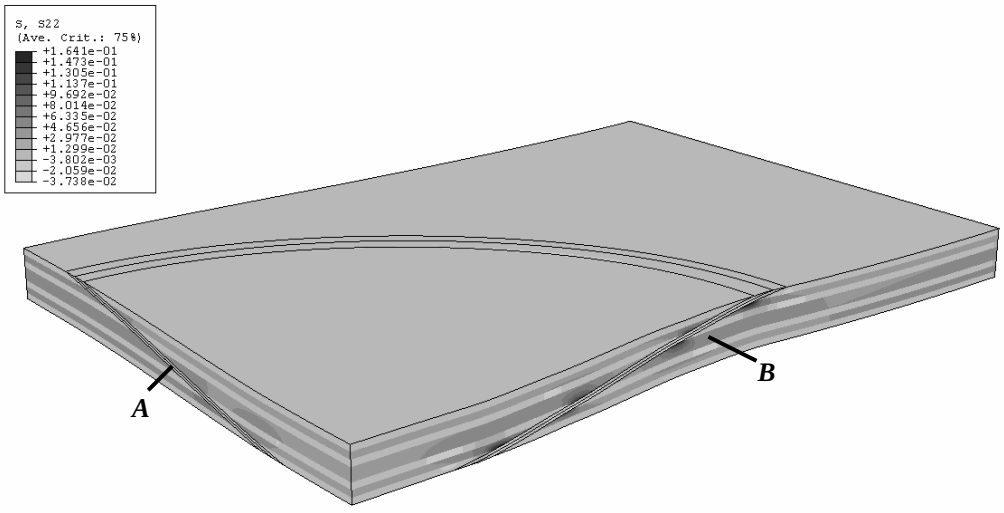

Fig. 267 – σ_y stresses at the repair region (3D repair).

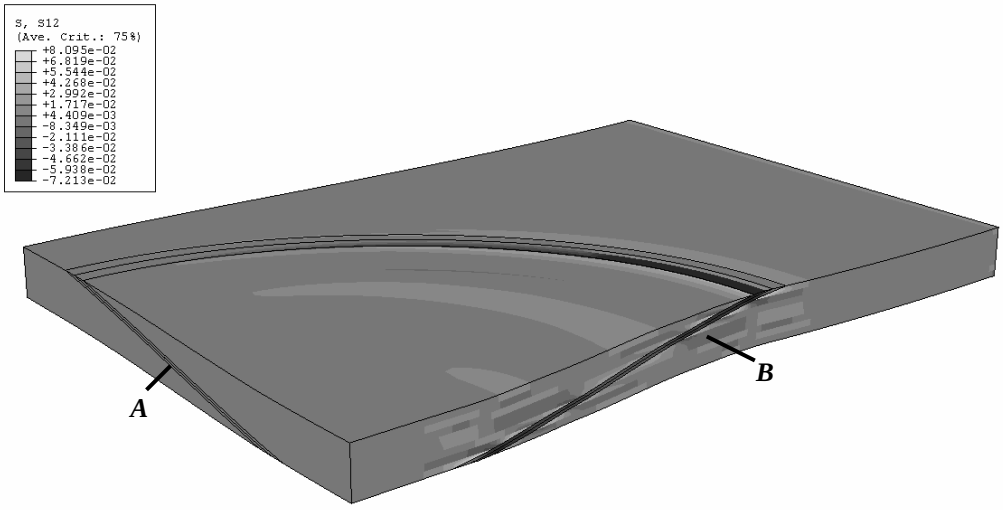

Fig. 268 – τ_{xy} stresses at the repair region (3D repair).

It should be emphasized that σ_y and τ_{xy} stresses in Fig. 267 and Fig. 268 were plotted in the coordinate system *x-y* (Fig. 248), while the corresponding distributions along L_S (Fig. 269 (a) and (b)) were obtained in the coordinate system *t-n* (Fig. 248). This difference, which prevents a direct comparison between both, was applied throughout Sub-Section 4.4, i.e., for all scarf repair studies. The stress fields in the coordinate system *x-y* were only included to present an overall idea of the repair critical regions. The ratio t/L_S represents the L_S normalized distance from the IES (Fig. 248). Additionally, for all analyses on scarf repairs, σ_n and τ_{tn} stress distributions are normalized by the τ_{avg}, the average shear stress at the middle of the adhesive (plane P2, Fig. 248).

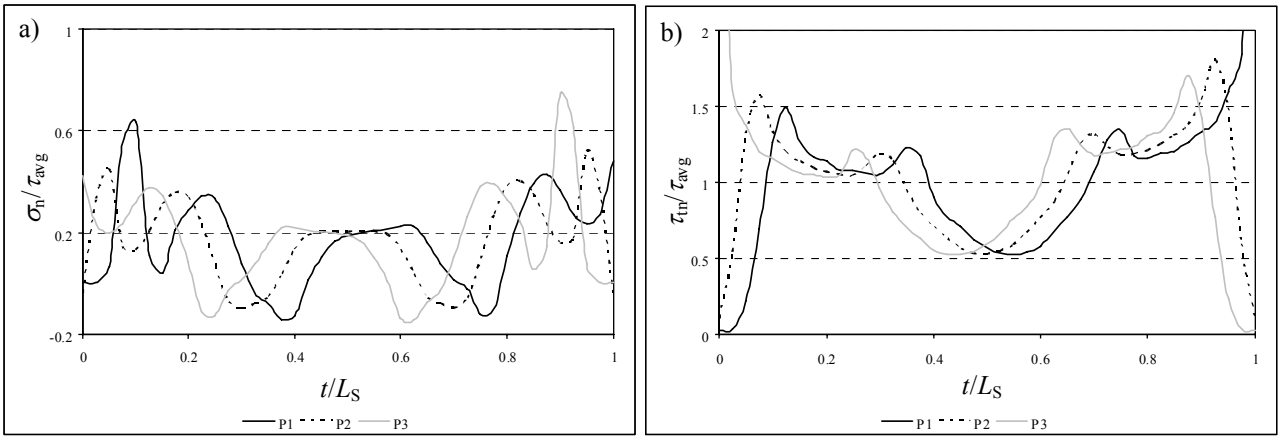

Fig. 269 – Normalized σ_n (a) and τ_{tn} (b) stress distributions at the repair region (3D repair).

It is known that normal and shear stresses in the adhesive layer of scarf assemblies are practically constant for isotropic adherends (Objois et al. 2000, Objois et al. 2005) or fibre reinforced ones, with unidirectional laminates (Odi and Friend 2002, Du et al. 2004, Campilho et al. 2007a). This can be justified by a smaller load eccentricity, comparing with lap geometries (Campilho et al. 2005, Kumar et al. 2005) and by the adherend tapering effect in scarf assemblies (Kumar et al. 2005, Campilho et al. 2009a). Moreover, for small values of α, normal stresses are almost nil and the adhesive layer is practically under pure shear (Hart-Smith 1973b, Campilho et al. 2007a), which helps to the high efficiency of these assemblies relatively to the bond area. However, for layered composites with differently oriented plies, the difference in compliance of each set of equally oriented plies leads to wavy stress distributions (Johnson 1989, Gunnion and

Herszberg 2006, Harman and Wang 2006, Wang and Gunnion 2008, Campilho et al. 2009a). Analysing the results of the previous figures, it can be concluded that σ_y/σ_n stresses (Fig. 267 and Fig. 269 a) are usually lower in magnitude than τ_{xy}/τ_{tn} stresses (Fig. 268 and Fig. 269 b). Only at localized regions in the laminate and patch normal stresses are higher in magnitude than shear ones (peel peak stresses near the adhesive layer, at the interfaces between differently oriented plies, Fig. 267). σ_y/σ_n stress distributions are identical between the three planes, without the presence of stress singularities (Fig. 269 a). No direct relation could be established between peel peak stresses and the ply orientations. Compared to the SS (Fig. 139) and DS (Fig. 156) repair techniques, peel peak stresses are usually smaller in magnitude. Only at the ply interfaces in the laminate and patch this does not apply. Shear stresses (Fig. 268 and Fig. 269 b) clearly reflect the differences in compliance between plies along L_S (Gunnion and Herszberg 2006, Harman and Wang 2006, Wang and Gunnion 2008). Thus, they peak near the 0º plies due to their higher stiffness in the load direction, exhibiting a globally increasing tendency towards the IES and OES. Stress singularities develop at planes P1 (OES) and P3 (IES). These results are consistent with the work of Campilho et al. (2007a), concerning the tensile behaviour of unidirectional scarf repairs. Under the same value of δ, shear stresses are slightly higher in magnitude than SS and DS repair ones (Fig. 140 and Fig. 157, respectively). However, smaller gradients were detected along L_S. This can be regarded as an advantage, since the adhesive layer becomes more homogeneously loaded. This stress analysis indicates that damage is prone to initiate at or near plane P1 (OES) and plane P3 (IES), since shear stress singularities develop at those regions.

Following, a comparison with the 3D analysis is performed using a 2D repair with the *initial dimensions* introduced in Sub-Section 4.4, to check the suitability of the 2D approximation to study this typically 3D geometry. Since some dimensions differ from the 3D repair ones, no direct comparison could be performed on the magnitude of stresses. Fig. 270 shows the respective deformed configuration. The repair layout of Fig. 270, i.e., patch at the left and laminate at the right, applies throughout this section. σ_x stresses at the scarf region are presented in Fig. 271.

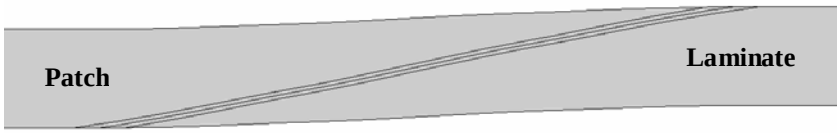

Fig. 270 – Deformed configuration of the scarf repair under a tensile load (2D repair).

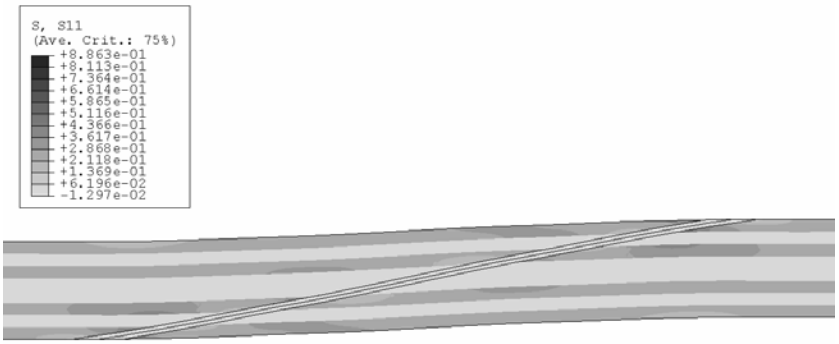

Fig. 271 – σ_x stresses at the repair region (2D repair).

The repair region undergoes moderate transverse flexure (Fig. 270), equally to the 3D analysis (Fig. 264). Moreover, an analogous behaviour to the 3D repair was identified for σ_x stresses at the repair region (Fig. 271 compared to Fig. 266). Actually, σ_x stresses are higher in magnitude in the load oriented plies. These stresses are practically uniform between

equally oriented plies along the repair thickness, following the 3D repairs behaviour. The figures below illustrate σ_y stresses (Fig. 272), σ_n stress distributions at three planes at the repair region (Fig. 274 a), τ_{xy} stresses (Fig. 273) and τ_{tn} stress distributions at three planes at the repair region (Fig. 274 b).

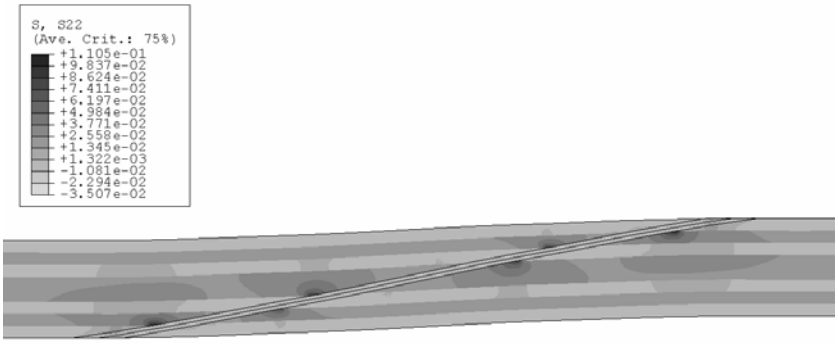

Fig. 272 – σ_y stresses at the repair region (2D repair).

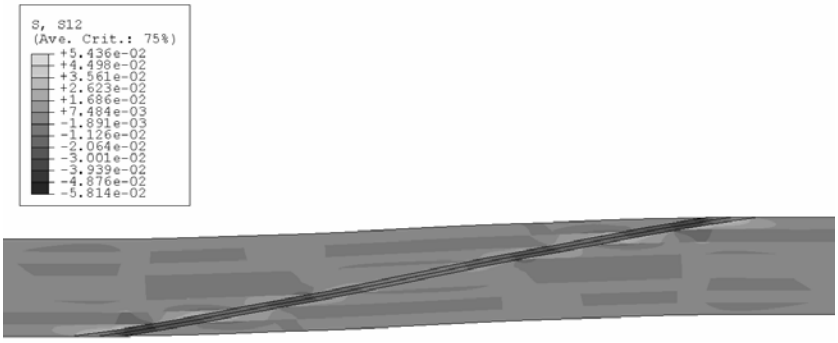

Fig. 273 – τ_{xy} stresses at the repair region (2D repair).

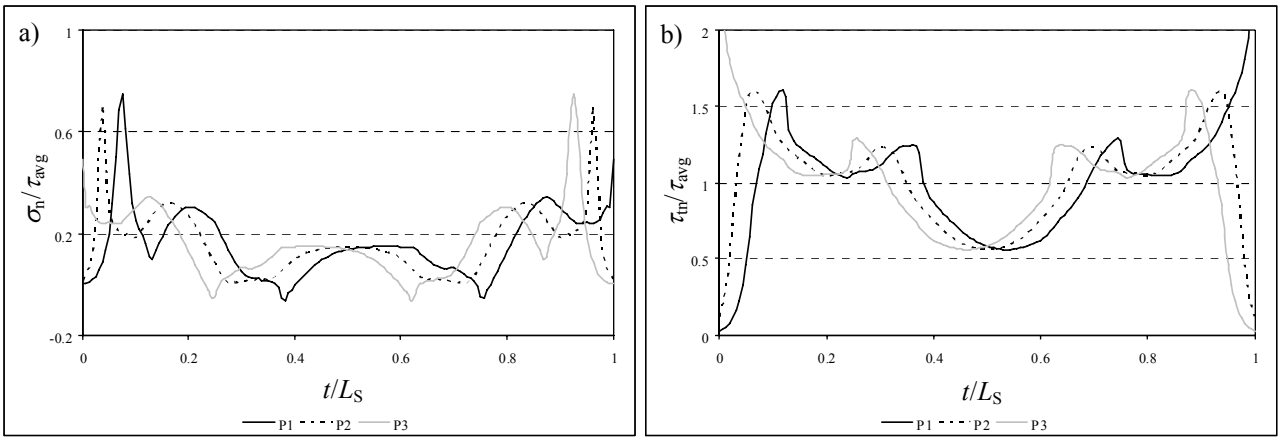

Fig. 274 – Normalized σ_n (a) and τ_{tn} (b) stress distributions at the repair region (2D repair).

The comparison between σ_y/σ_n stress distributions (Fig. 272 and Fig. 274 a) with the 3D ones (Fig. 267 and Fig. 269 a) allows emphasizing their similarity along L_S for the three planes evaluated. However, the 2D analysis yields slightly higher peak values. On the other hand, the τ_{xy}/τ_{tn} shear stress profiles are almost indistinguishable to the 3D repair ones (Fig. 273 and Fig. 274 (b) compared to Fig. 268 and Fig. 269 (b)). The results presented here, due to their similitude to the 3D repairs, point towards damage initiation at or near plane P1 (OES) and plane P3 (IES). **The comparative study**

presented in this Sub-Section, showing similar results for the 2D and 3D repair configurations on the stress distributions and their corresponding relative magnitude along L_S, is on the basis of the approximation made in this work, where 2D scarf repairs were examined as an approximation of this repair technique.

4.4.3.1.1. Scarf angle

A comparison on the values of α was performed for σ_n and τ_{tn} stress distributions at planes P1, P2 and P3 (Fig. 248). Fig. 275 corresponds to plane P1 (laminate/adhesive interface), Fig. 276 to plane P2 (adhesive layer mid-thickness) and Fig. 277 to plane P3 (adhesive/patch interface).

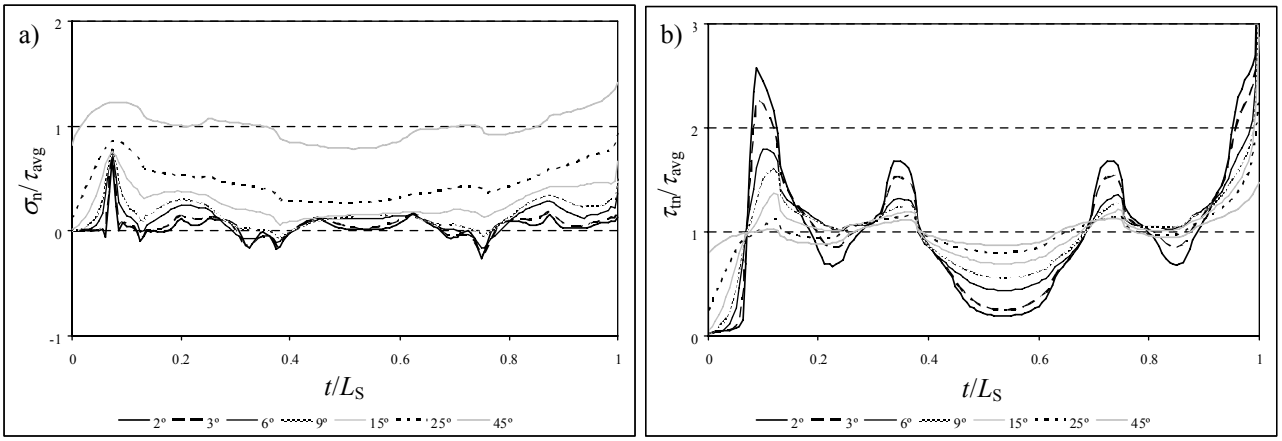

Fig. 275 – Normalized σ_n (a) and τ_{tn} (b) stress distributions at the laminate/adhesive interface (P1) as a function of α.

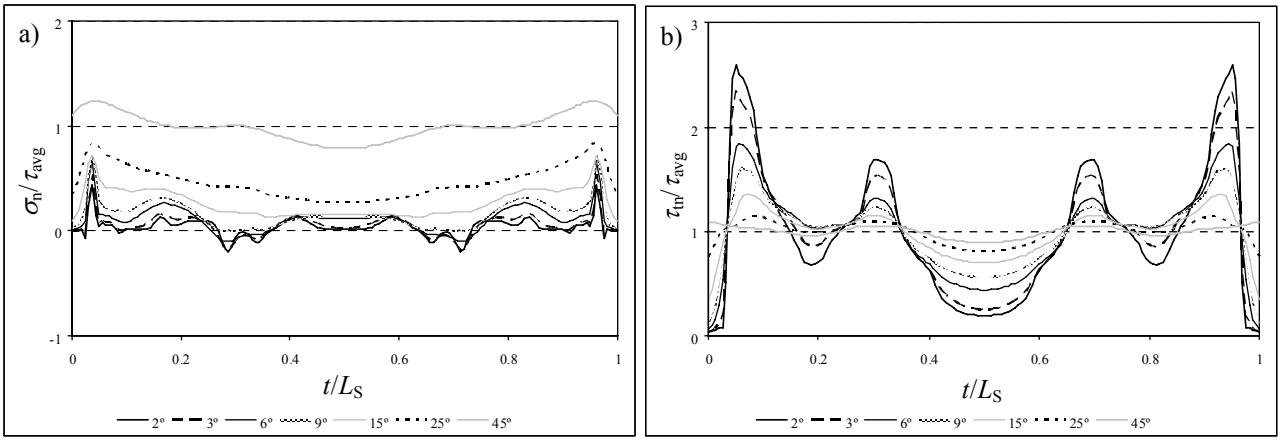

Fig. 276 – Normalized σ_n (a) and τ_{tn} (b) stress distributions at the middle of the adhesive (P2) as a function of α.

σ_n stresses are nearly nil for the smaller values of α, compared to τ_{tn} stresses. In fact, under these conditions, the repair is primarily loaded in shear (Hart-Smith 1973b, Campilho et al. 2007a). However, σ_n stresses gradually increase with α (Brink et al. 2000). Inclusively, for a α=45º repair, σ_n stresses approach τ_{avg} in magnitude. σ_n stress profiles are wavy, without a direct correspondence with the plies orientation. σ_n stresses are predominantly tractive along L_S. Only for the smaller values of α compressive peaks are identified at the scarf central region. σ_n stress distributions are identical for each value of α, regardless the plane. However, at plane P2 two σ_n peel stress peaks develop for the smaller values of α (located at the IES and OES), whilst at planes P1 and P3 this occurs only at the IES or OES, respectively.

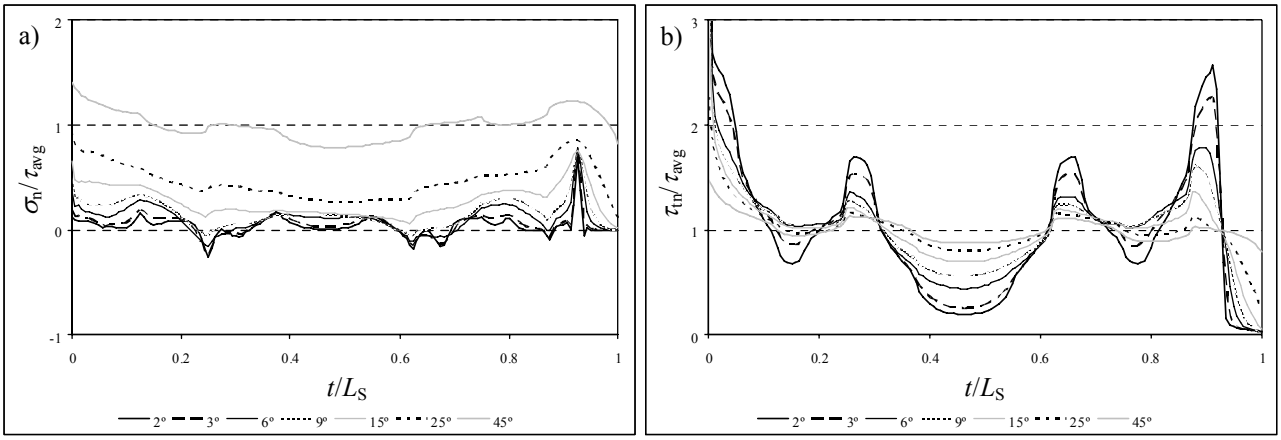

Fig. 277 – Normalized σ_n (a) and τ_{tn} (b) stress distributions at the adhesive/patch interface (P3) as a function of α.

Oppositely to σ_n stress distributions, τ_{tn} shear stresses relate directly to the plies orientation. In fact, for all values of α, τ_{tn} shear stresses are higher in magnitude near the 0º plies. The shear stress gradients between the 0º and transversely oriented plies gradually diminish with the increase of α. These stresses are identical between planes P1, P2 and P3, with the exception of the stress singularities at planes P1 (OES) and P3 (IES) (Campilho et al. 2007a). The results presented here are not conclusive in terms of strength evolution with the bond area. In fact, increasing the bond area (corresponding to a reduction of α), σ_n peel stresses diminish, while τ_{tn} shear stress gradients increase, which does not allow the establishment of design guidelines based only on this stress analysis.

4.4.3.2. Failure analysis

4.4.3.2.1. Mechanical behaviour

Two distinct failure mechanisms were identified experimentally: type A and type B (Fig. 278) failures. A type A failure was observed for the α=15º, 25º and 45º repairs, and consisted on a cohesive failure of the adhesive layer (Fig. 279 (a) shows a type A failure for a α=15º repair).

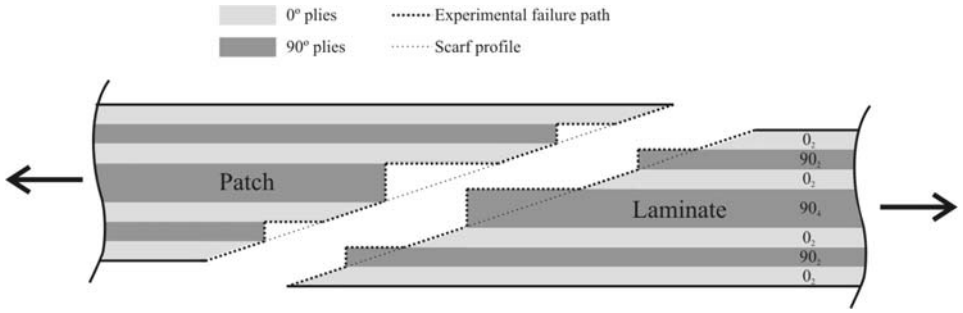

Fig. 278 – Schematic representation of the type B experimental failure.

A type B failure occurred for the other values of α, representing a mixed cohesive and interlaminar/intralaminar failure of the patch. Fig. 279 (b) shows the corresponding fractured surfaces for a α=3º repair. The difference on the failure

modes with α can be explained in light of the variation of stress distributions (Fig. 275, Fig. 276 and Fig. 277). In fact, for the bigger values of α, σ_n stress distributions are flatter and more significant, relatively to τ_{avg}. This also applies to τ_{tn} shear stress distributions, which are substantially more uniform for the bigger values of α. As a result, the adhesive is almost equally loaded along L_S, which leads to an entirely cohesive failure of the adhesive. On the other hand, for the smaller values of α, σ_n stresses diminish in relative magnitude to τ_{avg}. Consequently, it can be concluded that, under these conditions, τ_{tn} stresses govern the repairs behaviour (Hart-Smith 1973b, Campilho et al. 2007a). Since for these small values of α, τ_{tn} stresses in the adhesive layer near the 90º plies are smaller in magnitude, the intralaminar strength of the composite in tension is attained firstly. Interlaminar crack growth follows, leading to a type B failure.

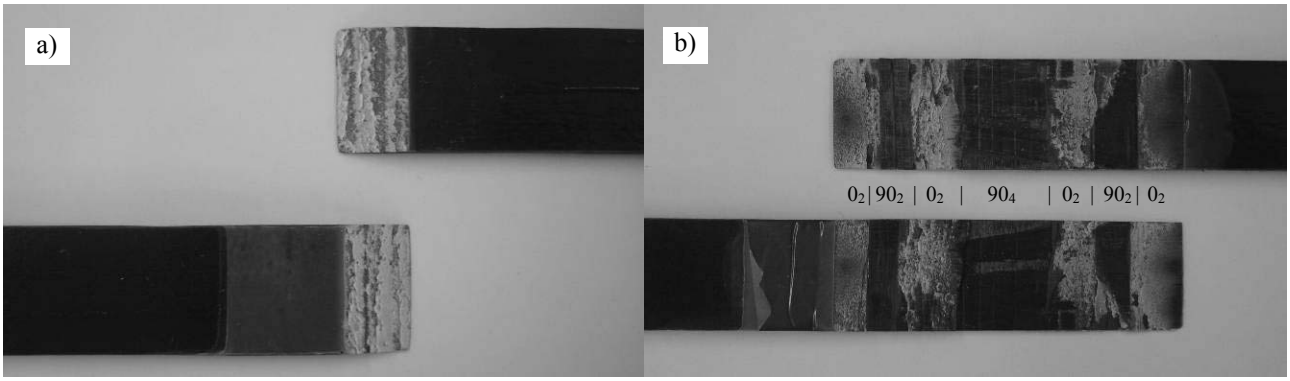

Fig. 279 – Experimental fracture surfaces for a α=15º (a) and α=3º (b) repair.

The numerical simulations predicted accurately the experimental fractures for all values of α. Fig. 280 (a) shows a type A failure for the α=45º repair, whilst Fig. 280 (b) relates to a type B failure for the α=9º repair.

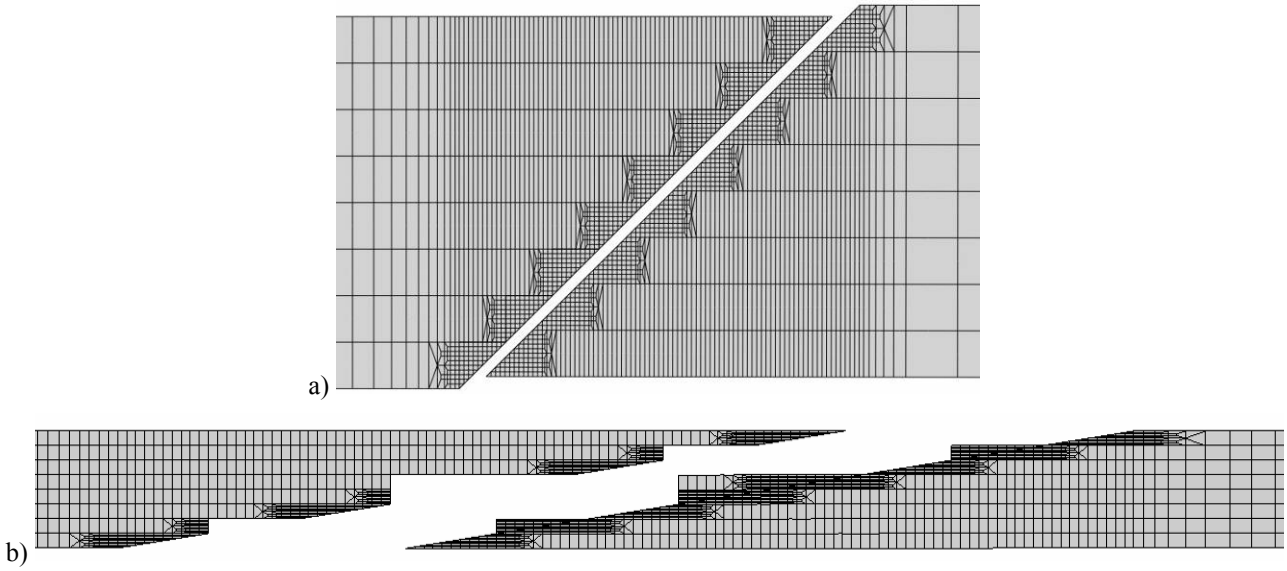

Fig. 280 – Numerical type A failure for a α=45º (a) and type B failure for a α=9º (b) repair.

Fig. 281 compares the experimental and numerical P-δ curves for the α=9º repair. These present a practically linear behaviour up to P_m, experiencing a small stiffness reduction near this value due to softening of the adhesive layer elements. Only one value of α is presented, owing to the similarity between the values of α evaluated.

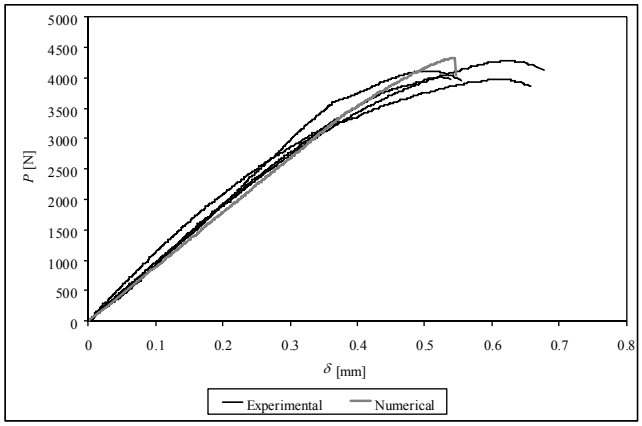

Fig. 281 – Experimental and numerical P-δ curves comparison for the α=9º repair.

4.4.3.2.2. Summary of the results

In this Sub-Section, a comparison is performed between the experiments and FEM simulations on the values of K (Fig. 282 a), maximum load displacement (δ_m, Fig. 282 b) and P_m (Fig. 283), incorporating the standard deviation of the experimental values. K was measured between the LVDT attachment points (Fig. 261). A small increasing trend of K was observed with the reduction of α (Fig. 282 a). The numerical simulations captured this tendency, although a small deviation to the experimental average values was found for the smaller values of α. Additionally, a substantial experimental scattering was found for these values of α. On the other hand, δ_m showed exponentially increasing values with the reduction of α, also with a bigger dispersion for the smaller values of α. The numerical simulations agreed reasonably with the experiments on this parameter. The experimental results scatter on K and δ_m for the smaller values of α is caused by the bigger difficulty to achieve the desired value of t_A, due to the laminates and patches bending near the scarf tips. This was caused by the introduction of thermal residual stresses during the laminate curing cycle, which led to a slight bending near the scarf tips after machining (Fredrickson et al. 2008, Campilho et al. 2009a).

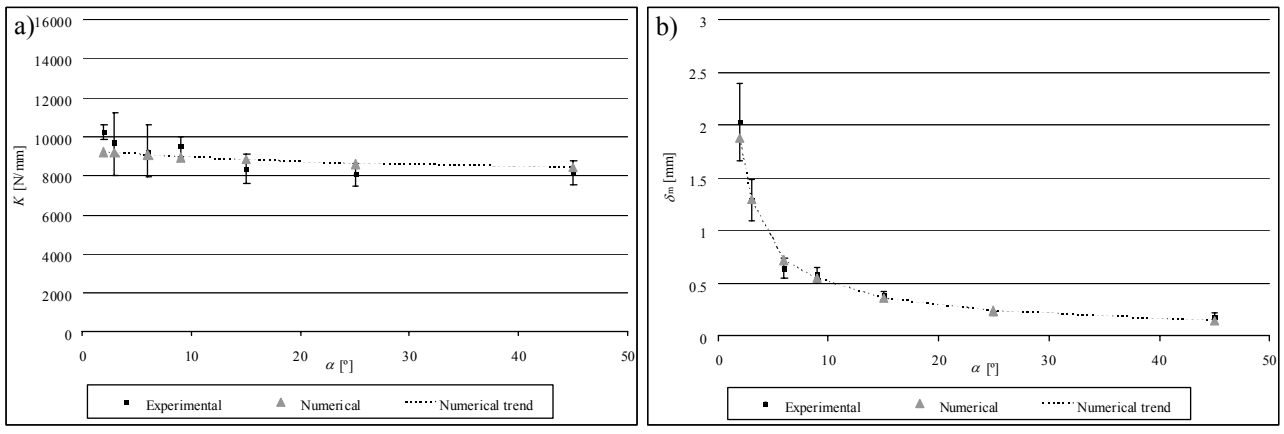

Fig. 282 – K as a function of α (a) and δ_m as a function of α (b).

A similar trend to δ_m was found for P_m, whose values increased exponentially with the reduction of α (Adkins and Pipes 1988, Du et al. 2004, Odi and Friend 2004, Objois et al. 2005, Campilho et al. 2007a, Wang and Gunnion 2008). The corresponding increase of the bond area justifies this trend. Generally, the experimental and numerical results showed a

good agreement on the three parameters studied. **It is thereby concluded that the α=2º repair is the best solution for the values of α studied, with an exponential increase on P_m with the reduction of α up to this value**.

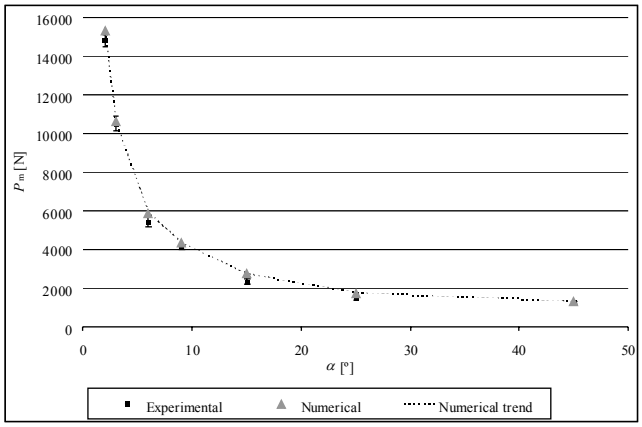

Fig. 283 – P_m as a function of α.

4.4.4. Compressive load

Following the tensile study of Sub-Section 4.4.3, the scarf repairs are subjected to a compressive load, without restraining to global buckling, similarly to the study on strap repairs. The initial stress analysis allowed the establishment of guidelines for the probable crack onset regions and influence of the parameter studied (α) on P_m.

4.4.4.1. Stress analysis

The deformed configuration of the scarf repair under a compression load is presented in Fig. 284. Fig. 285 shows σ_x stresses at the scarf region.

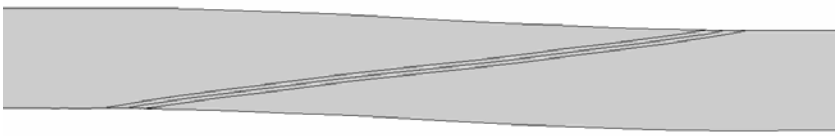

Fig. 284 – Deformed configuration of the scarf repair under a compressive load.

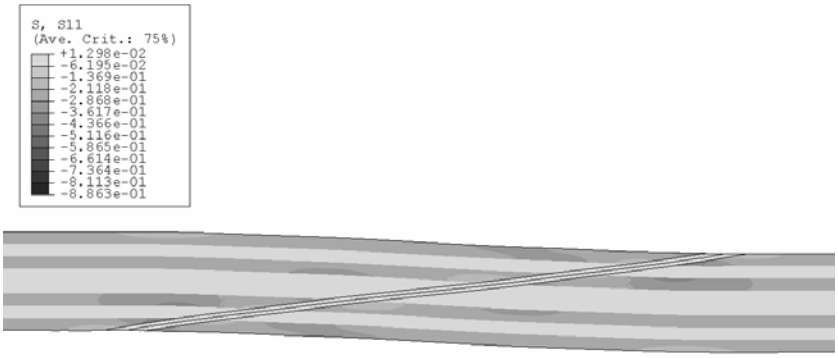

Fig. 285 – σ_x stresses at the repair region.

Under compression, the repair flexure develops in the opposite direction to the tensile load (Fig. 270). Additionally, σ_x stresses at the repair region (Fig. 285) are antisymmetric to the tensile load ones (Fig. 271). Thus, they are compressive at the repair region. These stresses are practically constant for each set of equally oriented plies and higher in magnitude in the 0º plies. Moreover, minor stress concentrations exist near the IES and OES, due to the flexure at those regions. Equally to the tensile load, no σ_x stress gradients were detected in the laminate thickness direction. The figures below show σ_y stresses at the repair region (Fig. 286), σ_n stress distributions at planes P1, P2 and P3 at the repair region (Fig. 288 a), τ_{xy} stresses (Fig. 287) and τ_{tn} stress distributions at the same three planes (Fig. 288 b).

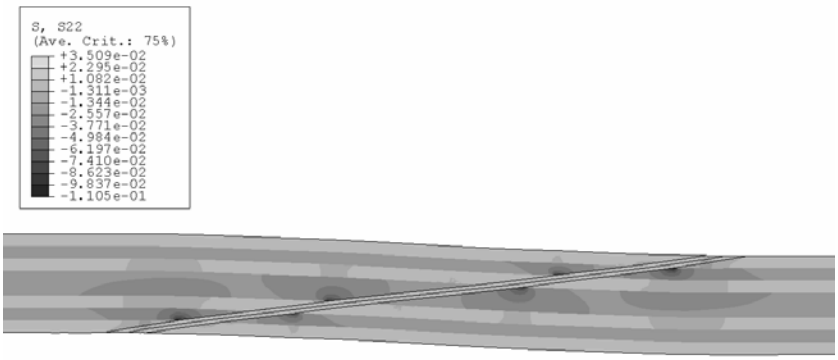

Fig. 286 – σ_y stresses at the repair region.

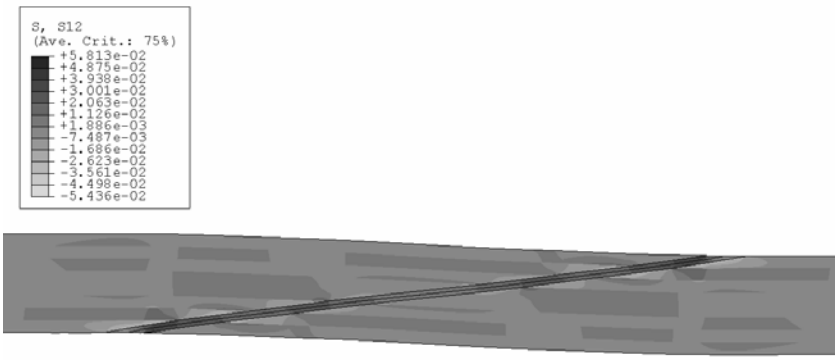

Fig. 287 – τ_{xy} stresses at the repair region.

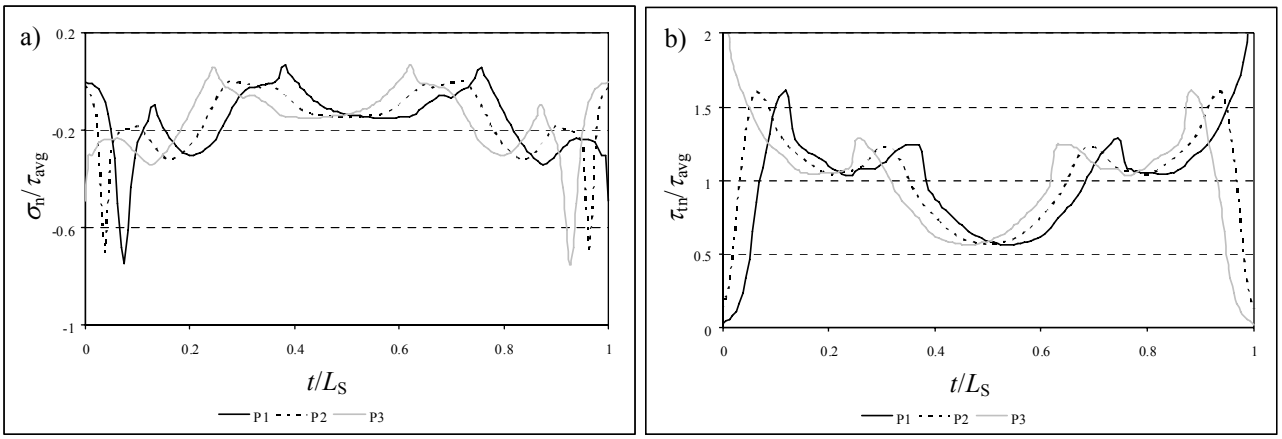

Fig. 288 – Normalized σ_n (a) and τ_{tn} (b) stress distributions at the repair region.

σ_y/σ_n stress distributions along L_S are antisymmetric to the corresponding scarf repairs under tension (Fig. 272 and Fig. 274 a). Thus, they are predominantly compressive and similar at the three planes, without a direct relation with the plies orientation (Campilho et al. 2009f). On the other hand, τ_{xy}/τ_{tn} stresses are equal to the tensile load ones (Fig. 273 and Fig. 274 b). As a result, these stresses peak near the load oriented plies, due to their higher stiffness in the load direction (Campilho et al. 2009f). Analysing these results, similar conclusions to the scarf repairs under tension are drawn on the most probable damage onset loci. Thus, damage is expected to initiate at or near plane P1 (OES) and plane P3 (IES), since shear stress singularities develop at those locations.

4.4.4.1.1. Scarf angle

Equally to the previous analyses, planes P1, P2 and P3 (Fig. 248) were selected to evaluate σ_n and τ_{tn} stress distributions as a function of α. Fig. 289, Fig. 290 and Fig. 291 pertain to planes P1 (laminate/adhesive interface), P2 (adhesive layer mid-thickness) and P3 (adhesive/patch interface), respectively.

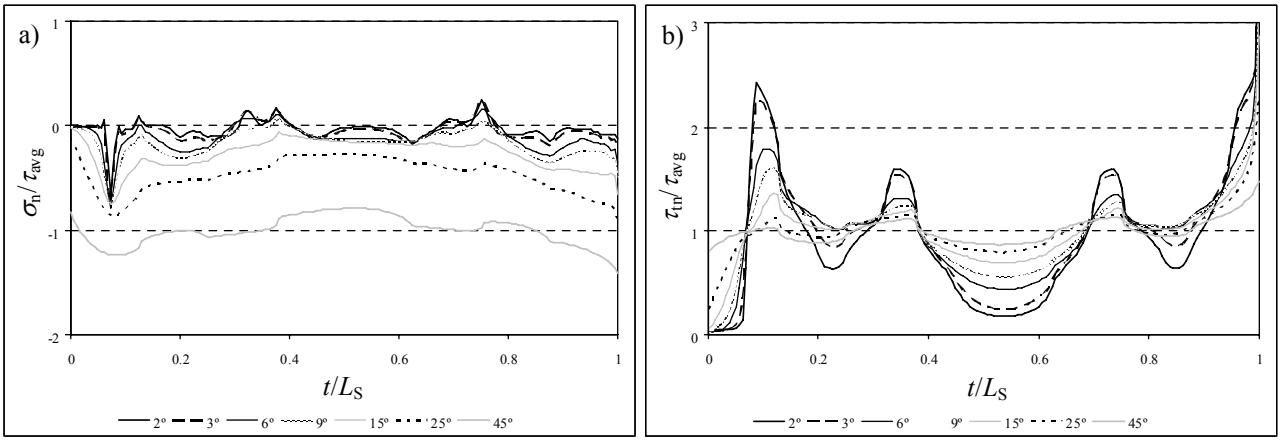

Fig. 289 – Normalized σ_n (a) and τ_{tn} (b) stress distributions at the laminate/adhesive interface (P1) as a function of α.

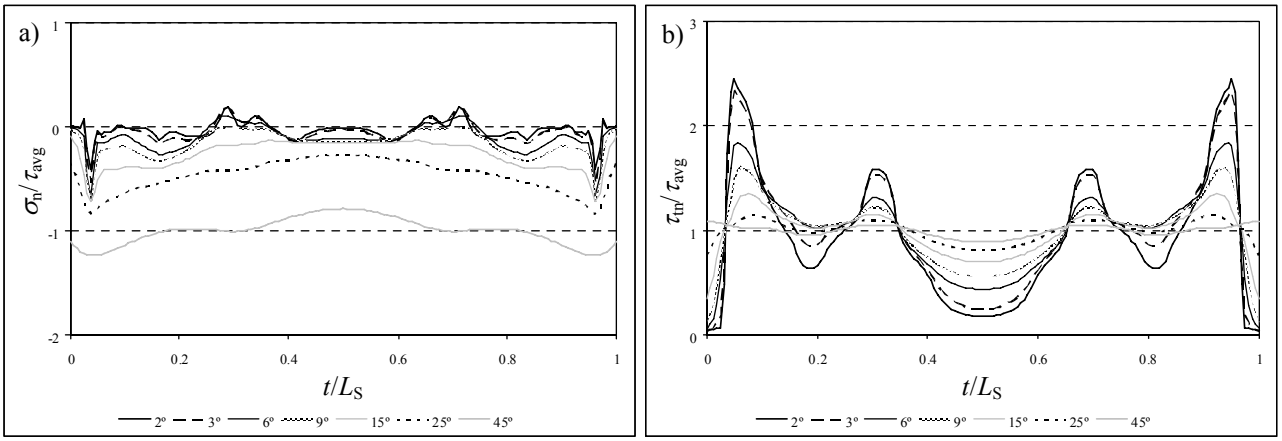

Fig. 290 – Normalized σ_n (a) and τ_{tn} (b) stress distributions at the middle of the adhesive (P2) as a function of α.

σ_n stresses are antisymmetric to the tensile load ones (Fig. 275 (a), Fig. 276 (a) and Fig. 277 (a)). As a result, these are mostly compressive along L_S. Only for the smaller values of α, σ_n peel stresses of small magnitude develop at localized regions. σ_n stresses only acquire relevance for the bigger values of α (Campilho et al. 2009f), whilst for the smaller

values the repairs behaviour is ruled by shear (Imanaka et al. 2000, Imanaka and Suzuki 2002). No significant differences were found on σ_n stress distributions between the three planes.

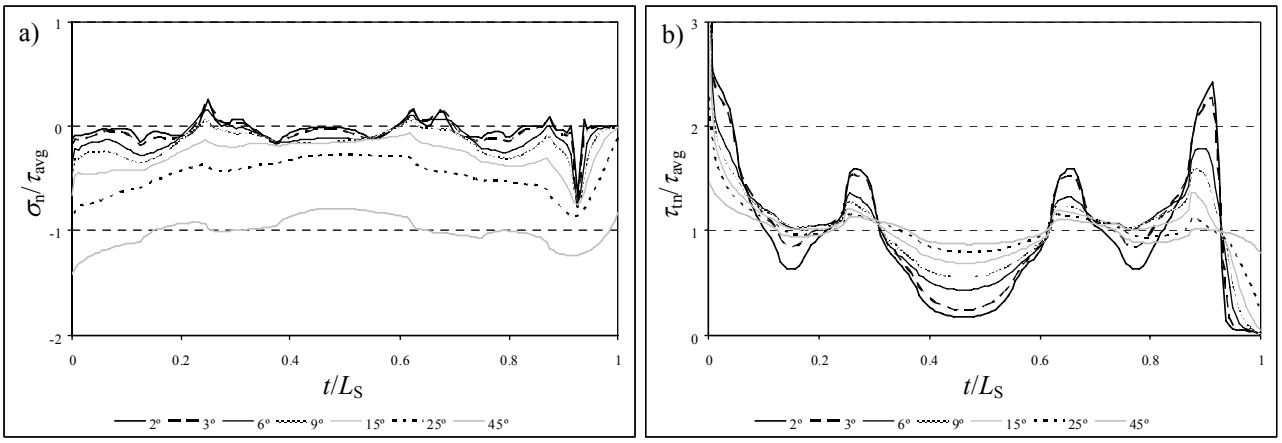

Fig. 291 – Normalized σ_n (a) and τ_{tn} (b) stress distributions at the adhesive/patch interface (P3) as a function of α.

τ_{tn} stresses are equal to the ones under tension (Fig. 275 (b), Fig. 276 (b) and Fig. 277 (b)), thus peaking near the 0º plies. Added to this, τ_{tn} stress gradients between 0º and 90º plies also diminish by increasing the value of α (Campilho et al. 2009f). Apart from the stress singularities at plane P1 (OES) and plane P3 (IES), τ_{tn} stress distributions are identical between planes P1, P2 and P3. No conclusions will be drawn at this stage concerning the influence of stresses on the repairs strength, since under compression the strength is ruled by the buckling of the repairs, rather than the strength properties of the materials involved (Finn et al. 1992, Helms et al. 2003).

4.4.4.2. Failure analysis

4.4.4.2.1. Mechanical behaviour

The experimental tests disclosed two dissimilar failure mechanisms for the scarf repairs under compression, depending on α: type A and type B (Fig. 292) failures. In fact, for the bigger values of α (15º, 25º and 45º), failure was entirely cohesive in the adhesive layer, near the patch/adhesive interface (type A failure, Fig. 293 (a) for a α=45º repair), which showed to be consistent with the FEM simulations (Fig. 294 a). Moreover, the plateau regions for these repairs were relatively small, corresponding to an equally minor buckling prior to failure.

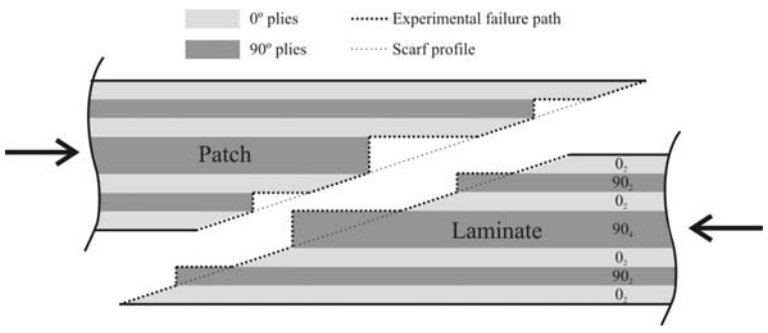

Fig. 292 – Schematic representation of the type B experimental failure.

On the other hand, the α=2º, 3º, 6º and 9º repairs experienced a mixed failure. Fig. 292 portrays a type B failure, characterized by a cohesive failure of the adhesive layer near the 0º plies and a interlaminar/intralaminar failure of the patch 90º plies. The fracture surfaces of a α=2º repair showing a type B failure are illustrated in Fig. 293 (b).

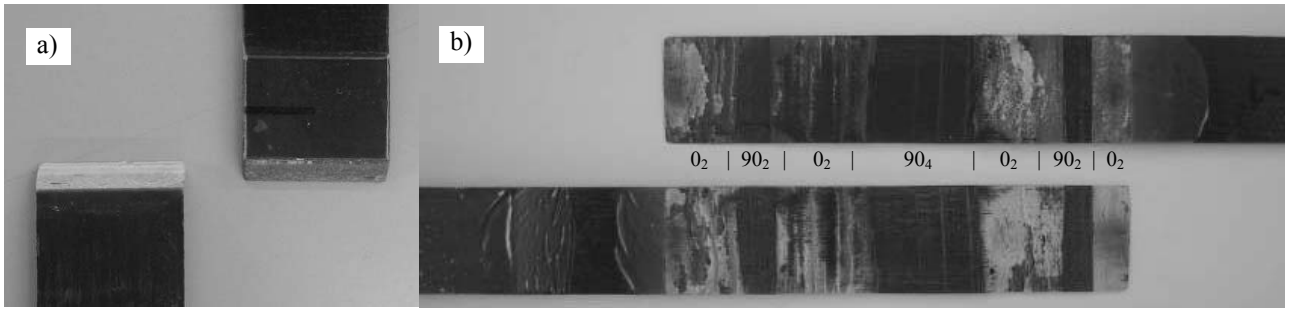

Fig. 293 – Experimental fracture surfaces for a α=45º (a) and α=2º (b) repair.

The simulations performed for these repair geometries agreed with the experiments (Fig. 294 (b); enlargement to the vertical coordinates was applied for clarity). The type B failure, observed for the smaller values of α, agrees with the tensile load analysis for these repairs, presented in Sub-Section 4.4.3.2.1.

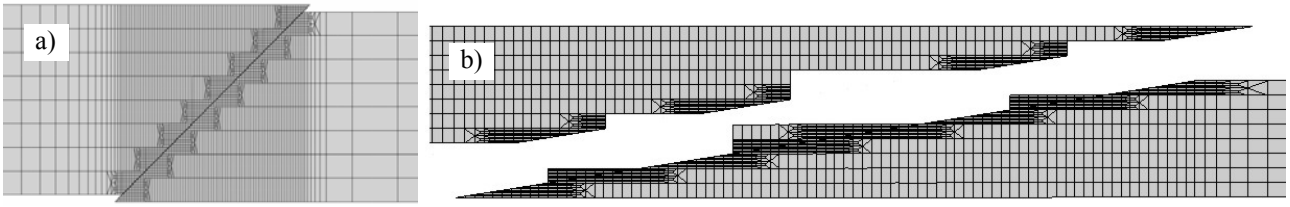

Fig. 294 – Numerical type A failure for a α=45º (a) and type B failure for a α=2º (b) repair.

Under compression, the difference in failure modes can also be explained in light of the same principles. Indeed, Fig. 289, Fig. 290 and Fig. 291 show that for the smaller values of α, the adhesive layer portions near the 90º plies are almost unloaded. Actually, σ_n stresses are nearly nil along L_S, while τ_{tn} shear stresses are markedly smaller in magnitude than near the 0º plies. This leads to a premature intralaminar fracture in the 90º plies (Fig. 292), which then propagates between differently oriented plies (interlaminar propagation), leading to a type B failure. The P-δ curves of the scarf repairs under compression revealed similar tendencies, regardless the value of α.

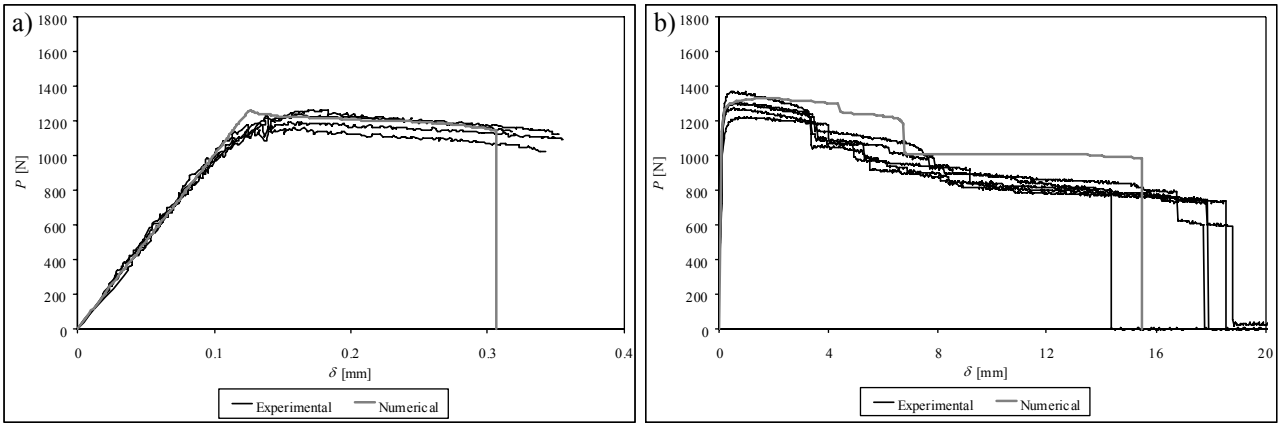

Fig. 295 – Experimental and numerical P-δ curves comparison for the α=45º (a) and α=2º (b) repairs.

Fig. 295 (a) and (b) compare the experimental and numerical P-δ curves for the α=45º and α=2º repairs, respectively. Initially, the repairs behaved elastically, without evidence of buckling. A plateau region followed, corresponding to the beginning and development of the global buckling of the repairs between the testing machine grips (Helms et al. 2003, Campilho et al. 2009f). Fig. 296 presents a comparison between the experimental and numerical deformed configurations of the α=2º repair immediately before failure.

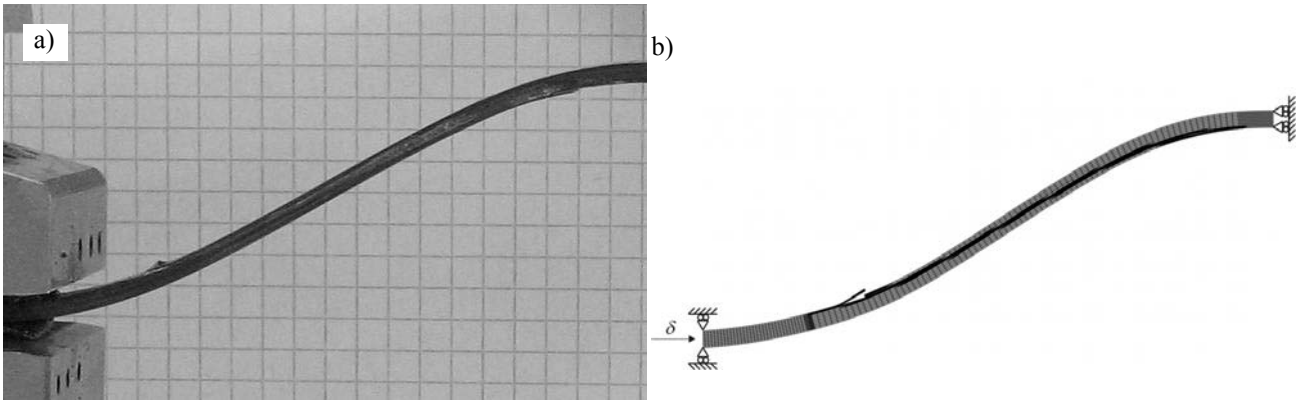

Fig. 296 – Experimental (a) and numerical (b) deformed configuration of the α=2º repair immediately before failure.

4.4.4.2.2. Summary of the results

This Sub-Section summarizes the experimental results and respective deviations, and the FEM predictions. The values of K (Fig. 297 a), P_m (Fig. 297 b), δ_m (Fig. 298a) and plateau displacement (δ_p, Fig. 298 b) were evaluated. K was measured between the testing machine grips (Fig. 262). δ_p corresponds to the failure displacement, during which the repair is able to sustain loads. K slightly increased with the reduction of α, from α=45º to α=3º. Below α=3º, K dropped abruptly (Helms et al. 2003), owing to a corresponding increase of the repaired length, which is more compliant than the undamaged composite. The buckling strength of slender structural elements under pure compression is ruled by the value of K, rather than the strength properties of the materials involved (Timoshenko and Gere 1961, Helms et al. 2003). Consequently, P_m reflected the global trend of K, i.e., a gradual increase from α=45º to α=3º, followed by an abrupt drop further decreasing α. For both K and P_m, the small deviation of the experimental data showed the repeatability of the tests conducted. In addition, a good correlation with the numerical predictions was found.

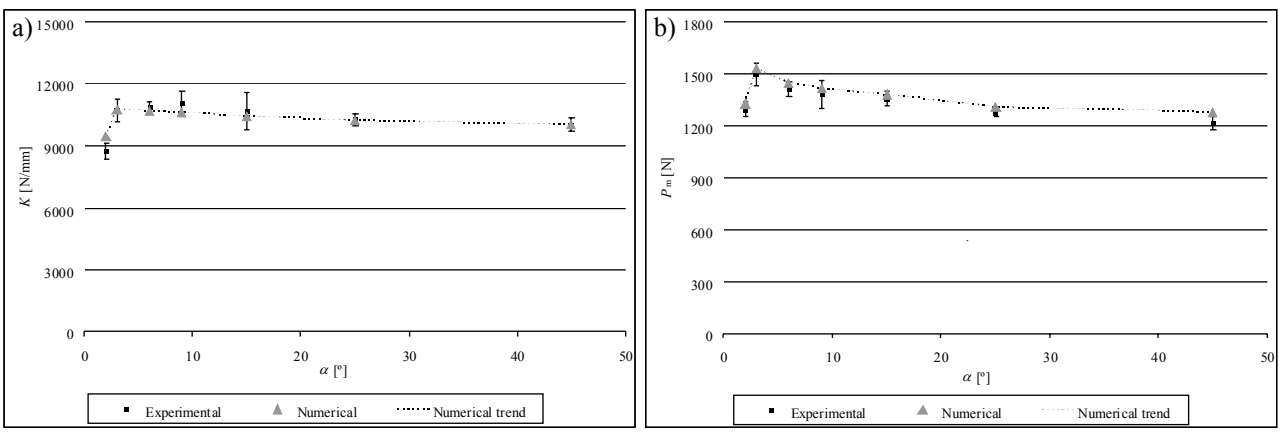

Fig. 297 – K as a function of α (a) and P_m as a function of α (b).

A similar tendency was identified experimental and numerically for the values of δ_m, characterized by a practically nil influence of α on δ_m for the 45º≤ α≤ 15º repairs and an exponential increase for the smaller values of α. This difference is caused by a smoother transition between the elastic and buckling regions of the P-δ curves with the reduction of α (Fig. 295), arising from the bigger stress gradients for the smaller values of α (Fig. 289, Fig. 290 and Fig. 291) and corresponding premature damage initiation in the adhesive layer. The values of δ_p also revealed a similar trend to δ_m, which is interpreted in light of the exponential enlargement of the bonded region with the reduction of α, which leads to correspondingly larger displacement bearing capabilities of the repairs. **For the materials, geometry and dimensions evaluated, the α=3º repair presents the highest value of P_m and is therefore considered as the optimal solution. However, smaller values of α may be recommended if the repaired region of the structure under analysis is mainly forced to bear a large displacement, rather than sustain heavy loads. This opposes to the repairs behaviour under tension, for which P_m increases exponentially with the reduction of α (Du et al. 2004, Campilho et al. 2007a, Wang and Gunnion 2008), due to the corresponding increase of the bond area**.

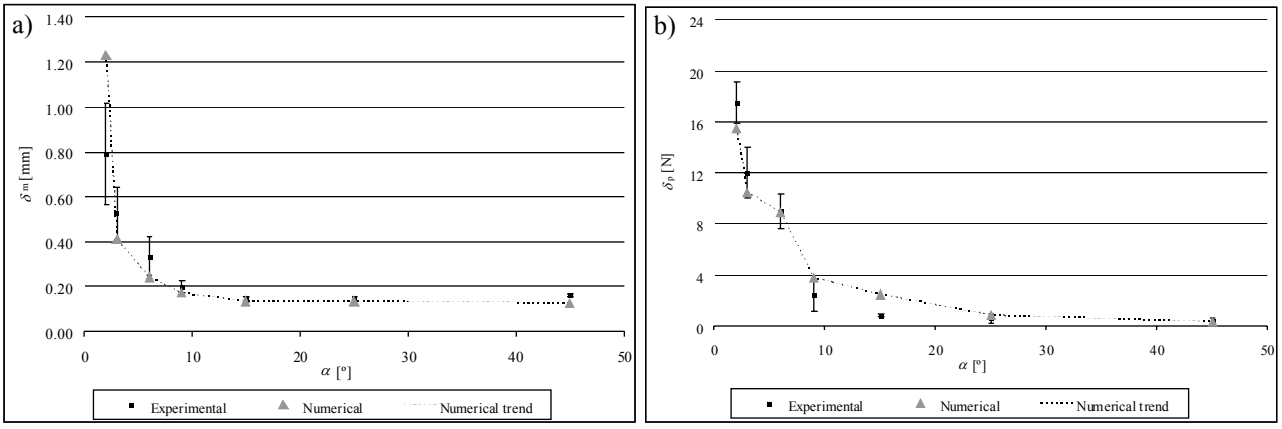

Fig. 298 – δ_m as a function of α (a) and δ_p as a function of α (b).

4.4.5. Bending load

As the final study of Section 4, the fracture behaviour of the scarf repairs under bending is described. The selected 4PB testing configuration allows a constant bending moment at the repaired region. Similarly to the previous studies, the analysis begins with a discussion of elastic stresses, followed by the failure mechanisms and summary of the results.

4.4.5.1. Stress analysis

The following figures report on the deformed shape of the scarf repair under a bending load (Fig. 299) and the respective σ_x stresses at the scarf region (Fig. 300).

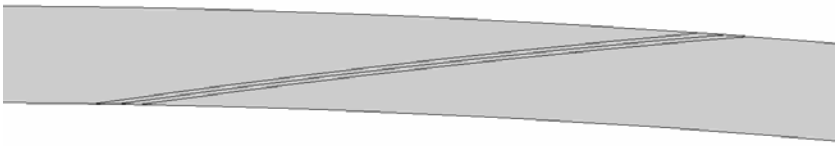

Fig. 299 – Deformed configuration of the scarf repair under a bending load.

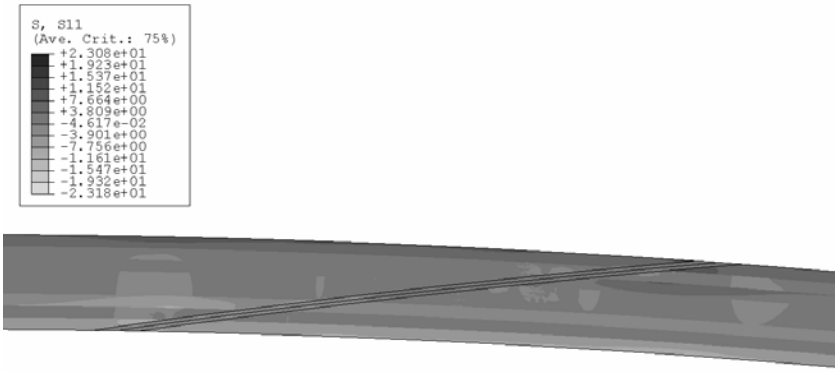

Fig. 300 – σ_x stresses at the repair region.

The constant bending moment at the repair region under 4PB reflects on a smooth curvature at the scarf region, opposed to the tensile and compressive loads (Fig. 270 and Fig. 284, respectively). σ_x stresses are highest at the inner (σ_x compressive stresses) and outer (σ_x tensile stresses) repair faces, with an approximate linear variation between these regions. Thus, at the inner plies, these stresses are small in magnitude. Oppositely to the tensile (Fig. 271) and compressive (Fig. 285) loads, significant σ_x stress gradients in the thickness direction develop under bending. However, no significant concentrations are introduced in the bonded region due to the repair procedure, unlike in the case of tensile and compressive loads. Fig. 272 corresponds to σ_y stresses and Fig. 274 (a) to σ_n stress distributions at planes P1, P2 and P3. Fig. 273 and Fig. 274 (b) present τ_{xy} stresses and τ_{tn} stress distributions at the same planes, respectively.

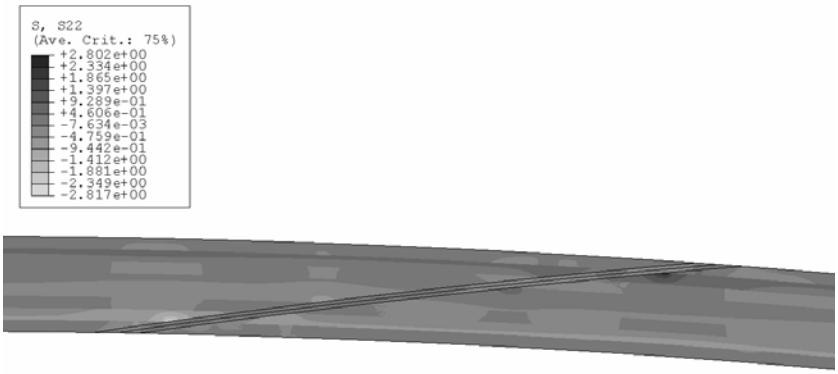

Fig. 301 – σ_y stresses at the repair region.

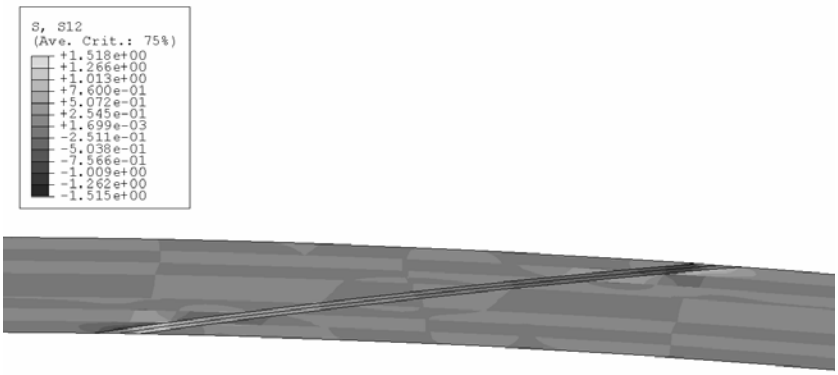

Fig. 302 – τ_{xy} stresses at the repair region.

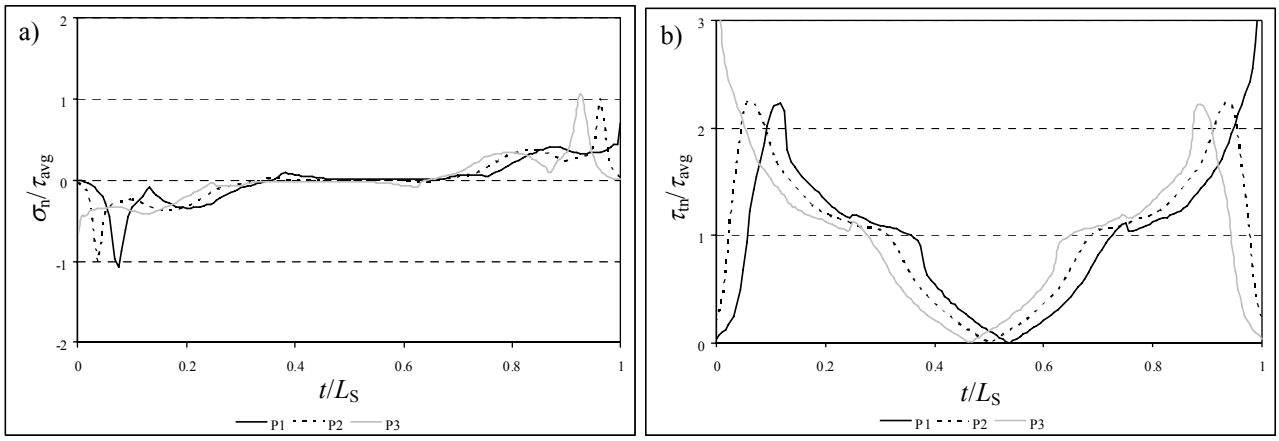

Fig. 303 – Normalized σ_n (a) and τ_{tn} (b) stress distributions at the repair region.

σ_y/σ_n stress distributions at plane P2 under bending are antisymmetric relatively to t/L_S=0.5, in opposition to the symmetric profiles of the tensile (Fig. 272 and Fig. 274 a) and compressive (Fig. 286 and Fig. 288 a) loads. In fact, peel peak stresses at the IEO oppose to compressive peak ones at the OEO. Identical σ_n stress distributions were found between the three planes. τ_{xy}/τ_{tn} stresses present some similarities to the corresponding tensile (Fig. 273 and Fig. 274 b) and compressive (Fig. 287 and Fig. 288 b) ones. Indeed, these are characterized by a higher magnitude near the 0º plies. However, the variation of stresses along the thickness with respect to the neutral axis, characteristic of structures under bending, also adds to this behaviour. As a result, shear stresses become nil at or in the vicinity of t/L_S=0.5, depending on the plane considered. This analysis shows that damage initiation under a bending load is likely to occur at the OES, where the highest magnitude peel and shear peak stresses coexist. Moreover, damage is prone to initiate at or near plane P1, since a stress singularity develops at this plane.

4.4.5.1.1. Scarf angle

σ_n and τ_{tn} stresses are presented at planes P1 (laminate/adhesive interface, Fig. 304), P2 (adhesive layer mid-thickness, Fig. 305) and P3 (adhesive/patch interface, Fig. 306).

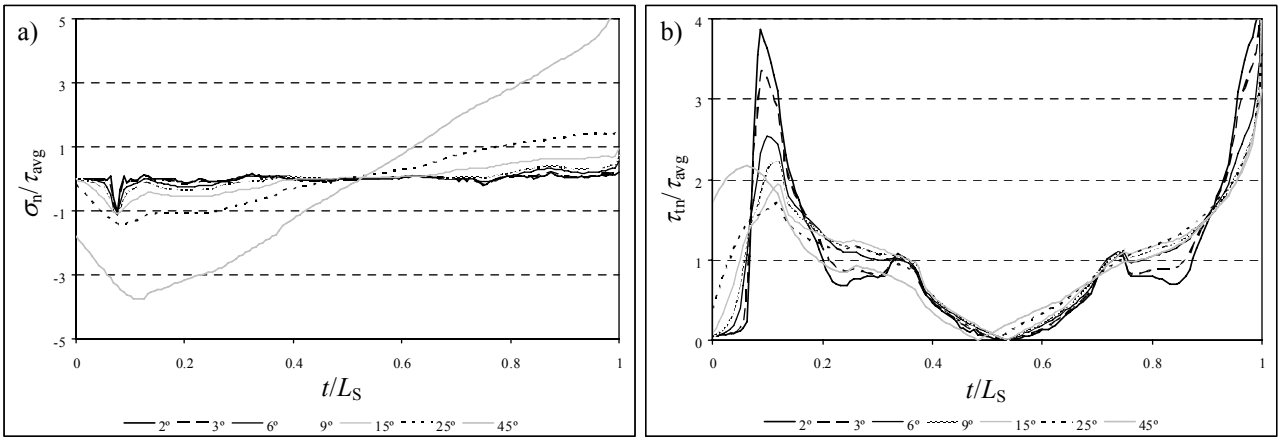

Fig. 304 – Normalized σ_n (a) and τ_{tn} (b) stress distributions at the laminate/adhesive interface (P1) as a function of α.

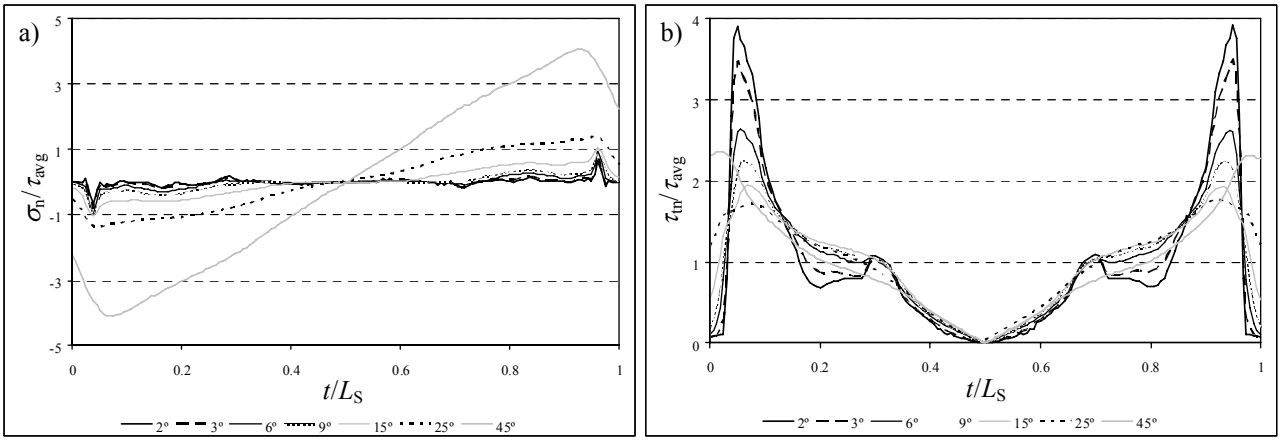

Fig. 305 – Normalized σ_n (a) and τ_{tn} (b) stress distributions at the middle of the adhesive (P2) as a function of α.

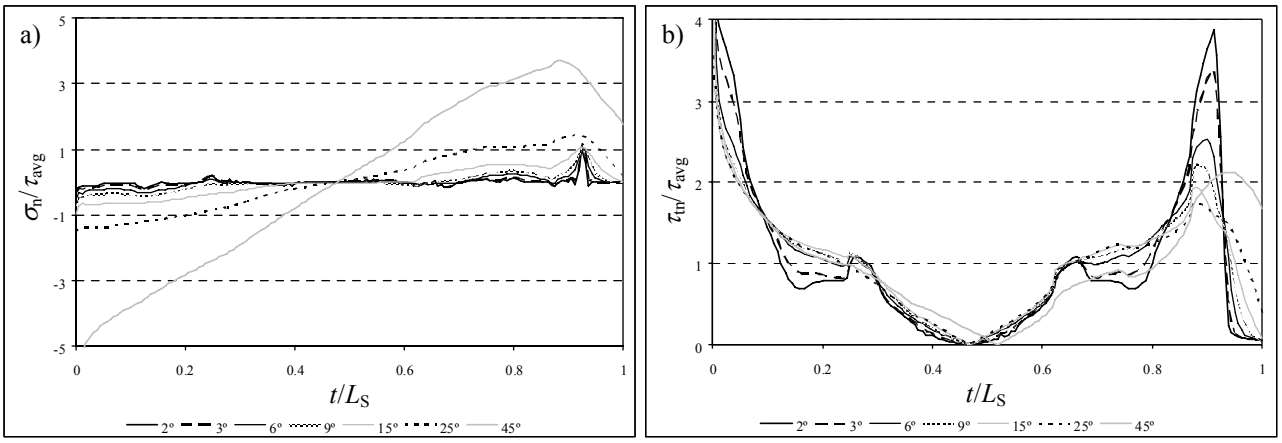

Fig. 306 – Normalized σ_n (a) and τ_{tn} (b) stress distributions at the adhesive/patch interface (P3) as a function of α.

σ_n stresses are negligible comparatively to τ_{avg} for the smaller values of α, gradually increasing with this parameter, which is consistent with the tension load results (Fig. 275 (a), Fig. 276 (a) and Fig. 277 (a)) and compression (Fig. 289 (a), Fig. 290 (a) and Fig. 291 (a)). σ_n stresses are nil at t/L_S=0.5, increasing linearly and antisymmetrically towards the IES and OES. This opposes to the tension and compression loads, for which σ_n stresses are flatter, especially for the bigger values of α. No significant variations were discovered between the three planes, except on the σ_n peak stresses at the adhesive layer edges. In fact, at plane P2 these are present at both edges, while at planes P1 and P3 they only subsist at the IES and OES, respectively. Conversely to σ_n stresses, τ_{tn} stresses present some similarities to the tensile (Fig. 275 (b), Fig. 276 (b) and Fig. 277 (b)) and compression loads (Fig. 289 (b), Fig. 290 (b) and Fig. 291 (b)). However, the linear thickness stress variation with respect to the neutral axis adds to the typical wavy distributions emerging from the different ply orientations. An increase of the stress gradients along L_S was identified with the reduction of α. Owing to the reduced τ_{tn} stresses magnitude at the scarf central region, higher τ_{tn}/τ_{avg} values were also found at the scarf edges. Stress singularities at plane P1 (OES) and plane P3 (IES) are the sole relevant differences between the three planes. Identically to the tensile and compression loads, no definitive conclusions can be drawn at this stage regarding the evolution of the repairs strength with the bond area.

4.4.5.2. Failure analysis

4.4.5.2.1. Mechanical behaviour

An identical failure mode of the scarf repairs under bending was found experimentally for all values of α, consisting on a mixed cohesive and interlaminar/intralaminar failure of the laminate at the scarf region. Fig. 307 shows schematically this failure, which can be described as a cohesive failure along L_S, except at the two sets of 90º plies closer to the IES, for which a mixed interlaminar/intralaminar failure of the laminate occurred.

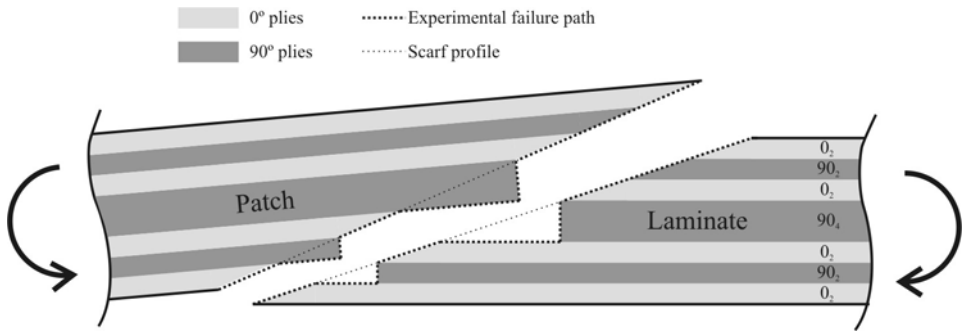

Fig. 307 – Schematic representation of the experimental failure.

Fig. 308 (a) and (b) display the fractured surfaces for a α=6º and α=25º repair, respectively. The experimental behaviour was partially captured by the FEM analysis. In fact, the α=45º repair showed numerically an interlaminar/intralaminar failure only at the set of two 90º plies nearest the IES, which is not consistent with the tests. For the other values of α, the experimental failure mode was accurately reproduced. Fig. 309 shows the numerical failures for a α=45º (a) and α=25º (b) repair.

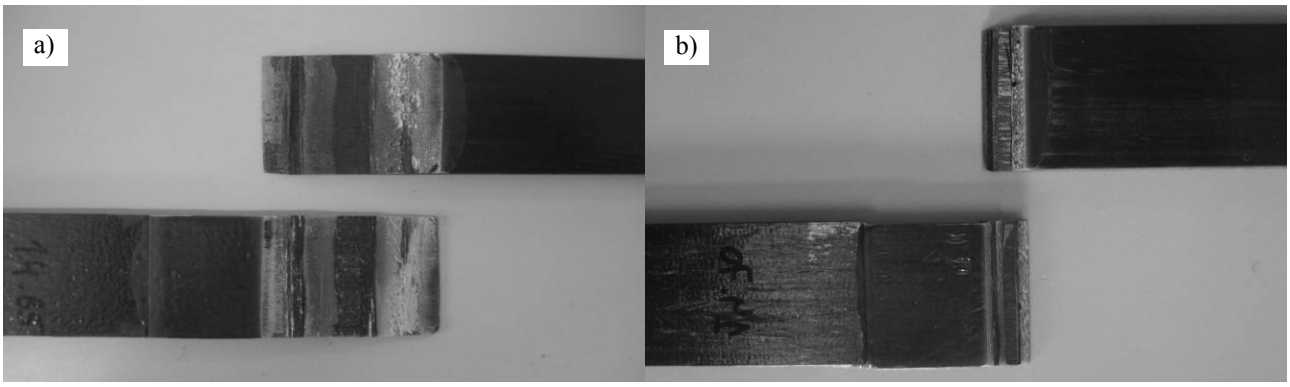

Fig. 308 – Experimental fracture surfaces for a α=6º (a) and α=25º (b) repair.

The described fracture can be explained in light of the antisymmetry of σ_n stresses along L_S (Fig. 304 (a), Fig. 305 (a) and Fig. 306 (a)). In fact, these are compressive at the scarf inner region ($0 \leq t/L_S \leq 0.5$). Since σ_n compressive stresses are not as harmful to the adhesive as σ_n peel ones (Tong and Steven 1999, Campilho et al. 2008a, Campilho et al. 2009g), the adhesive is not as severely loaded as at the scarf outer region ($0.5 \leq t/L_S \leq 1$). As a result, at the two sets of

90º plies closest to the IES, intralaminar failures of the laminate took place prior to failure in the adhesive layer. Interlaminar damage propagation followed at these regions, leading to the failure mode illustrated in Fig. 307.

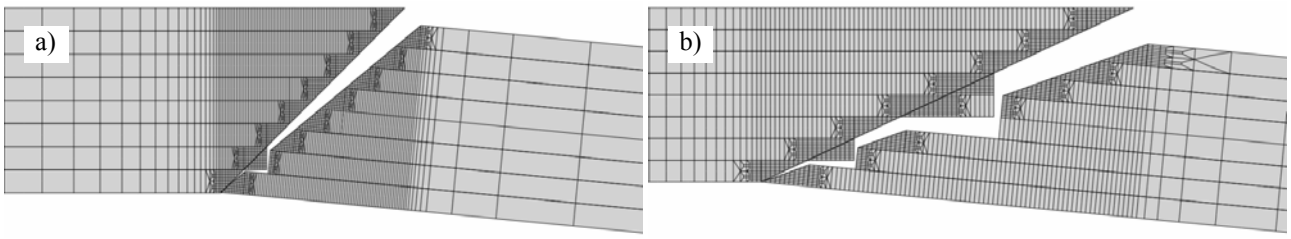

Fig. 309 – Numerical failure for a α=45º (a) and α=25º (b) repair.

Fig. 310 (a) and (b) compare the experimental and numerical P-δ curves for the α=6º and α=25º repairs, respectively. The numerical simulations predicted accurately the values of K, P_m and δ_m for these repairs, notwithstanding the slight difference on P_m and especially δ_m for some of the testing conditions (including the α=25º repair, Fig. 310 b). Although no definite conclusions could be drawn concerning these small deviations, the estimation procedure for the pure mode I cohesive law of the adhesive layer can be pointed out a probable cause (Sub-Section 3.2.2.1.2). Actually, it was mentioned that the values of $\sigma_{u,I}$ and $\delta_{2,I}$ practically did not affect the fitting procedure, which led to the use of simplification assumptions for the derivation of these parameters. Given that, for these particular loading conditions, peel stresses are particularly relevant (Fig. 304, Fig. 305 and Fig. 306), the scarf repairs under bending could show a higher sensitivity to small errors emerging from the estimation of the values of $\sigma_{u,I}$ and $\delta_{2,I}$.

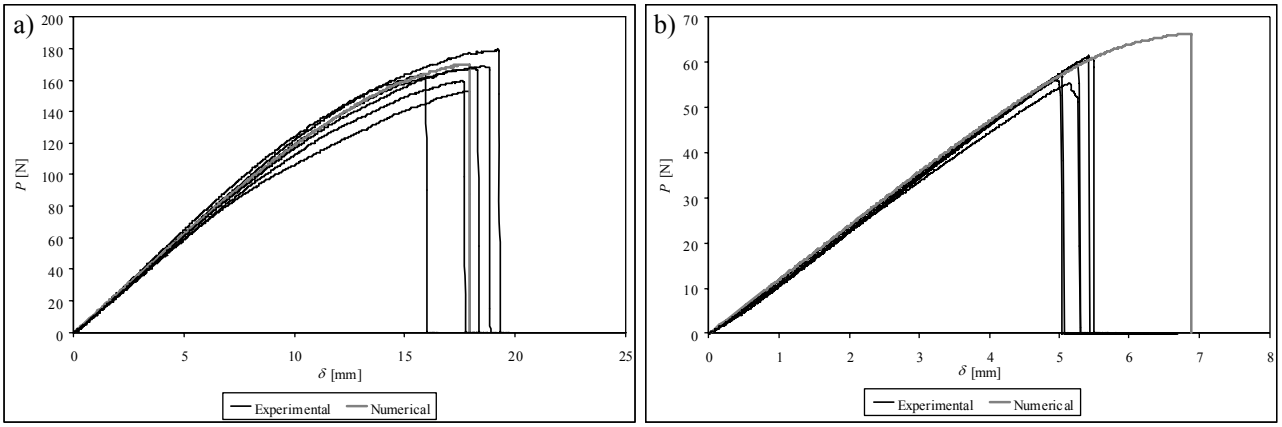

Fig. 310 – Experimental and numerical P-δ curves comparison for the α=6º (a) and α=25º (b) repairs.

4.4.5.2.2. Summary of the results

The average results of the tests and respective numerical predictions are summarized in terms of K (Fig. 311 a), δ_m (Fig. 311 b) and P_m (Fig. 312). The standard deviation of the experiments is also included. The value of δ for the calculation of K was equalled to the cross-head displacement of the testing machine. Identically to the tensile load (Fig. 282 a), a small increasing trend of K was observed with the reduction of α. This tendency was also obtained numerically, although a non-negligible deviation was detected for the α=3º repair. Small variations of t_A, whose cause was already discussed in Sub-Section 4.4.3.2.2, are the probable explanation for this inconsistency. On δ_m, the experimental

exponential increasing trend with the reduction of α was obtained numerically. However, slightly higher values of δ_m were generally detected in the FEM simulations, already discussed in the previous Sub-Section. Moreover, a minor reduction on δ_m was attained from α=3 to α=2º, which also is not consistent with the experiments. The exponential trend for δ_m is substantiated by the increase of L_S with the reduction of α and corresponding reduction of the repair bending stiffness at that region (Campilho et al. 2009g). As a result, the repair flexibility increases, being required bigger values of δ to attain the adhesive layer and interlaminar/intralaminar strengths and subsequent repair failure.

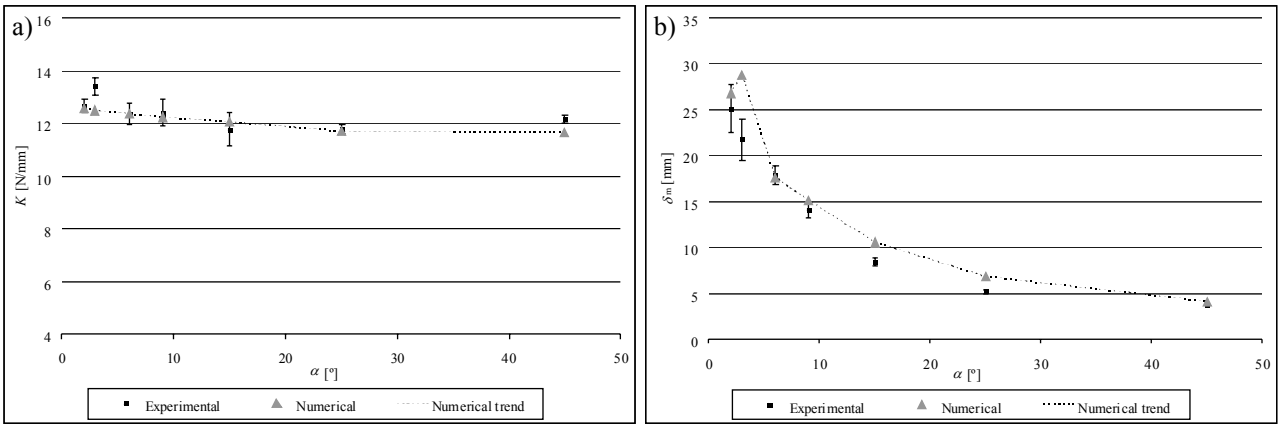

Fig. 311 – K as a function of α (a) and δ_m as a function of α (b).

The values of P_m followed this tendency, with an exponential increase with the reduction of α. This is explained by the corresponding reduction of the adhesive layer stresses magnitude (Campilho et al. 2009g), due to the laminates and patches higher flexibility at the scarf region (even though the gradients along L_S increase; Fig. 304, Fig. 305 and Fig. 306). Also on P_m the numerical simulations reproduced the experiments accurately. **Based on the results presented here, the α=2º and α=3º repairs are recommended. In fact, these present the highest values of P_m and δ_m. This conclusion is consistent with the tensile load analysis presented previously**.

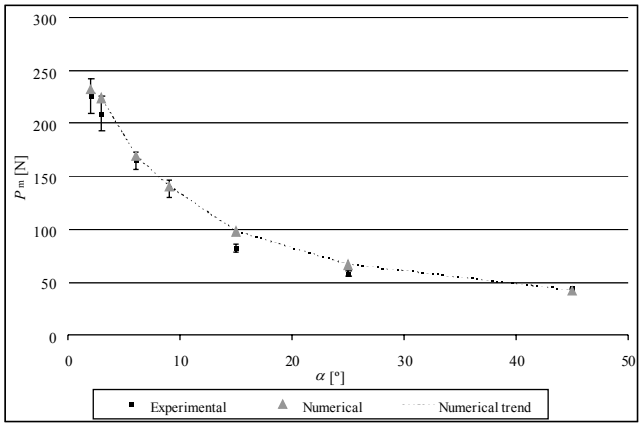

Fig. 312 – P_m as a function of α.

5. GEOMETRIC CHANGES IN COMPOSITE REPAIRS

Many works have been published regarding the influence of various geometric changes in structural adhesively-bonded assemblies, in order to increase their strength. The reduction of σ_y and τ_{xy} peak stresses at the critical regions of the structures (Groth and Nordlund 1992, Giare et al. 1992, Chaves 2005, Yan et al. 2007, You et al. 2008, Campilho et al. 2008a) or modifications of the failure mechanism emerging from these local changes (Guild et al. 2001, Potter et al. 2001, Campilho et al. 2008a) justify a strength improvement that, in many cases, can be substantial. Bogdanovich and Kizhakkethara (1999) performed a 2D FEM study on DS joints with CFRP adherends under a tensile displacement, analysing the effect of straight and curved fillets on σ_y and τ_{xy} stresses in the adhesive. The numerical models used plane-strain elements and a sub-modelling technique was employed to extract stresses at the critical regions. The fillet was found to significantly diminish σ_y peel and τ_{xy} peak stresses at the overlap edge near the fillet. Tsai and Morton (1995b) addressed the same issue experimentally and numerically using graphite-epoxy SL joints under tension. The MIM was used to extract shear strains near the fillet. It was concluded that a fillet effectively reduces shear strains, and σ_y peel and τ_{xy} peak stresses near the fillet, subsequently increasing the joint strength. Rispler et al. (2000) used a FEM optimization iterative method to ascertain the optimal fillet shape in CFRP tabs reinforced with adhesively-bonded titanium plates. Whilst the analysis initiated with a square-edge fillet, in each iteration the lower stressed fillet elements were removed to optimize the fillet shape. The process completed when all fillet elements attained 20% of the maximum stresses in the structure. A 45º straight fillet was found to be the optimal solution for the particular geometry tested. In this case, σ_y peel stresses in the adhesive and plate were reduced by 50% and 40%, respectively, compared to the square-edge geometry. A 2D FEM study was published by Lang and Mallick (1998), concerning the effect of the fillet shape on σ_y and τ_{xy} stresses in a SL joint loaded in tension. Reductions on σ_y peel and τ_{xy} peak stresses of 87 and 60% were achieved at the overlap edges using a curved fillet. A similar study regarding the geometry and load applied, and using CFRP adherends, was published by Quaresimin and Ricotta (2006b). Experimental results showed that efficiency improvements from 11.6 to 25.2% can be achieved with a 45º straight fillet, depending on the overlap length and adherends surface condition (with or without peel-ply). The FEM work of Belingardi et al. (2002) on tensile loaded SL joints showed that, amongst the fillet angles studied (from 15º to 75º), the 45º fillet yields the best results in reducing σ_y peel and τ_{xy} peak stresses at the overlap edges. A theoretical and experimental study was accomplished by Adams et al. (1986) on the tensile strength of CFRP/steel DL joints, including several geometric changes, such as filleting the plate edges and chamfering the inner and outer adherends faces. An inside taper in the outer adherends combined with an adhesive fillet proved to be the most efficient scenario. Between the fillet angles tested (17º, 30º and 45º), the 30º one was found to be the best solution. Overall, the theoretical predictions on the failure loads were accurate. The work of Campilho et al. (2009b) used a CZM with triangular laws in pure modes I and II to evaluate the tensile strength of adhesively-bonded SS and DS repairs with unidirectional CFRP adherends. Several geometric alterations, such as fillets, were analysed. Amongst the various fillet shapes considered, the 45º straight fillet led to the highest strength improvement for both SS and DS repairs. The use of fillets incorporating steel wires and wedges in SL joints with steel

adherends was investigated experimentally by You et al. (2003) for different shapes of these elements. Three shape/size combinations were tested, including circular and triangular shaped elements. These modifications significantly improved the joints tensile strength, reaching approximately 45% for a circular steel wire. Hu and Soutis (2000) carried out a FEM analysis on 3D DS repairs under compression and concluded that localized stresses develop at the overlap edges. The numerical simulations showed that shear peak strains can be markedly reduced increasing locally the value of t_A at these regions. Therefore, a repair with the patches tapered from the inside was considered to reduce stress concentrations in the adhesive layer, enhancing the repairs strength. No numerical or experimental analyses were performed to confirm this assumption. The taper slope for the patches proposed in this work is 1/10. A 2D study of tensile loaded aluminium and steel SL joints was accomplished by Sancaktar and Nirantar (2003). The authors focused on the adherend outside tapering technique, concluding that this modification significantly reduces σ_y peel and τ_{xy} peak stresses in the joints, increasing significantly their strength. The adherends notching at the overlap edges was used by Sancaktar and Simmons (2000) on aluminium SL joints under tension. The FEM analyses revealed a major reduction on σ_y peel peak stresses (maximum of 66%), whilst τ_{xy} stresses were kept identical. However, experimental tests showed only an 8% strength improvement, compared to the standard SL joint. Ganesh and Choo (2002) carried out a FEM study in which E modulus grading of the adherends of SL joints was applied at the overlap region to reduce stress concentrations. This technique showed a 20% reduction on τ_{xy} peak stresses in the adhesive at the overlap edges, increasing the load transfer at the overlap central region. σ_y stresses were not affected by this modification, while σ_x stresses slightly increased. No strength comparison to the standard SL joints was performed. Boss et al. (2003) addressed the same technique, considering additionally the geometrical thickness grading of the adherends at the overlap edges with the same purpose. Shear peak stresses at the adhesive layer edges were reduced with both the solutions tested, i.e., E modulus grading and chamfering of the adherends. σ_y peel stresses only diminished by the chamfering technique. Ávila and Bueno (2004a) studied a wavy-lap joint with E-glass/epoxy composite adherends under a tensile load. This geometry consisted on a sinusoidal adherends shape at the overlap region, instead of the traditional flat one. An experimental and numerical work was accomplished. The authors concluded that this modification increased on approximately 40% the standard SL joint strength, owing to the flatter σ_y and τ_{xy} stress distributions along the overlap. Kim et al. (2006) accomplished an experimental comparative study of CFRP SL joints under a tensile load, in which different joint configurations were considered: specimens with and without straight fillets of different dimensions, and co-cured specimens with or without adhesive film. The co-cured specimens without adhesive film were found to be the most efficient. The use of fillets has also proved to increase the standard SL joint strength. Potter et al. (2001) and Guild et al. (2001) performed a two-phase experimental and numerical study, respectively, concerning the tensile behaviour of adhesively-bonded CFRP DL joints with adhesive fillets at the overlap edges, adherends tapering, and also with modification layers inside the adhesive. These layers were intended to prevent crack propagation from the adhesive to the laminates, experimentally observed for the unmodified joints. This was accomplished more effectively with Kapton® films. Adhesive filleting was also judged essential in controlling the strength and failure mode of the joints. In fact, specimens with or without a 20º straight fillet were also tested, resulting on a 30% strength improvement with the fillet. da Silva and Adams (2007b) studied, using the DL geometry (CFRP inner adherend and titanium outer adherends), the effect of a patch internal taper (1/8 slope) and a straight adhesive fillet (17º) on the maximum σ_y stresses in the composite adherends and on the joints strength. Tensile loads, thermal loads and the combinations of both were examined with a 2D linear elastic FEM analysis. σ_y stresses greatly diminished under tensile loads, and also combining tensile and thermal loads. Under a purely thermal load, σ_y stresses slightly increased with the mentioned modifications. Experimental results showed that, as a rule, tapering and filleting increased

the joints strength at ambient temperatures. At low temperatures, the differences were not significant. Fessel et al. (2007) performed an experimental and 2D FEM work regarding tensile loaded steel SL joints, being tested wavy, improved wavy and reverse-bent geometries. These three modifications were regarded as extremely valuable, diminishing σ_y peel and τ_{xy} peak stresses at the overlap edges. Experimental tests were carried out for the reverse-bent joint, and strength improvements from 9 to 40% were found, compared to a standard SL joint.

In this Section, different geometric modifications for the 3D SS and DS repair techniques were evaluated numerically, using ABAQUS®, under tension, compression and bending (4PB). The choice of a purely numerical analysis is substantiated by the previous validations of the CZM approach employed in this work to simulate bonded assemblies. The specimens fabrication for some of the techniques would not be straightforward as well, requiring *Computer Numerical Control* (CNC) milling machines to fabricate the 3D shapes, added to the fastening difficulties for the circular patches (Campilho et al. 2008b). The geometric modifications tested consisted on adhesive thickening at the overlap edges, outer chamfers of the laminate and patch, adhesive fillets of various shapes at the OEO, and plug filling with adhesive the central hole of the repair. Additionally, combinations of these modifications were examined according to the results of the individual modifications for each repair technique/load, allowing maximizing the repairs strength. Initially, the material properties and analysis procedure are described. Following, this Section is divided into the two repair techniques evaluated: SS and DS repairs. Each one of these two Sub-Sections is separated into all the geometric changes considered and an additional one, addressing the combination of them. At the end of Section 5, the results are summarized in terms of failure modes and strength predictions for all individual changes and combinations. The list of the different failure modes identified for the repairs studied is presented in Table 19, while its correspondence with the repair configuration (SS or DS), load and geometry is summarized in Table 20. Table 21 lists the optimal repair configuration for each case and the respective percentile strength improvement to the standard repair.

5.1. Material properties

The materials and lay-ups of the laminates and patches are consistent with Section 4 (the mechanical properties of a unidirectional ply are detailed in Table 3, Sub-Section 3.2.2.1.2.1). The epoxy adhesive Araldite® 2015 was employed for the adhesive layer (characterized in Table 8, Sub-Section 3.2.2.1.4). In this Section, the value of t_A defined in the adhesive characterization procedure (t_A=0.2 mm) will be used. It should be emphasized that, for both stress and failure analyses, the adhesive representative solid elements were modelled as elastic isotropic, with the values of E and G moduli defined in Sub-Section 3.2.2.1.4 for this particular adhesive.

5.2. Procedure

The triangular CZM introduced in Section 3.2.1 was employed in this analysis for both stress and failure studies. From this statement, it can be concluded that solid elements were always used to model the adhesive. The cohesive elements were introduced in the numerical models at different planes in the repair thickness including the interfaces between different materials to allow the extraction of stresses and to promote damage onset and growth, allowing the characterization of the repairs up to failure. This procedure was adopted, because the trapezoidal CZM (Sub-Section 3.2.2) was developed to simulate a thin adhesive layer and, for this reason, is not applicable to some of the geometries

of this Section (e.g. adhesive thickness variations, plug filling or adhesive fillets). The geometric modifications will be applied to the SS and DS standard repair geometries (Fig. 121), with the *initial dimensions*, boundary and symmetry conditions detailed in Sub-Section 4.3. For the stress analysis, only one plane will be considered, since σ_y and τ_{xy} stresses are similar in the adhesive and respective interfaces with the laminate and patch (Fig. 141 (a) and (b) for the SS repairs, tensile load; Fig. 158 (a) and (b) for the DS repairs, tensile load). Plane P3 (laminate/adhesive interface, Fig. 122) will be addressed as a rule; only for the laminate outer chamfering plane P5 (adhesive/patch interface, Fig. 122) will be used instead, since the laminate/adhesive interface does not develop horizontally along all its length. σ_y and τ_{xy} stress distributions were always normalized by τ_{avg}, the average shear stress for the standard repair along the plane under evaluation (P3 or P5). This procedure was applied in all stress distributions in this Section. Only the symmetry plane ***B*** was evaluated, since this is the critical region of the repairs concerning the tensile (Fig. 137 – SS; Fig. 154 – DS), compressive (Fig. 180 – SS, Fig. 188 – DS) and bending loads (Fig. 204 – SS, Fig. 221 – DS). Moreover, in this Section, only the tensile stresses will be presented, since it is not the purpose of this work to study thoroughly the stress distributions for all geometric modifications and loads, but to optimize the geometry of the repairs. The failure analysis follows, considering the patch debonding onset load (P_d) instead of P_m, to characterize the strength improvement to the standard repair patch debonding onset load (P_{d0}), using the P_d/P_{d0} ratio. The cohesive elements were placed only at planes P3, P4 and P5, which implies that damage in the laminate and patches was not addressed. Additional planes were used according to the distinctive characteristics of each geometric modification. **It must be emphasized that it is not guaranteed that this modelling technique faithfully characterizes the repairs strength for all the repairs studied. In fact, it was observed in Section 4 that for some of the repairs, P_m was not ruled by patch debonding (e.g. axial splitting or delamination or compression failure in the laminate). Nonetheless, this procedure was adopted due to the difficulties and computational time required to simulate all the damage mechanisms in the laminates and patches for many different geometric scenarios. Other possibilities, such as the laminate load bearing capabilities after patch debonding (Hu and Soutis 2000, Campilho et al. 2005), were not addressed either in this analysis. In fact, it is not the objective of this work to validate or compare comprehensively the fracture behaviour and strength of the repairs with experiments, which, as mentioned previously, were not performed. Instead, this study only aims the qualitative comparison between different solutions to increase the repairs strength under different loadings, allowing the establishment of design guidelines for these repairs.**

5.3. Single-strap repairs

5.3.1. Patch outer chamfer

Fig. 313 details the mesh of the 0.3 mm (a) and 1.2 mm (b) patch outer chamfer repairs, with the last one comprising all the value of t_H at the OEO. The reduction of peel peak stresses at the OEO is the main goal of this modification (Mortensen and Thomsen 2002, Campilho et al. 2005, Kress et al. 2006), eventually increasing the repairs strength. Kaye and Heller (2002) emphasized that patch tapering distributes the loads more uniformly between the laminates and patches, which reflects on a strength improvement of bonded structures. Several t_H reductions at the OEO were tested, keeping a 1/10 chamfer slope. This slope was regarded as the most adequate by several investigators (Adams et al. 1986, Hu and Soutis 2000, da Silva and Adams 2007b). It must be emphasized, though, that tapering of thin composites

can be costly to incorporate in the components design or may not be practical due to possible damage to the components during machining (Fitton and Broughton 2005). Reductions on t_H of 0.3, 0.6, 0.9 and 1.2 mm were examined.

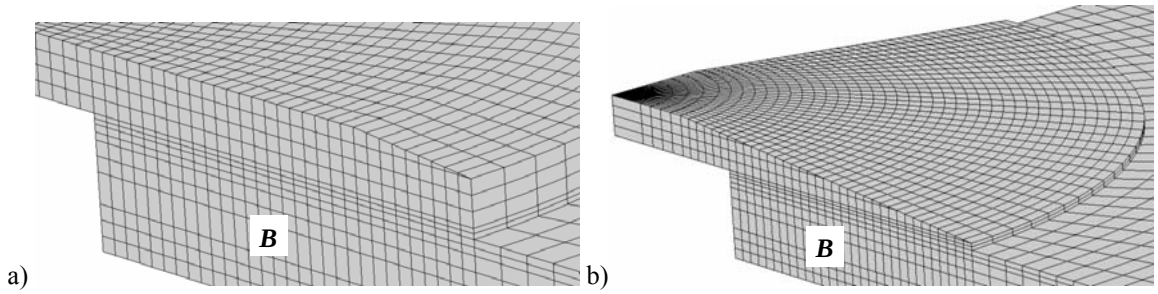

Fig. 313 – Detail of the mesh at the overlap region for the 0.3 mm (a) and 1.2 mm (b) patch outer chamfer repairs.

Fig. 314 (a) and (b) report on σ_y and τ_{xy} stress distributions, respectively, for a tensile load at the laminate/adhesive interface for all patch outer chamfer dimensions. A comparative analysis with the standard repair was performed in all the stress distributions of Section 5. σ_y stress distributions (Fig. 314 a) agree with the standard repair results, peaking at the overlap edges from lightly loaded and compressive inner regions. Whilst the 0.3 mm patch outer chamfer only alters marginally σ_y stresses, bigger chamfers lead to a gradual reduction of peak stresses at the IEO, giving rise to a tensile region of small magnitude, whose locus progressively moves towards the IEO with the chamfer dimensions. This modification is due to the corresponding decrease of load transmitted by the patch at its outer region. Identically, this geometric change shows a small influence on τ_{xy} stress distributions (Fig. 314 b), slightly reducing τ_{xy} stresses at the OEO. This reduction is more significant for the bigger dimensions patch outer chamfers (Campilho 2005). The repairs normalized patch debonding predictions for the five repairs (including the standard geometry), and for the tensile, compression and bending loads, are plotted in Fig. 315.

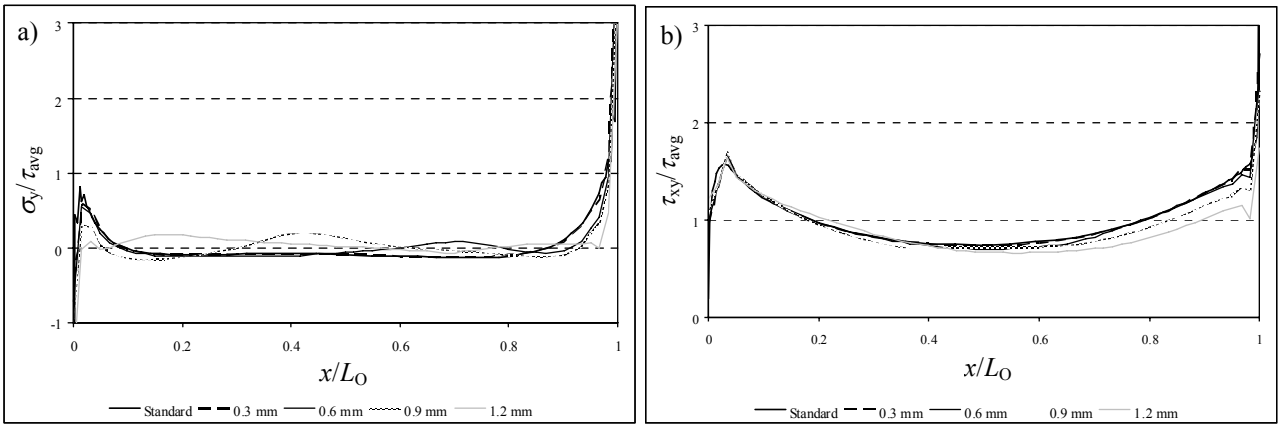

Fig. 314 – Normalized σ_y (a) and τ_{xy} (b) stress distributions at the laminate/adhesive interface (tensile load).

- In tension, P_d/P_{d0} increased exponentially as a function of the patch outer chamfer dimensions, attaining a 17.5% strength improvement for the 1.2 mm patch outer chamfer. Damage onset and growth for these repairs agrees with the standard repair, initiating at the symmetry plane ***B*** simultaneously at the OEO (laminate/adhesive interface) and at the IEO (adhesive/patch interface), with growth towards the overlap central region. These results can be explained in light of the reduction of the patch stiffness at the damage onset location (OEO), diminishing σ_y peel and shear peak stresses at this location, thus increasing P_d. Fig. 316

shows the deformed configuration of the standard (a) and the 1.2 mm patch outer chamfer (b) repairs under a tensile load. Both figures pertain to a value of δ corresponding to patch debonding onset for the 1.2 mm chamfer repair. Under these conditions, the patch has already debonded for the standard repair, due to its bigger stiffness and magnitude of stresses at the OEO.

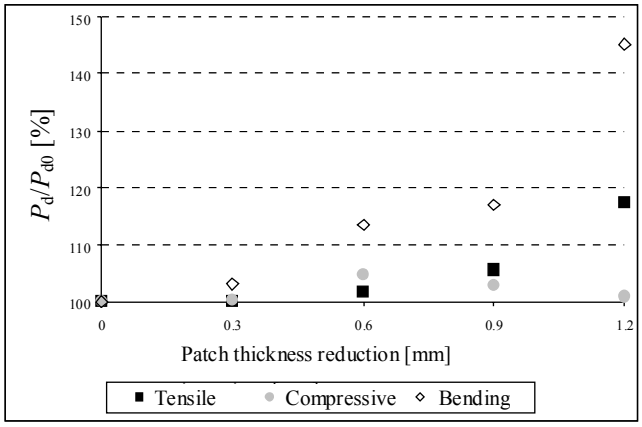

Fig. 315 – Normalized strength for different dimensions patch outer chamfer repairs.

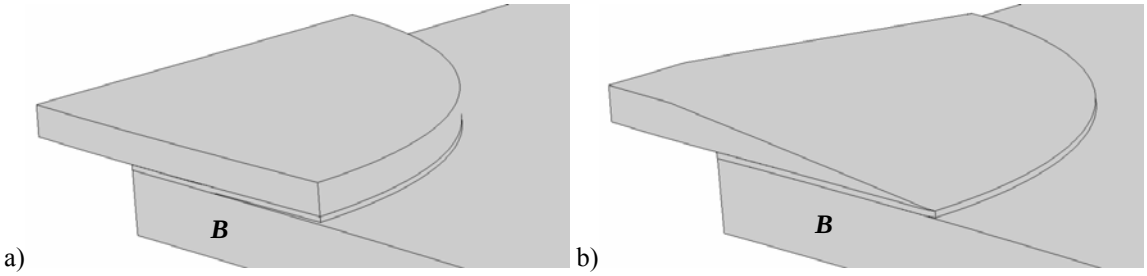

a) b)

Fig. 316 – Deformed shape of the standard (a) and 1.2 mm patch outer chamfer (b) repairs (tensile load).

- Under a compressive load, the highest strength improvement (4.6%) was attained with the 0.6 mm patch outer chamfer. For the standard, 0.3 and 0.6 mm patch outer chamfer repairs, damage initiated at the OEO at the laminate/adhesive interface (at a 45º angle of the symmetry plane ***B***), growing towards the IEO (Fig. 317 (a) shows damage onset for the 0.6 mm patch outer chamfer repair). For the other dimensions, damage initiated at the IEO (at a 45º angle of the symmetry plane ***B***) at the adhesive/patch interface, propagating to the OEO. Fig. 317 (b) shows damage onset for the 1.2 mm patch outer chamfer repair. The strength reduction from the 0.6 mm chamfer is caused by the corresponding marked decrease of the patch stiffness for the bigger chamfers. In fact, up to the 0.6 mm patch outer chamfer repair, the compressive displacement leading to patch debonding and value of P_d increase, due the reduction of stresses at the damage onset locus (OEO). Additionally, the chamfer leads to a more progressive damage growth, comparing with the standard repair. Bigger chamfers lead to a premature failure near the IEO (Fig. 317 b), justified by the increased patch flexure emerging from its stiffness reduction. This causes the strength reduction trend of Fig. 315.
- An almost 50% strength improvement was achieved under bending with this geometric alteration. However, the evolution of P_d/P_{d0} with the chamfer dimensions is far from being linear, mainly due to the significant differences between the 0.9 mm (17.0%) and the 1.2 mm (45.2%) chamfer repairs. The observed failure modes are similar to the standard repair, i.e., damage initiation at the OEO (laminate/adhesive interface) at symmetry

plane ***B*** and growth along the overlap and towards the IEO along the same interface until complete patch failure. The reduction of the patch stiffness at the damage onset locus (OEO) and the progressive increase on the patch debonding onset displacement with the chamfer dimensions explain this increasing strength tendency. Fig. 318 shows the deformed shape of the 0.3 mm (a) and 1.2 mm (b) patch outer chamfer repairs, under the patch debonding displacement for the 1.2 mm chamfer repair, clarifying the mentioned behaviour.

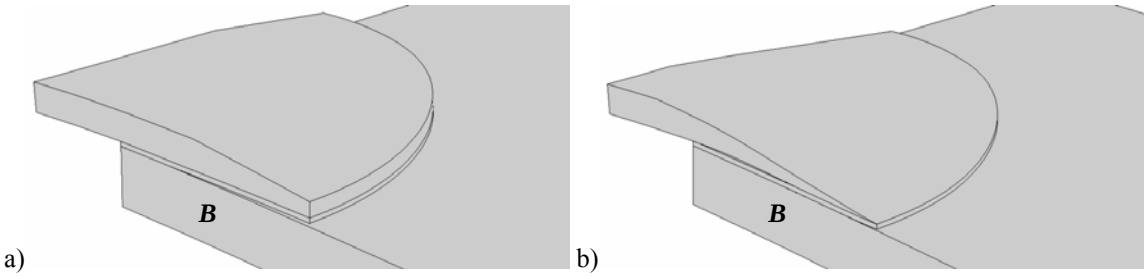

a) b)

Fig. 317 – Deformed shape of the 0.6 mm (a) and 1.2 mm (b) patch outer chamfer repairs (compressive load).

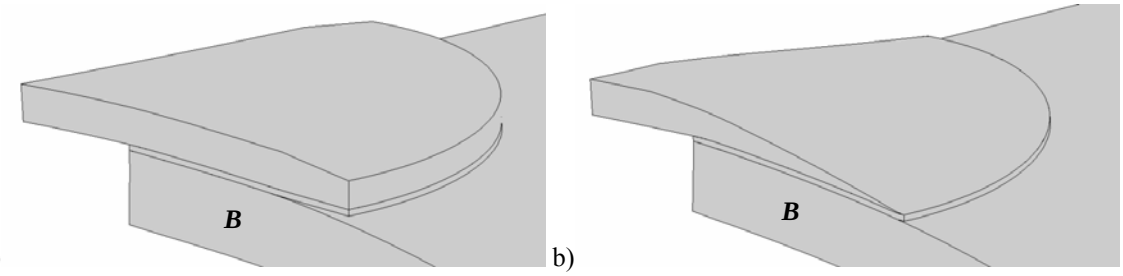

a) b)

Fig. 318 – Deformed shape of the 0.3 mm (a) and 1.2 mm (b) patch outer chamfer repairs (bending load).

5.3.2. Patch inner chamfer

The patch inner chamfering technique is widely regarded as a mean to reduce σ_y peel and τ_{xy} peak stresses at the OEO, therefore increasing the structures strength. Fig. 319 shows the mesh of the 0.3 mm (a) and 1.2 mm (b) patch inner chamfer repairs. The FEM study of Hu and Soutis (2000) demonstrated that shear peak strains in 2D DS repairs under compression diminished increasing t_A at the OEO. Therefore, patch inner chamfering was hypothetically judged to increase the repairs strength, despite the fact that no simulations were performed to corroborate this assumption. This geometric modification leads to an increase of t_A at the OEO. Although the optimal slope of the chamfer is considered to be 1/10 (Hu and Soutis 2000, da Silva and Adams 2007b), in this work a slope of 1.5/10 was used, due to geometric limitations (Fig. 319). Reductions of t_H at the OEO of 0.3, 0.6, 0.9 and 1.2 mm were evaluated.

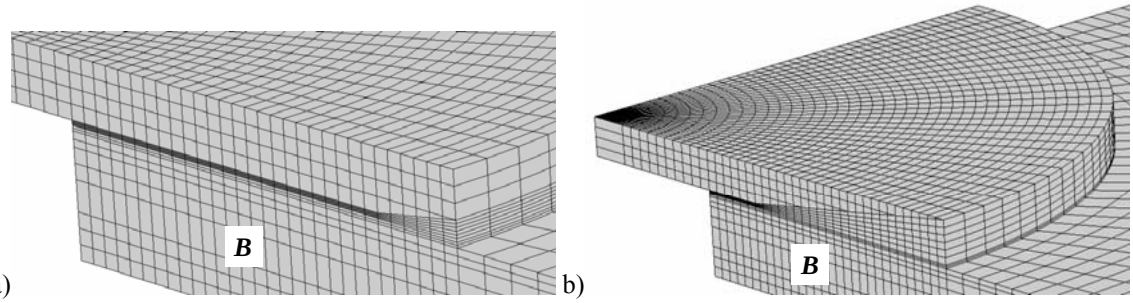

a) b)

Fig. 319 – Detail of the mesh at the overlap region for the 0.3 mm (a) and 1.2 mm (b) patch inner chamfer repairs.

The tensile σ_y and τ_{xy} stress distributions are presented in Fig. 320 (a) and (b), respectively, at the laminate/adhesive interface (plane P3, Fig. 122). σ_y stresses greatly differ between the standard and chamfered repairs. In fact, with this modification, σ_y compressive peak stresses develop at the IEO. σ_y stress distributions for the chamfered repairs are similar, regardless the patch inner chamfer dimensions. τ_{xy} stress distributions diminish significantly with this geometric modification, notwithstanding the chamfer dimensions (Hildebrand 1994, Belingardi et al. 2002, Campilho et al. 2009b). Moreover, significant variations were found, depending on the chamfer dimensions, with moderate magnitude τ_{xy} stress concentrations near the region of adhesive thickening initiation. Fig. 321 represents P_d/P_{d0} for all patch inner chamfer dimensions, under tensile, compression and bending loads.

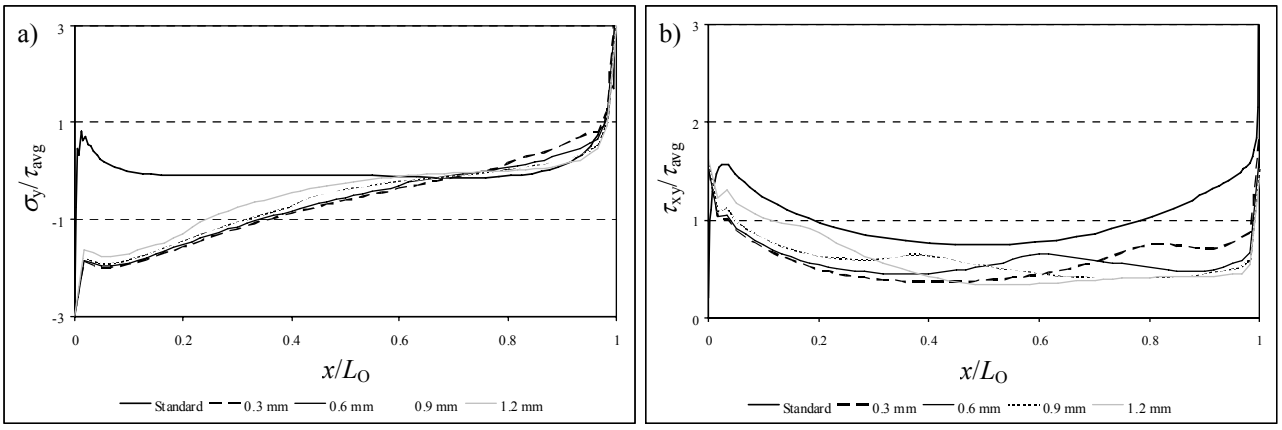

Fig. 320 – Normalized σ_y (a) and τ_{xy} (b) stress distributions at the laminate/adhesive interface (tensile load).

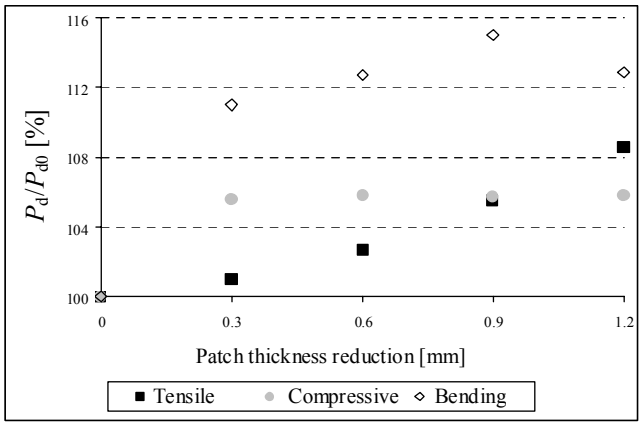

Fig. 321 – Normalized strength for different dimensions patch inner chamfer repairs.

- Under a tensile load, the patch inner chamfering technique leads to a strength improvement roughly proportional to its dimensions, reaching 8.5% for the 1.2 mm patch inner chamfer repair. Under tension, damage initiated at the OEO and IEO simultaneously, at the laminate/adhesive interface (symmetry plane ***B***), growing towards the overlap central region. The elimination of σ_y peel peak stresses and the major reduction of τ_{xy} peak stresses at the repair critical regions (OEO and IEO), caused by the reduction of the patch stiffness, justify the observed strength improvement. Fig. 322 compares the standard and 1.2 mm patch inner chamfer repairs, under the value of δ for patch debonding of the 1.2 mm chamfer repair. Under these conditions, damage in the standard repair extended almost to the middle of the overlap, due to the higher patch stiffness.

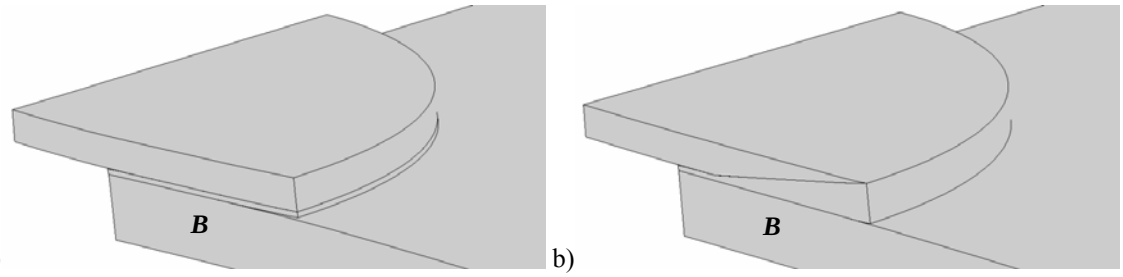

a) b)

Fig. 322 – Deformed shape of the standard (a) and 1.2 mm patch inner chamfer (b) repairs (tensile load).

- The strength improvements under compression are identical between all patch inner chamfer dimensions (≈5.7%). For this loading, damage initiated at the laminate/adhesive interface (OEO), growing in the direction of the IEO. Fig. 323 (a) corresponds to the standard repair after patch debonding. Fig. 323 (b) shows the 1.2 mm patch inner chamfer repair. Notwithstanding the chamfer dimensions, damage initiated at a 45º angle of the symmetry plane ***B***, growing towards this plane. It was found that the compressive displacement leading to patch debonding onset increased linearly with the chamfer dimensions, which would suggest a corresponding increase of the repairs compressive strength. However, since the patch cross-section also decreases with the chamfer dimensions, the P_d/P_{d0} ratio remains similar.

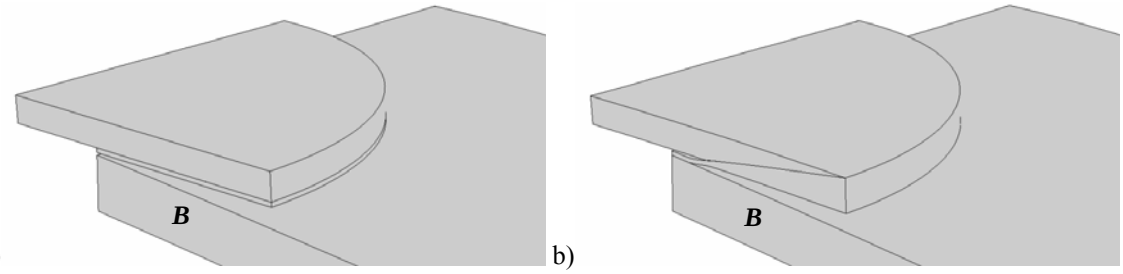

a) b)

Fig. 323 – Deformed shape of the standard (a) and 1.2 mm patch inner chamfer (b) repairs (compressive load).

- The most significant results were obtained under a bending load. In fact, a maximum of 15.0% strength improvement was achieved using a 0.9 mm chamfer. The other dimension chamfers showed smaller but still worth mentioning strength improvements. The failure modes were identical to the standard repair, i.e., damage onset at the OEO at the symmetry plane ***B*** (laminate/adhesive interface), with growth towards the IEO along the same interface. Fig. 324 shows the 1.2 mm patch inner chamfer repair at damage onset at the OEO (a) and after complete patch debonding (b).

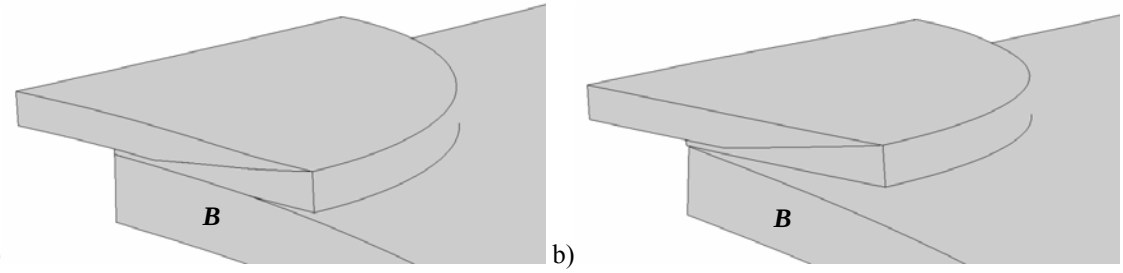

a) b)

Fig. 324 – Deformed shape of the 1.2 mm patch inner chamfer repair at damage onset (a) and patch debonding (b) (bending load).

5.3.3. Plug filling

Plug filling with adhesive the laminate hole was also examined in this analysis (Fig. 325). To simulate a plug filled repair, additional cohesive elements were employed vertically at the plug/laminate interface. The adhesive layer and plug filling representative elements are shaded in Fig. 325, for clarity. The numerical work of Campilho et al. (2009b) addressed this technique on 2D SS repairs with CFRP adherends in tension. This technique was found to slightly decrease the repair strength, due to a premature plug/laminate interface fracture, prior to failure in the adhesive layer.

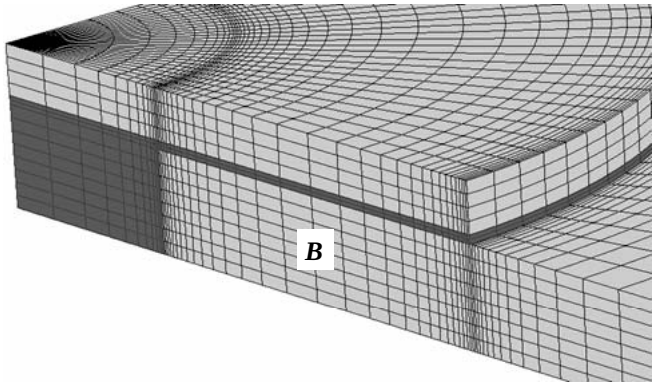

Fig. 325 – Detail of the mesh at the overlap region for the plug repair.

Fig. 326 (a) and (b) relate to σ_y and τ_{xy} stress distributions, respectively, for the standard and plug filled repairs, under a tensile load. σ_y peel peak stresses at the IEO diminished plug filling the repair (Fig. 326 a), with σ_y stresses being approximately nil at the plug region. However, plug filling also gives rise to a τ_{xy} stress singularity at the IEO (Fig. 326 b). Along the overlap, τ_{xy} stresses diminish with this technique, more significantly near the IEO. At the plug region, τ_{xy} stresses gradually become smaller with the distance to the IEO.

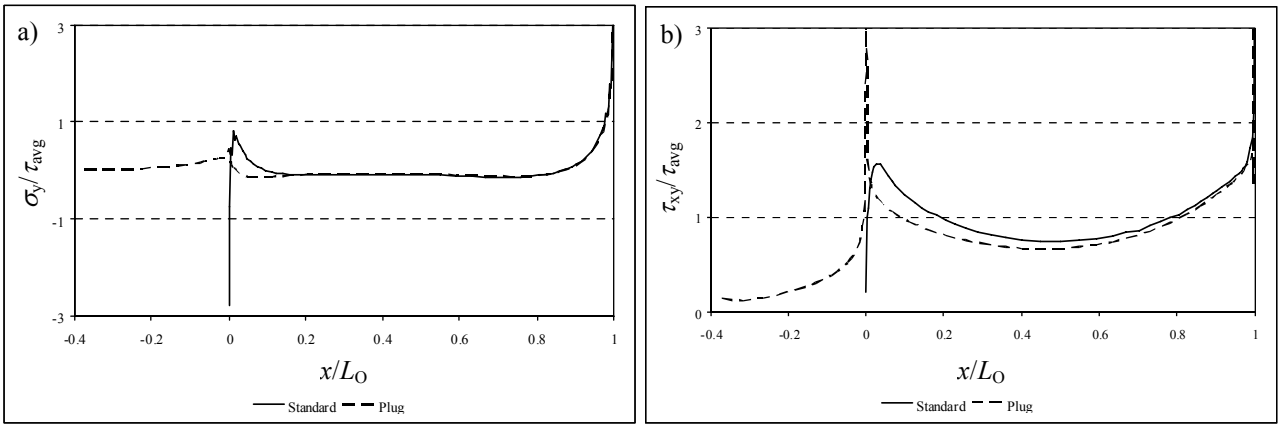

Fig. 326 – Normalized σ_y (a) and τ_{xy} (b) stress distributions at the laminate/adhesive interface (tensile load).

- A 0.8% tensile strength improvement was achieved by plug filling the repair. Under this loading, damage initiated at the symmetry plane ***B***, at the plug/laminate vertical interface (Fig. 327 a), with growth at the laminate/adhesive interface from the OEO towards the IEO (Fig. 327 b). The reduced strength improvement is justified by the plug/laminate vertical interface fracture occurring prior to damage initiation in the adhesive layer. Actually, at the time of patch debonding, the plug is not contributing to the repair strength, due to its

earlier failure. This result agrees with the numerical analysis of Campilho et al. (2009b) on the tensile strength of 2D SS adhesively-bonded repairs with CFRP adherends.

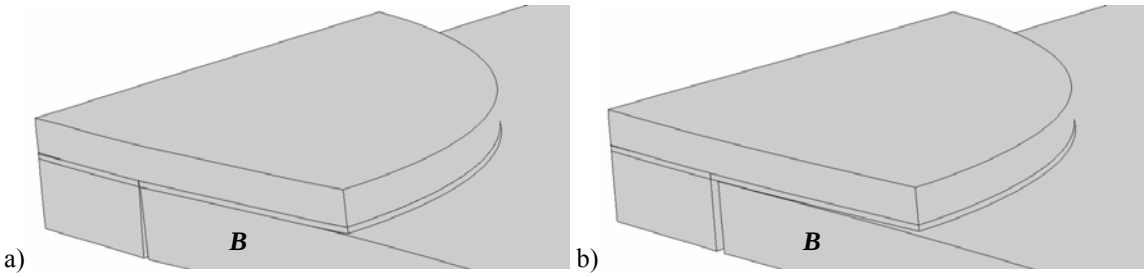

Fig. 327 – Deformed shape of the plug repair at damage onset (a) and patch debonding (b) (tensile load).

- A 5.8% strength improvement was achieved under compression. Damage onset occurs at a 45º angle of the symmetry plane ***B*** and then grows in the direction of plane ***B***, at the laminate/adhesive interface (growing from the OEO towards the IEO). After patch debonding, the plug is still intact at the plug/patch and the plug/laminate interfaces. Owing to this behaviour, plugging the repair proved to be effective under a compressive load. Plug filling also led to a 7.2% increase of the damage onset displacement. Fig. 328 represents the repair deformed shape at damage onset (a) and after damage growth in the adhesive layer (b).

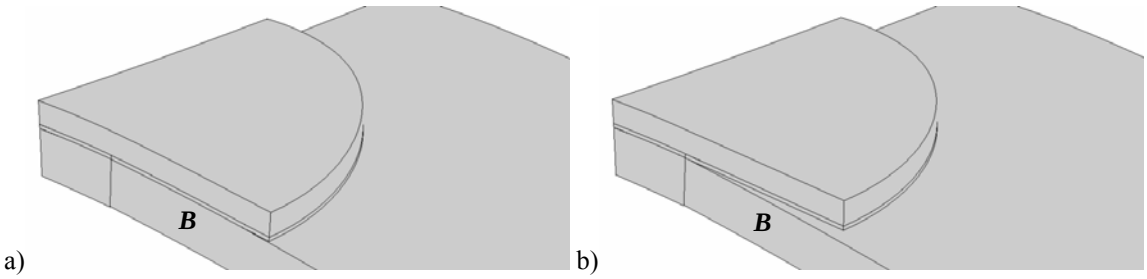

Fig. 328 – Deformed shape of the plug repair at damage onset (a) and patch debonding (b) (compressive load).

- The best results were obtained under a bending load (17.4% strength improvement). Under this loading, damage initiated at the OEO at the symmetry plane ***B*** (laminate/adhesive interface) and propagated towards the IEO until complete patch debonding. The plug/laminate vertical interface only failed after patch debonding, which explains the strength improvement. The progressive failure of the repair is shown in Fig. 329. Patch debonding at the OEO is presented in Fig. 329 (a), while Fig. 329 (b) shows damage onset at the plug/laminate vertical interface, occurring after patch debonding.

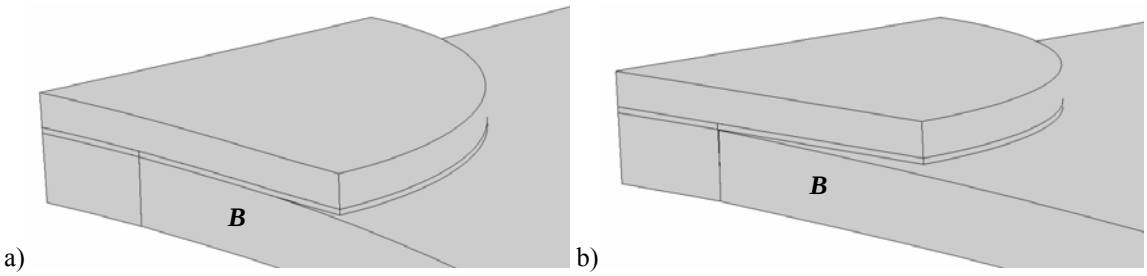

Fig. 329 – Deformed shape of the plug repair at damage onset (a) and patch debonding (b) (bending load).

5.3.4. Fillets

The use of fillets at the OEO was also examined in this work (Fig. 330), comprising four fillet shapes: a curved fillet (Fig. 330 (1)) and straight fillets with 45º, 30º and 15º slopes (Fig. 330 (2), (3) and (4), respectively). Additional cohesive elements were introduced at the patch/fillet vertical interface to account for the respective fracture possibility. It is known that the stress singularities at the overlap edges for structures with square-edges may lead to adhesion failures at those regions and consequently to a premature damage initiation (Gleich et al. 2001b, Panigrahi and Pradhan 2007c). Fillets are widely considered to reduce stresses at those regions and, as a result, to increase the structures strength (Adams and Peppiatt 1974, Adams and Harris 1987, Hildebrand 1994, Tsai and Morton 1995b, Bogdanovich and Kizhakkethara 1999, Campilho et al. 2008a, Ashcroft et al. 2001, Chaves et al. 2008, Campilho et al. 2009b, Reis et al. 2009). In this study, the fillets include all the patch thickness, minimizing σ_y peel and τ_{xy} peak stresses at the OEO (Lang and Mallick 1998, Cheuk and Tong 2002). In terms of fabrication of the filleted repairs, some difficulties on the curing process are expected, especially for low viscosity adhesives or if access is limited (Fitton and Broughton 2005).

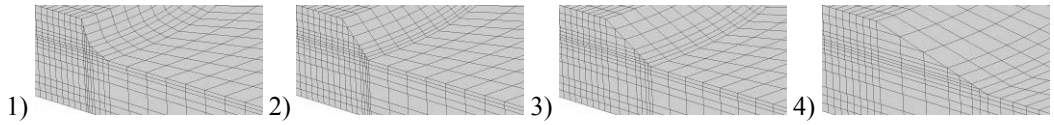

Fig. 330 – Fillet shapes studied.

σ_y and τ_{xy} stress distributions are presented in Fig. 331 (a) and (b), respectively, at the laminate/adhesive interface (tensile load) for all the fillet shapes evaluated. The use of fillets diminishes σ_y peak stresses at the OEO (Fig. 331 a), identically for the four fillet shapes of Fig. 330. This also applies to τ_{xy} stresses (Fig. 331 b), which display a similar reduction on τ_{xy} peak stresses at the OEO, disregarding the fillet shape. These results indicate that the use of a fillet will probably increase the repairs strength, since σ_y peel and τ_{xy} peak stresses at the damage onset region (OEO) diminish. Fig. 332 compares the P_d/P_{d0} ratio for all fillet shapes, under tensile, compression and bending loads.

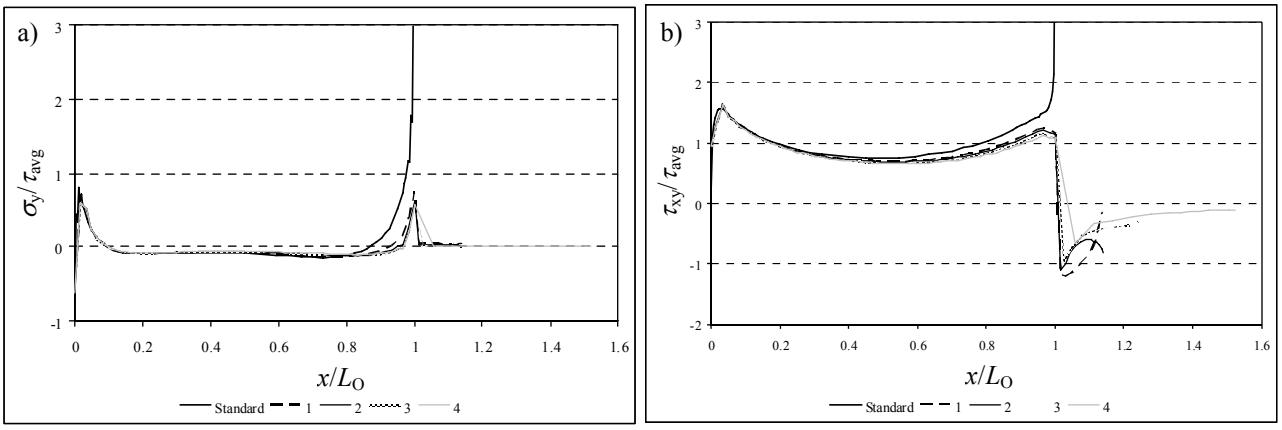

Fig. 331 – Normalized σ_y (a) and τ_{xy} (b) stress distributions at the laminate/adhesive interface (tensile load).

- Under tension, geometries 1 and 2 were the most effective (strength improvements of 6.0 and 8.0%, respectively). Geometries 3 and 4, pertaining to 30º and 15º straight fillets, lead to a strength improvement of approximately 2%. These results are in agreement with FEM analyses carried out by Belingardi et al. (2002)

and Rispler et al. (2000), and also the experimental work of de Morais et al. (2007). Regardless the fillet shape, damage initiated at the symmetry plane ***B*** at the patch/fillet vertical interface (Fig. 333), growing along the adhesive/patch interface from the OEO towards the IEO. The strength improvement in all cases results from the reduction of σ_y peel and τ_{xy} peak stresses at the OEO (damage onset region), whilst the smaller strength improvement for the 30º and 15º straight fillet repairs is related to the bigger stiffness of these fillets, promoting a premature failure of the fillet/patch vertical interface. Fig. 333 shows the deformed shape of the 45º (a) and the 15º (b) straight fillet repairs, pertaining to the value of δ corresponding to the patch/fillet vertical interface failure for the 45º straight fillet repair. It is observed that, for the 15º straight fillet repair, damage has already propagated to the adhesive layer by the adhesive/patch interface.

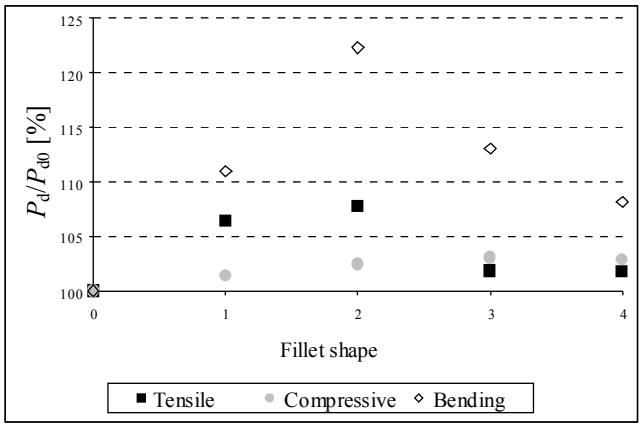

Fig. 332 – Normalized strength for different fillet shapes.

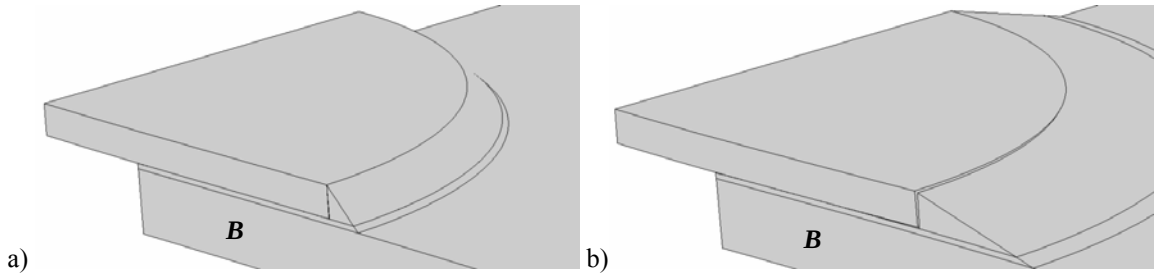

a) b)

Fig. 333 – Deformed shape of the 45º (a) and 15º (b) straight fillet repairs (tensile load).

- The maximum strength improvement under compression (3.1%) was achieved with the 30º straight fillet. For all the fillets, failure initiated at the patch/fillet vertical interface at 45º of the symmetry plane ***B***, propagating along the adhesive/patch interface. Fig. 334 shows damage onset (a) and patch debonding (b) for the 45º straight fillet repair. The reduction on τ_{xy} peak stresses at the OEO justifies the mentioned strength improvement. The smaller value of P_d/P_{d0} for the 15º straight fillet repair, compared to the 30º one, is related to its bigger fillet stiffness, causing a premature patch/fillet vertical interface failure. Fig. 335 displays the deformed shape of the 30º (a) and 15º (b) straight fillet repairs, under the same value of δ (corresponding to damage onset of the 30º straight fillet repair). For the 15º straight fillet repair, damage has already propagated to the adhesive layer, owing to the bigger fillet stiffness.

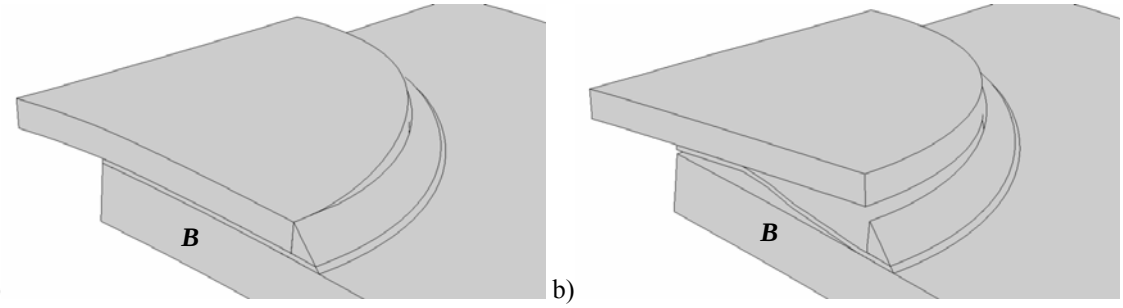

a) b)

Fig. 334 – Deformed shape of the 45º straight fillet repair at damage onset (a) and patch debonding (b) (compressive load).

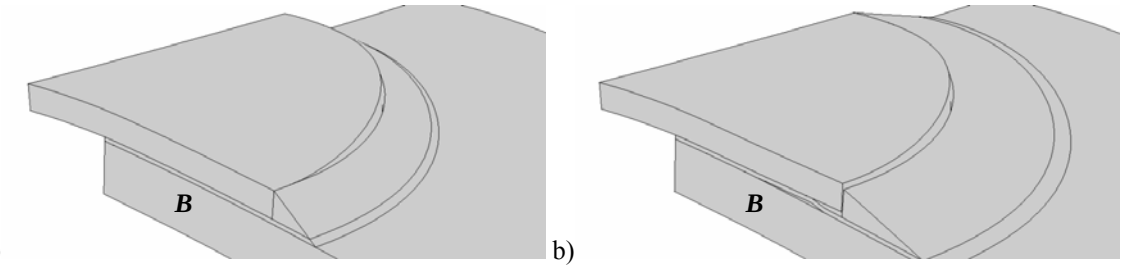

a) b)

Fig. 335 – Deformed shape of the 30º (a) and 15º (b) straight fillet repairs (compressive load).

- The most promising results were attained under bending, with a maximum strength improvement of 22.3% for the 45º straight fillet. For the curved and 45º fillets, damage initiated simultaneously at the adhesive/patch and patch/fillet interfaces, while for the 30º and 15º fillets, damage initiated at the patch/fillet vertical interface, and only after propagated to the adhesive layer, growing from the OEO to the IEO along the adhesive/patch interface. This difference comes from the bigger stiffness of the 30º and 15º fillets, sourcing a patch/fillet vertical interface fracture prior to failure in the adhesive layer and causing a reduction on P_d/P_{d0}. Fig. 336 and Fig. 337 picture the failure process for the 45º and 15º straight fillet repairs, respectively. Damage onset at the adhesive/patch and patch/fillet interfaces is shown in (a), while (b) relates to patch debonding.

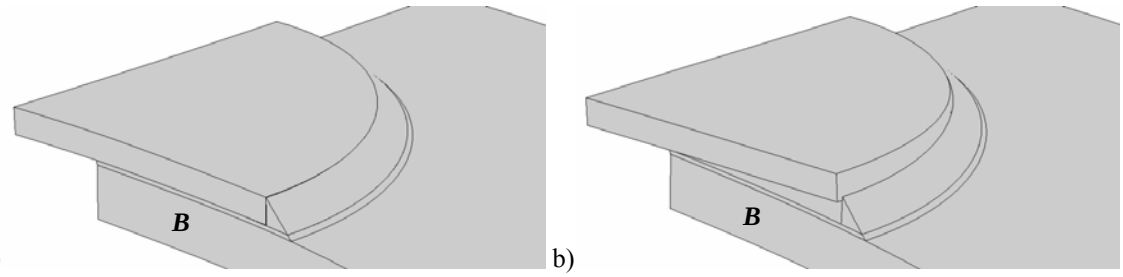

a) b)

Fig. 336 – Deformed shape of the 45º straight fillet repair at damage onset (a) and patch debonding (b) (bending load).

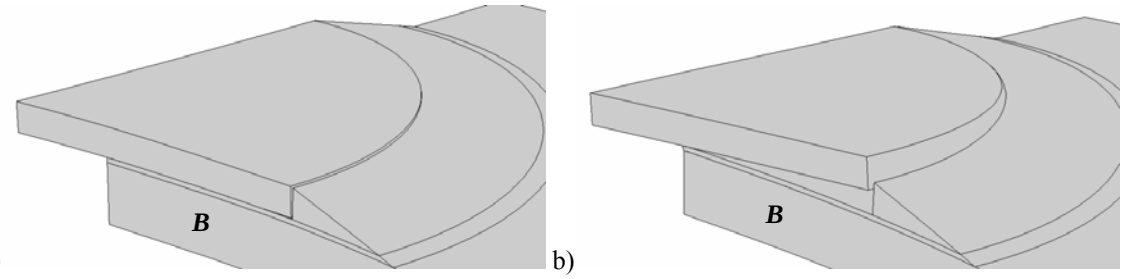

a) b)

Fig. 337 – Deformed shape of the 15º straight fillet repair at damage onset (a) and patch debonding (b) (bending load).

5.3.5. Laminate outer chamfer

Fig. 338 shows a detail of the mesh used for the 0.2 and 0.6 mm laminate outer chamfer repairs. A few investigators addressed this optimization technique. A recently published work of You et al. (2008) showed, using aluminium SL joints under tension, that peak stresses along the overlap diminished by chamfering the adherends at the overlap edges. Between the chamfer angles studied, ranging from 0º to 60º, the 30º chamfer led to the highest strength. Reductions on t_P of 0.2, 0.4 and 0.6 mm at the IEO were examined in this analysis, keeping a 1.5/10 chamfer slope.

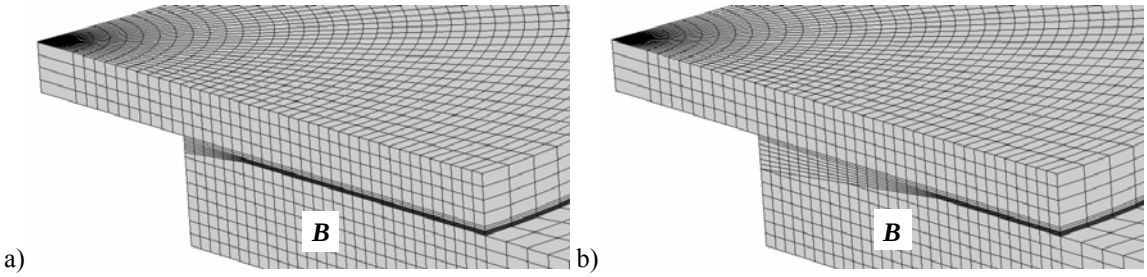

Fig. 338 – Detail of the mesh at the overlap region for the 0.2 mm (a) and 0.6 mm (b) laminate outer chamfer repairs.

Fig. 339 (a) and (b) relate to σ_y and τ_{xy} stress distributions, respectively, at the adhesive/patch interface (tensile load). σ_y stress distributions (Fig. 339 a) are highly dependent on this modification. Actually, σ_y peel peak stresses at the IEO are eliminated, giving rise to σ_y compressive ones. σ_y stresses are practically equal between the chamfer dimensions evaluated. Fig. 339 (b) shows a global reduction on the magnitude of τ_{xy} stresses for all the chamfered repairs from the standard repair. Equally to σ_y stresses, no considerable differences were found between the different chamfers studied. The FEM results concerning the P_d/P_{d0} ratio between the different laminate outer chamfer dimensions are portrayed in Fig. 340 for the three loads under analysis.

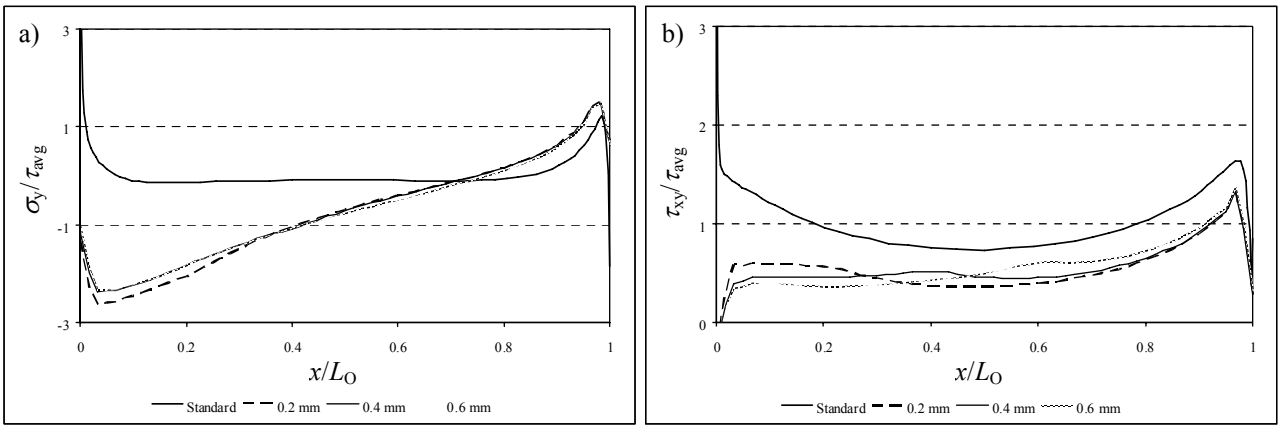

Fig. 339 – Normalized σ_y (a) and τ_{xy} (b) stress distributions at the adhesive/patch interface (tensile load).

- This modification only marginally affects the repairs tensile strength (Campilho et al. 2009b), which displays a minor reduction on P_d/P_{d0} with the laminate outer chamfer dimensions. Damage initiated at the symmetry plane ***B*** at the OEO (laminate/adhesive interface), growing towards the IEO, which explains the trend in Fig. 340. Indeed, no significant variations on the magnitude of stresses were found at the damage initiation locus (OEO), with only a slight reduction of τ_{xy} peak stresses and a minor increase of σ_y peel ones. The laminate

cross-sectional area reduction with the chamfer dimensions originates the mentioned decreasing trend. Fig. 341 compares the 0.6 mm laminate outer chamfer repair at damage onset (a) and after patch debonding (b).

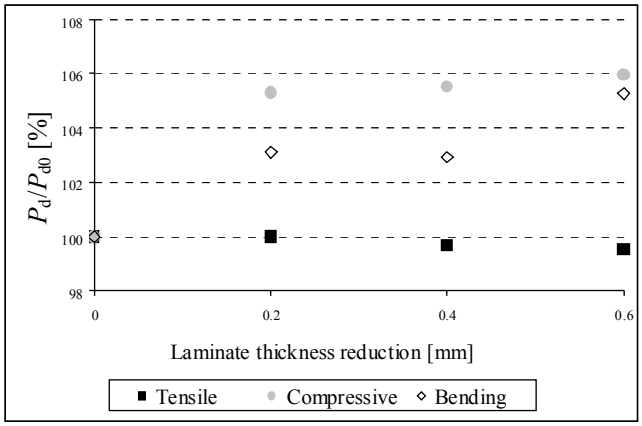

Fig. 340 – Normalized strength for different dimensions laminate outer chamfer repairs.

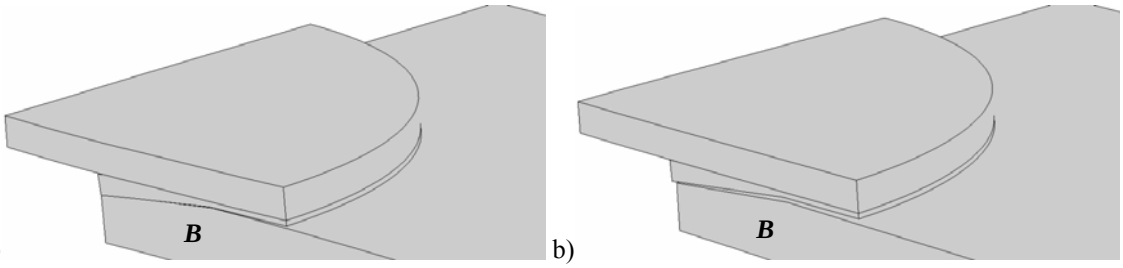

Fig. 341 – Deformed shape of the 0.6 mm laminate outer chamfer repair at damage onset (a) and patch debonding (b) (tensile load).

- The repairs compressive strength is not markedly affected by this chamfer, increasing moderately with its dimensions (from 5.3 to 6.0%). The failure mechanism is consistent with the standard repair, i.e., damage onset at 45º of the symmetry plane ***B*** at the OEO (laminate/adhesive interface), progressing towards the symmetry plane ***B*** and the IEO along the same interface until patch complete failure. The value of δ leading to patch debonding onset increased linearly with the chamfer dimensions, which would suggest a corresponding increasing trend of P_d/P_{d0}. However, the parallel reduction of the laminate cross-sectional area, bearing the majority of the loads transmitted by the repair, counteracts the influence of δ for patch debonding, yielding the results practically independent of the chamfer dimensions. Fig. 342 compares the standard (a) and the 0.6 mm laminate outer chamfer (b) repairs for the value of δ of damage onset for the chamfered repair.

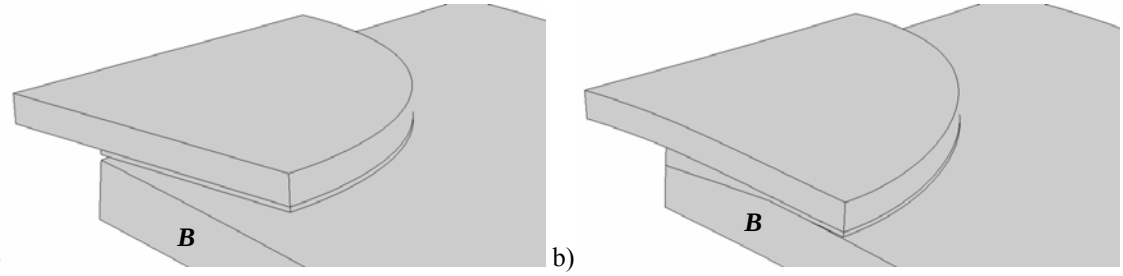

Fig. 342 – Deformed shape of the standard (a) and 0.6 mm laminate outer chamfer (b) repairs (compressive load).

- Laminate outer chamfering is also advisable under bending. In fact, a maximum 5.3% strength improvement was achieved with a 0.6 mm laminate outer chamfer. The failure mode observed is similar, regardless of the laminate outer chamfer dimensions. Damage initiates at the symmetry plane ***B*** at the OEO (laminate/adhesive interface) and then grows along the mentioned interface until complete patch failure. The increase on the patch allowable flexure originating from the adhesive thickening causes a reduction of stresses at the OEO and a smaller repair stiffness, explaining the reported increasing tendency. Fig. 343 represents damage onset at the OEO (a) and patch debonding (b) for the 0.6 mm laminate outer chamfer repair.

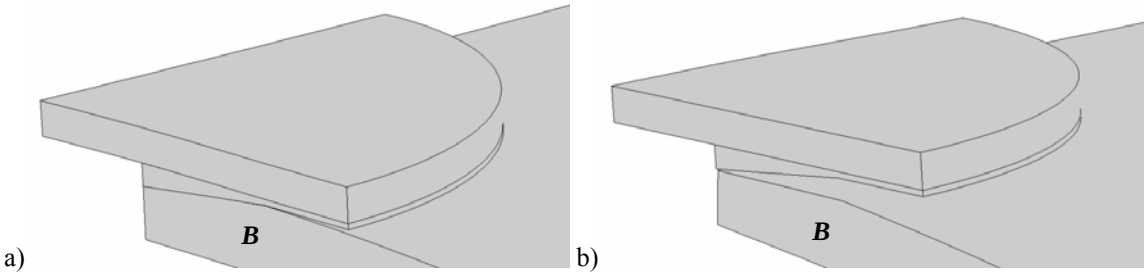

Fig. 343 – Deformed shape of the 0.6 mm laminate outer chamfer repair at damage onset (a) and patch debonding (b) (bending load).

5.3.6. Laminate inner chamfer

Fig. 344 shows the mesh for the 0.3 mm (a) and 1.5 mm (b) laminate inner chamfer repairs. Boss et al. (2003) examined this technique on SL joints, concluding that it diminishes σ_y peel and τ_{xy} peak stresses at the overlap edges. In this work, reductions on t_P at the IEO of 0.3, 0.6, 0.9, 1.2 and 1.5 mm were tested, considering a 1.5/10 chamfer slope.

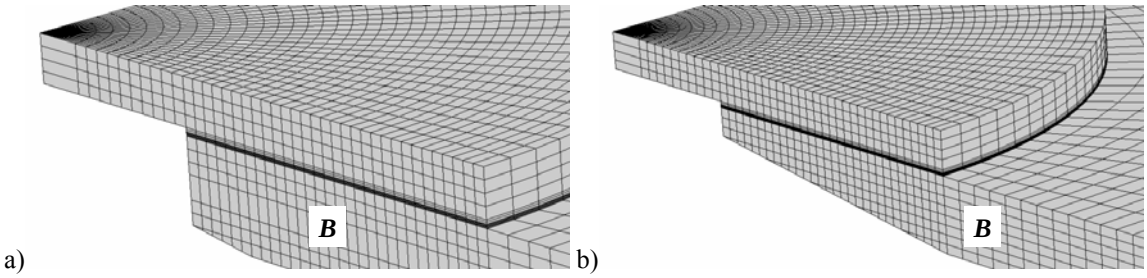

Fig. 344 – Detail of the mesh at the overlap region for the 0.3 mm (a) and 1.5 mm (b) laminate inner chamfer repairs.

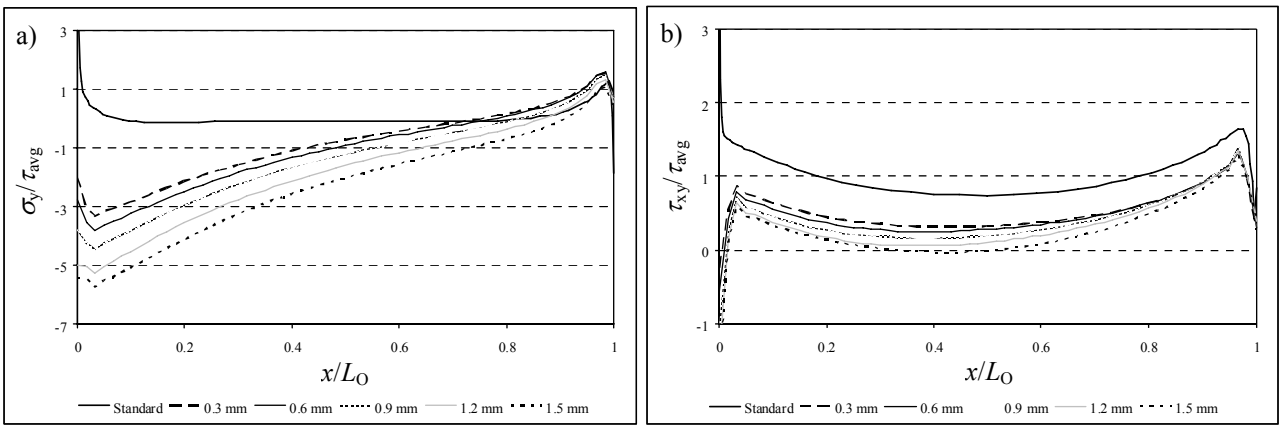

Fig. 345 – Normalized σ_y (a) and τ_{xy} (b) stress distributions at the laminate/adhesive interface (tensile load).

Fig. 345 (a) and (b) plot σ_y and τ_{xy} stress distributions, respectively, at the laminate/adhesive interface (tensile load). This modification revealed a reduction on σ_y and τ_{xy} stresses in the overlap. Actually, σ_y peel peak stresses at the IEO are eliminated and a compressive region develops from the IEO up to $x/L_O \approx 0.7$ (Fig. 345 a). The compressive stresses magnitude increase gradually with the laminate inner chamfer dimensions. τ_{xy} stresses (Fig. 345 b) diminish in magnitude along the entire overlap with the chamfer dimensions, which is consistent with the tendency of σ_y stresses. The P_d/P_{d0} ratio of the repairs is presented in Fig. 346 for the three loadings, as a function of the chamfer dimensions.

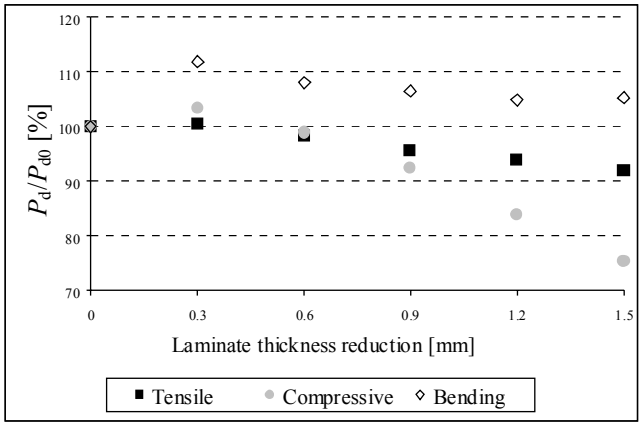

Fig. 346 – Normalized strength for different dimensions laminate inner chamfer repairs.

- The repairs tensile strength showed a decreasing tendency with the laminate inner chamfer dimensions, reaching 8.0% for the 1.5 mm laminate inner chamfer repair. The failure mode for the chamfered repairs was found to be identical to the standard repair. Therefore, damage initiated at the symmetry plane ***B*** at the OEO and IEO simultaneously (laminate/adhesive interface), propagating towards the overlap central region. The strength reduction under tension is mainly related to the laminate cross-sectional area reduction with the chamfer dimensions. In fact, the value of δ for patch debonding was found to be similar to the standard repair, which excludes this feature from affecting the repairs strength. In addition, σ_y and τ_{xy} stress distributions are not markedly affected by this parameter at one of the damage onset regions (OEO). This behaviour opposes to the 2D SS repair. In this case, a strength improvement is expected with this modification, due to the laminate stiffness reduction at the IEO and corresponding reduction of peak stresses at that particular region (Campilho et al. 2009b). Fig. 347 shows the deformed shape of the 1.5 mm laminate inner chamfer repair at damage onset (a) and after patch debonding (b).

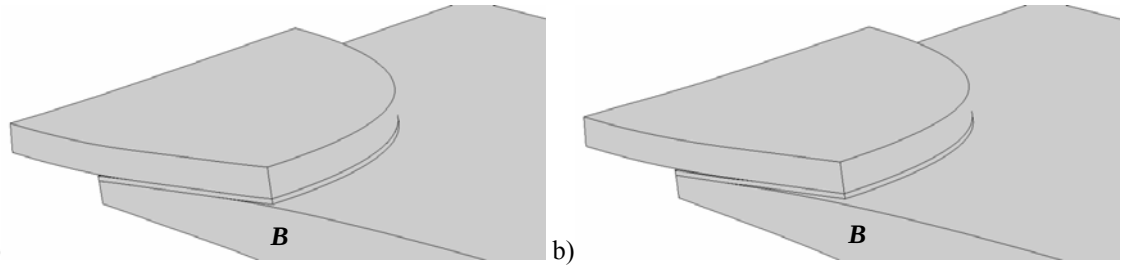

Fig. 347 – Deformed shape of the 1.5 mm laminate inner chamfer repair at damage onset (a) and patch debonding (b) (tensile load).

- Under compression, this modification showed a 3.3% strength improvement using a 0.3 mm chamfer. Bigger chamfers gradually diminished the repairs strength, up to 25% for the 1.5 mm chamfer. The failure modes were identical to the standard repair, i.e., damage onset at 45º of the symmetry plane ***B*** at the OEO (laminate/adhesive interface), progressing towards the symmetry plane ***B*** and the IEO along the mentioned interface until patch debonding. The reduction of τ_{xy} peak stresses led to the 3.3% strength improvement of the 0.3 laminate inner chamfer repair, also causing a 5.7% increase on the value of δ for patch debonding. Beyond this point, the value of δ for patch debonding gradually diminished, which helped to the strength reduction, concurrently with the reduction of the laminate cross-sectional area. Fig. 348 shows, for the 1.5 mm laminate inner chamfer repair, the repair at damage onset (a) and after patch debonding (b).

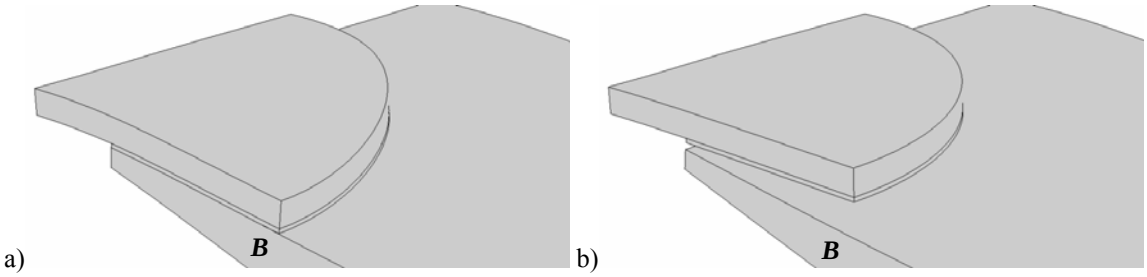

Fig. 348 – Deformed shape of the 1.5 mm laminate inner chamfer repair at damage onset (a) and patch debonding (b) (compressive load).

- The best results were achieved under bending, with the 0.3 mm laminate inner chamfer yielding the most significant strength improvement (11.7%). Bigger chamfers progressively reduce the repairs strength. The values of δ for patch debonding followed the same trend, justifying this behaviour. Equally to the standard repair, damage initiated at the symmetry plane ***B*** at the OEO, progressing towards the IEO along the laminate/adhesive interface. Fig. 349 represents the 1.5 mm laminate inner chamfer repair at damage onset at the OEO (a) and after growth towards the IEO (b).

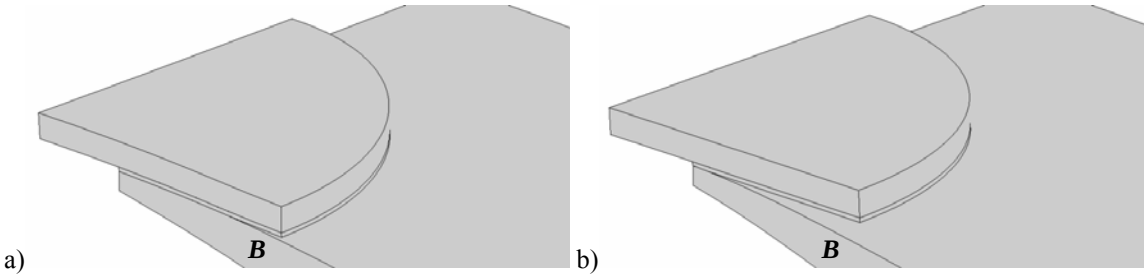

Fig. 349 – Deformed shape of the 1.5 mm laminate inner chamfer repair at damage onset (a) and patch debonding (b) (bending load).

5.3.7. Geometric changes combinations

In this work, the most effective geometric changes under tensile, compressive and bending loads were also tested simultaneously, in an effort to combine their characteristic advantages, thus maximizing the P_d/P_{d0} ratio. In some of the cases, when the optimal solution is not obvious from the individual data of the geometric modifications, more than one combination was tested, for completeness of the study.

5.3.7.1. Tensile load

Under a tensile load, the following geometric changes led to a strength improvement: the fillet (a 45º straight fillet leads to a 7.7% strength improvement), the patch outer chamfer (a 1.2 mm chamfer leads to a 17.4% strength improvement) and the patch inner chamfer (an 8.5% strength improvement was attained with a 1.2 mm chamfer). Fig. 350 shows a detail of the mesh combining the 45º straight fillet with the 1.2 mm patch inner chamfer. In this case, damage initiates at the IEO at the adhesive/patch interface (symmetry plane ***B***) (Fig. 351 a) and then grows along the same interface until patch debonding (Fig. 351 b). **The strength improvement reached 27.7% combining these two modifications, which corresponds to the optimal solution for the SS repair under a tensile load.**

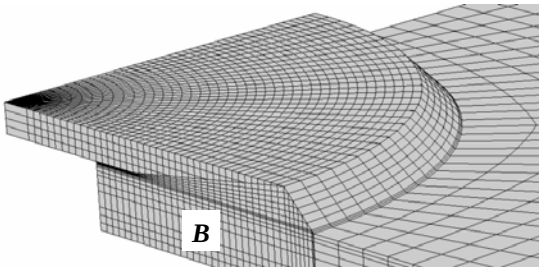

Fig. 350 – Detail of the mesh at the overlap region combining the 45º straight fillet and the 1.2 mm patch inner chamfer.

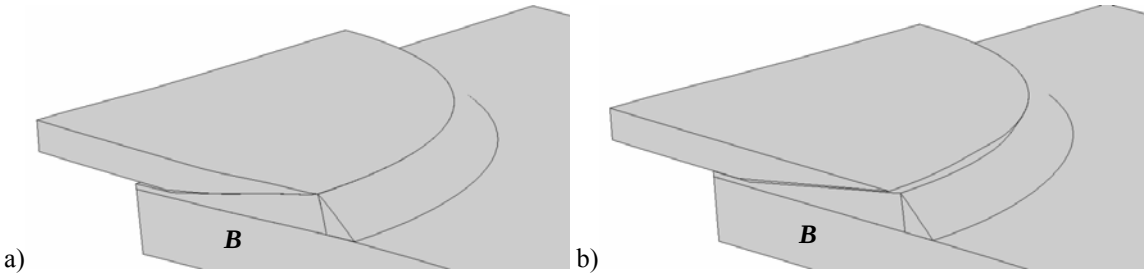

Fig. 351 – Deformed shape of the combination repair at damage onset (a) and patch debonding (b) (tensile load).

5.3.7.2. Compressive load

Under compression, the following geometric changes are beneficial: the fillet (3.1% strength improvement for a 30º straight fillet), the patch outer chamfer (a 0.6 mm chamfer leads to a 4.6% strength improvement), the patch inner chamfer (a 5.8% strength improvement for a 1.2 mm chamfer), the laminate inner chamfer (the 0.6 mm chamfer causes a 6.0% strength improvement, although the smaller ones present similar results), the laminate outer chamfer (only the 0.3 mm chamfer leads to a strength improvement, of 3.3%) and the plug (5.8% strength improvement). In view of these results, two different combinations were tested:

- **1 –** A 30º straight fillet + a 1.2 mm patch inner chamfer + a 0.2 mm laminate inner chamfer + a 0.3 mm laminate outer chamfer;
- **2 –** A 30º straight fillet + a 1.2 mm patch inner chamfer + a plug.

The mesh for combinations 1 and 2 is detailed in Fig. 352 (a) and (b), respectively. Combination 1 leads to a 3.8% strength improvement. With this geometry, damage initiates at the OEO, at 45º of the symmetry plane ***B*** (Fig. 353 a) and then grows along the adhesive/patch interface towards the IEO until patch debonding (Fig. 353 b). A 6.8% strength improvement was obtained with combination 2. Fig. 354 characterizes damage onset (a) and final patch failure (b) for this combination. The failure mode is consistent with combination 1. The plug remains intact after patch debonding (Fig. 354 b), corroborating the importance of this modification up to the repair failure. **The combination 2 repair corresponds to the optimal solution for the SS repair under a compressive load.**

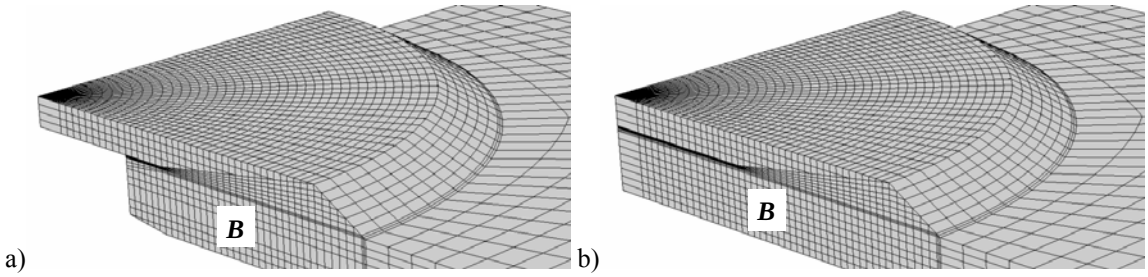

a) b)

Fig. 352 – Detail of the mesh at the overlap region for the combination 1 (a) and combination 2 (b) repairs.

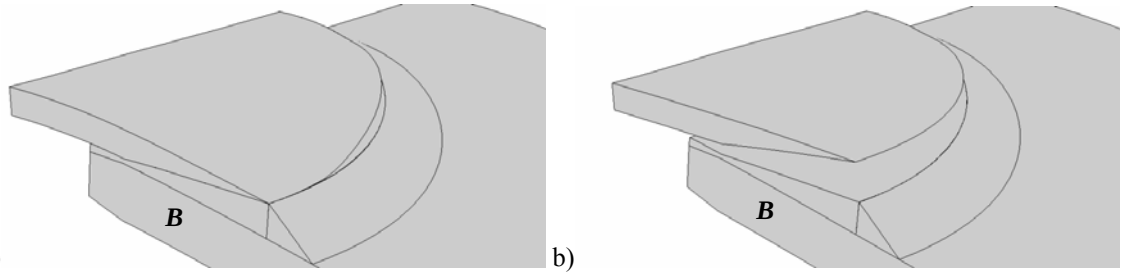

a) b)

Fig. 353 – Deformed shape of the combination 1 repair at damage onset (a) and patch debonding (b) (compressive load).

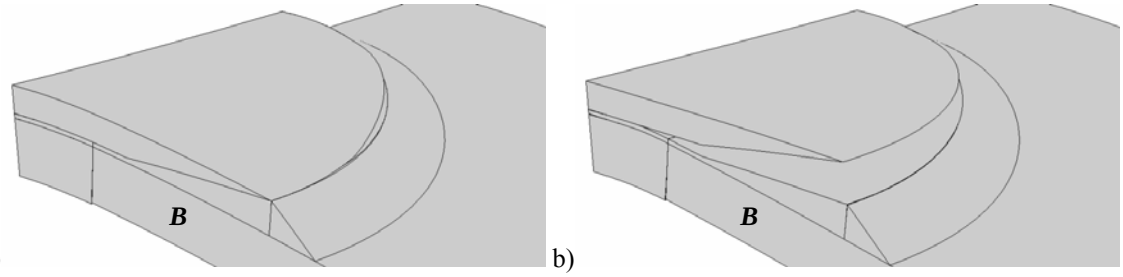

a) b)

Fig. 354 – Deformed shape of the combination 2 repair at damage onset (a) and patch debonding (b) (compressive load).

5.3.7.3. Bending load

Under bending, all the geometric changes shall be equated: the 45º straight fillet (22.3%), the 1.2 mm patch outer chamfer (45.2%), the 0.9 mm patch inner chamfer (15.0%), the 0.6 mm laminate inner chamfer (5.3%), the 1.5 mm laminate outer chamfer (11.7%) and the plug filling technique (17.4%). The individual use of the patch outer chamfer causes a 45.2% strength improvement, which suggests that the optimal repair under bending would include this geometric modification. However, for completeness of this study, the following combinations were tested:

- **1 –** A 45º straight fillet + a 1.2 mm patch inner chamfer + a 0.2 mm laminate inner chamfer + a 0.3 mm laminate outer chamfer;
- **2 –** A 45º straight fillet + a 1.2 mm patch inner chamfer + a plug;
- **3 –** A 1.2 mm patch outer chamfer + a 0.2 mm laminate inner chamfer + a 0.3 mm laminate outer chamfer;
- **4 –** A 1.2 mm patch outer chamfer + a plug.

Fig. 355 (a) and (b) details the mesh at the overlap region for combinations 1 and 2, respectively. Fig. 356 (a) and (b) correspond to combinations 3 and 4, by the respective order.

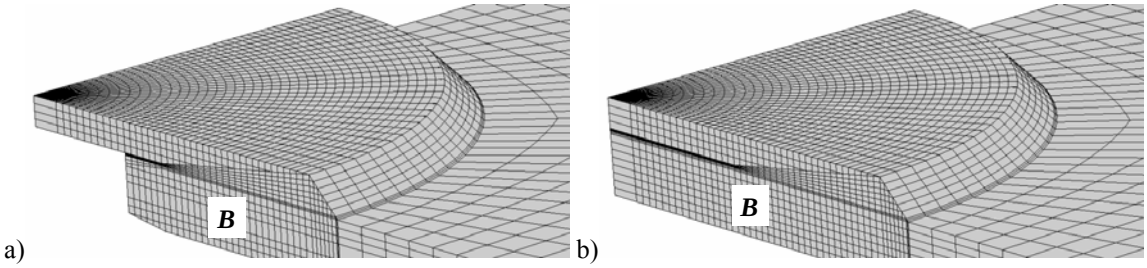

a) b)

Fig. 355 – Detail of the mesh at the overlap region for the combination 1 (a) and combination 2 (b) repairs.

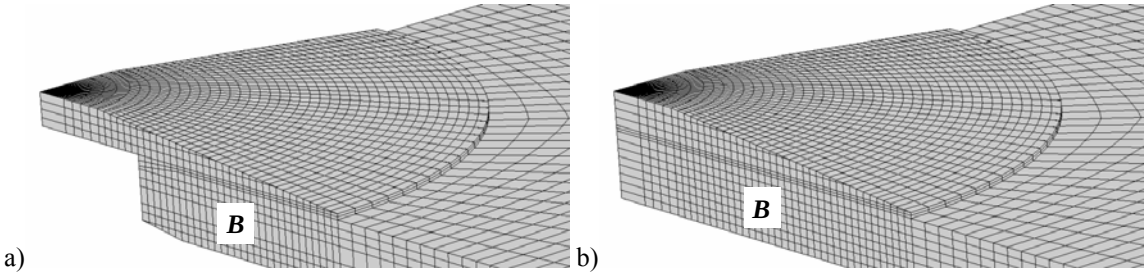

a) b)

Fig. 356 – Detail of the mesh at the overlap region for the combination 3 (a) and combination 4 (b) repairs.

Combination 1 resulted on a 39.0% strength improvement. Using this geometry, damage initiates at the OEO at the laminate/fillet interface (symmetry plane ***B***) (Fig. 357 a) and then propagates towards the IEO along the laminate/adhesive interface, up to patch debonding (Fig. 357 b).

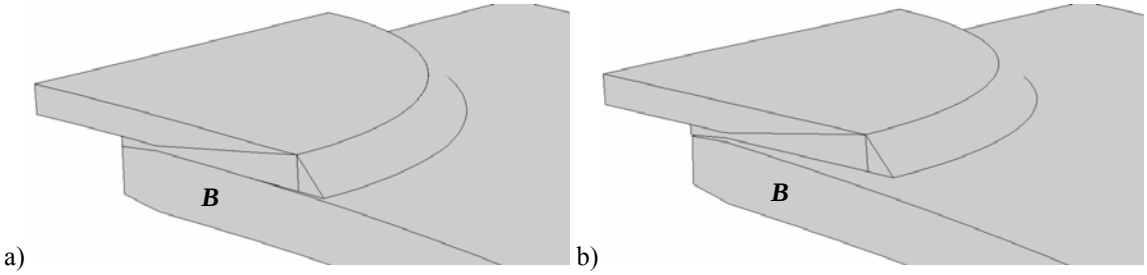

a) b)

Fig. 357 – Deformed shape of the combination 1 repair at damage onset (a) and patch debonding (b) (bending load).

Combination 2 caused a 36.6% strength improvement, displaying an equal failure mode to combination 1. Fig. 358 represents damage onset (a) and patch debonding (b) for this combination repair. The strength improvement reached 58.3% with combination 3. With these modifications, damage initiated at the OEO (symmetry plane ***B***) at the laminate/adhesive interface (Fig. 359 a), propagating along this interface towards the IEO until patch debonding (Fig.

359 b). Combination 4 led to a 49.3% strength improvement. For this combination, damage initiates at the laminate/adhesive interface at the OEO (symmetry plane ***B***) and then grows along this interface. Fig. 360 represents damage onset (a) and patch debonding (b) for this combination repair. **In view of these results, combination 3 is considered the optimal solution, pertaining to the SS repair under bending.**

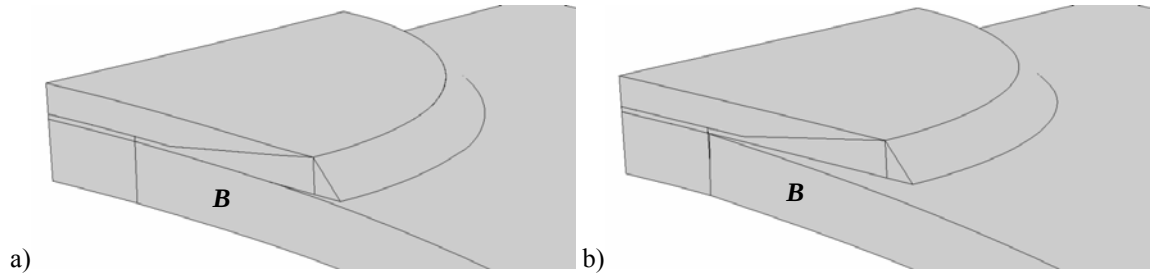

Fig. 358 – Deformed shape of the combination 2 repair at damage onset (a) and patch debonding (b) (bending load).

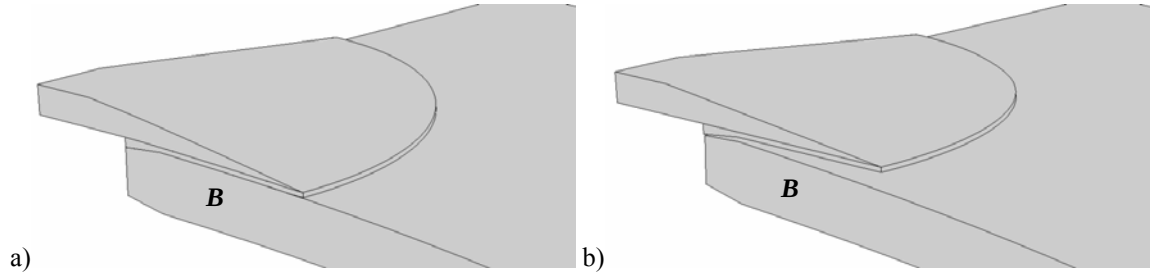

Fig. 359 – Deformed shape of the combination 3 repair at damage onset (a) and patch debonding (b) (bending load).

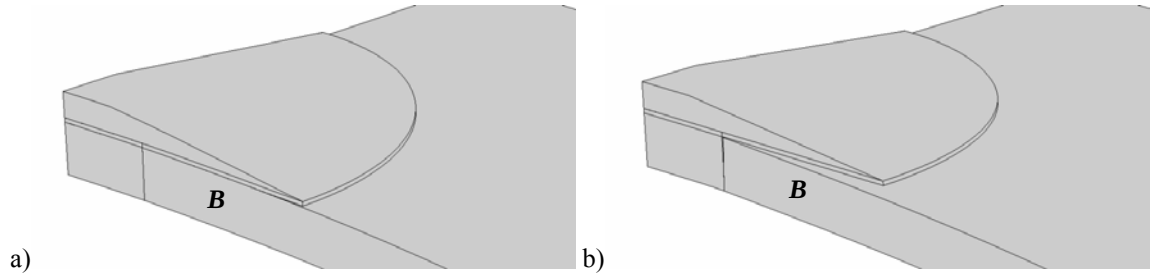

Fig. 360 – Deformed shape of the combination 4 repair at damage onset (a) and patch debonding (b) (bending load).

5.4. Double-strap repairs

5.4.1. Patch outer chamfer

Fig. 313 shows two of the chamfer dimensions considered. Kaye and Heller (2002) used an optimization procedure on DL joints to ascertain the optimal patch outer chamfer geometry that minimized stresses along the bond length. A linear chamfer led to a significant reduction on shear stresses near the chamfer, thus anticipating an improvement on the joints strength. **In this study, the same dimensions and slope for the patch outer chamfers of the SS repairs were employed. This applies to all the geometric modifications for the DS repairs (Sub-Section 5.4).** Fig. 361 (a) and (b) represent σ_y and τ_{xy} stress distributions, respectively, at the laminate/adhesive interface (tensile load) for all the patch outer chamfer dimensions. σ_y stresses (Fig. 361 a) are highly influenced by the dimensions of this modification. In fact,

a tensile peak develops near the tapering initiation region of the patch. τ_{xy} stresses are also influenced by this technique (Fig. 361 b). However, only a slight reduction of τ_{xy} stresses at the OEO and slight increase at the IEO are worth noticing (Potter et al. 2001). These tendencies agree with the SS repair behaviour. The normalized patch debonding predictions for the patch outer chamfer repairs are summarized in Fig. 362.

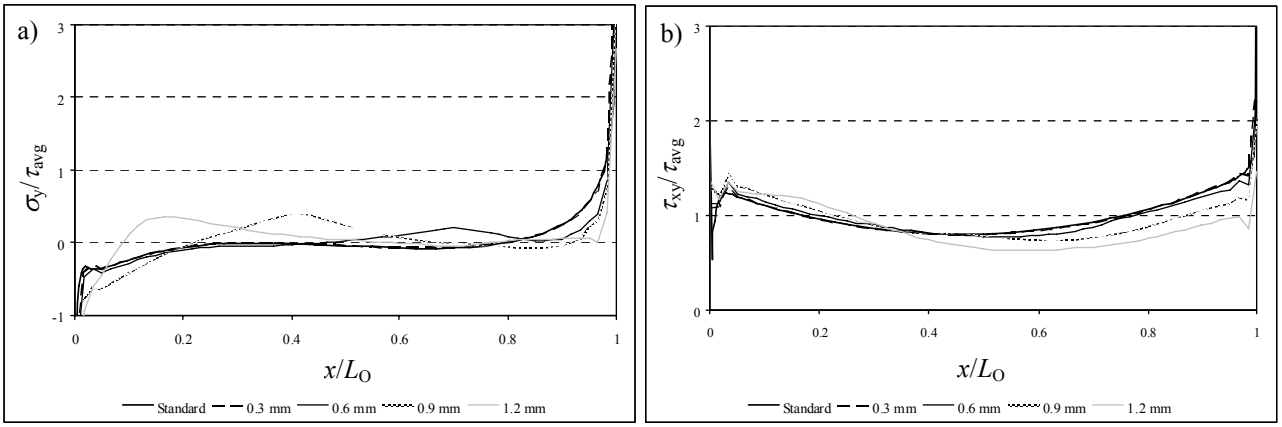

Fig. 361 – Normalized σ_y (a) and τ_{xy} (b) stress distributions at the laminate/adhesive interface (tensile load).

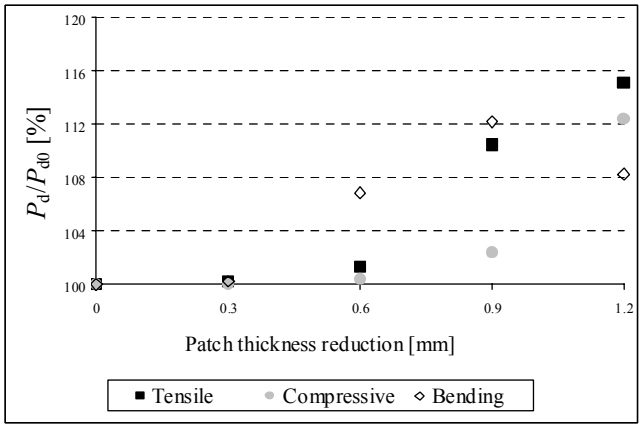

Fig. 362 – Normalized strength for different dimensions patch outer chamfer repairs.

- The tensile results are not significant for the smaller chamfers, whilst the bigger ones were valuable in increasing the strength of the repairs (reaching 15.0% for the 1.2 mm patch outer chamfer). For the 0.9 mm and 1.2 mm patch outer chamfer repairs, damage initiated at the symmetry plane ***B*** at the OEO (laminate/adhesive interface) and IEO (adhesive/patch interface) simultaneously and grows towards the overlap central region. For the other chamfers, damage initiates at the OEO at the laminate/adhesive interface (symmetry plane ***B***) and grows towards the IEO along this interface. This difference is substantiated by reduction of σ_y and τ_{xy} stresses at the patch debonding onset region (OEO). This increases the value of δ for patch debonding and, correspondingly, the value of P_d. Fig. 363 relates to the standard (a) and 1.2 mm patch outer chamfer (b) repairs, for the patch debonding value of δ for the chamfered repair. The comparative analysis between the two figures shows that damage in the standard repair grows prematurely to the modified repair.

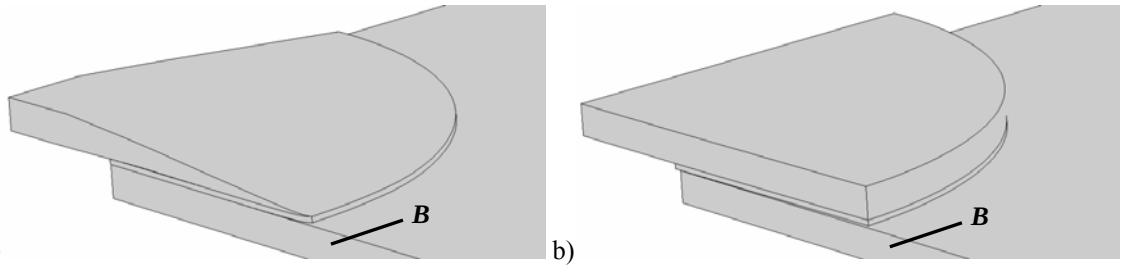

a) b)

Fig. 363 – Deformed shape of the standard (a) and 1.2 mm patch outer chamfer (b) repairs (tensile load).

- The increase on the repairs compressive strength is exponential with the patch outer chamfer dimensions, reaching 12.4% for the 1.2 mm chamfer. The failure mode was kept identical to the standard repair, i.e., damage onset at the IEO at the laminate/adhesive interface (symmetry plane ***B***) and progressive growth along the same interface. The reduction of the repair stiffness, yielding a reduction of stresses in the adhesive layer and consequent increase of the value of δ for patch debonding, justifies the strength improvement. Fig. 364 pertains to the deformed shape of the 0.6 mm (a) and 1.2 mm (b) patch outer chamfer repairs, for the value of δ corresponding to patch debonding of the 1.2 mm chamfer repair. In Fig. 364 (a), the patch debonded prematurely, as a result of its bigger stiffness.

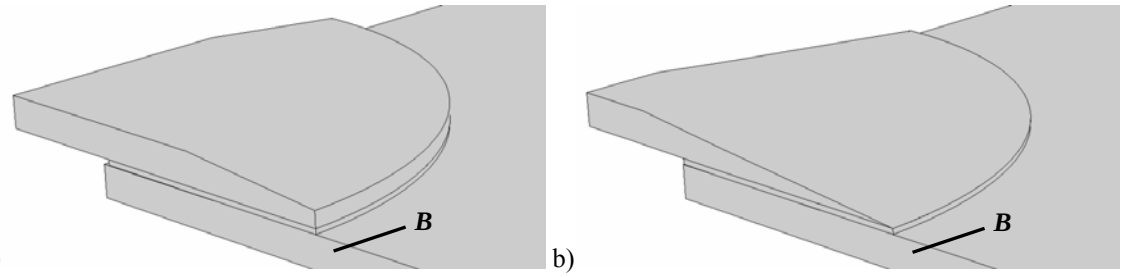

a) b)

Fig. 364 – Deformed shape of the 0.6 mm (a) and 1.2 mm (b) patch outer chamfer repairs (compressive load).

- The 0.9 mm patch outer chamfer proved to be the most efficient solution under bending, with a strength improvement of 12.2%. In all the modified repairs, damage onset and growth took place at the outer patch, initiating at the laminate/adhesive interface at the OEO (symmetry plane ***B***) and progressing towards the IEO. The value of δ for patch debonding is highest for the 0.9 mm patch outer chamfer, following the P_d/P_{d0} trend of Fig. 362, which explains these results. The deformed shape of the repair at damage onset is presented in Fig. 365 for the 0.6 mm (a) and 0.9 mm (b) patch outer chamfer repairs.

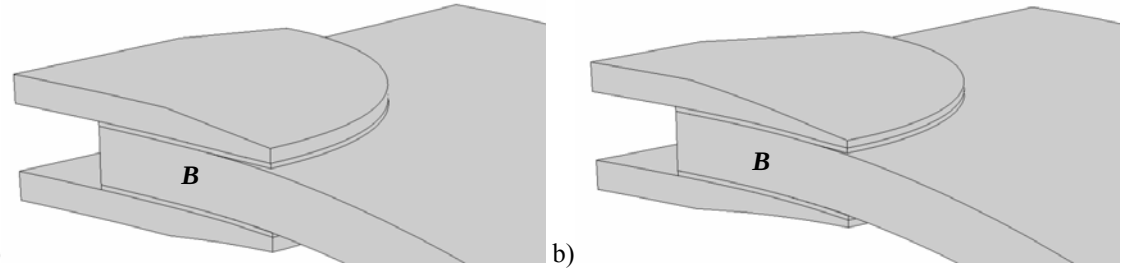

a) b)

Fig. 365 – Deformed shape of the 0.6 mm (a) and 1.2 mm (b) patch outer chamfer repairs (bending load).

5.4.2. Patch inner chamfer

Fig. 319 details the mesh for the 0.3 mm (a) and 1.2 mm (b) patch inner chamfer repairs. This procedure is regarded to reduce considerably stress concentrations near the adhesive thickening region in DL joints (Adams et al. 1986, Kaye and Heller 2002, da Silva and Adams 2007b, Marques 2008) and DS repairs (Campilho et al. 2009b). Fig. 366 (a) and (b) plot σ_y and τ_{xy} stress distributions, respectively, at the laminate/adhesive interface (tensile load). Oppositely to the patch outer chamfer, this alteration does not affect considerably σ_y stress distributions in the adhesive (Fig. 366 a). On the other hand, τ_{xy} stress distributions (Fig. 366 b) are highly dependent on the patch inner chamfer dimensions, always with a reduction in magnitude at the OEO. Additionally, τ_{xy} stresses peak near the adhesive thickening region. Fig. 367 shows the evolution of P_d/P_{d0} with the patch inner chamfer dimensions.

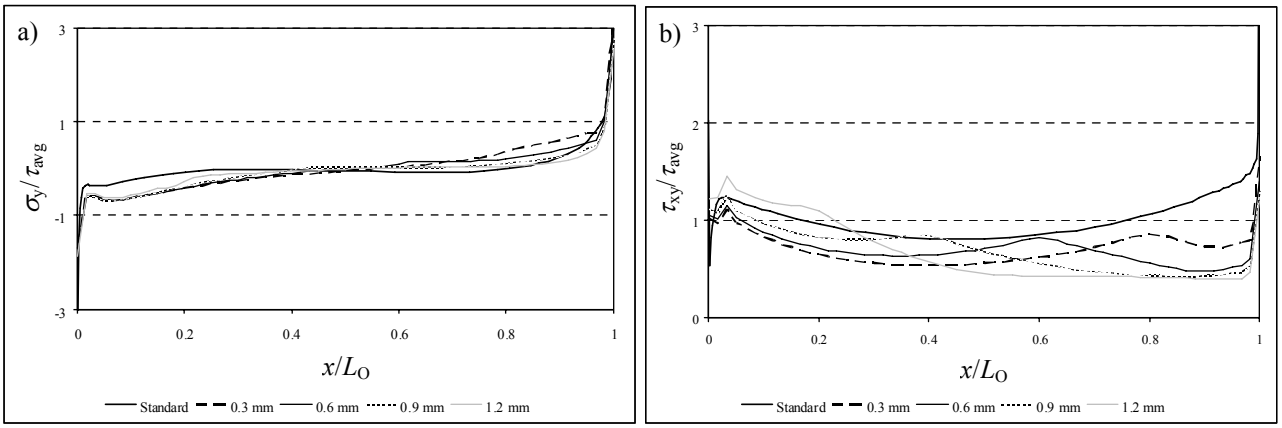

Fig. 366 – Normalized σ_y (a) and τ_{xy} (b) stress distributions at the laminate/adhesive interface (tensile load).

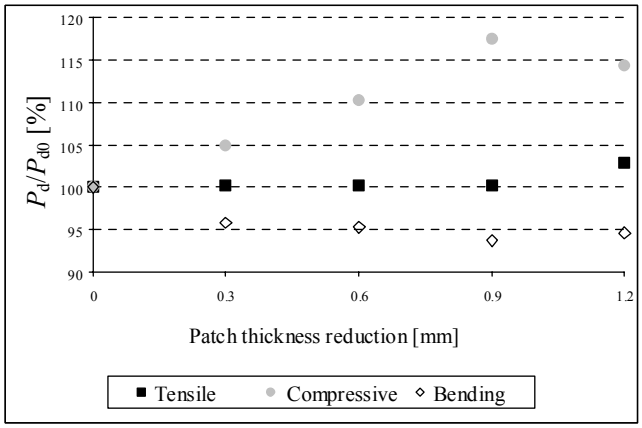

Fig. 367 – Normalized strength for different dimensions patch inner chamfer repairs.

- This modification only vaguely affects the repairs tensile strength, with the 1.2 mm patch inner chamfer composing the exception to this tendency (2.9% strength improvement). For the 0.9 and 1.2 mm patch inner chamfer repairs, damage initiated at the symmetry plane ***B*** simultaneously at the laminate/adhesive interface (OEO) and at the adhesive/patch interface (IEO), with growth towards the overlap central region. For the other chamfers, damage initiated simultaneously at the symmetry plane ***B*** at the adhesive/patch interface (OEO) and at the laminate/adhesive interface (IEO), growing along the mentioned interfaces towards the overlap central

region. The smaller influence of the chamfers on the repairs strength, compared to the SS repairs (Fig. 321), is related to the elimination of the laminate flexure for the DS repair, which yields σ_y stresses identical to the standard repair (Fig. 366 compared to Fig. 320). In fact, for the SS repairs, σ_y peak stresses at the IEO became compressive with this geometric modification, which led to an increased repair strength. For the DS repairs, this effect was cancelled, and only for the 1.2 mm chamfer the value of δ for patch debonding slightly increased (3.5%), which explains the results of Fig. 367. Fig. 368 (a) and (b) show the 0.3 mm and 1.2 mm patch inner chamfer repairs, respectively, after patch debonding.

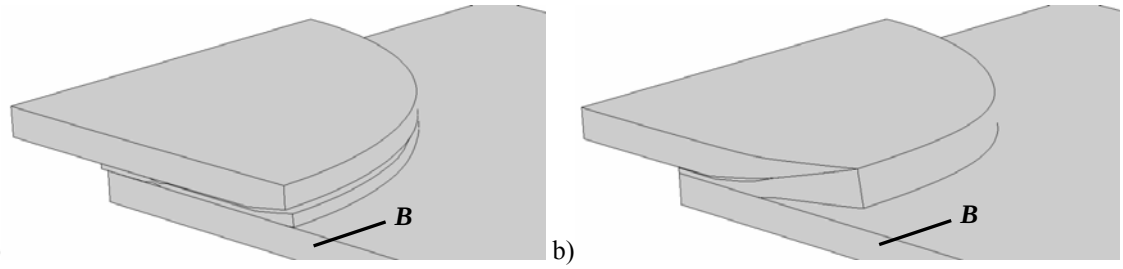

a) b)

Fig. 368 – Deformed shape of the 0.3 mm (a) and 1.2 mm (b) patch inner chamfer repairs (tensile load).

- The repairs compressive strength increased proportionally with the chamfer dimensions up to the 0.9 mm chamfer repair, slightly decreasing for the 1.2 mm one. For the 0.3, 0.6 and 0.9 mm chamfers, damage initiated at the laminate/adhesive interface at the IEO, followed by debonding at the adhesive/patch interface at the OEO (symmetry plane ***B***), growing towards the IEO. Oppositely, for the 1.2 mm patch inner chamfer repair, damage initiated at the laminate/adhesive interface at the IEO (symmetry plane ***B***) and, due to the lower patch stiffness, propagated along the same interface until complete patch failure, since the patch undergoes extensive flexure near the OEO. The proportional strength improvement up to the 0.9 mm patch inner chamfer repair is justified by the reduction of patch stiffness at the OEO, causing a modification of the failure path from the laminate/adhesive interface to the adhesive/patch interface. This also increased the value of δ for patch debonding, reaching 17.0% for the 0.9 mm chamfer, compared to the standard repair. Fig. 369 shows the deformed shape of the 0.9 mm chamfer repair, at damage onset (a) and after patch debonding (b). The extensive patch flexure of the 1.2 mm patch inner chamfer repair, caused by the lower patch stiffness, led to a slight reduction of the value of δ for patch debonding, and to damage growth along the laminate/adhesive interface along the entire overlap. Owing to this, the repair strength slightly diminished. Fig. 370 (a) represents damage onset and Fig. 370 (b) patch debonding for the 1.2 mm patch inner chamfer repair.

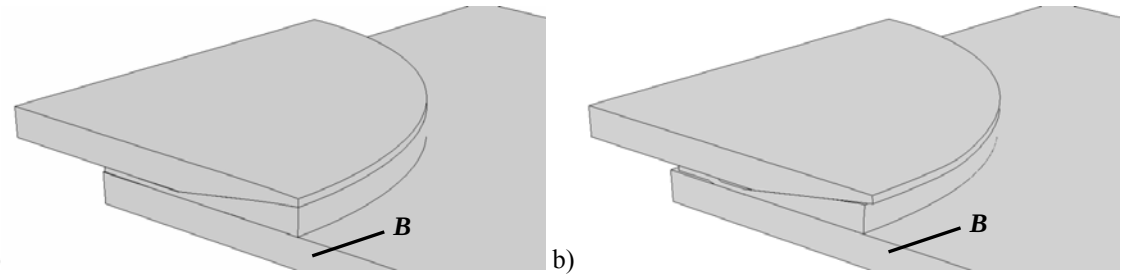

a) b)

Fig. 369 – Deformed shape of the 0.9 mm patch inner chamfer repair at damage onset (a) and patch debonding (b) (compressive load).

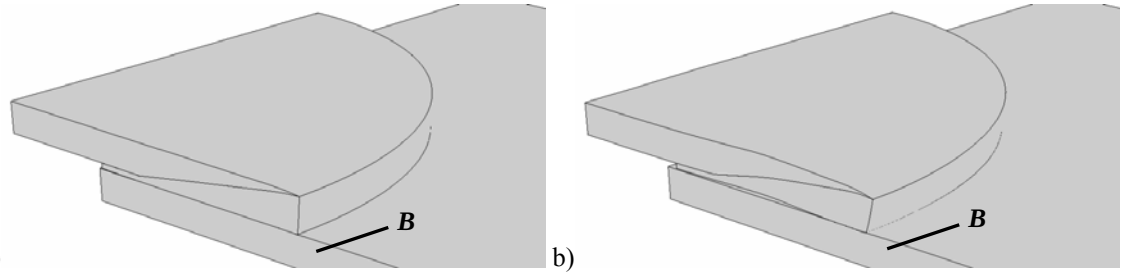

a) b)

Fig. 370 – Deformed shape of the 1.2 mm patch inner chamfer repair at damage onset (a) and patch debonding (b) (compressive load).

- In contrast to the tensile and compressive loads, the patch inner chamfer is not recommended under bending for these repairs, since it caused an approximate 5% strength reduction, regardless the chamfer dimensions. Damage onset and growth path was equal for all chamfers, occurring at the outer patch (Fig. 371), initiating at the laminate/adhesive interface at the OEO (symmetry plane ***B***) and progressing towards the IEO. The mentioned strength behaviour is due to the reduction of repair stiffness emerging from the chamfer. Fig. 371 shows patch debonding onset for the 0.3 mm (a) and 1.2 mm (b) patch inner chamfer repairs.

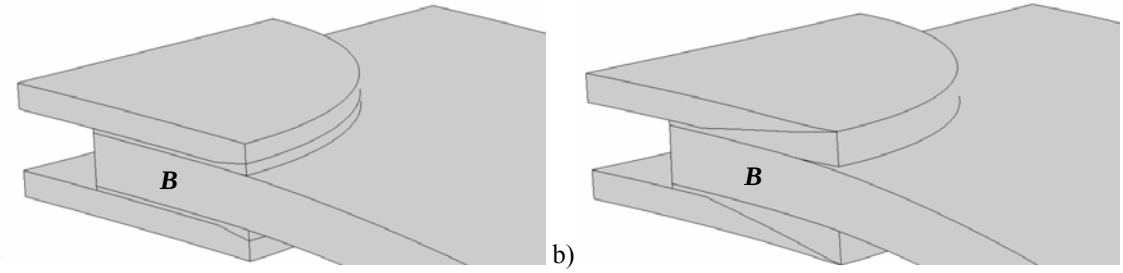

a) b)

Fig. 371 – Deformed shape of the 0.3 mm (a) and 1.2 mm (b) patch inner chamfer repairs (bending load).

5.4.3. Plug filling

Fig. 325 represents the mesh at the repair region, for the SS repair. Soutis et al. (1999) concluded that the compressive strength of 3D DS repairs increased filling with adhesive the open hole of the repairs, due to the reduction of stress concentrations at the hole edges. Almost 90% of the undamaged compressive strength of the laminate was achieved plug filling the repairs, compared to the 80% strength restitution using only the patches. Fig. 372 (a) and (b) show σ_y and τ_{xy} stress distributions, by this order, at the laminate/adhesive interface (tensile load). For both stresses, the deviation to the standard repair is not significant. In fact, σ_y stresses (Fig. 372 a) only show a minor modification at the IEO, with the elimination of compressive peak stresses. τ_{xy} stresses (Fig. 372 b) diminish at the overlap inner region. However, a τ_{xy} singularity appears at the IEO, at the plug/laminate vertical interface.

- The tensile strength of the repairs is not affected by the plug filling. An analogous justification to the SS repair is presented (Fig. 327). Actually, also for the DS repair the plug/laminate vertical interface fails prior to damage initiation in the adhesive layer. Only after the plug failure damage initiates in the adhesive layer, at the laminate/adhesive interface at the OEO (symmetry plane ***B***), growing towards the OEO. Fig. 373 presents the plug repair at damage onset (a) and after patch debonding (b), clarifying the described behaviour.

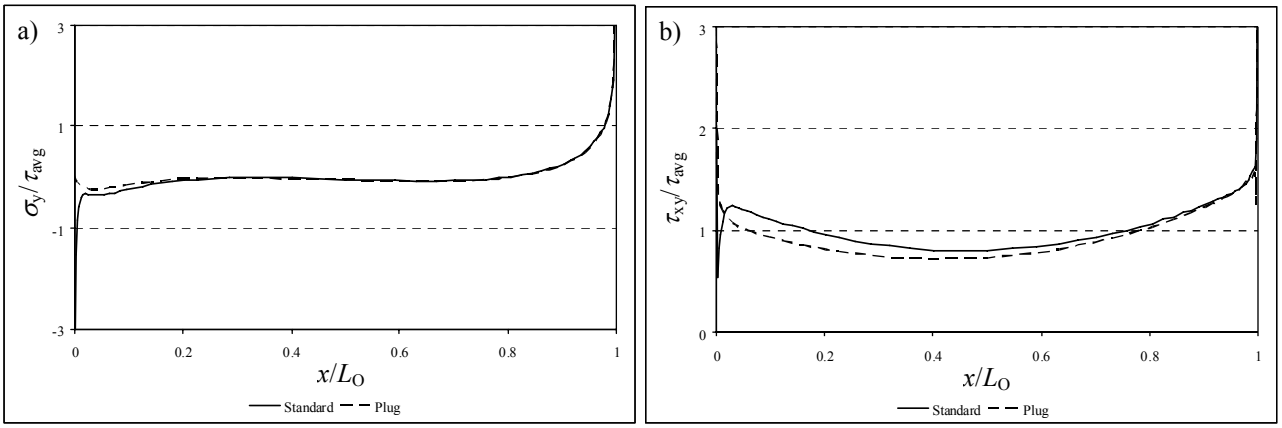

Fig. 372 – Normalized σ_y (a) and τ_{xy} (b) stress distributions at the laminate/adhesive interface (tensile load).

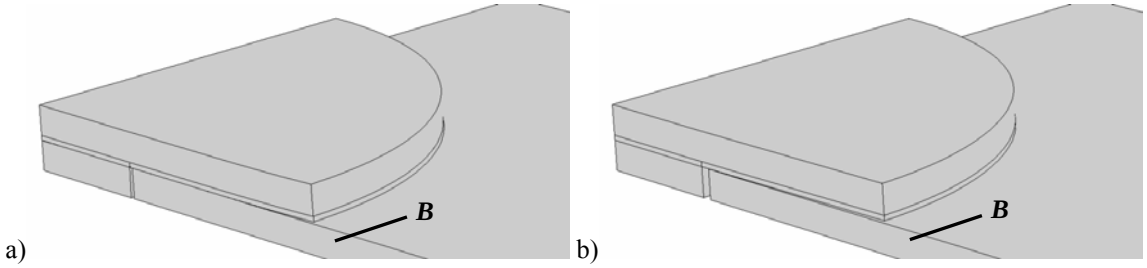

a) b)

Fig. 373 – Deformed shape of the plug repair at damage onset (a) and patch debonding (b) (tensile load).

- Under a compressive load, plug filling leads to a 13.6% strength improvement. Damage initiated at the laminate/adhesive interface simultaneously at the entire overlap (symmetry plane ***B***). After complete patch failure in the adhesive layer, the plug fails at the plug/patch interface. This opposed to the tensile behaviour, justifying the mentioned strength improvement. Fig. 374 (a) shows damage initiation at the IEO at the laminate/adhesive interface (which propagates almost simultaneously to the entire overlap). Fig. 374 (b) corresponds to patch debonding.

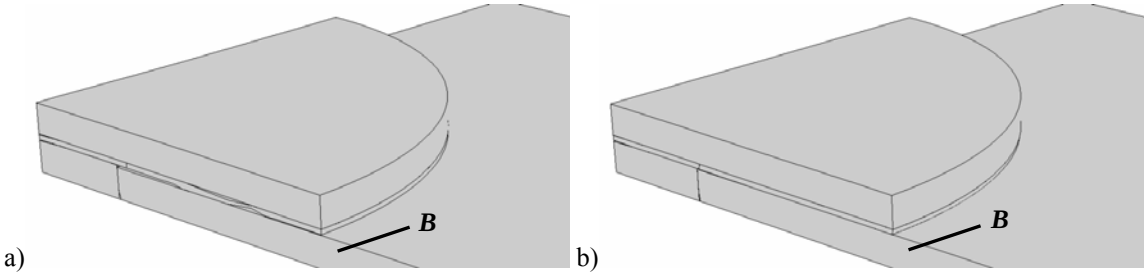

a) b)

Fig. 374 – Deformed shape of the plug repair at damage onset (a) and patch debonding (b) (compressive load).

- Plug filling revealed to be ineffective under bending. Damage initiated at the outer patch, at the laminate/adhesive interface at the OEO (symmetry plane ***B***), growing along this interface towards the IEO. The repair inner region, near the plug, remains undamaged until complete patch debonding. The negligible influence of the plug on P_d/P_{d0} is substantiated by the onset of damage at the OEO. Damage initiation at the outer patch is presented in Fig. 375 (a). Patch debonding is shown in Fig. 375 (b), being clearly visible that the plug is left undamaged after patch debonding.

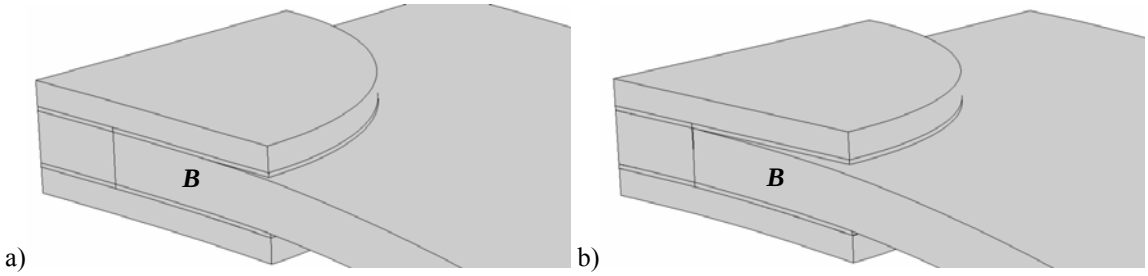

a) b)

Fig. 375 – Deformed shape of the plug repair at damage onset (a) and patch debonding (b) (bending load).

5.4.4. Fillets

Fig. 330 shows the fillet shapes evaluated. Vallée et al. (2006a, 2006b) studied the influence of curved fillets of different radius at the overlap edges in DL joints between GFRP pultruded adherends. Even though the fillet increased the joints strength, due to reduction of peak stresses at the overlap edges, only a marginal strength improvement was achieved increasing the fillet radius. σ_y and τ_{xy} stress distributions for the four fillet shapes considered in this work are presented in Fig. 376 (a) and (b), respectively, at the laminate/adhesive interface (tensile load). Equally to the SS repairs, σ_y and τ_{xy} stress distributions were similar, regardless the fillet shape. The use of a fillet leads to a major reduction on σ_y peel peak stresses at the OEO (Fig. 376 a). A reduction of the τ_{xy} peak stresses was also achieved at the overlap outer region (Fig. 376 b). As mentioned previously for the SS repairs, this geometric modification is prone to increase the repair strength, since the stress concentrations at the damage onset region (OEO) diminish significantly. Fig. 377 summarizes the values of P_d/P_{d0} for all fillet geometries tested and loads.

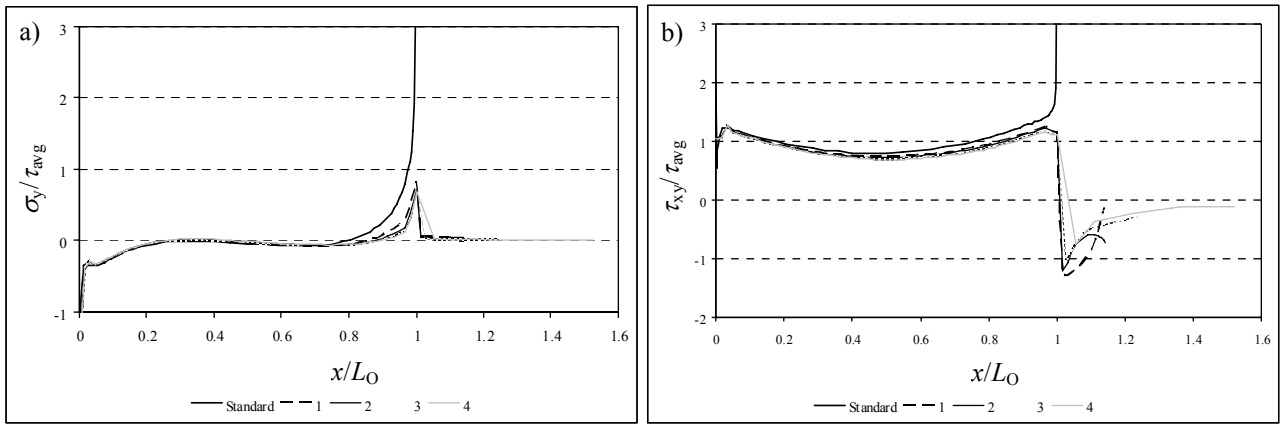

Fig. 376 – Normalized σ_y (a) and τ_{xy} (b) stress distributions at the laminate/adhesive interface (tensile load).

- Under a tensile load, the repairs behaviour agrees with the SS repairs, i.e., maximum strength improvement (7.5%) for the 45º straight fillet (Campilho et al. 2009b). The worst results were obtained for the 30º and 15º straight fillets. Equally to the SS repairs, damage initiated at the patch/fillet vertical interface at the symmetry plane ***B***, growing along the adhesive/patch interface from the OEO towards the IEO. The reduction on σ_y peel and τ_{xy} peak stresses at the damage onset region (OEO), notwithstanding the fillet shape, explains the strength improvement. These results agree with the works of Vallée et al. (2006a, 2006b). The smaller performance of the 30º and 15º straight fillet repairs is justified by the bigger fillet stiffness, causing a premature failure at the

fillet/patch interface. Fig. 378 illustrates the 45º (a) and 15º (b) straight fillet repairs under the same value of δ (corresponding to damage initiation for the 45º straight fillet repair), clarifying the described behaviour.

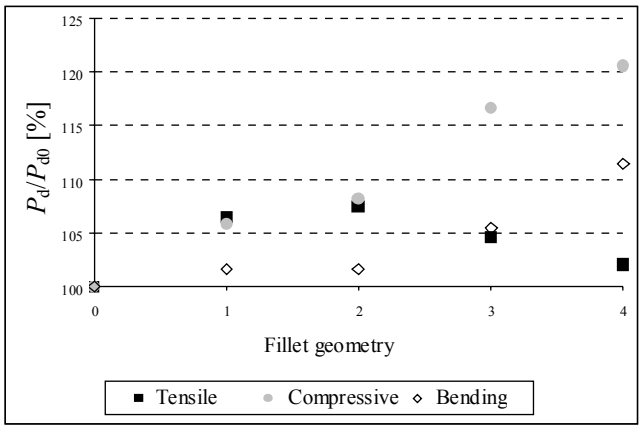

Fig. 377 – Normalized strength for different fillet shapes.

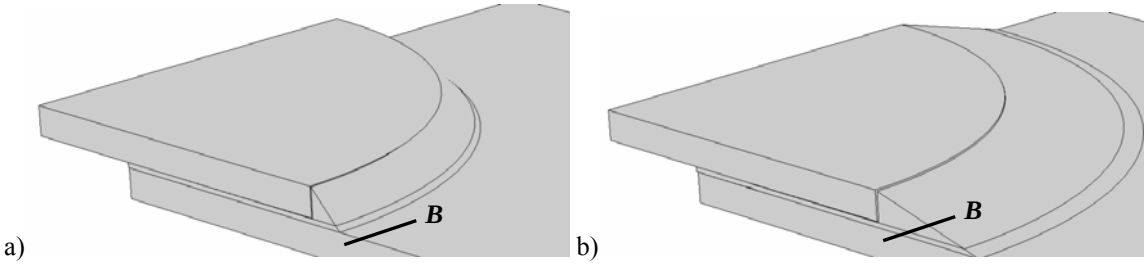

Fig. 378 – Deformed shape of the 45º (a) and 15º (b) straight fillet repairs (tensile load).

- Under a compressive load, a more substantial strength improvement was attained than under tension. The best results were achieved using a 15º straight fillet (strength improvement of 20.5%). For all fillet shapes evaluated, results showed damage initiation concurrently at the laminate/adhesive interface (IEO) and at the adhesive/patch interface (OEO) at the symmetry plane ***B***, growing towards the overlap central region with the increase on the applied load. The documented increasing improvement of the P_d/P_{d0} ratio with the reduction of the fillet angle is related to the fillet horizontal shear area. In fact, the reduction of the fillet angle increases the fillet shear resistant area, which correspondingly reflects on the strength of the repairs. Fig. 379 shows the deformed shape of the 45º (a) and 30º (b) straight fillet repairs, for the value of δ of debonding onset for the 30º straight fillet repair. The comparative analysis of these two figures reveals that the patch for the 30º straight fillet repair is still intact.

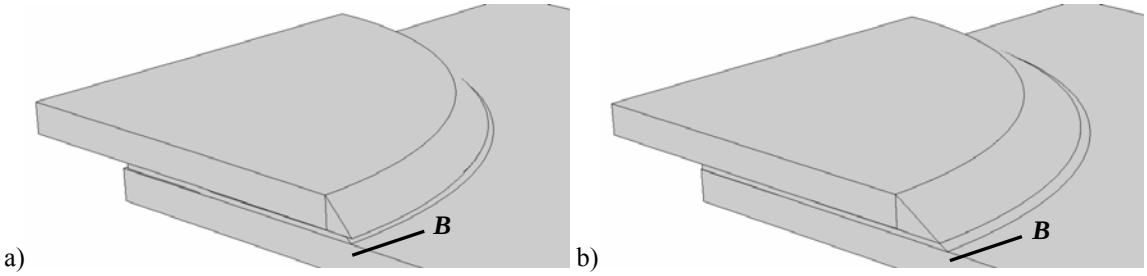

Fig. 379 – Deformed shape of the 45º (a) and 30º (b) straight fillet repairs (compressive load).

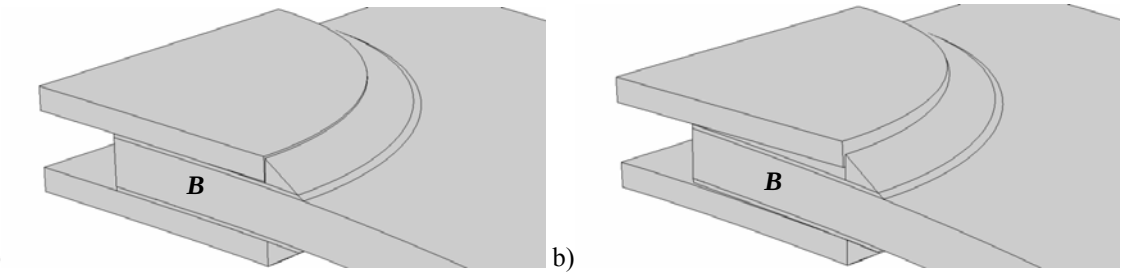

a) b)

Fig. 380 – Deformed shape of the 30º straight fillet repair at damage onset (a) and patch debonding (b) (bending load).

- Under bending, the 15º straight fillet repair led to the best results. The strength improvements were similar between the curved and 45º straight fillet repairs (approximately 1.7%). The repair strength then increased progressively with the reduction of the fillet angle, up to an 11.4% strength improvement for the 15º straight fillet repair. With this modification, damage initiated at the outer patch at the patch/adhesive interface at the OEO (symmetry plane ***B***), propagating to the adhesive/patch interface from the OEO towards the IEO. The increase of P_d/P_{d0} with the reduction of the fillet angle can be attributed to larger stiffening at the repair region. Fig. 380 shows the deformed shape of the 30º straight fillet repair at damage onset (a) and after damage propagation at the adhesive/patch interface (b).

5.4.5. Laminate outer chamfer

The laminate outer chamfering technique (Fig. 338) is the last modification examined for the DS repairs, since the laminate inner chamfer is not applicable to this repair technique. Adams et al. (1986) addressed the tensile behaviour of adhesively-bonded CFRP/steel DL joints with tapered outer adherends (1/10 slope). It was concluded that this geometry slightly diminished the standard DL joint strength, due to the small influence of this modification on the transverse normal stresses. σ_y and τ_{xy} stress distributions are shown in Fig. 381 (a) and (b), respectively, at the laminate/adhesive interface (tensile load). σ_y compressive stresses (Fig. 381 a) increased in magnitude at the IEO with this modification, while at the OEO σ_y peel peak stresses followed the same tendency. σ_y stress distributions were found to be similar, independently of the chamfer dimensions. τ_{xy} stresses (Fig. 381 b) diminish along the entire overlap with this modification, compared to the standard repair. The most substantial reduction occurred at the IEO, near the chamfer. The values of P_d/P_{d0} are summarized in Fig. 382 as a function of the laminate outer chamfer dimensions.

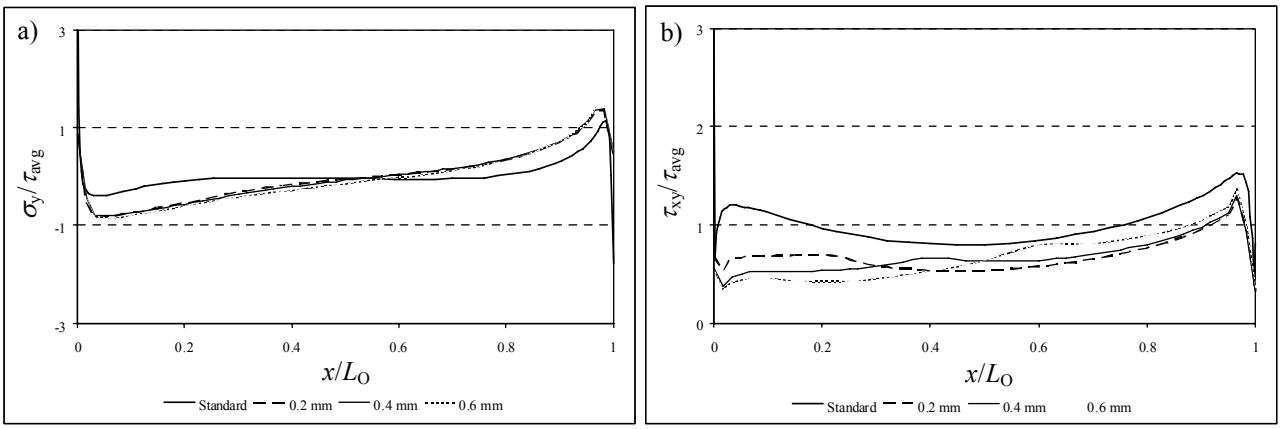

Fig. 381 – Normalized σ_y (a) and τ_{xy} (b) stress distributions at the adhesive/patch interface (tensile load).

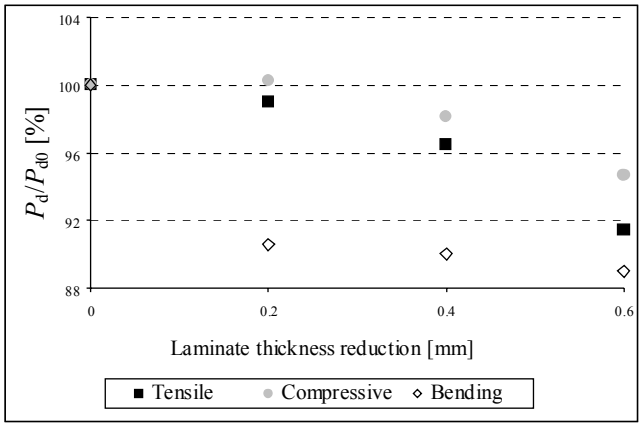

Fig. 382 – Normalized strength for different dimensions laminate outer chamfer repairs.

- The laminate outer chamfer leads to a gradual reduction of the repairs tensile strength as a function of its dimensions, reaching 8.5% for the 0.6 mm chamfer. Independently of the chamfer dimensions, damage initiated at the laminate/adhesive interface at the OEO (symmetry plane ***B***), growing along the same interface towards the IEO. It was found that the value of δ for patch debonding is identical between the chamfered repairs and the standard repair. The decreasing trend of P_d/P_{d0} is due to the reduction of the laminate cross-sectional area with the chamfer dimensions, despite the parallel reduction on τ_{xy} peak stresses at the OEO, where damage initiates (Campilho et al. 2009b). Fig. 383 concerns the deformed shape of the 0.6 mm laminate outer chamfer repair at damage onset (a) and after patch debonding (b).

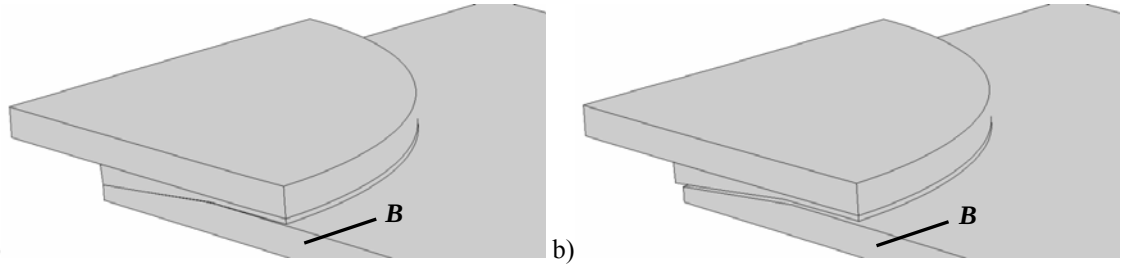

a) b)

Fig. 383 – Deformed shape of the 0.6 mm laminate outer chamfer repair at damage onset (a) and patch debonding (b) (tensile load).

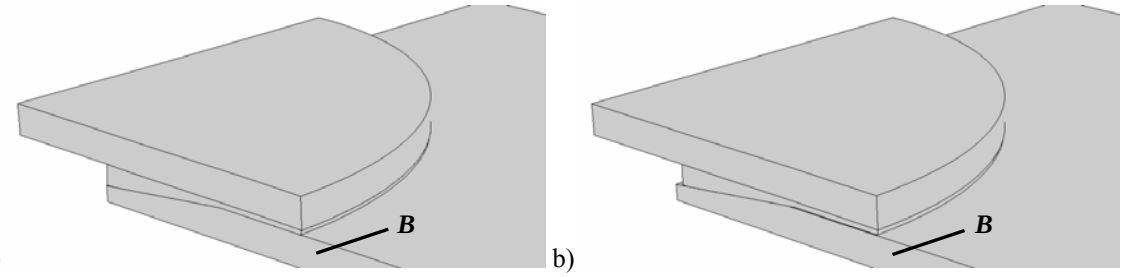

a) b)

Fig. 384 – Deformed shape of the 0.6 mm laminate outer chamfer repair at damage onset (a) and patch debonding (b) (compressive load).

- Also under compression the repairs strength diminished progressively as a function of the chamfer dimensions, reaching 5.5% for the 0.6 mm chamfer. In all cases, damage initiated at the laminate/adhesive interface (symmetry plane ***B***) simultaneously at the entire overlap. Despite this strength reduction, the value of δ for patch debonding is similar between all the chamfered repairs. Equally to the tensile load, the decreasing trend

of P_d/P_{d0} can be explained by the reduction of the laminate cross-sectional area, induced by the chamfer. Fig. 384 shows the 0.6 mm laminate outer chamfer repair at damage onset (a) and after patch debonding (b).

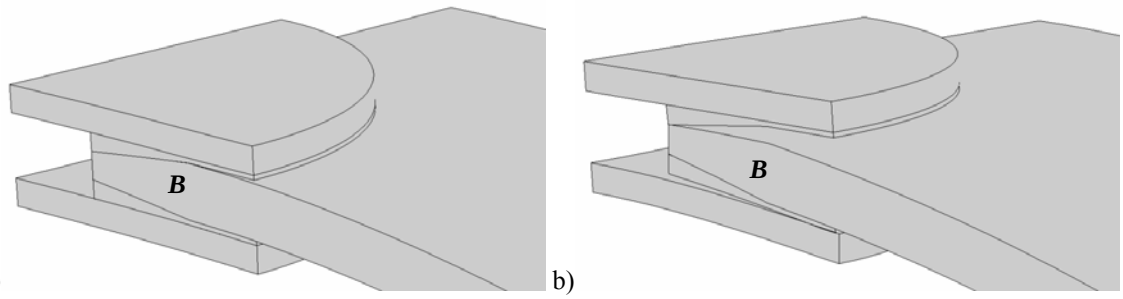

a) b)

Fig. 385 – Deformed shape of the 0.6 mm laminate outer chamfer repair at damage onset (a) and patch debonding (b) (bending load).

- The bending strength was reduced by approximately 10%, regardless the chamfer dimensions. The failure mechanism was similar to the standard repair, i.e., damage initiation at the outer patch at the laminate/adhesive interface at the OEO (symmetry plane ***B***), growing along the same interface towards the IEO. The strength reduction is explained in light of the reduction of stiffness at the repair region with this modification. Fig. 385 shows the 0.6 mm laminate outer chamfer repair at damage onset (a) and after patch debonding (b). In Fig. 385 (b) failure of the inner patch can also be visualized, which occurred only after the outer patch debonding.

5.4.6. Geometric changes combinations

Also for the DS repairs, the individual geometric changes that showed to be valuable under tension, compression and bending were combined, to achieve the biggest strength improvement possible. The following Sub-Sections summarize the individual results of the geometric changes, proposing different combinations based on these results.

5.4.6.1. Tensile load

The following geometric changes increased the repairs tensile strength: the 45º straight fillet (7.5% strength improvement), the patch outer chamfer (the 1.2 mm chamfer leads to a 15.0% strength improvement) and the patch inner chamfer (the 1.2 mm one results on a 2.9% strength improvement).

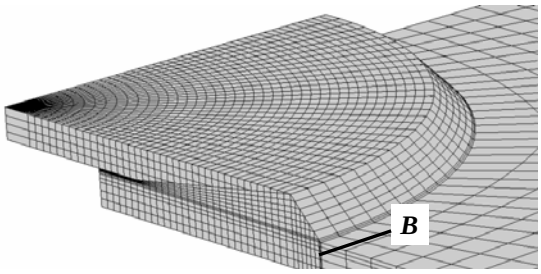

Fig. 386 – Detail of the mesh at the overlap region combining the 45º fillet and the 1.2 mm patch inner chamfer.

Fig. 386 details the FEM mesh at the overlap region of a repair combining a 45º straight fillet with a 1.2 mm patch inner chamfer. A 21.4% increase on P_{d0} was achieved. The failure path is similar to the SS equivalent combination, i.e.,

damage onset at the IEO at the adhesive/patch interface (symmetry plane ***B***) and growth along the same interface until patch debonding. Fig. 387 (a) shows damage onset, while Fig. 387 (b) represents patch debonding for this combination repair. **This combination represents the best solution for the DS repair under a tensile load**.

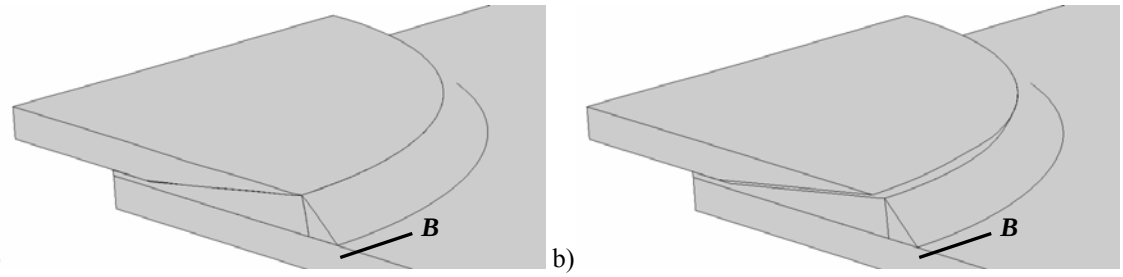

a) b)

Fig. 387 – Deformed shape of the combination repair at damage onset (a) and patch debonding (b) (tensile load).

5.4.6.2. Compressive load

Different guidelines for the individual changes were recommended under a compressive load. Actually, the 15º straight fillet led to a 20.5% strength improvement, the 1.2 mm patch outer chamfer resulted in a 12.4% strength improvement, the 0.9 mm patch inner chamfer led to a 17.5% strength improvement, and the plug filling caused a 13.6% strength improvement. A combination repair was analysed, merging a 15º straight fillet, a 1.2 mm patch inner chamfer and a plug. A patch inner chamfer comprising all the patch thickness was used, instead of a 3/4 patch thickness one, for mesh simplification purposes, since the difference between both was minimal. Fig. 388 details the mesh for this combination. The strength improvement for this combination reached 26.0%. With this geometry, damage initiated simultaneously at the overlap region, at the adhesive/patch interface (symmetry plane ***B***). Fig. 389 (a) represents the deformed shape of the repair at damage initiation, while Fig. 389 (b) shows the repair after patch debonding. **Analysing the presented results, this combination repair is regarded as the optimal solution for the DS repair under a tensile load**.

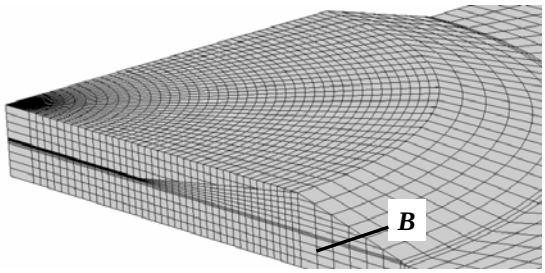

Fig. 388 – Detail of the mesh at the overlap region combining the 15º straight fillet, the 1.2 mm patch inner chamfer and the plug.

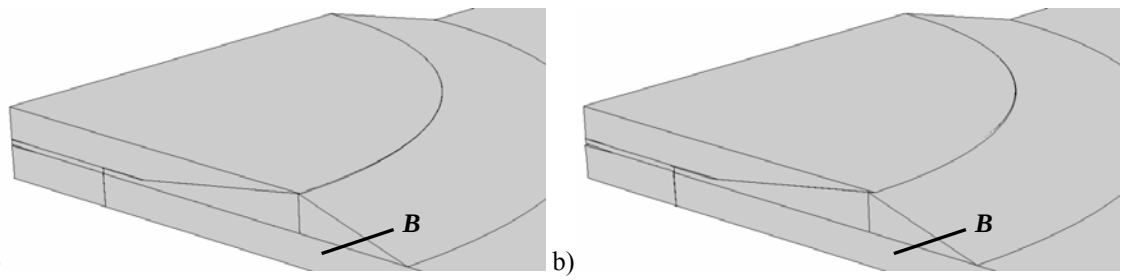

a) b)

Fig. 389 – Deformed shape of the combination repair at damage onset (a) and patch debonding (b) (compressive load).

5.4.6.3. Bending load

Under a bending load, the geometric changes leading to a strength improvement are the fillet (the 15º straight fillet causes an 11.4% strength improvement) and the patch outer chamfer (the 0.9 mm chamfer leads to a 12.2% strength improvement). Since merging of these two geometric changes is not feasible, **it is considered that the 0.9 mm patch outer chamfer is the optimal solution for the DS repairs under a bending load**.

5.5. Summary of the failure modes and optimal solutions

This Sub-Section summarizes the overall results of Section 5. The list of failure modes characterized in this Section for all the repair configurations is listed in Table 19. Table 20 establishes the correspondence between all the geometric modifications evaluated and the failure modes of Table 19, for all the loadings evaluated. Table 21 summarizes the optimal repair configuration for each repair technique/load combination and the respective percentile strength improvement to the standard repair.

Table 19 – List of failure modes.

Failure modes and respective description	
F1	Damage onset at symmetry plane ***B***, at the OEO (laminate/adhesive interface) and at IEO (adhesive/patch interface). Growth towards the central overlap region.
F2	Damage onset at symmetry plane ***B***, at the OEO (laminate/adhesive interface), growing along the same interface towards the IEO.
F3	Damage onset at symmetry plane ***B***, at the patch/fillet vertical interface and growth along the adhesive/patch interface from the OEO towards the IEO.
F4	Damage onset at symmetry plane ***B***, at the plug/laminate vertical interface, following growth at the laminate/adhesive interface at the OEO towards the IEO.
F5	Damage onset at symmetry plane ***B***, simultaneously at the laminate/adhesive interface at the IEO and at the adhesive/patch interface at the OEO.
F6	Damage onset at a 45º angle of the symmetry plane ***B***, at the laminate/adhesive interface at the OEO growing towards the IEO along the same interface.
F7	Damage onset at a 45º angle of the symmetry plane ***B***, at the adhesive/patch interface at the IEO, growing towards the OEO along this interface.
F8	Damage onset at a 45º angle of the symmetry plane ***B***, at the patch/fillet vertical interface, growth along the adhesive/patch interface from the OEO towards the IEO.
F9	Damage onset at symmetry plane ***B***, simultaneously at the entire overlap at the laminate/adhesive interface.
F10	Damage onset at symmetry plane ***B***, at the IEO at the laminate/adhesive interface, growing along the laminate/adhesive interface towards the OEO.

Table 20 – Failure modes of the repairs.

Geometry	SS			DS		
	Tensile	Compressive	Bending	Tensile	Compressive	Bending
Standard	F1	F6/F7	F2	F2	F9	F2*
Patch outer chamfering	F1	F6	F2	F1/F2	F9	F2*
Patch inner chamfering	F1	F6	F2	F1/F5	F5/F10	F2*
Laminate outer chamfering	F2	F6	F2	F2	F9	F2*
Laminate inner chamfering	F1	F6	F2	-	-	-
Fillet	F3	F8	F3	F3	F5	F3*
Plug filling	F4	F6	F2	F4	F9	F2*

* *at the outer patch*

Table 21 – Summary of the most efficient solutions.

Geometry	SS			DS		
	Tensile	Compressive	Bending	Tensile	Compressive	Bending
Strength improvement [%]	27.7	6.8	58.3	21.4	26.0	12.2
Patch outer chamfer [mm]	-	-	1.2	1.2	-	0.9
Patch inner chamfer [mm]	1.2	1.2	-	-	1.2	-
Laminate outer chamfer [mm]	-	-	0.3	-	-	-
Laminate inner chamfer [mm]	-	-	0.2	-	-	-
Fillet [º]	45	30	-	45	15	-
Plug filling	-	√	-	-	√	-

This study was intended to assess the influence of the most significant geometric changes on the strength of CFRP SS and DS repairs, under tensile, compressive and bending loads. Overall, significant strength improvements were achieved for the SS and DS repairs under all loadings. For the SS repairs, the best results were obtained under bending. The patch outer and inner chamfering techniques, as well as filleting at the OEO, were the most efficient geometric changes. Different combinations of these changes led to 27.7, 6.8 and 58.3% strength improvements under tensile, compressive and bending loads, respectively. The DS repairs strength was also studied. The patch outer and inner chamfers and the fillet were the most efficient modifications. Strength improvements of 21.4, 26.0 and 12.2% were obtained combining different geometric changes for the tensile, compressive and bending loads, respectively. Although the results presented in this Section may depend on the materials properties, lay-ups and geometric repair parameters, it can be concluded that the analysis methodology adopted simulates the different failure modes typical of these repairs and provides design guidelines to increase the residual strength of composite repairs.

6. REPAIR OF WOOD STRUCTURES WITH COMPOSITES

The experimental and numerical evaluation of repairs on wood beams with adhesively-bonded CFRP composites is the last topic examined in this work. Several studies addressed reinforcement and repairing techniques for large-scale wood structures, but only a few of these employed adhesive-bonding techniques. However, adhesive-bonding of strengthening elements has already proved to be structurally efficient and economically competitive, comparing with the traditional repair procedures (Dagher and Lindyberg 2000, Custódio et al. 2009). The importance of the proposed study lies on the extensive use of wood on large scale applications, added to the several potential damage mechanisms possible to occur (Triantafillou 1998a), which traditionally lead to the replacement of large scale beams, with the associated difficulties. The limited availability of these large beams is another factor encouraging the repair of wood members, instead of their replacement. The work presented here also acquires special significance because of the limited number of available studies on composite repairs of wood structures (Radford et al. 2002, Lopez-Anido et al. 2003, Lopez-Anido et al. 2005, Akbiyik et al. 2007, Alam et al. 2009). Additionally, these are limited to experimental studies that, most of the times, are not easily applicable. On the other hand, it is unrealistic to apply available empirical results to timber structures in need of repair, since much of the research is based upon timber reinforcement rather than repair (Jones 1997, Ogawa 2000), despite the fact that many papers published on timber reinforcement can be useful as a basis to devise suitable repair techniques for these structures (Sliker 1962, Peterson 1965, Coleman and Hurst 1974, Hoyle 1975, Bulleit et al. 1989). The proposed FEM methodology, including the inverse material characterization technique applied to wood repairs, will also allow the reduction of time and cost associated to extensive experimentation, otherwise necessary to allow the widespread use of these repairs, since no accurate numerical predictive tools were yet developed for adhesively-bonded repairs for wood members. Amongst the few researches focusing on the repair of wood structures with composites, the recently published work of Akbiyik et al. (2007) should not be disregarded. The authors addressed the repair of large-scale wood beams damaged by horizontal checking and splitting along the members length, using different approaches. These included the use of hex bolts and attachment of GFRP plates to the beam side faces with lag screws. Repairing with GFRP side plates was particularly effective for the beams with end-splitting (with crack initiation at one of the beam edges), by providing a larger equivalent cross-sectional area. Moreover, after testing the GFRP side plates did not exhibit signs of damage, apart from the lag screws loci. Radford et al. (2002) proposed a repair methodology for low aspect ratio wood beams damaged by a longitudinal crack along their length, which allowed overcoming the loss of shear properties. Steel nails or fibreglass pultruded rods were adhesively-bonded through the beams thickness. The suitability of this technique was performed with scaled tests, being the number of rods and respective loci the parameters investigated. The GFRP rods were found to be more effective than the steel ones in restoring the stiffness and strength of the undamaged beams. The works of Lopez-Anido et al. (2003, 2005) addressed a repair technique for decayed underwater wood piles in waterfront facilities, using GFRP shells and a grouting material. The proposed method consisted on applying a composite shield around the wood pile that enclosed its deteriorated portion. Following, the region between the shield and the wood pile was filled with a grouting material to transmit the

pile loads to the CFRP shield. Although no repairs were performed in-situ, the feasibility of the proposed repair methodology was demonstrated in the laboratory with full-size specimens. The results showed that the full recovery of the piles undamaged strength can be achieved with this technique. Alam et al. (2009) compared different repair strategies for wood beams damaged in the laboratory (to simulate structural damage), under a 4PB loading. The repair techniques consisted on routing grooves in the beams tension, compression or both faces along their length, and adhesively-bonding reinforcement rods with an epoxy adhesive. Steel and composite pultruded rods of CFRP, GFRP and FULCRUM (commercial designation of a glass fibre reinforced polyurethane composite) with a rectangular section were considered. The results were compared with the undamaged beam ones. The authors concluded that, regardless of the reinforcement material, the repairs stiffness and strength increased from repairing in the compression face to the repair on both faces. The steel and CFRP rods led to bigger strengths than the undamaged beam, whilst the other reinforcement materials were sufficient to restore the undamaged beam strength.

In this Section, repair techniques with adhesively-bonded composite patches are proposed for three of the most common damage types found in wood structures. These damage mechanisms were established from an extensive literature research (Ebeling 1990, Ritter 1990, Akhras and Foo 1993, Sullivan et al. 1994, Brebbia 2003, Lopez-Anido et al. 2003, Humphreys and Francey 2004, Yeomans 2004, Akbiyik 2005, Lopez-Anido et al. 2005, Akbiyik et al. 2007, Lamanna et al. 2007, Alam et al. 2009). Scaled specimens of the *Pinus Pinaster* species with a quadrangular section of 20x20 mm^2 and 300 mm length will be used to test, under 4PB, the proposed solutions of adhesive-bonding CFRP laminates in several configurations to strengthen the damaged beams. For the compression failure repair, the crushed material will also be removed prior to the patch application, extending the application of the proposed repair technique to other damage scenarios, like material imperfections, such as knots, or local damage, due to human intervention. The FEM simulations to predict the behaviour of these repairs were performed in ABAQUS®. The data obtained from the inverse material characterization technique is applied in this Section, including the trapezoidal CZM developed in Sub-Section 3.2.2 to simulate the adhesive layer. The epoxy adhesive Araldite® 2015, already characterized in Sub-Section 3.2.2.1 in pure modes I and II, will be applied to adhesively-bond the CFRP patches to the wood beams. The interlaminar fracture of the CFRP composite, as well as the wood beam failure through two different planes which occurred in the experiments, were also simulated numerically. The structure of this Section is as follows: the repair constituents used are firstly characterized, the analysis methodology is presented, and the repair technique (including the repair procedure, geometry and dimensions) is described. The numerical idealization of the repairs, comprising a detailed description of the mesh, planes for the evaluation of stresses, and cohesive elements loci to simulate the different fractures, are subsequently detailed. The experimental procedure follows, involving the repairs fabrication and testing procedures. The results for each of the three repair techniques are divided in Sub-Sections, initiating with an elastic stress analysis to the repair, followed by a failure analysis (comparison between the experiments and FEM simulations on the failure modes and values of K, δ_m and P_m of the repairs).

6.1. Material properties

Wood is a material with a hierarchically arranged and oriented anatomic structure, often showing a significant variability on the elastic and strength properties between specimens of the same species. At the macroscopic scale, characteristic of large-scale structures, wood is regarded as an orthotropic material (Hallstrom and Grenestedt 1997), with three orthogonal directions of symmetry (Fig. 390). These correspond to the fibres longitudinal directional (L),

radial direction of the annual rings (*R*) and tangential direction of the annual rings (*T*). Owing to these characteristics, six propagation systems must be distinguished for each elementary propagation mode (I, II and III): *TL*, *RL*, *LR*, *TR*, *RT* and *LT* (Fig. 391). The first letter represents the normal direction to the crack plane and the second letter the crack growth direction (Smith and Vasic 2003).

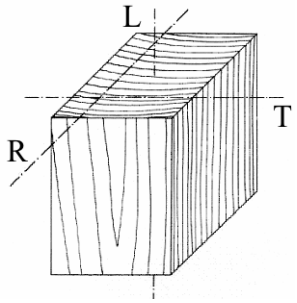

Fig. 390 – Wood directions of symmetry (Pereira 2005).

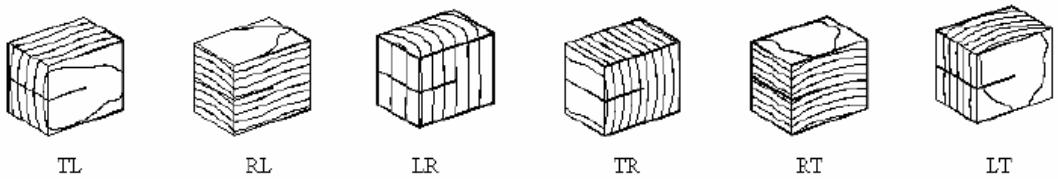

Fig. 391 – Crack propagation systems in wood (Pereira 2005).

Scaled specimens of the *Pinus Pinaster* species were considered in this study, whose elastic orthotropic properties and cohesive parameters used to simulate wood failures in two different propagation systems in pure modes I and II are presented in Table 22 and Table 23, respectively (Caumes 1987, Xavier 2003, Pereira 2005, Silva 2005). The pure mode III cohesive properties, also used in this Section whenever 3D models are employed, were considered equal to the pure mode II ones, as an approximation. It should be emphasized that the value of E_L was tuned to the test results, for a value of 10.20 GPa compared to the literature reference value of 15.13 GPa, for an accurate simulation of the repairs stiffness (Hallstrom and Grenestedt 1997). This is justified by the significant stiffness variation of this natural material between specimens of the same species (Malan et al. 1988a, Malan et al. 1988b, Downes et al. 1997, Bao et al. 2001, Baillères et al. 2005). The tensile fracture behaviour of wood was simulated with the triangular cohesive model presented in Sub-Section 3.2.1, due to the brittle nature of this material under tension (Gilfillan et al. 2003). For the CFRP patches, the same unidirectional pre-preg of carbon-epoxy used previously was considered (Table 3 shows the elastic orthotropic properties of a unidirectional ply and Table 9 the cohesive properties for an interlaminar failure). The epoxy adhesive Araldite® 2015 was used to bond the CFRP patches to the wood beams (the fracture characterization of this adhesive was performed in Sub-Section 3.2.2.1; its cohesive properties in pure modes I and II are presented in Table 8). On all the repairs, t_A=0.2 mm was considered, to be consistent with the adhesive characterization procedure.

Table 22 – Elastic orthotropic properties for the *Pinus Pinaster* wood.

E_L=10.20 GPa	ν_{LR}=0.47	G_{LR}=1120 MPa
E_R=1910 MPa	ν_{LT}=0.51	G_{LT}=1040 MPa
E_T=1010 MPa	ν_{RT}=0.59	G_{RT}=170 MPa

Table 23 – Cohesive parameters for wood fracture in the *RL* and *LR* propagation systems in pure modes I and II.

	RL Plane		*LR* Plane	
Pure mode	I	II	I	II
d_i [N/mm^3]	10^6	10^6	10^6	10^6
$\sigma_{u,i}$ [MPa]	16	16	65	16
J_i [N/mm]	0.2	1.2	25	1.2
$\delta_{1,i}=\delta_{2,i}$ [mm]	$1.6*10^{-5}$	$1.6*10^{-5}$	$6.5*10^{-5}$	$1.6*10^{-5}$
$\delta_{u,i}$ [mm]	0.025	0.15	0.77	0.15

6.2. Procedure

The damage mechanisms addressed in this Section are compression failure (Fig. 57 a), cross-grain tension (Fig. 57 b) and horizontal shear failure initiating at one of the beam edges (Fig. 57 c). As will be detailed and justified further in this work, the horizontal shear failure repair was simulated with 3D models, whilst for the other repairs, a 2D approximation was assumed. Since these fractures typically occur under pure bending, the repair techniques suggested will be tested under 4PB, assuring a constant bending moment at the repair region. The analysis of each of the repair techniques begins with an elastic stress analysis of the repairs. For the repairs modelled as 2D, stresses will be evaluated at different planes, such as the wood/adhesive interfaces, the middle of the adhesive, within the wood or between patch plies. For the horizontal shear failure repair, simulated with 3D models, an analysis of the stress fields at the repair region was carried out instead. This will allow a better understanding of the potential damage onset regions of the repairs, and also explain the stiffness/strength tendencies of the parametric studies performed. Equally to Section 4, the stress analysis was carried out with solid finite elements to model the adhesive layer. Stress distributions were extracted with triangular cohesive elements (Section 4.2). A failure analysis follows, in which the adhesive layer was simulated using cohesive elements with trapezoidal laws, whose parameters in pure modes I and II were previously determined (Section 3.2.2.1). An experimental/numerical comparison of K, δ_m and P_m was performed for these repairs. The fracture mechanisms of the repairs were addressed as well. In the repairs described in this Section, a FEM study was performed prior to the tests such that the biggest value of the quantity analysed in the parametric study (typically the patch length, L_P, or L_O) granted the re-establishment of the undamaged beam strength. In these preliminary studies, different fractures were introduced in the models using the pre-determined cohesive properties, based on the likely critical regions of the repairs established from the knowledge of the repair materials and literature results.

6.3. Pure bending damage

This Section addresses three of the most common damage types of large-scale wood beams under pure bending (Akbiyik 2005, Arbiyik et al. 2007, Lamanna et al. 2007, Alam et al. 2009). Repair techniques were proposed for compression failure (Fig. 392 a), cross-grain tension (Fig. 392 b) and horizontal shear failure initiating at one of the beam edges (Fig. 393). In the mentioned figures, the L, R, T coordinate system refers to the wood beam, while the coordinate system x, y, z pertains to the CFRP patch. At this stage, the *RL* plane (horizontal longitudinal plane of the beams) and *LR* plane (cross-sectional plane of the beams), whose fractures will be addressed, are introduced.

- **Compression failure** is the first damage mechanism evaluated (Fig. 57 a). This fracture is characterized by the crushing of the wood material at the compression half of an intermediate section of a wood beam under bending, being particularly probable for low-density wood species (Akbiyik 2005, Akbiyik et al. 2007). Under these circumstances, the repair technique proposed consists on the removal of the damaged material with a semi-circular shape, minimizing stress concentrations at the weakened region, and adhesively-bonding of a CFRP patch with the ductile adhesive Araldite® 2015 (Fig. 392 a). In this case, the patch will mainly bear compression loads in the beam length direction. Thus, unidirectional patches with the fibres aligned in this direction will be used. It should be mentioned that the repair procedure suggested can also be applied in other damage scenarios, such as deterioration caused by aging or adverse environmental conditions, wood imperfections (knots or checks), human intervention or in-service damage (Akbiyik 2005, Custódio et al. 2009). The following parameters are defined for this repair geometry: beam length (a), width (b) and height (h), hole diameter (d), adhesive thickness (t_A), patch thickness (t_H) and overlap length (L_O). It should be referred that the optimal value of t_H was established numerically before the experimental tests, as the minimum value avoiding patch buckling, which can occur in these situations due to the compressive loading applied to the patch, added to its slenderness (Moulin et al. 1990, Kim et al. 1997, Gilfillan et al. 2001).
- **Cross-grain tension** is also likely to occur under pure bending (Fig. 57 b), due to a misalignment of the wood fibres with the beam major axis (Radford et al. 2002, Lionetto and Frigione 2009). It consists on a tensile fracture perpendicularly to these fibres, at the beam tensile face, resulting in a quasi-horizontal crack ($\alpha_C \leq 15º$, Fig. 392 b). The proposed repair consists on adhesively-bonding of a CFRP patch in the face under tension to prevent further crack propagation (Fig. 392 b). Under these conditions, the patch will be under uniaxial tension. Consequently, it consists on a unidirectional lay-up with the fibres aligned along the beam length. The characteristic dimensions of the repair are the beam length (a), width (b) and height (h), crack length projection along the L direction (L_C'), cross-grain angle (α_c), adhesive thickness (t_A), patch thickness (t_H), and patch length (L_P). The value of t_H was defined numerically before the experimental tests as the minimum value assuring that the strength of the CFRP in the fibres direction was not exceeded, to avoid patch tensile failures.

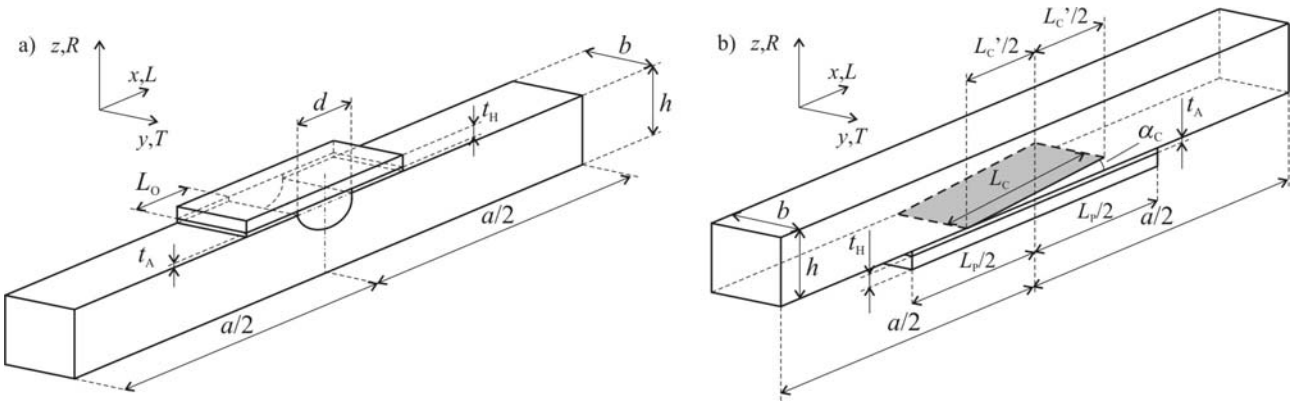

Fig. 392 – Compression failure (a) and cross-grain tension (b) repair procedures.

- Finally, **horizontal shear failure** at the middle of the beam height was addressed, initiating at one of the beam edges with propagation to the beam inner region (Fig. 57 c). The repair consists on adhesively-bonding CFRP patches on the vertical side faces of the beam at the cracked region (Fig. 393) to block sliding between the beam arms, to increase the strength of the damaged beams. The patches consist on unidirectional laminates

with the fibres aligned vertically, to maximize their shear strength in the horizontal *RL* plane. The dimensions of the repair are the beam length (a), width (b) and height (h), crack length (L_C), adhesive thickness (t_A), patch thickness (t_H), distance between the beam and patch edges (L_{PR}), and patch length (L_P) and width (w_P). In the repaired geometries, the value of L_{PR} was kept constant, while varying L_P. A smaller value of w_P was selected for the patches, compared to h, to avoid interferences between the patches and the cylinders. Also for this repair, t_H was tuned numerically as the minimum value assuring that the typical shear strengths of the CFRP patch in the *RL* plane were not attained up to the repair fracture, to avoid premature patch failures.

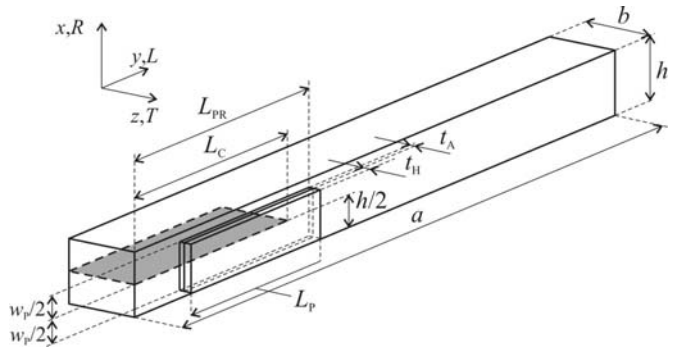

Fig. 393 – Horizontal shear failure repair procedure.

Table 24 presents the *initial dimensions* and patch lay-ups for the three repair techniques proposed in Fig. 392 and Fig. 393. Ply unit thickness is 0.15 mm. **The *initial dimensions* will be used in Section 6 for the initial stress analysis of each technique, varying only the values of L_O or L_P in the parametric studies performed, depending on the repair. These will comprise L_O=10, 20 and 30 mm for the compression failure repairs, L_P=40, 60 and 80 mm for the cross-grain tension repairs and L_P=45, 75 and 105 mm for the horizontal shear failure repairs. Moreover, 0º plies are assumed to be aligned with the *x* direction of each repair (Fig. 392 and Fig. 393).** The repairs were tested under 4PB, enabling a constant bending moment at the central region of the repair (this does not apply to the horizontal shear failure repair procedure, since the damage extends up to the beam edge).

Table 24 – *Initial dimensions* (in mm) of the repair techniques proposed for the beams damaged under pure bending.

Compression failure repair				
a=300	b=20	h=20	d=7.5	t_A=0.2
t_H=1.2	L_O=10	$[0_8]$ patch lay-up		
Cross-grain tension repair				
a=300	b=20	h=20	L_C'=20	α=15º
t_A=0.2	t_H=0.6	L_P=40	$[0_4]$ patch lay-up	
Horizontal shear failure repair				
a=300	b=20	h=20	L_{PR}=105	L_P=45
t_A=0.2	t_H=1.2	L_C=95	w_P=4.5	$[0_8]$ patch lay-up

Fig. 394 details the test configuration for the three repair techniques. ***D*** and ***E*** represent the loading and supporting cylinders, respectively. Values of S=260 mm, S'=130 mm, d_C=10 mm and b_C=70 mm were always considered. The value of e, specifying the distance between each supporting cylinder and the nearest beam edge, was fixed at 20 mm.

On the bending tests, d_C=10 mm was used. A different value of d_C to Sections 4 and 5 was considered, to minimize indentations in the wood beams, which are significantly more compliant than CFRP composites.

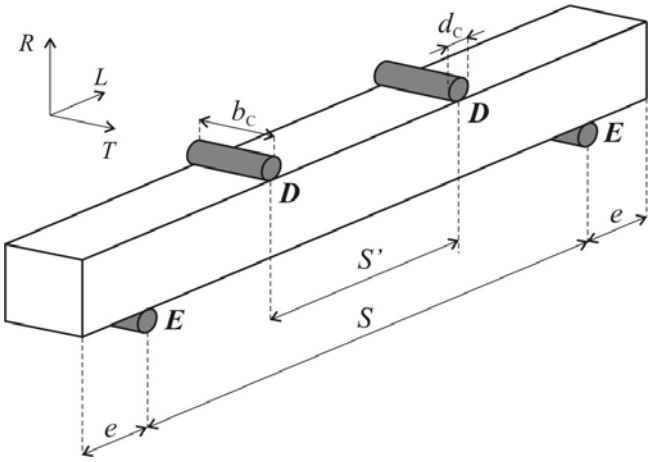

Fig. 394 – Test configuration under 4PB.

6.3.1. Numerical work

The FEM simulations were performed in ABAQUS®, using 2D models for the techniques of Fig. 392 (a) and (b), which can be accurately described in 2D due to their constant shape in the width direction. These repairs employed six and eight-node plane-strain solid finite elements and six-node cohesive elements for the stress and failure analyses. The horizontal shear failure repair (Fig. 393) was simulated with 3D models using twenty-seven-node full integration solid finite elements and eighteen-node cohesive elements for the stress analyses. The numerical models for the fracture characterization were built with eight-node reduced integration solid finite elements and eight-node cohesive elements, to reduce the computational effort. Non-linear geometric and material analyses were performed. σ_y and τ_{xy} stresses were evaluated at seven planes at the bond region in the beams height direction for the compression failure and cross-grain tension repairs (Fig. 395): within the wood beam at different distances to the wood/adhesive interface (P1 and P2), at the wood/adhesive interface (P3), at the middle of the adhesive (P4), at the adhesive/patch interface (P5) and in the patch between the two plies closest to the adhesive (P6) and between the second and third patch plies closest to the adhesive (P7). The loci of planes P1 and P2 will be defined later, taking into account the test results. The stress distributions in these planes were obtained with the cohesive elements, following the procedure of Sections 4 and 5. The stress analysis for the horizontal shear failure repairs was performed differently. Instead of evaluating stresses at different planes, a detailed analysis will be presented of the most significant stress fields at the repair region.

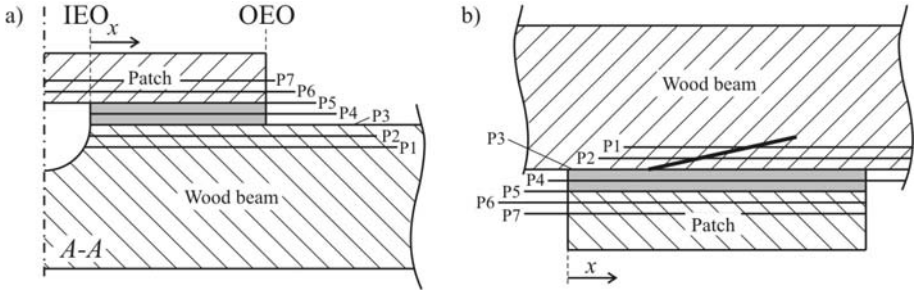

Fig. 395 – Cohesive elements in the compression failure (a) and cross-grain tension (b) repairs.

Whilst for the cross-grain tension repair (Fig. 392 b) the FEM models were built without symmetry conditions, due to the absence of vertical symmetry, the other repair techniques took advantage of symmetry conditions (Fig. 396). Only half length was used for the compression failure 2D models, due to the vertical symmetry of the repair (Fig. 396 a), while only half width was considered for the horizontal shear failure 3D models (Fig. 396 b).

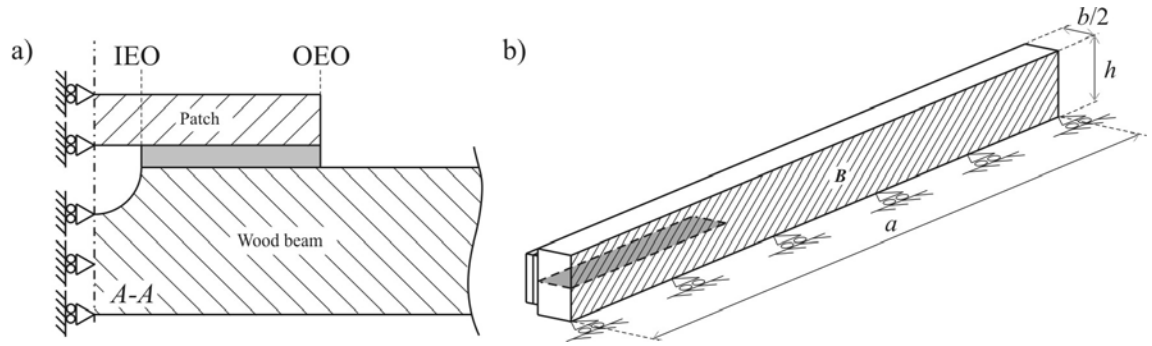

Fig. 396 – Symmetry conditions for the compression failure (a) and horizontal shear failure (b) repairs.

Fig. 397 to Fig. 401 describe the meshes, including details at the repair region for the failure models (which do not include solid finite elements to simulate the adhesive layer). A more refined mesh was built for the wood beams near the loading and supporting cylinders, for an improved numerical efficiency at the beam/cylinder contacting regions. To perform the stress analysis for the compression failure and cross-grain tension repairs, two solid elements through-thickness were employed for the adhesive layer, whilst only one solid element was considered in the horizontal shear failure 3D models with this purpose.

- The **compression failure repairs** 2D mesh (Fig. 397) was more refined near the cylinders (sixty elements over 6 mm). The mesh was built with fifteen solid elements for the beams height. Thirty elements were used along the overlap, using bias effects for a more refined mesh near the overlap edges, where stress concentrations are expected due to the evident dissimilar strains under loading experienced by the wood beam and patch along the overlap. The patch thickness was modelled with four elements. The two patch plies closer to the adhesive layer were modelled with one element each, to allow the extraction of stresses between the first and second, and also the second and third plies closer to the adhesive, using the cohesive elements, and to introduce the possibility of an interlaminar patch failure at these interfaces, as will be discussed later. The mesh was constructed to ensure that, within the wood beam, the element boundaries for the two elements closer to the adhesive layer were kept perfectly horizontal (Fig. 397 b), to allow the extraction of stresses and include the possibility of horizontal *RL* failures at these boundaries, as will be addressed later in this work.

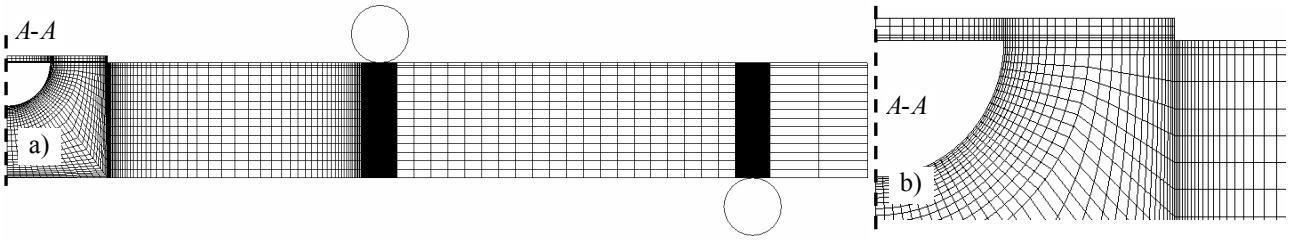

Fig. 397 – Mesh for the compression failure repair (a) and respective detail at the crack region (b).

- Fig. 398 and Fig. 399 pertain to the **cross-grain tension repairs** 2D mesh. Near the cylinders, sixty elements were employed over a length of 4 mm. In the repairs height, two mesh sizes were applied: a more refined mesh at the tensile region comprising the cross-grain crack, with twenty-two elements, and a coarser mesh with ten elements at the undamaged compressive region of the beam. In the beams length, a moderately refined mesh was along the extent of the crack, since this region is not expected to be severely loaded. The bonding regions at both sides of the crack were simulated with forty elements, being employed bias effects for an accurate characterization of the peak stresses expected near the overlap edges. The patch was modelled with four solid elements through thickness. The two plies closer to the adhesive were modelled by one solid element each, allowing the extraction of stresses and the possibility of patch interlaminar failures at planes P6 and P7 (Fig. 395 b). Within the wood beam, the mesh was set to include cohesive elements horizontally at established distances to the adhesive layer, to simulate *RL* failures. This option will be substantiated further in this Section.

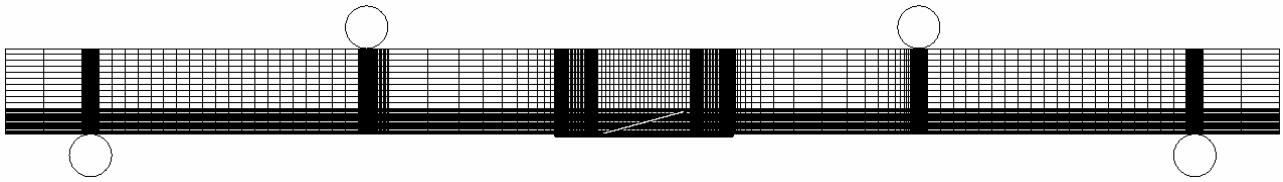

Fig. 398 – Mesh for the cross-grain tension repair.

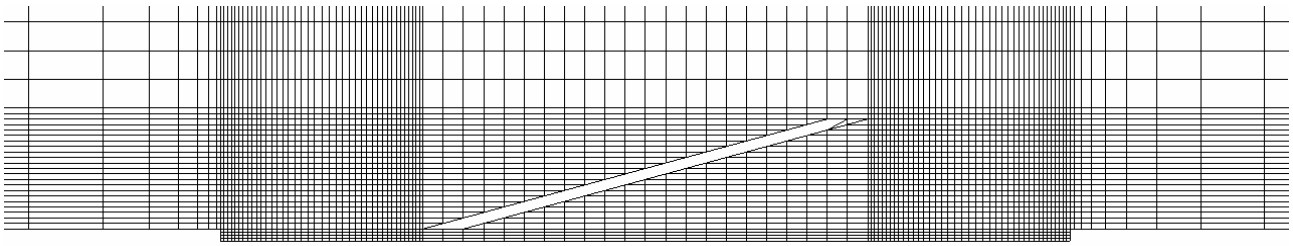

Fig. 399 – Mesh detail for the cross-grain tension repair at the repaired region.

- For the **horizontal shear failure repair** (Fig. 400 and Fig. 401), the beam regions contacting with the cylinders were refined with forty elements along a length of 2.5 mm. In addition, the mesh was particularly refined in the vicinity of the crack tip, to guarantee a stable crack initiation and growth. The repaired portion of the beam was also more refined than the undamaged portion. Four elements were employed to model the beams half-width, and eight elements to model their height. On both cases, different element sizes were selected along the respective dimension, using bigger elements where approximately constant stresses are expected. The patch thickness was modelled with two elements. For consistency with the fabricated specimens (following in Sub-Section 6.3.2.1.3), a 1 mm gap was left between the cracked beam arms (Fig. 401). A blunt region resulted from the mesh construction at the tip of the horizontal shear crack (Fig. 401 b). This corresponds approximately to the obtained shape after cutting the crack with a 1 mm thickness saw. To reproduce accurately the specimens tested, the cohesive elements integration points at the crack tip were opened from the beginning of the analysis ($\delta > \delta_{u,i}$ in Fig. 68), extending the crack of a length equal to the length of two solid elements (1 mm). Using this procedure, the sharp crack tip, which was induced in the specimens with a razor blade as will be detailed later, is simulated accurately. The value of L_C, extending up to the crack tip, corresponds in the FEM models to the initiation of the third cohesive element.

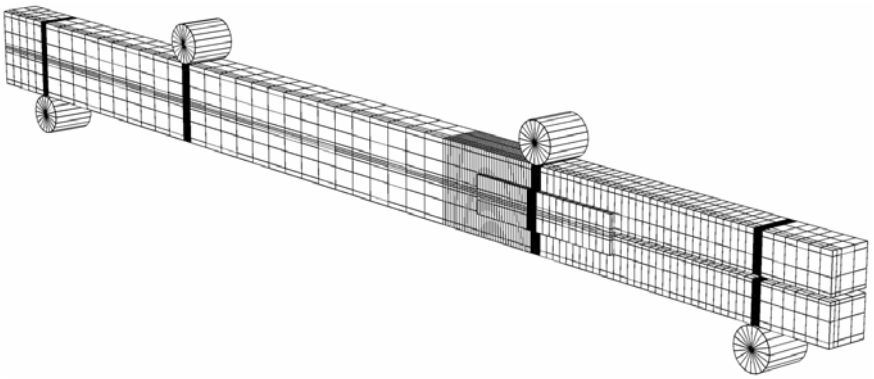

Fig. 400 – Mesh for the horizontal shear failure repair.

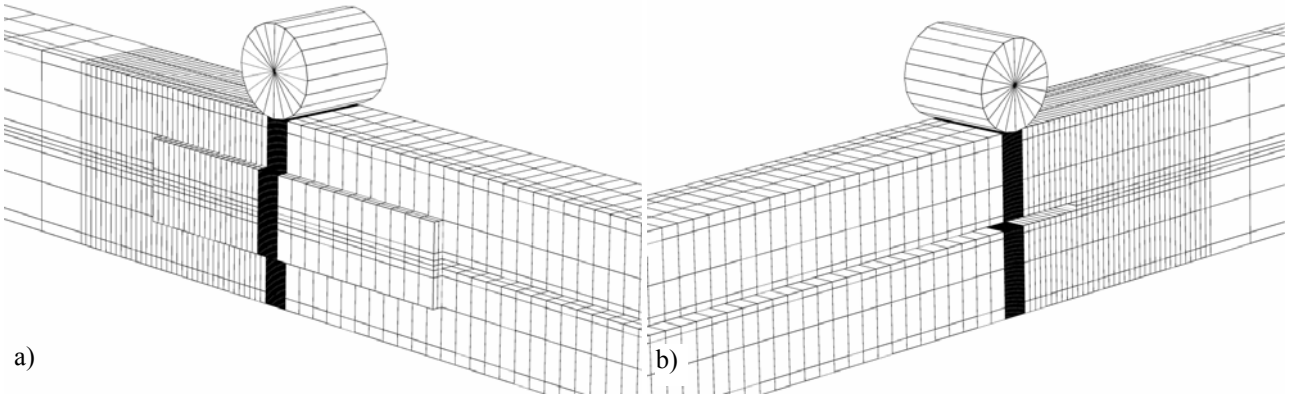

Fig. 401 – Mesh details for the horizontal shear failure repair: patch (a) and crack tip (b) regions.

Detailed models were built for the failure analyses, incorporating cohesive elements at additional locations with different cohesive laws to simulate damage initiation and propagation within the various constituents of the repairs or between their interfaces, for an accurate simulation of the experimental failure modes. The t_A=0.2 mm adhesive layer was simulated for all the repair techniques with cohesive elements with trapezoidal laws in each pure mode, in an analogous way to Section 4. The undamaged beam and the unrepaired beams, damaged by the three damage mechanisms, were also examined for comparison purposes.

- For the **compression failure repair** (Fig. 402 a), patch interlaminar failures were taken into consideration between the two plies closer to the adhesive (plane P6, Fig. 395 a) and between the second and third patch plies closer to the adhesive (plane P7, Fig. 395 a). Within the wood beams, the prospect of horizontal *RL* propagations was introduced at planes P1 and P2 (Fig. 395 a). Distances to the wood/adhesive interface of 0.4 and 0.8 mm were selected for these planes, respectively, corresponding to the limit values of the experimental wood failures. The possibility of vertical *LR* failures in the wood beam was also incorporated in the FEM models at the symmetry line *A-A* and below the loading cylinders. It should be mentioned that cross-graining was not equated in all the analyses in this Section.
- The failure modes equated for the **cross-grain tension repair** are specified in Fig. 402 (b). The possibility of CFRP patch interlaminar failures was included at the two planes mentioned for the compression failure repair. *RL* propagations in the wood beam between the loading cylinders were investigated at planes P1 and P2 (Fig. 395 b). The experiments allowed the establishment of the limit distances between these planes and the adhesive layer, defined at 0.3 and 0.6 mm. In Fig. 402 (b), failure paths A1 and A4 correspond to damage

propagation near the smaller and larger bonds, respectively, either in the patch, adhesive layer or wood beam at planes P1 or P2. *RL* damage propagations were also considered initiating at the crack tip and growing up to the rightmost (path A2) and leftmost (path A3) loading cylinders, and initiating at the middle of the cross-grain crack height up to the leftmost loading cylinder. *RL* transverse wood failures were equated below the loading cylinders and initiating at the crack tip. The propagation of the cross-grain crack with its initial orientation was not addressed, since this would pertain to a very specific set of conditions that are not satisfied in most fabricated repairs. In fact, these present the wood fibres almost perfectly aligned in the *L* direction and, under these conditions, the induced cross-grain crack is expected to propagate either in the *RL* or *LR* planes.

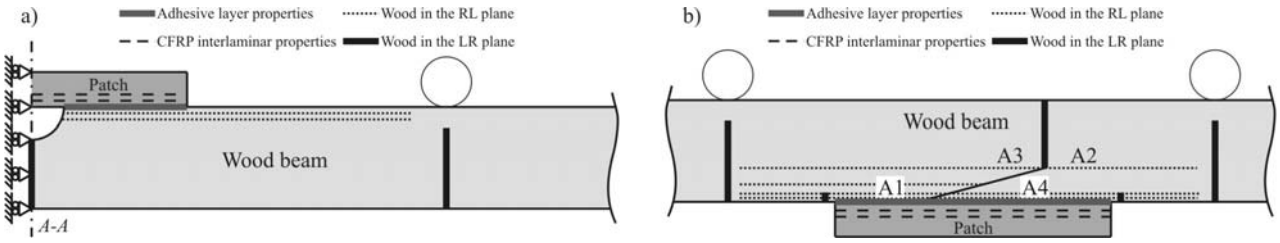

Fig. 402 – Cohesive elements loci for the compression failure (a) and cross-grain tension (b) repairs.

- Oppositely to the previous models, for the **horizontal shear failure repair**, failures within the CFRP patch and the wood beam were not equated, except for *RL* crack propagation initiating at the tip of the horizontal shear crack. This choice was made due to the 3D numerical idealization of these repairs, with the corresponding increased complexity, and also because in these repairs P_m was always related to patch detachment. Failures within the wood beam, either by tensile failure, cross-grain tension failure, or even *RL* horizontal shear propagation, always occurred after P_m. Thus, damage growth was only evaluated at the adhesive layer and horizontally in the *RL* plane, to simulate the growth of the horizontal shear crack.
- The **undamaged beam** and the **unrepaired beams**, damaged by each one of the three damage mechanisms, were also simulated numerically, for comparison with the repaired beams. In these models, only the *RL* and/or *LR* wood fracture possibilities were addressed, with the exception of the *RL* wood failures at planes P1 and P2 (Fig. 402 b), which become irrelevant due to the absence of the patch. Equally to the analysis in Section 4, a penalty function method was used for the failures within the wood and patch up to $\sigma_{u,i}$ (Fig. 68), considering $d_i=10^6$ N/mm^3 (de Moura et al. 1997). Also for these fractures, the assumption of $\delta_{2,i}=\delta_{1,i}$ was made, due to the brittle nature of these interfaces (Lee and Soutis 2008).

6.3.2. Experimental work

6.3.2.1. Specimens preparation

The repair techniques in this Section were evaluated with 300 mm x 20 mm x 20 mm scaled wood beams of the *Pinus Pinaster* species, prepared at the Forest Department of UTAD, with the orientation of Fig. 392 and Fig. 393. For all the repair geometries, the wood specimens were left in a dry environment at room temperature for at least one month to assure a strong bond to the adhesive layer, avoiding overheating and likely damage to the wood surfaces (Steiger 2002, Custódio et al. 2009). The unidirectional CFRP patches, used to repair the damaged beams, were fabricated following

the guidelines presented in Sub-Section 3.2.2.1.1. The techniques to artificially induce the three damage mechanisms in the wood members are initially described. The implementation of the repair procedures is also focused in detail.

6.3.2.1.1. Compression failure specimens

The compression damage is characterized by the crushing of wood at the compression region of an intermediate beam section. Initially, the damaged material is removed in a semi-circle shape, using a cylindrical end-mill. After this procedure, a patch is bonded over the weakened region for strengthening purposes.

Damaged material removal

The repair method initiated with the damaged material removal in a semi-circle shape, hypothetically developing at the middle of the beam length (Fig. 392 a). This operation was accomplished at UTAD, using an EFI FG2201 conventional drilling machine and a HSS 711PM30 Clarkson end-mill with a 15 mm diameter and two flutes. The holes were drilled with a rotational speed of 300 RPM using a manual feed. This operation was executed in several steps. In each step, the cutting tool was pulled out to allow a phased extraction of the drilling swarf, to assure a high quality surface finishing. Fig. 403 (a) shows the setup in the drilling machine. Since the material was to be removed in a semi-cylindrical shape, two specimens were fastened in the machine grips at a time with the correct wood fibres orientation, allowing the simultaneous material removal on the two beams. Besides the obvious fabrication speed advantages, this method also avoids using a sacrifice wood beam, which would be required to avoid a rough surface with chips at the hole region. Fig. 403 (b) presents a set of two beams after the drilling operation.

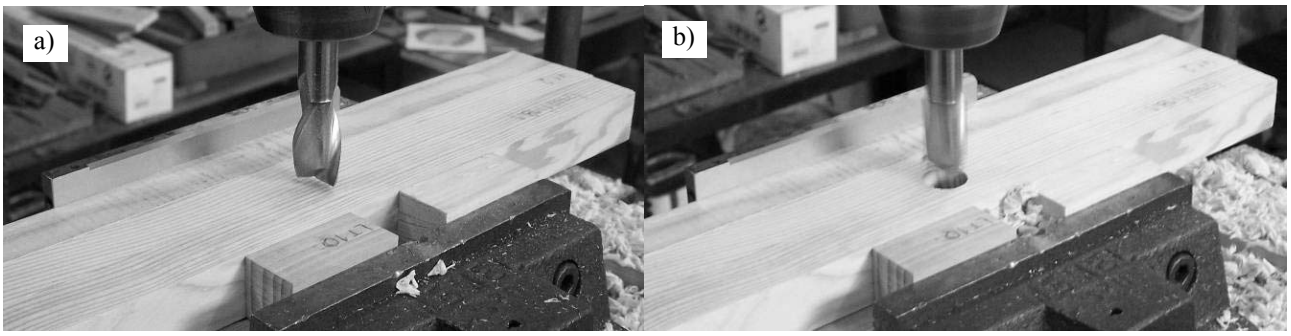

Fig. 403 – Setup in the drilling machine (a) and set of two beams after the drilling operation (b).

Adhesive bonding of the patches

It is known that the bond strength and durability between adhesives and wood members depends on many factors, such as the type and quality of wood, moisture content, use of primer, applied pressure during the adhesive curing, environmental exposures, operating environment, design life and type of adhesive, amongst others (Lyons and Ahmed 2005). Epoxy adhesives are regarded as one of the best choices to bond wood, provided that a set of premises are satisfied, being particularly suitable for wood bonds, due to their improved capability to fill gaps (Davis 1997, Wheeler and Hutchinson 1998, Lyons and Ahmed 2005) and polar surfaces of wood (Custódio et al. 2009). Additionally, they do not require high pressure during the curing process, are reasonably tolerant to small thickness variations and can be developed to cure under a wide variety of temperatures, which makes them particularly attractive for in-situ repairs (Custódio et al. 2009). Due to their ability to adhere strongly to materials other than wood, such as steel of CFRP, epoxy adhesives are also recommended for wood repairs (Plecnik et al. 1980, Aicher et al. 1998). However, epoxy adhesives

have already showed bonding difficulties to some wood species presenting particularly high moisture contents and acids concentrations, suck as oak (Wheeler and Hutchinson 1998). In fact, the study of Broughton and Hutchinson (2001) showed that the bond strength between two typical epoxy adhesives and wood was not affected up to 20% moisture content in the wood beams, but progressively diminished for higher moisture contents. Apart from the adhesive choice, the wood surface condition also has a major influence on the bond strength. It is known that a rough surface typically improves the bond strength (Lyons and Ahmed 2005). This is an extremely important issue to guarantee a strong wood/adhesive interface, affecting the initial strength and long-term durability of the bond (Marra 1992, Pocius 2002, Pizzi and Mittal 2003). In fact, abrasion raises the critical surface tension of wood, improving its wettability (Custódio et al. 2009). It also produces a freshly cut surface, free of machining marks and other surface irregularities, and eliminates contaminants, thus avoiding crushing or burnishing it, which would inhibit adhesive wetting and penetration (Adams and Wake 1984, Minford 1991, Mays and Hutchinson 1992, Richter and Steiger 2005). In this work, the wood bonding surfaces were abraded manually with 220 grit sandpaper and cleaned with compressed air, avoiding cleaning agents which would probably be absorbed by the wood beams and, consequently, affect the bonding. The wood surfaces were abraded with a fine mesh sandpaper, since it is known that heavy sanding leads to a poor bond performance, causing severe surface and subsurface damage to the wood cells (Murmanis and River 1983). The CFRP patches were also abraded with an equal mesh sandpaper and cleaned with acetone prior to bonding. For all repairs in this Section, the patches were always bonded less than one hour after sanding the wood surfaces, since these are particularly prone to loose their wettability and become chemically inactivated due to the exposal to atmospheric gases and pollutants (Mays and Hutchinson 1992, Nussbaum 1993, Davis 1997). Under these conditions, although the adhesive would still penetrate in the superficial wood gaps, it would not become molecularly bonded to the wood, resulting on a weak bond (Adams and Wake 1984, Marra 1992). The bonding procedure presented in Sub-Section 4.3.2.1 for the CFRP strap repairs was applied throughout this Section to bond the patches to the damaged wood beams.

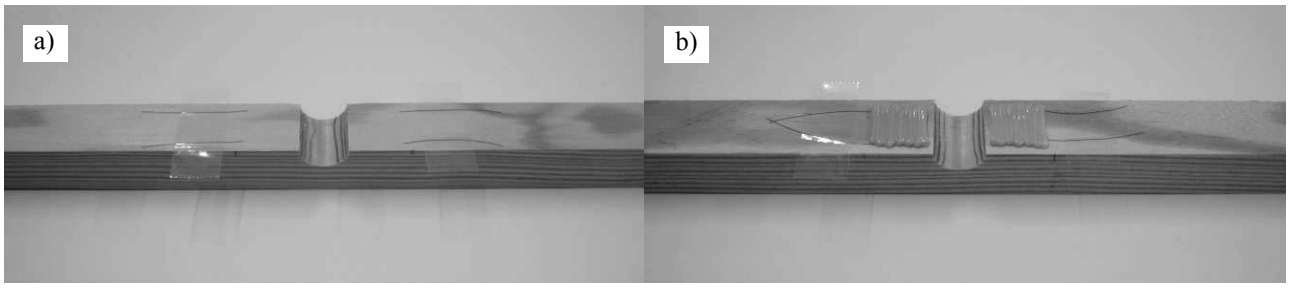

Fig. 404 – Application of the fishing lines with adhesive tape (a) and adhesive poured in the wood beam (b).

Fig. 404 (a) shows the application of the 0.2 mm diameter fishing lines at the patch edges (approximately 1-2 mm below the patch) for the L_O=20 mm repair, to provide a t_A=0.2 mm adhesive layer. In Fig. 404 (b) the adhesive was already poured in the wood beam. The patch application is shown in Fig. 405 (a). At this stage, the patch was adjusted to its final position, although without much care. Following, the patch was covered by a Teflon® film and pressed to the wood beam with grips (Fig. 405 b). Owing to the geometry of the repairs and value of t_H, an additional rigid element was not required to guarantee the uniformity of t_A. After approximately one hour of the grips application, with the adhesive still not completely cured, the fishing lines were removed and the adhesive excess at the patch edges was cleaned with a sharp blade, preventing t_A variations. The final position of the patch was then precisely adjusted in the length and width directions with a digital calliper (precision of 10 μm). The adhesive was left to cure for at least one week before testing. Fig. 406 shows a L_O=20 mm (a) and a L_O=10 mm (b) repair.

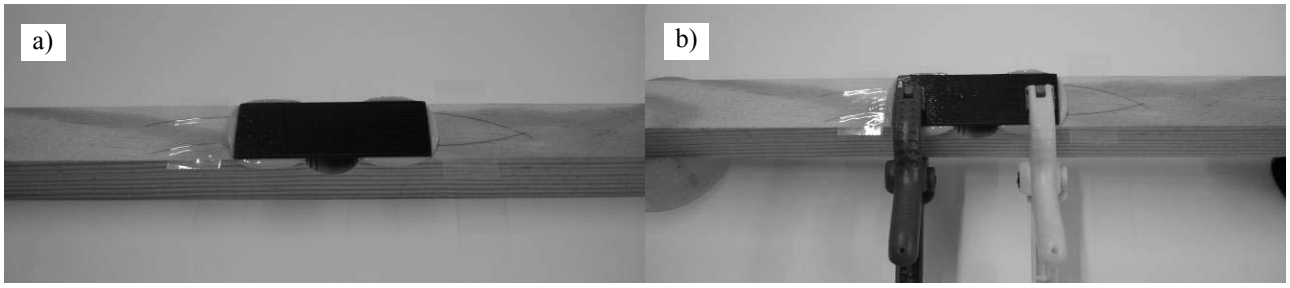

Fig. 405 – Repair after placing the patch (a) and application of pressure using grips (b).

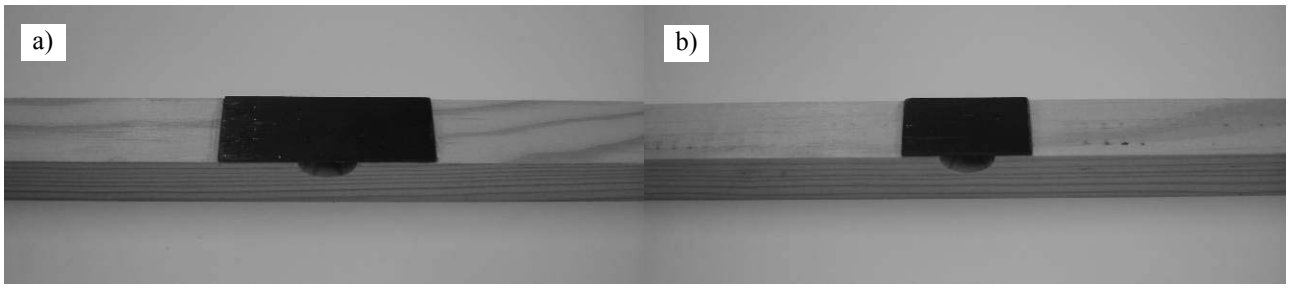

Fig. 406 – Final look of a L_O=20 mm (a) and a L_O=10 mm (b) repair.

6.3.2.1.2. Cross-grain tension specimens

To fabricate the cross-grain tension repairs, a crack was initially induced at the middle of the beams at a 15º angle to its longitudinal direction, to simulate a cross-grain fracture at the tensile region of an intermediate beam section. A CFRP patch was then adhesively-bonded at the cracked region in an attempt to restore the beam undamaged properties.

Cutting of the cross-grain tension crack

The cross-grain tension crack was induced at a 15º angle to the beams *RL* plane (Fig. 392 b), at an intermediate section of the tension region of the beam, to simulate cross-grain damage in a wood beam whose fibres are deviated of 15º to the *L* direction. The crack was cut at UTAD with a MICROCUT KV-50 vertical saw (Fig. 407) equipped with a 1 mm thickness HSS saw. The resulting approximate 1 mm gap between the crack faces, which does not exist in real damaged structures, will be also considered in the FEM simulations for an accurate reproduction of the experimental geometry.

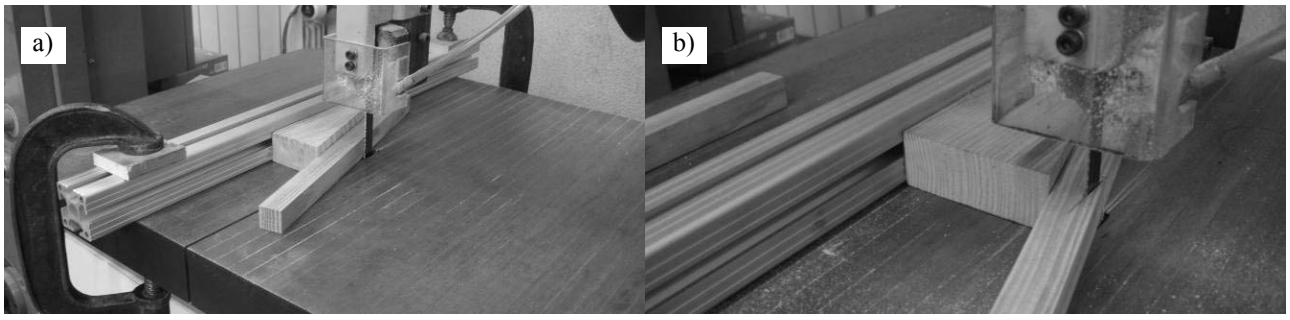

Fig. 407 – Cutting setup and specimen before (a) and after cutting the crack (b).

This approximation was imposed by limitations of the available equipments to perform this operation. The guiding system used to cut the crack is shown in Fig. 407, consisting on a 15º wood wedge supported on a guiding system

parallel to the saw, allowing cutting the crack at a 15º angle to the beams L direction. The specimens were adjusted in the wedge using a stopping system that allowed their rigid body movement, hindering sliding effects during the cutting operation. A crack was opened with this procedure up to L_C minus approximately 1 mm, to produce afterwards a sharp crack tip with a 0.1 mm thickness razor blade. This blade, which was initially centred in the 1 mm crack gap using calibrated steel bars, was used to extend the crack up to the value of L_C, measured with the digital calliper.

Adhesive bonding of the patches

The patch bonding method agrees with the technique described in Sub-Section 6.3.2.1.1 for the compression failure repairs. Initially, the wood bonding surfaces were abraded manually with 220 grit sandpaper and cleaned with compressed air. This also applied to the CFRP patches, despite being cleaned with acetone. To attain a t_A=0.2 mm adhesive layer, 0.2 mm diameter fishing lines were used. After pouring of the adhesive, the patch was aligned manually with the digital calliper. The methodology followed is detailed in the subsequent figures.

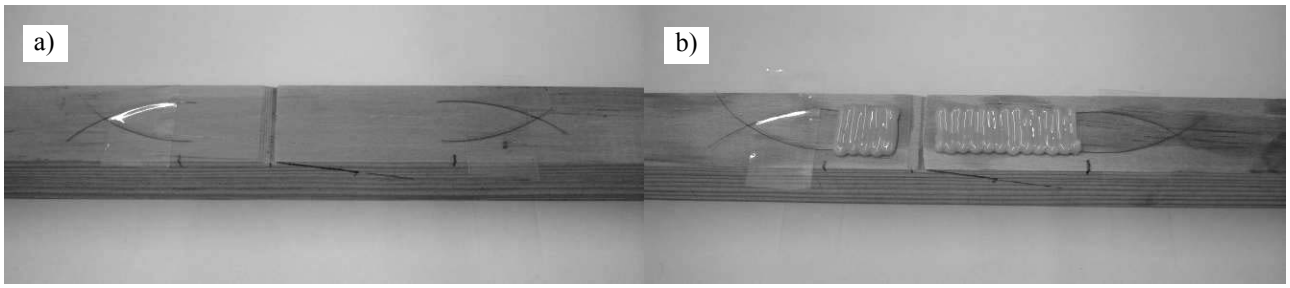

Fig. 408 – Application of the fishing lines with adhesive tape (a) and adhesive poured in the wood beam (b).

Fig. 408 illustrates a specimen after cutting of the crack and the positioning of the fishing lines (a), and the same specimen after pouring the adhesive (b). Identically to the compression failure repairs, a length of approximately 1-2 mm of fishing lines was left under the patch.

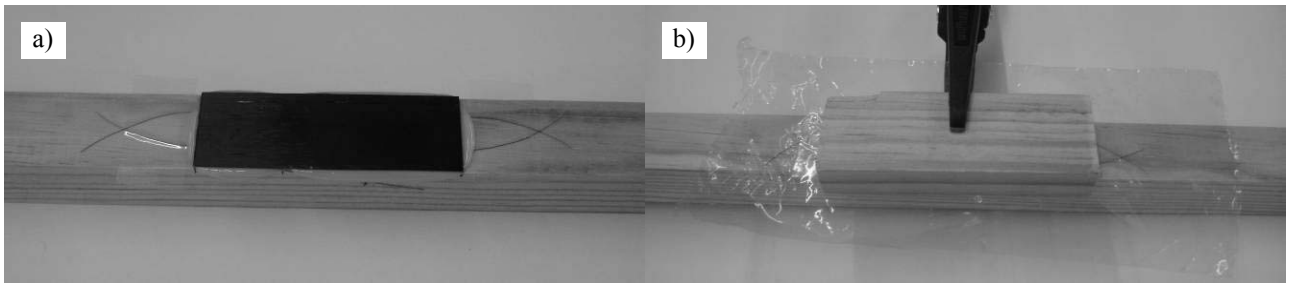

Fig. 409 – Repair after placing the patch (a) and application of pressure using a grip and a thick wood bar (b).

The patch was then applied and roughly adjusted to its final position (Fig. 409 a). After this, the patch was covered with a Teflon® film and a thick wood bar was used to assure the flatness of the patch after the application of pressure (Fig. 409 b). After approximately one hour after bonding, the fishing lines were removed and the adhesive excess at the patch edges was cleaned with a sharp blade. The patch was adjusted to its final position with the digital calliper. The final look of a L_P=60 mm and a L_P=40 mm repair is shown in Fig. 410 (a) and (b), respectively.

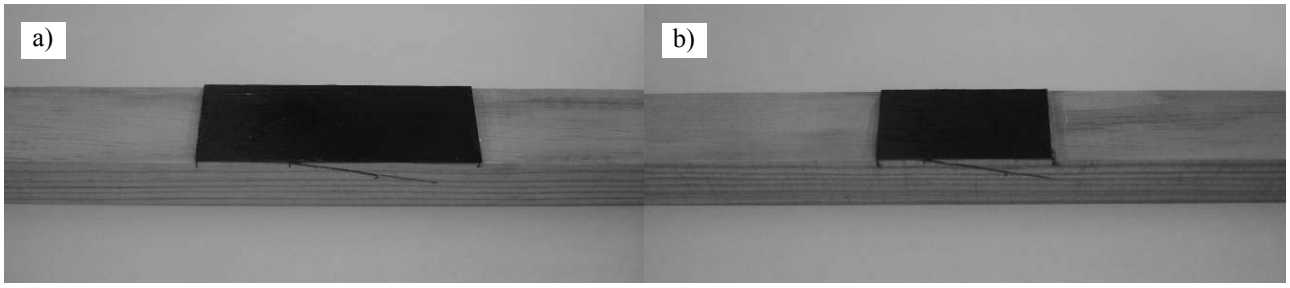

Fig. 410 – Final look of a L_P=60 mm (a) and a L_P=40 mm (b) repair.

6.3.2.1.3. Horizontal shear specimens

The repairs fabrication initiated with the cutting of the horizontal-shear crack, initiating at one of the beam edges, and respective finishing with a sharp blade. The repair procedure, which consisted on adhesive-bonding patches at the vertical faces of the wood beam at the cracked region, is also described.

Cutting of the horizontal shear crack

The fabrication of the horizontal shear crack in the wood beams was based on the guidelines of Sub-Section 6.3.2.1.2, regarding the cross-grain tension repair. A horizontal *RL* crack is initially introduced (Fig. 393), extending from one of the beam edges up to a pre-determined length (L_C in Fig. 393). This operation was performed in a MICROCUT KV-50 vertical saw available at UTAD (Fig. 411), using a 1 mm thickness HSS saw to produce a crack with a gap of approximately 1 mm between its faces. The FEM models for this repair were built to reproduce faithfully this geometry, for an accurate modelling of the repairs. Cutting of the horizontal shear crack was carried out with a guiding system parallel to the saw (Fig. 392), up to the value of L_C minus approximately 1 mm. In fact, this procedure would yield a blunt crack tip, which is not representative of the damage mechanism studied. Therefore, a sharp crack tip was induced up to the desired value of L_C, measured with the digital calliper, using a 0.1 mm thickness razor blade centred between the crack faces using calibrated steel bars.

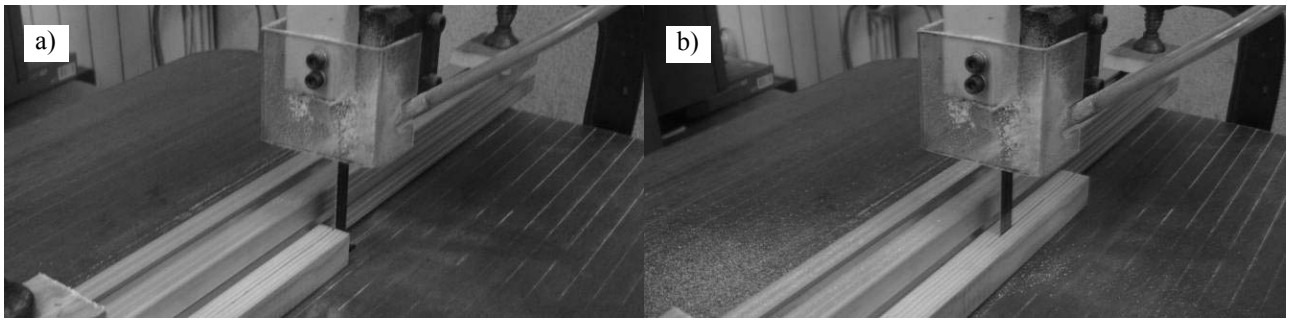

Fig. 411 – Cutting setup and specimen before (a) and after cutting the crack (b).

Adhesive bonding of the patches

The beams surface preparation involved manual abrasion with 220 grit sandpaper and cleaning with compressed air, while the patches were abraded with the same mesh sandpaper and cleaned with acetone. Bonding was performed using the 0.2 mm diameter fishing lines to assure the desired value of t_A and a manual patch positioning method using the digital calliper. The following figures detail the patch bonding procedure, in which the two patches of each repair were bonded separately. Fig. 412 (a) shows a wood beam after cutting the horizontal shear crack and placing the 0.2 mm

thickness fishing lines equally spaced at both the crack sides. The fishing lines were placed such that, after the patch application, 1-2 mm of fishing line lied under the patch. A 25 μm Teflon® film was inserted at the crack, along its full length and width, to avoid bonding of the crack faces near the repaired surfaces, due to the prospect of adhesive excess filling the crack gap, at the time of the patch application. In Fig. 412 (b), pouring of the adhesive was accomplished.

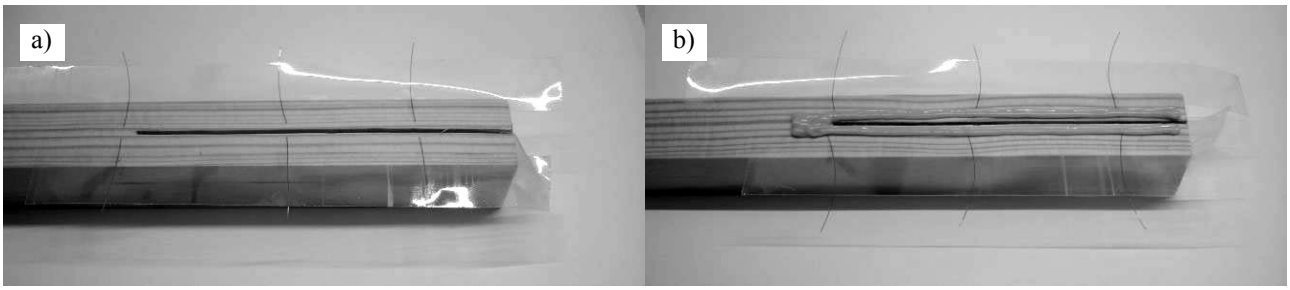

Fig. 412 – Application of the fishing lines with adhesive tape (a) and adhesive poured in the wood beam (b).

Following, the patch was applied and pressed to the wood beam until contacting with the fishing lines (Fig. 413 a). At this point, the patch was merely roughly adjusted to its final position. The patch was covered with a Teflon® film and a grip was employed to apply pressure uniformly to the patch, using a thick wood bar (Fig. 413 b). The adhesive was left to cure during approximately one hour. This is not sufficient for the adhesive to cure completely, but allows the removal of the fishing lines and cleaning of the adhesive excess at the patch edges with a sharp blade, without t_A variations. Fig. 414 shows the final look of a L_P=105 mm (a) and a L_P=75 mm (b) repair.

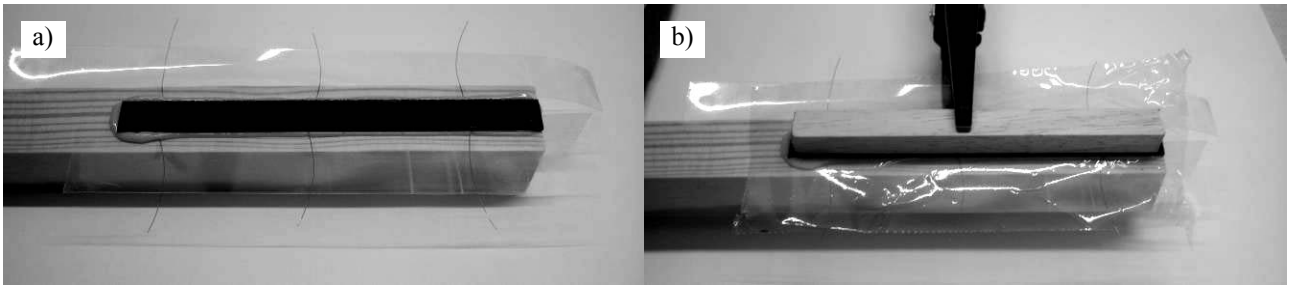

Fig. 413 – Repair after placing the patch (a) and application of pressure using grips and a thick wood bar (b).

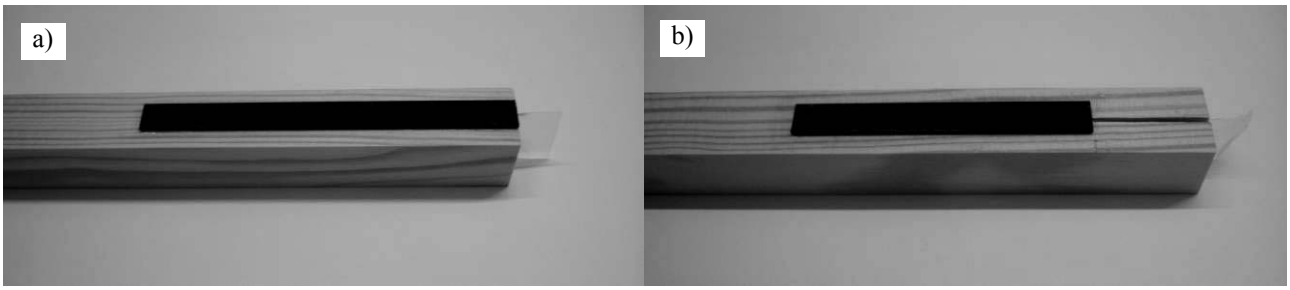

Fig. 414 – Final look of a L_P=105 mm (a) and a L_P=75 mm (b) repair.

6.3.2.2. Specimens testing

The testing equipment and conditions were identical for the three repair strategies evaluated in Section 6. The experimental tests under 4PB were carried out at UTAD in an Instron® 1125 electro-mechanical testing machine,

equipped with a 100kN load cell. The experiments were accomplished at room temperature and under displacement control (2 mm/min). The loading cylinders displacement was assumed equal to the testing machine cross-head displacement (neglecting the bending apparatus deformation). A sample rate of 5 points per second was used to extract the P-δ data. **Equally to the study of Section 4, all the tests in this Section were recorded with a 10 MPixel digital camera (one picture each 5 s) to allow an accurate characterization of the repairs fracture sequence up to failure. Ten specimens were tested for each condition, due to the known variability in wood elastic and strength properties (Malan et al. 1988a, Malan et al. 1988b, Downes et al. 1997, Bao et al. 2001, Baillères et al. 2005). At least seven valid results were always obtained**. Fig. 415 (a) illustrates the testing device and setup under 4PB for an unrepaired compression failure beam, after removal of the damaged wood portion. Fig. 415 (b) and (c) show a detail near the loading and supporting cylinders in the beginning and during the test, respectively.

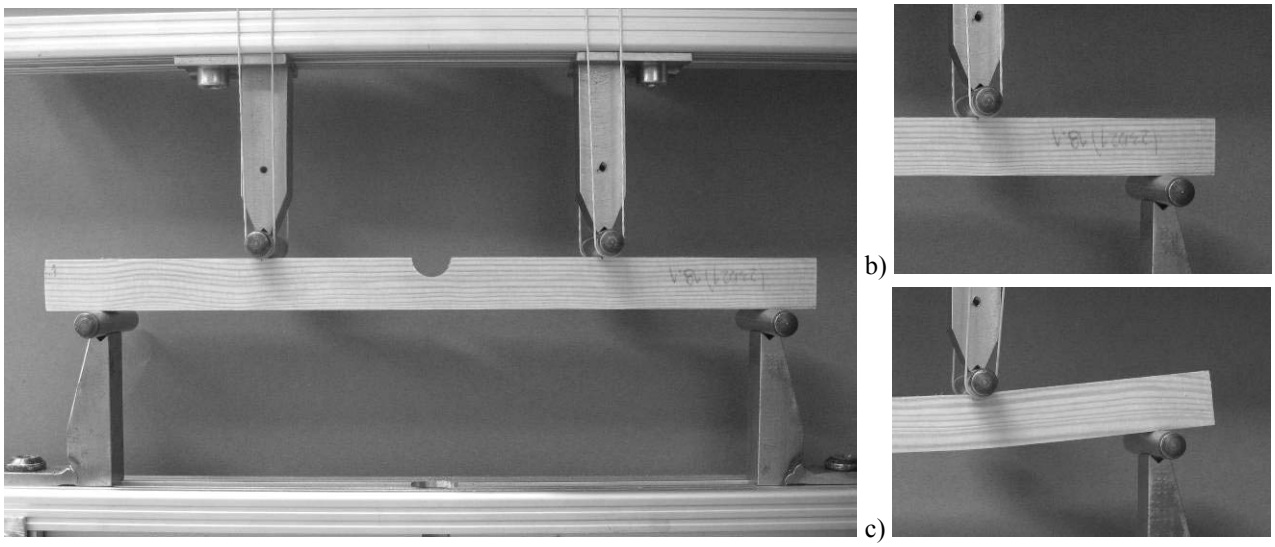

Fig. 415 – Experimental setup in the testing machine (bending load, unrepaired compression failure beam).

6.3.3. Compression failure repairs

6.3.3.1. Stress analysis

Fig. 416 shows the deformed shape of the repair, for δ=0.3 mm (applying a 50x enhancement to the displacements). **This value of δ and magnification, which are equal to the ones used in Section 4 for the composite repairs under a bending load, will be used in this Section for the stress analyses of all the repair techniques studied, except if mentioned otherwise.** Fig. 417 pictures σ_x stresses at the repair region.

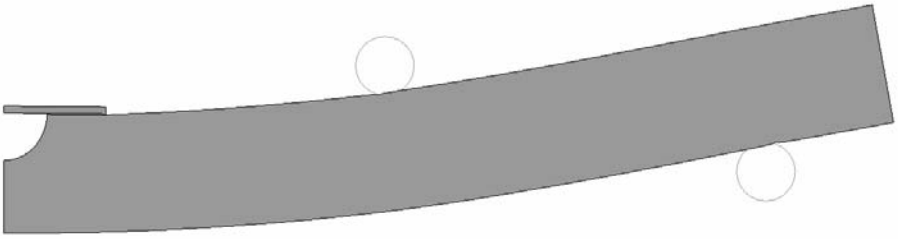

Fig. 416 – Deformed configuration of the compression failure repair under a bending load.

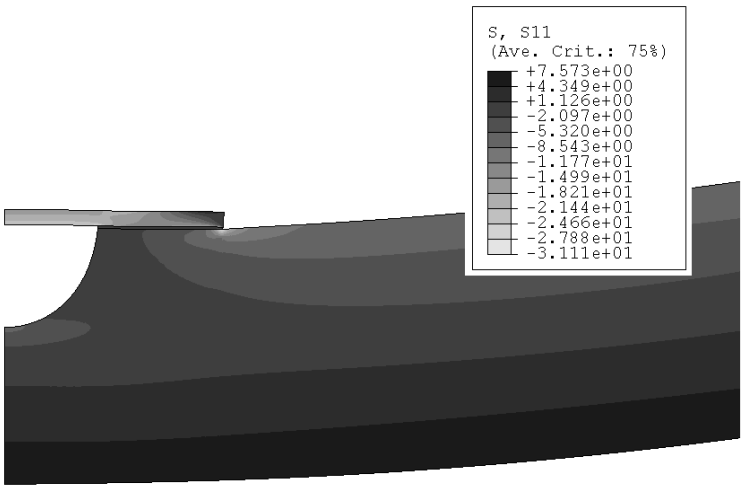

Fig. 417 – σ_x stresses at the repair region.

Between the loading cylinders, σ_x stresses along the beam height are proportional to the distance to the beam neutral axis, excepting near the hole. Thus, σ_x tensile stresses develop at the undamaged lower half of the beam, while at the repaired upper half, σ_x stresses are compressive. The damaged material removal and application of the patch revealed a small disturbance on the contour of σ_x stresses. In fact, the σ_x compressive peak stresses at a localized region near the OEO (Fig. 395 a) are the sole relevant difference. The patch is mainly under uniaxial compression, which could cause its buckling between bonds. As mentioned earlier, a preliminary FEM study was performed to avoid this occurrence, leading to the minimum value of t_H=1.2 mm.

Fig. 418 and Fig. 420 (a) detail σ_y stresses and σ_y stress distributions at planes P3, P4 and P5 (Fig. 395 a), respectively. Fig. 419 and Fig. 420 (b) correspond to τ_{xy} stresses and τ_{xy} stress distributions at the same planes (Fig. 395 a). x/L_O represents the overlap normalized distance from the IEO (Fig. 395 a). **The stress distributions presented are normalized by τ_{avg}, the average shear stress along L_O at plane P4, for the respective overlap length. This procedure is also applied to the cross-grain tension repair.**

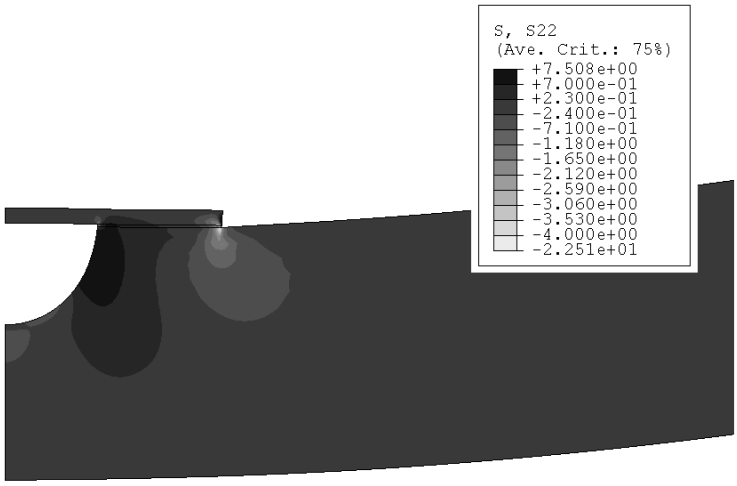

Fig. 418 – σ_y stresses at the repair region.

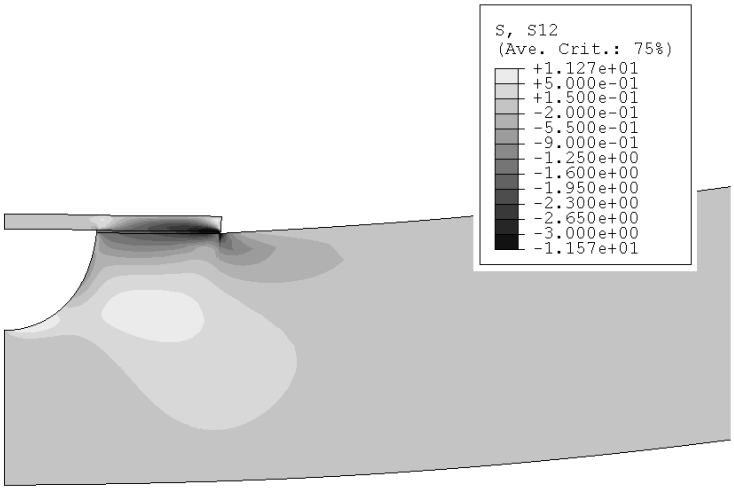

Fig. 419 – τ_{xy} stresses at the repair region.

σ_y peel stresses peak near the repair region, increasing in magnitude from the middle of the overlap in the direction of the IEO (Fig. 418 and Fig. 420 a). At the OEO, a σ_y compressive peak of significant magnitude grows towards x/L_O=1, emerging from the higher patch stiffness, compared to the wood beam (Fig. 418), and reducing the prospect of premature peel failures at this region, likely to occur in bonded assemblies under tension (Li et al. 1999, Mortensen and Thomsen 2002, Campilho et al. 2008b, Campilho et al. 2009b). At the IEO, localized σ_y compressive peak stresses develop. σ_y stress profiles are similar along L_O between the three planes. However, singular regions were found at the square-edges of the repair, i.e., at the OEO (plane P3, wood beam/adhesive interface) and IEO (plane P5, adhesive/patch interface). These results are consistent with the stress analyses of Section 4 (e.g. SS repair under a tensile load, Fig. 141 a). Fig. 419 and Fig. 420 (b) represent τ_{xy} stresses at the repair region and at three planes along the overlap, respectively. τ_{xy} stresses are smaller at the IEO, increasing gradually towards the OEO. The beam flexure leads to a predominant shear loading at the repair region. The gradual increase in magnitude of τ_{xy} stresses from the IEO to the OEO is caused by the differential straining between the patch and the wood beam in the length direction (Volkersen 1938, Adams et al. 1997, Zou et al. 2004, Campilho et al. 2005). τ_{xy} stresses are identical between planes P3, P4 and P5, with a stress singularity emerging at plane P3 (OEO). An analogy to the results of Section 4 can also be performed on τ_{xy} stresses (e.g. SS repair under a tensile load, Fig. 141 b).

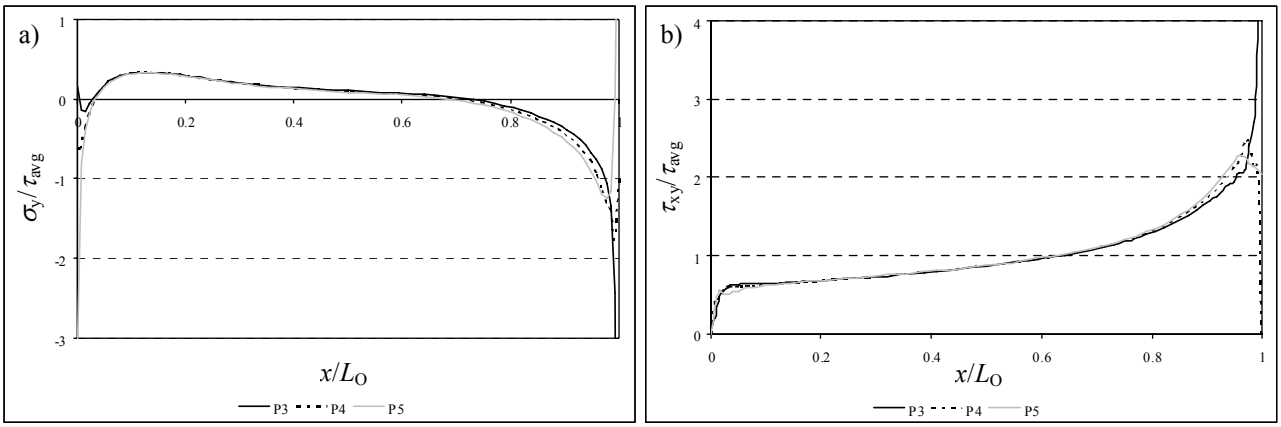

Fig. 420 – Normalized σ_y (a) and τ_{xy} (b) stress distributions at the repair region.

Fig. 421 and Fig. 422 present σ_y and τ_{xy} stress distributions, respectively, at the seven planes of Fig. 395 (a). Overall, σ_y stress profiles are identical between these planes, only showing slight variations at the overlap edges. Near the IEO (x/L_O=0), σ_y stresses are mostly compressive. Planes P1 and P2 are the sole exception to this tendency. At the inner region of the overlap, minor σ_y peel stresses are observed, while from approximately x/L_O=0.7 a compressive peak of significant magnitude develops near the OEO. A stress singularity emerges at the OEO at planes P5, P6 and P7.

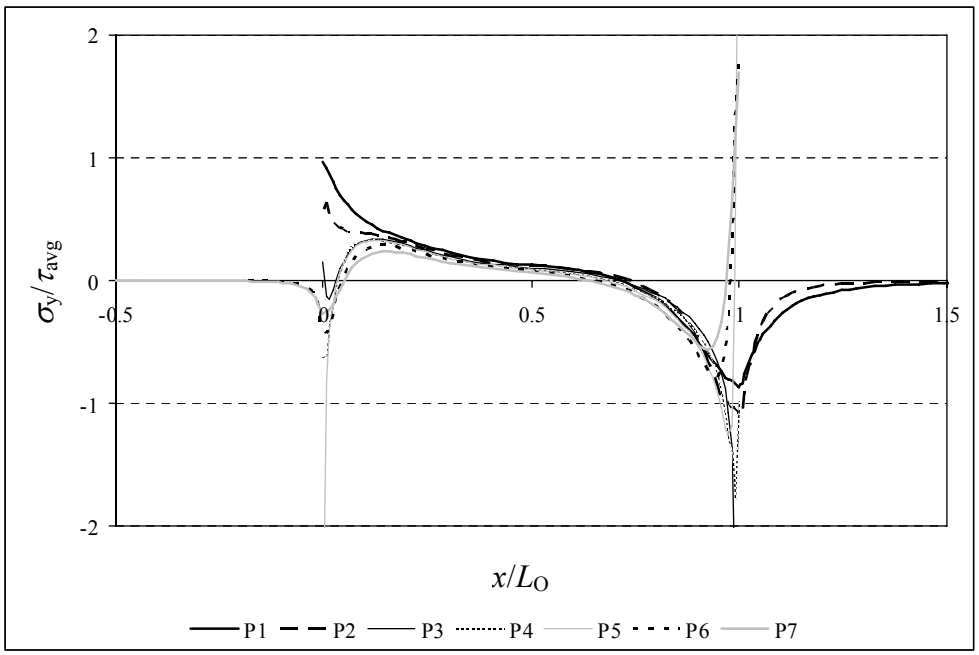

Fig. 421 – Normalized σ_y stress distributions at seven planes in the repair.

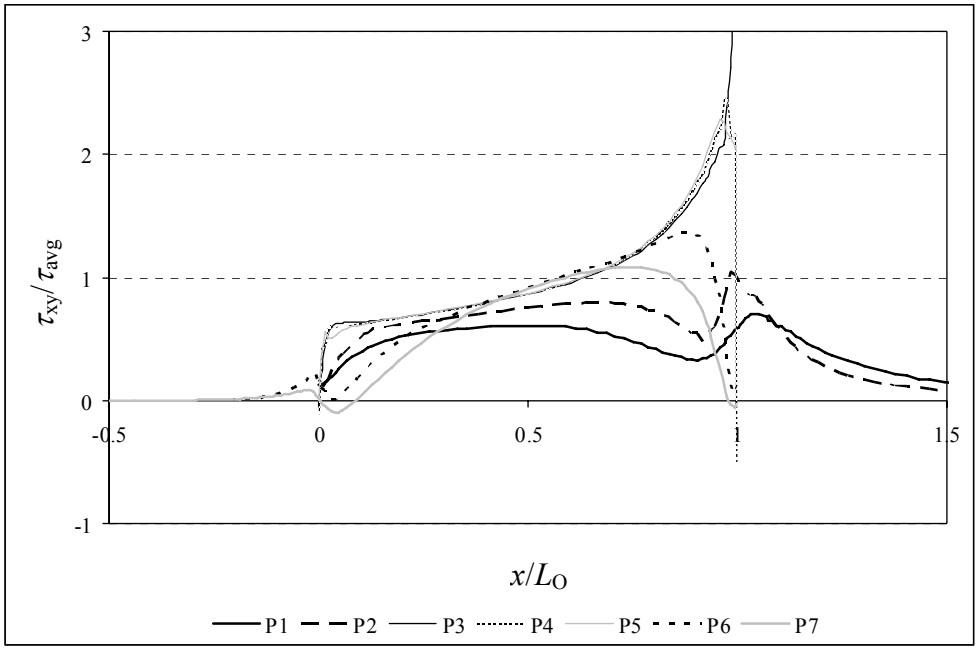

Fig. 422 – Normalized τ_{xy} stress distributions at seven planes in the repair.

Oppositely to σ_y stresses, τ_{xy} ones significantly vary between planes. Planes P3, P4 and P5 correspond to the loci of higher magnitude, especially at the OEO. Additionally, τ_{xy} stresses are higher in magnitude within the patch than in the

wood beam, owing to the bigger distance to the beam neutral axis. Both σ_y and τ_{xy} stresses tend to become nil within the wood beam and in the patch outside the overlap region ($x/L_O<0$ and $x/L_O>1$). This analysis points towards damage initiation close to or in the adhesive layer, at one of the overlap edges or simultaneously along the overlap. In fact, τ_{xy} stresses are highest at the OEO, while significant peel stresses at the IEO may also lead to damage initiation at this region. The exact loci of damage initiation will also depend on the properties of the different materials involved.

6.3.3.1.1. Overlap length

L_O is the parameter evaluated for the compression failure repair (Fig. 392 a), consisting on the bonded length between the wood beam and the patch, initiating at the hole edge (IEO) up to the patch edge (OEO). Fig. 423, Fig. 424 and Fig. 425 show σ_y and τ_{xy} stress distributions in the overlap at planes P3, P4 and P5, respectively. These relate, by the same order, to the wood beam/adhesive interface, the middle of the adhesive and the adhesive/patch interface (Fig. 395 a).

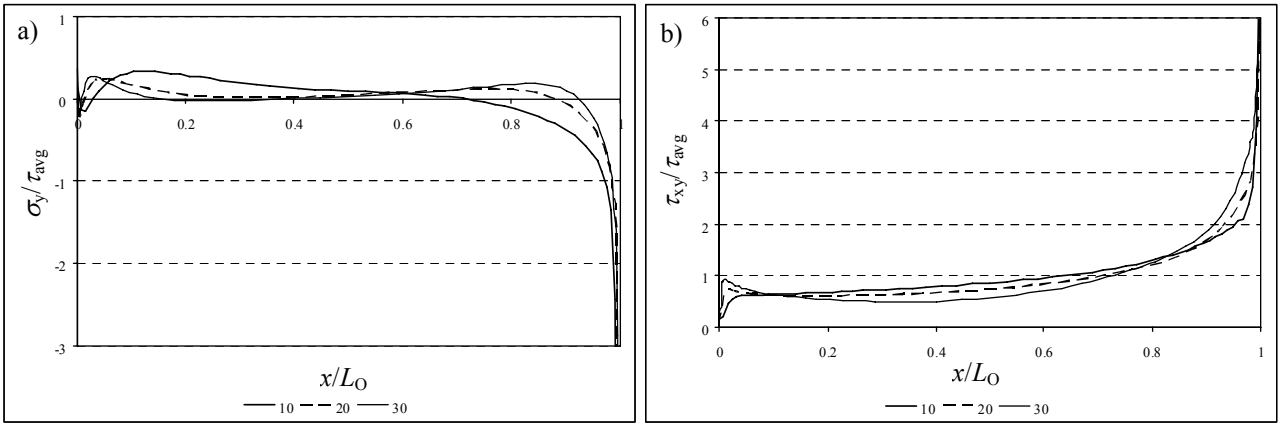

Fig. 423 – Normalized σ_y (a) and τ_{xy} (b) stress distributions at the laminate/adhesive interface (P3) as a function of L_O.

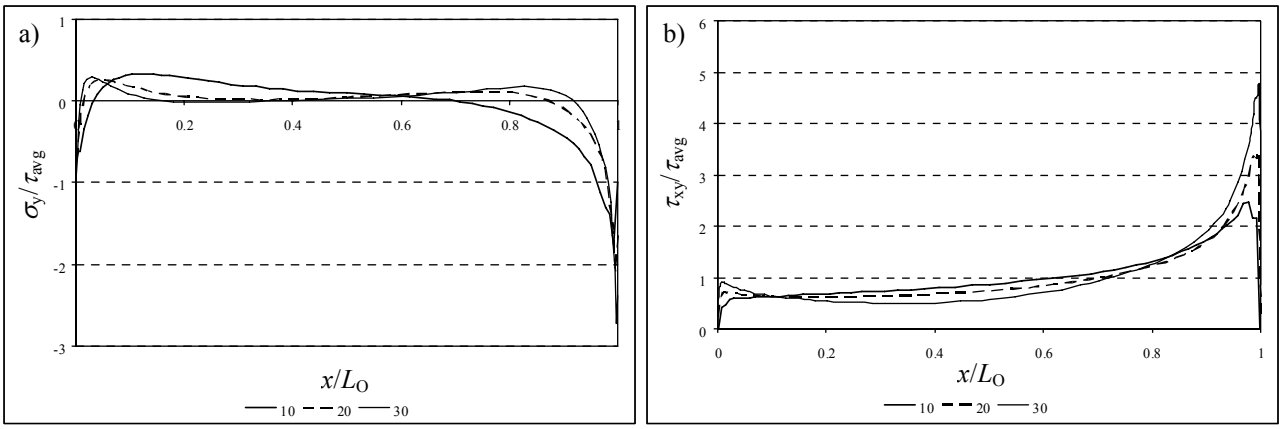

Fig. 424 – Normalized σ_y (a) and τ_{xy} (b) stress distributions at the middle of the adhesive (P4) as a function of L_O.

As a rule, σ_y stresses are identical along the overlap between the three planes, except at the overlap edges, where singular regions are noted. σ_y stresses are much smaller than τ_{xy} stresses at the inner region of the overlap, showing a compressive peak of moderate magnitude near the OEO. Despite no significant difference was found on σ_y stresses at the IEO for the values of L_O under analysis, at the OEO σ_y compressive peak stresses gradually increase in magnitude

with L_O. Moreover, increasing L_O diminishes σ_y stresses at the inner half of the overlap ($0 \leq x/L_O \leq 0.5$), giving rise to a minor peel region at the opposite half. At planes P3 and P5, stress singularities are present regardless the value of L_O, located at the OEO (plane P3) and at the IEO (plane P5).

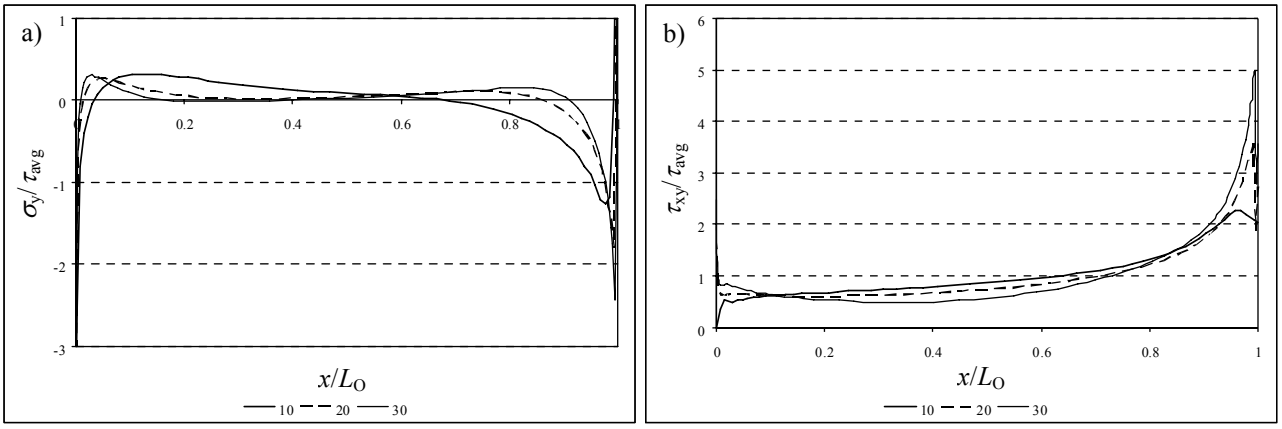

Fig. 425 – Normalized σ_y (a) and τ_{xy} (b) stress distributions at the adhesive/patch interface (P5) as a function of L_O.

τ_{xy} stresses are also practically impossible to differentiate between the three planes, except at the overlap edges. In all cases, τ_{xy} stresses show a gradual increase in magnitude from the IEO towards the OEO. Increasing L_O causes overall a slight reduction of these stresses at the inner region of the overlap, which increase at both overlap edges. For all the values of L_O, the stress singularities are located at plane P3 (OEO) and at plane P5 (IEO). The results presented in this Sub-Section suggest an increase of P_m at a decreasing rate with L_O, since τ_{xy} peak stress gradients at the bond edges increase with this quantity, which may lead to premature failures at these regions for the bigger values of L_O (Hu and Soutis 2000, Reis et al. 2005, Campilho et al. 2008a).

6.3.3.2. Failure analysis

6.3.3.2.1. Mechanical behaviour

In this Section, the undamaged wood beam behaviour was also characterized experimentally and numerically to evaluate the repairs capability to re-establish the beams strength. These results will thus be used for the three repair techniques in Section 6. In the analyses of this Section, the unrepaired damaged beams were always studied as well.

- Two different fracture mechanisms were identified for the undamaged beam. Seven of the ten specimens tested showed damage initiation by pure tension below one of the loading cylinders (Fig. 426 a), which corresponded to P_m in these beams, due to the concentration of σ_x stresses at these regions. Shortly after, this damage propagated as a predominantly horizontal *RL* crack between the loading cylinders (Fig. 426 b). The other three specimens tested displayed a gross-grain tension failure, with crack propagation between the loading cylinders at a small angle to the beams *L* direction, due to a small cross-graining of the wood fibres. This abrupt failure corresponded to P_m. Fig. 427 shows two examples of cross-grain tension fractures.

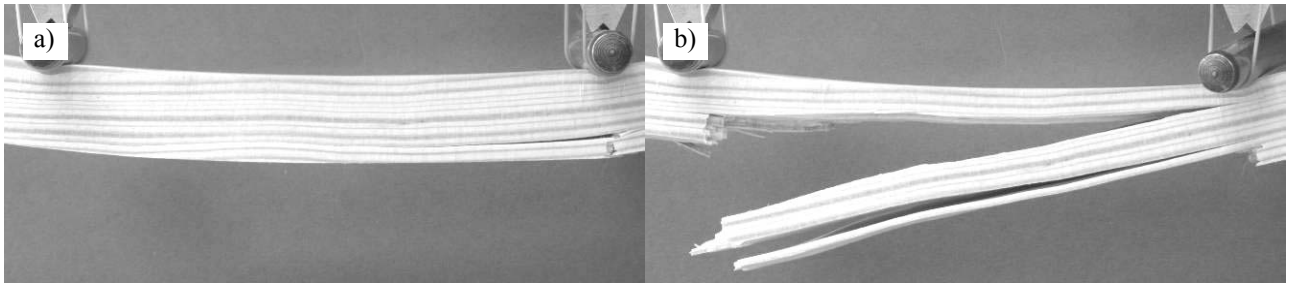

Fig. 426 – Pure tension failure onset below a loading cylinder (a) and longitudinal growth (b) for an undamaged beam.

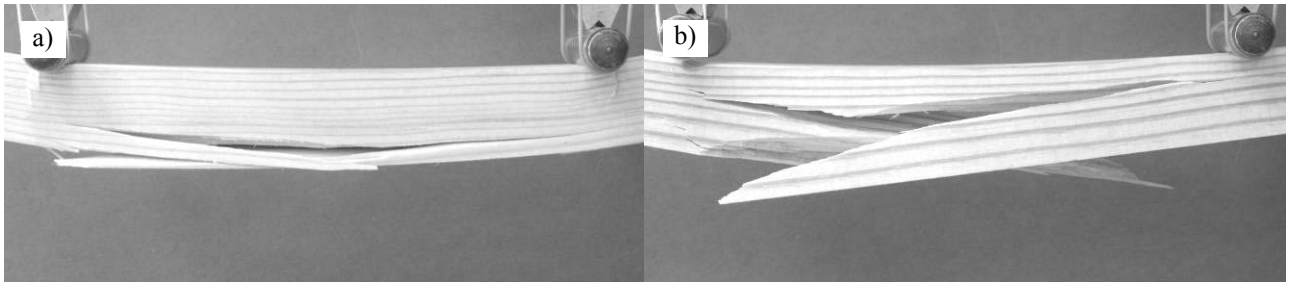

Fig. 427 – Two examples of cross-grain tension failures for an undamaged beam.

- For the compression failure repairs, the unrepaired beam includes the damaged material removal. Damage initiated by wood crushing near the symmetry plane *A-A* (Fig. 395 a) at the compression region of the beam cross-section (Fig. 428). This damage mechanism did not show a visible influence on the P-δ curves, causing only a small drop of P for some of the specimens. P_m occurred only after this event near the symmetry plane *A-A*, at the tension region of the beam. Two different scenarios emerged, depending on the alignment of the wood fibres. In fact, some of the beams failed by pure tension near the symmetry plane *A-A* (Fig. 429 a). However, for the specimens showing a non-negligible cross-graining, failure occurred by cross-grain tension (Fig. 429 b). In both situations, the fracture near line *A-A* is justified by the smaller cross-sectional area at this region.

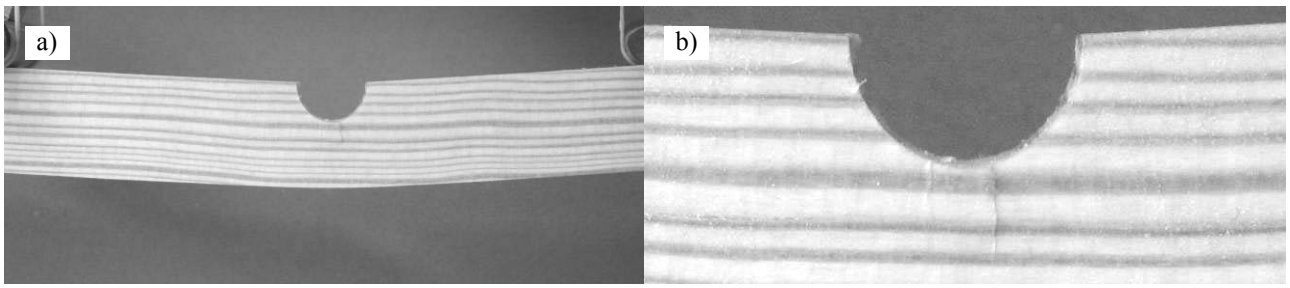

Fig. 428 – Compression failure (a) and corresponding detail (b) for an unrepaired beam.

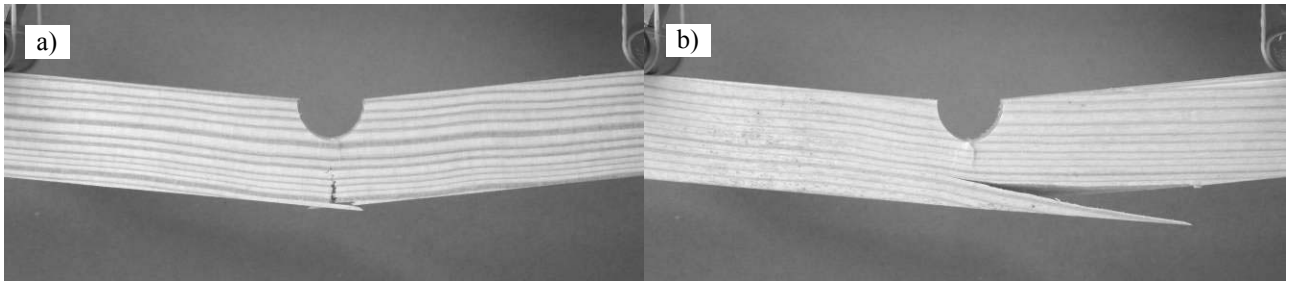

Fig. 429 – Pure tension failure (a) and cross-grain tension failure (b) for an unrepaired beam.

- The L_O=10 mm repairs showed two different failure mechanisms. Five specimens failed prematurely (before P_m) in the wood beam near the adhesive layer (Fig. 430 a), with crack onset near the two hole edges, followed by a fast *RL* propagation in the direction of the patch edges (Fig. 395 a). The measured distance between the wood fracture plane and the beam/adhesive interface varied from approximately 0.4 to 0.8 mm. After this event, which led to a corresponding abrupt drop on *P*, the specimens behaved similarly to an unrepaired beam, i.e., with P_m and final failure caused by pure tension (Fig. 430 b) or cross-graining. Failure within the wood beam near the adhesive layer was expected in these repairs, since stronger bonds than the wood properties are usual in these assemblies (Konnerth et al. 2006). The other specimens failed cohesively in the adhesive layer with initiation at the IEO (Fig. 431 a), which only led to an abrupt drop of *P*. An unrepaired beam behaviour followed up to P_m, by pure tension or cross-grain tension failure. These results show that σ_y peel peak stresses at the IEO, particularly at planes P1 and P2, overcome the differential shearing effects at the patch edges (Fig. 421 and Fig. 422), causing damage initiation at the IEO. The described fracture sequence point towards a negligible influence of the L_O=10 mm patch on the unrepaired beam value of P_m, due to the premature patch detachment. Fig. 431 (b) corresponds to the same specimen of Fig. 431 (a) after final failure by pure tension.

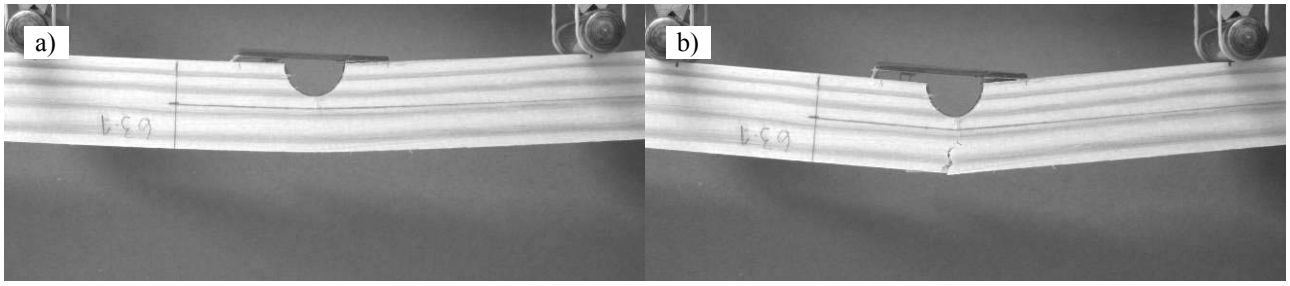

Fig. 430 – Damage onset in the wood beam (a) followed by pure tension failure (b) for a L_O=10 mm repair.

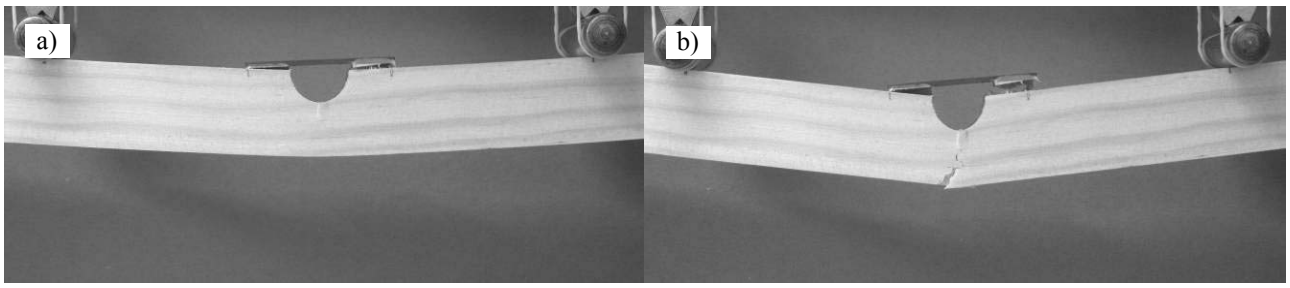

Fig. 431 – Cohesive failure of the adhesive (a) followed by pure tension failure (b) for a L_O=10 mm repair.

- The L_O=20 mm repairs also showed two different fracture mechanisms. For six specimens, P_m matched with damage in the wood beam at one of the overlaps, initiating at the hole region and growing rapidly to all the overlap. The measured distances to the beam/adhesive interface agrees with the results obtained for the L_O=10 mm repair. Thus, and given that this mode of failure did not occur for the L_O=30 mm repairs, these limit values were used to establish the fracture planes P1 and P2 in the FEM simulations. At the opposite side of the repair, a peel crack developed at a distance to the beam/adhesive interface between 2 and 4 mm (Fig. 432 a), due to the high stiffness of the CFRP patch. This event, which led to a sudden drop of P_m, occurred for a higher value of *P* than the unrepaired beam strength. After a typically reduced value of δ, the specimens fractured similarly to the unrepaired beam (Fig. 432 (b), failure by pure tension). For the other specimens, P_m coincided with a cohesive failure of the adhesive layer (Fig. 433 a). After a small value of δ, an unrepaired beam fracture

occurred (Fig. 433 (b), failure by cross-grain tension). For both fractures, damage initiated at the hole edges, despite the increase of τ_{xy} stresses at the OEO from the L_O=10 mm repair (Fig. 423, Fig. 424 and Fig. 425).

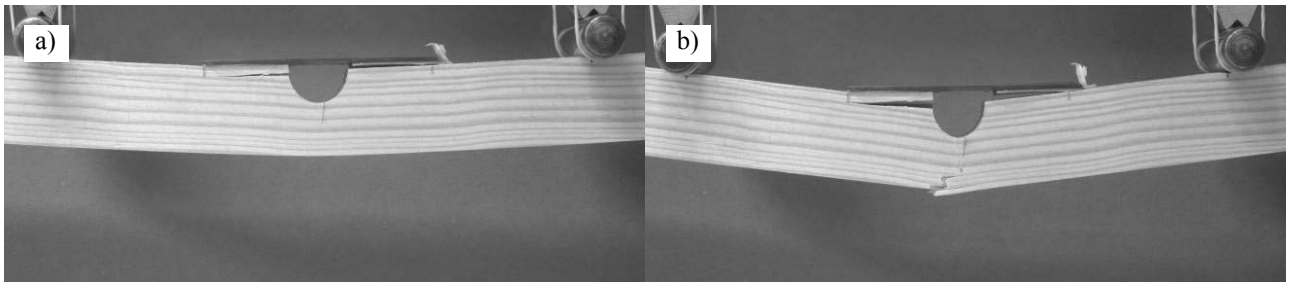

Fig. 432 – Damage onset in the wood beam (a) followed by pure tension failure (b) for a L_O=20 mm repair.

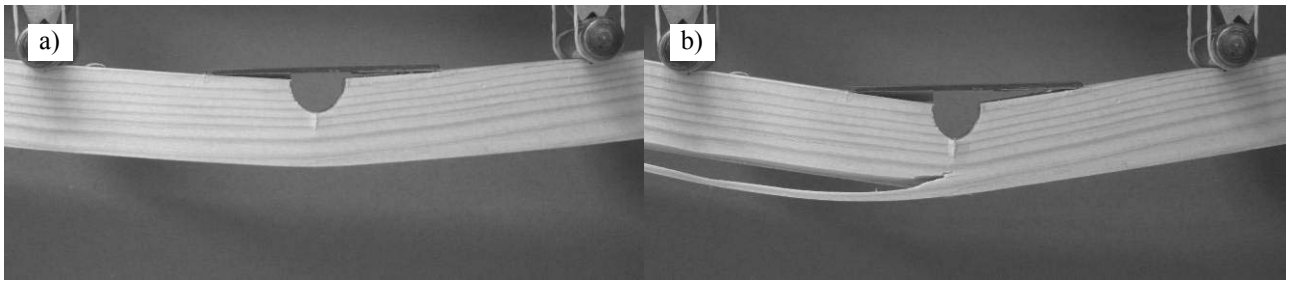

Fig. 433 – Cohesive failure of the adhesive (a) followed by cross-grain tension failure (b) for a L_O=20 mm repair.

- The L_O=30 mm repair did not reveal signs of damage at the repair region up to failure, for all specimens. In fact, fracture was always abrupt below the loading cylinders, either by pure tension (Fig. 434) or cross-graining (Fig. 435), suggesting that the undamaged beam strength is restored with this value of L_O, since the weakest region of the repair is no longer near the notch. On all the repairs where cohesive failures were reported, a thin layer of adhesive was clearly visible covering entirely both the wood beam and patch bonding surfaces.

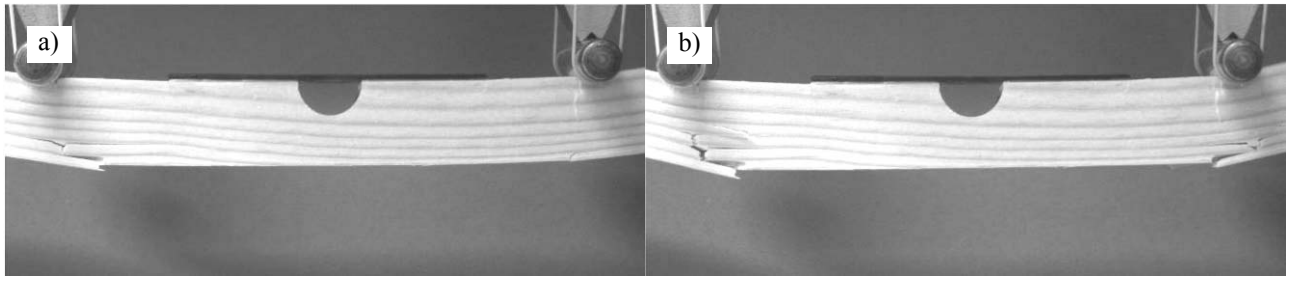

Fig. 434 – Damage onset by pure tension in the wood beam near the loading cylinders (a) and growth (b) for a L_O=30 mm repair.

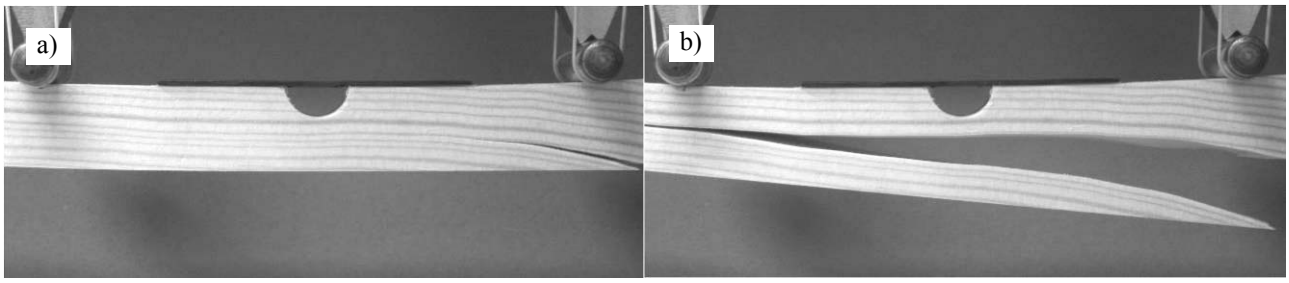

Fig. 435 – Damage onset by cross-graining in the wood beam near the loading cylinders (a) and growth (b) for a L_O=30 mm repair.

The FEM simulations were able to capture the experimental fractures with a reasonable accuracy.

- The undamaged beam fractured vertically (*LR* plane) below the loading cylinder (Fig. 436), which is consistent with the experimental failures (Fig. 426), neglecting the few specimens showing evidence of cross-graining.

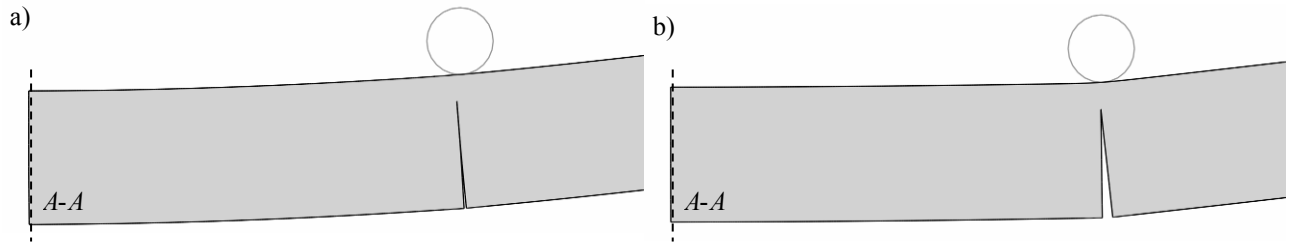

Fig. 436 – Numerical damage initiation (a) and growth (b) below the loading cylinder for the undamaged beam.

- Fig. 437 illustrates the numerical failure for the unrepaired beam, which consisted on a pure-tension failure at the symmetry line *A-A*, prior to an eventual tension failure below the loading cylinders, also considered in the simulations for the unrepaired beam (Fig. 402 a). This result also agrees with the experiments (Fig. 429), and is explained by the higher magnitude of σ_x stresses at this plane, due to the smaller cross-sectional area.

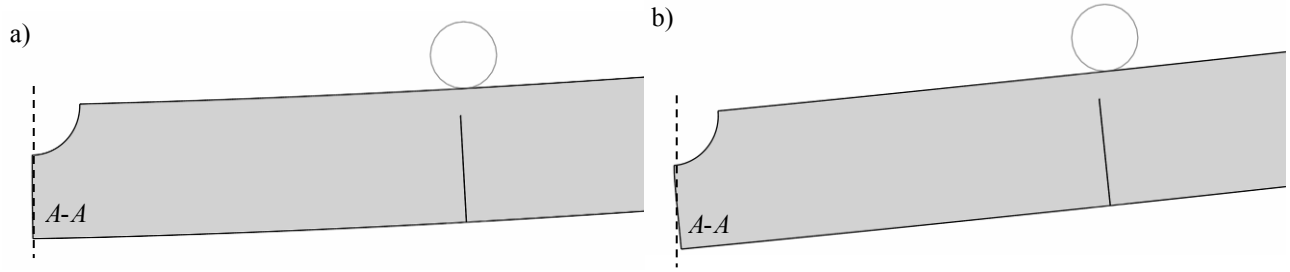

Fig. 437 – Numerical damage initiation (a) and growth (b) at the symmetry plane *A-A* for the unrepaired beam.

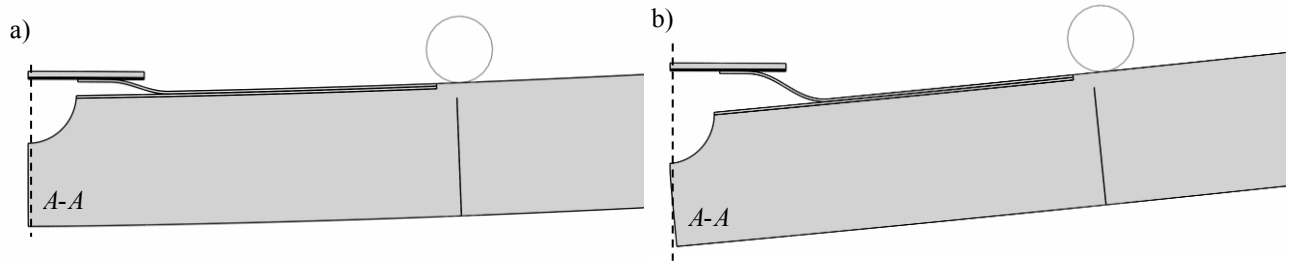

Fig. 438 – Numerical damage initiation at plane P2 (a) and failure at the symmetry plane *A-A* (b) for the L_O=10 mm repair.

- The numerical failure for the L_O=10 mm repair conformed to the firstly described of the two experimental fractures for these repairs (Fig. 430). In reality, damage initiated in the wood beam at plane P2 instantaneously in the entire overlap (Fig. 438 a), oppositely to the experiments, which showed damage initiation at the hole region, with fast growth to the patch edges. Since patch detachment was premature, leading only to a drop of P prior to P_m, no improvement on P_m is expected from the unrepaired beam. It should be mentioned that, at the time of failure, the adhesive layer cohesive elements that showed the highest τ_{xy} stresses (Fig. 422), were already under softening ($\delta_i > \delta_{1m,i}$ in Fig. 68). This indicates that both failures are likely to occur with this value

of L_O, due to small variations of the repair constituents properties. This applies particularly to the wood beams, which exhibit a significant variability of their elastic and strength properties between specimens of the same species (Malan et al. 1988a, Malan et al. 1988b, Downes et al. 1997, Bao et al. 2001, Baillères et al. 2005). P_m and final failure of the repair corresponded to a pure tension failure at the symmetry line *A-A* (Fig. 438 b).

- A similar FEM behaviour was identified for the L_O=20 mm repair, which partially agreed with one of the experimental fractures (Fig. 432). In fact, P_m was related to damage initiation in the wood beam at the IEO (plane P2), propagating rapidly towards the patch edge along the same plane (Fig. 439 a). After this, the repaired beam behaved similarly to an unrepaired beam, sustaining loads for a small value of δ, before final fracture in the wood beam at the symmetry line *A-A* by pure tension (Fig. 439 b). On the experiments, as mentioned previously, failure near the wood beam/adhesive interface (plane P2) occurred only at one of the overlaps. At the opposite side of the repair, a peel failure of the wood beam took place at a significantly bigger distance to the wood beam/adhesive interface (between 2 and 4 mm).

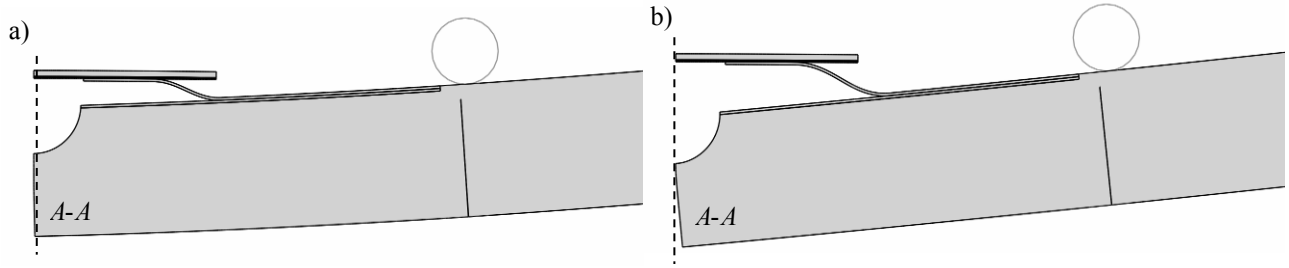

Fig. 439 – Numerical damage initiation at plane P2 (a) and failure at the symmetry plane *A-A* (b) for the L_O=20 mm repair.

- The L_O=30 mm repairs displayed an identical fracture between the experiments (Fig. 434) and simulations (Fig. 440), both failing by pure tension below the loading cylinders. This damage mechanism, similar to the one described for the undamaged wood beam, suggests a full strength recovery of the damaged beam, since the weakest region of the repair is no longer near the notch.

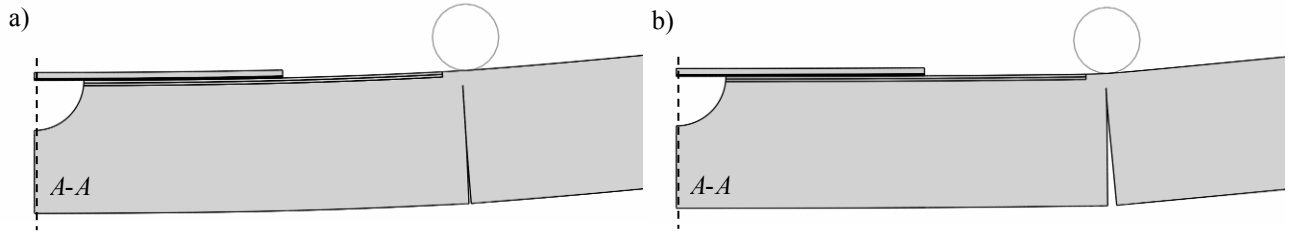

Fig. 440 – Numerical damage initiation (a) and growth (b) below the loading cylinder for the L_O=30 mm repair.

The experimental and numerical P-δ curves are compared in Fig. 441 for the unrepaired beam (a) and the L_O=10 mm repair (b), and in Fig. 442 for the L_O=20 mm (a) and 30 mm (b) repairs.

- A reasonable agreement was found for the unrepaired beam on K, P_m and δ_m (Fig. 441 a). P_m, experimentally related to a pure tension (Fig. 429 a) or cross-grain tension failure (Fig. 429 b), was slightly overpredicted.
- Equally, the experimental behaviour of the L_O=10 mm repair was simulated accurately, with a drop of P prior to P_m ($\delta \approx 3$ mm), relating to a premature patch detachment by a *RL* failure in the wood beam at plane P2 (Fig.

438 a). Experimentally, the drop of P occurred either by this event (Fig. 430 a) or due to a cohesive failure of the adhesive layer (Fig. 431 a). Subsequently, the repair behaved as an unrepaired beam, with P_m attained by a pure tension failure at the symmetry line *A-A* (Fig. 438 b).

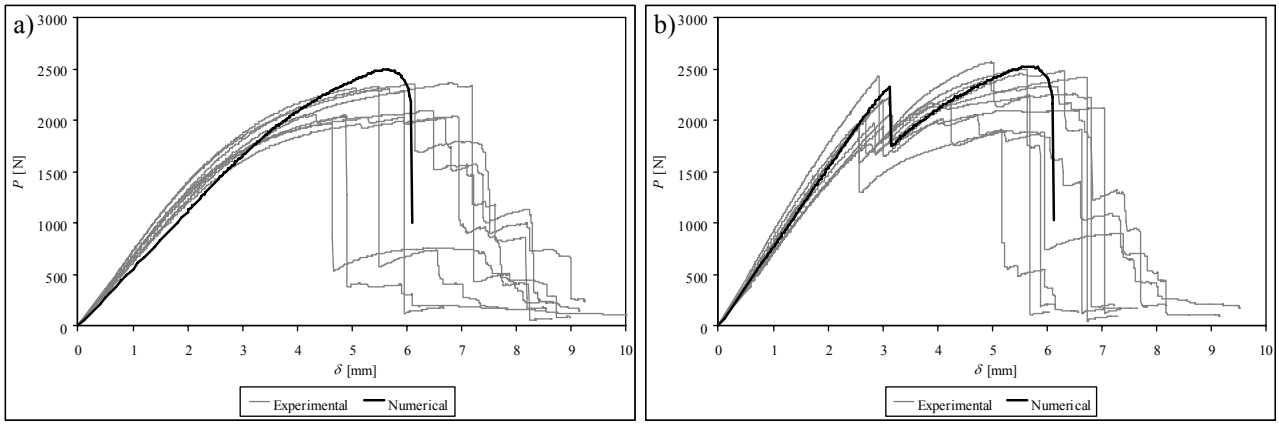

Fig. 441 – Experimental and numerical P-δ curves comparison for the unrepaired beam (a) and the L_O=10 mm repair (b).

- In the experimental P-δ curves of the L_O=20 mm repairs (Fig. 442 a) P_m correlates to a cohesive failure of the adhesive layer (Fig. 433 a) or failure within the wood beam near the beam/adhesive interface (Fig. 432 a). After the drop on P_m, a small plateau followed up to complete failure by pure tension (Fig. 432 b) or cross-grain tension (Fig. 433 b) near the symmetry line *A-A*. The simulations displayed a similar behaviour, with damage initiation at plane P2 at all the overlap (Fig. 439 a), leading to an abrupt drop on P_m. Complete failure was attained by pure tension near the symmetry line *A-A* (Fig. 439 b).
- The experimental value of P_m for the L_O=30 mm repairs related to a pure tension failure in the wood beam below the loading cylinders, either by pure tension (Fig. 434 a) or cross-graining (Fig. 435 a). The simulations were entirely consistent with the reported behaviour (Fig. 440).

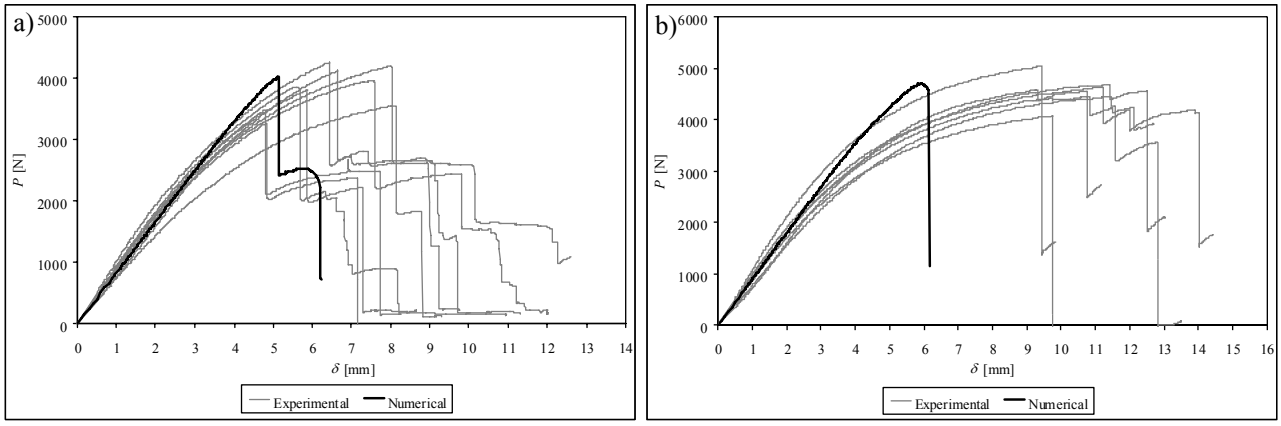

Fig. 442 – Experimental and numerical P-δ curves comparison for the L_O=20 mm (a) and L_O=30 mm (b) repairs.

6.3.3.2.2. Summary of the results

Fig. 443 summarizes the experimental and numerical results of K (a) and δ_m (b) as a function of L_O, while Fig. 444 compares the values of P_m. All these figures include the standard deviation of the experiments. The predictions of K

were reasonably accurate for all the beams tested (Fig. 443 a). Only for the unrepaired beam (L_O=0 mm) the value of K was underpredicted of a non-negligible amount. In fact, this beam showed experimentally a minor reduction of K compared to the undamaged beam, whilst the numerical simulations exposed a bigger difference. The gradual increase of K with L_O for the repaired beams is caused by the increase of the adhesive shear resistant area at the repair region (Lopez-Anido et al. 2003, Corradi et al. 2006). This tendency was accurately captured by the FEM models. Oppositely to the predictions of K, the numerical values of δ_m showed to be accurate only for the L_O=0 and 10 mm repairs, with a significant deviation being found for the L_O=20 and 30 mm repairs, and also the undamaged beam (Fig. 443 b). This can be explained by an indentation event at the contact regions of the wood beams with the cylinders, initiating for values of P between 2000-2500 N, and not captured in the FEM simulations due to the elastic orthotropic idealization of the wood beams (Campilho et al. 2009c). This phenomenon can be identified in Fig. 441 and Fig. 442 by the stiffness reduction of the P-δ curves at these values of P, being also particularly visible in Fig. 434, corresponding to a L_O=30 mm repair. Owing to the magnitude of P at which indentation initiates, δ_m predictions were accurate for the L_O=0 and 10 mm repairs, whose values of P_m did not exceed the indentation onset load by a significant amount (Fig. 441). The negligible indentation in these beams is also clearly perceptible in Fig. 430 and Fig. 431. Oppositely, for the L_O=20 and 30 mm repairs, and also the undamaged beam, indentation led to a substantial drop on K significantly before P_m (Fig. 442 (a) and (b)), which caused the reported divergence of Fig. 443 (b).

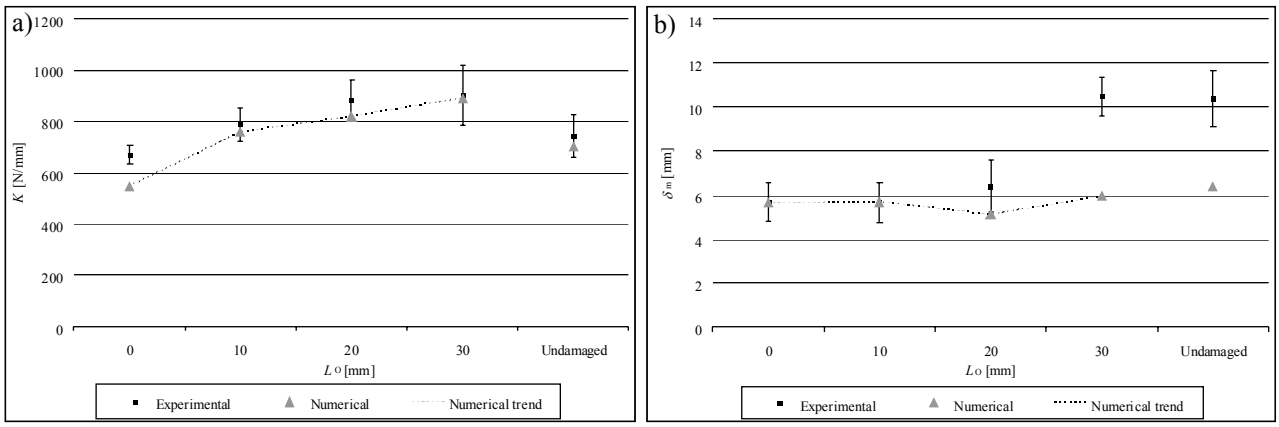

Fig. 443 – K as a function of L_O (a) and δ_m as a function of L_O (b).

Fig. 444 emphasizes the good agreement on P_m between the experiments and the simulations, in addition to the irrelevancy of using a L_O=10 mm repair, which was anticipated by the documented fracture for this repair (Campilho et al. 2009c). Actually, the premature failure in the wood beam yields the repair behaviour similar to an unrepaired beam. However, bigger values of L_O progressively increase P_m, being attained the undamaged beam strength with a L_O=30 mm repair. The damage mechanism for this repair, consistent with the undamaged wood beam, explains the full strength recovery, given that the weakest region of the repair is no longer near the notch. The significant scattering of the experiments on these three parameters is mainly caused by the known variability of the wood properties (Malan et al. 1988a, Malan et al. 1988b, Downes et al. 1997, Bao et al. 2001, Baillères et al. 2005). **The results presented in this Sub-Section allow concluding that, for the material properties and geometry under evaluation, the L_O=30 mm repair restores the undamaged strength of the wood beam. The L_O=20 mm repair, although not accomplishing this task, is also a viable option to increase the unrepaired beam strength. On the other hand, no advantage exists in repairing the damaged beam with a L_O=10 mm repair, due to a premature patch detachment**.

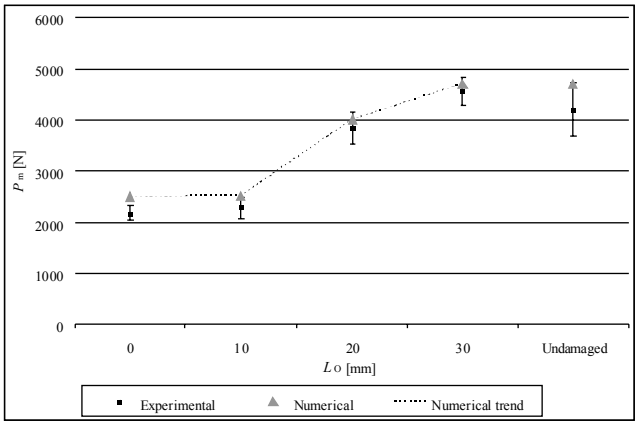

Fig. 444 – P_m as a function of L_O.

6.3.4. Cross-grain tension repairs

6.3.4.1. Stress analysis

Fig. 445 illustrates the deformed shape of the repair. σ_x stresses at the repair region are shown in Fig. 446.

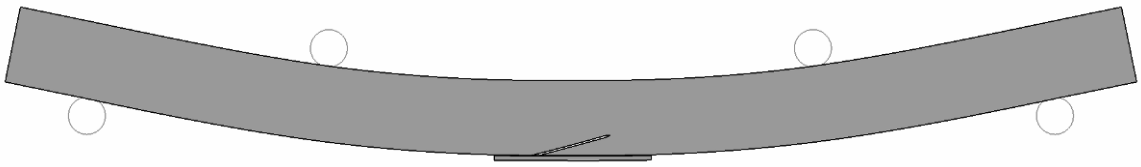

Fig. 445 – Deformed configuration of the cross-grain tension repair under a bending load.

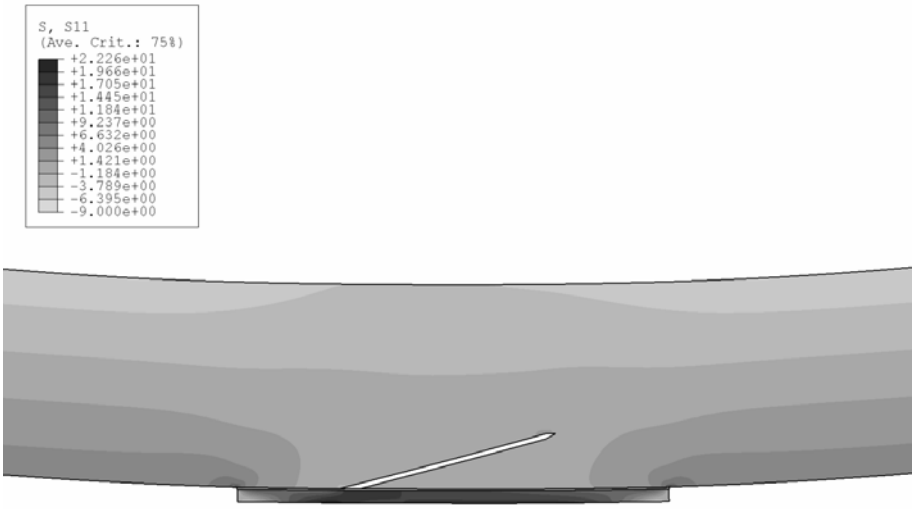

Fig. 446 – σ_x stresses at the repair region.

In the undamaged part of the beam, σ_x stresses along the beam thickness vary linearly with the distance to the beam neutral axis, which corresponds to the typical behaviour of beams under bending. The cross-grain crack and patch regions are under σ_x tensile stresses, whilst the undamaged region of the beam is under compressive loads. Near the

crack region, σ_x stresses are nearly nil, due to the deviation of loads from the tensile region of the repaired beam to the CFRP patch. The loads are transmitted through the adhesive layer mainly by shear, explaining the development of the highest σ_x stresses in the patch (reaching approximately 2.5x the maximum σ_x magnitude in the wood beam). The difference on σ_x stresses is also justified by the higher stiffness of the CFRP patch. The negligible magnitude of σ_x stresses at the cracked region of the wood beam, particularly at the crack tip, is highly advantageous, reducing the prospect of tensile fractures at this weakened region.

σ_y stresses and σ_y stress distributions at planes P3, P4 and P5 (Fig. 395 b) are shown in Fig. 447 and Fig. 449 (a), respectively. Fig. 448 and Fig. 449 (b) concern τ_{xy} stresses and τ_{xy} stress distributions at the same planes. In the following figures, x/L_P represents the distance from the leftmost edge of the patch, normalized by L_P (Fig. 395 b).

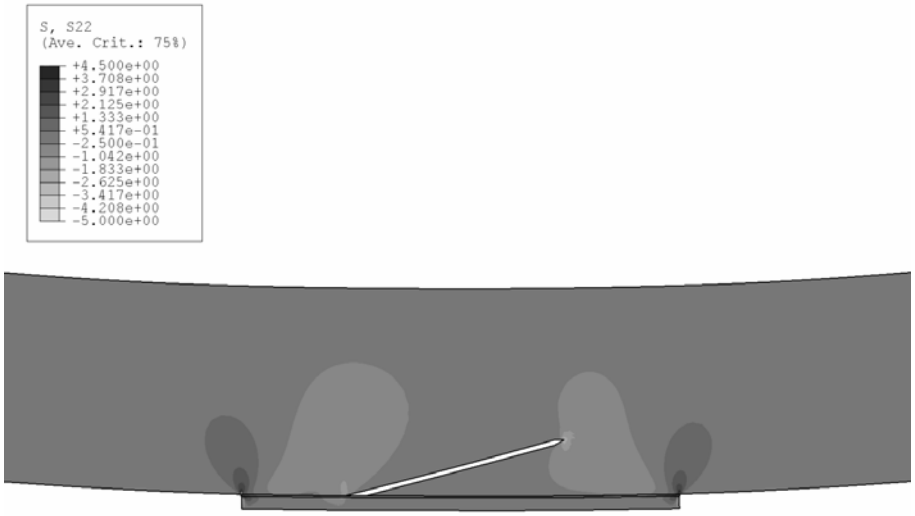

Fig. 447 – σ_y stresses at the repair region.

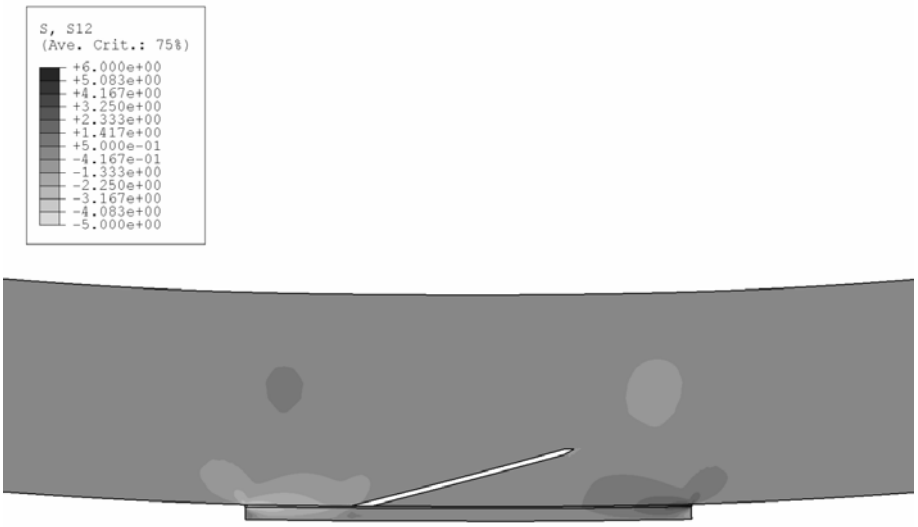

Fig. 448 – τ_{xy} stresses at the repair region.

σ_y stresses are approximately nil along the overlap, excluding at the bond edges. σ_y peel stresses concentrate towards the patch edges (corresponding to the square-edge corners). At the inner region of the bond, σ_y stresses are not

important, with the exception of a compressive singularity near the bond gap (x/L_P=0.25), induced by the cross-grain crack. At the inner bond region, σ_y peel stresses of small magnitude were only detected near the tip of the wood spike ($0.25 \leq x/L_P \leq 0.40$). σ_y stresses are usually significantly smaller in magnitude than τ_{xy} stresses along the bond length. Fig. 449 (a) also shows that σ_y stresses are almost impossible to differentiate between the three planes, with stress singularities at the patch edges at these planes. τ_{xy} stresses at the repair region (Fig. 448 and Fig. 449 a) are higher in magnitude near the patch edges, corresponding to the regions of load transfer between the wood beam and the patch. At the wood spike region ($0.25 \leq x/L_P \leq 0.75$), τ_{xy} stresses are nearly nil. The small magnitudes of σ_y and τ_{xy} stresses at this region also avoid premature failures of the wood spike by tension, since the load paths are deviated from this weakened region to the neighbouring undamaged regions of the beam. τ_{xy} stresses gradually increase towards the patch edges, where these stresses peak. A τ_{xy} singularity emerges near the bond gap (x/L_P=0.25) at plane P3, due to the material discontinuity at this region. Equally to σ_y stresses, τ_{xy} stress distributions are identical between the three planes, with the exception of the stress singularity at plane P3.

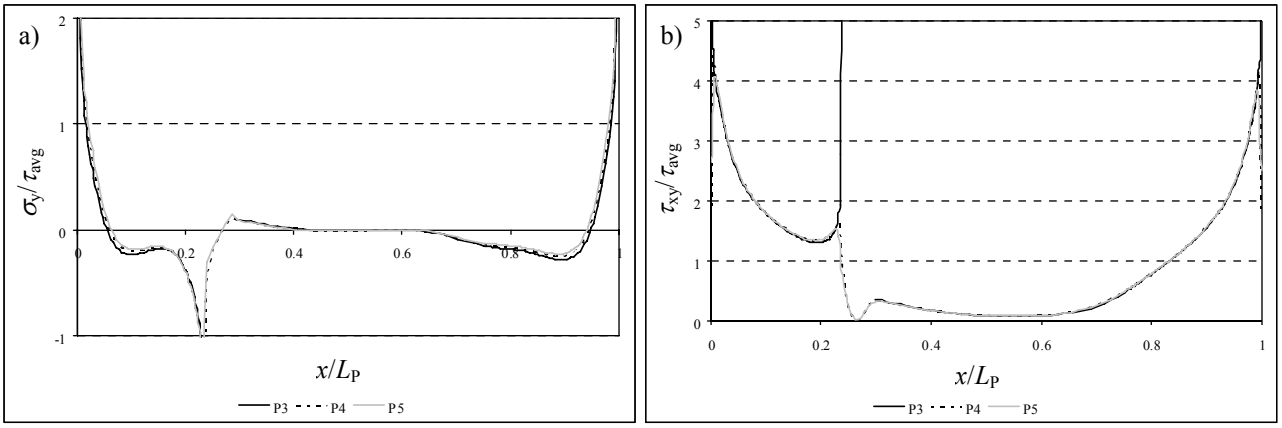

Fig. 449 – Normalized σ_y (a) and τ_{xy} (b) stress distributions at the repair region.

A detailed description of σ_y and τ_{xy} stress distributions at the repair region is presented in Fig. 450 and Fig. 451, respectively, including the seven planes of Fig. 395 (b). σ_y stress distributions do not differ significantly along L_P between these planes, only showing minor deviations in magnitude. As mentioned previously, σ_y stresses are mostly compressive and smaller than τ_{xy} stresses at the load bearing regions ($0 \leq x/L_P \leq 0.25$ and $0.75 \leq x/L_P \leq 1$). However, σ_y peel stresses grow in magnitude towards the patch edges (x/L_P=0 and x/L_P=1), with a stress singularity at plane P3 (this is not visible in Fig. 450, since the *y*-axis limits were defined for an easier understanding of stresses near σ_y/τ_{avg}=0). No significant differences on σ_y peel stresses at the patch edges were found between the seven planes, while the adjacent σ_y compressive stresses gradually diminish from plane P1 to plane P7. Substantial differences were detected for τ_{xy} stresses. In fact, despite showing identical profiles, higher magnitude τ_{xy} peak stresses at the patch edges were found at planes P3, P4 and P5. Although this is not visible in Fig. 451, τ_{xy} singularities develop at plane P3 at both patch edges and at the bond gap (x/L_P=0.25). Within the wood beam and the patch, τ_{xy} peak stresses at these regions are smaller in magnitude, diminishing with the distance to the adhesive layer (i.e., from plane P2 to plane P1 and from plane P6 to plane P7). This elastic stress analysis points towards damage initiation at one of the patch edges, since σ_y peel and τ_{xy} stresses concentrate at these regions. Between the two patch edges, the one at x/L_P =0 acquires special significance (Fig. 451), due to a smaller bond length up to the crack gap. Between the seven planes, considering similar mechanical and

fracture properties for the different repair constituents, damage would initiate at or near one of the two stress singularity regions (patch edges at plane P3). Owing to the different strength properties between the wood, adhesive and patch, no definite conclusions can be drawn at this stage of the analysis.

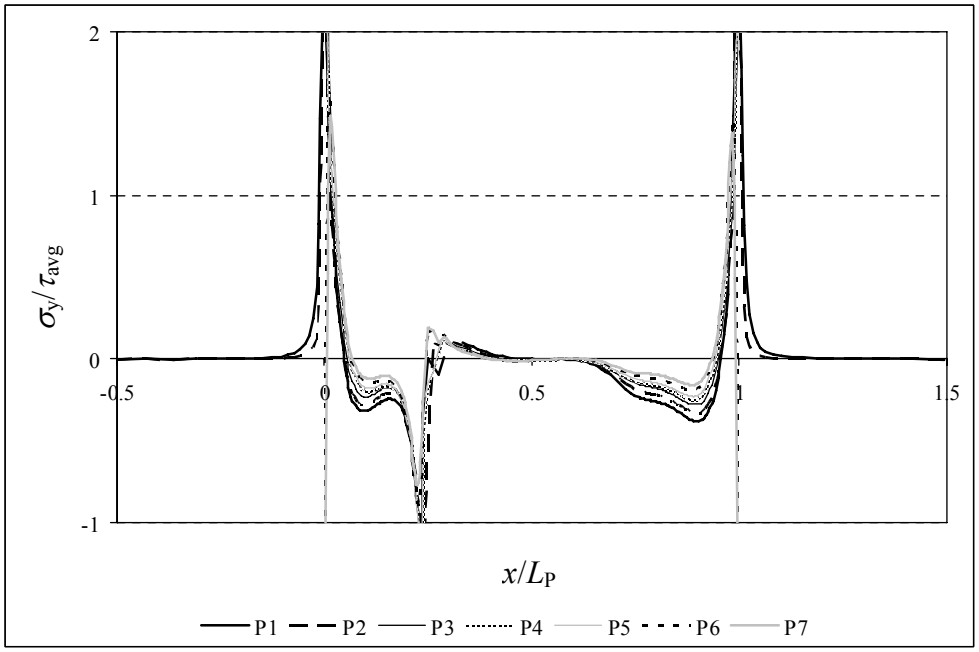

Fig. 450 – Normalized σ_y stress distributions at seven planes in the repair.

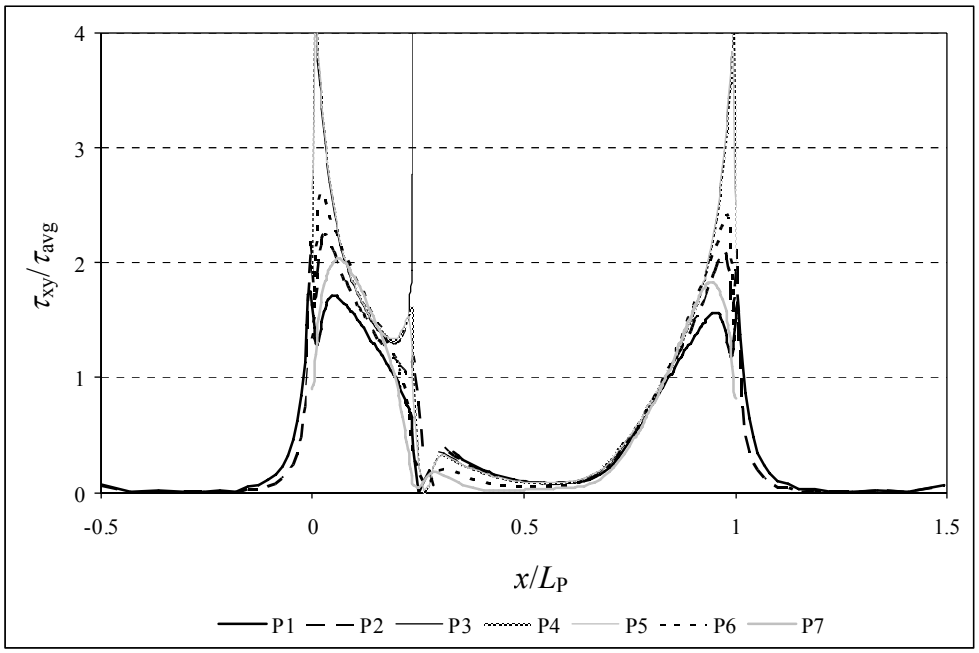

Fig. 451 – Normalized τ_{xy} stress distributions at seven planes in the repair.

6.3.4.1.1. Patch length

A parametric study on L_P was carried out for the cross-grain tension repairs. L_P represents the length of the patch, bonded at the tension face of the wood beam at the cross-grain crack region. σ_y and τ_{xy} stress distributions along L_P at

planes P3, P4 and P5 (Fig. 395 b) are shown in Fig. 452, Fig. 453 and Fig. 454, by the respective order. The mentioned planes correspond to the wood beam/adhesive interface (plane P3), the middle of the adhesive (plane P4) and the adhesive/patch interface (plane P5).

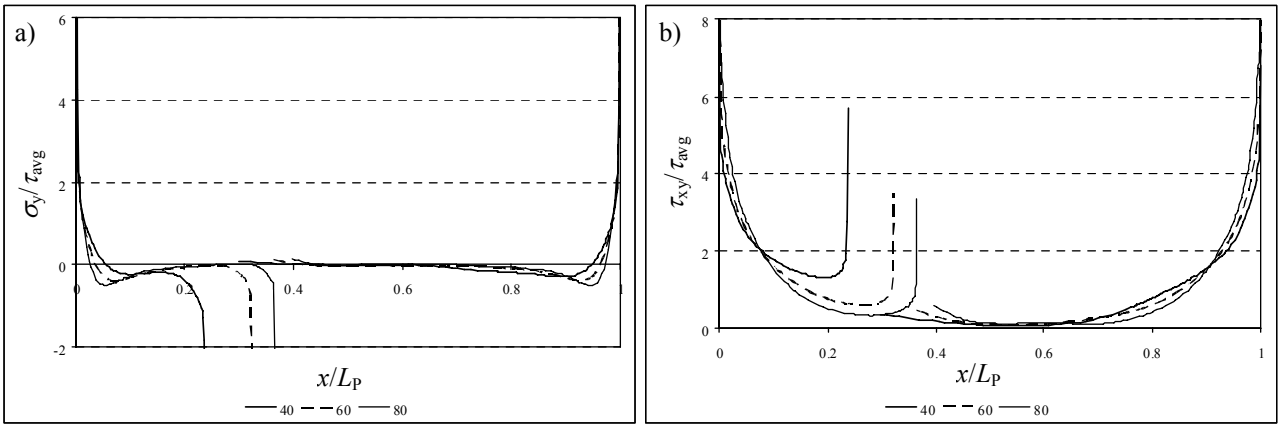

Fig. 452 – Normalized σ_y (a) and τ_{xy} (b) stress distributions at the laminate/adhesive interface (P3).

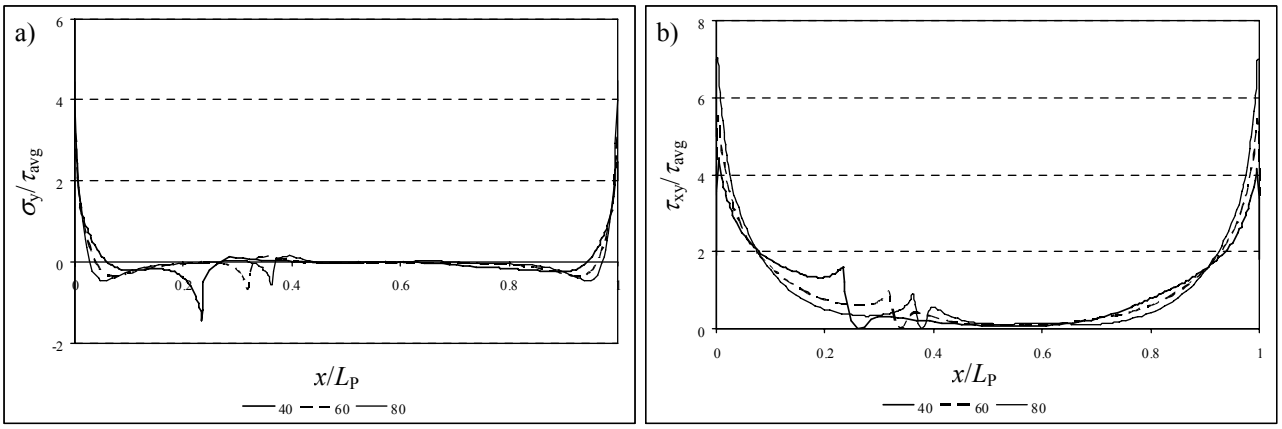

Fig. 453 – Normalized σ_y (a) and τ_{xy} (b) stress distributions at the middle of the adhesive (P4).

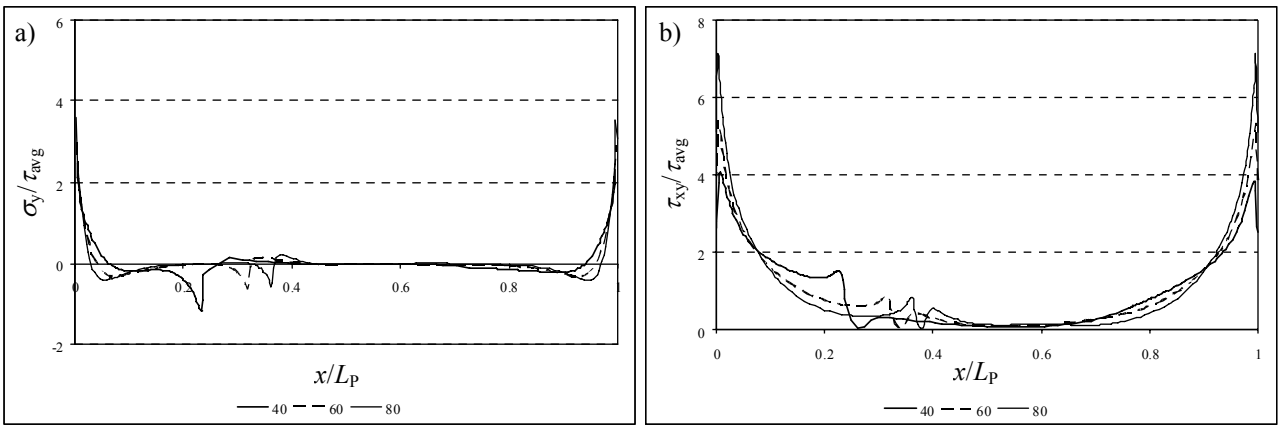

Fig. 454 – Normalized σ_y (a) and τ_{xy} (b) stress distributions at the adhesive/patch interface (P5).

These figures show identical σ_y stresses along L_P between planes P3, P4 and P5. The only differences worth mentioning arise at the patch edges and at the bond gap, with a singular region at plane P3 for the three values of L_P. These

discontinuities were expected, due to the square-edge corners (Campilho 2005, Campilho et al. 2005). σ_y stresses are nearly nil compared to τ_{xy} stresses, except at the singularities. With the increase of L_P, a slight reduction of σ_y compressive stresses at the bond gap and an increase near the patch edges should be emphasized. τ_{xy} stresses also behave similarly profiles at the three planes. Actually, the sole relevant differences are the τ_{xy} singularities at plane P3 at the same locations (i.e., at the patch edges and at the bond gap). Equally, τ_{xy} stresses between planes P4 and P5 are nearly impossible to differentiate. It is also emphasized that the smallest value of L_P yields significantly higher magnitude τ_{xy} stresses at the smaller bond ($0 \leq x/L_P \leq 0.25$), overloading this region, which may cause a premature failure. Increasing L_P gradually cancels this effect, as τ_{xy} stresses level between the two bonds. This analysis points to an increase of P_m with L_P. This conclusion is based on the increase of the shear area available to deviate loads from the cracked to the sane region of the beam, and due to the levelling of τ_{xy} stresses between the two bonds. The increase of σ_y and τ_{xy} stresses at the patch edges with L_P may be responsible for a P_m improvement at a decreasing rate with L_P.

6.3.4.2. Failure analysis

6.3.4.2.1. Mechanical behaviour

The fractures of the unrepaired and repaired beams, damaged by cross-graining, are characterized in this Sub-Section.

- Damage in the unrepaired damaged beam initiated by a *RL* propagation along path A2 (Fig. 402 b), causing only a reduction of stiffness. For seven of the specimens tested, crack propagation was practically horizontal (Fig. 455 a) since, as mentioned previously, although the wood beams were artificially damaged to simulate cross-graining, they were selected from specimens with a negligible fibre misalignment. For the other three specimens, the crack path followed the induced crack, propagating approximately at a 15º angle to the *RL* plane (Fig. 455 b). In both cases, damage continued to grow steadily up to P_m, occurring due to *RL* fractures at paths A2 and A3 (Fig. 402 b), instantaneously up to near the loading cylinders for three specimens, corresponding to complete failure ($P<50\%.P_m$). For the other specimens, smaller cracks opened, corresponding to a smaller drop of P_m (Fig. 456 a). After this, the specimens still sustained some load while damage propagated up to the loading cylinders (Fig. 456 b). **Final fracture for the unrepaired beam, and also for the subsequent repairs, occurred predominantly by a vertical *LR* failure initiating at the cross-graining crack tip. Since this fracture occurred subsequently to P_m and at a very reduced value of *P*, it will be omitted in the following analyses.**

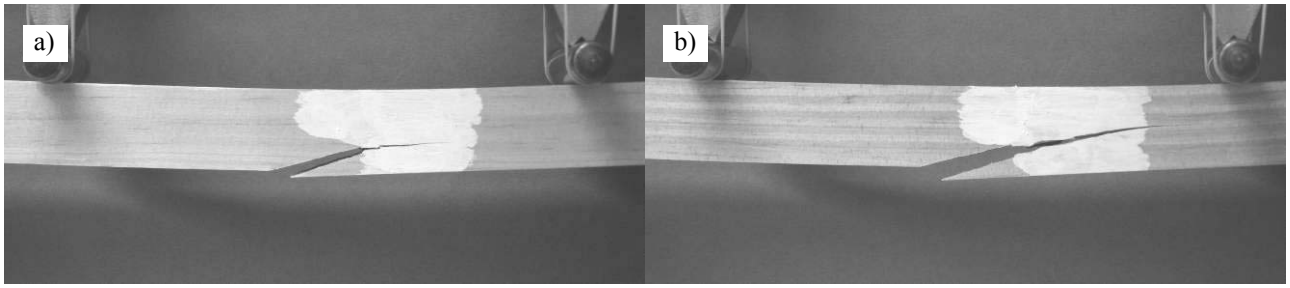

Fig. 455 – Damage onset at path A2 horizontally (a) and with cross-graining (b) for an unrepaired beam.

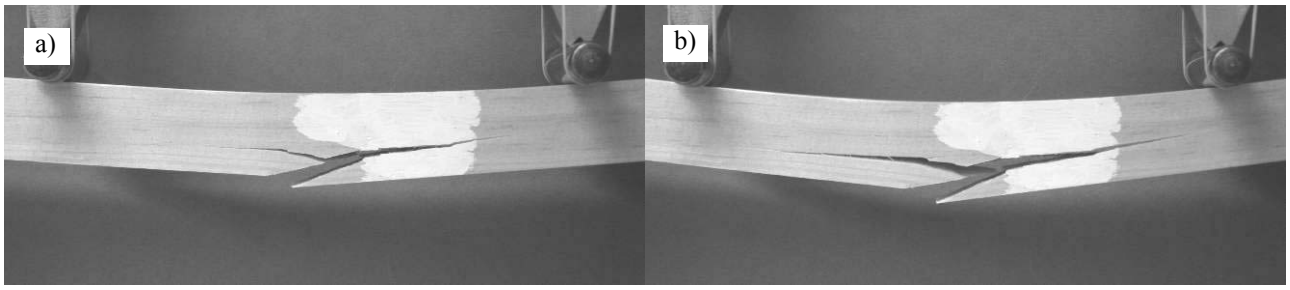

Fig. 456 – Damage initiation (a) and growth (b) along paths A2 and A3 for an unrepaired beam.

- The L_P=40 mm repairs displayed two different fractures. For six specimens, failure and P_m occurred abruptly without previous visual evidence of damage, with simultaneous *RL* failures at paths A1, A2 and A3 (Fig. 402 b). Fig. 457 relates to practically horizontal *RL* propagations (a) and for a specimen showing cross-graining (b). For the other specimens, damage initiated as shown in Fig. 458 (a), with simultaneous *RL* failures at paths A1 and A2 (Fig. 402 b), causing a drop of P_m. Subsequently, the repair still sustained loads until complete fracture (Fig. 458 b), with a horizontal *RL* failure at path A3 (Fig. 402 b). The fractures at path A1 within the wood beam denote a weaker strength of this material compared to the adhesive layer and respective interfaces, since τ_{xy} stresses, controlling the failure process in this repair, are higher at these particular regions (planes P3, P4 and P5 in Fig. 451). Fracture at path A1 is related to the smaller length of this bond, causing higher stresses than at the opposite bond (Fig. 452, Fig. 453 and Fig. 454). This is more evident for the smallest value of L_P. In all cases, failure along path A1 occurred at a measured distance to the adhesive/wood beam interface between approximately 0.3 and 0.7 mm (including the three repairs evaluated). For mesh simplification purposes, planes P1 and P2 were placed at 0.6 and 0.3 mm to the wood/adhesive interface, respectively.

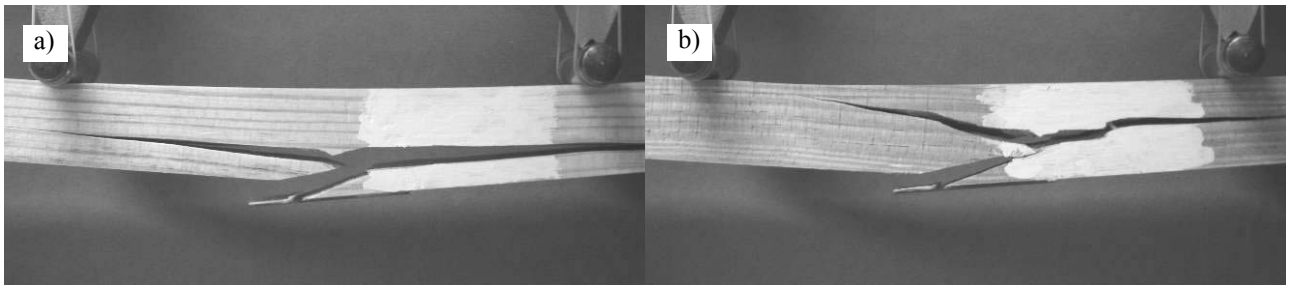

Fig. 457 – Instantaneous failure at paths A1, A2 and A3 horizontally (a) and with cross-graining (b) for a L_P=40 mm repair.

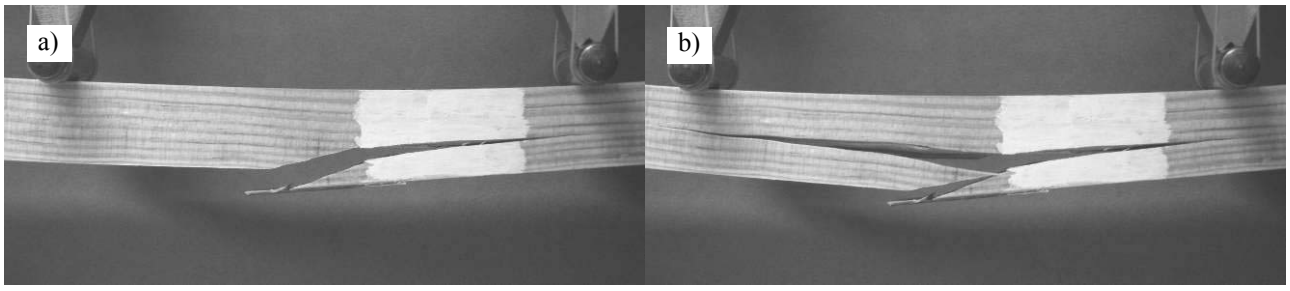

Fig. 458 – Damage initiation at paths A1 and A2 horizontally (a) and growth at path A3 (b) for a L_P=40 mm repair.

- The L_P=60 mm repairs also showed two different fractures, despite being nearly identical. For eight specimens, failure was similar to one of the failures of the L_P=40 mm repair (Fig. 457). In fact, three simultaneous *RL*

fractures within the wood beam, at paths A1, A2 and A3 (Fig. 402 b), led to P_m. Fig. 459 shows two examples of this failure for beams without cross-graining. Up to this failure, no evidence of damage was found. For the other specimens, the patch detached completely at paths A1 and A4 (Fig. 402 b). Fig. 460 illustrates these two specimens after failure. Only for the specimen of Fig. 460 (a), the tip of the wood spike fractured differently to the numerical idealizations. Fracture at paths A1, A2 and A3 always occurred concurrently, owing to the bigger values of P_m than for the previous repair, caused by a larger shear resistant area. The levelling of τ_{xy} stresses between the smaller and larger bond regions (Fig. 452, Fig. 453 and Fig. 454) justifies the complete patch detachment observed for the two repairs of Fig. 460, which did not occur for the L_P=40 mm repairs.

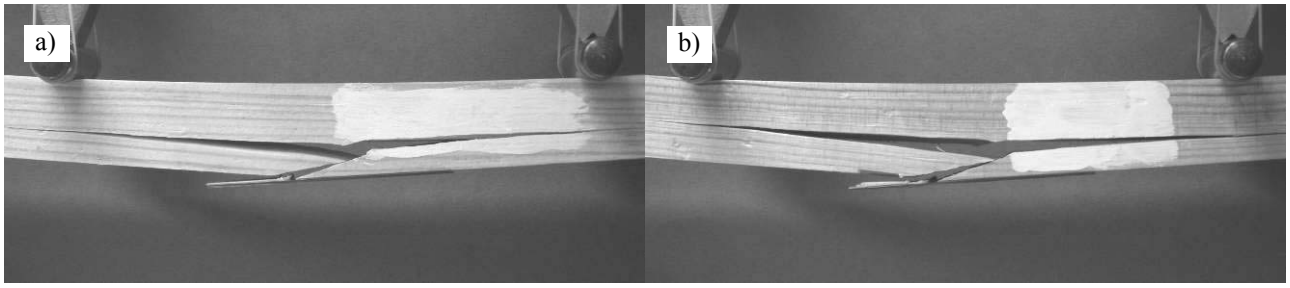

Fig. 459 – Instantaneous failure at paths A1, A2 and A3 horizontally (a) and with cross-graining (b) for a L_P=60 mm repair.

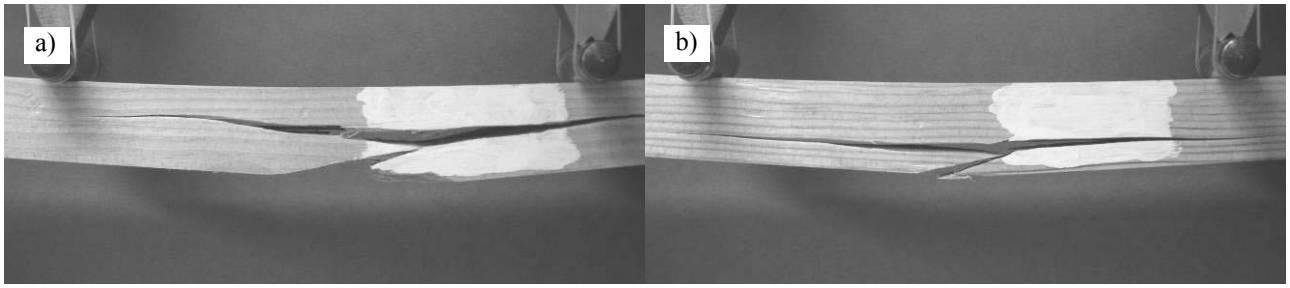

Fig. 460 – Two examples of instantaneous failure at paths A1, A2, A3 and A4 for a L_P=60 mm repair.

- The L_P=80 mm repairs fracture is entirely consistent with the L_P=60 mm repairs in terms of failure mechanisms and number of occurrences. Fig. 461 illustrates two of the eight specimens failing similarly to Fig. 459, i.e., concurrently at three *RL* planes in the wood beam (paths A1, A2 and A3, Fig. 402 b). In the other two specimens (shown in Fig. 462), the wood failure close to adhesive layer extended to the entire bond length, causing the patch detachment. In these specimens, failure near the spike tip was deeper in the wood than mentioned earlier (at 0.3-0.6 mm of the beam/adhesive interface). Failure at paths A1 and A4 in all the repairs was always abrupt, despite the peak stresses at the patch edges (Fig. 452, Fig. 453 and Fig. 454).

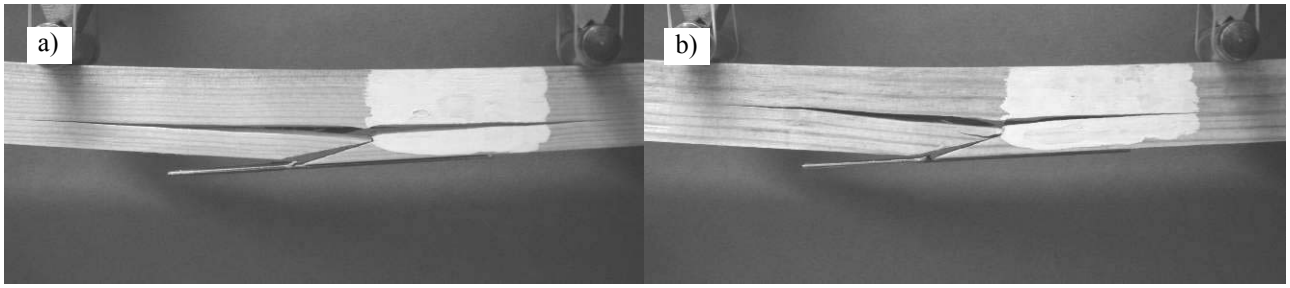

Fig. 461 – Instantaneous failure at paths A1, A2 and A3 horizontally (a) and with cross-graining (b) for a L_P=80 mm repair.

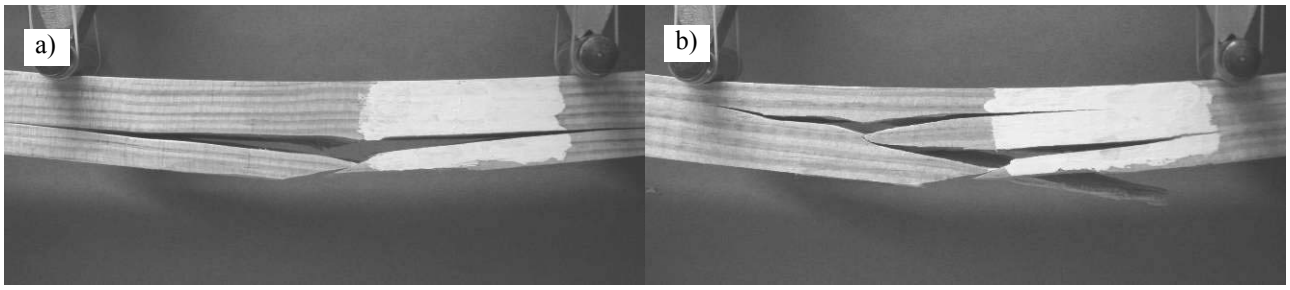

Fig. 462 – Two examples of instantaneous failure at paths A1, A2, A3 and A4 for a L_P=80 mm repair.

The aforementioned experimental behaviour of the unrepaired and repaired beams was simulated numerically with a reasonable degree of accuracy.

- Numerically, damage in the unrepaired beam initiated at the cross-grain crack tip, growing horizontally as an *RL* fracture along path A2 (Fig. 463 a). This led to a small drop on *P*, which then continued to increase as the *RL* crack propagated. P_m occurred after this crack approached the loading cylinder, by instantaneous failure at path A3 (Fig. 463 b). This behaviour is consistent with the experiments (Fig. 456).

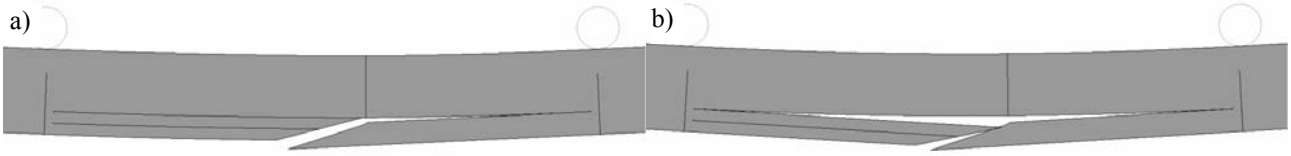

Fig. 463 – Numerical damage initiation at path A2 (a) and growth at path A3 (b) for the unrepaired beam.

- The FEM simulation of the L_P=40 mm repair showed to be equivalent to one of the experimental fractures (Fig. 458). In fact, the repair behaved linearly up to P_m, occurring due to simultaneous horizontal *RL* failures at path A1 at 0.3 mm of the adhesive layer (plane P2 in Fig. 395 b) and at path A2 (Fig. 464 a). At this instant, P_m dropped abruptly while the crack at path A2 continued to grow. Finally, the repair failed suddenly at path A3 (Fig. 464 b). It must be mentioned that, at the time of the initial failure, most of the adhesive layer cohesive elements were already in the softening stage ($\delta_i > \delta_{1m,i}$ in Fig. 68), which implies that small variations in the repair constituents properties, namely the wood beam, could result on a cohesive failure of the adhesive layer.

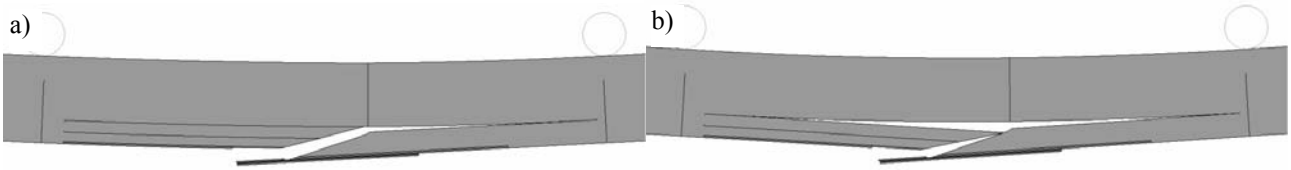

Fig. 464 – Numerical damage initiation at paths A1 and A2 (a) and growth at path A3 (b) for the L_P=40 mm repair.

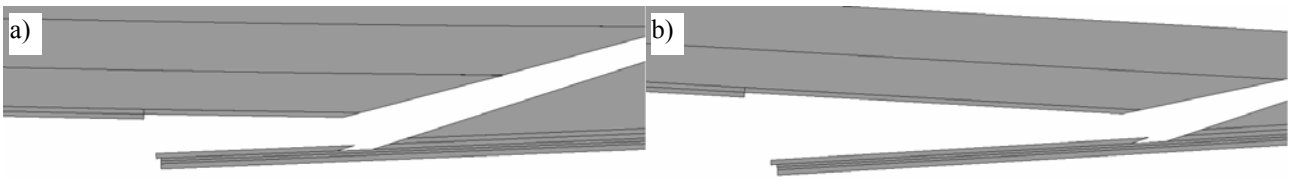

Fig. 465 – Detail of the failure at path A1 for the L_P=40 mm (a) and L_P=60 mm (b) repairs.

Fig. 465 (a) and (b) show a detail of the fracture at path A1 (plane P2 in Fig. 395 b) for the L_P=40 mm (a) and L_P=60 mm (b) repairs, for an easier visualization.

- Experimentally, the L_P=60 mm repairs fractured concurrently at paths A1, A2 and A3 (Fig. 402 b), neglecting the two specimens in which the patch detached completely. This was accurately simulated by the FEM models. Fig. 466 (a) relates to the instant before failure, and (b) immediately after failure.

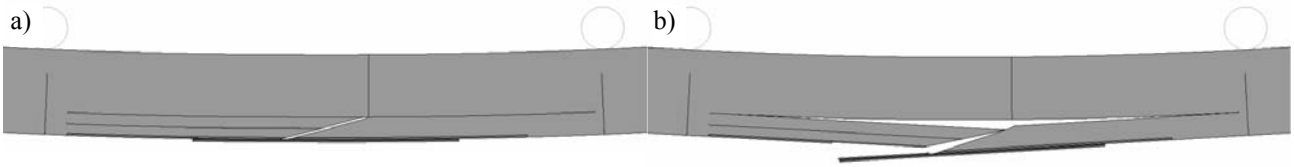

Fig. 466 –Numerical L_P=60 mm repair immediately before (a) and after abrupt failure at paths A1, A2 and A3 (b).

- Also for the L_P=80 mm repair, ignoring the two specimens showing a complete patch detachment, the simulations revealed to be in agreement with the experiments. Thus, the numerical fracture is equivalent to the L_P=60 mm repair (simultaneous fracture at the three *RL* planes). Fig. 467 shows the L_P=80 mm repair immediately before abrupt failure (a) and after failure (b).

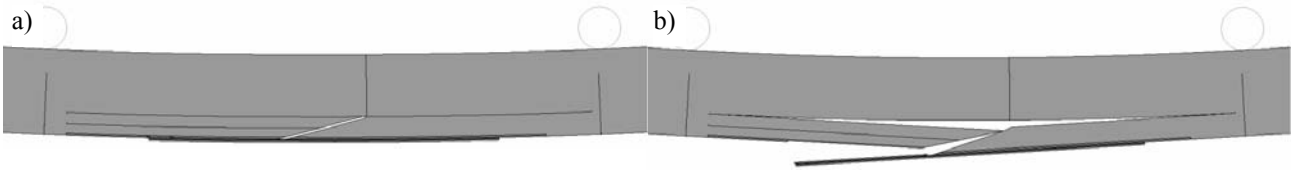

Fig. 467 – Numerical L_P=80 mm repair immediately before (a) and after abrupt failure at paths A1, A2 and A3 (b).

The following figures compare the experimental and numerical P-δ curves for the unrepaired beam (Fig. 468 a), and for the L_P=40 mm (Fig. 468 b), 60 mm (Fig. 469 a) and 80 mm (Fig. 469 b) repairs.

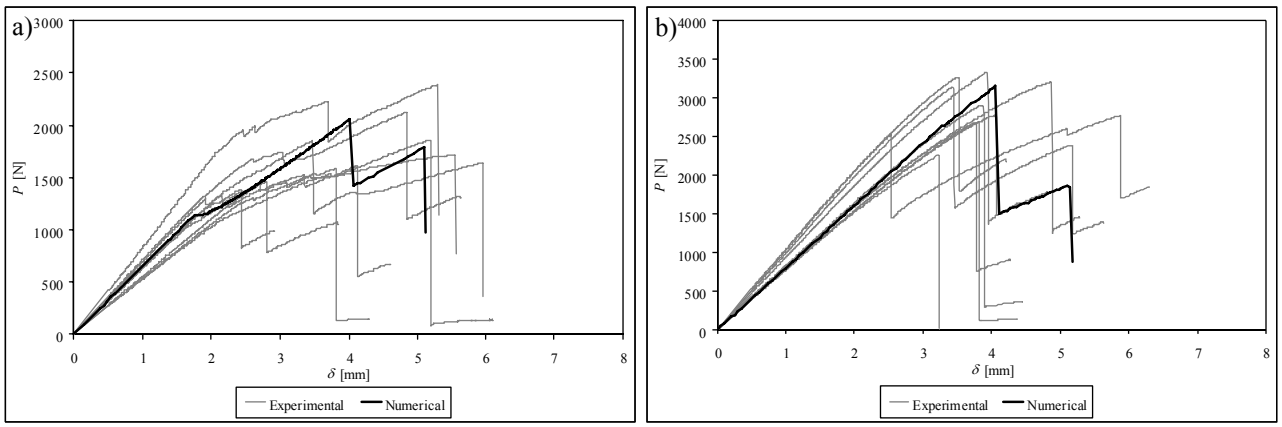

Fig. 468 – Experimental and numerical P-δ curves comparison for the unrepaired beam (a) and the L_P=40 mm repair (b).

- The unrepaired beam (Fig. 468 a) revealed numerically a drop of P owing to damage initiation at the tip of the cross-graining crack, which is clearly visible at δ≈1.8 mm and compares reasonably with the experimental curves, although in some specimens this occurred for a bigger value of δ. The numerical value of P_m, caused

by an abrupt *RL* failure at path A3 (Fig. 402 b), overpredicted the experiments for most of the specimens. After the drop of P_m, P increased up to complete failure, by tension above the cross-grain crack tip.

- Fig. 468 (b), representing the repair with L_P=40 mm, displays a nearly linear numerical P-δ curve up to P_m (δ≈4 mm), which agreed with the average of the experiments. As already discussed, the FEM value of P_m is related to simultaneous *RL* failures in the wood beam at paths A1 and A2 (Fig. 402 b). The repair still sustained loads up to fracture at path A3. In the experiments, for six of the specimens, failure occurred concurrently at the three paths referred (Fig. 457). For the other specimens, an equivalent tendency to the simulations was found (Fig. 458).

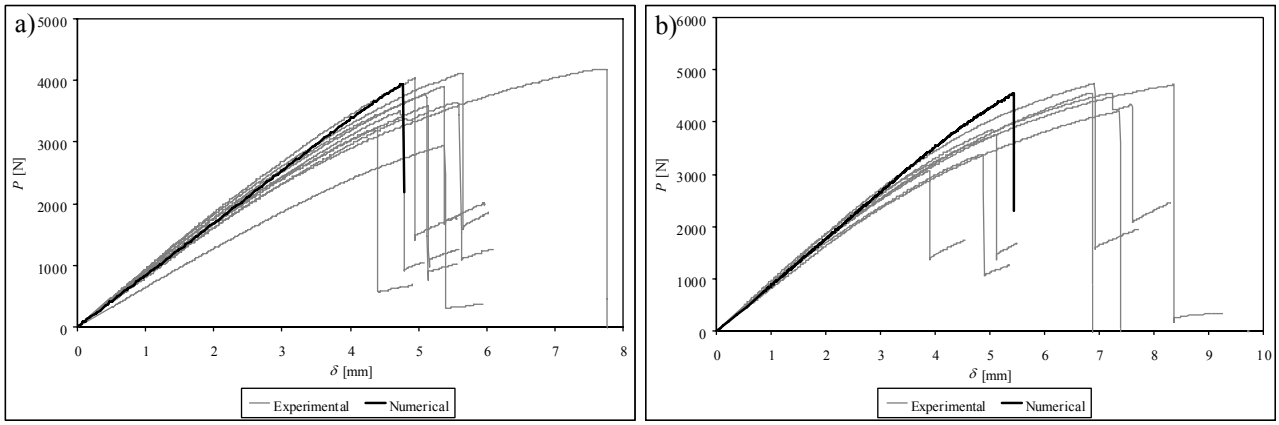

Fig. 469 – Experimental and numerical P-δ curves comparison for the L_P=60 mm (a) and L_P=80 mm (b) repairs.

- The experimental and numerical P-δ curves for the L_P=60 mm repair (Fig. 469 a) are nearly identical, apart from a higher value of δ_m for the experiments. In both cases, fracture developed abruptly at paths A1, A2 and A3 (Fig. 402 b), without previous perceptible damage. Owing to this, the P-δ curves were practically linear up to P_m. It must be mentioned that one of the specimens sustained a significantly bigger value of δ_m. However, this result was not discarded since the failure mode and value of P_m agreed with the overall trend of this repair geometry. Moreover, visual inspection after the test showed that this difference was caused by a bigger indentation of the cylinders than for the other specimens.
- The L_P=80 mm repair numerical P-δ curve also agrees with the tests (Fig. 469 b), where P_m occurs under the same conditions of the L_P=60 mm repair. The value of δ_m was also underpredicted for these repairs.

6.3.4.2.2. Summary of the results

Fig. 470 evaluates the experimental and FEM results, in terms of K (a) and δ_m (b) as functions of L_P (L_P=0 mm corresponds to the unrepaired beam). The values of P_m as a function of L_P are compared in Fig. 471. These figures also show the standard deviation of the experiments. The FEM predictions of K were found to be in close agreement with the tests for all configurations (Fig. 470 a), although in most cases the average experimental values of K were slightly underpredicted. The increase of the shear area with L_P is on the origin of this tendency (Lopez-Anido et al. 2003, Corradi et al. 2006). On the other hand, the simulations underpredicted the value of δ_m in some cases (Fig. 470 b), with an increasing difference with the value of P_m sustained by the respective specimens. Thus, the L_P=80 mm repair and undamaged beam showed the larger deviations. This divergence, which was already discussed in Sub-Section 6.3.3.2.2,

emerges from an indentation event initiating for values of P between 2000 N and 2500 N. The indentation caused a stiffness reduction in the experimental P-δ curves for the L_P=80 mm repair (Fig. 469 a) and undamaged beam (Fig. 469 b), initiating at the mentioned values of P. On the other hand, δ_m was accurately predicted for the L_P=0 and 40 mm repairs, whose values of P_m were similar to the loads of indentation initiation. This contrasting behaviour is also exemplified in the experimental fracture figures, with the unrepaired beam and L_P=40 mm repair (Fig. 455 to Fig. 458) showing little evidence of indentation, oppositely to the L_P=60 and 80 mm repairs (Fig. 459 to Fig. 462).

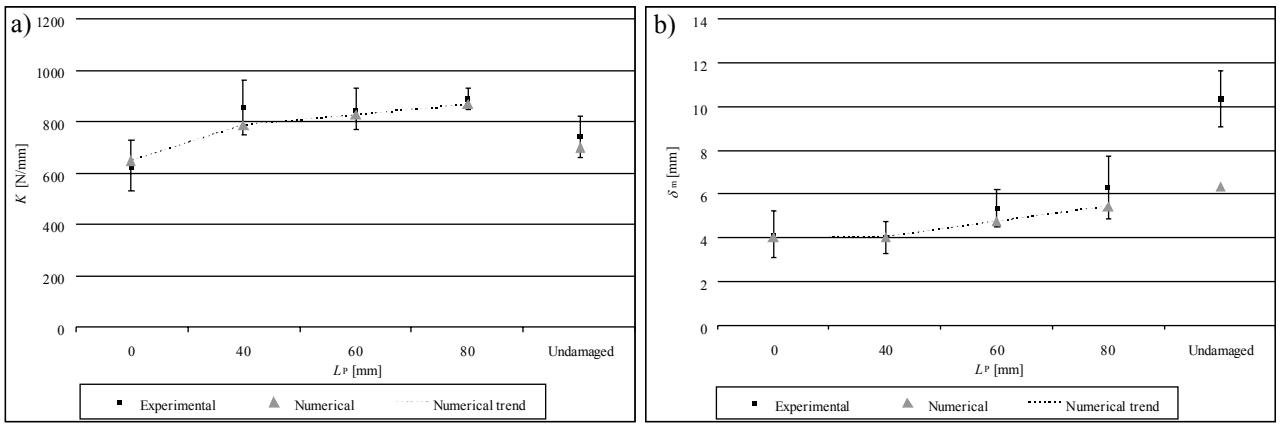

Fig. 470 – K as a function of L_P (a) and δ_m as a function of L_P (b).

The correlations between the experimental and the FEM values of P_m were accurate on all configurations tested (Fig. 471). The cross-graining crack led to a drop on P_m of slightly more than 50%. Repairing resulted on an approximately proportional increase of P_m with L_P, although at a decreasing rate. Given that in these repairs P_m is governed by wood failure at path A1 (Fig. 402 b), it can be concluded that the increasing magnitude of τ_{xy} peak stresses with L_P at the patch edges (x/L_P=1) is responsible for this non-proportional behaviour with L_P (Fig. 452, Fig. 453 and Fig. 454, although not relating to stresses within the wood, exemplify this tendency). The L_P=80 mm repair allows the re-establishment of the undamaged beam strength. The slightly smaller FEM value of P_m justifies the numerical failure at the repaired region (Fig. 467), rather than vertically below the loading cylinders. However, immediately before fracture, this failure mechanism was imminent, and would occur if P_m reached the undamaged beam value (which failed vertically below the loading cylinders; Fig. 426 and Fig. 436).

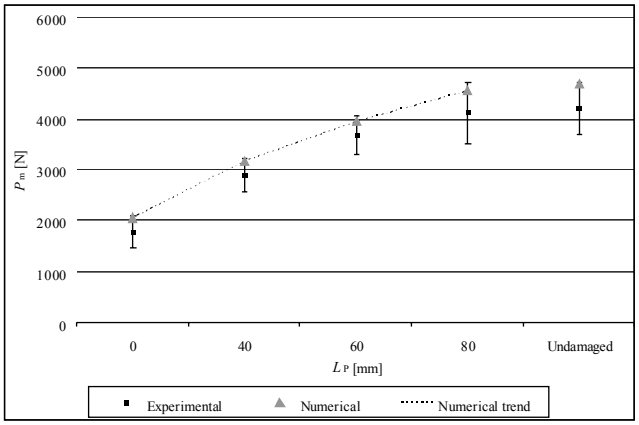

Fig. 471 – P_m as a function of L_P.

The experimental scatter on the three parameters is mainly attributed to the variability of the wood beam properties (Malan et al. 1988a, Malan et al. 1988b, Downes et al. 1997, Bao et al. 2001, Baillères et al. 2005). **The technique proposed in this Section for the beams damaged by cross-graining was found to be effective in restoring the undamaged beam strength. For the particular geometry and material properties considered, this is achieved with a L_P=80 mm patch. The smaller values of L_P tested, although not allowing the full strength recovery of the damaged beam, enhance its strength, with an approximately proportional increase of P_m with L_P.**

6.3.5. Horizontal shear failure repairs

6.3.5.1. Stress analysis

The stress analysis for the horizontal shear failure repairs was carried out differently to the other wood repair techniques proposed in Section 6. In fact, apart from the 3D FEM idealization of the horizontal shear failure repairs, these show significant stress variations at the repaired region in the beams height direction. Thus, the repairs do not possess a stress similarity in this direction that can be considered representative with a minimum degree of accuracy of the stress fields at the repair region. Moreover, different stress components, in addition to normal stresses in the adhesive thickness direction and shear stresses in the beam length direction (formerly addressed as σ_y and τ_{xy} stresses, respectively), emerge as relevant with this repair configuration. Consequently, for the horizontal shear failure repairs, the stress distributions evaluation at different planes is not addressed. Instead, a detailed analysis of the stress fields of the most significant stresses in the adhesive layer will be presented, allowing an easier interpretation of the experimental and numerical failure mechanisms and strength predictions. Fig. 472 shows the coordinate system used and the most relevant stress components for these repairs, based on a detailed analysis of the six stress components distributions at the repair region, particularly in the adhesive layer. σ_z, τ_{zx} and τ_{zy} stresses will be evaluated. The other stress components were found to be insignificant compared to these, and will not be studied.

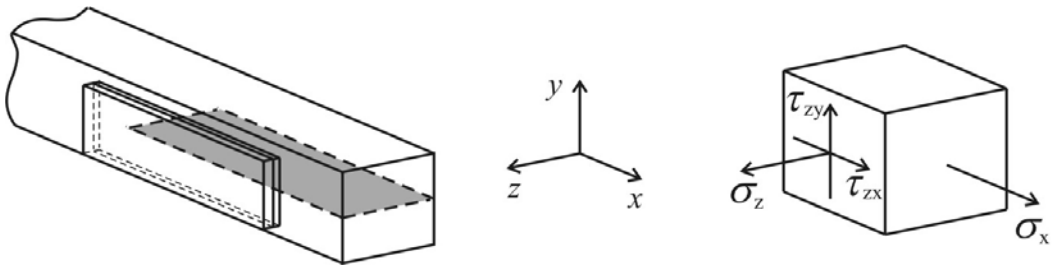

Fig. 472 – Stress components evaluated for the horizontal shear failure repair.

Fig. 473 shows the deformed shape of the L_P=45 mm repair. **For Fig. 473 and Fig. 474 only, the value of δ and magnification mentioned for these analyses were not employed, since the 50x amplification of the displacements would yield large interpenetrations at the wood beam cracked edge. In these figures, δ=15 mm was applied instead, without magnification.** σ_x stresses in the repair are initially presented to give an overall idea of these stresses (Fig. 474), which are induced by the bending of the beam, over the entire repair. The deformed configuration of the horizontal shear repair (Fig. 473) shows that the two beam arms at the cracked edge initiate contact with each other and relative sliding before the patch detachment.

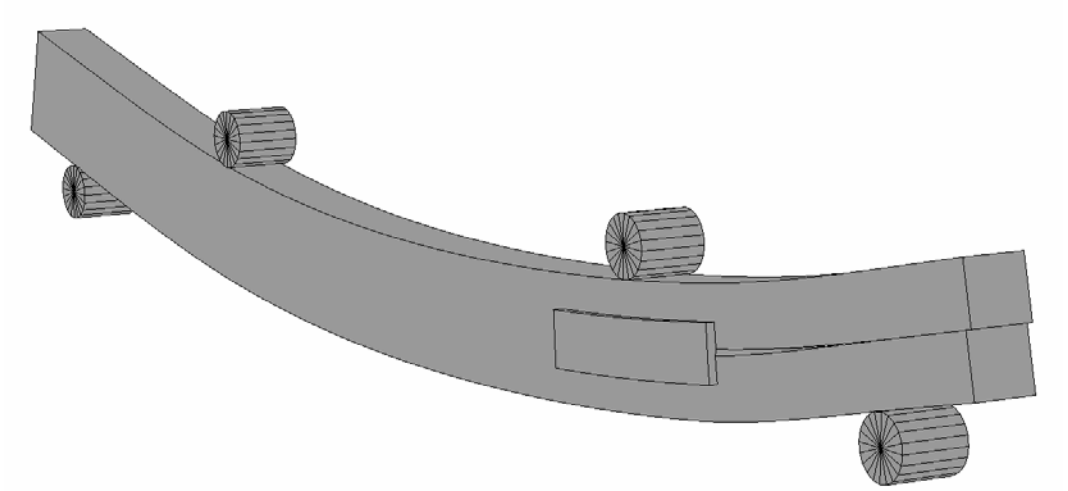

Fig. 473 – Deformed configuration of the horizontal shear failure repair under a bending load (L_P=45 mm repair).

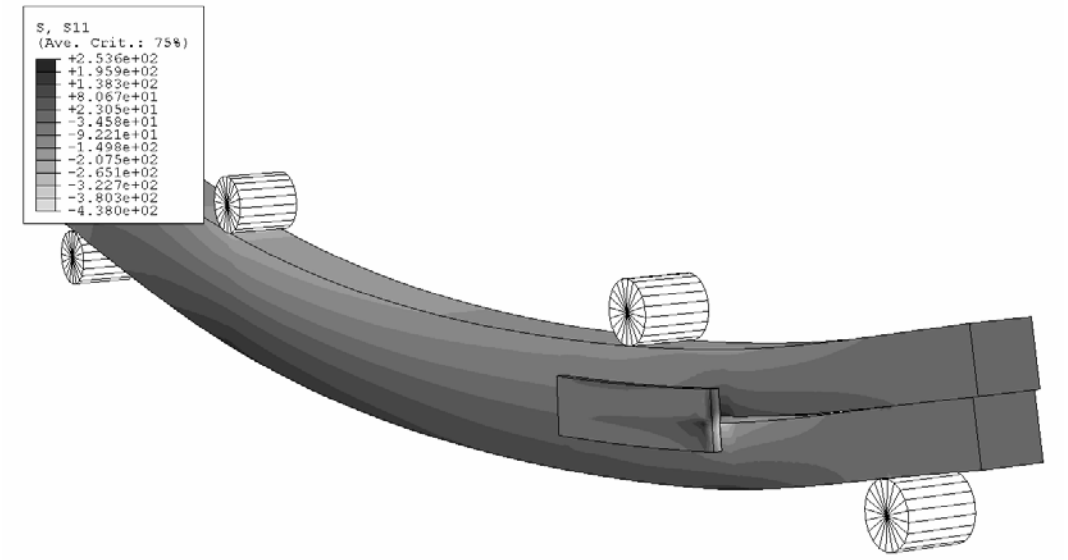

Fig. 474 – σ_x stresses at the repair region (L_P=45 mm repair).

σ_x stresses outside the repair region follow the expected behaviour of members under bending (Fig. 474), i.e., varying linearly in the thickness direction with the distance to the neutral axis (compressive stresses at its upper half and tensile ones at the lower half). σ_x stresses in the beam are smaller in magnitude near the patch, since at this region the loads are deviated to the patch. In the patch, σ_x stresses are approximately nil, except at its edge nearest to the cracked end of the beam (from this point addressed as *loaded edge*, for writing fluency purposes). At this region, stress perturbations emerge due to the deformations and shearing between the beam arms. The following figures illustrate the most significant stress components in the adhesive layer, expressed earlier in Fig. 472, considering the same repair orientation of Fig. 473 and Fig. 474. These include σ_z (Fig. 475), τ_{zx} (Fig. 476) and τ_{zy} (Fig. 477) stresses. It should be initially emphasized that σ_z, τ_{zx} and τ_{zy} stresses are approximately constant in the adhesive thickness direction in all the figures in this study, showing only minor variations near the patch loaded edge. σ_z stresses (Fig. 475) showed to be nearly nil in the adhesive layer, apart from its loaded edge, where σ_z peel stresses appear at the upper region of the adhesive, contrasting with σ_z compressive ones near the crack gap. Owing to this behaviour, eventual peel failures are likely to initiate at the loaded edge, either in the patch, in the adhesive or within the wood beam.

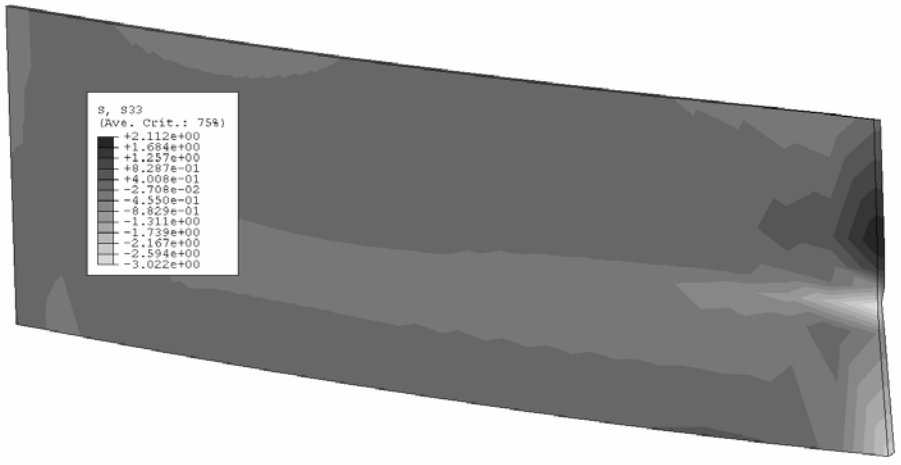

Fig. 475 – σ_z stresses at the repair region (L_P=45 mm repair).

τ_{zx} stresses in the adhesive layer (Fig. 476) emerge due to the shearing tendency between the upper and lower beam arms, being negligible in most of the adhesive layer, except at the loaded edge, where they peak near the crack gap. τ_{zx} shear stresses gradually diminish from the mentioned region towards the other edge of the adhesive layer, being approximately nil from roughly half the value of L_P. τ_{zy} stresses, on the other hand, appear due to the existence of the 1 mm gap between the wood beam arms, which tends to close due to the loading applied, causing vertical shear.

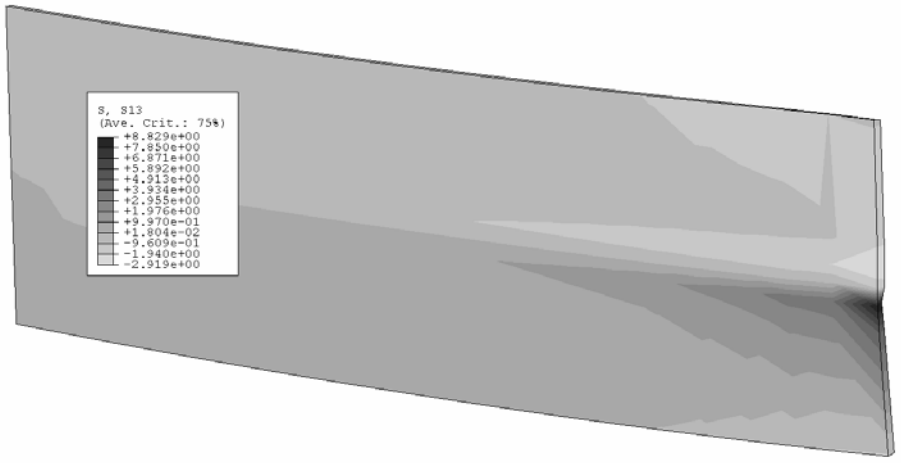

Fig. 476 – τ_{zx} stresses at the repair region (L_P=45 mm repair).

Oppositely to τ_{zx} stresses, τ_{zy} ones are more concentrated towards the loaded edge of the adhesive, peaking along all the lower half (Fig. 477). Near the upper beam arm, τ_{zy} stresses are smaller in magnitude. Comparing the stress magnitudes between τ_{zx} and τ_{zy} stresses, τ_{zy} stresses show slightly smaller values. The maximum values of σ_z peel stresses are less than 1/4 in magnitude compared to τ_{zx} peak stresses. Contrasting with this differences in magnitude, the locus of peak stresses is the same between the three stress components, i.e., at the loaded edge, suggesting that damage initiates at this region mostly by horizontal and vertical shear, with the prospect of propagation towards the other patch edge due to τ_{zx} stresses, followed by *RL* crack propagation initiating at the tip of the horizontal shear crack. This is deemed to occur when the patch is no longer capable of preventing the shearing between the two cracked arms and after the value of J_{IIc} of wood for *RL* propagation is attained at the crack tip.

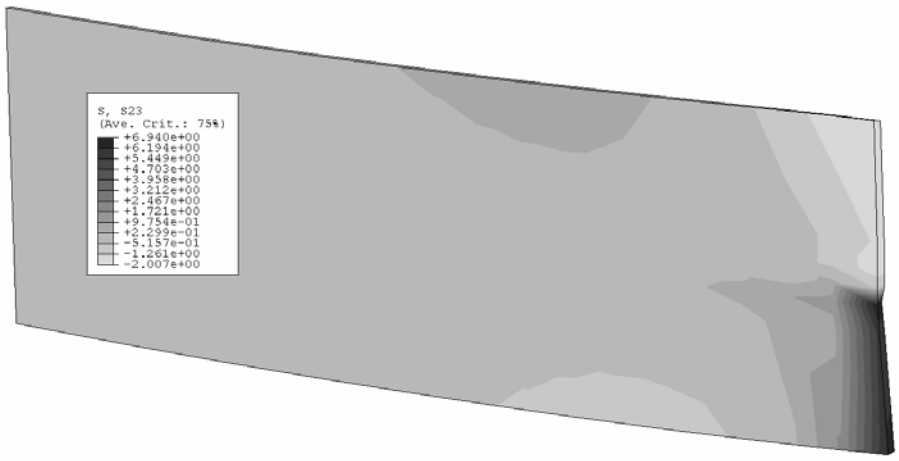

Fig. 477 – τ_{zy} stresses at the repair region (L_P=45 mm repair).

6.3.5.1.1. Patch length

A parametric study on L_P was performed for the horizontal shear failure repairs. The next figures show σ_z, τ_{zx} and τ_{zy} stresses in the adhesive layer for the L_P=75 and 105 mm repairs. Fig. 478 and Fig. 479 pertain to σ_z stresses, Fig. 480 and Fig. 481 to τ_{zx} stresses, and Fig. 482 and Fig. 483 to τ_{zy} stresses. These can be compared with the L_P=45 mm repairs stresses, presented previously in Fig. 475 (σ_z stresses), Fig. 476 (τ_{zx} stresses) and Fig. 477 (τ_{zy} stresses). σ_z stresses for the L_P=45 and 75 mm repairs (Fig. 475 and Fig. 478, respectively) present an analogous distribution in the adhesive layer, being approximately nil except at the loaded edge. At this region, as mentioned previously for the L_P=45 mm repair, σ_z peel stresses develop at the upper adhesive region, while at the lower region σ_z stresses are compressive and highest at the crack gap. In these repairs, the patches do not extend up to the supporting cylinder (Fig. 473 and Fig. 474), oppositely to the L_P=105 mm repair, where the patch attains the beam edge. Consequently, this last behaved differently (Fig. 479), with σ_z stress concentrations near the crack gap above the supporting cylinder (σ_z peel stresses at the lower beam arm region and compressive ones above the crack gap). Additionally, and opposing to the smaller L_P repairs, σ_z stresses also peak at the opposite edge of the adhesive layer, although at a very localized region. The magnitude of σ_z peak stresses diminishes gradually with L_P. τ_{zx} stresses are presented in Fig. 476, Fig. 480 and Fig. 481.

Fig. 478 – σ_z stresses at the repair region (L_P=75 mm repair).

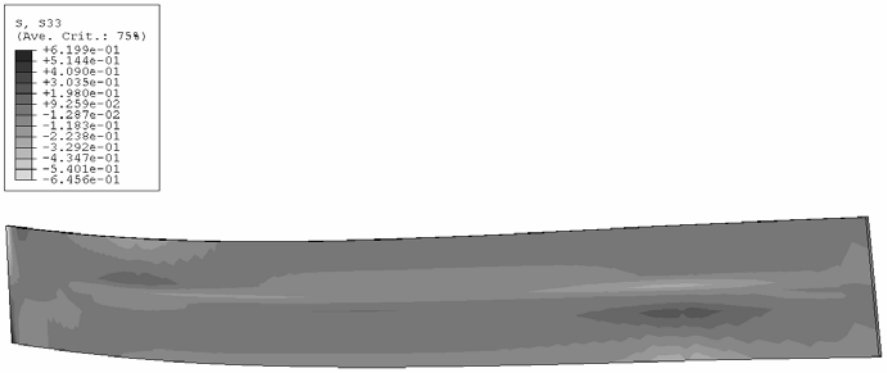

Fig. 479 – σ_z stresses at the repair region (L_P=105 mm repair).

The simulations show that τ_{zx} stresses in the adhesive layer behave similarly for the L_P=45 and 75 mm repairs. Thus, they are nearly nil in the adhesive layer, except at its loaded edge. At this region, τ_{zx} stresses at the lower beam arm peak near the crack gap. Conversely, for the L_P=105 mm repair, τ_{zx} stresses peak at both sides of the crack gap, extending from the tip of the horizontal shear crack to the supporting cylinder. These peak stresses are similar in magnitude at both sides of the crack gap. Outside this region, τ_{zx} stresses are approximately nil. τ_{zx} peak stresses also diminish progressively with the value of L_P, which is likely to increase the allowable value of δ sustained by the repair prior to failure in the adhesive layer, with the prospects of improving the repair strength.

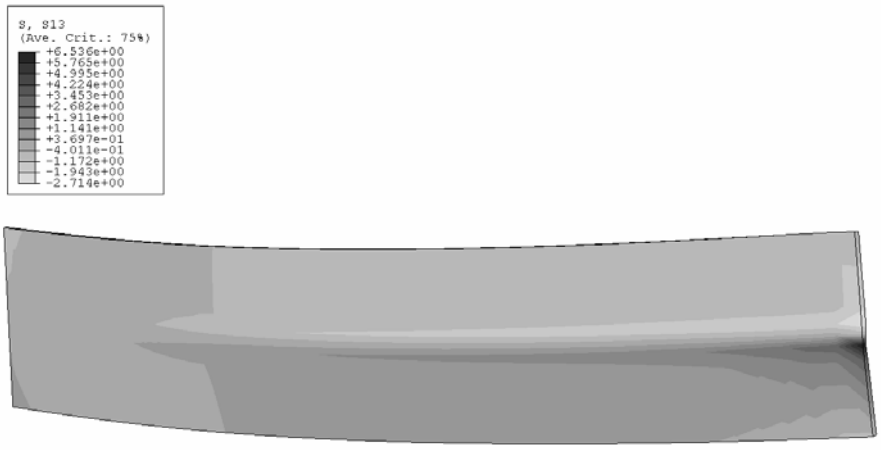

Fig. 480 – τ_{zx} stresses at the repair region (L_P=75 mm repair).

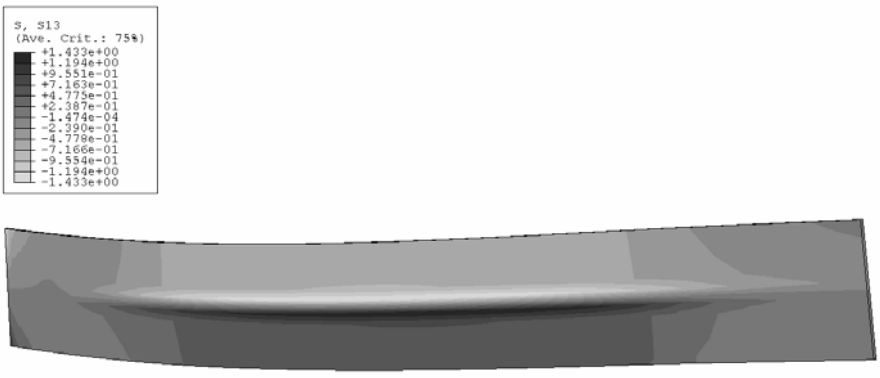

Fig. 481 – τ_{zx} stresses at the repair region (L_P=105 mm repair).

τ_{zy} stresses were also evaluated (Fig. 477, Fig. 482 and Fig. 483). For the L_P=45 and 75 mm repairs, these stresses concentrated at the loaded edge of the adhesive layer, peaking at its lower half. Following the global tendency of this stress analysis, for the L_P=105 mm repair, τ_{zy} peak stresses at the loaded edge disappear, giving rise to moderate τ_{zy} stresses above the supporting cylinder. The magnitude of τ_{zy} peak stresses slightly diminishes from the L_P=45 mm to the L_P=75 mm repair, being drastically reduced for the L_P=105 mm repair. In these repairs, damage is expected to initiate by an adhesive layer failure (or in the wood beam near the adhesive layer) due to the sliding between the beam arms, prior to damage propagation at the tip of the horizontal shear crack. The stress analysis conducted shows that P_m (hypothetically corresponding to damage initiation in the adhesive layer or near in the wood beam) is likely to increase with L_P, since all three stress components evaluated diminish progressively with this parameter. Additionally, bigger values of L_P increase the shearing resistant area between the two cracked arms of the wood beam.

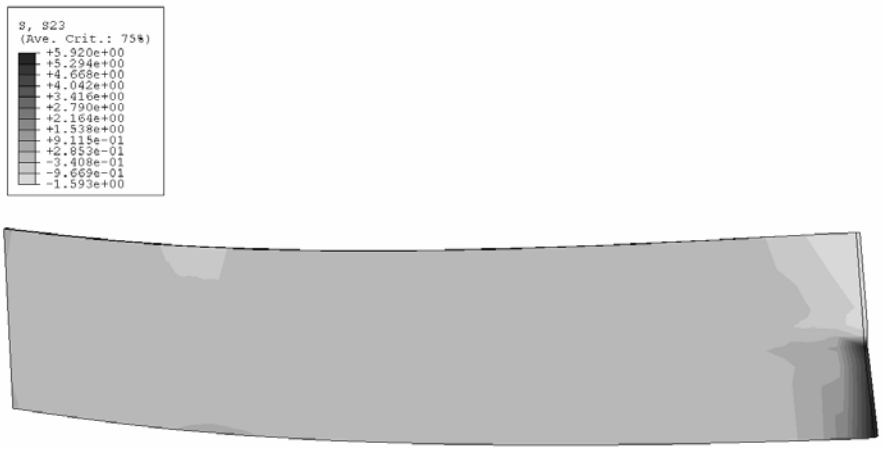

Fig. 482 – τ_{zy} stresses at the repair region (L_P=75 mm repair).

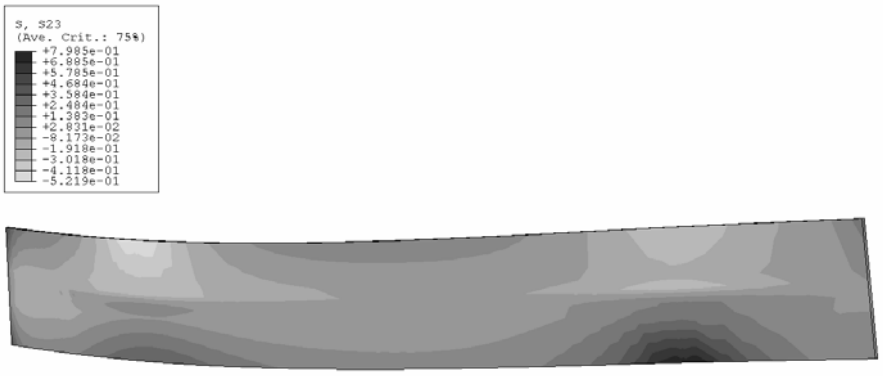

Fig. 483 – τ_{zy} stresses at the repair region (L_P=105 mm repair).

6.3.5.2. Failure analysis

6.3.5.2.1. Mechanical behaviour

This Sub-Section addresses the experimental and FEM fracture mechanisms of the repairs, including also the unrepaired beam, to ascertain the strength improvement of each repair.

- For the unrepaired beam, P_m is associated with extensive crack growth, initiating at the horizontal shear crack tip. Fig. 484 shows an unrepaired beam immediately before crack initiation (near P_m), where the vertical lines at the crack tip confirm the absence of sliding between the beam arms (a), and the same beam after crack propagation and the attainment of P_m (b). Even though crack growth is not clearly visible, which is characteristic of damage propagation in wood under shear (Corleto and Bradley 1989, O'Brien 1998, Silva et al. 2007), the vertical lines movement bears witness of this occurrence. Subsequently, the specimens still tolerated a relatively significant displacement under load before complete failure. Two different fractures were identified experimentally. Three specimens failed by tension at the lower beam arm (Fig. 485 a), whilst the other specimens, due to cross-graining between the loading cylinders, showed a cross-grain tension failure at the same region (Fig. 485 b).

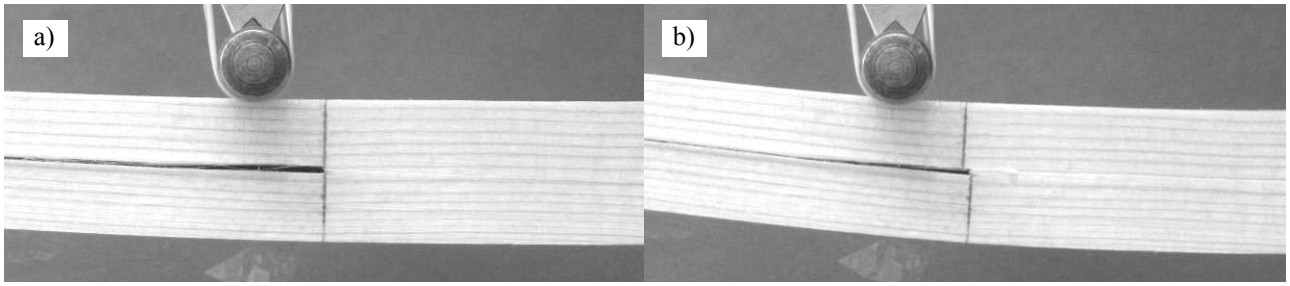

Fig. 484 – Unrepaired beam immediately before (a) and after crack propagation (b).

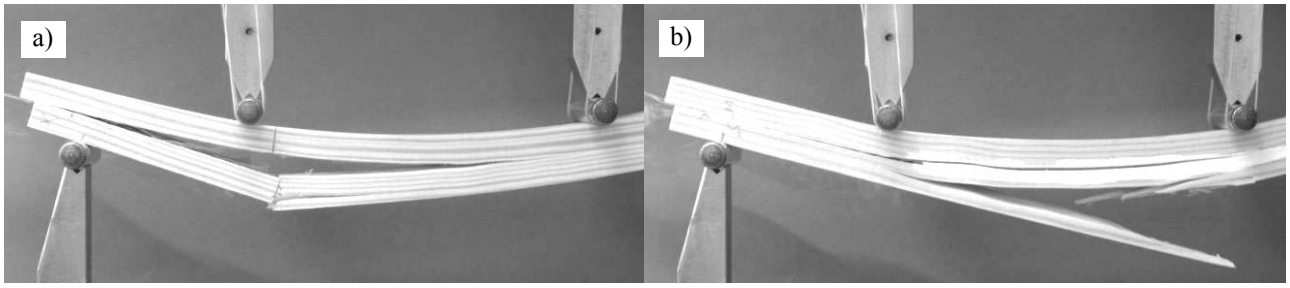

Fig. 485 – Tension failure of the lower beam arm (a) and cross-graining between the loading cylinders (b) for an unrepaired beam.

- All the L_P=45 mm repairs tested fractured identically, with a premature patch detachment prior to P_m at the loaded edge. This occurred either by a cohesive failure of the adhesive layer or by failure within the wood beam near the beam/adhesive interface, at the upper or lower beam arm regions. The locus of damage initiation is related to the regions of σ_z, τ_{zx} and τ_{zy} stress concentrations (respectively Fig. 475, Fig. 476 and Fig. 477). Fig. 486 (a) shows a L_P=45 mm repair immediately before sustaining the referred damage (the vertical line at the patch loaded edge can be used as a reference for the sliding between the patch and the upper beam arm). Fig. 486 (b) relates to the same specimen after failure within the wood beam at its upper arm. It should be emphasized that this damage mechanism occurred prior to P_m and simultaneously at the two patches, causing only a drop on P. Following, it continued to grow towards the horizontal shear crack tip as δ increased. After extensive patch damage, P_m was achieved similarly to the unrepaired beam, i.e., by crack propagation starting from the horizontal shear crack tip. Fig. 487 (a) represents a specimen after crack propagation almost up to the loading cylinder. Subsequently to this, the specimens still sustained loads prior to complete failure, either by

pure tension near the loading cylinders, propagating as a predominantly longitudinal crack between these cylinders (two specimens, Fig. 487 b) or by cross-graining between the loading cylinders (eight specimens).

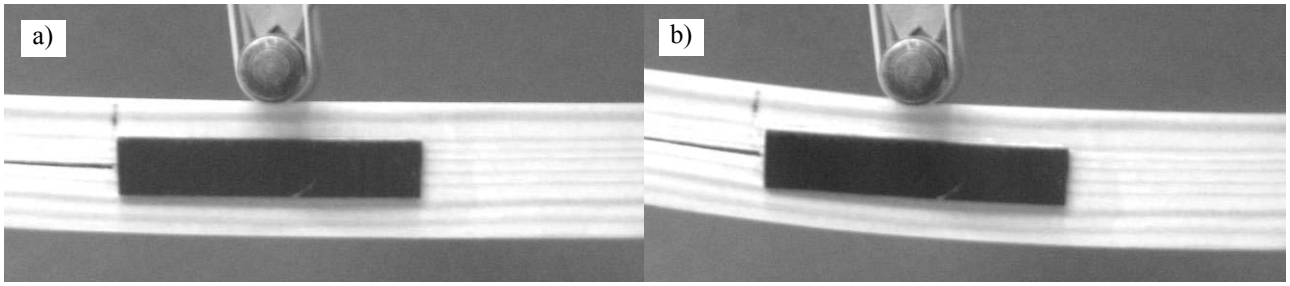

Fig. 486 – L_P=45 mm repair immediately before (a) and after patch detachment due to failure within the upper arm of the beam (b).

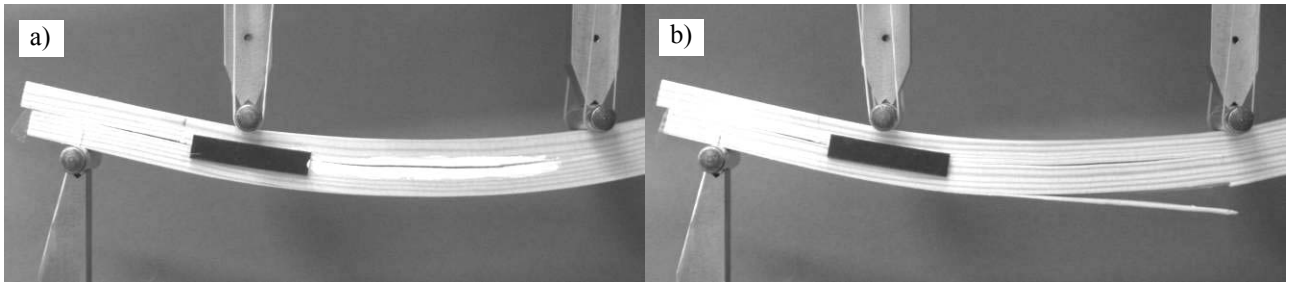

Fig. 487 – Crack propagation at the horizontal shear crack tip (a) and pure tension failure below a loading cylinder (b) for a L_P=45 mm repair.

- In the L_P=75 mm repairs, damage initiated due to a detachment of the patches at their loaded edge. Equally to the L_P=45 mm repairs, this occurred at the upper or lower beam arm regions by cohesive failure of the adhesive layer or failure within the wood beam, near the beam/adhesive interface, due to the peak stresses at this region (Fig. 478, Fig. 480 and Fig. 482). Fig. 488 concerns a cohesive failure of the adhesive layer at the upper beam arm (the upper beam arm and patch relative sliding is certified by the reference line). Damage was always simultaneous at the two patches, leading to P_m for six specimens, and only to an abrupt drop on P for the other ones, with P_m occurring after this event. The patches detached for values of P similar to the L_P=45 mm repairs, despite showing a smaller magnitude of stresses, as discussed in Sub-Section 6.3.5.1.1. The value of P then increased steadily up to crack propagation initiating at the tip of the horizontal shear crack (Fig. 489 a). This fracture resulted on a second drop of P. After carrying loads for a small value of δ, six specimens fractured by pure tension failure below one of the loading cylinders, followed by a typical longitudinal crack growth. The other specimens failed by cross-grain tension between the loading cylinders (Fig. 489 b).

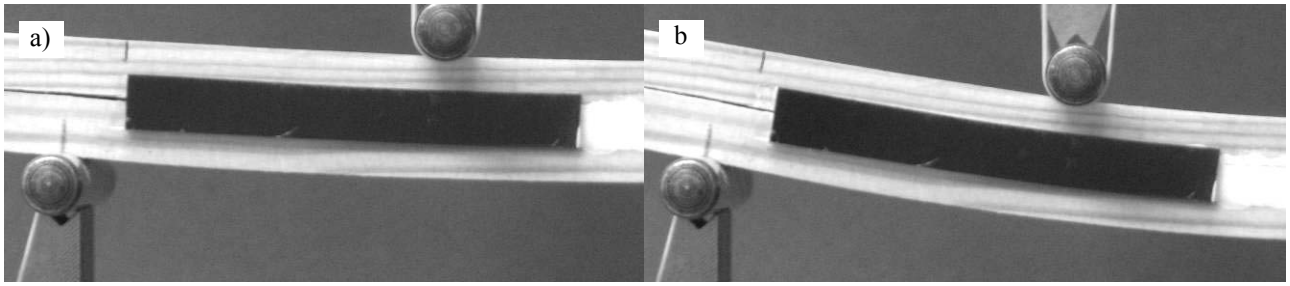

Fig. 488 – L_P=75 mm repair immediately before (a) and after patch detachment due to cohesive failure of the adhesive layer (b).

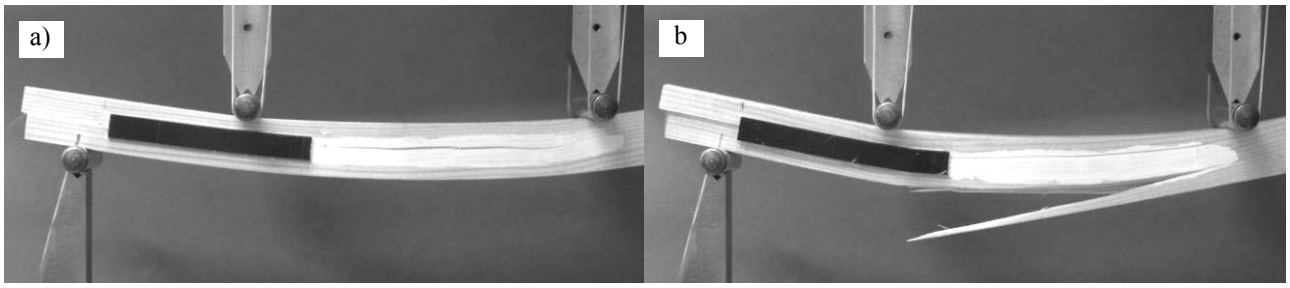

Fig. 489 – Crack propagation at the horizontal shear crack tip (a) and cross-graining between the loading cylinders (b) for a L_P=75 mm repair.

- For all the L_P=105 mm repairs, P_m was related to patch detachment at the upper or lower beam arm, by a cohesive failure of the adhesive layer or failure within the wood beam, near the beam/adhesive interface. This failure occurred abruptly from the repair edge to the vicinity of the loading cylinder (Fig. 490). This is consistent with the stress analysis performed, showing an identical magnitude of τ_{zx} stresses, which are the most significant stress component in the repair, between these two regions (Fig. 481). Fig. 490 portrays this scenario for a repair that suffered a cohesive failure of the adhesive layer at the upper beam arm region (the edge of the upper beam arm can be used as a reference to measure the sliding with the patch). Equally to the previous repairs analysed, this failure occurred simultaneously at the two patches. After sustaining loads for a typically small value of δ, a new drop on P followed due to a RL propagation from the horizontal shear crack tip (Fig. 491 a). Final failure for three specimens was due to pure tension below one of the loading cylinders, and by cross-graining between the loading cylinders, for seven specimens (Fig. 491 b).

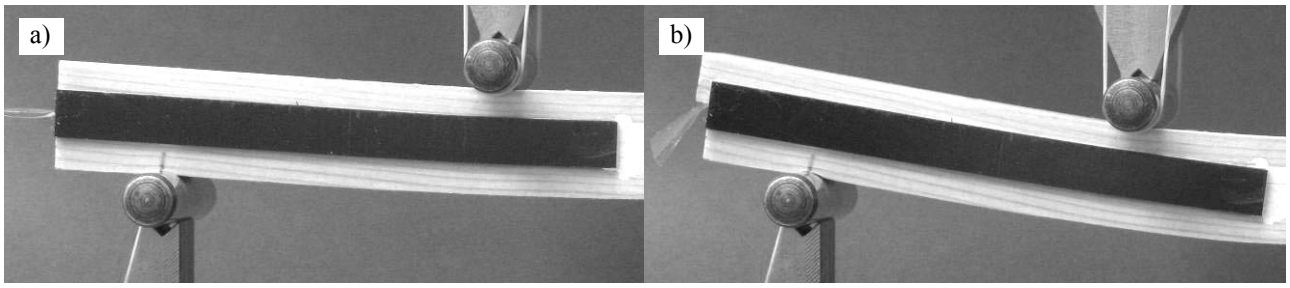

Fig. 490 – L_P=105 mm repair immediately before (a) and after patch detachment due to cohesive failure of the adhesive layer (b).

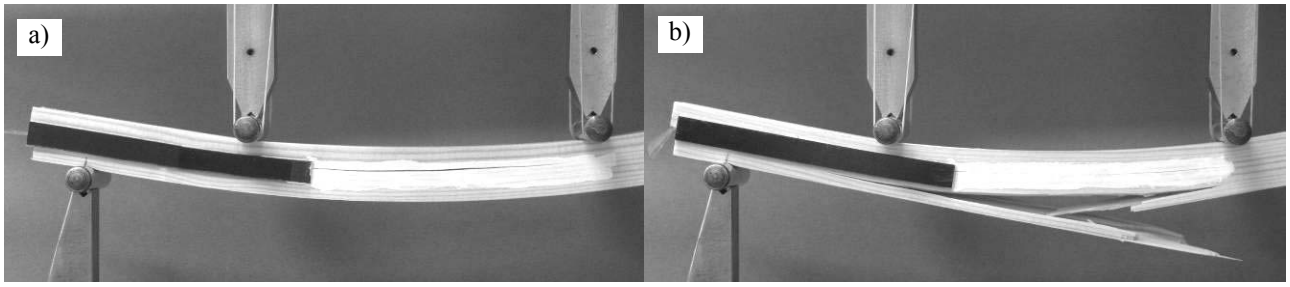

Fig. 491 – Crack propagation at the horizontal shear crack tip (a) and cross-graining between the loading cylinders (b) for a L_P=105 mm repair.

Prior to the description of the numerical failures, slight variations between the experimental and FEM fractures are acknowledged for some of the tested conditions. Though, this never compromised the accuracy of the

quantitative predictions of K, δ_m and P_m. Whilst no definitive conclusions could be drawn on the causes of this discrepancy, a probable justification is the elastic numerical idealization of the wood beam and CFRP patch, which prevented a localized plasticity at some regions. As already mentioned, the *LR* or cross-graining final fractures documented in the experiments were not addressed numerically.

- For the unrepaired beam, P_m was achieved due to a extensive *RL* propagation at the horizontal shear crack. Up to P_m, the beam behaved elastically. Fig. 492 represents the unrepaired beam before (a) and after *RL* crack propagation (b). This agrees with the experiments (Fig. 484 corresponds to a tested specimen immediately before crack initiation (a), and the same specimen after crack propagation (b)).

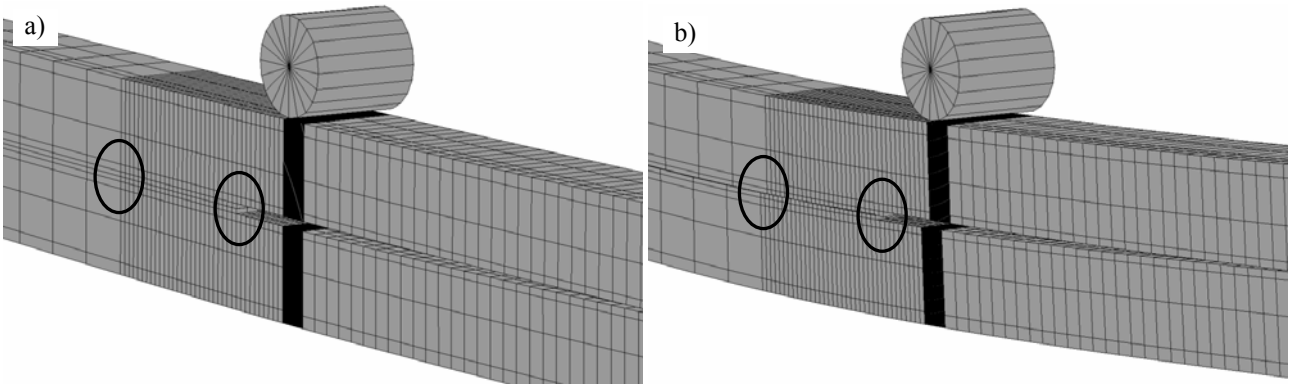

Fig. 492 – Numerical damage initiation (a) and growth (b) at the horizontal shear crack tip for the unrepaired beam.

- The L_O=45 mm repairs also fractured identically to the experiments. Thus, evidence of damage was found prior to P_m by patch debonding at the loaded edge (Fig. 493 a). After this, with the remaining of the bond still under load, P continued to increase up to P_m, occurring due to a complete debonding between the patch and the lower beam arm, concurrently with *RL* crack propagation starting at the tip of the horizontal shear crack (Fig. 493 b). **Although damage initiation at the tip of this crack cannot be clearly visualized, it can be testified by the sliding of the beam solid elements at the transition between the differently refined meshes (marked with a circle). This also applies to the subsequent repairs**. This damage sequence is consistent with the experimental observations (Fig. 486 relates to damage initiation at the patch loaded edge and Fig. 487 (a) to the P_m events, i.e., patch debonding and *RL* crack propagation).

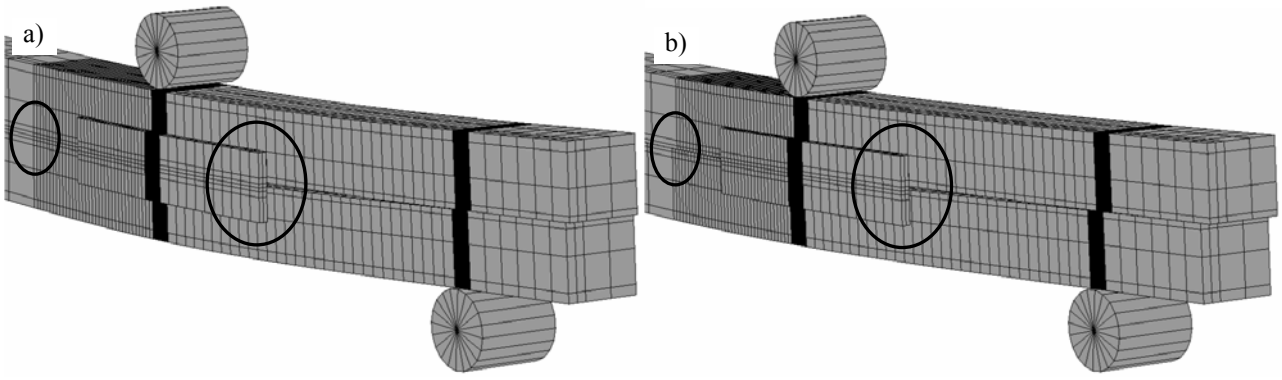

Fig. 493 – Numerical damage initiation at the adhesive loaded edge (a) and growth within the adhesive layer and by *RL* crack propagation (b) for the L_P=45 mm repair.

- The FEM analysis of the L_P=75 mm repairs showed a small deviation to the test results. In fact, the adhesive layer failed prematurely near its loaded edge, between the patch and the lower beam arm (Fig. 494 a). This resulted only on a small stiffness reduction in the P-δ curves. P_m was attained by an extensive cohesive failure of the adhesive layer between the patch and the lower beam arm, simultaneously with *RL* crack propagation initiating at the tip of the horizontal shear crack (Fig. 494 b). Recalling the experimental fracture, damage initiation and P_m were caused by a cohesive failure of the adhesive layer or failure within the wood beam between the patch and one of the beam arms, along practically all the patch length. The premature FEM failure at the loaded edge was not observed experimentally. The elastic idealization of the wood beam and patch is pointed out as the probable explanation, preventing local plasticization at the patch edge, hypothetically enough to avoid the premature failure. Added to this, in the experiments *RL* crack propagation (Fig. 489 a) took place only slightly after complete patch failure (Fig. 488 b). It should be emphasized that these small deviations did not yield a significant difference on the values of P_m and δ_m.

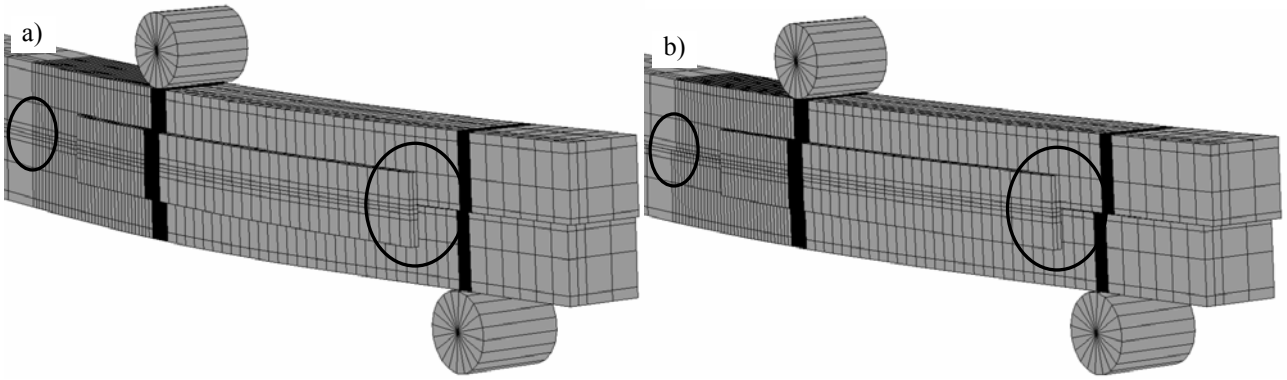

Fig. 494 – Numerical damage initiation at the adhesive loaded edge (a) and growth within the adhesive layer and by *RL* crack propagation (b) for the L_P=75 mm repair.

- The last repair (L_P=105 mm) showed numerically an abrupt cohesive failure of the adhesive layer between the patch and the lower beam arm, growing rapidly to all the extent of the patch (Fig. 495 a). This caused a drop of P_m, with final failure by *RL* propagation initiating at the horizontal shear crack (Fig. 495 b). The experiments showed equivalent results, with P_m relating to a cohesive fracture of the adhesive layer or failure within the wood beam (Fig. 490), followed by a subsequent drop of P due to *RL* propagation (Fig. 491 a).

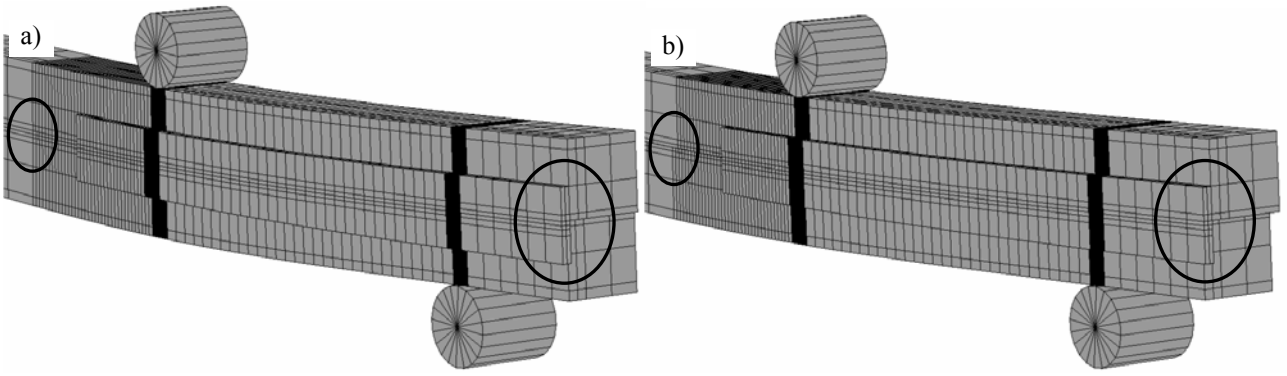

Fig. 495 – Numerical damage initiation extensively in the adhesive layer (a) and growth by *RL* crack propagation (b) for the L_P=105 mm repair.

Fig. 496 and Fig. 497 compare the experimental and numerical P-δ curves for the unrepaired and repaired beams. In these figures, the residual behaviour after *RL* crack propagation was discarded, since it was not considered relevant.

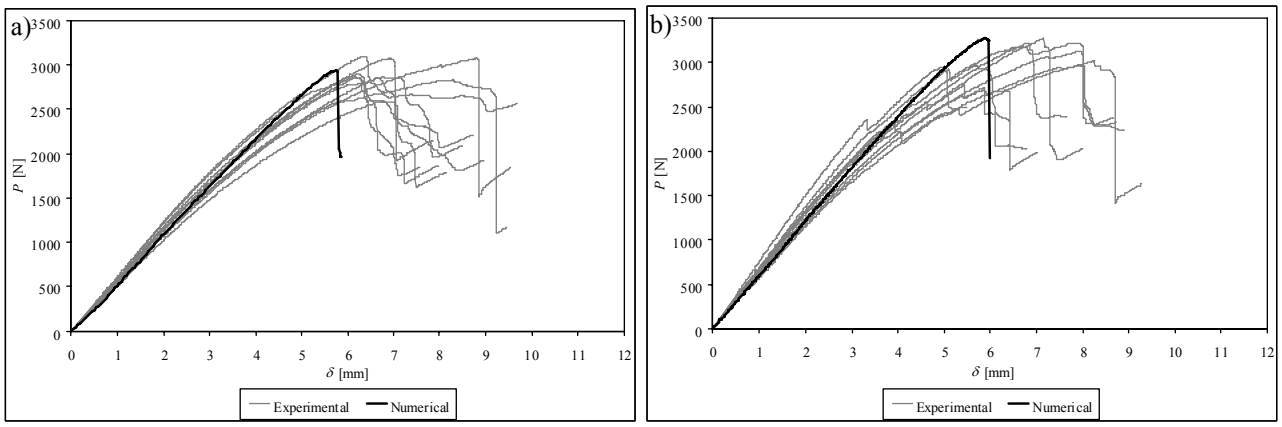

Fig. 496 – Experimental and numerical P-δ curves comparison for the unrepaired beam (a) and the L_P=45 mm repair (b).

- The unrepaired beam results (Fig. 496 a) showed to be in close agreement. In fact, for both the experiments and the simulations, P_m corresponded to extensive damage growth at the tip of the initial horizontal shear crack. This also applies to the values of K and δ_m, despite the slight underprediction of δ_m.
- The L_P=45 mm repairs also revealed an equivalent tendency between the tests and FEM analysis (Fig. 496 b), with a premature failure at the patch loaded edge. Numerically, this occurred progressively, without the abrupt drop on P observed in some of the tests at $\delta \approx 3.5$ mm. After this, P continued to increase until P_m, owing to a complete patch detachment by a cohesive failure of the adhesive layer or failure within the wood beam, concurrently with *RL* damage propagation initiating at the tip of the horizontal shear crack.

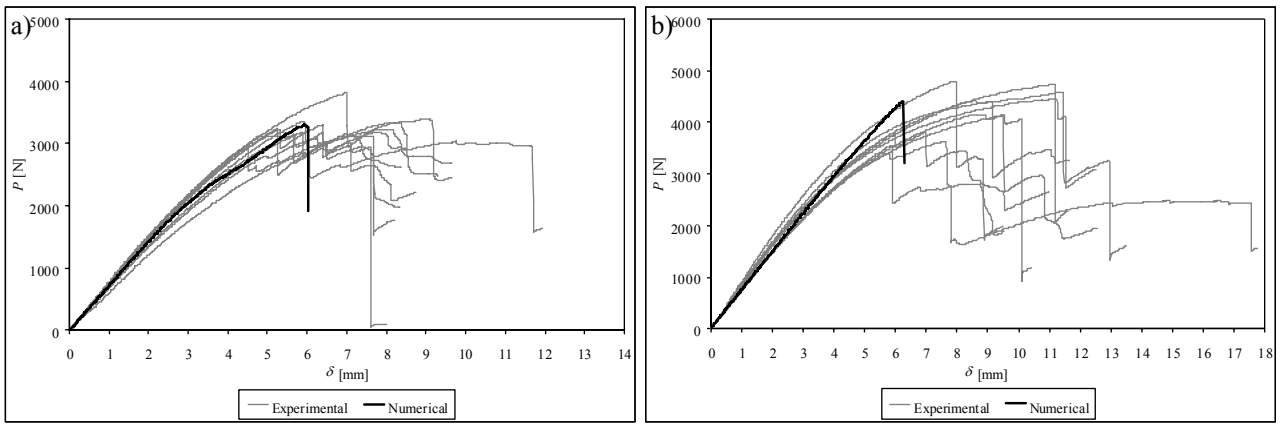

Fig. 497 – Experimental and numerical P-δ curves comparison for the L_P=75 mm (a) and L_P=105 mm (b) repairs.

- Some differences emerged on the L_P=75 mm repairs fractures (Fig. 497 a). As mentioned earlier, in the experiments no visible damage was detected up to P_m, which was related to a cohesive failure of the adhesive layer along the entire patch length or failure within the wood beam near the adhesive. In the simulations, a cohesive failure of the adhesive occurred at its loaded edge prior to P_m, leading to a substantial drop of the repair stiffness at $\delta \approx 4$ mm. In the experiments, P_m corresponded to a generalized patch detachment, with a subsequent *RL* failure. In the simulations, these two fractures were simultaneous.

- Fig. 497 (b) shows the good agreement between the tests and the FEM simulations of the L_P=105 mm repairs. In both cases, a global cohesive failure of the adhesive layer led to P_m, without previous evidence of damage. In the experiments, a few specimens failed within the wood beam. Following, another drop on P was detected due to a *RL* propagation near the mid-height of the beam, initiating at the horizontal shear crack tip.

6.3.5.2.2. Summary of the results

This Sub-Section summarizes the average results of the experimental tests with the respective deviations, and the corresponding FEM predictions. In the following figures, L_P=0 mm relates to the unrepaired beam. The predictions of K were fairly accurate (Fig. 498 a). Only for the L_P=0 mm repair the FEM value of K underpredicted the experiments. The increase of K with L_P was nearly linear from the L_P=0 mm to the L_P=105 mm repair, which is closely related to the increase of shear area between the patch and the beam arms. The value of K of the undamaged beam was attained with L_P=75 mm patches, with the L_P=105 mm repair exceeding this value. Following the results of the previous analyses in Section 6, some inconsistencies were found for the values of δ_m (Fig. 498 b), in this circumstances for the L_P=105 mm repair and the undamaged beam. For the other test configurations, including the unrepaired beam, the numerical predictions were accurate. This deviation follows the analyses of the previously studied repairs, being related with wood indentation initiating at P=2000-2500 N and being particularly significant for P>4000 N. Numerically, the elastic orthotropic idealization of the wood beams averted this occurrence. Given that the unrepaired beam and the L_P=45 and 75 mm repairs did not exceed the indentation initiation value of P by a significant amount, the predictions of δ_m for these beam configurations were reasonably accurate. This can be visualized contrasting the experimental P-δ plots of the unrepaired beam (Fig. 496 a), for which indentation was negligible, with the L_P=105 mm repair ones (Fig. 497 b), which present a minor reduction of stiffness at P≈2500 N, and noticeable indentation at P≈4000 N.

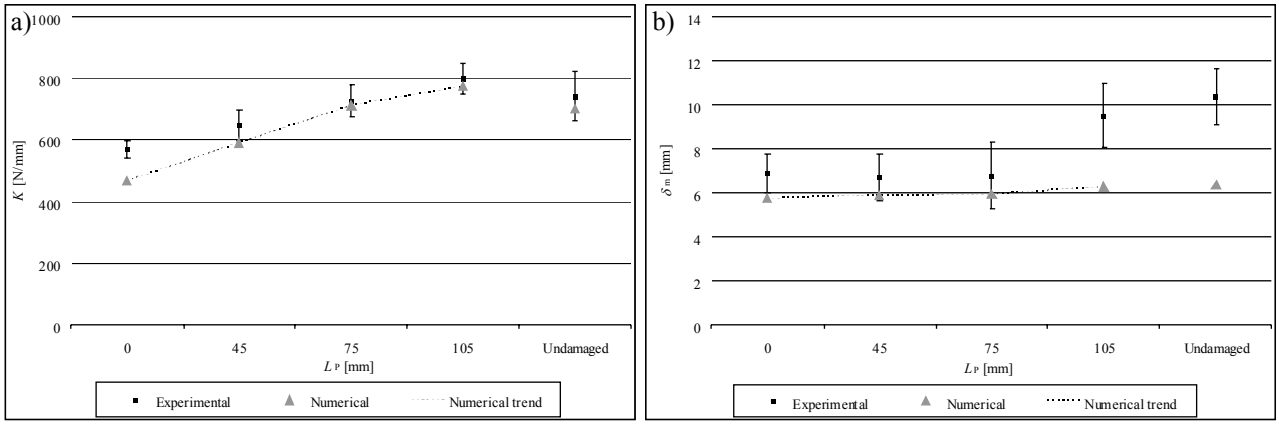

Fig. 498 – K as a function of L_P (a) and δ_m as a function of L_P (b).

The predictions of P_m and the corresponding experimental average values and deviations are compared in Fig. 499. The accurate predictions obtained confirm the suitability of the FEM methodology followed in this work. These results show an approximate 30% reduction of P_m inducing the horizontal shear crack in the specimens, and also that the L_P=45 and 75 mm repairs practically do not affect the value of P_m. This is related to two different scenarios. For the L_P=45 mm repair, a cohesive failure of the adhesive layer occurs prematurely to P_m, yielding the repair behaviour identical to an unrepaired beam. On the other hand, for the L_P=75 mm repair, P_m is related to patch detachment, which occurs at a

value of P near P_m for the unrepaired beam. Consequently, no significant improvement is attained. Oppositely, the L_P=105 mm repair led to a significant strength improvement, with P_m approaching the undamaged beam strength. Actually, under this configuration the patch prevented the sliding of the beam arms and consequent failure by *RL* propagation up to near the value of P_m of the undamaged beam. The experimental scatter of these results is justified mainly by variations on wood properties (Malan et al. 1988a, Malan et al. 1988b, Downes et al. 1997, Bao et al. 2001, Baillères et al. 2005). **A repair technique was projected for beams damaged by horizontal shear, being considered appropriate to restore the undamaged beam strength. For the particular materials and dimensions employed, this is accomplished with a L_P=105 mm repair. Smaller values of L_P, up to 75 mm, were found to be ineffective in increasing the unrepaired beam strength, due to patch detachment for values of P smaller or of the same order of magnitude than the unrepaired beam strength**.

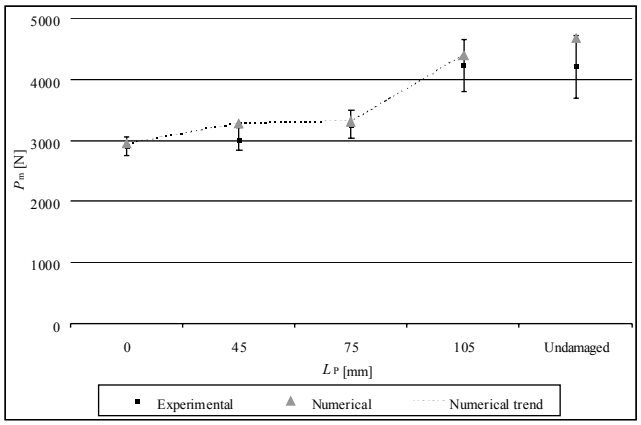

Fig. 499 – P_m as a function of L_P.

7. CONCLUDING REMARKS AND FUTURE WORK

In this dissertation, a comprehensive experimental and numerical study was performed on the repair of carbon-epoxy and wood structures, using carbon-epoxy patches. This is an extremely important topic owing to the increasing use of these composite materials in many applications. A state-of-the-art review on the different topics investigated is initially presented, for a broader understanding of the issues discussed, allowing also a clear insight on the contribution of this work to the current state of affairs. One of main objectives of this thesis consisted on the development of a numerical methodology, using the Finite Element Method, to predict the mechanical behaviour of bonded assemblies (either joints or repairs), allowing their full fracture characterization. This technique aims the reduction of costs and time associated to extensive experimentation, provided that an extensive validation is performed under all scenarios prone to emerge in bonded assemblies. This investigation is particularly meaningful for the adhesively-bonded repairs of wood members, for which no accurate predictive tools are yet available to the designer. Particular emphasis was paid to the development of a trapezoidal mixed-mode (I+II+III) cohesive damage model to simulate ductile adhesive layers. Actually, most structural adhesives used nowadays endure extensive plasticization in tension and shear after a predominantly elastic region, which is characterized by an approximately constant magnitude of stresses. The cohesive laws in pure modes I and II for the ductile adhesive used in this work were derived by an inverse data fitting procedure. For the three-dimensional simulations, the pure mode III cohesive parameters were equalled to the corresponding pure mode II values, as an approximation. The interlaminar and intralaminar fracture characterization of the composite used in this work as damaged structure or patch was also performed using the inverse technique.

A comprehensive parametric investigation of adhesively-bonded repairs on composite structures was carried out under tensile, compressive and four-point bending loadings, allowing the establishment of design guidelines for repairing. Carbon-epoxy laminates were repaired by the single and double-strap techniques (three-dimensional configuration), and the scarf technique (two-dimensional approximation). The overlap length and patch thickness (strap repairs) or scarf angle (scarf repairs) were the evaluated parameters for the composite repairs. An experimental and Finite Element investigation was carried out, to concurrently validate the proposed numerical technique under a broad variety of test conditions and mode-mixities, prone to emerge in structural applications. Preliminary validations were performed with parametric studies on two-dimensional single-strap repairs and single-lap joints under tension. Whilst in the first study, a different adhesive was used, whose cohesive properties were established based on the adhesive bulk characterization and a few approximations, the single-lap joints were simulated applying the inverse principles. The most important guidelines for repairing of carbon-epoxy structures on the different test conditions addressed are initially described, being emphasized their particular character to the specific set of testing, material and dimensional conditions selected. This applies globally to the conclusions presented in this Section.

- The **strap repairs under tension** showed a rather peculiar behaviour, with small overlaps diminishing the open-hole laminate strength, owing to the introduction of stresses in the laminate originating premature axial splitting of the outer load-oriented plies. Bigger overlaps were effective in increasing the damaged strength. Single-strap repairs were always ineffective under tension.
- **Under buckling unrestrained compression and also in bending, strap repairs** showed identical tendencies. Actually, single-strap repairs conceded only marginally improved the damaged strength, for all conditions tested. Double-strap repairs displayed a proportional increase of strength with the overlap length and an identical strength improvement for all values of patch thickness evaluated.
- The strength of **scarf repairs under tension and bending** grows exponentially with the reduction of the scarf angle. Under tension, this could be easily anticipated from the corresponding increase on the adhesive shear area. Under bending, the increase is exponential up to 3º, being kept nearly constant further reducing the scarf angle. The global trend is due to the reduction of bending stiffness with the reduction of the scarf angle, diminishing the magnitude of stresses at the critical regions of the repairs.
- Oppositely, the behaviour of **scarf repairs under buckling unrestrained compression** is ruled by the repairs stiffness rather than the strength of their constituents. A slight increasing trend was found with the reduction of the scarf angle up to 3º, following a substantial drop to the 2º scarf angle repair.

Prior to the study on wood repairs, a purely Finite Element study on geometric changes was carried out on single and double-strap repairs under the three loadings, attempting the maximization of their strength characteristics. Some of the geometric modifications regarded in the literature to increase the repairs strength were addressed, such as patch outer and inner chamfering, laminate outer and inner chamfering, adhesive filleting at the overlap outer edge and plug filling the repair hole with adhesive. Substantial strength improvements were attained.

- For the **single-strap repairs**, the best results were achieved under bending, being the patch outer and inner chamfering and filleting at the overlap outer edge the most efficient geometric changes. Different combinations led to 27.7, 6.8 and 58.3% strength improvements under tension, compression and bending, respectively.
- The patch outer and inner chamfers and the fillet were the most effective modifications for the **double-strap repairs**. Strength improvements of 21.4, 26.0 and 12.2% were achieved under tensile, compressive and bending loads, respectively, combining different geometric changes.

Repair solutions were also proposed for wood members under bending after sustaining three of the most common damage mechanisms found in large-scale wood structures, defined based on an extensive literature research. The parametric study performed focused on the overlap or patch length. The suitability of the proposed Finite Element methodology for the prediction of fracture and strength of these assemblies was also tested. The simulations included the possibility of wood failure in two propagation planes, in addition to interlaminar patch failure and cohesive failure of the adhesive layer. The damage mechanisms are individually addressed.

- For the **repairs damaged by compression**, the proposed repair methodology can be extended to other types of damage such as knots or human intervention. The irrelevance in repairing with short overlaps was exposed, due to patch detachment prior to the attainment of the damaged beam strength. The undamaged strength of the beam is re-established for bigger overlaps.

- The proposed repair method for the **cross-grain tension damage**, emerging from the misalignment of the wood fibres, showed to be effective in restoring the undamaged beam strength for the largest value of patch length evaluated, with an approximately proportional strength to the patch dimensions.
- **Horizontal-shear damage** was also studied. The repair consisted on adhesive-bonding of plates to obstruct sliding between the cracked arms. The smaller values of patch length tested were found to be worthless in increasing the damaged beam strength, owing to failure of the patches for loads smaller or of identical magnitude than the damaged beam. The biggest value of patch length fully restored the beam strength.

The overall results of this dissertation show that, despite introducing several possibilities in the numerical models, these were always accurate in modelling the repairs fracture behaviour. The precise quantitative predictions of the repairs elastic stiffness, maximum load and corresponding displacement, as well as other parameters defined by the characteristics of each technique/loading combination, certify the suitability of the proposed methodology in simulating the fracture behaviour of bonded assemblies. Thus, a good perspective emerges for a quicker design and reduction of costs due to extensive experimental characterization.

A few guidelines are also presented for possible continuation of these subjects, expanding the application of this predictive tool for a broader range of applications. In fact, this work comprehensively validated this technique under varying conditions and loadings, but was restricted to the quasi-static behaviour of bonded assemblies. On the other hand, real structural applications are hardly limited to static loadings during their service life, with high prospects of enduring other kinds of loads, such as fatigue, either by regular operation (aeronautic, aerospace and automotive carbon-epoxy structures), by moving loads (vehicles in wood bridges) or earthquakes, amongst many other scenarios.

- The **development of cohesive laws** to conform with material behaviours other than brittle or perfectly-plastic would expand the use of the proposed Finite Element technique to different materials.
- With the same purpose, modification of the cohesive elements formulation to **include friction effects** under compression after failure, would allow a more accurate characterization of fracture in particular applications showing sliding after failure.
- The extension of the proposed Cohesive Zone Model for the **simulation of fatigue loadings** cannot be forgotten, constituting an extremely important field of application of real structures and industry appliances, entailing also quite a challenge.
- In this work, results were regarded as independent of viscoelastic effects. Actually, based on literature results, neglecting of these questions does not compromise the accuracy of results for quasi-static loadings. Nevertheless, this discussion brings up the issue of **simulation of creep and high speed/impact loadings**, with particular emphasis on cohesive properties, whose characteristic features are still not fully understood.
- Transversely to these issues, the **creation of a database from the inverse characterization** of a wide range of structural adhesives and component materials under the different propagation planes (in the case of orthotropic materials) would also reduce the time needed to design bonded assemblies with different characteristics.
- The perception of the **influence of temperature and humidity effects** on the component materials and adhesive properties could permit an extension of the applications to be simulated. For these particular conditions, the suitability of the proposed cohesive laws shape would require verification.

8. REFERENCES

- **(Achour et al. 2003)** Achour T, Bouiadjra BB, Serier B. Numerical analysis of the performances of the bonded composite patch for reducing stress concentration and repairing cracks at notch. Computational Materials Science 2003;28:41-48.
- **(Adams 1989)** Adams RD. Strength predictions for lap joints, especially with composite adherends. A review. The Journal of Adhesion 1989;30:219-242.
- **(Adams and Comyn 2000)** Adams RD, Comyn J. Joining using adhesives. Assembly Automation 2000;20:109-117.
- **(Adams and Harris 1987)** Adams RD, Harris JA. The influence of local geometry on the strength of adhesive joints. International Journal of Adhesion & Adhesives 1987;7:69-80.
- **(Adams and Peppiatt 1974)** Adams RD, Peppiatt NA. Stress analysis of adhesive-bonded lap joints. Journal of Strain Analysis 1974;9:185-196.
- **(Adams and Wake 1984)** Adams RD, Wake WC. Structural adhesive joints in engineering. Elsevier Applied Science: London, UK; 1984.
- **(Adams et al. 1986)** Adams RD, Atkins RW, Harris JA, Kinloch AJ. Stress Analysis and Failure Properties of Carbon-Fibre-Reinforced-Plastic/Steel Double-Lap Joints. The Journal of Adhesion 1986;20:29-53.
- **(Adams et al. 1997)** Adams RD, Comyn JC, Wake WC. Structural adhesive joints in engineering. Second Edition. Chapman & Hall: London, UK; 1997.
- **(Adkins and Pipes 1988)** Adkins DW, Pipes RB. Tensile behaviour of bonded scarf joints between composite adherends. Proceedings of the Fourth Japan–US Conference on Composite Materials. Washington DC, USA. 27-29 June 1988.
- **(Ahn and Springer 1998a)** Ahn SH, Springer GS. Repair of composite laminates-I: test results. Journal of Composite Materials 1998;32:1036-1074.
- **(Ahn and Springer 1998b)** Ahn SH, Springer GS. Repair of composite laminates-II: models. Journal of Composite Materials 1998;32:1076-1114.
- **(Ahn et al. 1996)** Ahn SH, Springer GS, Shyprykevich P. Composite repair with wet lay-up and prepreg. Proceedings of Composites '96-Manufacturing and Tooling Conference. Anaheim, USA. 22-24 January 1996.
- **(Aicher et al. 1998)** Aicher S, Wolf M, Dill-Langer G. Heat flow in a glulam joist with a GISR subjected to variable ambient temperature. Otto Graf Journal 1998;9:185-204.
- **(Akbiyik 2005)** Akbiyik A. Feasibility investigation into shear repair of timber bridge stringers. M.Sc. Thesis. New Orleans, USA: Department of Civil and Environmental Engineering, Tulane University: 2005.
- **(Akbiyik et al. 2007)** Akbiyik A, Lamanna AJ, Hale WM. Feasibility investigation of the shear repair of timber stringers with horizontal splits. Construction and Building Materials 2007;21:991-1000.
- **(Akhras and Foo 1993)** Akhras G, Foo SHC. Inspection and repair of timber warren truss building using knowledge-based approach with graphics. Structures and Buildings 1993;99:429-438.

- **(Alam et al. 2009)** Alam P, Ansell MP, Smedley D. Mechanical repair of timber beams fractured in flexure using bonded-in reinforcements. Composites: Part B – Engineering 2009;40:95-106.
- **(Alfano 2006)** Alfano G. On the influence of the shape of the interface law on the application of cohesive-zone models. Composites Science and Technology 2006;66:723-730.
- **(Alfano and Crisfield 2001)** Alfano G, Crisfield MA. Finite element interface models for the delamination analysis of laminated composites: Mechanical and computational issues. International Journal for Numerical Methods in Engineering 2001;50:1701-1736.
- **(Allix and Corigliano 1996)** Allix O, Corigliano A. Modeling and simulation of crack propagation in mixed-modes interlaminar fracture specimens. International Journal of Fracture 1996;77:111-140.
- **(Allix et al. 1995)** Allix O, Ladeveze P, Corigliano A. Damage analysis of interlaminar fracture specimens. Composite Structures 1995;31:61-74.
- **(Allman 1977)** Allman DJ. A theory for elastic stresses in adhesive bonded lap joints. Quarterly Journal of Mechanics and Applied Mathematics 1977;30:415-436.
- **(Anderson and Trahair 1972)** Anderson JM, Trahair NS. Stability of monosymmetric beams and cantilevers. ASCE Journal of the Structural Division 1972;98:269-286.
- **(Anderson et al. 1988)** Anderson GP, Brinton SH, Ninow KJ, DeVries KL. A fracture mechanics approach to predicting bond strength. Proceedings of the Advances in Adhesively-Bonded Joints, Winter Annual Meeting. Chicago, USA. 28 November-2 December 1988.
- **(Andersson and Biel 2006)** Andersson T, Biel A. On the effective constitutive properties of a thin adhesive layer loaded in peel. International Journal of Fracture 2006;141:227-246.
- **(Andersson and Stigh 2004)** Andersson T, Stigh U. The stress-elongation relation for an adhesive layer loaded in peel using equilibrium of energetic forces. International Journal of Solids and Structures 2004;41:413-434.
- **(Andreassi et al. 2007)** Andreassi L, Baudille R, Biancolini ME. Spew formation in a single lap joint. International Journal of Adhesion & Adhesives 2007;27:458-468.
- **(Andrews et al. 1993)** Andrews SD, Ochoa OO, Owens SD. The effect of fastener hole defects. Journal of Composite Materials 1993;27:2-20.
- **(Andruet et al. 2001)** Andruet RH, Dillard DA, Holzer SM. Two- and three-dimensional geometrical nonlinear finite elements for analysis of adhesive joints. International Journal of Adhesion & Adhesives 2001;21:17-34.
- **(Apalak and Engin 2004)** Apalak MK, Engin A. Effect of adhesive free-end geometry on the initiation and propagation of damaged zones in adhesively bonded lap joints. Journal of Adhesion Science and Technology 2004;18:529-559.
- **(Apalak and Gunes 2005)** Apalak MK, Gunes R. Investigation of elastic stresses in an adhesively bonded single lap joint with functionally graded adherends in tension. Composite Structures 2005;70:444-467.
- **(Apalak and Gunes 2007)** Apalak MK, Gunes R. Elastic flexural behaviour of an adhesively bonded single lap joint with functionally graded adherends. Journal of Materials and Design 2007;28:1597-1617.
- **(Ashcroft et al. 2000)** Ashcroft IA, Hughes DJ, Shaw SJ. Adhesive bonding of fibre reinforced polymer composite materials. Assembly Automation 2000;20:150-161.

- **(Ashcroft et al. 2001)** Ashcroft IA, Abdel Wahab MM, Crocombe AD, Hughes DJ, Shaw SJ. The effect of environment on the fatigue of bonded composite joints. Part I: testing and fractography. Composites: Part A – Applied Science and Manufacturing 2001;32:45-58.
- **(Avent 1985)** Avent RR. Decay, weathering and epoxy repair of timber. ASCE Journal of Structural Engineering 1985;111:328-342.
- **(Avent 1986)** Avent RR. Design criteria for epoxy repair of timber structures. ASCE Journal of Structural Engineering 1986;112:222-240.
- **(Ávila and Bueno 2004a)** Ávila AF, Bueno PO. An experimental and numerical study on adhesive joints for composites. Composite Structures 2004;64:531-537.
- **(Ávila and Bueno 2004b)** Ávila AF, Bueno PO. Stress analysis on a wavy-lap bonded joint for composites. International Journal of Adhesion & Adhesives 2004;24:407-414.
- **(Awerbuch and Madhukar 1985)** Awerbuch J, Madhukar MS. Notched strength of composite laminates; prediction and Experiments – a review. Journal of Reinforced Plastics and Composites 1985;4:3-159.
- **(Bader et al. 2000)** Bader MG, Hamerton I, Hay JN, Kemp M, Winchester S. Double cantilever beam of repaired carbon fibre composites. Composites: Part A – Applied Science and Manufacturing 2000;31:603-608.
- **(Bahei-El-Din and Dvorak 2001)** Bahei-El-Din YA, Dvorak GJ. New designs of adhesive joints for thick composite laminates. Composites Science and Technology 2001;61:19-40.
- **(Baillères et al. 2005)** Baillères H, Vitrac O, Ramananantoandro T. Assessment of continuous distribution of wood properties from a low number of samples: application to the variability of modulus of elasticity between trees and within a tree. Holzforschung 2005;59:524-530.
- **(Bair et al. 1991)** Bair DL, Hudson PO, Ghanimati GR. Analysis and repair of damaged composite laminates. Proceedings of the 36th International SAMPE Symposium. San Diego, USA. 15-18 April 1991.
- **(Baker and Hatt 1973)** Baker RM, Hatt F. Analysis of bonded joints in vehicular structures. AIAA Journal 1973;11:1650-1654.
- **(Baker et al. 1999)** Baker AA, Chester RJ, Hugo GR, Radtke TC. Scarf repairs to highly strained graphite/epoxy structure. International Journal of Adhesion & Adhesives 1999;19:161-171.
- **(Baker et al. 2004)** Baker W, McKenzie I, Jones R. Development of life extension strategies for Australian military aircraft, using structural health monitoring of composite repairs and joints. Composite Structures 2004;66:133-143.
- **(Bakis et al. 2002)** Bakis CE, Bank LC, Brown VL, Cosenza E, Davalos JF, Lesko JJ, Machida A, Rizkalla SH, Triantafillou TC. Fiber-reinforced polymer composites for construction – State-of-the-art review. Journal of Composites for Construction 2002;6:73-87.
- **(Balkova et al. 2002)** Balkova R, Holcnerova S, Cech V. Testing of adhesives for bonding of polymer composites. International Journal of Adhesion & Adhesives 2002;22:291-295.
- **(Bao et al. 2001)** Bao FC, Jiang ZH, Jiang XM, Lu XX, Luo XQ, Zhang SY. Differences in wood properties between juvenile wood and mature wood in 10 species grown in China. Wood Science and Technology 2001;35:363-375.
- **(Barenblatt 1962)** Barenblatt GI. The mathematical theory of equilibrium cracks in brittle fracture. Advanced Applied Mechanics 1962;7:55-129.

- **(Bartholomeusz et al. 1999)** Bartholomeusz RA, Baker AA, Chester RJ, Searl A. Bonded joints with through-thickness adhesive stresses – reinforcing the F/A-18 Y470.5 bulkhead. International Journal of Adhesion & Adhesives 1999;19:173-180.
- **(Bascom and Cottingham 1976)** Bascom WD, Cottingham RL. Effect of temperature on the adhesive fracture behavior of an elastomer–epoxy resin. The Journal of Adhesion 1976;7:333-346.
- **(Bascom et al. 1975)** Bascom WD, Cottingham RL, Jones RL, Peyser P. The fracture of epoxy- and elastomer-modified epoxy polymers in bulk and as adhesives. Journal of Applied Polymer Science 1975;19:2545-2562.
- **(Bauld and Tzeng 1984)** Bauld NR, Tzeng L. A Vlasov theory for fiber-reinforced beams with thin-walled open cross sections. International Journal of Solids and Structures 1984;20:277-297.
- **(Bazant et al. 1996)** Bazant ZP, Daniel IM, Zhengzhi L. Size effect and fracture characteristics of composite laminates. Journal of Engineering Materials and Technology 1996;118:317-324.
- **(Belingardi et al. 2002)** Belingardi G, Goglio L, Tarditi A. Investigating the effect of spew and chamfer size on the stresses in metal/plastics adhesive joints. International Journal of Adhesion & Adhesives 2002;22:273-282.
- **(Bell and Kinloch 1997)** Bell AJ, Kinlock AJ. The effect of the substrate material on the value of the adhesive fracture energy, $G_{(c)}$. Journal of Materials Science Letters 1997;16;150-1453.
- **(Berbinau et al. 1999)** Berbinau P, Soutis C, Guzl IA. Compressive failure of 0º unidirectional carbon fiber-reinforced plastic (CFRP) laminates by biber microbuckling. Composites Science and Technology 1999;59:1451-1455.
- **(Berry and d'Almeida 2002)** Berry NG, d'Almeida JRM. The influence of circular centered defects on the performance of carbon-epoxy single lap joints. Polimer Testing 2001;21:373-379.
- **(Biel 2005)** Biel A. Constitutive behaviour and fracture toughness of an adhesive layer. Lic.Eng. Thesis. Göteborg, Sweden: Department of Applied Mechanics, Chalmers University of Technology: 2005.
- **(Biel and Stigh 2008)** Biel A, Stigh U. Effects of constitutive parameters on the accuracy of measured fracture energy using the DCB-specimen. Engineering Fracture Mechanics 2008;75:2968-2983.
- **(Bigwood and Crocombe 1989)** Bigwood DA, Crocombe AD. Elastic analysis and engineering design formulae for bonded joints. International Journal of Adhesion & Adhesives 1989;9:229-242.
- **(Bigwood and Crocombe 1990)** Bigwood DA, Crocombe AD. Non-linear adhesive bonded joint design analyses. International Journal of Adhesion & Adhesives 1990;10:31-41.
- **(Blackman et al. 2003)** Blackman BRK, Hadavinia H, Kinloch AJ, Williams JG. The use of a cohesive zone model to study the fracture of fibre composites and adhesively-bonded joints. International Journal of Fracture 2003;119:25-46.
- **(Blackman et al. 2005)** Blackman BRK, Kinloch AJ, Paraschi M. The determination of the mode II adhesive fracture resistance, G_{IIC}, of structural adhesive joints: an effective crack length approach. Engineering Fracture Mechanics 2005;72:877-897.
- **(Blackman et al. 2006)** Blackman BRK, Brunner AJ, Williams JG. Mode II fracture testing of composites: a new look at an old problem. Engineering Fracture Mechanics 2006;73:2443-2455.
- **(Bleich 1952)** Bleich F. Buckling strength of metal structures. McGraw-Hill: New York, USA; 1952.
- **(Bodig and Jayne 1982)** Bodig J, Jayne BA. Mechanics of Wood and Wood Composites. Van Nostrand Reinhold Company: New York, USA; 1982.

- **(Bodig and Jayne 1993)** Bodig J, Jayne BA. Mechanics of wood and wood composites. Krieger Publishing Company: Florida, USA; 1993.
- **(Bogdanovich and Kizhakkethara 1999)** Bogdanovich AE, Kizhakkethara I. Three dimensional finite element analysis of double-lap composite adhesive bonded joint using submodeling approach. Composites: Part B – Engineering 1999;30:537-551.
- **(Bogdanovich and Yushanov 1999a)** Bogdanovich AE, Yushanov SP. Progressive failure analysis of adhesive bonded joints with laminated composite adherends. Journal of Reinforced Plastics and Composites 1999;18:1689-1707.
- **(Bogdanovich and Yushanov 1999b)** Bogdanovich AE, Yushanov SP. 3D progressive failure analysis of bonded composite joints. Proceedings of the 40th AIAA/ASME/ASCE/AHS/ASC Structures, Structural Dynamics, and Materials Conference and Exhibit. Saint Louis, USA. 14-17 April 1999.
- **(Borri et al. 2005)** Borri A, Corradi M, Grazini A. A method for flexural reinforcement of old wood beams with CFRP materials. Composites: Part B – Engineering 2005;36:143-153.
- **(Boss et al. 2003)** Boss JN, Ganesh VK, Lim CT. Modulus grading versus geometrical grading of composite adherends in single-lap bonded joints. Composite Structures 2003;62:113-121.
- **(Botelho et al. 2006)** Botelho EC, Silva RA, Pardini LC, Rezende MC. A review on the development and properties of continuous fiber/epoxy/aluminum hybrid composites for aircraft structures. Materials Research 2006;9:247-256.
- **(Brebbia 2003)** Brebbia CA. Structural studies, repairs and maintenance of heritage architecture. WIT press: Southampton, UK; 2003.
- **(Brink et al. 2000)** Brink DD, Mailand JC, Levi CG, Leckie FA. Deformation behaviour of model MMC scarf joints. Materials Science and Engineering: A 2000;281:113-125.
- **(Brooks and Turvey 1995)** Brooks RJ, Turvey GJ. Lateral buckling of pultruded GRP I-section cantilever. Composite Structures 1995;32:203-215.
- **(Broughton and Hutchinson 2001)** Broughton JG, Hutchinson AR. Effect of timber moisture content on bonded-in rods. Construction and Building Materials 2001;15:17-25.
- **(Budiansky and Fleck 1993)** Budiansky B, Fleck NA. Compressive failure of fibre composites. Journal of the Mechanics and Physics of Solids 1993;41:183-211.
- **(Bulleit et al. 1989)** Bulleit WM, Sandberg LB, Woods GJ. Steel-reinforced glued laminated timber. ASCE Journal of Structural Engineering 1989;115:433-444.
- **(Campilho 2005)** Campilho RDSG. Modelação da Execução de Reparações em Materiais Compósitos. M.Sc. Thesis. Porto, Portugal: Department of Mechanical Engineering and Industrial Management, Enginnering Faculty of Porto University: 2005.
- **(Campilho et al. 2005)** Campilho RDSG, de Moura MFSF, Domingues JJMS. Modelling single and double-lap repairs on composite materials. Composites Science and Technology 2005;65:1948-1958.
- **(Campilho et al. 2007a)** Campilho RDSG, de Moura MFSF, Domingues JJMS. Stress and failure analyses of scarf repaired CFRP laminates using a cohesive damage model. Journal of Adhesion Science and Technology 2007;21:855-970.
- **(Campilho et al. 2007b)** Campilho RDSG, de Moura MFSF, Domingues JJMS. Efeito da geometria na resistência residual à tracção de juntas reparadas de sobreposição simples de carbono-epóxido. Ciência e Tecnologia dos Materiais 2007;19:68-74.

- **(Campilho et al. 2007c)** Campilho RDSG, de Moura MFSF. Modelação da execução de reparações por sobreposição simples e dupla em materiais compósitos. Revista Iberoamericana de Ingeniería Mecánica 2007;11:35-52.
- **(Campilho et al. 2008a)** Campilho RDSG, de Moura MFSF, Domingues JJMS. Using a cohesive damage model to predict the tensile behaviour of CFRP single-strap repairs. International Journal of Solids and Structures 2008;45:1497-1512.
- **(Campilho et al. 2008b)** Campilho RDSG, de Moura MFSF, Domingues JJMS, Morais JJL. Computational modelling of the residual strength of repaired composite laminates using a cohesive damage model. Journal of Adhesion Science and Technology 2008;22:1565-1591.
- **(Campilho et al. 2008c)** Campilho RDSG, de Moura MFSF, Domingues JJMS. Modelação numérica de reparações por sobreposição simples e dupla em materiais compósitos. Mecânica Experimental 2008;15:103-116.
- **(Campilho et al. 2008d)** Campilho RDSG, de Moura MFSF, Ramantani DA, Gonçalves JPM. Obtaining the cohesive laws of a trapezoidal mixed-mode damage model using an inverse method. Ciência e Tecnologia dos Materiais 2008;20:81-86.
- **(Campilho et al. 2009a)** Campilho RDSG, de Moura MFSF, Pinto AMG, Morais JJL, Domingues JJMS. Modelling the tensile fracture behaviour of CFRP scarf repairs. Composites: Part B – Engineering 2009;40:149-157.
- **(Campilho et al. 2009b)** Campilho RDSG, de Moura MFSF, Domingues JJMS. Numerical prediction on the tensile residual strength of repaired CFRP under different geometric changes. International Journal of Adhesion & Adhesives 2009;29:195-205.
- **(Campilho et al. 2009c)** Campilho RDSG, de Moura MFSF, Barreto AMJP, Morais JJL, Domingues JJMS. Fracture behaviour of damaged wood beams repaired with an adhesively-bonded composite patch. Submitted to Composites: Part A – Applied Science and Manufacturing.
- **(Campilho et al. 2009d)** Campilho RDSG, de Moura MFSF, Pinto AMG, Ramantani DA. Interlaminar fracture characterization of a carbon-epoxy composite in pure mode II. Submitted to Materials Science Forum.
- **(Campilho et al. 2009e)** Campilho RDSG, de Moura MFSF, Ramantani DA, Morais JJL, Domingues JJMS. Tensile behaviour of three-dimensional carbon-epoxy adhesively-bonded single and double-strap repairs. International Journal of Adhesion & Adhesives doi: 10.1016/j.ijadhadh.2009.02.004.
- **(Campilho et al. 2009f)** Campilho RDSG, de Moura MFSF, Ramantani DA, Morais JJL, Domingues JJMS. Buckling behaviour of carbon-epoxy adhesively-bonded scarf repairs. Accepted in Journal of Adhesion Science and Technology.
- **(Campilho et al. 2009g)** Campilho RDSG, de Moura MFSF, Pinto AMG, Ramantani DA, Morais JJL, Domingues JJMS. Strength prediction of adhesively-bonded scarf repairs in composite structures under bending. Submitted to Materials Science Forum.
- **(Carlberger and Stigh 2007)** Carlberger T, Stigh U. An explicit FE-model of impact fracture in an adhesive joint. Engineering Fracture Mechanics 2007;74:2247-2262.
- **(Carlsson et al. 1986)** Carlsson LA, Gillespie JW, Pipes RB. On the analysis and design of the end notched flexure (ENF) specimen for mode II testing. Journal of Composite Materials 1986;20:594-604.
- **(Caumes 1987)** Caumes P. Rupture d´un materiau anisotropic en conditions polymodales (Le bois). Ph.D. Thesis. Bordeaux, France: Université de Bordeaux I: 1987.
- **(Cavalli and Thouless 2001)** Cavalli MN, Thouless MD. The effect of damage nucleation on the toughness of an adhesive joint. The Journal of Adhesion 2001;76:75-92.

- **(Chai 1986)** Chai H. Bond thickness effect in adhesive joints and its significance for mode I interlaminar fracture of composites. Proceedings of the Seventh Conference on Composite Materials Testing and Design. Philadelphia, USA. 29 April – 01 May 1986.
- **(Chai 1988)** Chai H. Shear fracture. International Journal of Fracture 1998;37:137-159.
- **(Chai 1992)** Chai H. Experimental evaluation of mixed-mode fracture in adhesive bonds. Experimental Mechanics 1992;32:296-303.
- **(Chai 1993)** Chai H. Observation of deformation and damage at the tip of cracks in adhesive bonds loaded in shear and assessment of a criteria for fracture. International Journal of Fracture 1993;60:311-326.
- **(Chajes 1952)** Chajes A. Principle of structural stability theory. Prentice-Hall: New Jersey, USA; 1952.
- **(Chajes et al. 1995)** Chajes MJ, Kaliakin VN, Holsinger SD, Meyer AJ. Experimental testing of composite wood beams for use in timber bridges. Proceedings of the 4th International Bridge Conference. San Francisco, USA. 28-30 August 1995.
- **(Chamis and Murthy 1991)** Chamis CC, Murthy PLN. Simplified procedures for designing adhesively bonded composite joints. Journal of Reinforced Plastics and Composites 1991;10:29-41.
- **(Champaney and Valoroso 2001)** Champaney L, Valoroso N. Evaluation of interface models for the analysis of non-linear behaviour of adhesively bonded joints. Proceedings of the European Conference on Computational Mechanics. Cracow, Poland. 26-29 June 2001.
- **(Chan and Sun 1980)** Chan WS, Sun CT. Interfacial stresses and strength of lap joints. Proceedings of the 21st Conference of Structures, Structural Dynamics and Materials. Seattle, USA. 12-14 May 1980.
- **(Chan and Vedhagiri 2001)** Chan WS, Vedhagiri S. Analysis of composite bonded/bolted joints used in repairing. Journal of Composite Materials 2001;35:1045-1061.
- **(Chandra et al. 2002)** Chandra N, Li H, Shet C, Ghonem H. Some issues in the application of cohesive zone models for metal–ceramic interfaces. International Journal of Solids and Structures 2002;39:2827-2855.
- **(Chang et al. 1990)** Chang FK, Perez JL, Chang KY. Analysis of thick laminated composites. Journal of Composite Materials 1990;24:801-822.
- **(Charalambides et al. 1997)** Charalambides MN, Kinloch AJ, Matthews FL. Strength prediction of bonded joints. Proceedings of the 83rd meeting of the AGARD SMP Conference on Bolted/Bonded Joints in Polymeric Composites. Florence, Italy. 2-3 September 1996.
- **(Charalambides et al. 1998a)** Charalambides MN, Hardouin R, Kinloch AJ, Matthews FL. Adhesively-bonded repairs to fibre-composite materials II: Finite element modelling. Composites: Part A – Applied Science and Manufacturing 1998;29:1383-1396.
- **(Charalambides et al. 1998b)** Charalambides MN, Hardouin R, Kinloch AJ, Matthews FL. Adhesively-bonded repairs to fibre-composite materials I: Experimental. Composites: Part A – Applied Science and Manufacturing 1998:29:1371-1381.
- **(Chaves 2005)** Chaves FJP. Application of adhesive bonding in PVC windows. M.Sc. Thesis. Porto, Portugal: Department of Mechanical Engineering and Industrial Management, Enginnering Faculty of Porto University: 2005.
- **(Chaves et al. 2008)** Chaves FJP, da Silva LFM, de Castro PMST. Adhesively bonded T-joints in polyvinyl chloride windows. Journal of Materials: Design and Applications 2008;222:159-174.
- **(Cheikh et al. 2001)** Cheikh M, Coorevits P, Loredo A. Modelling the stress vector continuity at the interface of bonded joints. International Journal of Adhesion & Adhesives 2001;21:249-257.

- **(Chen 2002)** Chen J. Predicting progressive delamination of stiffened fibre-composite panel and by decohesion models. Journal of Thermoplastic Composite Materials 2002;15:429-441.
- **(Chen and Cheng 1983)** Chen D, Cheng S. An analysis of adhesive-bonded single-lap joints. Journal of Applied Mechanics 1983;50:109-115.
- **(Chen et al. 1999)** Chen J, Crisfield M, Kinloch AJ, Busso EP, Matthews FL, Qiu Y. Predicting progressive delamination of composite material specimens via interface elements. Mechanics of Advanced Materials and Structures 1999;6:301-317.
- **(Cheng et al. 2007)** Cheng J, Wu X, Li G, Taheri F, Pang S. Design and analysis of a smart adhesive single-strap joint system integrated with the piezoelectrics reinforced composite layers. Composites Science and Technology 2007;67:1264-1274.
- **(Cheuk and Tong 2002)** Cheuk PT, Tong L. Failure of adhesive bonded composite lap shear joints with embedded precrack. Composites Science and Technology 2002;62:1079-1095.
- **(Christy et al. 2005)** Christy AG, Senden TJ, Evans PD. Automated measurement of checks at wood surfaces. Measurement 2005;37:109-118.
- **(Chu and Ahn 2005)** Chu WS, Ahn SH. Internet-based composite repair. Journal of Composite Materials 2006;39:827-845.
- **(Cognard et al. 2006)** Cognard JY, Davies P, Sohier L, Créac'hcadec R. A study of the non-linear behaviour of adhesively-bonded composite assemblies. Composite Structures 2006;76:34-46.
- **(Cole 1999)** Cole WF. Technical justification of repairs to composite laminates. International Journal of Adhesion & Adhesives 1999;19:107-120.
- **(Coleman and Hurst 1974)** Coleman GE, Hurst HT. Timber structures reinforced with light gage steel. Forest Products Journal 1974;24:45-53.
- **(Colombi and Poggi 2006)** Colombi P, Poggi C. Strengthening of tensile steel members and bolted joints using adhesively bonded CFRP plates. Construction and Building Materials 2006;20:22-33.
- **(Corleto and Bradley 1989)** Corleto CR, Bradley WL. Mode II delamination fracture toughness of unidirectional graphite/epoxy laminates. ASTM Special Technical Publication 1989;1012:201-221.
- **(Corradi and Borri 2007)** Corradi M, Borri A. Fir and chestnut timber beams reinforced with GFRP pultruded elements. Composites: Part B – Engineering 2007;38:172-181.
- **(Corradi et al. 2006)** Corradi M, Speranzini E, Borri A, Vignoli A. In-plane shear reinforcement of wood beam floors with FRP. Composites: Part B – Engineering 2006;37:310-319.
- **(Cotterell and Reddell 1977)** Cotterell B, Reddell JK. The essential work of plane stress ductile fracture. International Journal of Fracture 1977;13:167-277.
- **(Crews et al. 1988)** Crews JH, Shivakumar KN, Raju IS. Factors influencing elastic stresses in double cantilever beam specimens. ASTM Special Technical Publication 1988;981:119-132.
- **(Crocombe 1989)** Crocombe AD. Global yielding as a failure criterion for bonded joints. International Journal of Adhesion & Adhesives 1989;9:145-153.
- **(Crocombe and Adams 1982)** Crocombe AD, Adams RD. An elastoplastic investigation of the peel test. The Journal of Adhesion 1982;13:241-267.

- **(Crocombe and Bigwood 1992)** Crocombe AD, Bigwood DA. Development of a full elasto-plastic adhesive joint design. Journal of Strain Analysis for Adhesive Design 1992;27:211-218.
- **(Crocombe and Moult 1987)** Crocombe AD, Moult AC. The effect of the adhesive thickness on the strength of bonded joint. Proceedings of the 25th Annual Conference on Adhesion and Adhesives 1987. London, UK. 31 March-1 April 1988.
- **(Cui and Wisnom 1993)** Cui W, Wisnom MR. A combined stress-based and fracture-mechanics-based model for predicting delamination in composites. Composites 1993;24:467-474.
- **(Custódio et al. 2009)** Custódio J, Broughton J, Cruz H. A review of factors influencing the durability of structural bonded timber joints. International Journal of Adhesion & Adhesives 2009;29:173-185.
- **(Czamocki and Piekarski 1986)** Czamocki P, Piekarski K. Fracture strength of an adhesive-bonded joint. International Journal of Adhesion & Adhesives 1986;6:93-95.
- **(da Silva and Adams 2007a)** da Silva LFM, Adams RD. Adhesive joints at high and low temperatures using similar and dissimilar adherends and dual adhesives. International Journal of Adhesion & Adhesives 2007;27:216-226.
- **(da Silva and Adams 2007b)** da Silva LFM, Adams RD. Techniques to reduce peel stresses in adhesive joints with composites. International Journal of Adhesion & Adhesives 2007;27:227-235.
- **(da Silva and Lopes 2009)** da Silva LFM, Lopes MJCQ. Joint strength optimization by the mixed-adhesive technique. International Journal of Adhesion & Adhesives doi: 10.1016/j.ijadhadh.2008.09.009.
- **(da Silva et al. 2004)** da Silva LFM, Adams RD, Gibbs M. Manufacture of adhesive joints and bulk specimens with high-temperature adhesives. International Journal of Adhesion & Adhesives 2004;24:69-83.
- **(da Silva et al. 2006)** da Silva LFM, Rodrigues TNSS, Figueiredo MAV, de Moura MFSF, Chousal JAG. Effect of adhesive type and thickness on the lap shear strength. The Journal of Adhesion 2006;82:1-25.
- **(da Silva et al. 2009a)** da Silva LFM, das Neves PJC, Adams RD, Spelt JK. Analytical models of adhesively bonded joints-Part I: Literature survey. International Journal of Adhesion & Adhesives 2009;29:319-330.
- **(da Silva et al. 2009b)** da Silva LFM, das Neves PJC, Adams RD, Wang A, Spelt JK. Analytical models of adhesively bonded joints-Part II: Comparative study. International Journal of Adhesion & Adhesives 2009;29:331-341.
- **(Dagher and Lindyberg 2000)** Dagher HJ, Lindyberg R. FRP-wood hybrids for bridges: a comparison of E-glass and carbon reinforcements. Proceedings of the Structures Congress 2000. Philadelphia, USA. 7-10 May 2000.
- **(Daghyani et al. 1995a)** Daghyani HR, Ye L, Mai YW. Mode I Fracture Behavior of Adhesive Joints. Part I. Relationship between Fracture Energy and Bond Thickness. The Journal of Adhesion 1995;53:149-162.
- **(Daghyani et al. 1995b)** Daghyani HR, Ye L, Mai YW.Mode I Fracture Behavior of Adhesive Joints. Part II. Stress Analysis and Constraint Parameters. The Journal of Adhesion 1995;53:163-172.
- **(Daghyani et al. 1996)** Daghyani HR, Ye L, Mai YW. Mixed-mode fracture of adhesively bonded CF/Epoxy composite joints. Journal of Composite Materials 1996;30:1248-1265.
- **(Daniel and Hsiao 1999)** Daniel HJ, Hsiao HM. Is there thickness effect on compressive strength of unnotched composite laminates? International Journal of Fracture 1999;95:143-158.
- **(Das et al. 2005)** Das M, Barut A, Madenci E, Ambur DR. Complete stress field in sandwich panels with a new triangular finite element of single-layer theory. Computer Methods in Applied Mechanics and Engineering 2005;194:2969-3005.

- **(Das et al. 2006)** Das M, Barut A, Madenci E, Ambur DR. A triangular plate element for thermo-elastic analysis of sandwich panels with a functionally graded core. International Journal for Numerical Methods in Engineering 2006;68: 940-966.
- **(Das et al. 2008)** Das M, Madenci E, Ambur DR. Three-dimensional nonlinear analyses of scarf repair in composite laminates and sandwich panels. Journal of the Mechanics of Materials and Structures 2008;3:1641-1658.
- **(Davalos et al. 1999)** Davalos J, Zipfel G, Qiao P. Feasibility study of prototype GFRP-reinforced wood railroad crosstie. Journal of Composites for Construction 1999;3:92-99.
- **(Davidson et al. 2006)** Davidson BD, Krüger R, König M. Effect of stacking sequence on energy release rate distributions in multidirectional DCB and ENF specimens. Engineering Fracture Mechanics 1996;55:557-569.
- **(Davis 1997)** Davis G. The performance of adhesive systems for structural timbers. International Journal of Adhesion & Adhesives 1997;17:247-255.
- **(Davis and Bond 1999)** Davis M, Bond D. Principles and practices of adhesive bonded structural joints and repairs. International Journal of Adhesion & Adhesives 1999;19:91-105.
- **(Davis and Petton 1999)** Davis P, Petton D. An experimental study of scale effects in marine composites. Composites: Part A – Applied Science and Manufacturing 1999;30:267-275.
- **(de Castro and Keller 2008a)** de Castro J, Keller H. Ductile double-lap joints from brittle GFRP laminates and ductile adhesives, Part I: Experimental investigation. Composites: Part B – Engineering 2008;39:271-281.
- **(de Castro and Keller 2008b)** de Castro J, Keller H. Ductile double-lap joints from brittle GFRP laminates and ductile adhesives, Part II: Numerical investigation and joint strength prediction. Composites: Part B – Engineering 2008;39:282-291.
- **(de Lorenzis et al. 2005)** de Lorenzis L, Scialpi V, Tegola AL. Analytical and experimental study on bonded-in CFRP bars in glulam timber. Composites: Part B – Engineering 2005;36:279-289.
- **(de Morais et al. 2007)** de Morais AB, Pereira AB, Teixeira JP, Cavaleiro NC. Strength of epoxy adhesive-bonded stainless-steel joints. International Journal of Adhesion & Adhesives 2007;27:679-686.
- **(de Moura 2006)** de Moura MFSF. Numerical Simulation of the ENF Test for the Mode II Fracture Characterization of Bonded Joints. Journal of Adhesion Science and Technology 2006;20:37-52.
- **(de Moura et al. 1997)** de Moura MFSF, Gonçalves JPM, Marques AT, de Castro PT. Modeling compression failure after low velocity impact on laminated composites using interface elements. Journal of Composite Materials 1997;31:1462-1479.
- **(de Moura et al. 2000)** de Moura MFSF, Gonçalves JPM, Marques AT, de Castro PMST. Prediction of compressive strength of carbon-epoxy laminates containing delamination by using a mixed-mode damage model. Composite Structures 2000;50:151-157.
- **(de Moura et al. 2004)** de Moura MFSF, Gonçalves JPM. Modelling the interaction between matrix cracking and delamination in carbon-epoxy laminates under low velocity impact. Composites Science and Technology 2004;64:1021-1027.
- **(de Moura et al. 2006a)** de Moura MFSF, Silva MAL, de Morais AB, Morais JJL. Equivalent Crack Based Mode II Fracture Characterization of Wood. Engineering Fracture Mechanics 2006;73:978-993.
- **(de Moura et al. 2006b)** de Moura MFSF, Daniaud R, Magalhães AG. Simulation of mechanical behaviour of composite bonded joints containing strip defects. International Journal of Adhesion & Adhesives 2006;26:464-473.

- **(de Moura et al. 2008a)** de Moura MFSF, Gonçalves JPM, Chousal JAG, Campilho RDSG. Cohesive and continuum mixed-mode damage models applied to the simulation of the mechanical behaviour of bonded joints. International Journal of Adhesion & Adhesives 2008;28:419-426.
- **(de Moura et al. 2008b)** de Moura MFSF, Campilho RDSG, Gonçalves JPM. Crack Equivalent Concept Applied to the Fracture Characterization of Bonded Joints under Pure Mode I Loading. Composites Science and Technology 2008;68:2224-2230.
- **(de Moura et al. 2009a)** de Moura MFSF, Fernandez MVC, de Morais AB, Campilho RDSG. Numerical analysis of the Edge Crack Torsion (ECT) test for mode III interlaminar fracture of composite laminates. Engineering Fracture Mechanics 2009;76:469-478.
- **(de Moura et al. 2009b)** de Moura MFSF, Campilho RDSG, Gonçalves JPM. Pure mode II fracture characterization of composite bonded joints. International Journal of Solids and Structures 2009;46:1589-1595.
- **(de Moura et al. 2009c)** de Moura MFSF, Campilho RDSG, Amaro AM, Reis PNB. Interlaminar and intralaminar fracture characterization of composites under mode I loading. Submitted to Engineering Fracture Mechanics.
- **(de Moura et al. 2009d)** de Moura MFSF, Campilho RDSG, Gonçalves JPM. Mixed-mode cohesive damage model applied to the simulation of the mechanical behaviour of laminate composite adhesive joints. Accepted in Journal of Adhesion Science and Technology.
- **(Deaton 1987)** Deaton JW. Repair of advanced composites commercial aircraft structures. Engineered Materials Handbook, ASM International 1987;3:829-839.
- **(Dedale et al. 1981)** Dedale F, Erdogan F, Aydinoglu MN. Stresses in adhesively bonded joints: a closed-form solution. Journal of Composite Materials 1981;15:249-271.
- **(Deng and Lee 2008)** Deng J, Lee MMK. Effect of plate end and adhesive spew geometries on stresses in retrofitted beams bonded with a CFRP plate. Composites: Part B – Engineering 2008;39:731-739.
- **(Ding 1999)** Ding W. Delamination Analysis of Composite Laminates. Ph.D. Thesis. Toronto, USA: Graduate Department of Chemical Engineering and Applied Chemistry, University of Toronto: 1999.
- **(Donaldson and Roy 1997)** Donaldson SL, Roy AK. Experimental studies on composite bonded joints. Proceedings of the 11th International Conference on Composite Materials. Gold Coast, Australia. 14-18 July 1997.
- **(Downes et al. 1997)** Downes GM, Hudson IL, Raymond CA, Dean GH, Michell AJ, Schmileck LR, Evans R, Muneri A. Sampling plantation eucalipts for wood and fibre properties. CSIRO Publishing: Collingwood, Australia; 1997.
- **(Dragoni and Mauri 2000)** Dragoni E, Mauri P. Intrinsic static strength of friction interfaces augmented with anaerobic adhesives. International Journal of Adhesion & Adhesives 2000;20:315-321.
- **(Du et al. 2004)** Du J, Salmon FT, Pocius AV. Modeling of cohesive failure processes in structural adhesive bonded joints. Journal of Adhesion Science and Technology 2004; 18:287-299.
- **(Duan et al. 2002)** Duan K, Hu XZ, Wittmann FH. Explanation of size effect in concrete fracture using non-uniform energy distribution. Materials and Structures 2002;35:326-331.
- **(Duan et al. 2003)** Duan K, Hu XZ, Wittmann FH. Boundary effect on concrete fracture and non-constant fracture energy distribution. Engineering Fracture Mechanics 2003;70:2257-2268.
- **(Duan et al. 2004)** Duan K, Hu X, Mai YW. Substrate constraint and adhesive thickness effects on fracture toughness of adhesive joints. Journal of Adhesion Science and Technology 2004;18:39-53.

- **(Ducept at al. 2000)** Ducept F, Davies P, Gamby D. Mixed mode failure criteria for a glass/epoxy composite and an adhesively bonded composite/composite joint. International Journal of Adhesion & Adhesives 2000;20:233-244.
- **(Dugdale 1960)** Dugdale DS. Yielding of steel sheets containing slits. Journal of the Mechanics and Physics of Solids 1960;8:100-104.
- **(Durão 2005)** Durão LMP. Machining of hybrid composites. Ph.D. Thesis. Porto, Portugal: Department of Mechanical Engineering and Industrial Management, Enginnering Faculty of Porto University: 2005.
- **(Dvorak et al. 2001)** Dvorak GJ, Zhang J, Canyurt O. Adhesive tongue-and-groove joints for thick composite laminates. Composites Science and Technology 2001;61:1123-1142.
- **(Ebeling 1990)** Ebeling WD. Repair and rehabilitation of heavy timber trusses. Journal of Performance of Constructed Facilities 1990;4:242-258.
- **(Ehsani et al. 2004)** Ehsani M, Larsen M, Palmer N. FRP Laminates and Epoxy Help Support New Loads in an Existing Wooden Gymnasium. Structure Magazine 2004;11:19-21.
- **(Erdogan and Ratwani 1971)** Erdogan F, Ratwani M. Stress distribution in bonded joints. Journal of Composite Materials 1971;5:378-393.
- **(Ersoy and Vardar 2000)** Ersoy N, Vardar O. Measurement of residual stresses in layered composites by compliance method. Journal of Composite Materials 2000;34:575-598.
- **(Eryigit et al. 2009)** Eryigit E, Zor M, Arman Y. Hole effects on lateral buckling of laminated cantilever beams. Composites: Part B – Engineering 2009;40:174-179.
- **(Falk et al. 2000)** Falk RH, Green D, Rammer D, Lantz SF. Engineering evaluation of 55-year-old timber columns recycled from an industrial military building. Forest Products Journal 2000;50:71-76.
- **(Fardis and Khalili 1981)** Fardis MN, Khalili H. Concrete encased in fiberglass reinforced plastic. ACI Structural Journal 1981;78:440-446.
- **(Feih and Shercliff 2005)** Feih S, Shercliff HR. Adhesive and composite failure prediction of single-L joint structures under tensile loading. International Journal of Adhesion & Adhesives 2005;25:47-59.
- **(Feraren and Jensen 2004)** Feraren P, Jensen HM. Cohesive zone modelling of interface fracture near flaws in adhesive joints. Engineering Fracture Mechanics 2004;71:2125-2142.
- **(Fernlund 2007)** Fernlund G. Stress analysis of bonded lap joints using fracture mechanics and energy balance. International Journal of Adhesion & Adhesives 2007;27:584-592.
- **(Fernlund et al. 1994)** Fernlund G, Papini M, McCammond D, Spelt JK. Fracture load predictions for adhesive joints. Composites Science and Technology 1994;51:587-600.
- **(Ferreira et al. 2005)** Ferreira JM, Silva H, Costa JD, Richardson M. Stress analysis of lap joints involving natural fibre reinforced interface layers. Composites: Part B – Engineering 2005;36:1-7.
- **(Fessel et al. 2007)** Fessel G, Broughton JG, Fellows NA, Durodola JF, Hutchinson AR. Evaluation of different lap-shear joint geometries for automotive applications. International Journal of Adhesion & Adhesives 2007;27:574-583.
- **(Finn et al. 1992)** Finn SR, He YF, Springer GS, Lee HJ. Compressive strength of damaged and repaired composite plates. Journal of Composite Materials 1992;26:1796-1825.
- **(Fitton and Broughton 2005)** Fitton MD, Broughton JG. Variable modulus adhesives: an approach to optimized joint performance. International Journal of Adhesion & Adhesives 2005;25:329-336.

- **(Found and Friend 1995)** Found MS, Friend MJ. Evaluation of CFRP panels with scarf repair patches. Composite Structures 1995;32:115-122.
- **(Fredell et al. 1999)** Fredell R, Guijt C, Mazza J. An integrated bonded repair system: a reliable means of giving new life to aging airframes. Applied Composite Materials 1999;6:269-277.
- **(Fredrickson et al. 2008)** Fredrickson BM, Schoeppner GA, Mollenhauer DH, Palazotto AN. Application of three-dimensional spline variational analysis for composite repair. Composite Structures 2008;83:119-130.
- **(Frostig et al. 1997)** Frostig Y, Thomsen OT, Mortensen F. Analysis of adhesive bonded joints, square-end and spew-fillet: higher-order theory approach. Journal of Engineering Mechanics 1997;125:1298-1307.
- **(Gacoin et al. 2007)** Gacoin A, Assih J, Objois A, Delmas Y. Experimental studies on adhesively-bonded scarf joints: influence of natural ageing on progressive damage. Journal of Adhesion Science and Technology 2007;21:871-882.
- **(Ganesh and Choo 2002)** Ganesh VK, Choo TS. Modulus graded composite adherends for single-lap bonded joints. Journal of Composite Materials 2002;36:1757-1767.
- **(Gardon 1963)** Gardon JL. Peel Adhesion. I. Some Phenomenological Aspects of the Test. Journal of Applied Polymer Science 1963;7:625–641.
- **(Gentile et al. 2000)** Gentile C, Svecova D, Saltzberg W, Rizkalla SH. Flexural strenghtening of timber beams using GFRP. Proceedings of the 3rd International Conference in Advanced Composites Materials in Bridge and Structures. Ottawa, Canada. August 15-18 2000.
- **(Giare et al. 1992)** Giare GS, Mulholland DJ, Felton RF. Experimental investigation of the effect of geometry on the efficiency of double lap joint using fracture mechanics technique in shear mode (mode II). Engineering Fracture Mechanics 1992;41:487-497.
- **(Gibson 1994)** Gibson RF. Principles of composite material mechanics. McGraw-Hill: New York, USA; 1994.
- **(Gilfillan et al. 2001)** Gilfillan R, Gilbert S, Patrick G. The improved performance of home-grown timber glulam beams using fibre reinforcement. Journal of the Institute of Wood Science 2001;15:307-317.
- **(Gilfillan et al. 2003)** Gilfillan JR, Gilbert SG, Patrick GRH. The use of FRP composites in enhancing the structural behavior of timber beams. Journal of Reinforced Plastics and Composites 2003;22:1373-1388.
- **(Gleich et al. 2000)** Gleich DM, Van Tooren MJL, De Haan PAJ. Shear and peel stress analysis of an adhesively bonded scarf joint. Journal of Adhesion Science and Technology 2000;14:879-893.
- **(Gleich et al. 2001a)** Gleich DM, Van Tooren MJL, Beukers A. Analysis and evaluation of bondline thickness effects on failure load in adhesively bonded structures. Journal of Adhesion Science and Technology 2001;15:1091-1101.
- **(Gleich et al. 2001b)** Gleich DM, Van Tooren MJL, Beukers A. A stress singularity approach to failure initiation in a bonded joint with varying bondline thickness. Journal of Adhesion Science and Technology 2001;15:1247-1259.
- **(Goland and Reissner 1944)** Goland M, Reissner E. The stresses in cemented joints. Journal of Applied Mechanics 1944;66:17-27.
- **(Gonçalves et al. 2000)** Gonçalves JPM, de Moura MFSF, de Castro PT, Marques AT. Interface element including point-to-surface constraints for three-dimensional problems with damage propagation. Engineering Computations: International Journal for Computer-aided Engineering & Software 2000;17:28-47.
- **(Gonçalves et al. 2002)** Gonçalves JPM, de Moura MFSF, de Castro PMST. A three-dimensional finite element model for stress analysis of adhesive joints. International Journal of Adhesion & Adhesives 2002;22:357-365.

- **(Gonçalves et al. 2003)** Gonçalves JPM, de Moura MFSF, Magalhães AG, de Castro PMST. Application of interface finite elements to three-dimensional progressive failure analysis of adhesive joints. Fatigue and Fracture of Engineering Materials and Structures 2003;26:479-486.
- **(Gong et al. 2007)** Gong XJ, Cheng P, Rousseau J, Aivazzadeh S. Effect of local stresses on static strength and fatigue life of patched composite panels. Proceedings of the 16th International Conference on Composite Materials. Kyoto, Japan. 8-13 July 2007.
- **(Goyal et al. 2008)** Goyal VK, Johnson ER, Goyal VK. Predictive strength-fracture model for composite bonded joints. Composite Structures 2008;82:434-446.
- **(Grant et al. 2009)** Grant LDR, Adams RD, da Silva LFM. Experimental and numerical analysis of single-lap joints for the automotive industry. International Journal of Adhesion & Adhesives 2009;29:405-413.
- **(Green et al. 1999)** Green DW, Winandy JE, Kretschmann DE. Mechanical properties of wood, chapter 4 in Wood handbook – Wood as an engineering material. Technical Report FPL-GTR-113. Madison, USA. Forest Products Laboratory, United States Department of Agriculture 1999.
- **(Green et al. 2001)** Green DW, Falk RH, Lantz SF. Effect of Heart Checks on Flexural Properties of Reclaimed 6 by 8 Douglas-fir Timbers. Forest Products Journal 2001;51:82-88.
- **(Greenwood et al. 1969)** Greenwood L, Boag TG, McLaren AS. Stress distribution in lap joints. McLaren: London, UK; 1969.
- **(Grimes 1971)** Grimes GC. Stress distribution in adhesive bonded lap joints. SAE Transactions 710107 1971;370-378.
- **(Groth and Nordlund 1992)** Groth HL, Nordlund P. Shape optimization of bonded joints. International Journal of Adhesion & Adhesives 1991;11:204-212.
- **(Guild et al. 2001)** Guild FJ, Potter KD, Heinrich J, Adams RD, Wisnom MR. Understanding and control of adhesive crack propagation in bonded joints between carbon fibre composite adherends II Finite element analysis. International Journal of Adhesion & Adhesives 2001;21:445-453.
- **(Gunnion and Herszberg 2006)** Gunnion AJ, Herszberg I. Parametric study of scarf joints in composite structures. Composite Structures 2006;75:364-376.
- **(Gurvish and Byron 1995)** Gurvish MR, Byron PR. Strength size effect of laminated composites. Composites Science and Technology 1995;55:95-105.
- **(Haberle 1991)** Haberle JG. Strength and failure mechanics of unidirectional carbon fibre-reinforced plastics under axial compression. Ph.D. Thesis. London, UK: Department of Aeronautics, Imperial College: 1991.
- **(Haengsoo et al. 1994)** Haengsoo L, Dong-Won J, Jin-Ho J, Seyoung I. Finite element analysis of lateral buckling for beam structures. Computers & Structures 1994;53:1357-1371.
- **(Hall et al. 1988)** Hall SR, Raizenne MD, Simpson DL. A proposed composites repair methodology for primary structure. Composites 1988;20:479-483.
- **(Hallstrom and Grenestedt 1997)** Hallstrom S, Grenestedt JL. Failure analysis of laminated timber beams reinforced with glass fibre composites. Wood Science and Technology 1997;31:17-34.
- **(Hamoush et at. 2005)** Hamoush S, Shivakumar K, Darwish F, Sharpe M, Swindell P. Defective repairs of laminated solid composites. Journal of Composite Materials 2005;39:2185-2196.

- **(Harman and Wang 2006)** Harman AB, Wang CH. Improved design methods for scarf repairs to highly strained composite aircraft structure. Composite Structures 2006;75:132-144.
- **(Harris and Adams 1984)** Harris JA, Adams RD. Strength prediction of bonded single-lap joints by non-linear finite element methods. International Journal of Adhesion & Adhesives 1984;4:65-78.
- **(Hart-Smith 1973a)** Hart-Smith LJ. Adhesive-bonded single-lap joints. NASA Technical Report CR-112236. Hampton, USA. Langley Research Centre 1973.
- **(Hart-Smith 1973b)** Hart-Smith LJ. Adhesive-bonded Scarf and Stepped-lap Joints. NASA Technical Report CR-112237. Hampton, USA. Langley Research Centre 1973.
- **(Hart-Smith 1981)** Hart-Smith LJ. Further developments in the design and analysis of adhesive-bonded structural joints. ASTM Special Technical Publication 1981;749:3-31.
- **(Hart-Smith 1987)** Hart-Smith LJ. Joints. Engineered Materials Handbook, ASM International 1987;1:479-495.
- **(Hart-Smith 1995)** Hart-Smith LJ. An engineer's viewpoint on design and analysis of aircraft structural joints. Journal of Aerospace Engineering 1995;209:226-238.
- **(Helms et al. 1996)** Helms JE, Yang C, Pang SS. Strain distribution in a taper-taper adhesive-bonded joint in a composite flat plate. Journal of Thermoplastic Composite Materials 1996;9:280-291.
- **(Helms et al. 2003)** Helms JE, Li G, Pang SS. Buckling analysis of a taper-taper adhesive-bonded composite joint. Polymer Composites 2003;24:45-52.
- **(Her 1999)** Her SC. Stress analysis of adhesively-bonded lap joints. Composite Structures 1999;47:673-678.
- **(Heslehurst 1999)** Heslehurst RB. Observations in the structural response of adhesive bondline defects. International Journal of Adhesion & Adhesives 1999;19:133-154.
- **(Hildebrand 1994)** Hildebrand M. Non-linear analysis and optimization of adhesively bonded single lap joints between fibre-reinforced plastics and metals. International Journal of Adhesion & Adhesives 1994;14:261-267.
- **(Hilleborg et al. 1976)** Hilleborg A, Modéer M, Petersson PE. Analysis of crack formation and crack growth in concrete by means of fracture mechanics and finite elements. Cement and Concrete Research 1976;6:773-782.
- **(Hindman et al. 2005)** Hindman DP, Manbeck HB, Janowiak JJ. Measuremennt and prediction of lateral torsional buckling loads of composite wood materials: Rectangular sections. Forest Products Journal 2005;55:42-47.
- **(Hodges and Peters 2001)** Hodges DH, Peters DA. Lateral-torsional buckling of cantilevered elastically coupled composite strip- and I-beams. International Journal of Solids and Structures 2001;38:1585-1603.
- **(Hogberg and Stigh 2006)** Hogberg JL, Stigh U. Specimen proposals for mixed mode testing of adhesive layer. Engineering Fracture Mechanics 2006;73:2541-2556.
- **(Hojo et al. 2006)** Hojo M, Ando T, Tanaka M, Adachi T, Ochiai S, Endo Y. Modes I and II interlaminar fracture toughness and fatigue delamination of CF/epoxy laminates with self-same epoxy interleaf. International Journal of Fatigue 2006;28:1154-1165.
- **(Hosseinzadeh et al. 2005)** Hosseinzadeh R, Shokrieh MM, Lessard L. Damage behavior of fiber reinforced composite plates subjected to drop weight impacts. Composites Science and Technology 2006;66:61-68.
- **(Hou and Liu 2003)** Hou L, Liu D. Size effects and thickness constraints in composite joints. Journal of Composite Materials 2003;37:1921-1938.
- **(Hoyle 1975)** Hoyle RJ. Steel-reinforced wood beam design. Forest Products Journal 1975;25:17-23.

- **(Hsial et al. 1995)** Hsial HM, Danial IM, Wooh SC. A new compression test method for thick composites. Journal of Composite Materials 1995;29:1789-1806.
- **(Hu and Soutis 2000)** Hu FZ, Soutis C. Strength prediction of patch repaired CFRP laminates loaded in compression. Composites Science and Technology 2000;60:1103-1114.
- **(Hu and Wittmann 1992)** Hu XZ, Wittmann FH. Fracture energy and fracture process zone. Materials and Structures 1992;25:319-326.
- **(Hu et al. 1997)** Hu FZ, Soutis C, Edge EC. Interlaminar stresses in composite laminates with a circular hole. Composite Structures 1997;37:223-232.
- **(Hua et al. 2006)** Hua Y, Crocombe AD, Wahab MA Ashcroft IA. Modelling environmental degradation in EA9321-bonded joints using a progressive damage failure model. The Journal of Adhesion 2006;82:135-160.
- **(Huang et al. 2000)** Huang H, Yang CC, Tomblin JS, Harter P. Stress and failure analyses of adhesive-bonded composite joints using ASTM D3165 specimen. Proceedings of the American Society for Composites 2000;15:599-608.
- **(Hug et al. 2006)** Hug G, Thévenet P, Fitoussi J, D. Baptiste. Effect of the loading rate on mode I interlaminar fracture toughness of laminated composites. Engineering Fracture Mechanics 2006;73:2456-2462.
- **(Humphreys and Francey 2004)** Humphreys MF, Francey KL. An investigation into the rehabilitation of timber structures with fibre composite materials. Proceedings of the 18th Australasian Conference on the Mechanics of Structures and Materials. Perth, Australia. 1-3 December 2004.
- **(Hunston et al. 1989)** Hunston DL, Kinloch AJ, Wang SS. Micromechanics of fracture in structural adhesive bonds. The Journal of Adhesion 1989;28:103-114.
- **(Hutchinson and Suo 1992)** Hutchinson JW, Suo Z. Mixed mode cracking in layered materials. Advances in Applied Mechanics 1992;29:63-191.
- **(Iarve 1996)** Iarve E, Spline variational three dimensional stress analysis of laminated composite plates with open holes. International Journal of Solids and Structures 1996;33:2095-2118.
- **(Iarve and Pagano 2001)** Iarve E, Pagano PJ. Singular full-field stresses in composite laminates with an open hole. International Journal of Solids and Structures 2001;38:1-28.
- **(Ikeda et al. 2000)** Ikeda T, Yamashita A, Lee D, Miyazaki N. Failure of a ductile adhesive layer constrained by hard adherends. Journal of Engineering Materials and Technology 2000;122:80-85.
- **(Ikegami et al. 1990)** Ikegami K, Takeshita T, Matsuo K, Sugibayashi T. Strength of adhesively bonded scarf joints between glass fibre-reinforced plastics and metal. International Journal of Adhesion & Adhesives 1990;10:199–206.
- **(Imanaka and Suzuki 2002)** Imanaka M, Suzuki Y. Yield behavior of rubber-modified epoxy adhesives under multiaxial stress conditions. Journal of Adhesion Science and Technology 2002;16:1687-1700.
- **(Imanaka et al. 2000)** Imanaka M, Fujinami A, Suzuki Y. Fracture and yield behaviour of adhesively bonded joints under triaxial stress conditions. Journal of Materials Science 2000;35:2481-2491.
- **(Ireman 1998)** Ireman T. Three-dimensional stress analysis of bolted single-lap composite joints. Composite Structures 1998;43:195-216.
- **(Ireman and Eriksson 1997)** Ireman T, Eriksson I. Strength of composite laminates containing holes and subjected to complex loading conditions. Journal of Composite Materials 1997;31:1214-1248.

- **(Irwin 1957)** Irwin GR. Analysis of stress and strains near the end of a crack traversing a plate. Journal of Applied Mechanics 1957;24:361-364.
- **(Itagaki et al. 2003)** Itagaki N, Iijima Y, Mihashi H. Design method of mechanical performance in fibre reinforced glulam beams. Proceedings of the 2nd International Conference of the European Society for Wood Mechanics. Stockholm, Sweden. 25-28 May 2003.
- **(Jackson et al. 1992)** Jackson KE, Kellas S, Morton J. Scale effects in the response and failure of fiber reinforced composite laminates loaded in tension and in flexure. Journal of Composite Materials 1992;26:2674-2705.
- **(Jain and Mai 1999)** Jain LK, Mai YW. Analysis of resin-transfer-moulded single-lap joints. Composites Science and Technology 1999;59:1513-1518.
- **(Joh et al. 1993)** Joh D, Byun KY, Ha J. Thermal residual stresses in thick graphite/epoxy composite laminates-uniaxial approach. Experimental Mechanics 1993;50:70-76.
- **(John et al. 1991)** John SJ, Kinloch AJ, Matthews FL. Measuring and predicting the durability of bonded carbon fibre/epoxy composite joints. Composites 1991;22:121-126.
- **(Johns and Lacroix 2000)** Johns KC, Lacroix S. Composite Reinforcement of Timber in Bending. Canadian Journal of Civil Engineering 2000;27:899-906.
- **(Johnson 1989)** Johnson CL. Effect of ply stacking sequence on stress in a scarf joint. AIAA Journal 1989;27:79-86.
- **(Jones 1997)** Jones R. Upgrading of timber members in historic buildings. Journal of the Institute of Wood Science 1997;14:192-203.
- **(Kafkalidis and Thouless 2002)** Kafkalidis MS, Thouless MD. The effects of geometry and material properties on the fracture of single lap-shear joints. International Journal of Solids and Structures 2002;39:4367-4383.
- **(Kairouz and Matthews 1993)** Kairouz KC, Matthews FL. Strength and failure modes of bonded single lap joints between cross-ply adherends. Composites 1993;24:475-484.
- **(Kanninen and Popelar 1985)** Kanninen MF, Popelar CH. Advanced Fracture Mechanics. Oxford University Press: Oxford, UK; 1985.
- **(Karaagaç et al. 2007)** Karaagaç C, Öztürk H, Sabuncu M. Lateral dynamic stability analysis of a cantilever laminated composite beam with an elastic support. International Journal of Structural Stability and Dynamics 2007;7:727-730.
- **(Karbhari and Shulley 1995)** Karbhari VM, Shulley SB. Use of composites for rehabilitation of civil structures – determination of bond durability. Journal of Materials in Civil Engineering 1995;7:239-245.
- **(Kaye and Heller 2002)** Kaye RH, Heller M. Through-thickness shape optimisation of bonded repairs and lap-joints. International Journal of Adhesion & Adhesives 2002;22:7-21.
- **(Kaye and Heller 2006)** Kaye RH, Heller M. Finite element-based three-dimensional stress analysis of composite bonded repairs to metallic aircraft structure. International Journal of Adhesion & Adhesives 2006;26:261-273.
- **(Kayupov and Dzenis 2001)** Kayupov M, Dzenis YA. Stress concentrations caused by bond cracks in single-lap adhesive composite joints. Composite Structures 2001;54:215-220.
- **(Kellas and Morton 1992)** Kellas S, Morton J. Strength scaling in fibre composites. AIAA Journal 1992;30:1074-1080.
- **(Keller and Vallée 2005a)** Keller T, Vallée T. Adhesively bonded lap joints from pultruded GFRP profiles. Part I: Stress-strain analysis and failure modes. Composites: Part B – Engineering 2005;36:331-340.

- **(Keller and Vallée 2005b)** Keller T, Vallée T. Adhesively bonded lap joints from pultruded GFRP profiles. Part II: Joint strength prediction. Composites: Part B – Engineering 2005;36:341-350.
- **(Kilic et al. 2006)** Kilic B, Madenci E, Ambur DR. Influence of adhesive spew in bonded single-lap joints. Engineering Fracture Mechanics 2006;73:1472-1490.
- **(Kim and Kim 1988)** Kim KS, Kim J. Elasto-plastic analysis of the peel test for thin film adhesion. Journal of Engineering Materials and Technology 1988;110:266-273.
- **(Kim et al. 1995)** Kim HS, Lee SJ, Lee DG. Development of a strength model for the cocured stepped lap joints under tensile loading. Composite Structures 1995;32:593-600.
- **(Kim et al. 1997)** Kim Y, Davalos JE, Barbero EJ. Delamination buckling of FRP layer in laminated wood beams. Composite Structures 1997;37:311-320.
- **(Kim et al. 2003)** Kim JK, Kim HS, Lee DG. Investigation of optimal surface treatments for carbon/epoxy composite adhesive joints. Journal of Adhesion Science and Technology 2003;17:329-352.
- **(Kim et al. 2006)** Kim KS, Yoo JS, Yi YM, Kim CG. Failure mode and strength of uni-directional composite single lap bonded joints with different bonding methods. Composite Structures 2006;72:477-485.
- **(Kim et al. 2008a)** Kim TH, Kweon JH, Choi JH. An experimental study on the eefect of overlap length on the failure of composite-to-aluminium single-lap bonded joints. Journal of Reinforced Plastics and Composites 2008;27:1071-1081.
- **(Kim et al. 2008b)** Kim KS, Yi YM, Cho GR, Kim CG. Failure prediction and strength improvement of uni-directional composite single-lap bonded joints. Composite Structures 2008;82:513-520.
- **(Kinloch 1987)** Kinloch AJ. Adhesion and adhesives: science and technology. Chapman & Hall: London, UK; 1987.
- **(Kinloch 1990)** Kinloch AJ. Adhesion and adhesives. Chapman & Hall: London, UK; 1990.
- **(Kinloch and Shaw 1981)** Kinloch AJ, Shaw SJ. The fracture-resistance of a toughened epoxy adhesive. The Journal of Adhesion 1981;12:59-77.
- **(Kocher and Cross 1972)** Kocher LH, Cross SL. Reinforced cutouts in graphite composite structures. ASTM Special Technical Publication 1972;497:382-395.
- **(Konnerth et al. 2006)** Konnerth J, Gindl W, Harm M, Muller U. Comparing dry bond strength of spruce and beech wood glued with different adhesives by means of scarf and lap joint testing method. Holz als Roh- und Werkstoff 2006;64:269-271.
- **(Kress et al. 2006)** Kress G, Naeff P, Niedermeier M, Ermanni P. The onsert: A new joining technology for sandwich structures. Composite Structures 2006;73:196-207.
- **(Krueger 2002)** Krueger R. The Virtual Crack Closure Technique: History, Approach and Applications, NASA Report CR-2002-211628. Hampton, USA. Langley Research Centre 2002.
- **(Kumar et al. 2005)** Kumar SB, Sivashanker S, Bag A, Sridhar I. Failure of aerospace composite scarf-joints subjected to uniaxial compression. Materials Science and Engineering: A 2005;412:117-122.
- **(Kumar et al. 2006)** Kumar SB, Sridhar I, Sivashanker S, Osiyemi SO, Bag A. Tensile failure of adhesively bonded CFRP composite scarf joints. Materials Science and Engineering: B 2006;132:113-120.
- **(Lai and Dillard 1997)** Lai YH, Dillard DA. Using the fracture efficiency to compare adhesion tests. International Journal of Solids and Structures 1997;34:509–525.

- **(Lai et al. 1996)** Lai YH, Rakestraw MD, Dillard DA. The cracked lap shear specimen revisited – a closed form solution. International Journal of Solids and Structures 1996;33:1725-1743.
- **(Lamanna et al. 2007)** Lamanna AJ, Akbiyik A, Ray JC, Velasquez GI. Feasibility investigation into strengthtening of timber bridge stringers. Technical Report A179864. Vicksburgh, USA. Enginner Research and Development Center. Geotechnical and Structures Laboratory 2007.
- **(Lammerant and Verpoest 1996)** Lammerant L, Verpoest I. Modelling of the interaction between matrix cracks and delaminations during impact of composite plates. Composites Science and Technology 1996;56:1171-1178.
- **(Lang and Mallick 1998)** Lang TP, Mallick PK. Effect of spew geometry on stresses in single lap adhesive joints. International Journal of Adhesion & Adhesives 1998;18:167-177.
- **(Lang and Mallick 1999)** Lang TP, Mallick PK. The effect of recessing on the stresses in adhesively bonded single-lap joints. International Journal of Adhesion & Adhesives 1999;257-271.
- **(Lankford 1997)** Lankford J. The compressive failure of polymeric composites under hydrostatic confinement. Composites: Part A – Applied Science and Manufacturing 1997:28:409-418.
- **(Lavoie et al. 2000)** Lavoie JA, Soutis C, Morton J. Apparent strength scaling in continuous fibre composite laminates. Composites Science and Technololy 2000;60:283-299.
- **(Lawson et al. 2006)** Lawson RM, Lim J, Hicks SJ, Simms WI. Design of composite asymmetric cellular beams and beams with large web openings. Journal of Constructional Steel Research 2006;62:614-629.
- **(Lazzarin et al. 2002)** Lazzarin P, Quaresimin M, Ferro P. A two-term stress function approach to evaluate stress distributions in bonded joints of different geometries. Journal of Strain Analysis 2002;37:385-398.
- **(Lee and Hyer 1993)** Lee HH, Hyer MW. Postbuckling failure of composite plates with holes. AIAA Journal 1993;31:1293-1298.
- **(Lee and Kim 2001)** Lee J, Kim S. Flexural-torsional buckling of thin-walled I-section composites. Comput Struct 2001;79:987-995.
- **(Lee and Kong 2000)** Lee KY, Kong BS. Theoretical and experimental studies for the failure criterion of adhesively bonded joints. Journal of Adhesion Science and Technology 2000;14:817-832.
- **(Lee and Lee 1992)** Lee SJ, Lee GL. Development of a failure model for the adhesively bonded tubular single lap joint. The Journal of Adhesion 1992;40:1-14.
- **(Lee and Mall 1989)** Lee JH, Mall S. Strength of composite laminate with reinforced hole. Journal of Composite Materials 1989;23:337-347.
- **(Lee and Soutis 2005)** Lee J, Soutis C. Thickness effect on the compressive strength of T800/924C carbon fibre-epoxy laminates. Composites Part A: Applied Science and Manufacturing 2005;36:213-227.
- **(Lee and Soutis 2007)** Lee J, Soutis CA. study on the compressive strength of thick carbon fibre-epoxy laminates. Composites Science and Technology 2007;67:2015-2026.
- **(Lee and Soutis 2008)** Lee J, Soutis C. Measuring the notched compressive strength of composite laminates: Specimen size effects. Composites Science and Technology 2008;68:2359-2366.
- **(Lee et al. 2002)** Lee J, Kim SE, Hong K. Lateral buckling of I-section composite beams. Engineering Structures 2002;24:955-964.

- **(Lee et al. 2003a)** Lee SM, Abbott AL, Schmoldt DL. Surface shape analysis of rough lumber for wane detection. Computers and Electronics in Agriculture 2003;41:121-137.
- **(Lee et al. 2003b)** Lee DB, Ikeda T, Miyazaki N, Choi NS. Fracture behavior around a crack tip in rubber-modified epoxy adhesive joint with various bond thicknesses. Journal of Materials Science Letters 2003;22:229-233.
- **(Lee et al. 2004)** Lee DB, Ikeda T, Miyazaki N, Choi NS. Effect of bond thickness on the fracture toughness of adhesive joints. Journal of Engineering Materials and Technology 2004;126:14-18.
- **(Leffler et al. 2007)** Leffler K, Alfredsson KS, Stigh U. Shear behaviour of adhesive layers. International Journal of Solids and Structures 2007;44:530-545.
- **(Leichti et al. 1993)** Leichti RJ, Gilham PC, Tingley DA. The Taylor Lake Bridge: a reinforced-glulam structure. Wood Design Focus 1993;4:3-4.
- **(Lessard and Chang 1991)** Lessard LB, Chang FK. Effect of load distribution on fiber buckling strength of unidirectional composites. Journal of Composite Materials 1991;25:65-87.
- **(Li and Sullivan 2001)** Li G, Sullivan PL. Finite element and experimental studies on single-lap balanced joints in tension. International Journal of Adhesion & Adhesives 2001;21:211-220.
- **(Li et al. 1999)** Li G, Lee-Sullivan P, Thring RW. Nonlinear finite element analysis of stress and strain distributions across the adhesive thickness in composite single-lap joints. Composite Structures 1999;46:395-403.
- **(Li et al. 2005a)** Li S, Thouless MD, Waas AM, Schroeder JA, Zavattieri PD. Use of a cohesive-zone model to analyze the fracture of a fiberreinforced polymer–matrix composite. Composites Science and Technology 2005;65:537-549.
- **(Li et al. 2005b)** Li S, Thouless MD, Waas AM, Schroeder JA, Zavattieri PD. Use of mode-I cohesive-zone models to describe the fracture of an adhesively-bonded polymer–matrix composite. Composites Science and Technology 2005;65:281-293.
- **(Li et al. 2006a)** Li S, Thouless MD, Waas AM, Schroeder JA, Zavattieri PD. Mixed-mode cohesive-zone models for fracture of an adhesively bonded polymer–matrix composite. Engineering Fracture Mechanics 2006;73:64-78.
- **(Li et al. 2006b)** Li HCH, Beck F, Dupouy O, Herszberg I, Stoddart PR, Davis CE, Mouritz AP. Strain-based health assessment of bonded composite repairs. Composite Structures 2006;76:234-242.
- **(Liljedahl et al. 2006)** Liljedahl CDM, Crocombe AD, Wahab MA, Ashcroft IA. Damage modeling of adhesive bonded joints. International Journal of Fracture 2006;141:147-161.
- **(Lin and Jen 1999)** Lin WH, Jen MHR. The strength of bolted and bonded single-lapped composite joints in tension. Journal of Composite Materials 1999;33:640-666.
- **(Lionetto and Frigione 2009)** Lionetto F, Frigione M. Mechanical and natural durability properties of wood treated with a novel organic preservative/consolidant product. Materials & Design doi:10.1016/j.matdes.2008.12.010.
- **(Liu and Wang 2007)** Liu X, Wang G. Progressive failure analysis of bonded composite repairs. Composite Structures 2007;81:331-340.
- **(Long 1991)** Long RS. Static strength of adhesively bonded ARALL-1 joints. Journal of Composite Materials 1991;25:391-415.
- **(Lopez-Anido et al. 2003)** Lopez-Anido R, Michael AP, Sandford TC. Experimental characterization of FRP composite-wood pile structural response by bending tests. Marine Structures 2003;16:257-274.

- **(Lopez-Anido et al. 2005)** Lopez-Anido R, Michael AP, Sandford TC, Goodell B. Repair of wood piles using prefabricated fiber-reinforced polymer composite shells. Journal of Performance of Constructed Facilities 2005;19:78-87.
- **(Lubkin 1957)** Lubkin JL. A theory of adhesive scarf joints. Journal of Applied Mechanics 1957;24:255-260.
- **(Luo and Tong 2007)** Luo Q, Tong L. Fully-coupled nonlinear analysis of single lap adhesive joints. International Journal of Solids and Structures 2007;44:2349-2370.
- **(Lyons and Ahmed 2005)** Lyons JS, Ahmed MR. Factors affecting the bond between polymer composites and wood. Journal of Reinforced Plastics and Composites 2005;24:405-412.
- **(Magalhães et al. 2005)** Magalhães AG, de Moura MFSF, Gonçalves JPM. Evaluation of stress concentration effects in single-lap bonded joints of laminate composite materials. International Journal of Adhesion & Adhesives 2005;25:313-319.
- **(Mahdi et al. 2003a)** Madhi S, Kim HJ, Gama BA, Yarlagadda S, Gillespie Jr JW. A comparison of oven-cured and induction-cured adhesively bonded composite joints. Journal of Composite Materials 2003:37:519-542.
- **(Mahdi et al. 2003b)** Mahdi S, Kinloch AJ, Matthews, Crisfield MA. The static mechanical performance of repaired composite sandwich beams: part I – experimental characterization. Journal of Sandwich Structures and Materials 2003;5:179-202.
- **(Mahdi et al. 2003c)** Mahdi S, Kinloch AJ, Matthews, Crisfield MA. The static mechanical performance of repaired composite sandwich beams: part II – finite element modelling. Journal of Sandwich Structures and Materials 2003;5:267-303.
- **(Mai and Cotterell 1980)** Mai YW, Cotterell B. Effects of pre-strain on plane stress ductile fracture in alpha-brass. Journal of Materials Science 1980;15:2296-2306.
- **(Malan 1988a)** Malan FS. Genetic variation in some growth properties among 18 full-sib families of South African grown Eucaliptus grandis: a preliminary investigation. Southern African Forestry Journal 1988;146:38-43.
- **(Malan 1988b)** Malan FS. Wood density variation in four trees of South African grown Eucaliptus grandis (Hill x Maiden). Southern African Forestry Journal 1988;144:36-42.
- **(Mallick 1988)** Mallick PK. Fiber-reinforced composites. Marcel Dekker: New York, USA; 1988.
- **(Malyshev and Salganik 1965)** Malyshev BM, Salganik RL. The strength of adhesive joints using the theory of cracks. International Journal of Fracture 1965;1:114-128.
- **(Marques 2008)** Marques EAS. Analysis of adhesive joints for aerospace applications. M.Sc. Thesis. Porto, Portugal: Department of Mechanical Engineering and Industrial Management, Enginnering Faculty of Porto University: 2008.
- **(Marques and da Silva 2008)** Marques EAS, da Silva LFM. Joint strength optimization of adhesively bonded patches. The Journal of Adhesion 2008;84:917-936.
- **(Marra 1992)** Marra AA. Technology for wood bonding – principles in practice. Van Nostrand Reinhold Company: New York, USA; 1992.
- **(Marshall 1998)** Marshall D. Understanding housing effects. Interprint Ltd: Knaresborough, UK; 1998.
- **(Mays and Hutchinson 1992)** Mays G, Hutchinson AR. Adhesives in civil engineering, 1st ed. Cambridge University Press; Cambridge, UK; 1992.
- **(Mehrkam and Cochran 1997)** Mehrkam PA, Cochran R. Evaluation of materials for composite repair applications. Journal of Thermoplastic Composite Materials 1997;10:51-60.
- **(Meier 1987)** Meier U. Bridge repair with high performance composite materials. Material and Technik 1987;4:125-128.

- **(Meier and Winistorfer 1995)** Meier U, Winistorfer A. Retrofitring of structures through external bonding of CFRP sheets. Proceedings of the 2nd International RILEM Symposium. Ghent, Belgium. 23-25 August 1995.
- **(Messler 1993)** Messler RW. Joining of advanced materials. Butterworths/Heinemann: Stoneham, USA; 1993.
- **(Mi et al. 1997)** Mi Y, Crisfield MA, Hellweg HB, Davies GAO. Finite element method and progressive failure modelling of composite structures. Proceedings of the Computational Plasticity: Fundamentals and Applications Conference. Barcelona, Spain. 17-20 March 1997.
- **(Mi et al. 1998)** Mi Y, Crisfield MA, Davies GAO, Hellweg HB. Progressive delamination using interface elements. Journal of Composite Materials 1998;32:1246-1272.
- **(Minford 1991)** Minford JD. Treatise on adhesion and adhesives, vol. 7. Marcel Dekker: New York, USA; 1991.
- **(Mohri et al. 2002)** Mohri F, Azrar L, Potier-Ferry M. Lateral post-buckling analysis of thin-walled open sections beams. Thin-Walled Structures 2002;40:1013-1036.
- **(Mortensen and Thomsen 1997)** Mortensen F, Thomsen OT. Simplified linear and non-linear analysis of stepped and scarfed adhesive-bonded lap-joints between composite laminates. Composite Structures 1997;38:281-294.
- **(Mortensen and Thomsen 2002)** Mortensen F, Thomsen OT. Analysis of adhesive bonded joints: a unified approach. Composites Science and Technology 2002;62:1011-1031.
- **(Mostovoy et al. 1971)** Mostovoy S, Ripling EJ, Bersch CF. Fracture toughness of adhesive joints. The Journal of Adhesion 1971;3:125-144.
- **(Moulin et al. 1990)** Moulin JM, Pluvinage G, Jodin P. FGRG: Fiberglass reinforced gluelam – A new composite. Wood Science and Technology 1990;24:289-294.
- **(Murillo et al. 2007)** Murillo CG, Fagan M, Ansell MP, Meo M. Experimental and finite element studies of adhesively bonded lap joints for natural fibre composites. Proceedings of the 16th International Conference on Composite Materials. Kyoto, Japan. 8-13 July 2007.
- **(Murmanis and River 1983)** Murmanis L, River BH. Microscopy of abrasive-planed and knife-planed surfaces in wood-adhesive bonds. Wood and Fiber Science 1983;15:102-115.
- **(Myhre 1981)** Myhre SH. Advanced composite repair-recent development and some problems. Composite Repairs. Proceedings of the 26th National SAMPE Symposium and Exhibition. Los Angeles, USA. 28-30 April: 1981.
- **(Myhre and Beck 1979)** Myhre SH, Beck CE. Repair concepts for advanced composite structures. Journal of Aircraft 1979;16:720-728.
- **(Myhre and Kiger 1981)** Myhre SH, Kiger RW. Problems and options in advanced composite repair. Proceedings of the Fibrous Composites in Structural Design Conference. New Orleans, USA. 27-29 January 1981.
- **(Nairn 2000)** Nairn JA. Energy release rate analysis for adhesive and laminate double cantilever beam specimens emphasizing the effect of residual stresses. International Journal of Adhesion & Adhesives 2000;20:59-70.
- **(Narasimhan et al. 2004)** Narasimhan S, Shenoil RA, Jeong HK. Three-dimensional stresses in adhesively bonded lap joints with non-identical adherends. Journal of Materials: Design and Applications 2004;218:283-298.
- **(Natterer 2002)** Natterer JK. New technologies for engineered timber structures. Progress in Structural Engineering and Materials 2002;4:245-263.
- **(Neale 2000)** Neale KW. FRPs for structural rehabilitation: a survey of recent progress. Progress in Structural Engineering and Materials 2000;2:133-138.

- **(Needleman 1987)** Needleman A. A continuum model for void nucleation by inclusion debonding. Journal of Applied Mechanics 1987;54:525-532.
- **(Needleman 1990)** Needleman A. An analysis of tensile decohesion along an interface. Journal of the Mechanics and Physics of Solids 1990;38:289-324.
- **(Nguyen 1997)** Nguyen BN. Three-dimensional modeling of damage in laminated composites containing a central hole. Journal of Composite Materials 1997;31:1672-1693.
- **(Nishino and Aoki 2006)** Nishino M, Aoki. Nonlinear analysis and damage monitoring of a one-sided patch repair with delamination. Composite Structures 2006;73:423-431.
- **(Nussbaum 1993)** Nussbaum RM. Oxidative activation of wood surfaces by flame treatment. Wood Science and Technology 1993;27:183-193.
- **(O'Brien 1998)** O'Brien TK. Composite interlaminar shear fracture toughness, G_{IIc}: shear measurement or sheer myth? ASTM Special Technical Publication 1998;1330:3-18.
- **(O'Neill 1982)** O'Neill SS. Asymmetric reinforcement of a quasi-isotropic Gr/Ep plates containing a circular hole. M.Sc. Thesis. Monterey, USA: Naval Postgraduate School: 1982.
- **(Objois et al. 1999)** Objois A, Gilibert Y, Fargette B. Theoretical and experimental analysis of the scarf joint bonded structure: Influence of the adhesive thickness on the micro-mechanical behaviour. The Journal of Adhesion 1999;70:13-32.
- **(Objois et al. 2000)** Objois A, Fargette B, Gilibert Y. The influence of the bevel angle on the micro-mechanical behaviour of bonded scarf joints. Journal of Adhesion Science and Technology 2000;14:1057-1070.
- **(Objois et al. 2005)** Objois A, Assih J, Troalen JP. Theoretical method to predict the first microcracks in a scarf joint. The Journal of Adhesion 2005;81:893-909.
- **(Odi 1998)** Odi RA. Bonded repair of composite structures: a finite element approach. Ph.D. Thesis. Cranfield, UK: School of Engineering, Cranfield University: 1998.
- **(Odi and Friend 2002)** Odi RA, Friend CM. A comparative study of finite element models for the bonded repair of composite structures. Journal of Reinforced Plastics and Composites 2002;21:311-332.
- **(Odi and Friend 2004)** Odi RA, Friend CM. An improved 2D model for bonded composite joints. International Journal of Adhesion & Adhesives 2004;24:389-405.
- **(Ogawa 2000)** Ogawa H. Architectural application of carbon fibers – Development of new carbon fiber reinforced glulam. Carbon 2000;38:211-226.
- **(Ojalvo and Eidinoff 1978)** Ojalvo IU, Eidinoff HL. Bond Thickness Effects upon Stresses in Single-Lap Adhesive Joints. AIAA Journal 1978,16:204-211.
- **(Olia and Rossetos 1996)** Olia M, Rossetos JN. Analysis of adhesively bonded joints with gaps subjected to bending. International Journal of Solids and Structures 1996;33:2681-2693.
- **(Ong and Shen 1991)** Ong CL, Shen SB. Repair of F-104 aircraft nosedome by composite patching. Theoretical and Applied Fracture Mechanics 1991;15:75-83.
- **(Osnes and Andersen 2003)** Osnes H, Andersen A. Computational analysis of geometric nonlinear effects in adhesively bonded single lap joints. Composites: Part B – Engineering 2003;34:417-427.
- **(Oterkus et al. 2005)** Oterkus E, Barut A, Madenci E, Ambur DR. Nonlinear analysis of a composite panel with a cutout repaired by a bonded tapered composite patch. International Journal of Solids and Structures 2005;42:5274-5306.

- **(Oterkus et al. 2006)** Oterkus E, Barut A, Madenci E, Smeltzer III SS, Ambur DR. Bonded lap joints of composite laminates with tapered edges. International Journal of Solids and Structures 2006;43:1459-1489.
- **(Ou and Weller 1986)** Ou FL, Weller C. An Overview of Timber Bridges. Transportation Research Record 1986;1053:1-12.
- **(Owens and Sullivan 2000a)** Owens JFP, Sullivan PL. Stiffness behaviour due to fracture in adhesively bonded composite-to-aluminium joints I. Theoretical model. International Journal of Adhesion & Adhesives 2000;20:39-45.
- **(Owens and Sullivan 2000b)** Owens JFP, Sullivan PL. Stiffness behaviour due to fracture in adhesively bonded composite-to-aluminium joints II. Experimental. International Journal of Adhesion & Adhesives 2000;20:47-58.
- **(Oztelcan et al. 1997)** Oztelcan O, Ochoa OO, Martin J, Sem K. Design and analysis of test coupons for composite blade repairs. Composite Structures 1997;37:185-193.
- **(Pandey and Narasimhan 2001)** Pandey PC, Narasimhan S. Three-dimensional nonlinear analysis of adhesively bonded lap joints considering viscoplasticity in adhesives. Computers & Structures 2001;79:769-783.
- **(Panigrahi and Pradhan 2007a)** Panigrahi SK, Pradhan B. Three dimensional failure analysis and damage propagation behavior of adhesively bonded single lap joints in laminated FRP composites. Journal of Reinforced Plastics and Composites 2007;26:183-201.
- **(Panigrahi and Pradhan 2007b)** Panigrahi SK, Pradhan B. Delamination damage analyses of adhesively bonded lap shear joints in laminated FRP composites. International Journal of Fracture 2007;148:373-385.
- **(Panigrahi and Pradhan 2007c)** Panigrahi SK, Pradhan B. Adhesion failure propagation in adhesively-bonded single-lap laminated FRP composite joints. Journal of Adhesion Science and Technology 2007;21:379-398.
- **(Papanikos et al. 2005)** Papanikos P, Tserpes KI, Labeas G, Pantelakis S. Progressive damage modelling of bonded composite repairs. Theoretical and Applied Fracture Mechanics 2005;43:189-198.
- **(Papini et al. 1994)** Papini M, Fernlund G, Spelt JK. The effect of geometry on the fracture of adhesive joints. International Journal of Adhesion & Adhesives 1994;14:5-13.
- **(Pardoen et at. 2005)** Pardoen T, Ferracin T, Landis CM, Delannay F. Constraint effects in adhesive joint fracture. Journal of the Mechanics and Physics of Solids 2005;53:1951-1983.
- **(Penado 1998)** Penado FE. A simplified method for the geometrically nonlinear analysis of the single lap joint. Journal of Thermoplastic Composite Materials 1998;11:272-287.
- **(Penado 2000)** Penado FE. Analysis of singular regions in bonded joints. International Journal of Fracture 2000;105:1-25.
- **(Pereira 2005)** Pereira JL. Comportamento mecânico da madeira em tracção nas direcções de simetria material. M.Sc. Thesis. Vila Real, Portugal: Department of Engineering, University of Trás-os-Montes and Alto Douro: 2005.
- **(Pereira and de Morais 2003)** Pereira AB, de Morais AB. Strength of adhesively bonded stainless steel joints. International Journal of Adhesion & Adhesives 2003;23:315-322.
- **(Peterson 1965)** Peterson J. Wood beams prestressed with bonded tension elements. ASCE Journal of the Structural Division 1965;91:103-119.
- **(Petrossian and Wisnom 1998)** Petrossian Z, Wisnom MR. Prediction of delamination initiation and growth from discontinuous plies using interface elements. Composites: Part A – Applied Science and Manufacturing 1998;29:503-515.
- **(Pi and Trahair 1992)** Pi YL, Trahair NS. Prebuckling deflections and lateral buckling II: Applications. ASCE Journal of Structural Engineering 1992;118:2967-2985.

- **(Pinto et al. 2008)** Pinto AMG, Magalhães AG, Silva FG, Baptista APM. Shear strength of adhesively bonded polyolefins with minimal surface preparation. International Journal of Adhesion & Adhesives 2008;28:452-456.
- **(Pinto et al. 2009)** Pinto AMG, Magalhães AG, Campilho RDSG, de Moura MFSF, Baptista APM. Single-lap joints of similar and dissimilar adherends bonded with an acrylic adhesive. Accepted in The Journal of Adhesion.
- **(Pires et al. 2003)** Pires I, Quintino L, Durodola JF, Beevers. Performance of bi-adhesive bonded aluminium lap joints. International Journal of Adhesion & Adhesives 2003;23:215-223.
- **(Pirvics 1974)** Pirvics J. Two dimensional displacement-stress distributions in adhesive bonded composite structures. The Journal of Adhesion 1974;6:207-228.
- **(Pirvu et al. 2004)** Pirvu A, Gardner DJ, Lopez-Anido R. Carbon fiber-vinyl ester composite reinforcement of wood using the VARTM/SCRIMP fabrication process. Composites: Part A - Applied Science and Manufacturing 2004;35:1257-1265.
- **(Pizzi and Mittal 2003)** Pizzi A, Mittal KL. Handbook of adhesive technology. 2nd ed. CRC Press: Boca Raton, USA; 2003.
- **(Plecnik et al. 1980)** Plecnik JM, Iding RI, Cunningham JD, Bresler B. Temperature effects on epoxy adhesives. ASCE Journal of the Structural Division 1980;106:99-113.
- **(Plevris and Triantafillou 1992)** Plevris N, Triantaflllou TC. FRP-reinforced wood as structural material. Journal of Materials in Civil Engineering 1992;4:300-317.
- **(Pocius 2002)** Pocius AV. Adhesion and adhesives technology: an introduction, 2nd ed. Hanser Gardner Publications: Cincinnati, USA; 2002.
- **(Potter et al. 2001)** Potter KD, Guild FJ, Harvey HJ, Wisnom MR, Adams RD. Understanding and control of adhesive crack propagation in bonded joints between carbon fibre composite adherends I. Experimental. International Journal of Adhesion & Adhesives 2001;21:435-443.
- **(Pradhan et al. 1994)** Pradhan SC, Iyengar NGR, Kishore NN. Parametric study of interfacial debonding in adhesively bonded composite joints. Composite Structures 1994;29:119-125.
- **(Premrov et al. 2004a)** Premrov M, Dobrila P, Bedenik BS. Analysis of timber-framed walls coated with CFRP strips strengthened fibre-plaster boards. International Journal of Solids and Structures 2004;41:7035-7048.
- **(Premrov et al. 2004b)** Premrov M, Dobrila P, Bedenik BS. Approximate analytical solutions for diagonal reinforced timber-framed walls with fibre-plaster coating material. Constrution and Building Materials 2004;18:727-735.
- **(Qian and Akisanya 1999)** Qian ZQ, Akisanya AR. An investigation of the stress singularity near the free edge of scarf joints. European Journal of Mechanics - A/Solids 1999;18:443-463.
- **(Qiao et al. 1998)** Qiao P, Davalos JF, Zipfel M. Modeling and optimal design of composite-reinforced wood railroad crosstie. Composite Structures 1998;41:87-96.
- **(Qin and Dzenis 2003)** Qin M, Dzenis Y. Analysis of single-lap adhesive composite joints with delaminated adherends. Composites: Part B – Engineering 2003;34:167-173.
- **(Quaresimin and Ricotta 2006a)** Quaresimin M, Ricotta M. Stress intensity factors and strain energy release rates in single lap bonded joints in composite materials. Composites Science and Technology 2006;66:647-656.
- **(Quaresimin and Ricotta 2006b)** Quaresimin M, Ricotta M. Fatigue behaviour and damage evolution of single lap bonded joints in composite material. Composites Science and Technology 2006;66:176-187.

- **(Radford et al. 2002)** Radford DW, Van Goethem D, Gutkowski RM, Peterson ML. Composite repair of timber structures. Construction and Builing Materials 2002;16:417-425.
- **(Radice and Vinson 2006)** Radice J, Vinson J. On the use of quasi-dynamic modeling for composite material structures: analysis of adhesively bonded joints with midplane asymmetry and transverse shear deformation. Composites Science and Technology 2006;66:2528-2547.
- **(Radice and Vinson 2008)** Radice JJ, Vinson JR. On the analysis of adhesively bonded structures: A high order semi-elastic adhesive layer model. Composites Science and Technology 2008;68:376-386.
- **(Raghava et al. 1973)** Raghava R, Caddell RM, Yeh GS. The macroscopic yield behaviour of polymers. Journal of Materials Science 1973;8:225-232.
- **(Ramantani et al. 2009)** Ramantani DA, Campilho RDSG, de Moura MFSF, Marques AT. Stress and failure analysis of repaired sandwich composite beams using a cohesive damage model. Accepted in Journal of Sandwich Structures and Materials.
- **(Rammer 1999)** Rammer DR. Evaluation of recycled timber members. Materials and construction. Proceedings of the 5th ASCE Materials Engineering Congress. Cincinnati, USA. 10-12 May 1999.
- **(Rammer and McLean 1996)** Rammer DR, McLean DI. Shear Strength of Wood Beams. Proceedings of the National Conference on Wood Transportation Structures. Madison, USA. 23-25 October 1996.
- **(Rammer et al. 1998)** Rammer DR, McLean DI, Cofer WF. In-place Shear Strength of Wood Beams. Proceedings of the 5th World Conference on Timber Engineering. Montreux, Switzerland. 17-20 August 1998.
- **(Rastogi et al. 1998)** Rastogi N, Soni SR, Denney JJ. Analysis of bonded composite patch repaired metallic structures – an overview of aging aircraft. Proceedings of the AIAA SDM Conference. Long Beach, USA. 20-23 April 1998.
- **(Reis et al. 2005)** Reis P, Antunes F, Ferreira JAM. Influence of superposition length on mechanical resistance of single-lap adhesive joints. Composite structures 2005;67:125-133.
- **(Reis et al. 2009)** Reis PNB, Amaro AM, Magalhães AM, de Moura MFSF, Campilho RDSG. Optimization of the taper angle on adhesive single-lap joints. Submitted to Engineering Fracture Mechanics.
- **(Renton and Vinson 1975a)** Renton WJ, Vinson JR. On the behaviour of bonded joints in composite material structures. Engineering Fracture Mechanics 1975;7:41-60.
- **(Renton and Vinson 1975b)** Renton WJ, Vinson JR. The efficient design of adhesive bonded joints. The Journal of Adhesion 1975;7:175-193.
- **(Renton and Vinson 1975c)** Renton WJ, Vinson JR. Fatigue behaviour of bonded joints in composite material structures. Journal of Aircraft 1975;12:442-447.
- **(Richardson 1995)** Richardson B. Remedial treatment of buildings, 2nd ed. Butterworths/Heinemann: Stoneham, USA; 1995.
- **(Richardson et al. 1993)** Richardson G, Crocombe AD, Smith PA. A comparison of two- and three-dimensional finite element analysis of adhesive joints. International Journal of Adhesion & Adhesives 1993;13:193-200.
- **(Richter and Steiger 2005)** Richter K, Steiger R. Thermal stability of wood-wood and wood-FRP bonding with polyurethane and epoxy adhesives. Advanced Engineering Materials 2005;7:419-426.
- **(Ripling et al. 1963)** Ripling EJ, Mostovoy S, Patrick RL. Application of Fracture Mechanics to Adhesive Joints. ASTM Special Technical Publication 1963;360:5-19.

- **(Rispler et al. 2000)** Rispler AR, Tong L, Steven GP, Wisnom MR. Shape optimization of adhesive fillets. International Journal of Adhesion & Adhesives 2000;20:221-231.
- **(Ritter 1990)** Ritter MA. Timber bridges: design, construction, inspection and maintenance. Report EM 7700-8. Washington, USA. United States Department of Agriculture 1990.
- **(Robinson and Das 2004)** Robinson P, Das S. Mode I DCB testing of composite laminates reinforced with z-direction pins: a simple model for the investigation of data reduction strategies. Engineering Fracture Mechanics 2004;71:345-364.
- **(Robson et al. 1992)** Robson JE, Matthews FL, Kinloch AJ. The strength of composite repair patches: a laminate analysis approach. Journal of Reinforced Plastics and Composites 1992;11:729-742.
- **(Romilly and Clark 2008)** Romilly DP, Clark RJ. Elstic analysis of hybrid bonded joints and bonded composite repairs. Composite Structures 2008;82:563-576.
- **(Rostasy 1987)** Rostasy FS. Bonding of steel and GFRP plates in the area of coupling joints. Research Report Nº 3126/1429. Braunschweig, Germany. Federal Institute for Materials Testing 1987.
- **(Roy et al. 1997)** Roy AK, Donaldson SL, Schoeppner GA. Bonded joints of unidirectional and cross-ply laminates: an experimental study. Proceedings of the 38th AIAA/ASME/ASCE/AHS/ASC Structures, Structural Dynamics and Materials Conference. Florida, USA. 7-10 April 1997.
- **(Salmon and Pocius 2004)** Salmon FT, Pocius AV. Modeling of cohesive failure processes in structural adhesive bonded joints. Journal of Adhesion Science and Technology 2004;18:287-299.
- **(Sancaktar and Nirantar 2003)** Sancaktar E, Nirantar P. Increasing strength of single-lap joints of metal adherends by taper minimization. Journal of Adhesion Science and Technology 2003;17:655-675.
- **(Sancaktar and Simmons 2000)** Sancaktar E, Simmons SR. Optimization of adhesively-bonded single lap joints by adherend notching. Journal of Adhesion Science and Technology 2000;14:1363-1404.
- **(Sandhu 1972)** Sandhu RS. A survey of failure theories of isotropic and anisotropic materials. Technical report AFFDL-TR-72-71. Dayton, USA. Air force flight dynamics laboratory. Wright Aeronautical Labs 1972.
- **(Sapkas and Kollar 2002)** Sapkas A, Kollar LP. Lateral–torsional buckling of composite beams. International Journal of Solids and Structures 2002;39:2939-2963.
- **(Savage 2007)** Savage G. Failure prevention in bonded joints on primary load bearing structures. Engineering Failure Analysis 2007;14:321-348.
- **(Sawa and Uchida 1997)** Sawa T, Uchida H. A two-dimensional stress analysis and strength evaluation of band adhesive butt joints subjected to tensile loads. Journal of Adhesion Science and Technology 1997;11:811-833.
- **(Schroeder 1990)** Schroeder JA. Photoelastic stress analysis of bonded lap shear joints having thermoplastic adherends. The Journal of Adhesion 1990;32:89-103.
- **(Schubbe and Mall 1998)** Schubbe JJ, Mall S. Fatigue behaviour in thick aluminium panels with a composite repair. Proceedings of the AIAA SDM Conference, Long Beach, USA. 20-23 April 1998.
- **(Schuecker and Davidson 2000)** Schuecker C, Davidson BD. Effect of friction on the perceived mode II delamination toughness from three and four point bend end notched flexure tests. ASTM STP 2000;1383:334-344.
- **(Seo and Lee 2002)** Seo DC, Lee JJ. Fatigue crack growth behaviour of cracked aluminium plate repaired with composite patch. Composite Structures 2002;57:323-330.

- **(Shanmugam and Thevendran 1992)** Shanmugam NE, Thevendran V. Critical loads of thin-walled beams containing web openings. Thin Walled Structures 1992;14:291-305.
- **(Sheppard et al. 1998)** Sheppard A, Kelly D, Tong L. A damage zone model for the failure analysis of adhesively bonded joints. International Journal of Adhesion & Adhesives 1998;18:385-400.
- **(Sherwin 1999)** Sherwin GR. Non-autoclave processing of advanced composite repairs. International Journal of Adhesion & Adhesives 1999;19:155-159.
- **(Shin and Lee 2003)** Shin KC, Lee JJ. Bond parameters to improve tensile load bearing capacities of co-cured single and double lap joints with steel and carbon-fiber-epoxy composite adherends. Journal of Composite Materials 2003;37:401-420.
- **(Shin et al. 2003)** Shin KC, Lim JO, Lee JJ. The manufacturing process of co-cured single and double lap joints and evaluation of the load-bearing capacities of co-cured joints. Journal of Materials Processing Technology 2003;138:89-96.
- **(Siener 1992)** Siener MP. Stress field sensivity of a composite patch repair as a result of varying patch repair thickness. ASTM Special Technical Publication 1992;1120:444-464.
- **(Silva 2005)** Silva MAL. Estudo das propriedades de fractura em modo II e em modo III da madeira de pinus pinaster ait. M.Sc. Thesis. Porto, Portugal: Department of Mechanical Engineering and Industrial Management, Enginnering Faculty of Porto University: 2005.
- **(Silva et al. 2007)** Silva MAL, Morais JJL, de Moura MFSF, Lousada JL. Mode II wood fracture characterization using the ELS test. Engineering Fracture Mechanics 2007;74:2133-2147.
- **(Sliker 1962)** Sliker A. Reinforced wood laminated beams. Forest Products Journal 1962;12:91-96.
- **(Smith and Vasic 2003)** Smith I, Vasic S. Fracture behaviour of softwood. Mechanics of Materials 2003;35:803-815.
- **(Soltis et al. 1998)** Soltis LA, Ross RJ, Windorski DF. Fiberglass-reinforced bolted wood connections. Forest Products Journal 1998;48:63-67.
- **(Soutis and Hu 1996)** Soutis C, Hu FZ. Design and performance of bonded patch repairs of composite structures. Proceedings of the IMechE Conference on Airworthiness Aspects of New Technologies. Bristol, UK. 10 November 1996.
- **(Soutis and Hu 1997)** Soutis C, Hu FZ. Repair design of composites and efficiency of scarf patch repairs. Proceedings of the 11th International Conference on Composite Materials. Gold Coast, Australia. 14-18 July 1997.
- **(Soutis et al. 1999)** Soutis C, Duan DM, Goutas P. Compressive behaviour of CFRP laminates repaired with adhesively bonded external repairs. Composite structures 1999;45:289-301.
- **(Soutis et al. 2002)** Soutis C, Lee J, Kong C. Size effects on compressive strength of T300/924C carbon fibre-epoxy laminates. Plastics, Rubber and Composites 2002;3:364-370.
- **(Spaun 1981)** Spaun FD. Reinforcement of wood with fiberglass. Forest Products Journal 1981;31:26-33.
- **(Steiger 2002)** Steiger R. Fibre reinforced plastics (FRP) in timber structures: Investigations and developments. Proceedings of the EUROWOOD Workshop 2002 on “Engineered wood products – Innovation and exploitation”. Helsinki, Finland. 1-5 June 2002.
- **(Stone 1985)** Stone RH. Development of repair procedures for graphite/epoxy structures on commercial transports. SAMPE Monograph No. 1: Covina, USA; 1985.
- **(Suemasu et al. 2006)** Suemasu H, Takahashi H, Ishikawa T. On failure mechanisms of composite laminates with an open hole subjected to compressive load. Composites Science and Technology 2006;66:634-641.

- **(Sullivan et al. 1994)** Sullivan GR, Hamilton MH, McCarthy JE. Bridge inspection, maintenance and repairs. Technical Report TM 5-600/AFJPAM 32-1088. Washington DC, USA. Joint Departments of the Army and Air Force 1994.
- **(Svecova and Eden 2004)** Svecova D, Eden RJ. Flexural and Shear Strengthening of Timber Beams Using Glass Fiber Reinforced Polymer Bars-An Experimental Investigation. Canadian Journal of Engineering 2004;31:45-55.
- **(Svensson 1985)** Svensson SE. Lateral buckling of beams analyzed as elastically supported columns subject to a varying axial force. Journal of Constructional Steel Research 1985;5:179-193.
- **(Szépe 1966)** Szépe F. Strength of adhesive-bonded lap joints with respect to change of temperature and fatigue. Experimental Mechanics 1966;6:280-286.
- **(Tai 2004)** Tai T. The lateral-torsional buckling analysis of composite laminated beams. M.Sc. Thesis. Taichung, Taiwan: Graduate Institute of Aeronautical Engineering, Feng Chia University: 2004.
- **(Taib et al. 2006a)** Taib AA, Boukhili R, Achiou S, Boukehili H. Bonded joints with composite adherends. Part II. Finite element analysis of joggle lap joints. International Journal of Adhesion & Adhesives 2006;26:237-248.
- **(Taib et al. 2006b)** Taib AA, Boukhili R, Achiou S, Gordon S, Boukehili H. Bonded joints with composite adherends. Part I. Effect of specimen configuration, adhesive thickness, spew fillet and adherend stiffness on fracture. International Journal of Adhesion & Adhesives 2006;26:226-236.
- **(Tamuzs et al. 2003)** Tamuzs V, Tarasovs S, Vilks U. Delamination properties of translaminar-reinforced composites. Composites Science and Technology 2003;63:1423-1431.
- **(Tan and Tsai 1987)** Tan SC, Tsai SW. Notched strength. Composites Design, 3rd ed. Springer-Verlag: New-York, USA; (1987).
- **(Thamm 1976)** Thamm F. Stress distribution in lap joints with partially thinned adherends. The Journal of Adhesion 1976;7:301-309.
- **(Theakston 1965)** Theakston FH. A feasibility study for strengthening timber beams with fiberglass. Canadian Agriculture Engineering 1965;January:17-19.
- **(Thevendran and Shanmugam 1992)** Thevendran V, Shanmugam NE. Lateral buckling of narrow rectangular beams containing openings. Computers & Structures 1992;43:247-254.
- **(Timoshenko and Gere 1961)** Timoshenko SP, Gere JM. Theory of Elastic Stability. McGraw-Hill: New York, USA; 1961.
- **(Tingley 1994)** Tingley DA. Aligned fiber reinforcement panel for structural wood members. US Patent 5362545.
- **(Tomblin et al. 2004)** Tomblin JS, Salah L, Welch JM, Borgman MD. Bonded repair of aircraft composite sandwich structures. Report PB2004-105463. Wichita, USA. Boeing Co 2004.
- **(Tong 1996)** Tong L. Bond strength for adhesive bonded single lap joints. Acta Mechanica 1996;117:103-113.
- **(Tong 1997)** Tong L. An assessment of failure criteria to predict the strength of adhesively bonded composite double lap joints. Journal of Reinforced Plastics and Composites 1997;16:698-713.
- **(Tong and Steven 1999)** Tong L, Steven GP. Analysis and design of structural bonded joints. Kluwer Academic Publishers: Boston, USA; 1999.
- **(Tong et al. 1995)** Tong L, Sheppard A, Kelly D. Relationship between surface displacement and adhesive peel stress in bonded double lap joints. International Journal of Adhesion & Adhesives 1995;15:43-48.

- **(Tong et al. 1997)** Tong L, Kuruppu M, Kelly M. Analysis of adhesively bonded composite double lap joints. Journal of Thermoplastic Composite Materials 1997;10:61-75.
- **(Towse et al. 1997)** Towse A, Davies RGH, Clarke A, Wisnom MR, Adams RD, Potter KD. The design and analysis of high load intensity adhesively bonded double lap joints. Proceedings of the 4th International Conference on Deformation and Fracture of Composites. Manchester, London. 24-26 March 1997.
- **(Towse et al. 1999)** Towse A, Potter KD, Wisnom MR, Adams RD. The sensitivity of a Weibull failure criterion to singularity strength and local geometric variations. International Journal of Adhesion & Adhesives 1999;19:71-82.
- **(Trahair 1993)** Trahair NS. Flexural–torsional buckling of structures. CRC Press: Boca Raton, USA; 1993.
- **(Trantina 1972)** Trantina GG. Fracture mechanics approach to adhesive joints. Journal of Composite Materials 1972;6:192-207.
- **(Triantafillou 1997)** Triantafillou TC. Shear Reinforcement of Wood Using FRP Materials. Journal of Materials in Civil Engineering 1997;9:65-69.
- **(Triantafillou 1998a)** Triantafillou TC. Strengthening of structures with advanced FRPs. Progress in Structural Engineering and Materials 1998;1:126-134.
- **(Triantafillou 1998b)** Triantafillou TC. Composites: a new possibility for the shear strengthening of concrete, masonry and wood. Composites Science and Technology 1998;58:1285-1295.
- **(Triantafillou and Deskovic 1992)** Triantafillou T, Deskovic N. Pre-stressed FRP sheets as external reinforcement of wood members. ASCE Journal of Structural Engineering 1992;118:1270-1284.
- **(Triantafillou and Plevris 1991)** Triantafillou TC, Plevris N. Post-strengthening of r/c beams with epoxy-bonded fiber-composite materials. Proceedings of the ASCE Conference on Advanced Composite Materials in Civil Engineering Structures. Las Vegas, USA. 31 January-1 February 1991.
- **(Tsai and Morton 1994)** Tsai MY, Morton J. An evaluation of analytical and numerical solutions to the single-lap joint. International Journal of Solids and Structures 1994;31:2537-2563.
- **(Tsai and Morton 1995a)** Tsai MY, Morton J. An experimental investigation of non-linear deformations in single-lap joints. Mechanics of Materials 1995;20:183-194.
- **(Tsai and Morton 1995b)** Tsai MY, Morton J. The effect of a spew fillet on adhesive stress distributions in laminated composite single-lap joints. Composite Structures 1995;32:123-131.
- **(Tsai and Wu 1971)** Tsai SW, Wu EM. A general theory of strength for anisotropic materials. Journal of Composite Materials 1971;5:58-81.
- **(Tsai et al. 1995)** Tsai MY, Morton J, Matthews FL. Experimental and numerical studies of a laminated composite single-lap adhesive joint. Journal of Composite Materials 1995;29:1154-1275.
- **(Tsai et al. 1998)** Tsai MY, Oplinger DW, Morton J. Improved theoretical solutions for adhesive lap joints. International Journal of Solids and Structures 1998;35:1163-1185.
- **(Tsuji and Kubomura 1992)** Tsuji N, Kubomura K. Non-linear compression stress-strain curve of pitch-based high modulus carbon fibre composites and structural responses. Journal of Materials Science 1992;27:3782-3788.
- **(Turon et al. 2007)** Turon A, Dávila CG, Camanho PP, Costa J. An engineering solution for mesh size effects in the simulation of delamination using cohesive zone models. Engineering Fracture Mechanics 2007;74:1665-1682.

- **(Turvey 1996a)** Turvey GJ. Effects of load position on the lateral buckling response of pultruded GRP cantilevers-comparisons between theory and experiment. Composite Structures 1996;35:33-47.
- **(Turvey 1996b)** Turvey GJ. Lateral buckling tests on rectangular cross section pultruded GRP Cantilever beams. Composites: Part B – Engineering 1996;27:35-42.
- **(Tvergaard and Hutchinson 1992)** Tvergaard V, Hutchinson, JW. The relation between crack growth resistance and fracture process parameters in elastic-plastic solids. Journal of the Mechanics and Physics of Solids 1992;40:1377-1397.
- **(Tvergaard and Hutchinson 1993)** Tvergaard V, Hutchinson, JW. The influence of plasticity on the mixed-mode interface toughness. Journal of the Mechanics and Physics of Solids 1993;41:1119-1135.
- **(Tvergaard and Hutchinson 1996)** Tvergaard V, Hutchinson JW. On the toughness of ductile adhesive joints. Journal of the Mechanics and Physics of Solids 1996;44:789-800.
- **(Tzetzis and Hogg 2008)** Tzetzis D, Hogg PJ. Experimental and finite element analysis on the performance of vacuum-assisted resin infused single scarf repairs. Materials and Design 2008;29:436-449.
- **(Uenoya and Redwood 1978)** Uenoya M, Redwood RG. Buckling of webs openings. Computers & Structures 1978;9:191-199.
- **(Vable and Maddi 2006)** Vable M, Maddi JR. Boundary element analysis of adhesively bonded joints. International Journal of Adhesion & Adhesives 2006;26:133-144.
- **(Vallée and Keller 2006)** Vallée T, Keller T. Adhesively bonded lap joints from pultruded GFRP profiles. Part III: Effects of chamfers. Composites: Part B – Engineering 2006;37:328-336.
- **(Vallée et al. 2006a)** Vallée T, Correia JR, Keller T. Probabilistic strength prediction for double lap joints composed of pultruded GFRP profiles – Part I: Experimental and numerical investigations. Composites Science and Technology 2006;66:1903-1914.
- **(Vallée et al. 2006b)** Vallée T, Correia JR, Keller T. Probabilistic strength prediction for double lap joints composed of pultruded GFRP profiles – Part II: Strength prediction. Composites Science and Technology 2006;66:1915-1930.
- **(Valoroso and Champaney 2006)** Valoroso N, Champaney L. A damage-mechanics-based approach for modelling decohesion in adhesively bonded assemblies. Engineering Fracture Mechanics 2006;73:2774-2801.
- **(Van Tooren et al. 2004)** Van Tooren MJL, Gleich DM, Beukers A. Experimental verification of a stress singularity model to predict the effect of bondline thickness on joint strength. Journal of Adhesion Science and Technology 2004;18:395-412.
- **(Vinson and Sierakowski 1987)** Vinson JR, Sierakowski RL. The behaviour of structures composed of composite materials. Martinus Nijhoff: Dordrecht, The Netherlands; 1987.
- **(Volkersen 1938)** Volkersen O. Die nietkraftoerteilung in zubeanspruchten nietverbindungen konstanten loschonquerschnitten. Luftfahrtforschung 1938;15:41-47.
- **(Volkersen 1965)** Volkersen O. Recherches sur la theorie des asssemblages collés. Construction Metallique 1965:4;3-13.
- **(Wang and Gunnion 2008)** Wang CH, Gunnion AJ. On the design methodology of scarf repairs to composite laminates. Composites Science and Technology 2008;68:35-46.
- **(Wang and Rose 1997)** Wang CH, Rose LRF. Determination of triaxial stresses in bonded joints. International Journal of Adhesion & Adhesives 1997;17:17-25.

- **(Wang and Rose 2000)** Wang CH, Rose LRF. Compact solutions for the corner singularity in bonded lap joints. International Journal of Adhesion & Adhesives 2000;20:145-154.
- **(Wang and Williams 1992)** Wang Y, Williams JG. Corrections for Mode II Fracture Toughness Specimens of Composite Materials. Composites Science and Technology 1992;43:251-256.
- **(Wang et al. 1996)** Wang HS, Hung CL, Chang FK. Bearing failure of bolted composite joints. Part I: Experimental characterization. Journal of Composite Materials 1996;30:1284-1313.
- **(Wang et al. 2004)** Wang CM, Wang CY, Reddy JN. Exact solutions for buckling of structural members. CRC Press: Boca Raton, USA; 2004.
- **(Watt and Swallow 1996)** Watt D, Swallow P. Surveying historic buildings. Donhead Publishing: Shaftesbury, UK; 1996.
- **(Wei and Hutchinson 1997)** Wei Y, Hutchinson JW. Nonlinear delamination mechanics for thin films. Journal of the Mechanics and Physics of Solids 1997;45:1137-1159.
- **(Wei and Hutchinson 1999)** Wei Y, Hutchinson JW. Interface strength, work of adhesion and plasticity in the peel test. International Journal of Fracture 1999;93:315-333.
- **(Wheeler and Hutchinson 1998)** Wheeler AS, Hutchinson AR. Resin repairs to timber structures. International Journal of Adhesion & Adhesives 1998;18:1-13.
- **(Whitney and Nuismer 1974)** Whitney JM, Nuismer RJ. Stress fracture criteria for laminated composites containing stress concentrations. Journal of Composite Materials 1974;8:253-265.
- **(Winandy 1994)** Winandy JE. Wood properties. Encyclopedia of Agricultural Science vol 4. Academic Press: Orlando, USA; 1994.
- **(Windorski et al. 1997)** Windorski DF, Soltis LA, Ross RJ. Feasibility of fibreglass-reinforced bolted wood connections. Research paper FPL-RP-562. Madison, USA. Forest Products Laboratory, United States Department of Agriculture 1997.
- **(Wisnom 1991a)** Wisnom MR. The effect of specimen size on the bending strength of unidirectional carbon fibre-epoxy. Composite Structures 1991;18:47-63.
- **(Wisnom 1991b)** Wisnom MR. Relationship between strength variability and size effect in unidirectional carbon fibre-epoxy. Composites 1991;22:47-52.
- **(Wooley and Carver 1971)** Wooley GR, Carver DR. Stress concentration factors for bonded lap joint. Journal of Aircraft 1971;8:817-820.
- **(Wu et al. 1997)** Wu ZJ, Romeijn A, Wardenier J. Stress expressions of single-lap adhesive joints of dissimilar adherends. Composite Structures 1997;38:273-280.
- **(Xavier 2003)** Xavier JC. Caracterização ao corte da madeira usando o ensaio de Iosipescu. M.Sc. Thesis. Vila Real, Portugal: Department of Engineering, University of Trás-os-Montes and Alto Douro: 2003.
- **(Xiao et al. 2004a)** Xiao XS, Foss PH, Schroeder JA. Stiffness prediction of the double lap shear joint. Part 1: Analytical solution. International Journal of Adhesion & Adhesives 2004;24:229-237.
- **(Xiao et al. 2004b)** Xiao XS, Foss PH, Schroeder JA. Stiffness prediction of the double lap shear joint. Part 2: Finite element modeling. International Journal of Adhesion & Adhesives 2004;24:239-246.
- **(Xu and Needleman 1994)** Xu XP, Needleman A. Numerical simulations of fast crack growth in brittle solids. Journal of the Mechanics and Physics of Solids 1994;42:1397-1434.

- **(Yan et al. 2001a)** Yan C, Mai YW, Ye L. Effect of bond thickness on fracture behaviour in adhesive joints. The Journal of Adhesion 2001;75:27-44.
- **(Yan et al. 2001b)** Yan C, Mai YW, Yuan Q, Ye L, Sun J. Effects of substrate materials on fracture toughness measurement in adhesive joints. International Journal of Mechanical Sciences 2001;43:2091-2102.
- **(Yan et al. 2007)** Yan ZM, You M, Yi XS, Zheng XL, Li Z. A numerical study of parallel slot in adherend on the stress distribution in adhesively bonded aluminium single lap joint. International Journal of Adhesion & Adhesives 2007;27:687-695.
- **(Yang and Thouless 2001)** Yang QD, Thouless MD. Mixed-mode fracture analyses of plastically deforming adhesive joints. International Journal of Fracture 2001;110:175-187.
- **(Yang et al. 1999)** Yang QD, Thouless MD, Ward SM. Numerical simulations of adhesively-bonded beams failing with extensive plastic deformation. Journal of the Mechanics and Physics of Solids 1999;47:1337-1353.
- **(Yang et al. 2000)** Yang QD, Thouless MD, Ward SM. Analysis of the symmetrical 90º peel test with extensive plastic deformation. The Journal of Adhesion 2000;72:115-132.
- **(Yang et al. 2001)** Yang QD, Thouless MD, Ward SM. Elastic-plastic mode-II fracture of adhesive joints. International Journal of Solids and Structures 2001;38:3251-3262.
- **(Yang et al. 2004)** Yang C, Huang H, Tomblin JS, Sun W. Elastic-plastic model of adhesive-bonded single-lap composite joints. Journal of Composite Materials 2004;38:293-309.
- **(Yang et al. 2008)** Yang QD, Thouless MD, Ward SM. Numerical simulations of adhesively-bonded beams failing with extensive plastic deformation. Journal of the Mechanics and Physics of Solids 2008;47:1337-1353.
- **(Ye 1988)** Ye L. Role of matrix resin in delamination onset and growth in composite laminates. Composites Science and Technology 1988;33:257-277.
- **(Yeh and Tandjung 2005)** Yeh HY, Tandjung D. Mixed mode fracture analysis of the lap shear specimen test per ASTM D1002. Journal of Reinforced Plastics and Composites 2005;24:839-853.
- **(Yeomans 2004)** Yeomans D. The repair of historic timber structures. ASCE press: New-York, USA; 2004.
- **(Yoshihara 2007)** Yoshihara H. Simple estimation of critical stress intensity factors of wood by tests with double cantilever beam and three-point end-notched flexure. Holzforschung 2007;61:182-189.
- **(You et al. 2003)** You M, Zheng Y, Zheng XL, Liu WJ. Effect of metal as part of fillet on the tensile shear strength of adhesively bonded single lap joints. International Journal of Adhesion & Adhesives 2003;23:365-369.
- **(You et al. 2008)** You M, Yan ZM, Zheng XL, Yu HZ, Li Z. A numerical and experimental study of adhesively bonded aluminium single lap joints with an inner chamfer on the adherends. International Journal of Adhesion & Adhesives 2008;28:71-76.
- **(Yuan and Xu 2008)** Yuan H, Xu Y. Computational fracture mechanics assessment of adhesive joints. Computational Materials Science 2008;43:146-156.
- **(Yurgartis 1987)** Yurgartis SW. Measurement of small angle fiber misalignments in continuous fiber composites, Composites Science and Technology 1987;30:279-293.
- **(Zandbergs and Smith 1988)** Zandbergs JG, Smith FW. Finite element fracture prediction for wood with knots and cross grain. Wood and Fiber Science 1988;20:97-106.

- **(Zemlyanova 2007)** Zemlyanova A. Singular integral equations for a patch repair problem. International Journal of Solids and Structures 2007;44:6860-6877.
- **(Zhang and Keller 2008)** Zhang Y, Keller T. Progressive failure process of adhesively bonded joints composed of pultruded GFRP. Composites Science and Technology 2008;68:461-470.
- **(Zhao 1991)** Zhao X. Stress and failure analysis of adhesively bonded lap joints. Ph.D. Thesis. Bristol, UK: Department of Mechanical Engineering, University of Bristol: 1991.
- **(Zimmerman and Liu 1995)** Zimmerman K, Liu D. Geometrical parameters in composite repair. Journal of Composite Materials 1995;29:1473-1487.
- **(Zimmerman and Liu 1996)** Zimmerman KB, Liu D. An experimental investigation of composite repair. Experimental Mechanics 1996;36:142-147.
- **(Zou et al. 2004)** Zou GP, Shalin K, Taheri F. An analytical solution for the analysis of symmetric composite adhesively bonded joints. Composite Structures 2004;65:499-510.
- **(Zweben 1994)** Zweben C. Is there a size effect in composite? Composites 1994;25:451-454.